FROM BIOMASS TO ADVANCED BIO-BASED CHEMICALS & MATERIALS: A MULTIDISCIPLINARY PERSPECTIVE

EDITED BY: Gabriel Paës, Caroline Rémond, Xavier Coqueret, Florent Allais, Thomas James Farmer and Warwick Douglas Raverty

PUBLISHED IN: Frontiers in Chemistry

frontiers Research Topics

Frontiers eBook Copyright Statement

The copyright in the text of individual articles in this eBook is the property of their respective authors or their respective institutions or funders. The copyright in graphics and images within each article may be subject to copyright of other parties. In both cases this is subject to a license granted to Frontiers.

The compilation of articles constituting this eBook is the property of Frontiers.

Each article within this eBook, and the eBook itself, are published under the most recent version of the Creative Commons CC-BY licence. The version current at the date of publication of this eBook is CC-BY 4.0. If the CC-BY licence is updated, the licence granted by Frontiers is automatically updated to the new version.

When exercising any right under the CC-BY licence, Frontiers must be attributed as the original publisher of the article or eBook, as applicable.

Authors have the responsibility of ensuring that any graphics or other materials which are the property of others may be included in the CC-BY licence, but this should be checked before relying on the CC-BY licence to reproduce those materials. Any copyright notices relating to those materials must be complied with.

Copyright and source acknowledgement notices may not be removed and must be displayed in any copy, derivative work or partial copy which includes the elements in question.

All copyright, and all rights therein, are protected by national and international copyright laws. The above represents a summary only. For further information please read Frontiers' Conditions for Website Use and Copyright Statement, and the applicable CC-BY licence.

ISSN 1664-8714
ISBN 978-2-88963-619-8
DOI 10.3389/978-2-88963-619-8

About Frontiers

Frontiers is more than just an open-access publisher of scholarly articles: it is a pioneering approach to the world of academia, radically improving the way scholarly research is managed. The grand vision of Frontiers is a world where all people have an equal opportunity to seek, share and generate knowledge. Frontiers provides immediate and permanent online open access to all its publications, but this alone is not enough to realize our grand goals.

Frontiers Journal Series

The Frontiers Journal Series is a multi-tier and interdisciplinary set of open-access, online journals, promising a paradigm shift from the current review, selection and dissemination processes in academic publishing. All Frontiers journals are driven by researchers for researchers; therefore, they constitute a service to the scholarly community. At the same time, the Frontiers Journal Series operates on a revolutionary invention, the tiered publishing system, initially addressing specific communities of scholars, and gradually climbing up to broader public understanding, thus serving the interests of the lay society, too.

Dedication to Quality

Each Frontiers article is a landmark of the highest quality, thanks to genuinely collaborative interactions between authors and review editors, who include some of the world's best academicians. Research must be certified by peers before entering a stream of knowledge that may eventually reach the public - and shape society; therefore, Frontiers only applies the most rigorous and unbiased reviews.
Frontiers revolutionizes research publishing by freely delivering the most outstanding research, evaluated with no bias from both the academic and social point of view. By applying the most advanced information technologies, Frontiers is catapulting scholarly publishing into a new generation.

What are Frontiers Research Topics?

Frontiers Research Topics are very popular trademarks of the Frontiers Journals Series: they are collections of at least ten articles, all centered on a particular subject. With their unique mix of varied contributions from Original Research to Review Articles, Frontiers Research Topics unify the most influential researchers, the latest key findings and historical advances in a hot research area! Find out more on how to host your own Frontiers Research Topic or contribute to one as an author by contacting the Frontiers Editorial Office: researchtopics@frontiersin.org

FROM BIOMASS TO ADVANCED BIO-BASED CHEMICALS & MATERIALS: A MULTIDISCIPLINARY PERSPECTIVE

Topic Editors:
Gabriel Paës, URD Agro-Biotechnologies Industrielles (ABI), CEBB, AgroParisTech, France
Caroline Rémond, FARE Laboratory, INRAE, Université de Reims Champagne-Ardenne, France
Xavier Coqueret, Institut de Chimie Moléculaire de Reims, CNRS UMR 7312, Université de Reims Champagne-Ardenne, France
Florent Allais, AgroParisTech Institut des Sciences et Industries du Vivant et de L'environnement, France
Thomas James Farmer, University of York, United Kingdom
Warwick Douglas Raverty, Monash University, Australia

Citation: Paës, G., Rémond, C., Coqueret, X., Allais, F., Farmer, T. J., Raverty, W. D., eds. (2020). From Biomass to Advanced Bio-Based Chemicals & Materials: A Multidisciplinary Perspective. Lausanne: Frontiers Media SA.
doi: 10.3389/978-2-88963-619-8

Table of Contents

frontiers in Chemistry

EDITORIAL
published: 25 February 2020
doi: 10.3389/fchem.2020.00131

Editorial: From Biomass to Advanced Bio-Based Chemicals & Materials: A Multidisciplinary Perspective

Florent Allais [1], Xavier Coqueret [2]*, Thomas Farmer [3]*, Warwick Raverty [4]*, Caroline Rémond [5]* and Gabriel Paës [5]**

[1] URD Agro-Biotechnologies Industrielles (ABI), CEBB, AgroParisTech, Pomacle, France, [2] Institut de Chimie Moléculaire de Reims, CNRS UMR 7312, Université de Reims Champagne-Ardenne, Reims, France, [3] Department of Chemistry, University of York, York, United Kingdom, [4] Department of Chemical Engineering, Monash University, Melbourne, VIC, Australia, [5] FARE Laboratory, INRAE, Université de Reims Champagne-Ardenne, Reims, France

Keywords: biomass, lignocellulose, cellulose, hemicellulose, lignin, biochemicals, biomaterials, catalysis

OPEN ACCESS

Edited and reviewed by:
Steve Suib,
University of Connecticut,
United States

****Correspondence:***
Florent Allais
florent.allais@agroparistech.fr
Xavier Coqueret
xavier.coqueret@univ-reims.fr
Thomas Farmer
thomas.farmer@york.ac.uk
Warwick Raverty
warwick.raverty@gmail.com
Caroline Rémond
caroline.remond@univ-reims.fr
Gabriel Paës
gabriel.paes@inrae.fr

Specialty section:
This article was submitted to
Chemical and Process Engineering,
a section of the journal
Frontiers in Chemistry

Received: *04 February 2020*
Accepted: *13 February 2020*
Published: *25 February 2020*

Citation:
Allais F, Coqueret X, Farmer T, Raverty W, Rémond C and Paës G (2020) Editorial: From Biomass to Advanced Bio-Based Chemicals & Materials: A Multidisciplinary Perspective. Front. Chem. 8:131. doi: 10.3389/fchem.2020.00131

Editorial on the Research Topic

From Biomass to Advanced Bio-Based Chemicals & Materials: A Multidisciplinary Perspective

Lignocellulosic biomass, one of the major feedstocks of the emerging bioeconomy, will play a key role in the replacement of petroleum-based chemicals and materials and will help to fight against global warming by providing renewable, carbon-neutral sources of energy. Nevertheless, because of its chemical and structural complexity, the transformation of lignocellulose into commodity and higher-valued products requires a combination of physical, biological, and chemical processes and a better understanding of both its composition and architecture at different scales, in order to render this transformation efficient and economically competitive. Importantly, lignocellulose transformation can also bring to the market novel and sustainable chemicals that can lead to new applications and new industries that can replace the mining and burning of fossil carbon. In particular, exploitation of aromatic molecules in lignin and of cellulose and hemicelluloses can produce biobased solvents, surfactants, plasticizers, functional additives for nutrition and cosmetics and life-saving medicines. In addition to this broad range of chemicals, cellulosic fibers, and particles fractionated from lignocellulosic biomass are increasingly used to produce composite materials. Overall, this Research Topic aims to illustrate how complementary approaches are relevant in addressing questions regarding the deconstruction of different forms of lignocellulosic biomass and the various processes required to turn them into valuable bio-based, renewable products.

The Research Topic comprises a collection of 16 original contributions: 14 research papers, one review and one mini-review dedicated to the modification, characterization and preparation of bio-based chemicals and materials using advanced chemical, physical and biochemical routes.

The review by Glasser is dedicated to lignin applications in materials, presenting how this group of aromatic bio-polymers can readily be tailored to get specific properties through chemical modification, and how compatibilization strategies such as lignin chemical functionalization can overcome the usual limitations encountered with unmodified-lignins for making advanced materials. The mini review by Zoghlami and Paës presents an up-to-date survey of the relative impact of chemical and structural factors on lignocellulosic biomass recalcitrance and of the most advanced techniques to evaluate these factors, together with recent spectral and water-related measurements to predict ease of hydrolysis.

Besides these two review articles, several articles detail how pre-treatments are necessary to facilitate subsequent reactions in biomass processing. Sipponen and Österberg assess aqueous ammonia for the separation of lignin from hydrothermally pre-treated wheat straw prior to enzymatic saccharification. The resulting lignin particles have potential in water remediation applications. A contribution by Lahtinen et al. focuses on extraction by pressurized hot water treatment, characterization, and concentration of phenolic residues from wood and their role in physical and oxidative stabilization of emulsions. Araya-Farias et al. have implemented a statistical approach to optimize several parameters during the pre-treatment of biomass with ionic liquids, leading to a useful mathematical model that predicts sugar release after enzymatic hydrolysis.

Chemical routes provide new perspectives for upgrading biomass to bio-based products. Flourat et al. have designed a new chemo-enzymatic route to synthesize advanced lignin models. Starting with lignocellulose-derived ferulic acid the first syntheses of two trimers of monolignol G possessing side-chains and both robust β-5 bonds and labile β-*O*-4 bonds have been achieved. Moore et al. report another chemo-enzymatic pathway, demonstrating that iodine supported on acidic alumina is a very effective catalyst for aza-Michael additions on bio-based itaconate polyesters. This reaction might reduce lengthy reaction sequences and produce new bio-based polyesters. The action of pyranose dehydrogenases on various xylo-oligosaccharides was assayed by Karppi et al. and demonstrated the potential to synthesize bifunctional molecules directly from hemicellulose fragments. This discovery could be the starting point for further derivatization and/or polymerization into bio-based chemicals and materials. Kammoun et al. investigated the possibility of using seawater to convert C5- and C6-sugars by hydrothermal conversion to furanic and acidic products, especially to lactic acid, offering interesting new chemical transformations in combination with dehydration catalysts or in biphasic systems.

Finally, the last group of articles illustrate some useful conversions of biomass into bio-based materials. In the case of lignin, Szabó et al. performed immobilization of lignin on carbon fiber and highlighted the importance of considering both the physicochemical properties of the matrix and of the polymer in order to design bio-composites with well-defined properties. Reactive extrusion was used by Milotskyi et al. to esterify kraft lignin with succinic and maleic anhydrides. Extensive characterization of the resulting materials demonstrated their potential for further polymerization or copolymerization and for combination with other polymers to produce new plastics with a significant bio-based content. Successful esterification of several industrial lignins with maleic acid in an acidic ionic liquid was achieved by Husson et al. resulting in increased solubility in polar and protic solvents without affecting thermal stability and opening the way to new polyolefin-lignin blends. Using vanillin as substrate, Savonnet et al. have synthesized bio-based aromatic diamines which were tested as curing agents for the design of bio-based epoxy thermosets. Further optimization of the synthetic pathways described are still necessary but thermomechanical properties in terms of glass transition temperature and char residue are considered promising.

Other bio-based polymers have demonstrated potential to create completely novel materials. For instance, a double-reagent simultaneous functionalization was used by Wang et al. in order to prepare porous polysilsesquioxanes having bifunctional groups. These novel materials were found to be nanoparticulate with morphology that could be controlled with the proportion of the reactants. Their meso- or macro-porous features are considered to have potential applications in environmental remediation. Moyer et al. showed that nanocellulose can serve as an effective templating agent by introducing controlled porosity and morphology to enhance surface area and introduce higher order architecture within catalyst particles, resulting in improved catalytic activities. Le Guen et al. have prepared and characterized biomass powders compounded in polylactic acid by twin screw extrusion to produce filaments for fused-deposition modeling 3D printing. The mechanical properties of the printed samples were found to be more affected by the printing direction than by the presence or type of biomass powder used.

The Editors hope that this collection, showing a great diversity of transformation pathways, characterization techniques and practical applications, will be of significant interest to Frontiers readers and will inspire significant progress in the field of biomass valorisation.

AUTHOR CONTRIBUTIONS

All authors listed have made a substantial, direct and intellectual contribution to the work, and approved it for publication.

Conflict of Interest: The authors declare that the research was conducted in the absence of any commercial or financial relationships that could be construed as a potential conflict of interest.

Copyright © 2020 Allais, Coqueret, Farmer, Raverty, Rémond and Paës. This is an open-access article distributed under the terms of the Creative Commons Attribution License (CC BY). The use, distribution or reproduction in other forums is permitted, provided the original author(s) and the copyright owner(s) are credited and that the original publication in this journal is cited, in accordance with accepted academic practice. No use, distribution or reproduction is permitted which does not comply with these terms.

frontiers in Chemistry

ORIGINAL RESEARCH
published: 22 March 2019
doi: 10.3389/fchem.2019.00132

Hydrothermal Dehydration of Monosaccharides Promoted by Seawater: Fundamentals on the Catalytic Role of Inorganic Salts

Maroua Kammoun[1]*, *Thibaut Istasse*[1], *Haitham Ayeb*[2], *Neila Rassaa*[3], *Taoufik Bettaieb*[4] *and Aurore Richel*[1]

[1] *Laboratory of Biomass and Green Technologies, University of Liege Gembloux Agro Bio-Tech, Gembloux, Belgium,* [2] *Louvain Institute of Biomolecular Science and Technology, University of Louvain, Louvain-la-Neuve, Belgium,* [3] *Laboratory of Agricultural Production Systems Sustainability in Northern Region of Tunisia, University of Jendouba, Le kef, Tunisia,* [4] *Laboratory of Horticultural Sciences, University of Carthage National Agronomic Institute of Tunis, Tunis, Tunisia*

In biorefining, the conversion of carbohydrates under subcritical water conditions is a field of extensive studies. In particular, the hydrothermal decomposition of benchmark C6- and C5-monosaccharides, i.e., D-glucose and D-xylose, into furanics and/or organic acids is fully considered. Herein, we propose to establish the fundamentals of the decomposition of D-glucose and D-xylose under subcritical water conditions in the presence of specific salts (i.e., NaCl and KI) and in seawater. Our results demonstrated that the introduction of inorganic salts was found to modify sugars dehydration yields. Different NaCl concentrations from 0.21 to 1.63 mol L^{-1} promoted the conversion of D-xylose to 2-furfural (2-F) from 28 to 44% (molar yield). NaCl also improved 5-hydroxymethylfurfural (5-HMF) generation from D-glucose as well as rehydration of 5-HMF to levulinic and formic acid. KI favored other pathways toward formic acid production from D-glucose, reaching 20% in the upper concentration. Compared to a solution of equivalent NaCl concentration, seawater enhanced selectivity toward lactic acid which was raised by 10% for both monosaccharides, and sugars conversion, especially for D-glucose whose conversion was increased by 20%. 5-HMF molar yield around 30% were achieved from D-glucose in seawater at 211°C and 20 bars after 15 min.

Keywords: D-glucose, D-xylose, dehydration, seawater, inorganic salts, hydrothermal, lactic acid, levulinic acid

OPEN ACCESS

Edited by:
Florent Allais,
AgroParisTech Institut des Sciences et Industries du Vivant et de L'environnement, France

Reviewed by:
Arnaud Haudrechy,
Université de Reims Champagne-Ardenne, France
Claudia Antonetti,
University of Pisa, Italy

***Correspondence:**
Maroua Kammoun
mkammoun@doct.uliege.be

Specialty section:
This article was submitted to Green and Sustainable Chemistry, a section of the journal Frontiers in Chemistry

Received: *14 January 2019*
Accepted: *20 February 2019*
Published: *22 March 2019*

Citation:
Kammoun M, Istasse T, Ayeb H, Rassaa N, Bettaieb T and Richel A (2019) Hydrothermal Dehydration of Monosaccharides Promoted by Seawater: Fundamentals on the Catalytic Role of Inorganic Salts. Front. Chem. 7:132. doi: 10.3389/fchem.2019.00132

INTRODUCTION

Upgrading of biomass is a field of extensive efforts. In particular, its hydrothermal conversion into valuable products has been extensively proposed in the state of the art (Tekin et al., 2014).

In fact, Biomass represents a renewable resource contributes to the development of a new-bioeconomy and to sustainable chemical industry. Several literatures reported the production of biobased molecules, from various sources such as giant reed (Licursi et al., 2018b), corncobs (Peleteiro et al., 2018), eucalyptus globulus wood (Peleteiro et al., 2018; Rivas et al., 2018), hazelnut shells (Licursi et al., 2017), and fructose (Antonetti et al., 2017). In these studies, the conversion carried in hydrothermal media using acid hydrolysis mostly with hydrochloric, sulfuric acids and acid resin (Amberlyst-7) in a microwave and autoclave reactors. The synthetic route employs monosaccharides as starting substrate, which, under hydrothermal conditions, undergoes dehydration to form the biobased molecules.

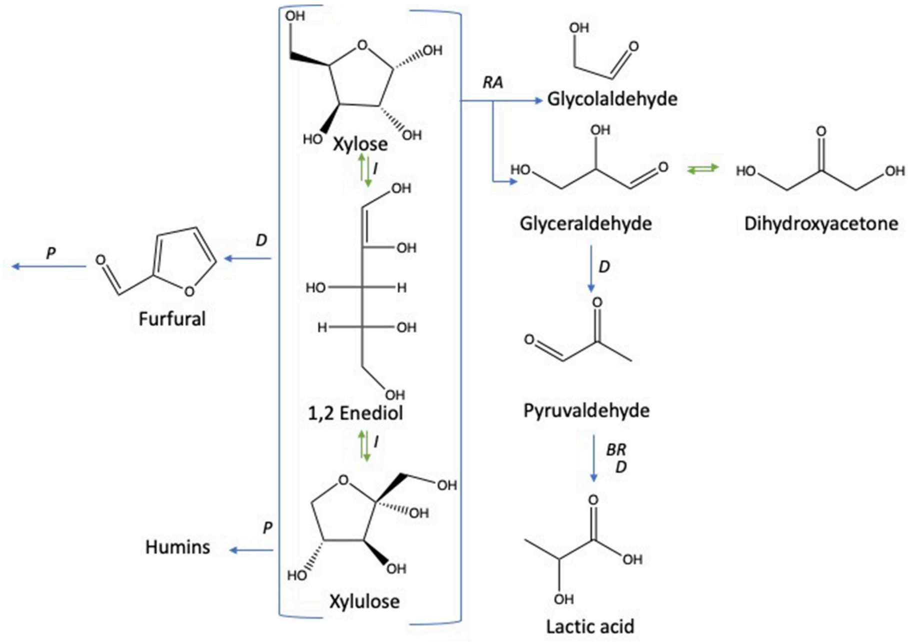

FIGURE 1 | D-xylose conversion pathways in subcritical water adapted from the works of Aida et al. (2010), You et al. (2014), and Delbecq et al. (2018). Reactions: D, dehydration; P, polymerization; BR, benzilic acid rearrangement; I, isomerization; RA, retro-aldol.

The understanding of the fundamentals of the conversion of "model" monosaccharides (including representative C5 sugars as D-xylose or C6 entities as D-glucose, D-fructose or D-mannose) under subcritical water conditions (namely between 100 and 374°C at a pressure high enough to maintain the liquid state) is still under investigations as the mechanisms governing the monosaccharides decomposition are complex and numerous (Srokol et al., 2004).

Under subcritical water conditions, it is nowadays well-established that monosaccharides undergo numerous reactions like isomerization, condensation into disaccharides, dehydration, and fragmentation. The dehydration of C6- and C5-monosaccharides typically leads to the respective formation of 5-hydroxymethylfurfural (5-HMF) and 2-furfural (2-F) together with variable amount of organic acids (resulting partially from the subsequent rehydration of furanic compounds) together with variable amounts of humins (Kabyemela et al., 1999). Fragmentation reactions result in the formation of erythrose, glycolaldehyde, and glyceraldehyde, which yields low molecular weight organics including acetic acid and lactic acid as final products. pH conditions strongly impact monosaccharides conversion pathways. Dehydration paths are favored in acidic conditions while the formation of glycolaldehyde and glyceraldehyde as well as isomerization are mainly base-catalyzed mechanisms. The major conversion pathways of D-xylose and D-glucose in subcritical water are depicted in **Figures 1**, **2**, respectively.

Among the products presented in **Figures 1**, **2**, furanic compounds and levulinic acid are the most promising to develop new bio-derivatives (i.e., solvents, fuels, and polymers) (Bozell and Petersen, 2010). Levulinic acid is easily produced through different processes such as biphasic [paraffin oil/water] (Licursi et al., 2018c), acid catalyst (Rivas et al., 2015, 2016) catalytic system [Ru/C + zeolite HY] (Licursi et al., 2018a). These studies investigated the important potential to convert biomass to value-added product, in particular the biobased platform molecules and their promising applications.

With the ambition to accelerate monosaccharides conversion under hydrothermal conditions and/or to improve the selectivity of this conversion, some studies have therefore reported the introduction of Brönsted acid catalysts (typically HCl or H_2SO_4) or bases (sodium hydroxide notably), and/or specific inorganics salts (Assary et al., 2012; Li et al., 2017). Indeed, it has been described that specific ions (i.e., metal cations as Al^{3+}, Cr^{3+}, Zn^{2+}, Cu^{2+}, Ag^{+}, etc.) enhance the conversion rate of C6-monosaccharides into 5-HMF (Wang et al., 2015). In particular, $MgCl_2$ was found to increase significantly the formation of levulinic acid when using HCl as the acid catalyst. Zn^{2+} or Co^{2+} salts were found to increase the formation of lactic acid. Due to the ability of Lewis acid to convert triose like glyceraldehyde and dihydroxyacetone to lactic acid (Rasrendra et al., 2010). The ionic strength of the reaction medium was also reported as a key point for modulating the selectivity and kinetics of the dehydration of D-glucose into 5-HMF. In this sense, (Tang et al., 2017) reported on the impact of the adjunction of sodium chloride to a biphasic THF/water system. The formation of hydrogen bond between the ion Cl^{-} and glucose in the position (C6)O-H leads to a ring-opening of glucose and to a mutarotation from α-D-Glucose to β-D-Glucose. Nevertheless, in the NaCl reaction media, the ratio of β-D-glucose/α-D-glucose at mutarotation equilibrium is

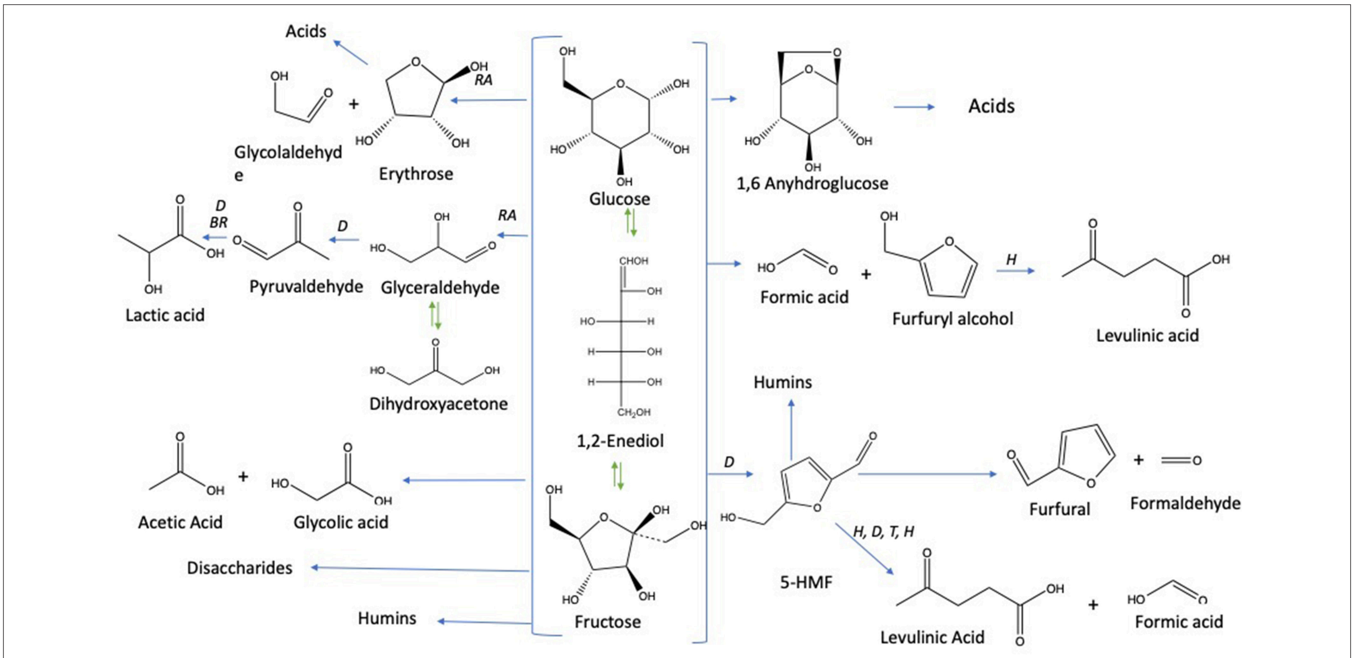

FIGURE 2 | D-glucose conversion pathways in subcritical water adapted from the works of Kabyemela et al. (1999); Watanabe et al. (2005); Rasrendra et al. (2010); Assary et al. (2012), and Aida et al. (2007). Reactions: D, dehydration; P, polymerization; BR, *benzilic acid* rearrangement; I, isomerization by Lobry de Bruyn–van Ekenstein transformation, RA: retro -aldol, H: hydration.

lower than that without NaCl. This affect glucose by decelerating its isomeration to fructose and suppressing its polymerization of humins. Actually, extensive R&D efforts are directed on the evaluation of biphasic or triphasic (organic) media as well as the selection of options as ionic liquids, deep eutectic solvents, etc. However, it appears that water plays a crucial role in the monosaccharide dehydration, catalyzing proton transfer and speeding up so the reaction (Zhou et al., 2017). Besides their influence on monosaccharides conversion pathways, inorganic salts also improve partition coefficients during the extraction of 5-HMF, 2-F and levulinic acid, which is of primary importance for purification steps (Sindermann et al., 2016).

As a cheap, abundant and salts rich medium, seawater could present interesting qualities for monosaccharides conversion. This natural source of salts ions (i.e., Na^+, Cl^-, K^+, Mg^{2+}) could be used as a processing medium at large scale especially for coastal cities while preserving drinkable water resources. Seawater is nowadays no longer limited to salts and seafood production. Due to its great potential, biorefinery concepts could benefit of it for aqueous-based processes as suggested in previous works. Lin et al. (2012) proved that seawater is a suitable medium for *Actinobacillus succinogenes* growth and also offers a complete nutrient medium for succinic acid production. Some papers investigate seawater as a solvent in furfural production processes using different catalysts, such as $FeCl_3$, NaCl, oxalic, and acetic acids, in which furfural production rate was enhanced (Vomstein et al., 2011; Grande et al., 2012; Mao et al., 2013; Hongsiri et al., 2014). Moreover, seawater would supply the appropriate source of sodium chloride for effective sugar dehydration. Chloride ions promote the formation of 1,2-enediol from the acyclic form of D-xylose, which is then dehydrated to furfural in the presence of acid catalysts (Marcotullio and De Jong, 2010).

KCl, $CaCl_2$ and $MgCl_2$ have also been used as main catalysts or co-catalysts for efficient sugar dehydration (Liu and Wyman, 2006; Zhou et al., 2014). However, the effect of potassium iodide on monosaccharides dehydration has not been studied yet in deionized water. Also, in biorefinery, hydrothermal treatment of some biomasses, such as halophyte plants in pilot reactor like steam explosion, allows the extraction of some components among which salts and monosaccharides. Some interactions are established between extracted sugars and salts during pretreatments and form other products like lactic acid, formic acid, levulinic acid, 2-furfural, 5-HMF. Depending on the envisaged application, their generation is favored or disadvantaged. In bioethanol production, these resulting products are avoided since they are considered as inhibitory compounds for microorganism during enzymatic hydrolysis. Contrariwise they are considered as platform products for chemical production.

In this study, pentose and hexose dehydration to furanic compounds and organic acids were investigated in the presence of inorganic salts in hydrothermal conditions at 211°C. The main salts found in biomass and seawater, i.e., NaCl and KI, were selected as benchmarks for this fundamental study. The objective is to assess the decomposition features of D-glucose and D-xylose in different mixtures of salts: (i) both aqueous solutions of sodium chloride and potassium iodide at increasing salts molarity from 0.21 to 1.63 mol L^{-1}; (ii) seawater from different geographical origins without additional inorganic catalysts.

EXPERIMENTAL SECTION

Materials

D-glucose (98%), D-xylose (98%), and D-fructose (99%) were supplied by Sigma Aldrich lactic acid (88%) from VWR, formic acid (99%) from Biosolv LTD, levulinic acid (98%), 5-hydroxymethylfurfural (5-HMF 98%) and 2-furfural from Alfa Aesar (98%), NaCl and KI were purchased from VWR and used as received.

Seawater samples were collected from three different locations presented in **Figure 3** between October and December 2017: Zeeland in the Netherlands (pH 8.04), Salakta in Tunisia collected (pH 7.93) and Kerkenah in Tunisia too (pH 8.19). Seawater samples characterization was carried out in a Laboratory called "Green lab" in Tunisia which is accredited by TUNAC according to ISO/IEC17025 standard. The composition of seawater samples is reported in **Table 1**.

Monosaccharides Conversion to Organic Acids and Furanic Compounds

The hydrothermal decomposition of monosaccharides (D-xylose and D-glucose) was performed in a Series 5,500 Parr reactor (600 mL) which is equipped with a temperature probe connected to a 4,848 Parr reactor controller and a mechanical stirring. The reactor was heated during 40 min to reach a target temperature of 211°C which was then maintained during 15 min. At the end of the treatment, the reactor was cooled down until 40°C (**Figure S1**). This process has been realized for monosaccharides (70 g/L) in deionized water, in solutions of NaCl or KI (from 35 to 70 g/L), in solutions containing a mixture of NaCl and KI and also in seawater. Each experiment was performed in triplicate. Before analysis, samples were filtered with 0.45 μm syringe filter and diluted with distilled water.

Analytic of Methods

Monosaccharides (D-xylose, D-glucose, and D-fructose) were determined using a high-performance liquid chromatography (HPLC) system Dionex 5,000 with acarbo Pac PA-100 (4 × 250 mm) anion exchange column and pulsed amperometric detection. Four different eluents were used: (A) 100 mM NaOH, (B) 100 mM NaOH + 600 mM NaCl, (C) 500 mM NaCl, and (D) ultra-deionized water. The decomposition products were analyzed using high performance liquid chromatography coupled with UV detection at 210 nm for organic acids and 284 nm for furanic compounds. 5 mM sulfuric acid was used as the elution solvent with a flow rate of 0.6 mL/min on a Aminex HPX-87H column (300 × 7.8 mm) at 45°C (Istasse et al., 2018).

The yield of all the compounds were defined by calculating the molar ratio between the generated product and the initial monosaccharides concentration (**Figure S2**).

Chemical Structure

Molecules were drawn using Chem Draw professional 15 (http://www.perkinelmer.com/fr/product/chemdraw-professional-chemdrawpro).

Data Treatment and Statistical Analyses

Results presented in Violin plot figures are the means of nine replicates. Scatter plot and Anova one-way analysis of variance as well as the Bartlett's test for equal variances were achieved using Graphpad Prism 7 (https://www.graphpad.com/scientific-software/prism/).Means were compared according to Tukey's multiple comparison test. The principal component analysis (PCA) was done using XLSTAT software (https://www.xlstat.com/fr/). Correlation matrix were realized using R Corrplot package. The geographic map was developed by integrating spatial data of sea zone map using ArcGIS (ArcInfo edition, ESRI, Redlands, CA: https://www.arcgis.com/index.html).

RESULTS AND DISCUSSIONS

Hydrothermal Conversion of Monosaccharides in Deionized Water

The dehydration of D-glucose and D-xylose in deionized water was selected as the benchmark and was achieved in a high-pressure reactor at 211°C corresponding to an internal reactor pressure of 20 bars. A preliminary kinetic investigation allowed to identify that 15 min was the optimal reaction time required to obtain the maximum yields in 2-furfural (2-F) and 5-hydroxymethylfurfural (5-HMF) in deionized water from respectively D-xylose and D-glucose (**Figure S3**). Classically, it appeared that D-glucose underwent a dehydration path with a successive formation of D-fructose through isomerization and subsequent dehydration into 5-HMF, whilst D-xylose was dehydrated in a single step into 2-F′. **Figures S4** and **S5** show the HPLC_UV chromatograms for products obtained from the reaction of D-glucose and D-xylose, respectively, in deionized water at 211°C. An average molar yield of 19.61% was recorded for 5-HMF from D-glucose compared to about 28.05% for 2-F from D-xylose. Rehydration of these molecules was expected to generate a mixture of both levulinic (LA) and formic acids (FA). At first sight, it appeared however that LA was not detected in the reaction media, whilst FA accounted for more than 11% when investigating D-glucose (FA was not detected in the case of D-xylose). This observation supports that other major pathways are responsible for formic acid generation in deionized water as mentioned in **Figure 2**. (Assary et al., 2012) proposed a mechanism initiated by the protonation of the glucose at the (C_2)-OH group which leads to the production of furfuryl alcohol and formic acid. A series of reactions take place including a dehydration followed by the hydration to the aldehyde group. Then, a deprotonation gives a gem-diol which undergoes a C-C scission to release the formic acid and a thermodynamically stable intermediate (5-hydroxymethyl)tetrahydrofuran-2,4-diol. This reaction pathway leads to the production of furfuryl alcohol (**Figure 4**). This latest compound can also undergo rehydration into levulinic acid. The absence of 5-HMF rehydration in the tested conditions suggests however that furfuryl alcohol could be stable enough, which could explain the formation of formic acid without levulinic acid. The pH of the solution shifted from 6 to 3 after the treatment of D-xylose and D-glucose. Lactic acid was also detected as a by-product with a substantial production reaching 13.36 and 7.16% for D-glucose and D-xylose, respectively.

The Effect of Inorganic Salts Concentration on D-xylose Conversion

Experiments were conducted to probe the role of NaCl and KI in D-xylose dehydration into 2-furfural and lactic acid. **Figures 5A–C** depict xylose conversion, the lactic acid yield and the 2-F yield under the reaction temperature at 211°C for 15 min. D-xylose conversion significantly increased with the overall molar salt concentration shifting from 67% when dehydration was performed in deionized water to more than 90% when introducing salts. Conversion was also boosted when NaCl and KI molarity increased. Addition of sodium chloride at concentrations of 35 and 70 g/L improved the formation of 2-F from D-xylose reaching a yield of about 43% for the upper NaCl concentration. This is in accordance with the results of (Marcotullio and De Jong, 2010), which show that Cl^- ions promote 1,2-enediol formation and thus dehydration to furfural. Levulinic acid and formic acid were not detected. Surprisingly, KI showed a different effect on 2-F production, a higher KI concentration seemed to significantly decrease 2-F yield. Lactic acid was also monitored with a production ranging from 2 to 6%. Lactic acid yield was significantly reduced by increasing molar concentration for both salts, namely NaCl and KI.

The Effect of Inorganic Salts Concentration on D-glucose Conversion

When the hydrothermal treatment of D-glucose was investigated in the presence of the same salts, we found that conversion was also significantly higher compared to deionized water. The results are demonstrated in **Figures 6A–F**. D-glucose reactivity was enhanced at high NaCl molarity. Similar D-glucose conversions were achieved in KI at 0.21 mol L^{-1} and NaCl at 0.60 mol L^{-1} (75.39 and 74.88%, respectively). Concerning D-fructose, no significant effect was detected in salts treatment, under different concentrations, and deionized water. Its yield was low and did not exceed 0.7%. 5-HMF yield significantly increased in upper concentration 70 g/L of both KI and NaCl compared to their lower 35 g/L. Levulinic acid (LA) was not detected in KI processes, while it was detected in NaCl treatments and its yield was significantly higher in the upper concentration 70 g/L (1.19 mol L^{-1}) than the lower 35 g/L (0.6 mol L^{-1}). Lactic acid quantification through HPLC afforded values ranging from 7 to 11% as in terms of the inorganic salt used for the hydrothermal treatment. Variance analysis (ANOVA) showed that its yield was significantly lower than that in deionized water, while formic acid (FA) showed the opposite trend: significantly higher in both NaCl and KI processes whose yields were noticeable culminating at more than 15% and reaching up to 20% for the upper KI concentration. According to **Figure 2**, the rehydration of 5-HMF produces a fair ratio of LA and FA. If the majority of LA is obtained from 5-HMF rehydration and considering that no LA was produced in distillated water, the addition of salts improves the dehydration of D-glucose. By summing produced moles of 5-HMF and LA, it was found that the overall generated 5-HMF increased with salts concentration until 0.81 M where a plateau is reached. The total production of 5-HMF for this salt concentration can be estimated at around 27%. Since LA is observed in the presence of NaCl in contrast to distillated water and KI solution, it is likely that NaCl promoted 5-HMF rehydration. When performing reactions in both NaCl or KI media, the pH tended to decrease due to the formation of organic acid side-products, i.e., LA and FA. The acidity of the reaction media after the process was quite stable whatever the monosaccharide or the nature of the inorganic salt. Indeed, the pH value was measured at a constant value of about pH 2.5.

Effect of Salts Combination on D-xylose Conversion

To better understand the different effects of the previous salts on monosaccharides degradation, a combination of KI and NaCl was done, first with the lower concentration 35 g/L and second with the upper concentration of 70 g/L of each salts.

According to **Figures 5A–C**, it can be seen that the conversion of D-xylose was significantly increased parallelly with the increased total molarity of salts. It was boosted by 10% and 12% in 0.81 mol L^{-1} (the lower combination solution) and at 1.63 mol L^{-1} (the upper combination solution) compared to KI solution at 0.21 and 0.42 mol L^{-1}, respectively. Besides, the higher the salt concentration, the lower the lactic acid detection. The variance analysis showed that lactic acid yield in combination solutions (0.81 and 1.63 mol) was significantly lower than that in KI solutions and which is not the case for NaCl, this can be explained maybe by the effect of sodium chloride on the appearance of some modifying functional groups to the intermediate molecule glycolaldehyde and pyruvaldehyde. Furfural yield was improved with increased salt concentration. Compared to KI solutions (0.2 and 0.42 mol L^{-1}), 2-F increased significantly in the mixture salt at 0.81 and 1.63 mol L^{-1}, which is not the case in NaCl solution and so this highlights that NaCl has a higher effect than KI salt on D-xylose dehydration to furfural production.

Effect of Salts Combination on D-glucose Conversion

Figures 6A–F show the effect of the amount of salts on D-glucose dehydration. Similarly to xylose conversion, the conversion of glucose increased parallelly by increasing the molarity of salts and reached 84%. Fructose yield remained low and no significant differences between treatments. As expected, lactic acid was significantly decreased by increasing salts molarity recording 3% for 1.63 mol L^{-1}. These results revealed that salts concentration had an antagonistic effect on lactic acid production for pentoses as well as hexoses. LA which was not detected in KI processes, was identified in the presence of salts mixture. Variance analysis showed that its yield was significantly increased in upper combination (1.19 mol L^{-1}) compared to the lower combination (0.81 mol L^{-1}). This result was in agreement with those previous results of NaCl processes. Formic acid yield was up to 20% in the upper combination (1.63 mol L^{-1}) which gave the same yield in KI process in upper concentration (0.42 mol L^{-1}). This yield was significantly higher than that in NaCl processes. This result stuck very well with previous results of KI.

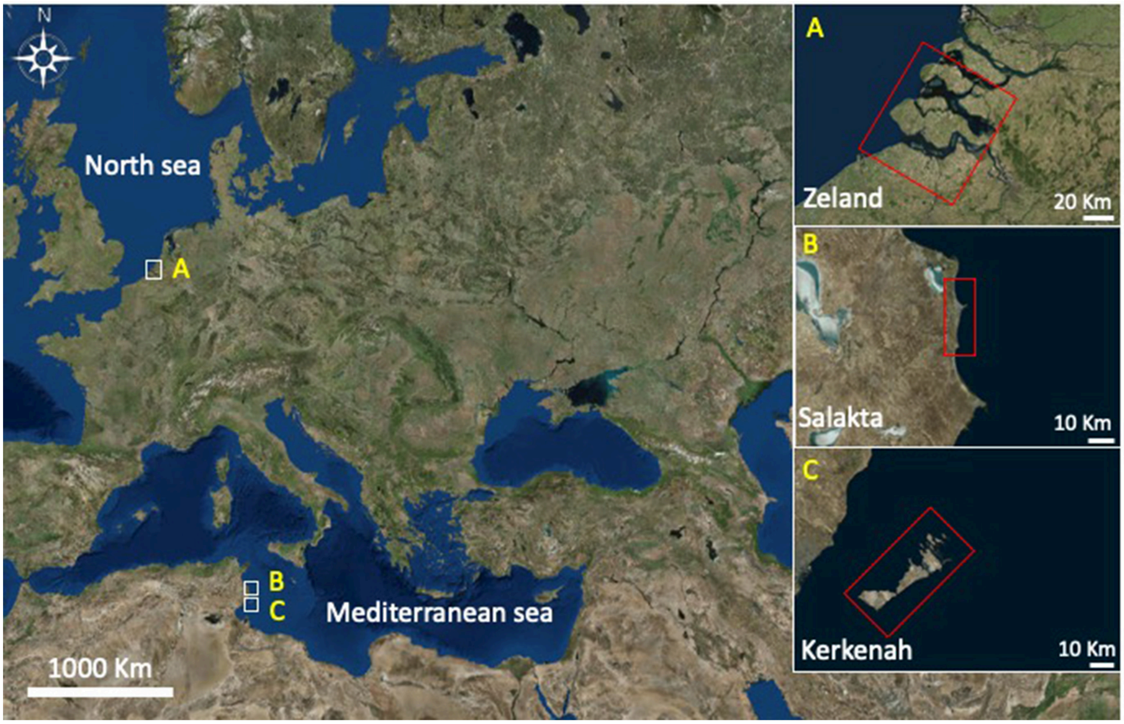

FIGURE 3 | Seawater samples locations. **(A)** Zeland, **(B)** Kerkenah, **(C)** Salakta.

TABLE 1 | Seawater samples composition by Green lab-TUNAC-Tunisia (All parameters are expressed in mg L^{-1}).

Seawater	Dry Residues	Chlorides	Sodium	Sulfates	Magnesium	Potassium	Calcium
Zeland	$38.4\ 10^3$	$18.3\ 10^3$	$11.3\ 10^3$	$2.66\ 10^3$	$1.48\ 10^3$	359	425
Kerkenah	$43.2\ 10^3$	$21.0\ 10^3$	$13.3\ 10^3$	$2.41\ 10^3$	$1.61\ 10^3$	398	419
Salakta	$36.4\ 10^3$	$18.2\ 10^3$	$11.1\ 10^3$	$2.26\ 10^3$	$1.39\ 10^3$	339	370

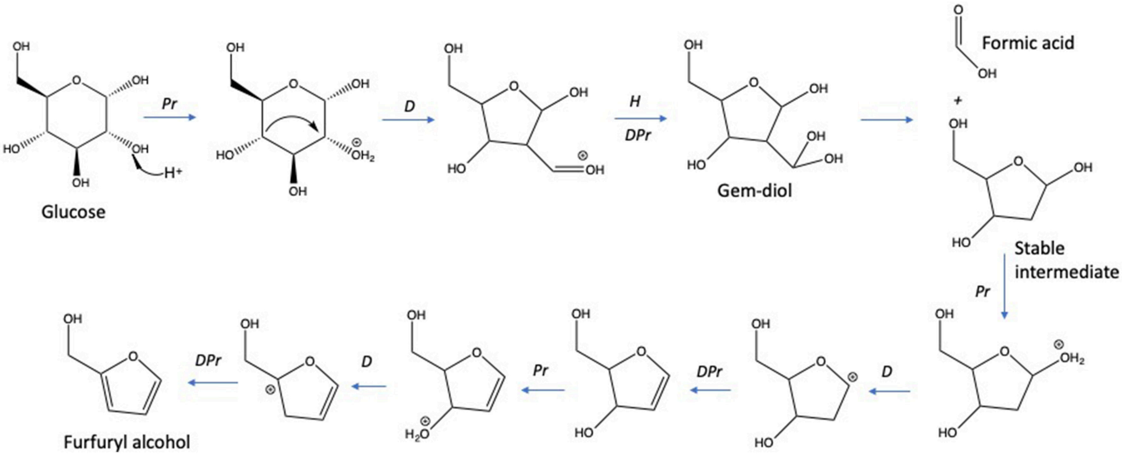

FIGURE 4 | Hydrothermal decomposition of D-glucose to formic acid and furfuryl alcohol (Assary et al., 2012). Reactions: Pr, protonation; H: hydration; D, dehydration; DPr, deprotonation.

Seawater's Effect on Xylose Conversion and Dehydration

Further experiments were performed under the same conditions at 211°C for 15 min in a natural source of salts, cheap and abundant, the seawater. **Table 1** highlights samples compositions in main salts. Molarities, been estimated on the basis of chloride concentration (mass concentration of chlorides / molar mass of chlorine). Zeland and Salakta seawater had almost the same molarity 0.51 and 0.52 mol L^{-1}, respectively, while Kerkenah was 0.59 mol L^{-1}. **Figure 7** recaps the effects of three seawaters samples on D-xylose dehydration compared to previous treatments. Interestingly, the yield of lactic acid was remarkably enhanced. **Figures S6A–C** show the effect of seawater samples on the D-xylose conversion, the 2-F and lactic acid yield. Conversion of D-xylose was higher than 96% for the three samples of seawater, which was significantly higher compared to distilled water. ANOVA showed that sugar conversion was also significantly higher not only compared to that in KI and NaCl solutions for concentrations < 0.5 mol L^{-1} (0.21 mol L^{-1}; 0.42 mol L^{-1}; 0.6 mol L^{-1}) but surprisingly comparable to the results obtained in combined solution (0.8 mol L^{-1}; 1.19 mol L^{-1}). This observation suggests that other factors than salt concentration are responsible for sugar conversion in seawater. The yield of 2-F reached around 31% for Kerkenah which was significantly higher compared to Zeland, Salakta, and deionized water. This yield is consistent regarding the previous results achieved at different NaCl concentrations. Seawater also favored lactic acid production with yields reaching 14 to 17% for Zeland and Kerkenah, respectively. Variance analysis showed that these yields were significantly higher to lactic acid yield produced in deionized water and different salt concentrations. De Bruijn et al. (1986) indicated that calcium ions enhance lactic acid production by increasing monosaccharides retro-aldolization.

Seawater's Effect on D-glucose Conversion and Dehydration

Figure 7 and **Figures S7A–C** represent the effect of seawaters samples on D-glucose conversion into furanic compounds and organic acids. Regarding D-glucose reactions in seawater, the conversion yield was significantly higher compared to deionized water and different salts concentrations. More than 94% of D-glucose was converted in seawater while only 81.98% of D-glucose was converted in the NaCl solution at 1.19 mol L^{-1}. The highest yield of levulinic and formic acid were detected in Kerkenah seawater compared to Zeland and Salakta seawater, but it remained significantly lower than the yield recorded for NaCl solutions. Compared to distillated water and salts solutions, 5-HMF formation was significantly improved in seawater media. Again, with the assumption that levulinic acid is generated from 5-HMF rehydration, overall 5-HMF yields higher than 30% are estimated. Lactic acid yield was also significantly enhanced compared to deionized water and salts solutions, because of calcium ions as previously explained for D-xylose. The highest yield was recorded in Kerkenah seawater relative to Zeland and Salakta seawater. Moreover, D-fructose molar yields of ∼4% were observed in seawater which was significantly

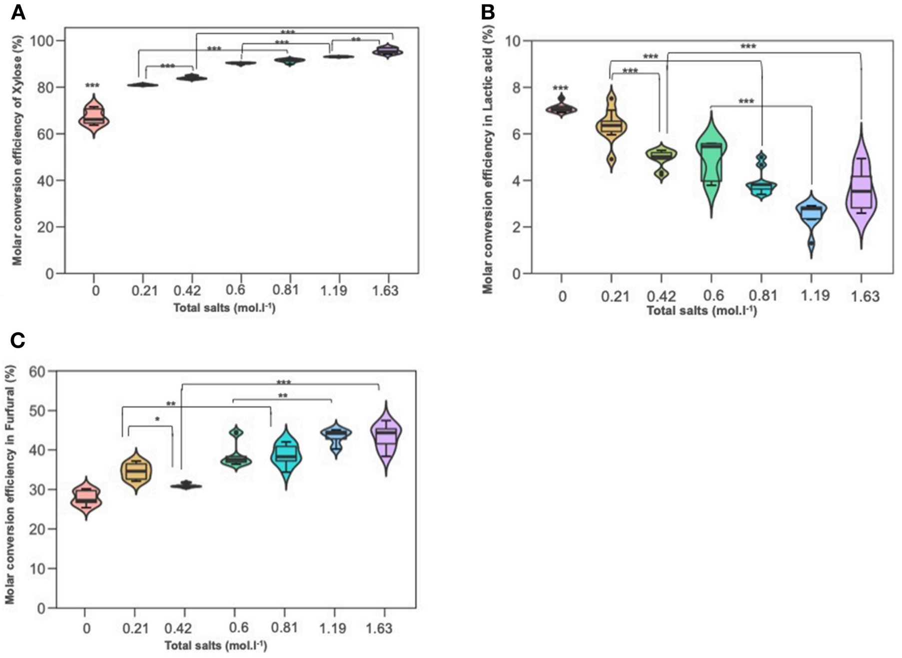

FIGURE 5 | The effect of adding NaCl and KI in hydrothermal dehydration of D-xylose: **(A)** molar conversion efficiency of D-xylose **(B)** molar conversion efficiency into lactic acid and **(C)** molar conversion effeciency into furfural **(C)**. Molarities 0; 0.21; 0.42; 0.6; 0.81; 1.19; 1.63 corresponding g/L to deionized water 35KI; 70KI; 35NaCl; 35 KI+ 35NaCl; 70NaCl; 70KI+70NaCl, respectively. Significant differences were determinated with on-way ANOVA and Tukey HSD *post hoc* test (*$P <$ 0.05; **$P <$ 0.01; ***$P <$ 0.001).

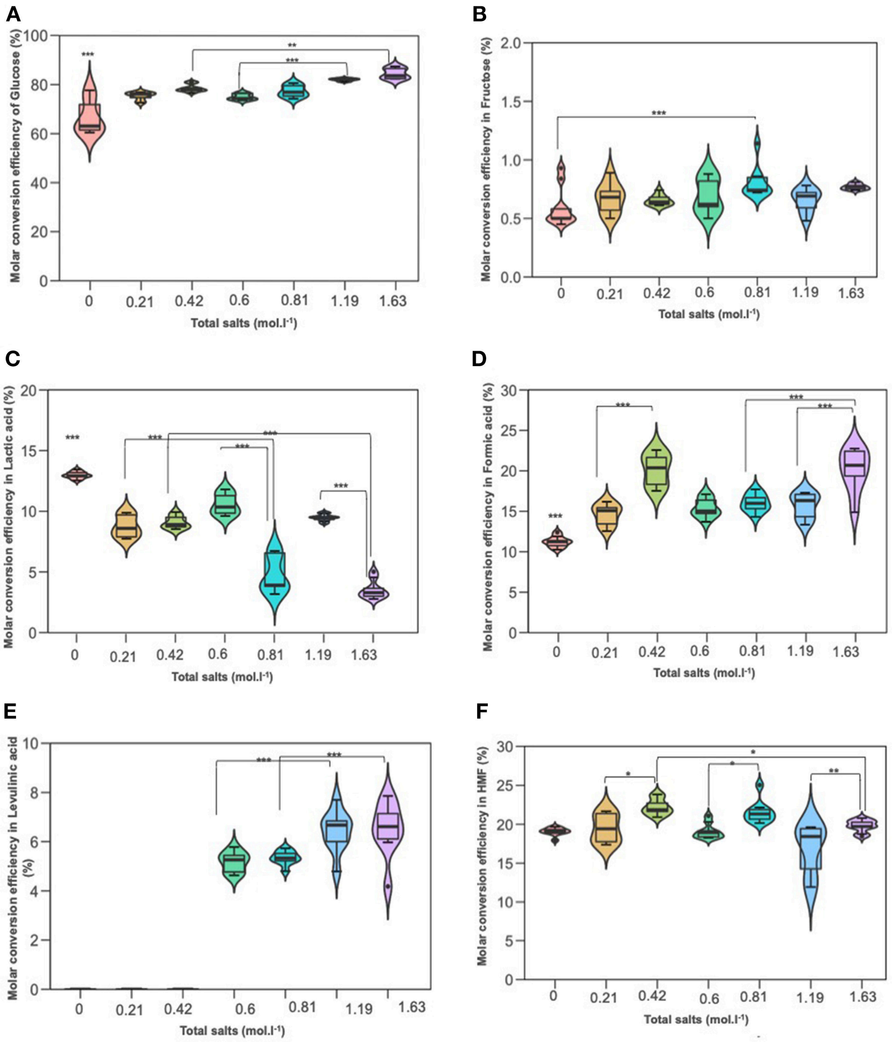

FIGURE 6 | The effect of adding NaCl and KI in hydrothermal dehydration of D-glucose: **(A)** molar conversion efficiency of D-glucose, **(B)** molar conversion efficiency to fructose, **(C)** molar conversion efficiency to lactic acid, **(D)** molar conversion efficiency to Formic acid, **(E)** molar conversion efficiency to levulinic acid, and **(F)** molar conversion efficiency to HMF. Molarities 0; 0.21; 0.42; 0.6; 0.81; 1,19; 163 corresponding g/L to deionized water; 35KI; 70KI; 35NaCl; 35 KI+ 35NaCl; 70NaCl; Q19 70KI+70NaCl, respectively. $^*P < 0.05$; $^{**}P < 0.01$; $^{***}P < 0.001$.

higher related to previous treatment. D-fructose could imply that the isomerization rate is higher in this medium compared to deionized water or tested saline solutions. Several factors could promote isomerization including the higher initial pH of seawater which could favor the Lobry de Bruyn–van Ekenstein transformation (Kobayashi et al., 2016). D-fructose being an intermediate in 5-HMF generation, the enhanced isomerization rate could explain the high amounts of 5-HMF observed in seawater. Since D-fructose is more readily converted into products than D-glucose, this improved isomerization could also explain the observed conversion.

Impact of Salts Concentrations and Seawater on Furanic Compounds and Organic Acids Production

Monosaccharides dehydration results showed significant differences in molar conversion efficiency into furanic compounds and organic acids. These differences are explained by the effect of salts type and concentration. So analyses under different salts composition for each monosaccharide were completed by a PCA.

Concerning D-xylose, PCA has been performed by considering three parameters and ten treatments. **Figures 8A–C** show the correlation circle, the observations and the correlation plot. The correlation circle explained 95.20% of the total variation. The first component F1 (axis 1) explained 54.22% of the variation, followed by 40.99% for the second component (axis 2). Observations explained 97.87% of total variation. PCA1 and PCA2 explained 56.684 and 41.186%, respectively. The correloplot is a correlation matrix which informs about correlation intensity. Conversion was positively correlated with furfural production (Pearson correlation coefficient $R = 0.32$) and with lactic acid appearance ($R = 0.33$), which could be explained by the pH shift during the treatment. Conversion of

D-xylose to organic acids progressively decreases pH, favoring the generation of products by acid catalyzed pathways like the production of furfural. Lactic acid was positively correlated with seawater media with a correlation coefficient of 0.4 for Zealand and Salakta seawater and of 0.7 for Kerkenah seawater. This perfectly matches previous analysis. Seawater is a catalytic media to produce lactic acid from monosaccharides. 2-furfural showed a positive correlation with NaCl compared to KI. It presents a better correlation with the highest concentration of NaCl.

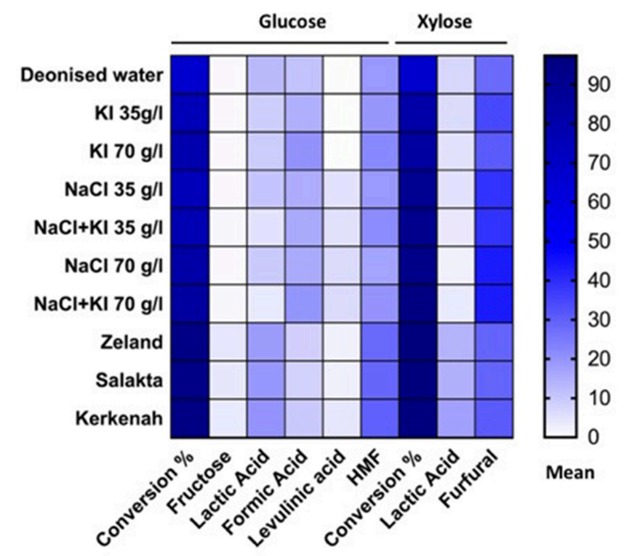

FIGURE 7 | The effect of inorganic salts and seawater on D-xylose and D-glucose conversion.

Concerning D-glucose, results are depicted in **Figures 9A–C**. Observations explained 89.848% of the total variation (PCA1 69.04%, PCA2 20.79%) followed by the correlation circle (F1 66.16% and F2 20.69%). PCA effected by considering six parameters and ten treatments. Conversion was highly positively correlated with HMF production and fructose formation with a Pearson correlation coefficient of 0.82 and 0.87, respectively. It was also moderately correlated with lactic acid ($R = 0.61$) and weakly correlated with levulinic acid (R = 0.24). On the other hand, negatively correlated with formic acid ($R = -0.48$). So, PCA analyses confirm clearly that HMF is positively correlated to fructose, which explains the increase of HMF production when fructose yield enhanced in seawater media. Fructose and HMF are highly negatively correlated to formic acid ($R = 0.86$ and $R = 0.795$, respectively) and weakly to levulinic acid production ($R = -0.068$ and $R = -0.148$, respectively). This negative correlation evinces HMF rehydration into formic acid and levulinic acid as shown in **Figure 3**, and thus HMF yield decreases when formic acid and levulinic acid were formed. Possibly levulinic acid reacts in the media and transformed into another molecule as its yield is lower than that of formic acid. Lactic acid is highly negatively correlated to formic acid ($R = -0.895$), and this may be explained by the different reactions types to form them from glucose based on **Figure 3**. Unlike lactic acid and furfural production from D-xylose, lactic acid generation and 5-HMF appearance from D-glucose are positively correlated. This observation does not seem consistent with their formation pathways requiring different pH conditions. D-glucose is however highly resilient to conversion in a slightly acidic medium. 5-HMF production is therefore facilitated by neutral or slightly alkaline conditions which favor D-glucose transformation to D-fructose by the Lobry Debruin VanEkenstein mechanism prior to the dehydration reaction.

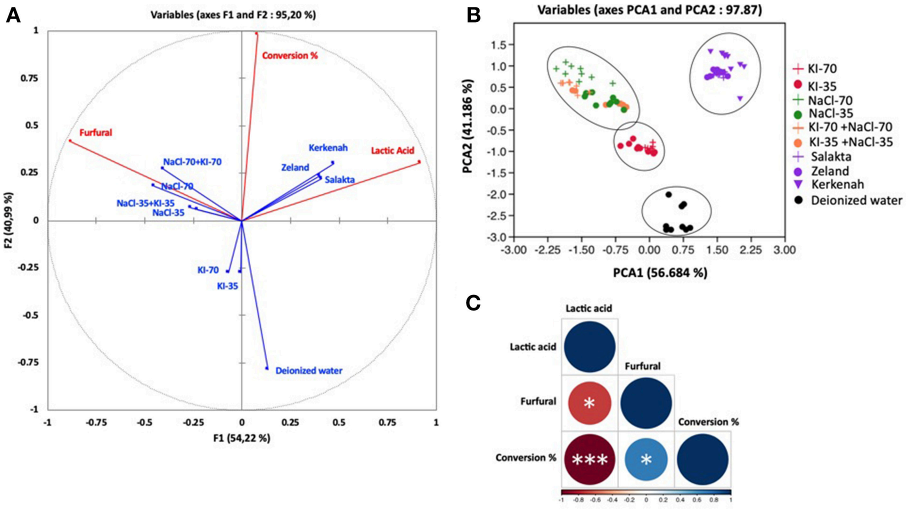

FIGURE 8 | Principal component analysis of molar conversion of D-xylose and its molar conversion efficiency into furfural and lactic acid under different salts concentration and seawater treatment. **(A)** Correlation circle: red lines represent parameters (active variables) and blue lines show the treatments (supplemental variables), **(B)** Observations, and **(C)** correlation plot. *$P < 0.05$; ***$P < 0.001$.

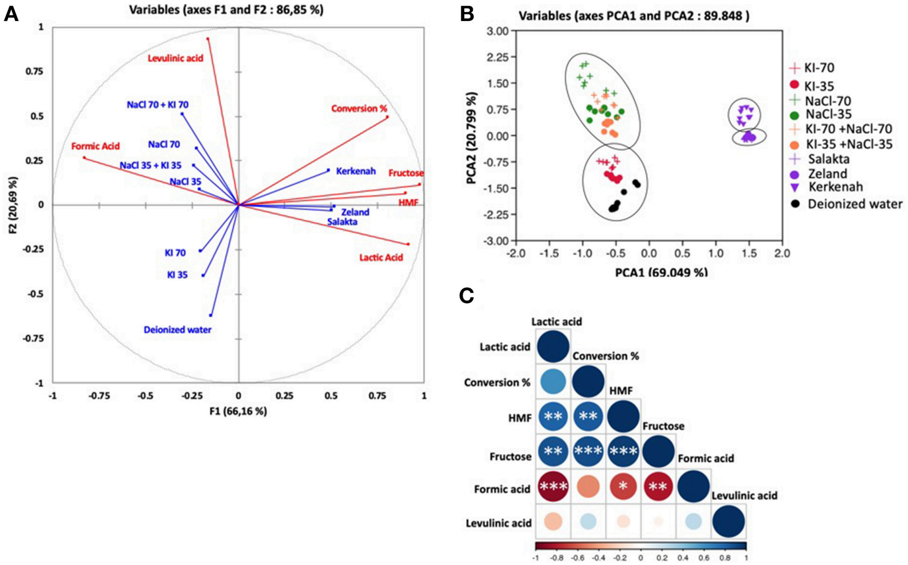

FIGURE 9 | Principal component analysis of molar conversion of D-glucose and its molar conversion efficiency into fructose, formic acid, lactic acid, levulinic acid, and HMF under different salts concentration and seawater treatment. **(A)** Correlation circle: red lines represent parameters and blue lines refer to the treatments, **(B)** Observations, and **(C)** correlation plot. *$P < 0.05$; **$P < 0.01$; ***$P < 0.001$.

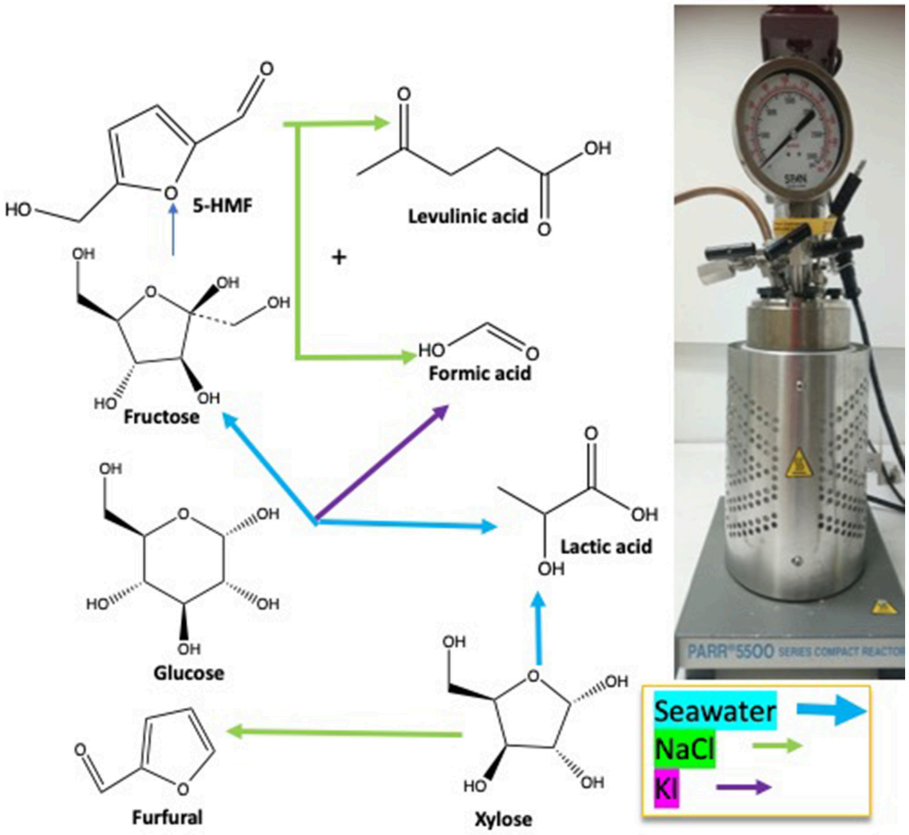

FIGURE 10 | Seawater is a cheap, abundant and safe medium able to improve conversion and dehydration reactions of monosaccharides compared to salts aqueous medium.

CONCLUSIONS

This study was focused on the different products generated during hydrothermal treatment of D-xylose and D-glucose at 211°C in deionized water, NaCl and KI solutions at various concentrations and seawater. Typical reaction products were mixtures of lactic acid, formic acid, levulinic acid, 5-HMF and 2-F. **Figure 10** shows the main products of each sugar under different treatments.

2-F yield from D-xylose is especially enhanced by the addition of NaCl and increases with salt concentration. The addition of NaCl to a D-glucose solution improves 5-HMF rehydration to levulinic and formic acid. KI favored other pathways toward formic acid production from D-glucose. 5-HMF production was improved in seawater as well as D-fructose concentration which indicates that this medium can promote isomerization. Seawater is consequently a cheap and suitable medium to perform C5- and C6-sugars conversion to furanic and acidic products especially to lactic acid production. The use of seawater in combination with dehydration catalysts or in biphasic systems could offer interesting performances while sparing drinkable water resources and should be investigated for developed costal countries.

AUTHOR CONTRIBUTIONS

All experiments, data analysis, discussion, and the manuscript preparation were done by MK. AR carried out the development and discussion of this work. TI assisted with discussion. HA conducted statistical analyses and figures preparations. NR and TB realized the manuscript recension. All authors have approved the submitted manuscript.

FUNDING

This work was funded by the Minister of Higher Education and Scientific Research of Tunisia and the European Regional Development.

ACKNOWLEDGMENTS

MK and TI thank the University of Carthage, the Minister of Higher Education, Scientific Research of Tunisia, and the European Regional Development Funds in the frame of the Low Carbon Footprint Materials portfolio (project BIOMAT_3) for their financial support. MK thanks the Green Lab for Seawater analysis.

SUPPLEMENTARY MATERIAL

The Supplementary Material for this article can be found online at: https://www.frontiersin.org/articles/10.3389/fchem.2019.00132/full#supplementary-material

REFERENCES

Aida, T. M., Sato, Y., Watanabe, M., Tajima, K., Nonaka, T., Hattori, H., et al. (2007). Dehydration of d -glucose in high temperature water at pressures up to 80 MPa. *J. Supercrit. Fluids* 40, 381–388. doi: 10.1016/j.supflu.2006.07.027

Aida, T. M., Shiraishi, N., Kubo, M., Watanabe, M., and Smith, R. L. (2010). Reaction kinetics of D-xylose in sub- and supercritical water. *J. Supercrit. Fluids* 55, 208–216. doi: 10.1016/j.supflu.2010.08.013

Antonetti, C., Raspolli Galleti, A. M., Fulignati, S., and Licursi, D. (2017). Amberlyst A-70: a surprisingly active catalyst for the MW-assisted dehydration of fructose and inulin to HMF in water. *Catal. Commun.* 97, 146–150. doi: 10.1016/j.catcom.2017.04.032

Assary, R. S., Kim, T., Low, J. J., and Curtiss, L. A. (2012). Glucose and fructose to platform chemicals : understanding the thermodynamic landscapes of acid-catalysed reactions using high-level ab initio methods. *RSC* 14, 16603–16611. doi: 10.1039/c2cp41842h

Bozell, J. J., and Petersen, G. R. (2010). Technology development for the production of biobased products from biorefinery carbohydrates - The US Department of Energy's "top 10" revisited. *Green Chem.* 12, 539–554. doi: 10.1039/b922014c

De Bruijn, J. M., Kieboom, A. P. G., and Van Bekkum, H. (1986). Alkaline degradation of monosaccharides III. Influence of reaction parameters upon the final product composition. *Recl. Des Trav. Chim. des Pays-Bas* 105, 176–183. doi: 10.1002/recl.19861050603

Delbecq, F., Wang, Y., Muralidhara, A., El Ouardi, K., Marlair, G., and Len, C. (2018). Hydrolysis of hemicellulose and derivatives-a review of recent advances in the production of furfural. *Front. Chem.* 6:146. doi: 10.3389/fchem.2018.00146

Grande, P. M., Bergs, C., and Domíngue De María, P. (2012). Chemo-enzymatic conversion of glucose into 5-hydroxymethylfurfural in seawater. *ChemSusChem* 5, 1203–1206. doi: 10.1002/cssc.201200065

Hongsiri, W., Danon, B., and De Jong, W. (2014). Kinetic study on the dilute acidic dehydration of pentoses toward furfural in seawater. *Ind. Eng. Chem. Res.* 53, 5455–5463. doi: 10.1021/ie404374y

Istasse, T., Bockstal, L., and Richel, A. (2018). Production of 5-Hydroxymethylfurfural from D-fructose in low-transition-temperature mixtures enhanced by chloride anions and low amounts of organic acids. *Chempluschem* 83, 1135–1143. doi: 10.1002/cplu.201800416

Kabyemela, B. M., Adschiri, T., Malaluan, R. M., and Arai, K. (1999). Glucose and fructose decomposition in subcritical and supercritical water : detailed reaction pathway, mechanisms, and kinetics. *Ind. Eng. Chem. Res.* 2888–2895. doi: 10.1021/ie9806390

Kobayashi, T., Khumijitjaru, P., and Adachi, S. (2016). Decomposition kinetics of glucose and fructose in subcritical water containing sodium chloride. *JAGlyco* 63, 99–104. doi: 10.5458/jag.jag.JAG-2016

Li, M., Li, W., Lu, Y., Jameel, H., Chang, H. M., and Ma, L. (2017). High conversion of glucose to 5-hydroxymethylfurfural using hydrochloric acid as a catalyst and sodium chloride as a promoter in a water/γ-valerolactone system. *RSC Adv.* 7, 14330–14336. doi: 10.1039/c7ra00701a

Licursi, D., Antonetti, C., Fulignati, S., Giannoni, M., and Raspolli Galleti, A. M. (2018a). Cascade Strategy for the Tunable Catalytic to 2-methyltetrahydrofuran and alcohols. *Catalysts* 8, 277–292. doi: 10.3390/catal8070277

Licursi, D., Antonetti, C., Fulignati, S., Vitolo, S., Puccini, M., Ribechini, E., et al. (2017). In-depth characterization of valuable char obtained from hydrothermal conversion of hazelnut shells to levulinic acid. *Bioresour. Technol.* 244, 880–888. doi: 10.1016/j.biortech.2017.08.012

Licursi, D., Antonetti, C., Mattonai, M., Pérez-Armada, L., Rivas, S., Ribechini, E., et al. (2018b). Multi-valorisation of giant reed (*Arundo Donax* L.) to give levulinic acid and valuable phenolic antioxidants. *Indus. Crops Produc.* 112, 6–17. doi: 10.1016/j.indcrop.2017.11.007

Licursi, D., Antonetti, C., Parton, R., and Raspolli Galletti, A. M. (2018c). A novel approach to biphasic strategy for intensification of the hydrothermal process to give levulinic acid: use of an organic non-solvent. *Bioresou. Technol.* 246, 180–189. doi: 10.1016/j.biortech.2018.05.075

Lin, C. S. K., Luque, R., Clark, J. H., Webb, C., and Du, C. (2012). Wheat-based biorefining strategy for fermentative production and chemical transformations of succinic acid. *Biofuels, Bioprod. Biorefin.* 6, 88–104. doi: 10.1002/bbb.328

Liu, C., and Wyman, C. E. (2006). The enhancement of xylose monomer and xylotriose degradation by inorganic salts in aqueous solutions at 180°C. *Carbohydr. Res.* 341, 2550–2556. doi: 10.1016/j.carres.2006.07.017

Mao, L., Zhang, L., Gao, N., and Li, A. (2013). Seawater-based furfural production via corncob hydrolysis catalyzed by FeCl3 in acetic acid steam. *Green Chem.* 15, 727–737. doi: 10.1039/C2GC36346A

Marcotullio, G., and De Jong, W. (2010). Chloride ions enhance furfural formation from D -xylose in dilute aqueous acidic solutions. *Green Chem.* 12, 1739–1746. doi: 10.1039/b927424c

Peleteiro, S., Raspolli Galletti, A. M., Antonetti, C., Santos, V., and Parajó, J. C. (2018). Manufacture of furfural from xylan-containing biomass by acidic processing of hemicellulose- derived saccharides in biphasic media using microwave heating. *J. Wood Chem. Technol.* 38, 198–213.doi: 10.1080/02773813.2017.1418891

Rasrendra, C. B., Makertihartha, I. G. B. N., Adisasmito, S., and Heeres, H. J. (2010). Green Chemicals from D-glucose : systematic studies on catalytic effects of inorganic salts on the chemo-selectivity and yield in aqueous solutions. *Topics Cata.* 1241–1247. doi: 10.1007/s11244-010-9570-0

Rivas, S., Raspolli Galletti, A. M., Antonetti, C., Licursi, D., Santos, V., et al. (2018). A biorefinery cascade conversion of hemicellulose-free eucalyptus globulus wood : production of concentrated levulinic acid solutions for -valerolactone sustainable preparation. *Catalysts* 8, 169–184. doi: 10.3390/catal8040169

Rivas, S., Raspolli-Galletti, A. M., Antonetti, C., Santos, V., and Paraj, ó, J. C. (2015). Sustainable production of levulinic acid from the cellulosic fraction of *pinus* pinaster wood : operation in aqueous media under microwave irradiation. *J. Wood Chem. Technol.* 35, 315–324. doi: 10.1080/02773813.2014.962152

Rivas, S., Raspolli-Galletti, A. M., Antonetti, C., Santos, V., and Paraj,ó, J. C. (2016). Sustainable conversion of *Pinus* pinaster wood into biofuel precursors : a biorefinery approach. *Fuel* 164, 51–58. doi: 10.1016/j.fuel.2015.09.085

Sindermann, E. C., Holbach, A., De Haan, A., and Kockmann, N. (2016). Single stage and countercurrent extraction of 5-hydroxymethylfurfural from aqueous phase systems. *Chem. Eng. J.* 283, 251–259. doi: 10.1016/j.cej.2015.07.029

Srokol, Z., Bouche, A.-G., van Estrik, A., Strik, R. C., Maschmeyer, T., and Peters, J. A. (2004). Hydrothermal upgrading of biomass to biofuel; studies on some monosaccharide model compounds. *Carbohydr. Res.* 339, 1717–1726. doi: 10.1016/J.CARRES.2004.04.018

Tang, J., Zhu, L., Fu, X., Dai, J., Guo, X., and Hu, C. (2017). Insights into the kinetics and reaction network of aluminum chloride-catalyzed conversion of glucose in NaCl-H2O/THF biphasic system. *ACS Catal.* 7, 256–266. doi: 10.1021/acscatal.6b02515

Tekin, K., Karagöz, S., and Bektaş, S. (2014). A review of hydrothermal biomass processing. *Renew. Sustain. Energy Rev.* 40, 673–687. doi: 10.1016/j.rser.2014.07.216

Vomstein, T., Grande, P. M., Leitner, W., and Domínguez de maría, P. (2011). Iron-catalyzed furfural production in biobased biphasic systems: From pure sugars to direct use of crude xylose effluents as feedstock. *ChemSusChem* 4, 1592–1594. doi: 10.1002/cssc.201100259

Wang, T., Glasper, J. A., and Shanks, B. H. (2015). Applied catalysis a : general kinetics of glucose dehydration catalyzed by homogeneous lewis acidic metal salts in water. *Appl. Catal. A, Gen.* 498, 214–221. doi: 10.1016/j.apcata.2015.03.037

Watanabe, M., Aizawa, Y., Iida, T., Levy, C., Aida, T. M., and Inomata, H. (2005). Glucose reactions within the heating period and the effect of heating rate on the reactions in hot compressed water. *Carbohydrate Res.* 340, 1931–1939. doi: 10.1016/j.carres.2005.05.019

You, S. J., Kim, Y. T., and Park, E. D. (2014). Liquid-phase dehydration of D-xylose over silica-alumina catalysts with different alumina contents. *React. Kinet. Mech. Catal.* 111, 521–534. doi: 10.1007/s11144-013-0655-1

Zhou, F., Sun, X., Wu, D., Zhang, Y., and Su, H. (2017). Role of water in catalyzing proton transfer in glucose dehydration to 5-hydroxymethylfurfural. *ChemCatChem* 9, 2784–2789. doi: 10.1002/cctc.201601522

Zhou, X., Zhang, Z., Liu, B., Zhou, Q., Wang, S., and Deng, K. (2014). Catalytic conversion of fructose into furans using FeCl3as catalyst. *J. Ind. Eng. Chem.* 20, 644–649. doi: 10.1016/j.jiec.2013.05.028

Conflict of Interest Statement: The authors declare that the research was conducted in the absence of any commercial or financial relationships that could be construed as a potential conflict of interest.

Copyright © 2019 Kammoun, Istasse, Ayeb, Rassaa, Bettaieb and Richel. This is an open-access article distributed under the terms of the Creative Commons Attribution License (CC BY). The use, distribution or reproduction in other forums is permitted, provided the original author(s) and the copyright owner(s) are credited and that the original publication in this journal is cited, in accordance with accepted academic practice. No use, distribution or reproduction is permitted which does not comply with these terms.

frontiers in Chemistry

ORIGINAL RESEARCH
published: 02 July 2019
doi: 10.3389/fchem.2019.00465

Amino- and Thiol- Polysilsesquioxane Simultaneously Coating on Poly(*p*-Phenylenetherephthal Amide) Fibers: Bifunctional Adsorbents for Hg(II)

Yunfeng Wang, Rongjun Qu*, Yinglei Mu, Changmei Sun*, Chunnuan Ji, Ying Zhang, Kai An, Xinhua Jia and Yu Zhang

School of Chemistry and Materials Science, Ludong University, Yantai, China

OPEN ACCESS

Edited by:
Florent Allais,
AgroParisTech Institut des Sciences et Industries du Vivant et de L'environnement, France

Reviewed by:
Tianyi Ma,
University of Newcastle, Australia
Kei Saito,
Monash University, Australia

****Correspondence:***
Rongjun Qu
rongjunqu@sohu.com
Changmei Sun
sunchangmei0535@126.com

Specialty section:
This article was submitted to Chemical and Process Engineering, a section of the journal Frontiers in Chemistry

Received: *11 March 2019*
Accepted: *11 June 2019*
Published: *02 July 2019*

Citation:
Wang Y, Qu R, Mu Y, Sun C, Ji C, Zhang Y, An K, Jia X and Zhang Y (2019) Amino- and Thiol- Polysilsesquioxane Simultaneously Coating on Poly(p-Phenylenetherephthal Amide) Fibers: Bifunctional Adsorbents for Hg(II). Front. Chem. 7:465. doi: 10.3389/fchem.2019.00465

A double reagents simultaneous functionalization (DRSF) was used to prepare porous polysilsesquioxane with NH_2 and SH bifunctional groups (PAMPSQ) coated poly(*p*-phenylenetherephthal amide) (PPTA) fibers adsorbents (PPTA-AM), via *in situ* condensations with aminopropyltriethoxysilane (APTES) and mercaptopropyltriethoxysilane (MPTES). The PAMPSQ coated on the PPTA surface was in the form of nanoparticles and its morphology varied with the proportion of the reactants. The PAMPSQ exhibited loose open meso- or macroporous features. The functional groups utilization of PAMPSQ was much higher than those of polysilsesquioxane on the mono-functional adsorbents with thiol or amino groups. The selective adsorption of PPTA-AM adsorbents for Hg(II) in binary component metal ion systems indicated their potential application in environmental remediation. The adsorption mechanism of Hg(II) onto PPTA-AM was proposed.

Keywords: polysilsesquioxane, poly(*p*-phenylenetherephthal amide), bifunctional adsorbent, adsorption, Hg(II)

INTRODUCTION

Water contamination caused by heavy metal ions has become a serious worldwide environmental problem that threatens the ecosystem, food safety, and human health. Thus far, many technologies such as adsorption, solvent extraction, ion exchange, reverse osmosis, membrane filtration, chemical precipitation, and electrolysis have been developed to remove heavy metal ions from contaminated water samples (Huang et al., 1996; Basso et al., 2002; Gomez-Salazar et al., 2003). Among them, adsorption is considered to be the optimum choice because it is facile and highly effective (Zub et al., 2005; Li et al., 2011).

One particular type of adsorbents is based on polysilsesquioxanes, which have desirable properties such as good hydrophilicity, chemical stability, and thermal stability (Hua et al., 2012; Sun et al., 2014). However, there are also unresolved issues regarding easy agglomerate and low utilization rate of the functional groups that eventually limit their applications (Liu et al., 2011). Attempts were made by our group to solve some of these issues. Two types of mono-functionalized fibrous adsorbents were prepared via the sol-gel condensation reactions (Wang et al., 2017). PPTA fibers were separately coated with amino-polysilsesquioxane and thiol-polysilsesquioxane. The resulting adsorbents, denoted as PPTA-A and PPTA-M, respectively, showed enhanced adsorption capacity for Hg(II) as compared to common silica adsorbents and amino- or thiol- functionalized polysilsesquioxane alone, due to the increase in specific surface area and functional group utilization rate. In principle, adsorption capacity of this type of functionalized adsorbents depends on the affinity of the functional group to the metal ion, as well as the morphology of the adsorbent material which affects the functional group utilization rate. PPTA-A is supposed to have similar or slightly better adsorption capacity compared to PPTA-M because of the superior hydrophilicity of the amino group vs. the thiol group. However, PPTA-A exhibited compact gel structures due to existence of lots of hydrogen bond while PPTA-M was able to form loose meso- or macro-porous structures under similar conditions. The overall effect of these two contradicting factors was that the adsorption capacities of PPTA-A samples were much lower than those of PPTA-M ones. It is our assumption that the strong hydrogen bonds between amino groups and PPTA fibers resulted in the compact structures, while the lack of such interaction between thiol groups and PPTA fibers led to the formation of meso- or macro-porous structures. But problems still remain, as the utilization ratio of SH in PPTA-M is unsatisfactory.

In current work, in order to obtain a more ideal adsorbent owning amino and thiol groups at the same time, amino-polysilsesquioxane, and thiol-polysilsesquioxane were introduced onto PPTA by a process named double reagents simultaneous functionalization (DRSF). The combination of weak alkaline amino groups and weak acidic thiol groups, on one hand can reduce the hydrogen bond interactions between the PPTA and functional groups then form porous structures on the surface of PPTA; and introduce simultaneously two kinds of functional groups only via one step on the other. Thus, the adsorbents might enhance Hg(II) separation effect and the utilization of functional groups. The synthesis proportions of amino groups and thiol groups were optimized. The adsorption kinetics, isotherms, selectivity, and adsorption mechanism of the resulting bi-functionalized adsorbent were investigated and discussed. This novel adsorbent showed favorable pore structures and enhanced adsorption capacities.

EXPERIMENTAL

Materials and Characterization Methods

PPTA were provided by Yantai Tayho Advanced Materials Co. Ltd., China. 3-Amino-propyltriethoxysilane (APTES) and 3-mercaptopropyltriethoxysilane (MPTES) were bought from Qufu Wanda Chemical Industry Co. Ltd., China. Dimethylsulfoxide (DMSO) and sodium hydride (NaH) were provided from Kishida Chemicals (Tokyo, Japan). Other reagents and solvents were all of analytical grade and were used as received directly.

Infrared (IR) spectra were measured on a fourier transform infrared (FTIR) spectrophotometer Nicolet iS50 (Nicolet, American). Surface morphologies were examined using Field Emission Scanning Electron Microscope (FE-SEM SU8010) (Hitachi, Japan). Thermogravimetric analysis (TGA) was analyzed on a TA instrument for thermogravimetric analysis (NETZSCHSTA 409 thermal analyzer, Germany). Elemental analysis was obtained using an Elementar Vario EL b model elemental analyzer (Elementar, Germany). Wide-angle X-ray diffraction (WAXD) curves were carried out on a Rigaku-D/max-2500VPC (Japan). X-ray photoelectron spectroscopy (XPS) was performed on ESCALAB Xi$^+$ (Thermo Fisher Scientific, American). The parameters of the porous structures were determined using an automatic physisorption analyzer (ASAP 2020, Micromeritics, USA). Analysis of various metal ions was performed on a flame atomic absorption spectrophotometer (Varian AA240, American). The contents of -NH$_2$ and -SH groups were determined by elemental analysis.

Preparation of PPTA-AM

Preparation of PPTA-ECH and PPTA-APTES followed the method in our previous work (Xu et al., 2016; Wang et al., 2017). Then different molar ratios of APTES and MPTES (see **Table 1**) were dissolved in 150 mL DMSO and added to PPTA-APTES in the flask. The mixture was subsequently stirred at 60°C for 12 h and was cooled to room temperature. NH$_4$F of 4 mL (0.014 g mL^{-1}) was added gradually with stirring and the resulting mixture was stirred for an additional 24 h. Solid fibers and solution were then poured into a Teflon-lined reactor and let to stand for 7 days, maintained at a near-constant temperature of 80°C. Finally, the resulted fibers were separated from the solution, extracted using re-fluxing ethanol for 48 h and dried under vacuum at 60°C for 80 h. The final products were denoted as PPTA-AM-n as shown in **Table 1**, where n corresponds to the percentage of APTES added. The synthetic route for the preparation of PPTA-AM samples is illustrated in **Scheme 1**.

Adsorption Experiments

The adsorption experiments were carried out using 20 mL of different concentrations of Hg(II) solution with predetermined amounts of PPTA-AM. The mixture solution was shaken at 25°C and pH 5.0 for 24 h. The equilibrium concentration of each solution was measured by Varian AA240. The adsorption capacity of Hg(II) was calculated according to Equation (1):

$$q_e = \frac{(C_0 - C)V}{W} \tag{1}$$

where q_e represents the adsorption amount (mmol g^{-1}); C_0 and C represent the initial and final concentrations, respectively (mmol mL^{-1}); V, the volume of solution (mL); W, the weight of adsorbents (g).

Adsorption kinetics were investigated from 0 to 7 h and the amount of adsorbent used was 20 mg. In addition, the effect of Hg(II) initial concentration was also studied. The initial concentrations were varied from 1 to 5 mmol L^{-1} at 25°C.

Adsorption selectivity of PPTA-AM-n was established by analyzing a solution containing Hg(II) and a coexisting ion including Cu(II), Ni(II), Pb(II), Ag(I), and Cd(II). The used adsorbents, PPTA-AM-n with adsorbed Hg(II), were eluted using different percentages (0, 1, 2, 3, 4, and 5%) of thiourea in 0.5 M HCl. The most effective eluent of 4% thiourea in 0.5 M HCl was used in five adsorption-desorption cycles on each adsorbent sample.

TABLE 1 | Formulations, element concentrations and binding energies of N_{1S}, S_{2p}, and Si_{2P} of PPTA and PPTA-AM samples.

Samples	APTES (mol)/ MPTES (mol) (Molar ratio)	Element concentrations Atomic %					Functional groups content (mmol g^{-1})	
		C_{1S}	N_{1S}	O_{1S}	Si_{2P}	S_{2P}	NH_2	SH
PPTA	0/0	73.68	7.85	19.47				
PPTA-AM-90	136.17/15.13 (9/1)	67.14	6.07	16.37	8.63	1.79	1.25	0.55
PPTA-AM-70	105.91/45.39 (7/3)	58.26	5.94	19.52	11.91	4.37	0.95	0.97
PPTA-AM-50	75.65/75.65 (1/1)	53.35	5.61	23.74	11.97	5.33	0.73	1.27
PPTA-AM-30	45.39/105.91 (3/7)	52.04	5.26	22.49	13.30	6.91	0.42	1.58
PPTA-AM-10	15.13/136.17 (1/9)	51.75	5.06	22.16	13.19	7.84	0.13	1.75

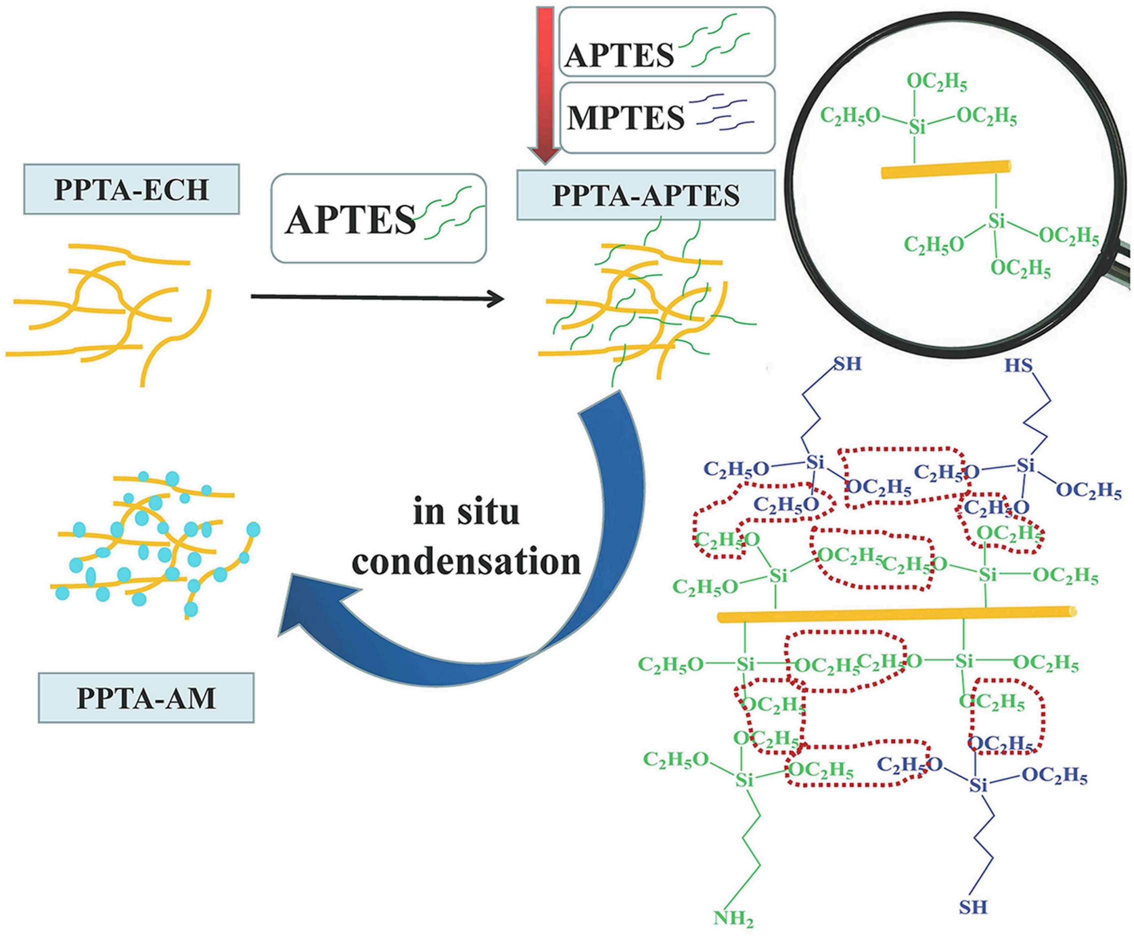

SCHEME 1 | Schematic diagram of the simultaneous functionalization process for PPTA-AM.

RESULTS AND DISCUSSION

Characterization of PPTA-AM

IR Spectroscopy Analysis

The IR spectra of PPTA-AM samples are presented in **Figure 1**. It can be observed that the absorption peaks around 1,640 and 1,545 cm^{-1} in PPTA fiber, which correspond to the C=O stretching vibration of amide and C-N stretching vibration, respectively (Yang et al., 2011), were weakened after modifications and appeared red-shifted in PPTA-AM samples. The peak at 1,574 cm^{-1} attributed to the in-plane bending vibration absorption of $-NH_2$ (from APTES) (Mehdipouratae et al., 2013) was present in PPTA-PAPSQ (Wang et al., 2017) but absent in all PPTA-AM samples. This may be due to the interactions between the thiol groups in MPTES and the amino groups in APTES. Two broad and strong absorption peaks around 1,104 and 1,010 cm^{-1} in PPPTA-AM samples as compared to one intense absorption peak at about 1,130 cm^{-1} in both PPTA-A and PPTA-M samples,

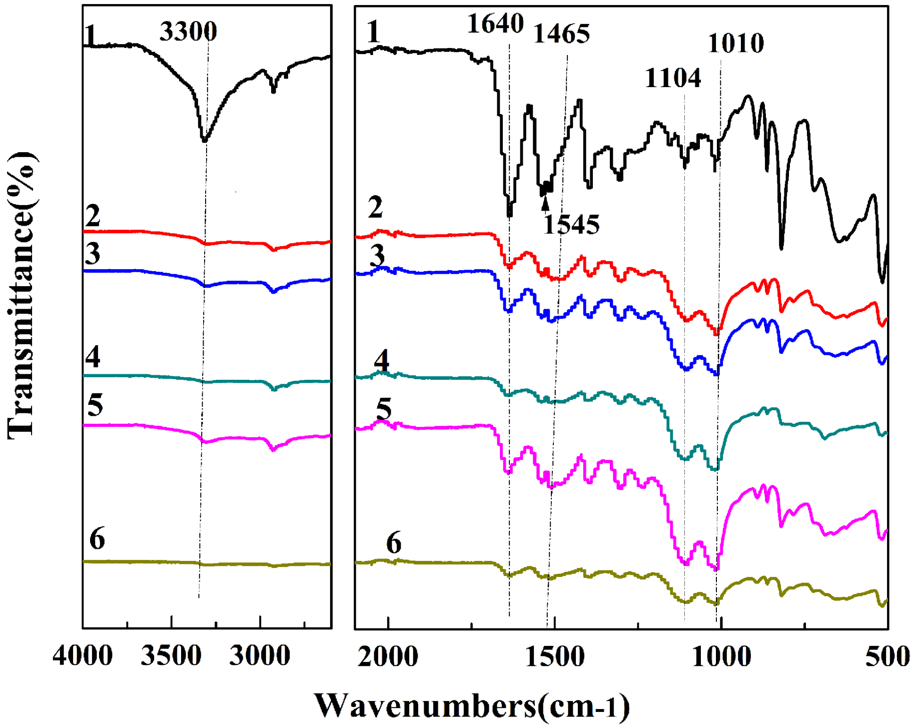

FIGURE 1 | IR spectra of PPTA and PPTA-AM samples. PPTA (1), PPTA-AM-90 (2), PPTA-AM-70 (3), PPTA-AM-50 (4), PPTA-AM-30 (5), and PPTA-AM-10 (6).

which can be attributed to –Si–O–Si– structure (Wang et al., 2017). This indicated that the structures of polysilsesquioxane with bifunctional groups of thiol- and amino- in PPTA-AM samples were different from those in mono-functional PPTA-A and PPTA-M adsorbents.

FE-SEM Images

As shown in **Figure 2**, PPTA-AM samples coated with various amounts of polysilsesquioxane exhibited varied surface morphologies. PPTA-AM-90 possessed a compact porous surface coating, and the surface nanoparticles of polysilsesquioxane (NPPSQ) were tightly cemented together. Conversely, there were a large number of NPPSQs densely aggregated in the form of "pearl chains" on the surface of PPTA-AM-70. The NPPSQs were relatively evenly distributed on the surface of PPTA-AM-50 and PPTA-AM-30, but severely agglomerated on the surface of PPTA-AM-10. The above observations indicated that the ratio of APTES and MPTES had important effects on the morphology and structures of NPPSQs on the surface PPTA-AM samples. When the proportion of APTES was higher than that of MPTES, NPPSQs tended to form compact porous structures shown on PPTA-AM-90 and PPTA-AM-70, which was due to the hydrogen-bonding interaction of -NH_2 in APTES (Wang et al., 2017). When the proportion of APTES were equal to (in the cases of PPTA-AM-50) or lower than that of MPTES (in the cases of PPTA-AM-30 and PPTA-AM-10), NPPSQs tended to form loose and porous structures because of the weakened hydrogen-bonding interaction of -NH_2 caused by its interaction with –SH in MPTES.

XPS Analysis

XPS results of wide-scan spectra of PPTA and PPTA-AM are shown in **Figure 3**. The element concentrations (**Table 1**) of N showed a gradually decreasing trend while those of S showed a gradually increasing trend. However, the ratio of N to S on the surface of PPTA-AM was not the same as that in the reactant mixture of APTES and MPTES. The binding energies of N_{1s} showed three peaks of N_{1S} in PPTA-AM-90–PPTA-AM-30 that appeared at about 399, 400, and 401 eV, which can be assigned to NH_2 (Metwalli et al., 2006; Majumder et al., 2009), amide (Giordani et al., 2009), and the protonated NH_2 adjacent to Si-OH, respectively (Acres et al., 2012). The binding energies of Si_{2p} that appeared at about 102 and 103 eV indicated there were two types of Si in the polysilsesquioxane structure, which could be assigned to Si–O–Si and Si–OH, respectively (Kropman et al., 1997; Qiao et al., 2015). But in the spectrum of PPTA-AM-10, only one peak of Si_{2p} appeared at 102.45 eV, which was attributed to Si-O-Si due to the highest MPTES proportion. It should be noted that the binding energy of S_{2P} increased gradually from PPTA-AM-90 to PPTA-AM-10 due to the interaction between SH and NH_2, indicating that the ratio of APTES and MPTES may have contributed to the difference of polysilsesquioxane structure in the PPTA-AM surface.

XRD Analysis and Nitrogen Adsorption Measurements

The WAXD patterns of PPTA and PPTA-AM samples and their corresponding crystalline parameters are presented in **Figure 4** and **Table 2**, respectively. As shown in **Table 2**, the Bragg angle

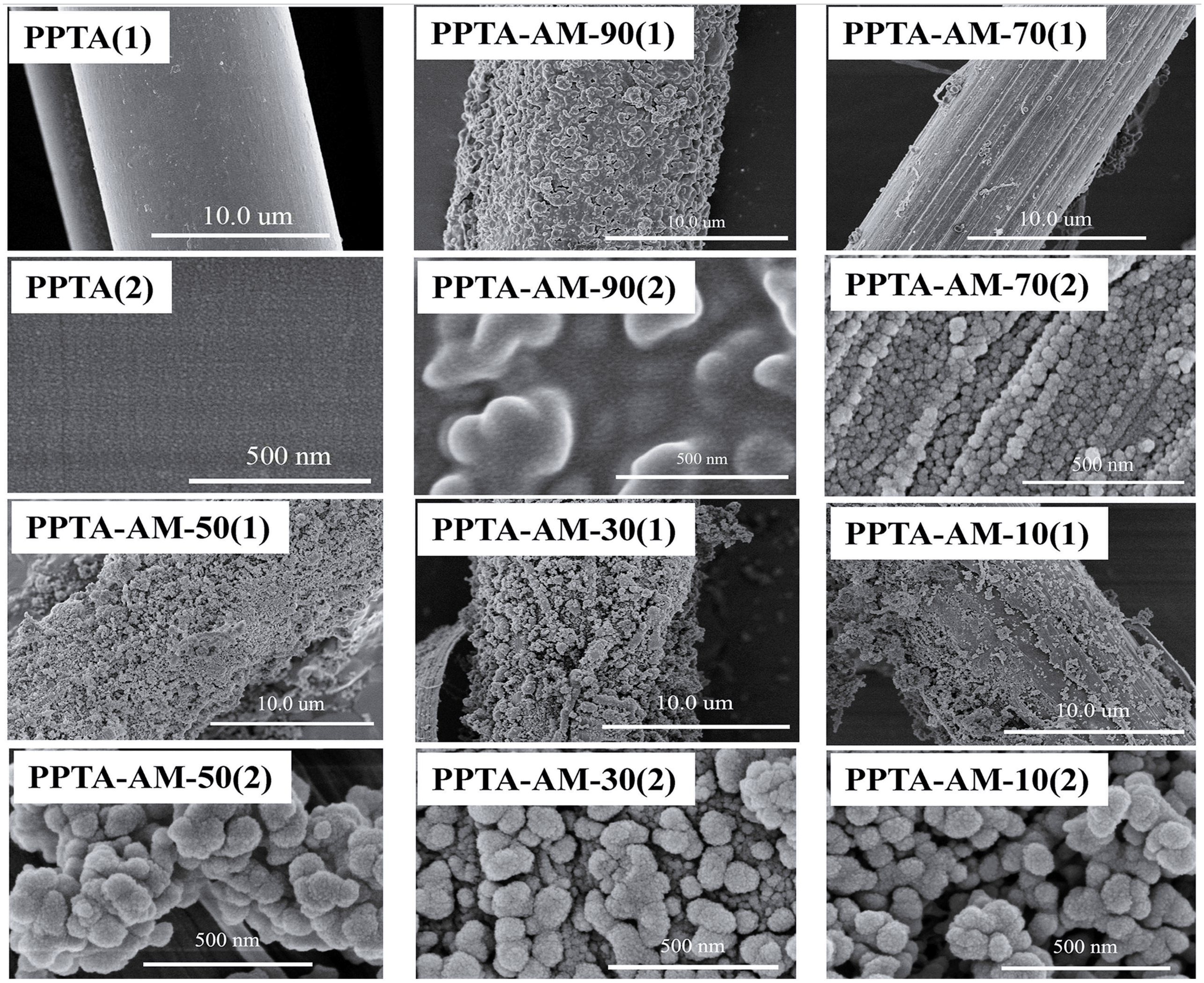

FIGURE 2 | FE-SEM images of PPTA and PPTA-AM samples.

(2θ) of (110), (200), and (211) crystal planes in PPTA-AM samples, slightly decreased compared with those of PPTA fibers, implying that the inter-planar spacing of each plane increased and the stacking density of the crystallite decreased (Zhang et al., 2006). Meanwhile, the values of full-width at half maximum (fwhm) and the average sizes of crystallites perpendicular to their diffracting planes (L_{hkl}) of modified PPTA fibers (PPTA-AM) slightly increased. All the results suggested that the crystal structures of PPTA fibers were affected significantly after modifications, so that their relative crystallinity (crystalline index, CI) was decreased. The CI of PPTA-AM samples were lower than those of PPTA-A and closer to those of PPTA-M. This may be due to the weakened effect of NH_2 on the crystal structure of PPTA fibers caused by the interaction between NH_2 and SH. Similarly to findings in our previous work, the intensities of the diffraction peaks at 20.5 and 22.6° in PPTA-AM samples decreased compared with those of the PPTA fibers. This indicated the amorphous structures of polysilsesquioxane with thiol and amino of bifunctional groups on the surface of PPTA-AM (Li et al., 2015).

Nitrogen Adsorption Measurements

Results from the nitrogen adsorption-desorption experiments are shown in **Figure 5**. It can be seen that the curves of nitrogen adsorption -desorption isotherms PPTA-AM samples were classified as type IV with H3 type hysteresis loop according to the IUPAC classification (Zhao et al., 2012), suggesting that PPTA-AM samples contained meso- or macroporous structures. The hysteresis loops of all the PPTA-AM samples extrapolated almost to $P/P0 = 1$, suggesting complete filling of the mesopores (Adam et al., 2010), which is also regarded as one of the characteristics of solids consisting of aggregates or agglomerate particles forming slit-shaped pores with non-uniform size and shape (Ahmed and Adam, 2007).

Table 2 showed that the BJH desorption pore size distributions of PPTA-AM-90–PPTA-AM-10 were

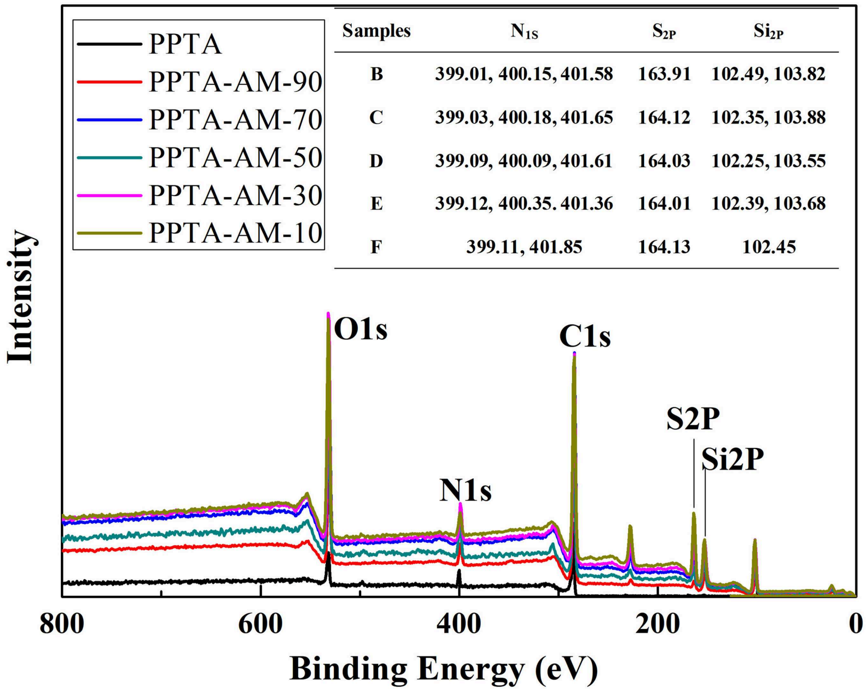

Samples	N_{1S}	S_{2P}	Si_{2P}
B	399.01, 400.15, 401.58	163.91	102.49, 103.82
C	399.03, 400.18, 401.65	164.12	102.35, 103.88
D	399.09, 400.09, 401.61	164.03	102.25, 103.55
E	399.12, 400.35. 401.36	164.01	102.39, 103.68
F	399.11, 401.85	164.13	102.45

FIGURE 3 | XPS spectra of PPTA and PPTA-AM samples.

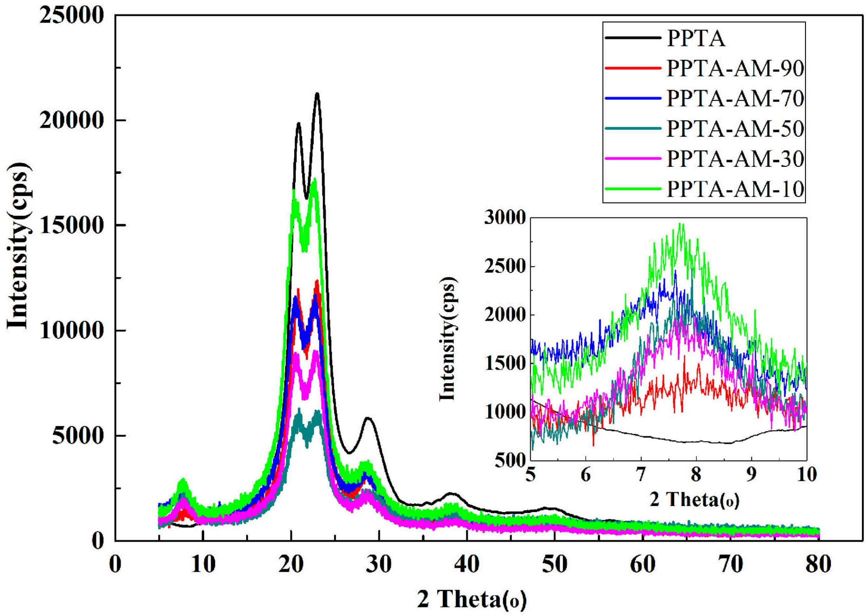

FIGURE 4 | XRD patterns of PPTA and PPTA-AM samples.

predominately in the ranges of 10∼85, 5∼80, 5∼60, 1∼65, and 1∼70 nm, respectively, which were slightly lower than that of PPTA- M (5–107 nm). The above results demonstrated that the adsorbents with porous structures can be obtained by using the DRSF method.

Saturated Adsorption

The saturated adsorption capacities of PPTA-AM for Hg(II) are presented in **Figure 6A**. For PPTA-A obtained using different quantity of APTES, the amounts of NH_2 are 0.63, 0.99, 1.31, 1.51, and 1.52, and the adsorption amounts are 0.07, 0.20,

TABLE 2 | Formulations, element concentrations, parameters of porous structures and ratio of functional group to metal ionon the surfaces of PPTA and PPTA-AM samples.

Samples	BET surface area ($m^2 g^{-1}$)	BJH desorption cumulative pore volume ($cm^3 g^{-1}$)	BJH desorption pore diameter (nm)	2θ (°)			fwhm (°)			L_{hkl} (nm)			CI (%)
				(110)	(200)	(211)	(110)	(200)	(211)	(110)	(200)	(211)	
PPTA	–	–	–	20.89	22.98	28.76	2.38	2.06	2.48	4.26	3.86	3.10	82.06
PPTA-AM-90	2.04	0.03	10∼85	20.83	22.95	28.64	2.49	2.11	2.52	4.31	3.88	3.12	75.58
PPTA-AM-70	6.57	0.04	5∼80	20.79	22.96	28.61	2.53	2.12	2.54	4.35	3.87	3.13	74.89
PPTA-AM-50	7.16	0.15	1∼60	20.80	22.96	28.65	2.51	2.05	2.57	4.30	3.86	3.11	71.14
PPTA-AM-30	6.32	0.13	1∼65	20.81	22.93	28.68	2.50	2.15	2.55	4.29	3.86	3.11	72.91
PPTA-AM-10	16.51	0.14	1∼70	20.85	22.95	28.66	2.53	2.14	2.64	4.28	3.87	3.12	78.91

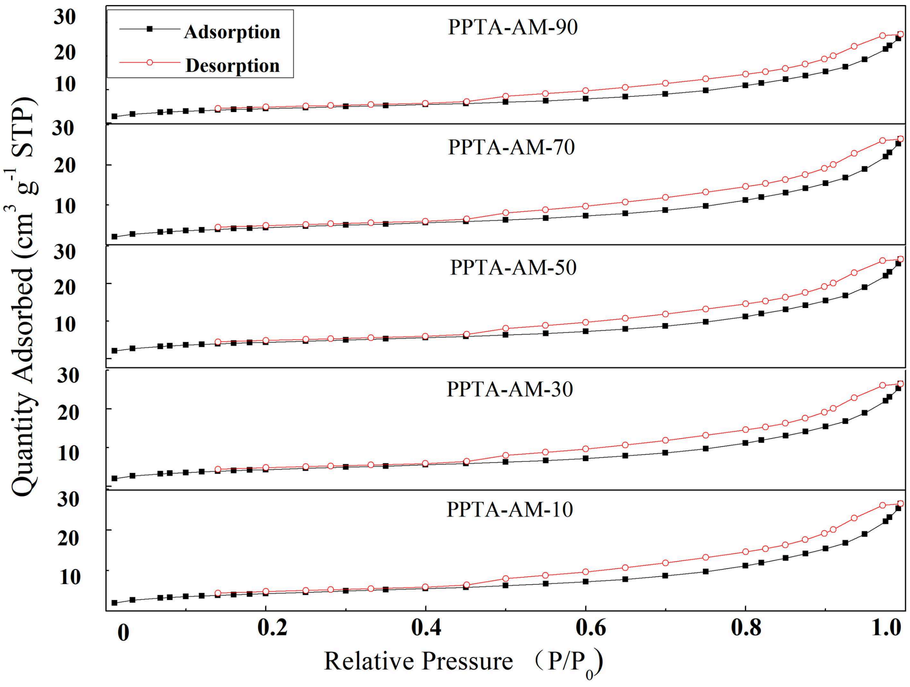

FIGURE 5 | Nitrogen adsorption–desorption isotherms of PPTA-AM samples.

0.26, 0.28, and 0.28 mmol g^{-1}. And for PPTA-M obtained using different quantity of MPTES, the amounts of SH are 1.41, 2.04, 2.18, 3.45, and 3.51 mmol g^{-1}, and the adsorption amounts are 0.32, 0.58, 0.65, 0.78, and 0.78 mmol g^{-1}. As shown in **Figure 6A**, the saturated adsorption capacities of PPTA-AM-90–PPTA-AM-10 for Hg(II) were 1.13, 1.36, 1.32, 1.22, and 1.19 mmol g^{-1}, respectively. That is, anyone is much higher than that adsorption maximum of PPTA-A (0.28 mmol g^{-1}, with the highest amount of NH_2 is 1.52 mmol g^{-1}) and that adsorption maximum of PPTA-M (0.78 mmol g^{-1}, with the highest amount of SH is 3.51 mmol g^{-1}). Obviously, the adsorption effect of amino- and thiol- polysilsesquioxane simultaneously coating on poly(*p*-phenylenetherephthal amide) fibers were much better than mono-functionalized poly(p-phenylenetherephthal amide) fibers (PPTA-A and PPTA-M) befitting from the synergistic effect. The adsorption capacity of PPTA-A was lower than those of PPTA-AM, which could be attributed to the lower loading of polysilsesquioxanes coating on the surface. The only explanation for the much higher adsorption capacities of PPTA-AM is that the polysilsesquioxanes with bifunctional groups in PPTA-AM samples were of different form and more conducive to Hg(II) adsorption than those in PPTA-M. Meanwhile, the Hg(II) adsorption capacities of PPTA-AM followed the descending order of PPTA-AM-70, PPTA-AMPPTA-AM-50, PPTA-AM-90, PPTA-AM-30, and PPTA-AM-10. This may be caused by a variety of factors such as the content of functional groups, pore structure and morphology of polysilsesquioxanes coating.

Determination of the Optimum pH Value

The pH value of the metal ions solution can impact the interaction between metal ions and the surface structure of adsorbents. The relationship between the saturated adsorption capacities and pH is shown in **Figure 6B**. It was found that

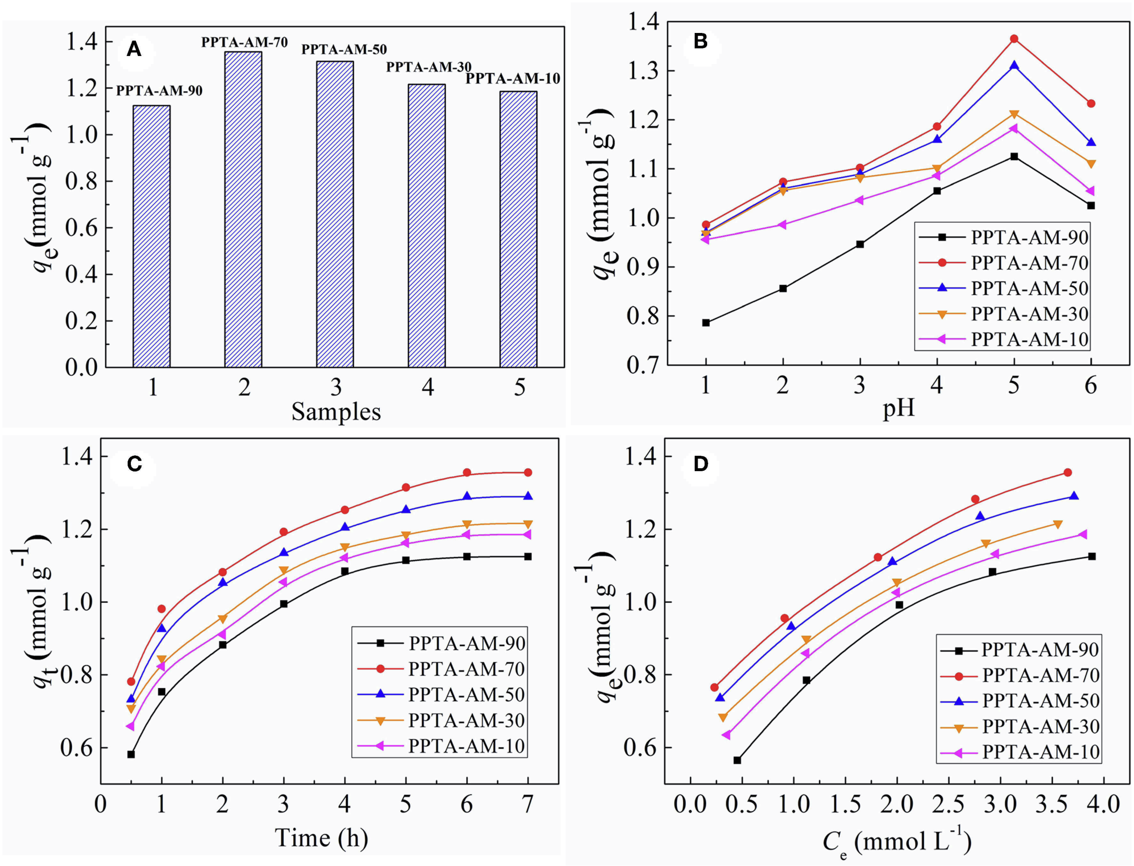

FIGURE 6 | Saturated adsorption capacities **(A)**, effect of pH **(B)**, adsorption kinetics **(C)**, and adsorption isotherms for Hg(II) onto PPTA-AM samples **(D)**.

the maximum adsorption values for the Hg(II) onto PPTA-AM samples appeared at pH = 5.0. At low pH, NH_2, and SH on the surface of adsorbents were positively charged owing to protonation, thus the adsorption was dominated by electrostatic repulsion and disfavored. Moreover, the existence of a large amount of H^+ in the solution may compete adsorption with Hg(II). With the increase of pH, the electrostatic repulsion between PPTA-AM and Hg(II) reduced for deprotonation and the deprotonated NH_2 and SH can effectively coordinate with Hg(II), thus the adsorption capacity of PPTA-AM for Hg(II) increased (Ma et al., 2017). The uptake of Hg(II) beyond pH 5.0 is decreased, which might attribute the formation of metal hydroxide species such as soluble $Hg(OH)^+$. Therefore, the optimum value pH = 5.0 was chosen in the subsequent experiments. This value was the same for PPTA-A and PPTA-M, implying that the interaction of NH_2 and SH did not affect the optimum pH values.

Adsorption Kinetics and Adsorption Isotherms

The adsorption kinetics for Hg(II) of PPTA-AM were determined to investigate the adsorption behavior and the results are shown in **Figure 6C**. As shown in **Figure 6C**, the adsorption for Hg(II) of PPTA-AM samples that reached equilibrium required a minimum of 6 h. The experimental data were tested by using to Pseudo-first-order (Barkat et al., 2009) and pseudo-second-order (Ho et al., 2000) models and the adsorption kinetic process were thus elucidated. The adsorption kinetics for Hg(II) of PPTA-AM were better described by pseudo-second-order model and equilibrium required a minimum within 6 h as shown in **Figure 6B**. The adsorption rate and adsorption capacities of PPTA-AM-70 were maximum, due to porous structure and to proceed the bicontinuum process, which occurred either in series or in parallel, being the more common bicontinuum conceptualization (Brusseau et al., 1989).

The pseudo-first-order and pseudo-second order models are, respectively, expressed by Equations (2) and (3).

$$\ln(q_e - q_t) = \ln q_e - k_1 t \tag{2}$$

$$\frac{t}{q_t} = \frac{1}{k_2 q_e^2} + \frac{t}{q_e} \tag{3}$$

q_e and q_t (mmol g^{-1}) are the adsorption amounts of Hg(II) at equilibrium and time t (min), respectively. k_1 and k_2 are the rate constants of pseudo-first-order (h^{-1}) and pseudo-second-order (g mmol^{-1} h^{-1}) adsorption. The experimental and calculated q_e

values, rate constants and regression coefficient (R^2) values are all presented in **Table 3**.

As shown in **Table 3**, the adsorption process followed the pseudo-second-order model well and had better correlation coefficients than the pseudo-first-order model for samples. Therefore, the adsorption kinetics of Hg(II) onto the adsorbents was better described by pseudo-second-order model.

The isotherm adsorption of PPTA-AM for Hg(II) was investigated and the results are shown in **Figure 6D**. The Langmuir and Freundlich equations were adopted to fit the experimental data. The linear expressions of Langmuir and Freundlich models can be written as Equations (4) and (5) (Zhang et al., 2015):

$$\frac{C_e}{q_e} = \frac{C_e}{q} + \frac{1}{qK_L} \tag{4}$$

$$\ln q_e = \ln K_F + \frac{\ln C_e}{n} \tag{5}$$

where q_e is the equilibrium concentration of Hg(II) on the adsorbent (mg g^{-1}), C_e is the equilibrium concentration of Hg(II) in solution (mg L^{-1}), q is the maximum capacity of adsorbent (mg g^{-1}), and K_L is the Langmuir adsorption constant (L mg^{-1}). K_F is the binding energy constant reflecting the affinity of the adsorbents to metal ions; n is the Freundlich exponent related to adsorption intensity.

The corresponding Langmuir and Freundlich constants and correlation coefficients (R^2) are listed in **Table 4**. From the correlation coefficients in **Table 4**, it can be concluded that the experiment data fitted Langmuir equation better than Freundlich equation, revealing the adsorption of Hg(II) adsorption on PPTA-AM obeyed the Langmuir adsorption isotherm. This implies that the adsorption of Hg(II) on PPTA-AM followed the mechanism of monolayer adsorption (chemisorption) (Qu et al., 2013).

Based on the q_{the} values in **Table 4**, these values have a significant advantage over other silica adsorption materials, e.g., silica–dithizone at 0.22 mmol g^{-1} (Cestari et al., 2004), and pure functionalized polysilsesquioxane, e.g., diethylenetriamine-bridged polysilsesquioxanes at 1.81 mmol g^{-1} (Sun et al., 2014), POSS-SH at 0.06 mmol g^{-1} (Wang et al., 2014). They are

TABLE 5 | Adsorption selectivity of PPTA-AM-70 toward Hg(II) at 25°C (pH 5.0).

System	Mental ions	q (mmol g^{-1})	Selectivity coefficient*
Hg(II)-Pb(II)	Hg(II)	1.36	∞
	Pb(II)	0.00	
Hg(II)-Cu(II)	Hg(II)	1.35	∞
	Cu(II)	0.00	
Hg(II)-Ni(II)	Hg(II)	1.36	∞
	Ni(II)	0.00	
Hg(II)-Cd(II)	Hg(II)	1.36	∞
	Zn(II)	0.00	
Hg(II)-Ag(I)	Hg(II)	1.31	10
	Ag(I)	0.13	

**The selective coefficient was the ratio of adsorption capacities of metal ions in a binary system.*

TABLE 3 | Kinetic parameters for the adsorption of Hg(II) on PPTA-AM samples.

Adsorbents	q_{exp} (mmol g^{-1})	Pseudo-first-order kinetics			Pseudo-second-order kinetics		
		k_1 (h^{-1})	$q_{e(cal)}$ (mmol g^{-1})	R_1^2	k_2 (g $mmol^{-1}$ h^{-1})	q_e (mmol g^{-1})	R_2^2
PPTA-AM-90	1.125	0.156	0.858	0.9412	1.579	1.118	0.9972
PPTA-AM-70	1.365	0.197	1.154	0.9695	1.891	1.356	0.9973
PPTA-AM-50	1.315	0.183	0.109	0.9754	1.645	1.321	0.9975
PPTA-AM-30	1.216	0.173	0.965	0.9855	1.441	1.210	0.9973
PPTA-AM-10	1.186	0.160	0.956	0.9653	1.370	1.185	0.9962

TABLE 4 | Langmuir and Freundlich isotherm constants for the adsorption of Hg(II) on PPTA-AM at 25°C (pH 5.0).

Adsorbents	Langmuir			Freundlich			Ratio of functional group to metal ion*
	q_{the} (mmol g^{-1})	K_L (L $mmol^{-1}$)	R_L^2	K_F (mmol g^{-1})	n	R_F^2	(NH_2+SH)/Hg(II)
PPTA-AM-90	1.32	1.42	0.9982	0.051	1.80	0.9802	1.36
PPTA-AM-70	1.54	0.41	0.9961	0.10	2.42	0.9775	1.25
PPTA-AM-50	1.41	0.43	0.9914	0.11	1.98	0.9682	1.42
PPTA-AM-30	1.34	0.45	0.9912	0.15	1.68	0.9743	1.49
PPTA-AM-10	1.33	0.54	0.9941	0.041	1.57	0.9891	1.42

The Ratio of functional group to metal ion is equal to M/q; wherein, M presents the amount of functional group (NH_2 + SH) in PPTA-AM (Table 1**).*

also higher than those of the monofuctional polysilsesquioxanes coated PPTA fibers, e.g., PPTA-A at 10.64 mmol g^{-1} and PPTA-M at 10.22 mmol g^{-1} (Wang et al., 2017). This implies that PPTA-AM with amino- and thiol- bifunctional groups possessed higher functional group utilization rates of polysilsesquioxanes than PPTA-A and PPTA-M adsorbents with amino- or thiol-monofunctional groups.

Adsorption Selectivity

The adsorption selectivities of PPTA-AM-70 were chosen as representatives in binary ion systems to compare the differences in adsorption properties between adsorbents with bifunctional groups and those with monofunctional groups. The results are presented in **Table 5**. From **Table 5**, it was found that PPTA-AM-70 exhibited excellent selectivity toward Hg(II) in the presence of Pb(II), Cu(II), Ni(II), and Cd(II), implying that bifunctionalization had no significant effect on its adsorption selectivity.

Adsorption Mechanism

The adsorption mechanism of PPTA-AM for Hg(II) using the XPS technique by comparing the changes of binding energies of N_{1s}, S_{2p}, and Hg_{4f} before and after adsorption. **Figure 7** shows the N_{1s}, S_{2p}, and Hg_{4f} spectra of PPTA-AM-70 after adsorbing Hg(II). From **Figure 7**, it can be found that the binding energies of N_{1s} in NH_2 and S_{2p} in SH in PPTA-AM-70 were shifted from 399.03 to 399.68 eV and from 164.12 to 164.32 eV, respectively, while that of Hg_{4f} was shifted from 104.00 to 101.98 eV after adsorption, implying that both NH_2 and SH were involved in the coordination with Hg(II). The binding energy of N_{1s} of amide 400.18 eV in PPTA-AM-70 had no change before and after adsorption, indicating that N of amide was not involved in adsorption process. The binding energy of S_{2p} at 168.32 eV implied that there was a certain degree of redox reaction in the adsorption process (Qu et al., 2006).

According to the data in **Table 4**, the coordination ratio of (NH_2 + SH) to Hg(II) of PPTA-AM samples can be calculated to be 1.36, 1.25, 1.42, 1.49, and 1.42, respectively, which were much lower than 2.4–2.89 of NH_2/Hg(II) for PPTA-A and 2.56–3.96 of SH/Hg(II) for PPTA-M ones. This suggested that PPTA-AM adsorbents needed only 1.25–1.49 (NH_2+SH) to chelate one Hg(II) ion. In other words, the bifunctional adsorbents prepared by the DRSF method had higher functional group utilization than those with monofunctional groups. This may be a result of their unique loose open meso- or macroporous features of PAMPAQ. Based on the above analysis, the adsorption mechanism of the PPTA-AM samples is proposed as illustrated in **Scheme 2**. The structures of chelates depended on the proportion of NH_2 and SH in PAMPSQ. When the proportion of NH_2 was greater than SH, the structure was dominated by I, II and IV. When the proportion

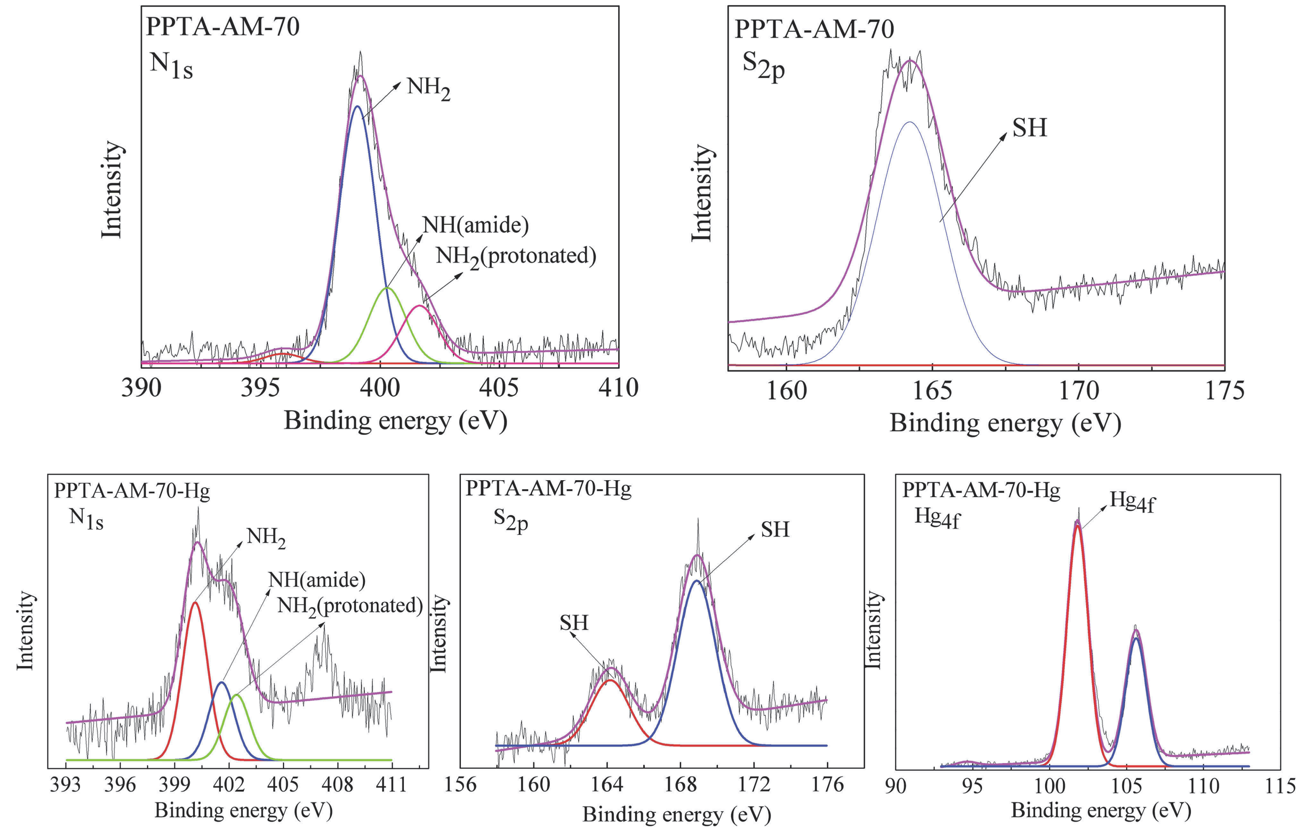

FIGURE 7 | N_{1s}, S_{2p}, Hg_{4f} spectra of PPTA-AM-70 after Hg(II) adsorption.

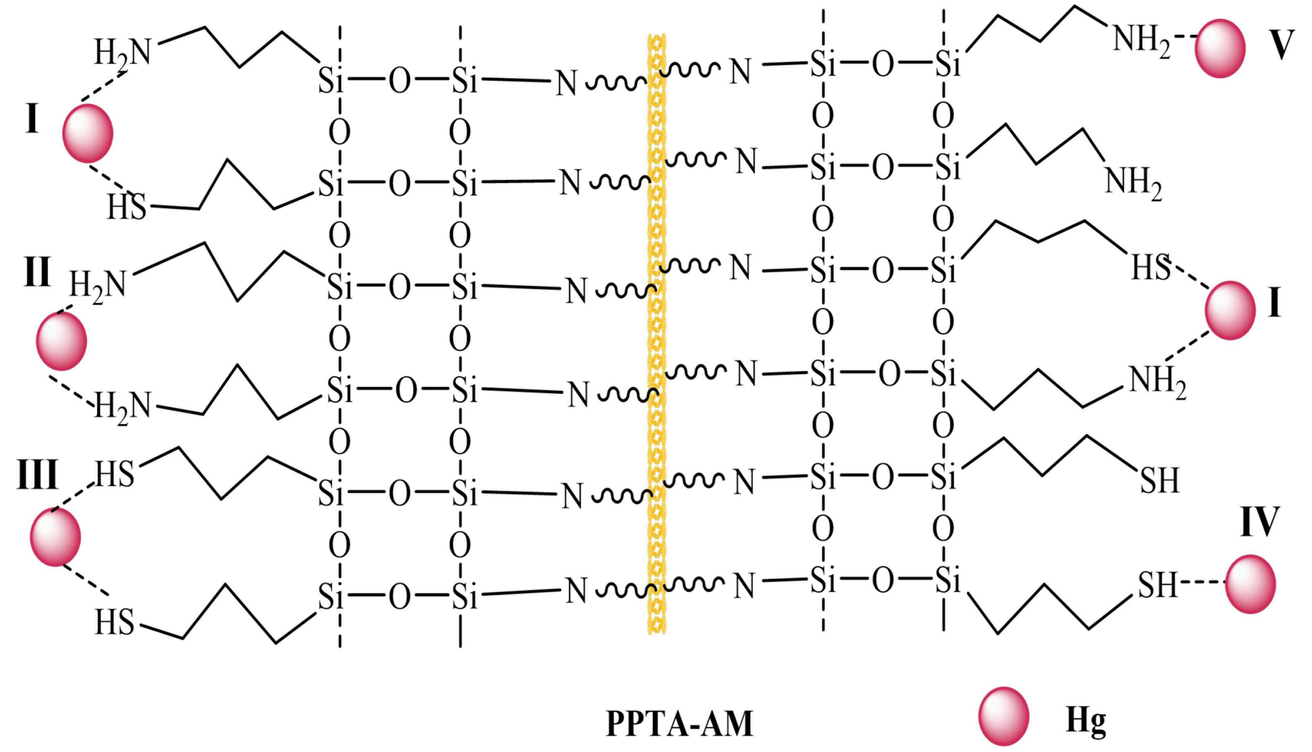

SCHEME 2 | Possible chelating structures of PPTA-AM with Hg(II).

of NH_2 was lower than SH, the structure was dominated by I, III, and V. When the proportion of NH_2 was equal to SH, the structure was dominated by I, IV, and V.

Regeneration

PPTA-AM-70 was chosen as a representative to test the reusability. The elution rate was over 95% eluted by the eluent system of 4% thiourea in 0.5 M HCl. Thiourea in HCl is frequently used for the desorption of Hg(II) from adsorbent surfaces because the sulfur and nitrogen present in thiourea can form a coordination interaction with Hg(II) ions, and because thiourea dissolved in HCl is expected to have more of a desorption effect (Velempini et al., 2019). Five cycles of adsorption-desorption were carried out on a single adsorbent sample and the results are shown in **Table 6**. As can be seen from **Table 6**, the adsorption properties of PPTA-AM-70 had only a small decrease after five cycles of adsorption-desorption, with the uptake all being above 90%. Therefore, the adsorbent was suitable for repeated use at a diminishing rate in the adsorption capacity.

TABLE 6 | Regeneration properties of PPTA-AM-70 for Hg(II) adsorption.

Regeneration times	Q_e (mmol g^{-1})	Desorption rate (%)
1	1.365	94.52
2	1.355	93.53
3	1.341	92.23
4	1.325	90.56
5	1.306	90.55

CONCLUSION

Bifunctional adsorbents PPTA-AM, amino- and thiol-polysilsesquioxane (PAMPSQ) simultaneously coated poly(*p*-phenyleneterephthal amide) fibers were successfully prepared by developed DRSF method. The loose and meso- or macro-porous structures of PAMPSQs in the form of nanoparticles were formed on the surface of PPTA fibers. The morphologies of the PAMPSQ coatings were dependent on the the proportion of reactants of APTES and MPTES. PPTA-AM adsorbents just need 1.25–1.49 NH_2+SH chelate one Hg(II) ion, indicating that the PAMPSQ coating in these bifunctionals adsorbents had much higher functional group utilization than pure functionalized polysilsesquioxane adsorption materials, and the corresponding monofunctional polysilsesquioxane coated PPTA fibrous adsorbents for Hg(II) adsorption.

DATA AVAILABILITY

The datasets generated for this study are available on request to the corresponding author.

AUTHOR CONTRIBUTIONS

RQ: work design. YW: data collection and organize the draft. YM, KA, XJ, and YuZ: data collection. CS and CJ: characterization. YiZ: make important changes to the paper.

ACKNOWLEDGMENTS

We are grateful for the financial support by the National Natural Science Foundation of China (Grant No. 51673089, 51373074, 51073075, 51302127, 51143006).

REFERENCES

Acres, R. G., Ellis, A. V., Alvino, J., Lenahan, C. E., Khodakov, D. A., Metha, G. F., et al. (2012). Molecular structure of 3-aminopropyltriethoxysilane layersformed on silanol-terminated silicon surfaces. *J. Phys. Chem C* 116, 6289–6297. doi: 10.1021/jp212056s

Adam, F., Appaturi, J. N., Thankappan, R., and Nawi, M. A. M. (2010). Silica-tin nanotubes prepared from rice husk ash by sol-gel method: characterization and its photocatalytic activity. *Appl. Surf. Sci.* 257, 811–816. doi: 10.1016/j.apsusc.2010.07.070

Ahmed, A. E., and Adam, F. (2007). Indium incorporated silica from rice husk and its catalytic activity. *Micropor. Mesopor. Mater.* 103, 284–295. doi: 10.1016/j.micromeso.2007.01.055

Barkat, M., Nibou, D., Chegrouche, S., and Mellah, A. (2009). Kinetics and thermodynamics studies of chromium(VI) ions adsorption onto activated carbon from aqueous solutions. *Chem. Eng. Process.* 48, 38–47. doi: 10.1016/j.cep.2007.10.004

Basso, M. C., Cerrella, E. G., and Cukierman, A. L. (2002). Activated carbons developed from a rapidly renewable biosource for removal of cadmium(II) and. nickel(II) from dilute aqueous solutions. *Ind. Eng Chem. Res.* 41, 180–189. doi: 10.1021/ie010664x

Brusseau, M. L., Rao, P. S. C., and Gillham, R. W. (1989). Sorption non-ideality during organic contaminant transport in porous media. *CRC Crit. Rev. Environ. Control* 19, 33–99. doi: 10.1080/10643388909388358

Cestari, A. R., Vieira, E. F. S., Lopes, E. C. N., and Silva, R. G. D. (2004). Kinetics and equilibrium parameters of Hg(II) adsorption on silica–dithizone. *J. Colloid. Interf. Sci.* 272, 271–276. doi: 10.1016/j.jcis.2003.09.019

Giordani, S., Colomer, J. F., Cattaruzza, F., Alfonsi, J., and Meneghetti, M. (2009). Multifunctional hybrid materials composed of fullerene-based functionalized-single-walled carbon nanotubes. *Carbon* 47, 578–588. doi: 10.1016/j.carbon.2008.10.036

Gomez-Salazar, S., Lee, J. S., Heydweiller, J. C., and Tavlarides, L. L. S. (2003). Analysis of cadmium adsorption on novel organo-ceramic adsorbents with a thiol functionality. *Ind. Eng. Chem. Res.* 42, 3403–3412. doi: 10.1021/ie020840h

Ho, Y. S., McKay, G. J., Wase, D. A., and Foster, C. F. (2000). Study of the sorption of divalent metal ions on to peat. *Adsorpt. Sci. Technol.* 18, 639–650. doi: 10.1260/0263617001493693

Hua, M., Zhang, S., Pan, B., Zhang, W., Lv, L., and Zhang, Q. (2012). Heavy metal removal from water/wastewater by nanosized metal oxides: a review. *J. Hazard. Mater*. 211–212, 317–331. doi: 10.1016/j.jhazmat.2011.10.016

Huang, C. P., Chung, Y. C., and Liou, M. R. (1996). Adsorption of Cu(II) and Ni(II) by pelletized biopolymer. *J. Hazard. Mater.* 45, 265–277. doi: 10.1016/0304-3894(95)00096-8

Kropman, B. L., Blank, D. H. A., and Rogalla, H. (1997). Self-assembled monolayers of alkylsiloxanes on $SrTiO_3$ substrates. *Supramol. Chem.* 4, 59–65. doi: 10.1016/S0968-5677(96)00043-0

Li, B., Li, X. H., Zhang, K. Q., Li, H., Zhao, Y. H., Ren, L. H., et al. (2015). Synthesis of POSS containing fluorosilicone block copolymers via RAFT polymerization for application as non-wetting coating materials. *Prog. Org. Coat.* 78, 88–199. doi: 10.1016/j.porgcoat.2014.09.004

Li, G., Zhao, Z., Liu, J., and Jiang, G. (2011). Effective heavy metal removal from aqueous systems by thiol functionalized magnetic mesoporous silica. *J. Hazard. Mater.* 192, 277–283. doi: 10.1016/j.jhazmat.2011.05.015

Liu, T. M., Zheng, Y. S., and Hu, J. (2011). Surface modification of aramid fibers with novel chemical approach. *Polym. Bull.* 66, 259–275. doi: 10.1007/s00289-010-0313-y

Ma, Y. X., Xing, D., Shao, W. J., Du, X. Y., and La, P. Q. (2017). Preparation of polyamidoamine dendrimers functionalized magnetic graphene oxide for the adsorption of Hg(II) in aqueous solution. *J. Colloid Interf. Sci.* 505, 352–363. doi: 10.1016/j.jcis.2017.05.104

Majumder, S., Priyadarshini, M., Subudhi, U., Chainy, G. B. N., and Varma, S. (2009). X-ray photoelectron spectroscopic investigations of modifications in plasmid DNA after interaction with Hg nanoparticles. *Appl. Surf. Sci.* 256:438–442. doi: 10.1016/j.apsusc.2009.06.097

Mehdipouratae, S., Mosslemin, M. H., Kholghi, S., and Mohaghegh, S. M. S. (2013). Soluble, thermally stable poly(amide-ester)s containing pyridine pendent group. *e-Polymers* 9, 527–537. doi: 10.1515/epoly.2009.9.1.527

Metwalli, E., Haines, D., Becker, O., Conzone, S., and Pantano, C. G. (2006). Surface characterizations of mono-, di-, and tri-aminosilane treated glass substrates. *J. Colloid Interf. Sci.* 298, 825–831. doi: 10.1016/j.jcis.2006.03.045

Qiao, B., Wang, T. J., Gao, H., and Jin, Y. (2015). High density silanization of nano-silica particles using c-aminopropyltriethoxysilane (APTES). *Appl. Surf. Sci.* 351, 646–654. doi: 10.1016/j.apsusc.2015.05.174

Qu, R. J., Sun, C. M., Ji, C. N., Xu, Q., Wang, C. H., and Cheng, G. X. (2006). The sorption mechanism of Au(III) on sulfur-containing chelating resin poly[4-vinylbenzyl (2-hydroxyethyl) sulfide. *Eur. Polym. J.* 42, 254–258. doi: 10.1016/j.eurpolymj.2005.07.001

Qu, R. J., Zhang, Y., Qu, W. W., Sun, C. M., Chen, J., Ping, Y., et al. (2013). Mercury adsorption by sulfur- and amidoxime-containing bifunctional silica gel based hybrid materials. *Chem. Eng. J.* 219, 51–61. doi: 10.1016/j.cej.2012.12.070

Sun, C. M., Li, C. X., Qu, R. J., Zhang, Y., Zhang, B. D., and Kuang, Y. Z. (2014). Syntheses of diethylenetriamine-bridged poly-silsesquioxanes and their structure–adsorption properties for Hg(II) and Ag(I). *Chem. Eng. J.* 240, 369–378. doi: 10.1016/j.cej.2013.11.092

Velempini, T., Pillay, K., Mbianda, X. Y., and Arotiba, O. A. (2019). Carboxymethyl cellulose thiol-imprinted polymers: synthesis, characterization and selective Hg(II) adsorption. *J. Environ. Sci.* 79, 280–296. doi: 10.1016/j.jes.2018.11.022

Wang, W. J., Chen, M. L., Chen, X. W., and Wang, J. H. (2014). Thiol-rich polyhedral oligomeric silsesquioxane as a novel adsorbent for mercury adsorption and specification. *Chem. Eng. J.* 242, 62–68. doi: 10.1016/j.cej.2013.12.063

Wang, Y. F., Qu, R. J., Pan, F. W., Jia, X. H., Sun, C. M., Ji, C. N., et al. (2017). Preparation and characterization of thiol- and amino-functionalized polysilsesquioxane coated poly(p-phenylenetherephthal amide) fibers and their adsorption properties towards Hg(II). *Chem. Eng. J.* 317,187–203. doi: 10.1016/j.cej.2017.02.073

Xu, C. Z., Qu, R. J., Li, S. S., Sun, C. M., Zhang, Y., Gao, J. J., et al. (2016). Preparation, characterization, and rapid adsorption of Hg^{2+} on nanoscale aramid-based adsorbent. *J. Polym. Environ.* 24, 206–220. doi: 10.1007/s10924-016-0764-9

Yang, M., Cao, K. Q., Sui, L., Qi, Y., Zhu, J., Waas, A., et al. (2011). Dispersions of aramid nanofibers: a new nanoscale building block. *ACS. Nano* 5, 6945–6954. doi: 10.1021/nn2014003

Zhang, H. P., Zhang, J. C., Chen, J. Y., Hao, X. M., Wang, S. Y., Feng, X. X., et al. (2006). Effects of solar UV irradiation on the tensile properties and structure of PPTA fiber. *Polym. Degrad. Stab.* 91, 2761–2767. doi: 10.1016/j.polymdegradstab.2006.03.025

Zhang, Y., Qu, R. J., Sun, C. M., Ji, C. N., Chen, H., and Yin, P. (2015). Improved synthesis of silica-gel-based dendrimer-like highly branched polymer as the Au(III) adsorbents. *Chem. Eng. J.* 270, 110–121. doi: 10.1016/j.cej.2015.02.006

Zhao, B., Song, J., Fang, T., Liu, P., Jiao, Z., Zhang, H. J., et al. (2012). Hydrothermal method to prepare porous NiO nanosheet. *Mater. Lett.* 67, 24–27. doi: 10.1016/j.matlet.2011.09.057

Zub, Y. L., Stolyarchuk, N. V., Chuiko, A. A., Dabrowski, A., and Barczak, M. (2005). New adsorbents based on bridged polysilsesquioxanes containing 3-mercaptopropyl functional groups. *Mendeleev. Commun.* 15, 168–170. doi: 10.1070/MC2005v015n04ABEH002096

Conflict of Interest Statement: The authors declare that the research was conducted in the absence of any commercial or financial relationships that could be construed as a potential conflict of interest.

Copyright © 2019 Wang, Qu, Mu, Sun, Ji, Zhang, An, Jia and Zhang. This is an open-access article distributed under the terms of the Creative Commons Attribution License (CC BY). The use, distribution or reproduction in other forums is permitted, provided the original author(s) and the copyright owner(s) are credited and that the original publication in this journal is cited, in accordance with accepted academic practice. No use, distribution or reproduction is permitted which does not comply with these terms.

frontiers in Chemistry

ORIGINAL RESEARCH
published: 15 July 2019
doi: 10.3389/fchem.2019.00501

Improving the Post-polymerization Modification of Bio-Based Itaconate Unsaturated Polyesters: Catalyzing Aza-Michael Additions With Reusable Iodine on Acidic Alumina

Oliver B. Moore, Polly-Ann Hanson, James W. Comerford, Alessandro Pellis and Thomas J. Farmer**

Green Chemistry Centre of Excellence, Department of Chemistry, University of York, York, United Kingdom

Bio-based platform molecules such as itaconic, fumaric, and muconic acid offer much promise in the formation of sustainable unsaturated polyester resins upon reaction with suitable diols and polyols. The C=C bonds present in these polyester chains allows for post-polymerization modification and such moieties are conventionally utilized in curing processes during the manufacture of coatings. The C=C modification sites can also act as points to add useful pendants which can alter the polymers final properties such as glass transition temperature, biodegradability, hardness, polarity, and strength. A commonly observed modification is the addition of secondary amines via an aza-Michael addition. Conventional procedures for the addition of amines onto itaconate polyesters require reaction times of several days as a result of undesired side reactions, in particular, the formation of the less reactive mesaconate regioisomer. The slow reversion of the mesaconate back to itaconate, followed by subsequent amine addition, is the primary reason for such extended reaction times. Herein we report our efforts toward finding a suitable catalyst for the aza-Michael addition of diethylamine onto a model substrate, dimethyl itaconate, with the aim of being able to add amine onto the itaconate units without excessive regioisomerization to the inactive mesaconate. A catalyst screen showed that iodine on acidic alumina results in an effective, heterogeneous, reusable catalyst for the investigated aza-Michael addition. Extending the study further, itaconate polyester was prepared by *Candida Antartica Lipase B* (CaL-B) via enzymatic polytranesterification and subsequently modified with diethylamine using the iodine on acidic alumina catalyst, dramatically reducing the required length of reaction (>70% addition after 4 h). The approach represents a multidisciplinary example whereby biocatalytic polymerization is combined with chemocatalytic modification of the resultant polyester for the formation of useful bio-based polyesters.

Keywords: biopolymer, itaconic acid, enzymatic polycondenzation, heterogeneous catalyst, Michael addition, mesaconate

OPEN ACCESS

Edited by:
Svetlana Ivanova,
Universidad de Sevilla, Spain

Reviewed by:
Dimitrios Bikiaris,
Aristotle University of Thessaloniki, Greece
Vincent Blay,
The Ohio State University, United States

***Correspondence:**
Alessandro Pellis
ale.pellis@york.ac.uk
Thomas J. Farmer
thomas.farmer@york.ac.uk

Specialty section:
This article was submitted to Green and Sustainable Chemistry, a section of the journal Frontiers in Chemistry

Received: 15 May 2019
Accepted: 01 July 2019
Published: 15 July 2019

Citation:
Moore OB, Hanson P-A, Comerford JW, Pellis A and Farmer TJ (2019) Improving the Post-polymerization Modification of Bio-Based Itaconate Unsaturated Polyesters: Catalyzing Aza-Michael Additions With Reusable Iodine on Acidic Alumina. Front. Chem. 7:501. doi: 10.3389/fchem.2019.00501

INTRODUCTION

An over-reliance of the chemical industry on non-renewable feedstocks has resulted in an ever growing interest in the utilization of bio-derived platform molecules to substitute petroleum-derived base chemicals as fundamental building-blocks for the synthesis of higher value products (Werpy and Petersen, 2004; Farmer and Mascal, 2014). Due to the sheer volumes produced coupled with enormous diversity of applications, it is not surprising that the field of polymer science has shown particular interest in using platform molecules to sustainably source monomers or monomer precursors (Mathers, 2012; Gandini and Lacerda, 2015; Isikgor and Becer, 2015; Llevot et al., 2016; Zhu et al., 2016). Plastics such as poly(lactic acid) (PLA), poly(butylene succinate) (PBS), and poly(ethylene furanoate) (PEF) demonstrate how polymers with favorable properties can be partly or wholly derived from platform molecules. A more recent trend has been toward the synthesis of functionalizable polymers and in particular, the polymerization of common platform molecules, itaconic acid, muconic acid, and fumaric acid with a range of diols/polyols such as 1,2-ethanediol, 1,2-propandiol, 1,3-propandiol, 1,4-butanediol, and glycerol (**Figure 1**) and to produce novel, 100% bio-derived unsaturated polyesters (UPEs) (Fonseca et al., 2015, 2017; Robert and Friebel, 2016; Rorrer et al., 2016; Costa et al., 2017; Kumar et al., 2017; Patil et al., 2017; Farmer et al., 2018a). Synthesis of these sustainable UPEs often employs conventional melt polymerization methods using well established metal catalysts (Ti, Al, Sn, and Zn) (Sakuma et al., 2008; Chanda and Ramakrishnan, 2015; Farmer et al., 2015; Winkler et al., 2015; Rowe et al., 2016; Schoon et al., 2017). Although valuable C=C groups present on such monomers offer enhanced functionality to the UPEs, they can also create many issues with the formation of undesired side reactions during the polymerization. In the case of itaconates, fumarates, and muconates typical side reactions include isomerization, radical cross-linking (**Figure 2A**) and Ordelt saturation (an oxo-Michael addition where an R-OH end-group attacks the conjugated C=C through a β-addition, **Figure 2B**; Farmer et al., 2015; Schoon et al., 2017).

To prevent radical crosslinking during conventional polyesterification of such monomers, scavengers such as quinol (Chanda and Ramakrishnan, 2015) and 4-methoxyphenol are used as quenchers (Schoon et al., 2017). Enzyme catalyzed polytransesterifications have proven somewhat effective in limiting isomerization but achieving high degrees of polymerization and efficient scaling-up these methods had proven elusive (Corici et al., 2015; Pellis et al., 2015). Limiting Ordelt saturation has proven even harder to achieve, most likely due to the fact that Lewis acid catalysts promoting polytransesterification will also increases the ability of the conjugated C=C to act as a Michael acceptor to a hydroxyl end-group. Once extensive crosslinking occurs the resultant UPEs, for example when using itaconates, are typically soft and rubbery and thus are only suitable for applications which do not require inherent strength (Singh et al., 1991; Guo et al., 2011; Wei et al., 2012; Dai et al., 2015a,b,c). Undesirable isomerization of the C=C is also widely reported for UPEs of itaconate, muconate fumarate, and maleate monomers, with the latter two able to interchange between one another (**Figure 3A**). In the case of itaconate containing polyesters, regioisomerization during polyesterification results in the formation of mesaconate (major) and citraconate (minor) units (**Figure 3B**). Formation of these regio-isomer units lead to greater complexity in the analysis of the polyesters, whilst also effecting reproducibility of the polymers final thermal and mechanical properties.

Previous research has continually observed regioisomerization of itaconate during polyester synthesis. The extent of this undesired reaction ranges from <10% (relative to itaconate) as described by Teramoto (9%) (Teramoto et al., 2005), Farmer (8%) (Farmer et al., 2015), and Spavojevic (7%) (Panic et al., 2017), increasing up to nearly 60% in the Takasu's protocol using itaconic anhydride as the monomer (Takasu et al., 1999). In the majority of the above examples the typical reaction conditions are elevated temperatures above 160°C, high vacuum to remove excess diol and relatively long reaction times and acidic catalysts or polymer chain ends; these conditions contribute to the promotion of mesaconate formation. The most effective method to avoid underdesired regioismerization during polycondenzation is to carry out the reaction under milder enzyme-catalyzed conditions (Pellis et al., 2019). However, regioisomerization has also been reported to occur during addition of pendants to free unsaturated sites, with a significantly increased proportion of mesaconate being seen for high (>75%) but not complete addition (Clark et al., 2009; Farmer et al., 2016). Pendant addition to itaconate UPEs remains a very desirable pathway as significant alterations to the polymers physical properties can be achieved, whilst the pendants themselves exhibit behavior such as metal chelation. Several recent studies have demonstrated post-polymerization modification (PPM) of bio-based UPEs, allowing these polyester backbones to be altered via facile Michael additions (Fonseca et al., 2015, 2017; Robert and Friebel, 2016; Rorrer et al., 2016; Costa et al., 2017; Kumar et al., 2017; Patil et al., 2017; Farmer et al., 2018a). Additions of thiols, amines and metal-chelating 1,3-dicarbonyls to bio-based UPEs have been recently demonstrated, tailoring the properties of the polyesters to suit a range of applications (Lv et al., 2014; Chanda and Ramakrishnan, 2015; Farmer et al., 2016). For example Hoffmann et al. showed that amine pendant addition to itaconate polyesters can tune the hydrophilicity of resultant gels and be tailored depending on the choice of amine donor (Hoffmann et al., 2015). Amine pendant itaconate polyesters have recently been used to produced temperature switchable materials, with examples of low-temperature depolymerization promoted by primary amine addition (Guarneri et al., 2019) or secondary amine release at elevated temperatures (>190°C) (Pellis et al., 2019). However, in many instances long reaction times for the addition of the pendants are quoted with little or no discussion as to why this is necessary. Lv et al. reported the need for 14–20 h reaction times for the addition of thiols and amines, despite the Michael donors being used in a 15-times molar excess (Lv et al., 2014). Chanda reported 3 day long additions of both thiols and amines to poly(dodecyl itaconate) UPEs (Chanda and

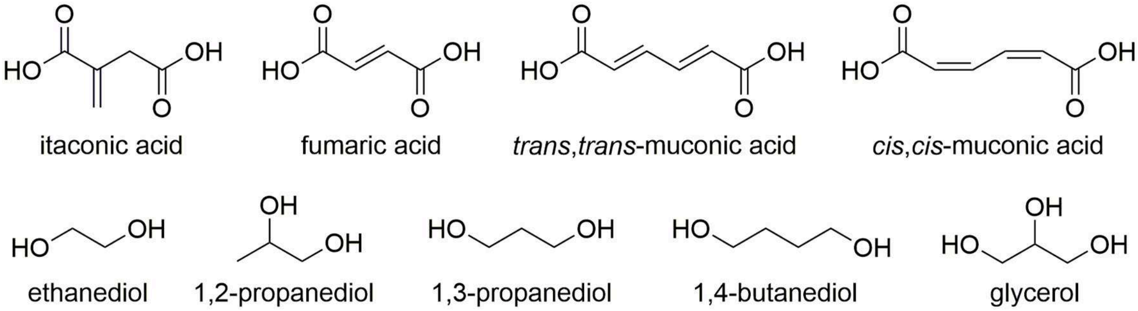

FIGURE 1 | Common bio-derivable unsaturated diesters, diols, and polyols used in the synthesis of unsaturated polyester resins (UPEs).

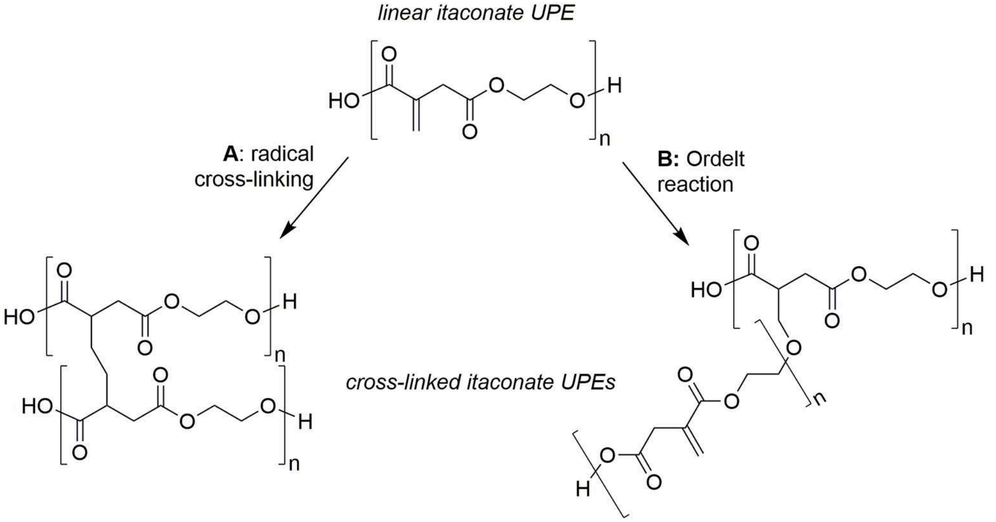

FIGURE 2 | Typical undesired side-reactions of bio-based unsaturated polyesters (UPEs), example for poly(ethylene itaconate). **(A)** Radical induced cross-linking via C=C, **(B)** Ordelt saturation (oxo-Michael addition of –OH end-group onto C=C) inducing crosslinking.

Ramakrishnan, 2015), while Winkler published thio-Michael additions that ran overnight using a 5-times molar excess of donor, and requiring 10 mol% hexylamine as a catalyst (Winkler et al., 2015). In a recent study it was shown that during aza-Michael addition of diethyl amine (DEA) onto dimethyl itaconate (DMI, a mimic for the itaconate unit in polyesters) regioisomerization (k_2) is in direct competition with desired addition (k_1) (**Figure 4**; Farmer et al., 2018b). Mesaconate (DMMes) formation was proven to be catalyzed by the amine Michael donor (DEA) but because the DMMes itself does not act as an acceptor (compounds **2** or **3** were not detected, **Figure 4**) the lengthy reaction times were deemed to be necessary. These long reaction times were found to be a result of the slow reformation of DMI from DMMes (k_2^*, **Figure 4**), with k_2^* being an order of magnitude slower than k_1. It was deduced that a suitable catalyst might be able to selectively catalyze the desired aza-Michael addition before extensive undesired regioisomerization occurs, resulting in significantly reduced post-polymerization modification reaction times from several days to just hours. Herein we report a study into finding a suitable catalyst for the aza-Michael addition of DEA onto DMI and an extension of this method to an addition onto poly(1,8-octylene itaconate) UPE.

MATERIALS AND METHODS

Chemicals and Enzymes

Dimethyl itaconate (DMI) and cerium (III) ammonium nitrate (CAN) were purchased from Alfa Aesar. Cerium (IV) ammonium nitrate (CAN) was purchased from FSA. All other chemicals and solvents were purchased from Sigma-Aldrich and used as received if not otherwise specified. For the powdered supports used as received in this study the following information is available from the supplier (Sigma-Aldrich): acidic alumina (19996-6), Brockmann I, 58 Å pore size, 150 mesh; neutral alumina (199974), Brockmann I, 58 Å pore size; basic alumina (199443), Brockmann I, 58 Å pore size; silica K60 (60738), 60 Å pore size, 220–240 mesh. *Candida Antarctica* lipase B (CaLB) immobilized onto methacrylic resin was purchased from Sigma-Aldrich (product code L4777, also known as Novozym 435). The enzyme was dried under

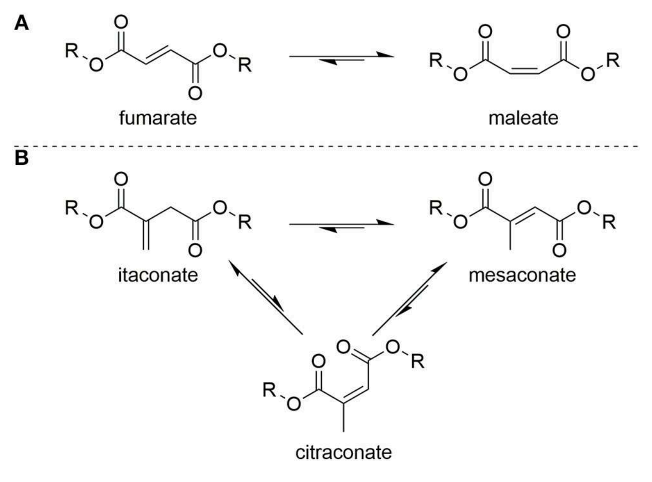

FIGURE 3 | Isomerization between **(A)** fumarate and maleate units in UPEs or **(B)** itaconate and mesaconate/citraconate units in UPEs.

vacuum for 96 h at 25°C and stored in a desiccator prior to use.

Preparation of CAN on Silica

Immobilization 1: To a 50 mL round bottomed flask, 1 gram from K60 silica gel was added with 0.2 mmols (109.7 mg) of $(NH_4)Ce(NO_3)_6$ and 20 mL of MeOH. Equipped with a reflux condenser, the solution was stirred slowly using a magnetic stirrer bar, at room temperature for 2 h. The solvent was then slowly evaporated over an hour under increasing reduced pressure until 10 mbar vacuum was achieved. The resultant bright orange material was then place under high vacuum (<1 mbar) for 2 h and then stored under an inert purge until required. Actual quantities used resulted in a loading of 0.156 mmol g^{-1} CAN on silica.

Immobilization 2: Increased concentrations of physisorbed $(NH_4)Ce(NO_3)_6$ were prepared as shown above, but using 0.5 mmol of $(NH_4)Ce(NO_3)_6$ with 1 g of silica giving a loading of 0.403 mmol g^{-1}.

Preparation of Iodine on Alumina or Silica

For the generation of the various forms of iodine (I_2) on alumina or silica, the standard loading of I_2 was 0.1 mmol (as $I_2 \equiv$ 0.2 mmol elemental I) per gram of alumina/silica (Deka and Sarma, 2001). To create this, 0.3804 g of I_2 was dissolved in 30 mL dichloromethane, before 15 g of the either alumina or silica was added to the reaction mixture. This suspension was then stirred for 30 min, before the excess solvent was removed under reduced pressure at 40°C. The orange/red powder obtained was then left to dry fully overnight before use. For higher loadings the iodine amount was multiplied (2x, 3x, and 4x) as required while all other reagent amounts and procedures were followed as above.

Enzymatic Polycondenzation for Formation of Poly(1,8-Octylene Itaconate) (POI)

The solventless synthesis procedure was taken from previous literature (Pellis et al., 2018, 2019). Briefly: 6 mmols of dimethyl itaconate and 6 mmols of 1,8-octanediol were accurately weighed into a 25 mL round bottom flask. The mixture was then stirred at 85 °C until a homogeneous melt was obtained. Ten percent w w^{-1} calculated on the total amount of the monomers of Novozym 435 was then added to the reaction mixture. The reactions were run for 6 h at 1,013 mbar. A vacuum of 20 mbar was subsequently applied for an additional 18 h maintaining the initial reaction temperature (total reaction time: 24 h). The reaction product was recovered by adding THF to dissolve the POI, the supported CaLB catalyst was removed *via* vaccum-assisted Buchner filtration (Fisherbrand filter paper QL100, 70 mm diameter), and the solvent from the filtrate evaporated under vacuum to yield the POI polymer product. The polymer was characterized (^1H-NMR spectroscopy in $CDCl_3$, **Figure S10**) without any additional purification steps prior to use.

Aza-Michael Addition of Diethylamine (DEA) Onto Dimethyl Itaconate (DMI) Using Cerium Catalysts

2.5 mmol of dimethyl itaconate and the selected catalyst (2 mol% Ce relative to DMI) were accurately weighed into an 8 mL flat bottomed sample vial. Twenty millimoles of diethylamine was added to the reaction and stirred at room temperature for 2 or 6 h when kinetic studies were made (taking aliquots at 2 hourly intervals for analysis by ^1H-NMR spectroscopy, $CDCl_3$ solvent). For the recovery of the catalyst the reaction mixture was filtered via vacuum-assisted Buchner filtration (Fisherbrand filter paper QL100, 70 mm diameter), with no solvent washing, the collected catalyst was left to air-dry over night between reuses.

Aza-Michael Addition of Diethylamine (DEA) Onto Dimethyl Itaconate (DMI) Using Molecular Iodine Catalysts

2.5 mmol of dimethyl itaconate and the selected amount of catalyst (no catalyst, 1.5, 5, 12.5 mol% of I_2 relative to DMI) were accurately weighed into an 8 mL flat bottomed sample vial. Twenty millimoles of diethylamine was added to the reaction and stirred at room temperature for 2 h. An aliquot of the reaction mixture was dissolved in $CDCl_3$ for analysis by ^1H-NMR spectroscopy.

Aza-Michael Addition of Diethylamine (DEA) Onto Dimethyl Itaconate (DMI) Supported Iodine Catalysts

2.5 mmol of dimethyl itaconate and the selected catalyst (5%mol w.r.t. I_2 per mole of DMI = 1.28 g of standard catalyst 1x loading catalyst) were accurately weighed into an 8 mL flat bottomed sample vial. Twenty millimoles of diethylamine was added to the reaction and stirred at room temperature for 2 h. The catalyst was removed by filtration and an aliquot of the filtrate was dissolved in $CDCl_3$ for analysis by ^1H-NMR spectroscopy. For the recovery of the catalyst the reaction mixture was filtered *via* vacuum-assisted Buchner filtration (Fisherbrand filter paper QL100, 70 mm diameter), with no solvent washing, the collected catalyst was left to air-dry over night between reuses. A dry free-flowing powder was obtained from each air drying. For the iodine

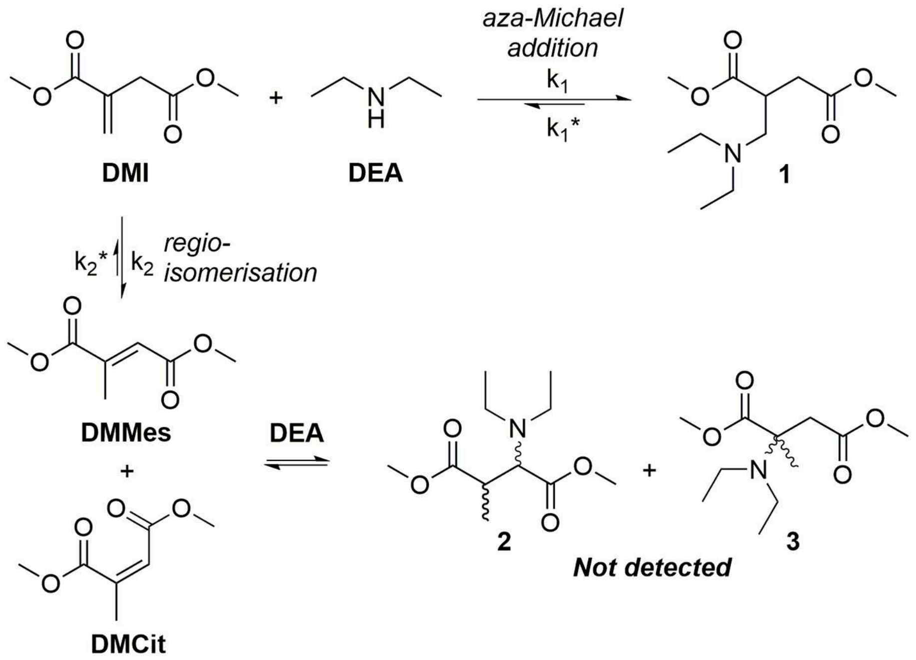

FIGURE 4 | Competitive reaction between either the addition of diethyl amine (DEA) to dimethyl itaconate (DMI) or regioisomerization of DMI to form dimethyl mesaconate (DMMes, dominant isomer) or dimethyl citraconate (DMCit, minor isomer).

on alumina loading study the relative quantity of I_2 (relative to DMI) was increased to 12.5%mol.

Extended Recovery and Reuse (10 Cycles) of Iodine on Acidic Alumina for the Aza-Michael Addition of Diethylamine (DEA) Onto Dimethyl Itaconate (DMI)

2.5 mmol of dimethyl itaconate and 1.28 g of 0.1 mmol g^{-1} I_2 on Al_2O_3 catalyst (5%mol w.r.t. I_2 per mole of DMI) were accurately weighed into an 8 mL flat bottomed sample vial. 20 mmol of diethylamine was added to the reaction and stirred at room temperature for 2 h. The catalyst was removed via vacuum-assisted Buchner filtration (Fisherbrand filter paper QL100, 70 mm diameter), with no solvent washing, the collected catalyst was left to air-dry over night between reuses. For each used an aliquot of the filtrate was dissolved in $CDCl_3$ for analysis by ^{1}H-NMR spectroscopy.

Aza-Michael Addition of Diethylamine (DEA) Onto Poly(1,8-Octyleneitaconate) (POI)

2.5 mmol of POI (0.6 g, based on constitutional repeat unit of 240.29 g mol^{-1}) and 0.64 g of 0.2 mmol g^{-1} I_2 on Al_2O_3 catalyst were accurately weighed into an 8 mL flat bottomed sample vial. Twenty millimoles of diethylamine was added to the vial and stirred for 24 h with aliquots taken at various intervals for analysis by ^{1}H-NMR spectroscopy ($CDCl_3$ solvent). After 24 h the reaction mixture was filtered to remove the spent catalyst (where used), excess DEA was removed *in vacuo* and the resultant viscous polymer analyzed by ^{1}H-NMR ($CDCl_3$ solvent) to compare against known previous literature characterization for this material (Pellis et al., 2019). For the non-catalyzed reaction 0.52 g and 0.54 g (duplicate) of polymer was recovered, for the catalyzed reaction 0.33 g and 0.22 g (duplicate) of polymer was recovered.

Nuclear Magnetic Resonance (NMR) Spectroscopy

^{1}H, ^{13}C, DEPT and HMQC NMR spectroscopic analysis were performed on a JEOL JNM-ECS400A spectrometer at a frequency of 400 MHz. $CDCl_3$ was used as the NMR solvent for itaconate-based polymers and for the aza-Michael addition experiments.

Gel Permeation Chromatography (GPC)

GPC was carried out using a PSS SDV High set composed of 3 analytical columns (300 × 8 mm, particle diameter 5 μm) of 1,000, 1,000 × 10^5 and 10^6 Å pore sizes, plus guard column (Polymer Standards Service GmbH, PSS) installed in a PSS SECcurity SEC system. Elution was with THF at 1 mL min^{-1} with a column temperature of 30 °C and detection by refractive index. Twenty microliter of a ∼2 mg mL^{-1} sample in THF, adding a drop of toluene as reference standard, was injected for each measurement and eluted for 50 min. Calibration was carried out in the molecular weight range 370–25,20,000 Da using the ReadyCal polystyrene standards supplied by Sigma Aldrich and referenced to the toluene peak.

Nitrogen Porosimetry

Nitrogen adsorption measurements were carried out at 77 K using a Micromeritics Tristar Porosimeter. Prior to analysis, the catalyst samples were outgassed at 180°C for 8 h under a flow of nitrogen gas. The specific surface areas were evaluated using the Brunauer–Emmett–Teller (BET) method in the P/P_0 range 0.05–0.3 (linear range). Pore size distribution curves were calculated using the adsorption branch of the isotherms and the Barrett–Joyner–Halenda (BJH) method, and pore sizes were obtained from the peak positions of the distribution curves.

Thermogravitmetric Analysis (TGA)

TGA was performed on a PL Thermal Sciences STA 625 thermal analyzer. 10 mg of sample was weighed into an aluminum cup, placed in the furnace with a N_2 flow of 100 mL min^{-1} and heated from 30 to 625°C at a heating rate of 10°C min^{-1}.

RESULTS AND DISCUSSION

Aza-Michael addition onto unsaturated polyesters are typically performed without catalyst, however as previously mentioned this requires extensive reaction times (Blaha et al., 2018; Pellis et al., 2019). Contrastingly, catalysts are often used for aza-Michael additions when synthesizing drug molecules, allowing lower activation energies and thus increased rates of reaction. Example catalysts include boric acid (Chaudhuri et al., 2005), lipases (Dhake et al., 2010), sulfonated zirconia (Reddy et al., 2008), copper(II) acetylacetonate (Kantam et al., 2005), and indium trichloride (Yang et al., 2007) but more commonly observed is the use of lanthanide metal-centered catalysts (e.g., SmI_2 Reboule et al., 2005 and $Yb(OTf)_2$ Jenner, 1995). Such catalysts have been shown to be particularly efficient for promoting aza-Michael additions, their activity assumed to be a result of Lewis acid behavior drawing electron density away from the C=C and making the β-position

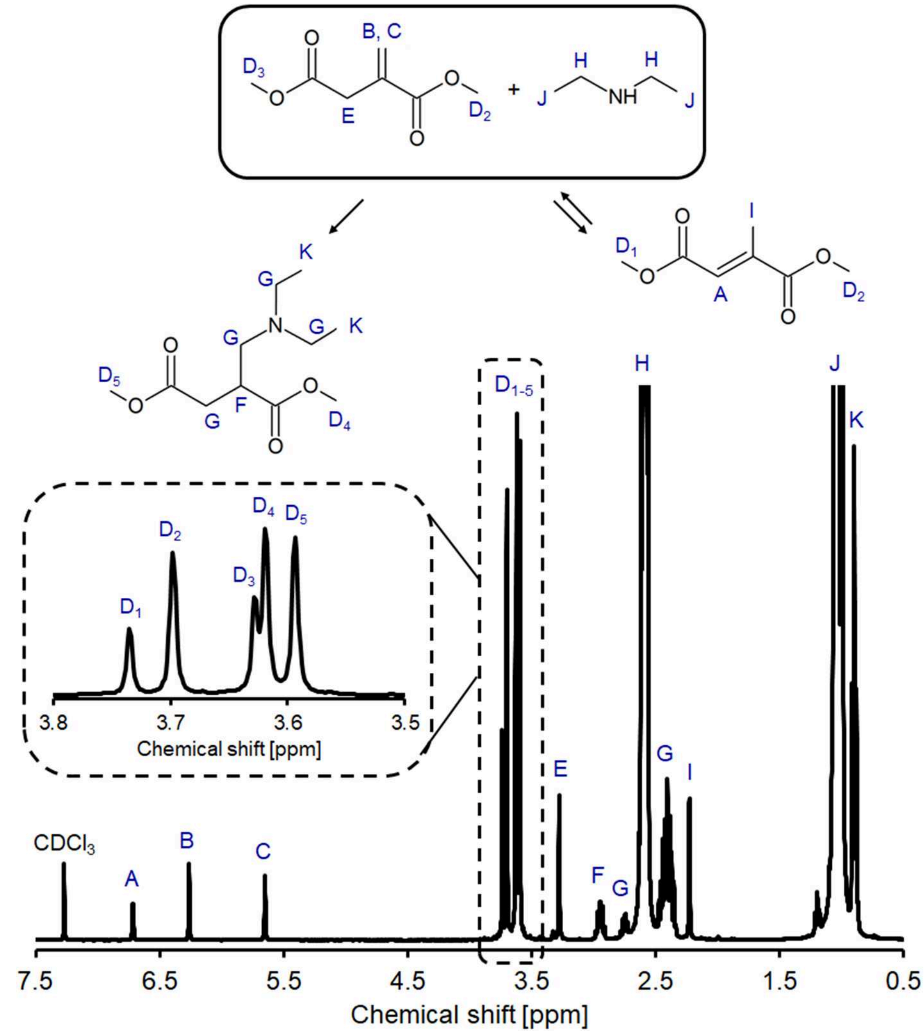

FIGURE 5 | Example ^1H NMR spectrum of the crude product from aza-Michael reaction between DMI and DEA with 3.8–3.5 ppm expanded region of the spectrum shown. Spectra of the crude reaction mixture was recorded in $CDCl_3$ after 2 h of reaction.

more susceptible to attack from the nucleophilic amine. Of the lanthanide series, cerium (Ce) is one of the most intriguing as it can readily switch between the (IV) and (III) oxidation states whereas other lanthanides generally tend to only be stable in the (III) oxidation state. Cerium's (IV) state has high oxidizing power (Kilbourn, 1986) and high redox potential meaning that cerium has been widely used as a single electron oxidant, though the salts of cerium as Lewis acids have received somewhat less attention (Sridharan et al., 2007).

Investigations Into Cerium Ammonium Nitrate as a Catalyst for Aza-Michael Additions

Cerium ammonium nitrate (CAN) is one of the most documented amongst the cerium-based catalysts (Sridharan and Menendez, 2010; So and Leung, 2017). CAN is able to act as a catalyst for a multitude of reactions, including carbon-nitrogen bond forming reactions such as aza-Michael additions (Nair and Deepthi, 2007) and has the benefit of being widely available and relatively cheap. Furthermore, it has also been shown to be an efficient catalyst toward both aliphatic and aromatic amine additions to Michael acceptors, thus offering a broad substrate scope (Duan et al., 2006).

Despite its high activity, recycling of cerium complexes as catalysts has not been well-documented in the literature and whilst a recent review (Molnar and Papp, 2017) on catalyst recycling mentioned two cerium containing complexes, both catalysts had cerium as a minor component. As such, we additionally sought to find an appropriate means of catalyst recovery and reuse in this work.

In alignment with our previous study into the un-catalyzed addition of amines on polyesters (Farmer et al., 2018b; Pellis et al., 2019), we first elected to study the room temperature addition of DEA using DMI as a model compound (**Figure 4**) representing the UPRs constitutional repeat unit (CRU). Use of a small model compound also aided analysis and avoided issues of changing reaction viscosity and consequently, effects of mass transfer. ^{1}H NMR analysis of the DMI and DEA reaction mixture showed peaks **A** and **I,** confirming the presence of regioisomerization product DMMes (**Figure 5**). Peak **H** shows CH_2 of the excess unreacted DEA, whilst there is significant overlap between the amine protons and CH_3 peaks **J**, making these unquantifiable for some samples. Peaks **F** is a complex multiplet as the surrounding H atoms are inequivalent, with a similar observation seen for signal **G**. To calculate the relative amounts of DMI and DMMes, peaks labeled **D** (methyl ester groups, CO_2CH_3) were integrated as 6 protons. These peaks are expanded in **Figure 5** to demonstrate the detectable difference. Although 6 different environments are possible for the methyl ester groups only five signals are observed; **D2** is a combination of the unsaturated ester of DMI and one of the ester groups of DMMes. Using these signals we were able to quantify the relative molar ratios of DMI (**D2** + **D3**), DMMes (**D1** + **D2**) and desired adduct **1** (**D4** + **D5**) during the course of reaction. The following equation was used (PI = peak integral):

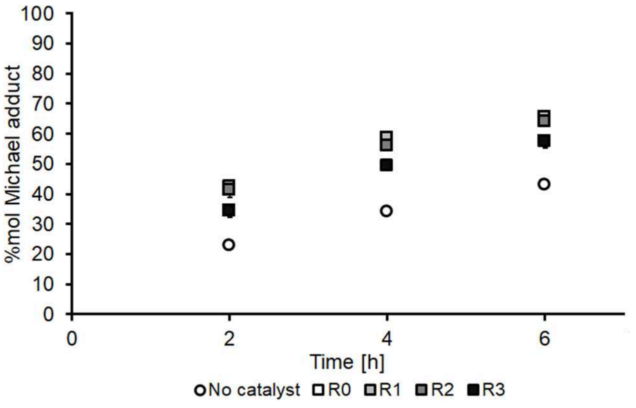

FIGURE 6 | Time course for aza-Michael addition of DEA onto DMI using CAN(IV) as catalyst, showing the first use (R0) and the subsequent three recycles (R1–R3) of the free catalyst and comparison to the no catalyst control. All experiments were performed in duplicates and are shown in the figure as the average of two independent experiments ± the standard deviation. The catalyst was used as received (Sigma-Aldrich) without pre-treatment.

$$\%\ adduct\ \mathbf{1} = 100\ x\ \frac{(PI_{D4} + PI_{D5})}{(PI_{D1} + PI_{D2} + PI_{D3} +\ PI_{D4} + PI_{D5})} \quad (1)$$

As shown in **Figure 6**, non-immobilized CAN(IV) (**Figure 6**, R0, white boxes) noticeably increases the formation of aza-adduct over the studied timescale (2–6 h) relative to the conventional un-catalyzed system (**Figure 6**, white circles). Interestingly, the CAN(IV) catalyst remained insoluble in the reaction media for the duration of the reaction and was therefore investigated as a potentially recoverable and reusable heterogeneous catalyst (**Figure 6**, R1–R3, shades of gray boxes). However, CAN's activity was found to steadily decrease upon re-use, particularly upon the third reuse (R3, **Figure 6**). As such, experiments were conducted to further understand the mechanism of the catalyst deactivation in the DMI + DEA model system, in the hope that it would highlight approaches to both improved adduct yield and enhanced catalyst recycling.

The reduction of Ce(IV) to Ce(III), with regeneration of Ce(IV) by an external oxidant was considered as one possible mechanism of catalysis. If this was the case, it was thought that the addition of a constant supply of oxygen to act as an oxidizing agent for Ce(III), would improve the recyclability allowing Ce(IV) to be constantly regenerated. However, as shown in **Figure S1**, this was not successful, where the two Ce oxidation states might exhibit similar activity and the addition reaction could be independent of oxidation state. Decrease in catalytic activity of the recycled catalyst was possibly due to the CAN itself deactivating overtime. CAN(IV) has 2 ammonium and 6 nitrate groups, and CAN(III) has 2 ammonium and 5 nitrate groups. In order to test whether the CAN(IV) was losing its nitrate groups, and consequently catalytic ability, the molar equivalent of sodium nitrate was added to the reaction on CAN's 4th recycle in an attempt to regenerate the CAN(IV). However, there appeared to be little benefit in addition of the sodium nitrate to prevent deactivation of either CAN(III) or CAN(IV), though the latter did show a slightly higher activity after 4 reuses with nitrate addition (**Figure S2**).

Activity of CAN (IV) and CAN(III) was shown to exhibit slight differences, where CAN(IV) was found to be more efficient at maintaining recyclability but the CAN(III) more efficient for the initial run. The increasing ionic charge might explain this, where increased Lewis acid capability allows CAN(IV) to act as a better catalyst. As for explaining the cases where CAN(III) is a better catalyst, further experiments were conducted. Michael additions with CAN were attempted with various amines to see how steric bulk affected the Michael addition and further probe differences between the two oxidation states; **Figure S3** shows the dipropylamine (DPA, **Figure S3A**) and dibutylamine (DBA, **Figure S3B**). Interestingly, the difference between CAN(IV) and CAN(III) appears to increase with increasing steric bulk of the amine. Dicyclohexane (DCHA) and diisopropylamine (DIPA) were also tested however no reaction appeared to take place, most likely due to the much more bulky sterics of diisopropyl and cyclohexyl groups. Ce(III) is a bigger ion due to reduced orbital contraction and the increased relative size may have the effect of allowing increasing co-ordination with substrates. This together with one less nitrate group and the increased nucleophilicity of dibutylamine (and relatively small increase in sterics in comparison with the propyl group) might explain the increase rates of reaction seen with the large amine group and Ce(III).

Another consideration was that the Michael adduct, **1**, might be hindering the catalytic ability of CAN (both III and IV). Therefore, prior to the Michael addition reaction, CAN(IV) and CAN(III) were stirred for 2 h with a small amount of purified product **1**, this was then removed before performing the reaction as normal. The results are shown in **Figure S4** (**Figure S4B**, shows a comparison without this extra pre-reaction step). Initial observations suggest that the addition of product **1** actually improves the reaction; however this is very unlikely to be the case. Incomplete removal of the addition product from the CAN increases the amount of addition product in the reaction, which invalidates the experiment. However, considering the increases in adduct yield as time passes, it is reasonable to conclude that the addition product had no effect, positive or negative, on the catalytic ability of CAN.

Interestingly, a consistent observation was that the CAN(IV) catalyst starts as an orange powder, but after the first reuse the color changes dramatically to give a brown sticky residue that adheres to the side of the reaction vessel. It was considered that this change in physical state might reduce available reactive surface area as well as the catalyst structure itself. In order to avoid agglomeration of the catalyst to a residue, CAN (IV) was physisorbed on to silica, with the aim of retaining small particle sizes with good accessibility. Two different loadings of CAN(IV) on silica were prepared to investigate the effect of loading on reuse and catalytic activity. **Figure S5** shows a comparison of catalytic activity between the free and two different immobilized CAN(IV) catalysts and surprisingly, the same loss of activity after reuse is observed and appears to be independent of catalyst loading. Although catalytic activity appears not to be a result of surface area loss, the immobilized CAN(IV) was more easily recovered a reused and therefore this approach still offers some merit, despite not overcoming the catalyst deactivation.

Alternative Catalysts to CAN for Aza-Michael Additions

CANs deactivation issues led us to search for alternative catalysts for the reaction between DMI and DEA. Complexes containing trifluoromethanesulfonate (OTf) ligands are known to be useful in metal-centered catalysis due to their ability to make the central metal ion highly electrophilic, and further to this, there have been many literature reports of complexes containing OTf being recyclable as well as efficient for Michael additions (Kobayashi et al., 1992). Both Ce(IV) and Ce(III) OTf were tested and initially showed much more promising yields to Michael adduct **1**, being considerably higher than those achieved with the CAN catalyst (**Figure 7A**). Unfortunately, **Figure 7B** shows that the catalytic ability of CeOTfs reduces significantly upon reuse, achieving similar conversions to the non-catalyzed background syntheses, suggesting almost total deactivation. A comparison between the two oxidation states for the OTf salts showed that the 4+ state is a better catalyst until it is consumed or made ineffective, thereafter the 3+ state dominants, contrary to the trend observed for the CAN catalysts. It is possible that in CeOTf, Lewis acidity is the primary mechanism of catalysis (more so than the CAN) in which case a more electrophilic Ce(IV) is a better Lewis acid.

This data led us to seek an alternative to lanthanide catalysts. A further screen of the literature suggested molecular iodine (I_2) as a promising candidate since it is reported to catalyze the addition of various aliphatic Michael acceptors and donors at high yields (>80%) (Borah et al., 2010). The amount of catalyst (based on relative %mol of I_2 to Michael acceptor) was screened at 1.5, 5, and 12.5%mol (entries 2–4, **Table 1**). Molecular iodine gave impressive yields (76–90%) for all three loadings, giving considerably higher yields than using no catalyst (entry 1, 26–28%), and producing limited amounts of the unwanted DMMes isomer. However, the molecular I_2 dissolved entirely in the excess of DEA, making it unrecoverable. Saikia et al. previously showed that I_2 can be supported onto alumina and used for other aza-Michael additions. This approach was therefore considered and further investigated (Saikia et al., 2009). Acidic alumina (i.e., without I_2), used as received, was found to have no catalytic ability (entry 5, **Table 1**), giving similar results to the no catalyst system (entry 1) with the exception of a slight increase in the isomerization of DMI to DMMes. The low catalytic ability of acidic alumina differs from observations of Bosica and Abdilla who found it to be suitable catalyst for aza-Michael additions of aromatic amines (Bosica and Abdilla, 2016). However, acidic alumina was found to be a suitable support for supporting I_2. Using the preparation method given by Deka and Sarma a free-flowing heterogeneous catalyst was prepared and found to give reasonable yields of adduct even upon recovery (*via* vacuum-assisted Buchner filtration and air drying) an subsequent reuse (entry 6, **Table 1**; Deka and Sarma, 2001). Nitrogen porosimetry (**Figure S6**) showed the BET surface area of the acidic alumina (120 m^2 g^{-1}) decreased slightly upon supporting 0.1 mmol g^{-1}

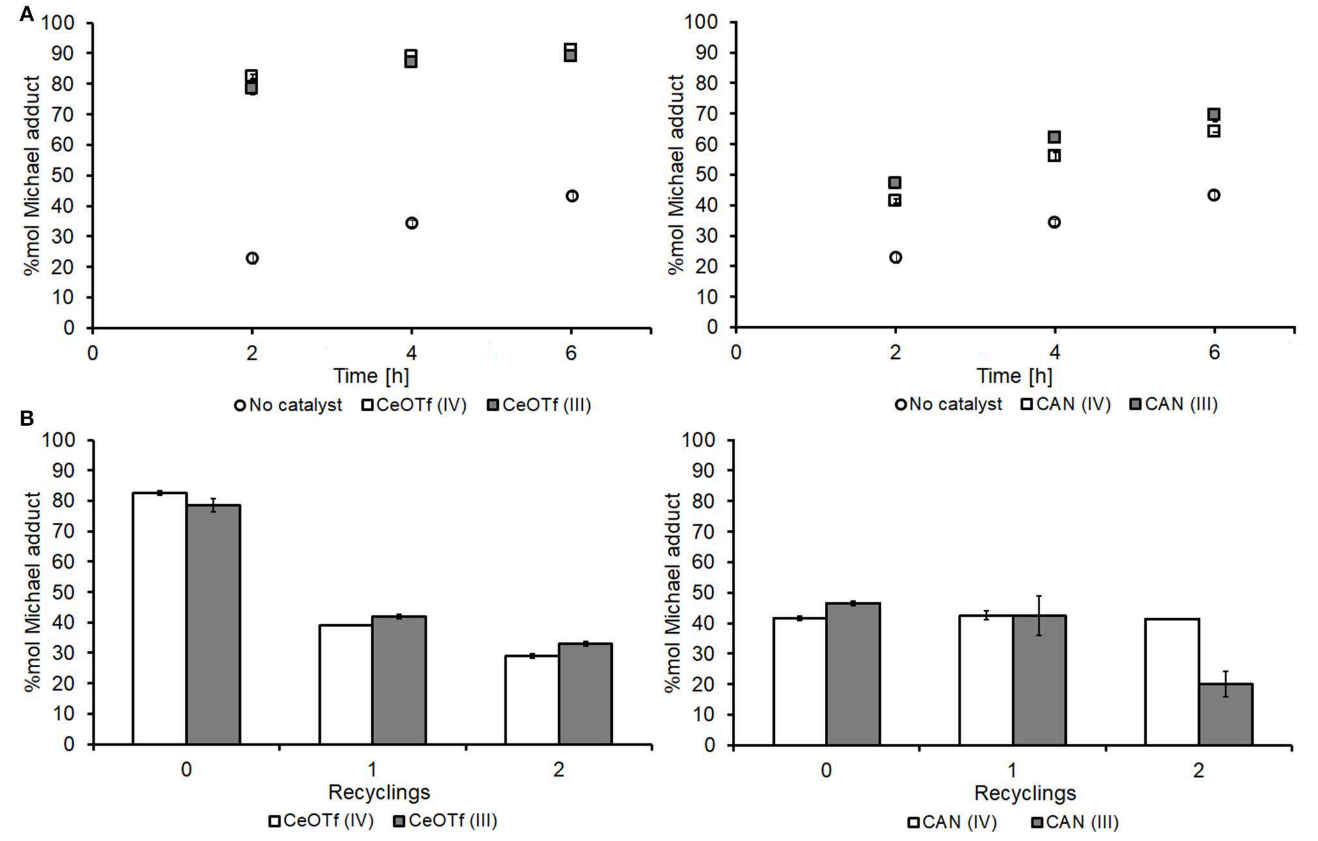

FIGURE 7 | Comparison and recyclability of the CAN vs. the CeOTf catalysts. **(A)** Time course of the aza-Michael addition of DEA on DMI using the CeOTF (left) and the CAN (right) catalysts alongside no catalyst control; **(B)** recyclability of the CeOTf (left) and the CAN (right) catalysts. Spectra of the crude reaction mixture was recorded in $CDCl_3$ after 2 h of reaction. All experiments were performed in duplicates and are shown in the figure as the average of two independent experiments ± the standard deviation. The catalysts were used as received (Sigma-Aldrich) without pre-treatment.

fresh I_2 (110 m^2 g^{-1}), and decreased further for the recovered catalyst (86 m^2 g^{-1}). Pore size distribution would suggest this reduction in surface area was a result of partial blocking of the mesopores (**Figure S7**), though despite this reduction in surface area the 0.1 mmol g^{-1} I_2 on acidic alumina maintained its catalytic ability upon reuse (entry 6, **Table 1**). Thermogravimetric analysis (TGA) corresponds to the porosimetry trends, showing the mass loss up to 625°C for the acidic alumina support (~5% loss, **Figure S8A**) increases slightly to 7–8% loss following 0.1 mmol g^{-1} loading of I_2 (**Figure S8B**). Of note is that the loss of I_2 does not appear to give a specific narrow temperature range for desorption, but instead seems to occur over a broad temperature range. The recovered catalyst's TGA trace (**Figure S8C**) shows an additional mass loss over the 30–220°C range, this attributed both to some residual amine (30–80°C, diethylamine b.p. is 55.5°C) and trapped itaconate, mesaconate, and adduct (100–220°C). The residual organics observed by TGA likely also caused the surface area and pore size reduction seen from porosimetry.

Equivalent supported forms of 0.1 mmol g^{-1} I_2 on neutral (entry 7, **Table 1**) and basic (entry 8, **Table 1**) alumina were also prepared and trialed for the addition of DEA to DMI, but the original system on acid alumina was found to remain superior. 0.1 mmol g^{-1} I_2 on K60 silica (I_2-SiO_2) was also assessed as a potential heterogeneous form of iodine (entry 10, **Table 1**), though this proved less efficient than the alumina supported systems. The I_2-SiO_2 seemingly promoted undesirable isomerization to a greater extent (>30%) compared to the other catalysts, an observation similarly observed for K60 silica without iodine (entry 9, **Table 1**). Amberlyst-15, an acidic heterogeneous resin, has also been reported to catalyze aza-Michael additions though for our substrate was found to have limited activity (entry 11, **Table 1**; Das and Chowdhury, 2007).

Extended Re-use Study for I_2 on Acidic Alumina

An extended recyclability study to 10 full cycles was carried out using the standard loading 0.1 mmol g^{-1} I_2 on acidic alumina catalyst (**Figure 8**) for the addition of DEA onto DMI. The first use and subsequent first four recycles retain good catalytic activity, whilst a slight reduction in activity was observed after the 5th recycle. Despite yields to adduct **1** dropping to ~48% for the last three uses, this remained considerably higher than with no catalyst at all (26–28% entry 1, **Table 1**, and **Figure 9**) or

TABLE 1 | Catalyst screen for the solvent-less reaction of DEA with DMI after 2 h.

Entry	Catalyst	1st or reuse	%mol DMI	%mol DMMes	%mol Michael adduct 1
1	No Catalyst	1st use	50	22	28
		Repeat	51	23	26
2	Iodine (I_2)[a] (1.5%mol)	1st use	13	20	67
		Re-use		Homogeneous—not recoverable and reusable	
3	Iodine (I_2)[a] (5%mol)	1st use	4	16	80
		Re-use		Homogeneous—not recoverable and reusable	
4	Iodine (I_2)[a] (12.5%mol)	1st use	9	1	90
		Re-use		Homogeneous—not recoverable and reusable	
5	Acidic alumina[b]	1st use	44	27	29
		Re-use	47	27	26
6	I_2 on acidic alumina (0.1 mmol g^{-1} I_2 loading)	1st use	6	21	73
		Re-use	4	22	74
7	I_2 on neutral alumina (0.1 mmol g^{-1} I_2 loading)	1st use	20	27	53
		Re-use	14	28	58
8	I_2 on basic alumina (0.1 mmol g^{-1} I_2 loading)	1st use	5	25	70
		Re-use	7	24	69
9	K60 silica[c]	1st use	41	29	30
		Re-use	35	30	35
10	I_2 on K60 silica (0.1 mmol g^{-1} I_2 loading)	1st use	22	35	43
		Re-use	14	31	55
11	Amberlyst-15 (0.25 g)	1st use	40	29	31
		Re-use	26	34	40

2.5 mmol DMI, 20 mmol DEA, 5%mol (w.r.t. I_2 per mole of DMI = 1.28 g of standard catalyst) catalyst unless otherwise stated, stirred for 2 h at room temperature, analysis by NMR spectroscopy ($CDCl_3$ solvent).

[a] *Molecular iodine had no Run 2 as it was not recoverable from the reaction mixture.*

[b] *Mass of acidic alumina used equals that used for I_2 on alumina catalyst (1.25 g).*

[c] *Mass of K60 silica used equals that used for I_2 on K60 silica (1.25 g).*

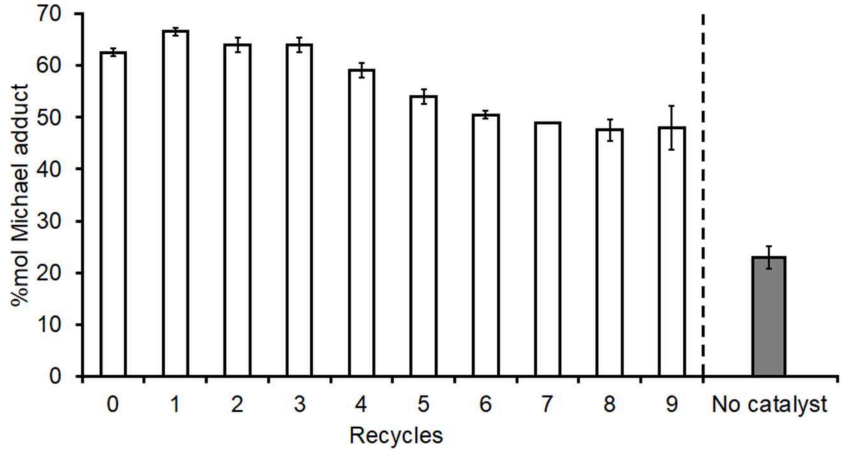

FIGURE 8 | Extended re-use study of I_2 on acidic alumina catalyst for addition of diethyl amine onto dimethyl itaconate. 2.5 mmol DMI, 20 mmol DEA, 1.28 g of 0.1 mmol g^{-1} I_2 on Al_2O_3 (standard loading) catalyst, stirred for 2 h at room temperature, reaction mixture filtered then filtrate analyzed by NMR spectroscopy ($CDCl_3$ solvent) while catalyst was recovered and reused with fresh reactants. Following filtration the catalyst was air-dried overnight prior to reuse between each run. All experiments were performed in duplicates and are shown in the figure as the average of two independent experiments ± the standard deviation.

when acidic alumina without I_2 was used (29%, entry 5, **Table 1**). The catalyzed experiment started with 1.28 g of catalyst but after the 10 full cycles 1.06 and 0.97 g (duplicate) of final catalyst was recovered. As such the final runs had catalyst loadings reduced to 76–83% of the original and this mass loss may have contributed to some of the reduced adduct yield observed over

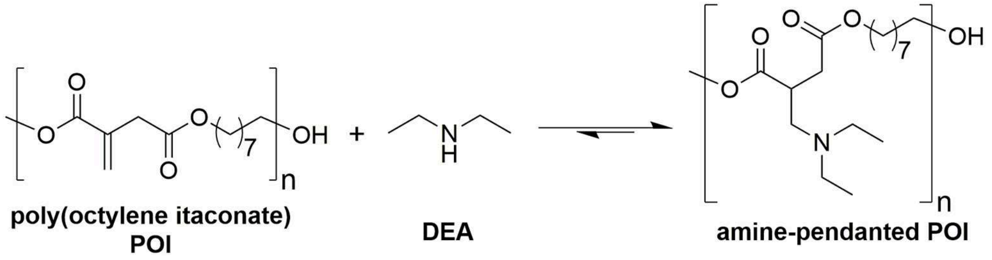

FIGURE 9 | Reaction scheme for addition of diethyl amine (DEA) pendant onto poly(octylene itaconate) (POI).

TABLE 2 | Effect of increased I_2 loading on acidic alumina for the Michael addition between DEA and DMI.

Entry	I_2 loading on acidic alumina	1st or reuse	%mol DMI	%mol DMMes	%mol Michael adduct 1
1	1x (standard)	1st use	3	22	75
		Re-use	4	18	78
2	2x	1st use	2	22	76
		Re-use	3	20	77
3	3x	1st use	2	17	81
		Re-use	2	18	80
4	4x	1st use	1	15	84
		Re-use	4	20	76

2.5 mmol DMI, 20 mmol DEA, 12.5%mol I_2 catalyst relative to DMI (3.2 g 1x loading, 1.6 g, 0.8 g and 0.67 g for 2x, 3x, and 4x loading, respectively), stirred for 2 h at room temperature, reaction mixture filtered then filtrate analyzed by ^{1}H-NMR spectroscopy ($CDCl_3$ solvent).

the extended reuse study. TGA analysis of the fresh (B, **Figure S9**) and recovered catalyst after 10 uses (C, **Figure S9**) suggest the latter contains 10–11% additional mass contributed by residual organics, this likely blocking some active sites and further reducing catalytic activity as observed in **Figure 8**. Nevertheless, I_2-Al_2O_3 was proven to be a more appropriate heterogeneous and recyclable catalyst for the aza-Michael addition compared to the lanthanide catalysts trialed above.

Effects of I_2 Loading on I_2 on Acidic Alumina Catalyst

Increasing I_2 loading on acidic alumina was investigated by multiplying the amounts of I_2 deposited onto the same amounts of catalyst (2x, 3x, and 4x). For their use in the aza-Michael addition the mass of each catalyst was concurrently reduced so as to ensure the same amount of I_2 (12.5%mol of I_2 with respect to DMI) was present in each run despite less acidic alumina support as loading increased. Results in **Table 2** show that the standard loading (1x = 0.1 mmol g^{-1} I_2-Al_2O_3) and double loading (2x = 0.2 mmol g^{-1} I_2-Al_2O_3) gave very similar results for 1st use and reuse, suggesting these suffer little from I_2 leaching. Increasing to 3x and 4x loadings both gave marginally higher yields of adduct for the first use, and the 4x loading suffered from a noticeable drop in yield upon reuse suggesting some leaching of I_2 occurred during the first run. Free, homogenous I_2 is extremely active as a catalyst for this reaction (see entries 2–4, **Table 1**, entry 4 being the direct comparison with 12.5%mol I_2 relative to DMI) and therefore leaching for the 4x, and possibly 3x, is likely responsible for the 1st use giving a greater yield. Based on this data it was concluded that the 2x loading (0.2 mmol g^{-1} I_2-Al_2O_3) was the optimum catalyst and this was used for a study into the catalyzed addition of DEA onto an itaconate polyester.

Use of I_2 on Acid Alumina for Catalyzing the Aza-Michael Addition Onto Itaconate Polyesters

DEA addition onto poly(1,8-octylene itaconate) (POI, **Figure 9**) was selected as an example reaction to study whether iodine on acidic alumina remained catalytic for reactions involving polymer substrates where viscosity is significantly increased and mass transfer thus reduced. The 2x loaded catalyst (0.2 mmol g^{-1} I_2 on Al_2O_3) was selected from the screen above. Maximizing the loading of I_2 would reduce the mass transfer limitations by lowering the overall quantity of required solid. A comparison against the uncatalysed system was made, and in both instances an 8:1 molar ratio of DEA to itaconate units was used, thus the excess DEA also acting as a solvent. The POI polyester was prepared using a previously reported enzymatic catalyzed polymerization method, this to minimize isomerization caused during polymerization. The method used for determining the extent of addition and isomerization via ^{1}H-NMR spectroscopy was modified from the model system (**Figure 5**) as a result of some peak overlap and loss of resolution (**Figure S10** for POI, **Figure S11** following addition of DEA to the polymer). The reference peak changed from the methyl ester group to the combined signals around 4.2 ppm set to an integral of 4 (CH_2s of the 1,8-octanediol nearest to the esters). The amount of addition was determined based on loss of alkene proton signals (5.5–6.8 ppm), whilst the amount of isomerization to mesaconate was determined by comparing signal integrals of the alkene protons of mesaconate (6.8 ppm, 1H) and itaconate (5.7 and 6.3 ppm, 1H each). A dramatic increase in rate of formation of aza-Michael adduct pendanted polyester was seen when using the I_2 on acidic alumina catalyst, monitored over a 24 h period (**Figure 10**). The catalyzed reaction had a 92% conversion rate to the Michael adduct polyester after 24 h, with only 60% seen for the conventional uncatalysed system. The catalyst also attained adduct yields of >70% after just

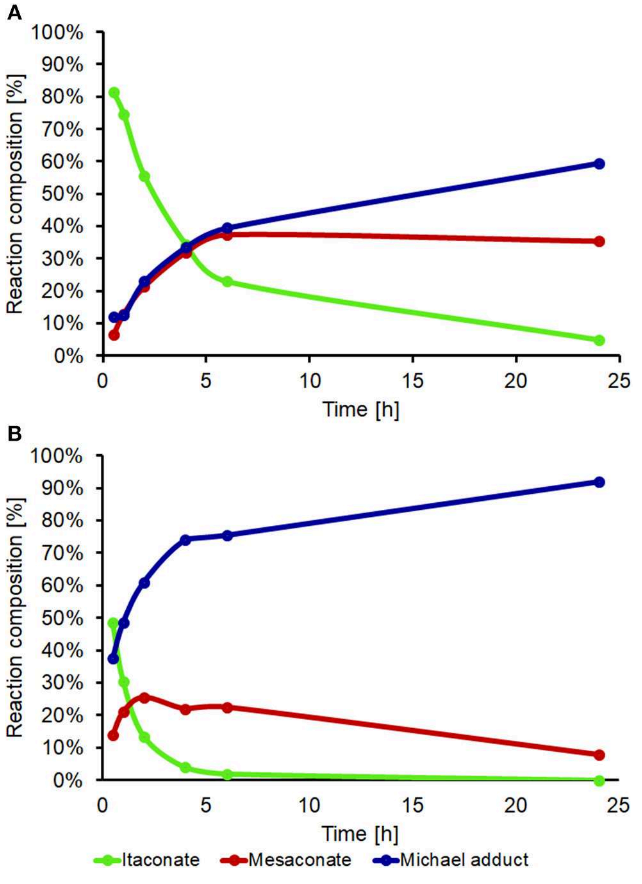

FIGURE 10 | Aza-Michael addition of DEA on poly(1,8-octylene itaconate) (POI). **(A)** Non-catalyzed reaction and **(B)** I_2 on Al_2O_3 as the catalyst. 2.5 mmol of POI (0.6 g, based on constitutional repeat unit of 240.29 g mol^{-1}), 20 mmol DEA, 0.64 g of 0.2 mmol g^{-1} I_2 on Al_2O_3 catalyst added to **(B)**, room temperature, aliquots analyzed by ^{1}H-NMR spectroscopy ($CDCl_3$ solvent) at 0.5, 1, 2, 4, 6, and 24 h.

4 h, and this with a concurrent significant reduction in extent of isomerization to mesaconate. The rapid reduction in the amount of itaconate units, with nearly complete conversion after 6 h, further demonstrates this catalyst to be very effective in promoting aza-Michael additions onto itaconate whilst not promoting undesired regio-isomerization. It was noted that the catalyzed reaction resulted in a polymer of darker orange coloration compared to that of no catalyst. Thermogravimetric analysis (**Figure S12**) of the fresh and recovered catalyst was thus used to ascertain if an appreciable quantity of I_2 was lost from the surface of the catalyst during the course of the reaction. The fresh 0.1 mmol g^{-1} I_2 on Al_2O_3 catalyst showed a prolonged gradual mass loss over the full TGA range (30–625°C) representing ∼7–8%. Complete loss of all I_2 from this sample should have resulted in a mass loss of just 2.5%, therefore it was hypothesized that water adsorbed onto the Al_2O_3 was also contributing to the observed mass loss. This was confirmed by comparison to the acidic alumina as received (Sigma-Aldrich), where a gradual mass loss of ∼5% is indeed also observed (**Figure S8A**). The recovered spent catalyst following the addition of DEA to DMI also shows this prolonged mass lost but has an additional mass loss at 190–270°C. This new mass loss event matches the previously reported temperature for retro-aza-Michael addition of the DEA unit from the polymer, suggesting residual polymer is contained on or within the catalyst (Pellis et al., 2019). The gradual mass loss associated to I_2 and H_2O release matches roughly with that for the fresh catalyst suggesting leaching of I_2 was only a minimal cause of the observed coloration, and further supports the sound reusability of this catalyst.

CONCLUSION

Although a versatile and useful reaction for the derivatization of α,β-unsaturation carbonyls, aza-Michael additions typically require long reaction times of several days. This is particularly problematic for the addition of amine pendants onto bio-based itaconate polyesters as undesired regioisomerization results in formation of mesaconate units which significantly reduce the rate of aza-Michael addition. A screen of various heterogeneous catalysts using the model reaction of addition of diethylamine onto dimethylitaconate found that I_2 supported onto acidic alumina produced an effective, recoverable and reusable catalyst for this aza-Michael addition. Although initially promising it was eventually concluded that various catalysts based on a cerium metal center were ineffective due to rapid deactivation after their first use. Despite extensive studies we were unable to fully ascertain the cause of this deactivation and hence sought an alternative. I_2 supported on acidic alumina demonstrated far better reusability, with an extended reuse study still showing significant catalytic activity remained. The best supported iodine catalyst gave yields of aza-Michael adduct of >70% after 2 h, even after reuse, while the equivalent non-catalyzed reaction had yields of adduct of 26–28%. A screen of I_2 loading found that catalysts of ≤0.2 mmol g^{-1} I_2 on alumina maintained their original efficiency upon reuse, while higher loadings of I_2 saw a drop that was likely caused by leaching of iodine into the reaction media. The optimum catalyst was subsequently used for the addition of diethylamine onto poly(1,8-octylene itaconate), this unsaturated polyester prepared via enzymatic polycondenzation. Use of the catalyst for post-polymerization modification showed that >90% amine pendant addition was possible after 24 h, this was far greater than the non-catalyzed equivalent with just 60% adduct and extensive undesired mesaconate units remaining. More impressively the catalytic system showed >70% addition after just 4 h, the non-catalyzed equivalent reached than half this over the same period. This study thus concludes that I_2 supported on acidic alumina is a very effective catalyst for aza-Michael additions on bio-based itaconate polyesters, and holds much promise in considerably reducing the lengthy times typically used for these reactions.

DATA AVAILABILITY

The raw data generated for the iodine on acidic alumina study and used to confirm the results can be found via doi: 10.15124/0bf5104e-70aa-4bb8-958b-a7501dcd2b48. Raw data for the cerium catalyst section of the study is available from the authors upon request.

AUTHOR CONTRIBUTIONS

TF developed the initial concept. TF, AP, and JC supervised the study. JC prepared immobilized CAN samples. AP prepared poly(1,8-octylene itaconate) and carried out TGA analysis. P-AH carried out the Ce catalyzed reactions, OM carried out the I_2 catalyzed reactions (DMI and polymer), and porosimetry analysis of the catalysts. TF and AP led preparation of the manuscript but were assisted by all the authors.

FUNDING

AP thanks the Austrian Science Fund (FWF) for the Schrödinger Fellowship (grant agreement J4014-N34). OM thanks the Department of Chemistry, University of York, for funding his summer vacation placement to undertake this research.

SUPPLEMENTARY MATERIAL

The Supplementary Material for this article can be found online at: https://www.frontiersin.org/articles/10.3389/fchem.2019.00501/full#supplementary-material

REFERENCES

Blaha, M., Trhlikova, O., Podesva, J., Abbrent, S., Steinhart, M., Dybal, J., et al. (2018). Solvent-free, catalyst-free aza-Michael addition of cyclohexylamine to diethyl maleate: reaction mechanism and kinetics. *Tetrahedron* 74, 58–67. doi: 10.1016/j.tet.2017.11.033

Borah, K. J., Phukan, M., and Borah, R. (2010). Aza-Michael addition of amines to alpha,beta-unsaturated compounds using molecular iodine as catalyst. *Synth. Commun.* 40, 2830–2836. doi: 10.1080/00397910903320241

Bosica, G., and Abdilla, R. (2016). Aza-Michael mono-addition using acidic alumina under solventless conditions. *Molecules* 21:E815. doi: 10.3390/molecules21060815

Chanda, S., and Ramakrishnan, S. (2015). Poly(alkylene itaconate)s - an interesting class of polyesters with periodically located exo-chain double bonds susceptible to Michael addition. *Polym. Chem.* 6, 2108–2114. doi: 10.1039/C4PY01613K

Chaudhuri, M. K., Hussain, S., Kantam, M. L., and Neelima, B. (2005). Boric acid: a novel and safe catalyst for aza-Michael reactions in water. *Tetrahedron Lett.* 46, 8329–8331. doi: 10.1016/j.tetlet.2005.09.167

Clark, J. H., Farmer, T. J., and Macquarrie, D. J. (2009). The derivatization of bioplatform molecules by using KF/alumina catalysis. *ChemSusChem* 2, 1025–1027. doi: 10.1002/cssc.200900193

Corici, L., Pellis, A., Ferrario, V., Ebert, C., Cantone, S., and Gardossi, L. (2015). Understanding potentials and restrictions of solvent-free enzymatic polycondensation of itaconic acid: an experimental and computational analysis. *Adv. Synth. Catal.* 357, 1763–1774. doi: 10.1002/adsc.201500182

Costa, C. S. M. F., Fonseca, A. C., Moniz, J., Godinho, M., Coelho, J. F. J., and Serra, A. C. (2017). Going greener: synthesis of fully biobased unsaturated polyesters for styrene crosslinked resins with enhanced thermomechanical properties. *Expr. Polym. Lett.* 11, 885–898. doi: 10.3144/expresspolymlett.2017.85

Dai, J. Y., Ma, S. Q., Liu, X. Q., Han, L. J., Wu, Y. G., Dai, X. Y., et al. (2015a). Synthesis of bio-based unsaturated polyester resins and their application in waterborne UV-curable coatings. *Progr. Organic Coat.* 78, 49–54. doi: 10.1016/j.porgcoat.2014.10.007

Dai, J. Y., Ma, S. Q., Wu, Y. G., Han, L. J., Zhang, L. S., Zhu, J., et al. (2015b). Polyesters derived from itaconic acid for the properties and bio-based content enhancement of soybean oil-based thermosets. *Green Chem.* 17, 2383–2392. doi: 10.1039/C4GC02057J

Dai, J. Y., Ma, S. Q., Wu, Y. G., Zhu, J., and Liu, X. Q. (2015c). High bio-based content waterborne UV-curable coatings with excellent adhesion and flexibility. *Progr. Organic Coat.* 87, 197–203. doi: 10.1016/j.porgcoat.2015.05.030

Das, B., and Chowdhury, N. (2007). Amberlyst-15: An efficient reusable heterogeneous catalyst for aza-Michael reactions under solvent-free conditions. *J. Mol. Catal. Chem.* 263, 212–215. doi: 10.1016/j.molcata.2006.08.082

Deka, N., and Sarma, J. C. (2001). Highly efficient dithioacetalization of carbonyl compounds catalyzed with iodine supported on neutral alumina. *Chem. Lett.* 794–795. doi: 10.1246/cl.2001.794

Dhake, K. P., Tambade, P. J., Singhal, R. S., and Bhanage, B. M. (2010). Promiscuous Candida antarctica lipase B-catalyzed synthesis of beta-amino esters via aza-Michael addition of amines to acrylates. *Tetrahedron Lett.* 51, 4455–4458. doi: 10.1016/j.tetlet.2010.06.089

Duan, Z., Xuan, X. J., Li, T., Yang, C. F., and Wu, Y. J. (2006). Cerium(IV) ammonium nitrate (CAN) catalyzed aza-Michael addition of amines to alpha,beta-unsaturated electrophiles. *Tetrahedron Lett.* 47, 5433–5436. doi: 10.1016/j.tetlet.2006.05.182

Farmer, T. J., Castle, R. L., Clark, J. H., and Macquarrie, D. J. (2015). Synthesis of unsaturated polyester resins from various bio-derived platform molecules. *Int. J. Mol. Sci.* 16, 14912–14932. doi: 10.3390/ijms160714912

Farmer, T. J., Clark, J. H., Macquarrie, D. J., Ogunjobi, J. K., and Castle, R. L. (2016). Post-polymerisation modification of bio-derived unsaturated polyester resins via Michael additions of 1,3-dicarbonyls. *Polym. Chem.* 7, 1650–1658. doi: 10.1039/C5PY01729G

Farmer, T. J., Comerford, J. W., Pellis, A., and Robert, T. (2018a). Post-polymerization modification of bio-based polymers: maximizing the high functionality of polymers derived from biomass. *Polym. Int.* 67, 775–789. doi: 10.1002/pi.5573

Farmer, T. J., Macquarrie, D. J., Comerford, J. W., Pellis, A., and Clark, J. H. (2018b). Insights into post-polymerisation modification of bio-based unsaturated itaconate and fumarate polyesters via aza-Michael addition: understanding the effects of C=C isomerisation. *J. Polym. Sci. Part A Polym. Chem.* 56, 1935–1945. doi: 10.1002/pola.29079

Farmer, T. J., and Mascal, M. (2014). "Chapter 4: platform molecules," in *Introduction to Chemicals from Biomass 2nd edn,* eds J. H. Clark and F. E. I. Deswarte (Weinheim: Wiley VCH), 89–155. doi: 10.1002/9781118714478.ch4

Fonseca, A. C., Costa, C. S. M. F., Marques, T. M. P., Coelho, J. F. J., and Serra, A. C. (2017). The impact of a designed lactic acid-based crosslinker in the thermochemical properties of unsaturated polyester resins/nanoprecipitated calcium carbonate composites. *J. Mater. Sci.* 52, 1272–1284. doi: 10.1007/s10853-016-0422-6

Fonseca, A. C., Lopes, I. M., Coelho, J. F. J., and Serra, A. C. (2015). Synthesis of unsaturated polyesters based on renewable monomers: structure/properties relationship and crosslinking with 2-hydroxyethyl methacrylate. *React. Funct. Polym.* 97, 1–11. doi: 10.1016/j.reactfunctpolym.2015.10.002

Gandini, A., and Lacerda, T. M. (2015). From monomers to polymers from renewable resources: recent advances. *Prog. Polym. Sci.* 48, 1–39. doi: 10.1016/j.progpolymsci.2014.11.002

Guarneri, A., Cutifani, V., Cespugli, M., Pellis, A., Vassallo, R., Asaro, F., et al. (2019). Functionalization of enzymatically synthesized rigid poly(itaconate)s via post-polymerization aza-Michael addition of primary amines. *Adv. Synth. Catal.* 361, 2559–2573. doi: 10.1002/adsc.201900055

Guo, B. C., Chen, Y. W., Lei, Y. D., Zhang, L. Q., Zhou, W. Y., Rabie, A. B. M., et al. (2011). Biobased poly(propylene sebacate) as shape memory polymer with tunable switching temperature for potential biomedical applications. *Biomacromolecules* 12, 1312–1321. doi: 10.1021/bm2000378

Hoffmann, C., Stuparu, M. C., Daugaard, A., and Khan, A. (2015). Aza-Michael addition reaction: post-polymerization modification and preparation of PEI/PEG-based polyester hydrogels from enzymatically synthesized reactive polymers. *J. Polym. Sci. Part A Polym. Chem.* 53, 745–749. doi: 10.1002/pola.27498

Isikgor, F. H., and Becer, C. R. (2015). Lignocellulosic biomass: a sustainable platform for the production of bio-based chemicals and polymers. *Polym. Chem.* 6, 4497–4559. doi: 10.1039/C5PY00263J

Jenner, G. (1995). Catalytic high-pressure synthesis of hindered beta-aminoesters. *Tetrahedron Lett.* 36, 233–236. doi: 10.1016/0040-4039(94)02215-W

Kantam, M. L., Neeraja, V., Kavita, B., Neelima, B., Chaudhuri, M. K., and Hussain, S. (2005). Cu(acac)(2) immobilized in ionic liquids: a recoverable and reusable catalytic system for aza-Michael reactions. *Adv. Synth. Catal.* 347, 763–766. doi: 10.1002/adsc.200404361

Kilbourn, B. T. (1986). The role of the lanthanides in applied catalysis. *J. Less Common Metals* 126, 101–106. doi: 10.1016/0022-5088(86)90254-7

Kobayashi, S., Hachiya, I., Takahori, T., Araki, M., and Ishitani, H. (1992). Lanthanide trifluoromethanesulfonates as reusable catalysts - michael and diels-alder reactions. *Tetrahedron Lett.* 33, 6815–6818. doi: 10.1016/S0040-4039(00)61783-5

Kumar, S., Krishnan, S., Samal, S. K., Mohanty, S., and Nayak, S. K. (2017). Itaconic acid used as a versatile building block for the synthesis of renewable resource-based resins and polyesters for future prospective: a review. *Polym. Int.* 66, 1349–1363. doi: 10.1002/pi.5399

Llevot, A., Dannecker, P. K., Von Czapiewski, M., Over, L. C., Soyler, Z., and Meier, M. A. R. (2016). Renewability is not enough: recent advances in the sustainable synthesis of biomass-derived monomers and polymers. *Chem. A Eur. J.* 22, 11509–11520. doi: 10.1002/chem.201602068

Lv, A., Li, Z. L., Du, F. S., and Li, Z. C. (2014). Synthesis, functionalization, and controlled degradation of high molecular weight polyester from itaconic acid via ADMET polymerization. *Macromolecules* 47, 7707–7716. doi: 10.1021/ma5020066

Mathers, R. T. (2012). How well can renewable resources mimic commodity monomers and polymers? *J. Polym. Sci. Part A Polym. Chem.* 50, 1–15. doi: 10.1002/pola.24939

Molnar, A., and Papp, A. (2017). Catalyst recycling-A survey of recent progress and current status. *Coord. Chem. Rev.* 349, 1–65. doi: 10.1016/j.ccr.2017.08.011

Nair, V., and Deepthi, A. (2007). Cerium(IV) ammonium nitrate - a versatile single-electron oxidant. *Chem. Rev.* 107, 1862–1891. doi: 10.1021/cr068408n

Panic, V. V., Seslija, S. I., Popovic, I. G., Spasojevic, V. D., Popovic, A. R., Nikolic, V. B., et al. (2017). Simple one-pot synthesis of fully biobased unsaturated polyester resins based on itaconic acid. *Biomacromolecules* 18, 3881–3891. doi: 10.1021/acs.biomac.7b00840

Patil, D. M., Phalak, G. A., and Mhaske, S. T. (2017). Design and synthesis of bio-based UV curable PU acrylate resin from itaconic acid for coating applications. *Desig. Monom. Polym.* 20, 269–282. doi: 10.1080/15685551.2016.1231045

Pellis, A., Comerford, J. W., Maneffa, A. J., Sipponen, M. H., Clark, J. H., and Farmer, T. J. (2018). Elucidating enzymatic polymerisations: chain-length selectivity of Candida antarctica lipase B towards various aliphatic diols and dicarboxylic acid diesters. *Eur. Polym. J.* 106, 79–84. doi: 10.1016/j.eurpolymj.2018.07.009

Pellis, A., Corici, L., Sinigoi, L., D'amelio, N., Fattor, D., Ferrario, V., et al. (2015). Towards feasible and scalable solvent-free enzymatic polycondensations: integrating robust biocatalysts with thin film reactions. *Green Chem.* 17, 1756–1766. doi: 10.1039/C4GC02289K

Pellis, A., Hanson, P. A., Comerford, J. W., Clark, J. H., and Farmer, T. J. (2019). Enzymatic synthesis of unsaturated polyesters: functionalization and reversibility of the aza-Michael addition of pendants. *Polym. Chem.* 10, 843–851. doi: 10.1039/C8PY01655K

Reboule, R., Gil, R., and Collin, J. (2005). Aza-Michael reactions catalyzed by samarium diiodide. *Tetrahedron Lett.* 46, 7761–7764. doi: 10.1016/j.tetlet.2005.09.039

Reddy, B., Patil, M., and Reddy, B. (2008). An efficient protocol for aza-Michael addition reactions under solvent-free condition employing sulfated zirconia catalyst. *Catal. Letters* 126, 413–418. doi: 10.1007/s10562-008-9646-7

Robert, T., and Friebel, S. (2016). Itaconic acid - a versatile building block for renewable polyesters with enhanced functionality. *Green Chem.* 18, 2922–2934. doi: 10.1039/C6GC00605A

Rorrer, N. A., Dorgan, J. R., Vardon, D. R., Martinez, C. R., Yang, Y., and Beckham, G. T. (2016). Renewable unsaturated polyesters from muconic acid. *Acs Sustain. Chem. Eng.* 4, 6867–6876. doi: 10.1021/acssuschemeng.6b01820

Rowe, M. D., Eyiler, E., and Walters, K. B. (2016). Bio-based plasticizer and thermoset polyesters: a green polymer chemistry approach. *J. Appl. Polym. Sci.* 133. doi: 10.1002/app.43917

Saikia, M., Kakati, D., Joseph, M. S., and Sarma, J. C. (2009). Iodine-alumina catalyzed aza- Michael addition under solvent free conditions. *Lett. Org. Chem.* 6, 654–658. doi: 10.2174/157017809790442961

Sakuma, T., Kumagai, A., Teramoto, N., and Shibata, M. (2008). Thermal and dynamic mechanical properties of organic-inorganic hybrid composites of itaconate-containing poly(butylene succinate) and methacrylate-substituted polysilsesquioxane. *J. Appl. Polym. Sci.* 107, 2159–2164. doi: 10.1002/app.27112

Schoon, I., Kluge, M., Eschig, S., and Robert, T. (2017). Catalyst influence on undesired side reactions in the polycondensation of fully bio-based polyester itaconates. *Polymers* 9:693. doi: 10.3390/polym9120693

Singh, M., Rathi, R., Singh, A., Heller, J., Talwar, G. P., and Kopecek, J. (1991). Controlled release of Lhrh-Dt from bioerodible hydrogel microspheres. *Int. J. Pharm.* 76, R5–R8. doi: 10.1016/0378-5173(91)90283-T

So, Y. M., and Leung, W. H. (2017). Recent advances in the coordination chemistry of cerium(IV) complexes. *Coord. Chem. Rev.* 340, 172–197. doi: 10.1016/j.ccr.2016.12.009

Sridharan, V., Avendano, C., and Menendez, J. C. (2007). General, mild and efficient synthesis of beta-enaminones catalyzed by ceric ammonium nitrate (pg 881, 2007). *Synlett* 1330–1330. doi: 10.1055/s-2007-977447

Sridharan, V., and Menendez, J. C. (2010). Cerium(IV) ammonium nitrate as a catalyst in organic synthesis. *Chem. Rev.* 110, 3805–3849. doi: 10.1021/cr100004p

Takasu, A., Ito, M., Inai, Y., Hirabayashi, T., and Nishimura, Y. (1999). Synthesis of biodegradable polyesters by ring-opening copolymerization of cyclic anhydrides containing a double bond with 1,2-epoxybutane and one-pot preparation of the itaconic acid-based polymeric network. *Polym. J.* 31, 961–969. doi: 10.1295/polymj.31.961

Teramoto, N., Ozeki, M., Fujiwara, I., and Shibata, M. (2005). Crosslinking and biodegradation of poly(butylene succinate) prepolymers containing itaconic or maleic acid units in the main chain. *J. Appl. Polym. Sci.* 95, 1473–1480. doi: 10.1002/app.21393

Wei, T., Lei, L. J., Kang, H. L., Qiao, B., Wang, Z., Zhang, L. Q., et al. (2012). Tough bio-based elastomer nanocomposites with high performance for engineering applications. *Adv. Eng. Mater.* 14, 112–118. doi: 10.1002/adem.201100162

Werpy, T., and Petersen, G. (2004). *Top Value Added Chemicals from Biomass: Vol. 1 - Results of Screening for Potential Candidates from Sugars and Synthesis Gas*. Oak Ridge, TN: U.S. Department of Energy. doi: 10.2172/15008859

Winkler, M., Lacerda, T. M., Mack, F., and Meier, M.,a.R. (2015). Renewable polymers from itaconic acid by polycondensation and ring-opening-metathesis polymerization. *Macromolecules* 48, 1398–1403. doi: 10.1021/acs.macromol.5b00052

Yang, L., Xu, L. W., and Xia, C. G. (2007). Efficient catalytic aza-Michael additions of carbamates to enones: revisited dual activation of hard nucleophiles and soft electrophiles by InCl3/TMSCI catalyst system. *Tetrahedron Lett.* 48, 1599–1603. doi: 10.1016/j.tetlet.2006.12.137

Zhu, Y. Q., Romain, C., and Williams, C. K. (2016). Sustainable polymers from renewable resources. *Nature* 540, 354–362. doi: 10.1038/nature21001

Conflict of Interest Statement: The authors declare that the research was conducted in the absence of any commercial or financial relationships that could be construed as a potential conflict of interest.

Copyright © 2019 Moore, Hanson, Comerford, Pellis and Farmer. This is an open-access article distributed under the terms of the Creative Commons Attribution License (CC BY). The use, distribution or reproduction in other forums is permitted, provided the original author(s) and the copyright owner(s) are credited and that the original publication in this journal is cited, in accordance with accepted academic practice. No use, distribution or reproduction is permitted which does not comply with these terms.

frontiers in Chemistry

ORIGINAL RESEARCH
published: 02 August 2019
doi: 10.3389/fchem.2019.00545

Aqueous Ammonia Pre-treatment of Wheat Straw: Process Optimization and Broad Spectrum Dye Adsorption on Nitrogen-Containing Lignin

Mika Henrikki Sipponen and Monika Österberg*

Department of Bioproducts and Biosystems, School of Chemical Engineering, Aalto University, Espoo, Finland

Biorefineries need cost-efficient pretreatment processes that overcome the recalcitrance of plant biomass, while providing feasible valorization routes for lignin. Here we assessed aqueous ammonia for the separation of lignin from hydrothermally pretreated wheat straw prior to enzymatic saccharification. A combined severity parameter was used to determine the effects of ammonia concentration, treatment time and temperature on compositional and physicochemical changes [utilizing elemental analysis, cationic dye adsorption, FTIR spectroscopy, size-exclusion chromatography (SEC), and ^{31}P nuclear magnetic resonance (NMR) spectroscopy] as well as enzymatic hydrolysability of straw. Pretreatment at the highest severity (20% NH_3, 160°C) led to the maximum hydrolysability of 71% in a 24 h reaction time at an enzyme dosage of 15 FPU/g of pretreated straw. In contrast, hydrolysabilities remained low regardless of the severity when a low cellulase dosage was used, indicating competitive adsorption of cellulases on nitrogen-containing lignin. In turn, our results showed efficient adsorption of cationic, anionic and uncharged organic dyes on nitrogen-containing lignin, which opens new opportunities in practical water remediation applications.

Keywords: biorefinery, environment, lignocellulose, plant biomass, sustainable materials, water purification

OPEN ACCESS

Edited by:
Gabriel Paes,
Fractionnation of AgroResources and Environment (INRA), France

Reviewed by:
Brigitte Chabbert,
Institut National de la Recherche Agronomique (INRA), France
Zhibao Huo,
Shanghai Ocean University, China

****Correspondence:***
Mika Henrikki Sipponen
mika.sipponen@aalto.fi

Specialty section:
This article was submitted to Chemical and Process Engineering, a section of the journal Frontiers in Chemistry

Received: *14 May 2019*
Accepted: *16 July 2019*
Published: *02 August 2019*

Citation:
Sipponen MH and Österberg M (2019) Aqueous Ammonia Pre-treatment of Wheat Straw: Process Optimization and Broad Spectrum Dye Adsorption on Nitrogen-Containing Lignin. Front. Chem. 7:545. doi: 10.3389/fchem.2019.00545

INTRODUCTION

The hierarchical and recalcitrant structure of renewable plant biomass hampers its enzymatic hydrolysis for the production of biofuels (Himmel et al., 2007; Chundawat et al., 2011a,b). One of the main constraints arises from the presence of lignin that functions as a natural resin within and between plant cell walls, and adsorbs cellulases in the saccharification step (Chen and Dixon, 2007; Li et al., 2016; Liu et al., 2016; Sipponen et al., 2017a). Various acid, base, and solvent-based pretreatments increase saccharification yields by removing/altering lignin and by causing complex physical-chemical changes in the plant cell walls (Paës et al., 2017).

Hydrothermal and thermochemical pre-treatments have predominated in commercial and pre-commercial biorefinery concepts (Pihlajaniemi et al., 2016; Auxenfans et al., 2017). Although steam-explosion, autohydrolysis, and dilute acid hydrolysis pre-treatments require no or low chemical input, these processes do not generate a soluble lignin fraction. Instead, lignin ends up to the residual solids after incomplete enzymatic hydrolysis (and fermentation) of the pre-treated biomass. Such residual lignin is usually heavily contaminated with unhydrolyzed cellulose. On the contrary, organosolv and alkaline pre-treatments dissolve lignin and allow for its isolation in a relatively pure form (Hage et al., 2009; Mousavioun and Doherty, 2010). This is important since besides its detrimental effects on enzyme activity, lignin is a potential raw material for aromatic chemicals (Zakzeski et al., 2010) and biobased polymers (Laurichesse and Avérous, 2014), with substantial effect on the profitability of cellulosic ethanol plants (Ragauskas et al., 2014).

Lignin is thus indirectly and directly involved in the two central challenges of the 2G bioethanol production: (1) Development of cost-efficient pre-treatments to open up the recalcitrant structure of lignocellulose (2) Demonstration of applications for lignin that secure sufficient volume and profits to compensate for the total costs of the multistep biorefinery operations. Such pre-treatment processes require cost-efficient cooking chemicals. Due to its alkalinity and volatility, ammonia is a plausible option as a reusable chemical catalyst. In addition to the processes using anhydrous or low-moisture ammonia (Cayetano and Kim, 2017, 2018; Mittal et al., 2017; Flores-Gómez et al., 2018; Guo et al., 2018; Sakuragi et al., 2018; Zhou et al., 2018), aqueous ammonia pre-treatments have been studied intensively in recent years (Sipponen, 2015; Domanski et al., 2016; Phitsuwan et al., 2016; Chong et al., 2017; Li et al., 2017; Niemi et al., 2017; Tolbert et al., 2017; Yoo et al., 2017; Du et al., 2018; Huo et al., 2018; Zhu et al., 2018; An et al., 2019; Xiao et al., 2019). In contrast to anhydrous ammonia, pre-treatment of plant biomass with aqueous ammonia dissolves lignin that can be isolated from the spent cooking liquor. It is known that oxidative cleavage of lignin occurs when ammonolysis is performed under oxygen atmosphere at elevated temperatures (Lapierre et al., 1994; Nascimento et al., 1994; Capanema et al., 2006), but reports on the characterization and applications of ammonolysis lignin from actual biomass pre-treatments are scarce.

Some earlier works have investigated oxidative ammonolysis of technical lignins to produce slow-release nitrogen fertilizers (Nascimento et al., 1994; Ramírez et al., 1997; Capanema et al., 2001). Aqueous ammonia-based biomass pre-treatment processes have seen steady development because of the lower basicity and milder cooking temperatures compared to hydrothermal pre-treatments (Du et al., 2018; Huo et al., 2018; Zhu et al., 2019). However, one drawback of any alkaline pre-treatment is the consumption of effective alkali due to the alkaline hydrolysis of ester-linked moieties of biomass. A two-stage process with a pre-hydrolysis step could alleviate the neutralization issue. Such sequential pre-treatments involving aqueous ammonia have been studied recently (Chong et al., 2017; An et al., 2019; Xiao et al., 2019) but information is lacking regarding how the severity of the aqueous ammonia delignification affects the yield and applicability of soluble lignin along with the hydrolysability of the solid fraction.

In the present work, a two-stage hydrothermal-aqueous ammonia pre-treatment of wheat straw was studied. We used response surface modeling and fitted a combined severity parameter to evaluate the effects of various cooking conditions on the fractionation and enzymatic saccharification of wheat straw. The pre-treated straw and the lignin fractions were characterized using an array of techniques (elemental analysis, dye adsorption, ^{31}P NMR and infrared spectroscopy, size-exclusion chromatography, and transmission electron microscopy) and the results are discussed in relation to the process conditions. Finally, using dye adsorption as a model system, we show that nitrogen-containing lignin holds potential as a broad-range adsorbent for cationic, anionic, and uncharged organic pollutants.

MATERIALS AND METHODS

Materials

Commercial soda lignin (GreenValue SA, Switzerland) and soda lignin isolated from hydrothermally pre-treated wheat straw were used as reference materials in this study. Characterization of these lignins has been performed in the prior literature (Sipponen, 2015).

Wheat Straw Pre-treatments and Isolation of N-lignin

Wheat straw (14 kg, dry basis) was collected from southern Finland during harvest, ground to pass a 1 mm screen in a Wiley mill, and subjected to hydrothermal (HT) pre-treatment at 140°C for 5 h (severity Log $R_0 = 3.8$, see Equation 1). The solid fraction collected after water-washing of pre-treated straw was dried at 40°C to 10 wt-% moisture content and termed HT-straw. Small portions of HT-straw (12.5 g on dry basis) were subjected to aqueous ammonia extraction at a liquid to solid ratio of 12. The cubic experimental design varied non-isothermal target temperature (100, 130, 160°C) and ammonia concentration (0, 4, 12, 20%, w/w) in the aqueous phase. The actual temperature as a function of treatment time was recorded for the calculation of severity parameters. The solid fraction was washed with deionized water, dried under ambient conditions, and subjected to enzymatic hydrolysis.

A larger batch of lignin was isolated from wheat straw in a two-stage pre-treatment. In the first step, 33.4 kg of wheat straw at a liquid to solid ratio of 10 was subjected to HT pre-treatment at 177°C (Log $R_0 = 4.1$). After separation of the liquid fraction, the solids were washed, pressed, and extracted with 7.5 wt% aqueous ammonia at a liquid to solid ratio of 7. Heating of the reactor to a maximum temperature of 140°C took ∼3 h. The solid/liquid separation was made by filtration in a hermetic Nutsche equipment. Residual ammonia in the solid fraction was removed by evaporation at reduced pressure and captured in 6 M sulfuric acid. Lignin was precipitated from the spent aqueous ammonia cooking liquor (30 kg fraction sampled from the cooking liquor, pH 8.5) by acidification to pH 5 (100 mL of 6 M hydrochloric acid), filtration, four sequential washing steps by making a dilute water suspension and separating the liquid fraction from the lignin solids by centrifugation, and freeze-drying. The corresponding mass yield of the dry N-lignin from the initial HT-straw was 17%. The above described pre-treatments and resulting liquid and solid fractions obtained from wheat straw are summarized in **Scheme 1**.

Combined Severity Parameter Fitting

Severity parameters have been previously used for acid- and base-catalyzed lignocellulose pre-treatments (Pedersen and Meyer, 2010). Here, we used a severity factor Equation (1) that combines

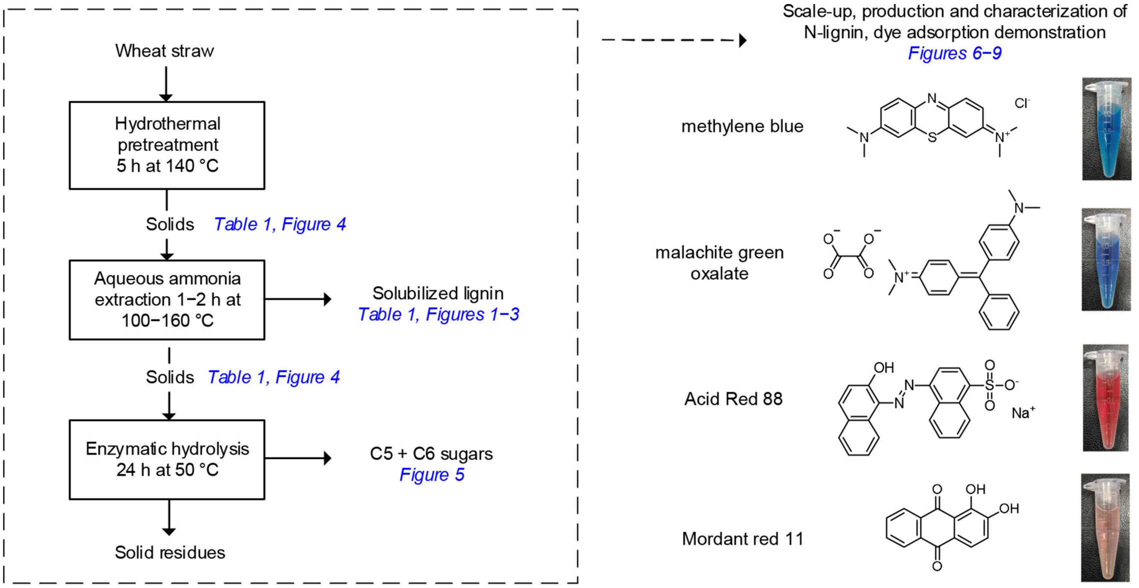

SCHEME 1 | Overview of the research approach involving a two-stage pre-treatment and enzymatic hydrolysis of wheat straw, analysis of the liquid and solid fractions, scale-up and isolation of N-lignin for characterization and dye adsorption tests. Photographs show appearance of the dye solutions prior to adsorption.

the effects of time, temperature, and the alkaline catalyst on biomass during the aqueous ammonia pre-treatment.

$$Log\ M_0 = Log\ R_0 + Log\ C^n \tag{1}$$

$R_0 = \int_0^t \exp^{\frac{T(t)-100}{14.75}} dt$, where $T(t)$ = treatment temperature at time t. The concentration of ammonia is given in the term C^n as weight percentage in the aqueous phase. The exponential factor n was obtained by iterative least squares linear fitting of the percentage of straw dissolved as a function of $Log\ M_0$.

Compositional Analysis of Lignin and Carbohydrates

The compositions of the straw fractions and N-lignin were determined following the two-stage sulfuric acid hydrolysis procedure (Sluiter et al., 2010). Sugar content of N-lignin was analyzed after hydrolysis of 20 mg dry material in 1.4 mL of 4 wt-% sulfuric acid (1 h, 121°C). The amount of dissolved lignin in the aqueous ammonia extracts was determined using the spectrophotometric method (Dence, 1992). Lignin concentration was calculated based on the absorbance reading at 280 nm using N-lignin for calibration (ε = 20.0 L/g/cm). Elemental carbon, hydrogen, nitrogen, and sulfur contents of various straw fractions and isolated ammonia lignin were analyzed with Perkin-Elmer (PE) 2400 Series II CHNS/O Analyzer. Sample weight was 2 mg.

Characterization of Pre-treated Straw by Dye Adsorption

Adsorption of the cationic dye Azure B was used to estimate the accessible surface area of lignin (Sipponen, 2015). Adsorption of Azure B (0, 0.1, 0.3, 0.5, 0.7, 0.8, and 1.0 g/L) on 50 mg of HT-straw before and after aqueous ammonia extraction was performed at 25°C in 0.05 M Na-phosphate buffer (pH 7). The soluble dye concentration after 24 h contact time was calculated from the absorbance reading at 647 nm. The maximum monolayer adsorption capacity was obtained by non-linear fitting of the Langmuir equation to the adsorption isotherms. Additionally, adsorption capacities of all pre-treated straw fractions were determined at 0.1 g/L initial dye concentration to assess the effect of pre-treatment severity on the equilibrium adsorption capacity.

Enzymatic Hydrolysis of Pre-treated Wheat Straw

Enzymatic hydrolysis assays were performed on the solid fractions either at 2 wt-% or 5 wt-% concentration of solids in the whole slurry with respective enzyme dosages of 15 FPU/g and 2 FPU/g. The enzyme mixture consisted on volume basis of 85% Econase CE (AB enzymes), 10% Novozyme 188 (Sigma-Aldrich/Novozymes), and 5% GC 140 (Genencor). The hydrolysis reactions were carried out in capped flasks agitated at 50°C. The liquid phase was sampled after 24 h reaction time for sugar analysis with HPLC. Briefly, the system included a Micro- Guard De-Ash pre-column (Bio-Rad, USA) connected to a SPO810 analytical column (Shodex). The analytical column was eluted with degassed deionized water at a flowrate of 0.7 mL/min isothermally at 60°C. A refractive index detector RID-10A was used to quantify monosaccharides identified based on their retention times and external calibration. Enzymatic hydrolysability was calculated as follows:

$$Enzymatic\ hydrolysability = 100\% \cdot \frac{m_{sugar\ (enzymatic\ hydrolysis)}}{m_{sugar\ (acid\ hydrolysis)}} \tag{2}$$

where $m_{sugar\ (enzymatic\ hydrolysis)}$ and $m_{sugar\ (acid\ hydrolysis)}$ are the total amounts of monosaccharides released from 1 g of pre-treated straw in enzymatic and analytical acid hydrolysis (two-step hydrolysis in concentrated and dilute sulfuric acid, see section Compositional Analysis of Lignin and Carbohydrates). Sugar recovery yield was calculated as follows:

$$Sugar\ recovery\ yield = \frac{m_{solid\ fraction}}{m_{HT-straw}} \cdot Enzymatic\ hydrolysability \tag{3}$$

where $m_{solid\ fraction}$ is the mass of straw recovered after aqueous ammonia extraction of $m_{HT-straw}$ amount of HT-straw (both on dry basis). Reported results are mean values of two independent experiments.

Characterization of Aqueous Ammonia-Soluble Lignins

Molecular weight distributions and weight average molar masses of lignin fractions from aqueous ammonia treatments were analyzed by aqueous high-performance size-exclusion chromatography (HPSEC). The first system was equipped with three Ultrahydrogel columns (Waters) eluted with aqueous 0.01 M sodium hydroxide containing 0.1 M sodium nitrate. The second system used a series of three PSS MCX 5 μm 300 mm × 8 mm, 100, 500, and 1,000 Å columns eluted with aqueous 0.1 M sodium hydroxide. Both systems were calibrated with poly(styrenesulfonate) standards and used a variable wavelength detector set at 280 nm.

N-lignin from the up-scaled process was analyzed by ^{31}P NMR spectroscopy (Granata and Argyropoulos, 1995). The samples were phosphitylated using 2-chloro-4,4,5,5-tetramethyl-1,3,2-dioxaphospholane and analyzed as described more in detail elsewhere (Sipponen et al., 2017b) except that the relaxation delay d1 of 15 s was used in the present work. Reported results are mean values of two independent experiments.

FTIR spectra of ammonolysis lignin and wheat straw soda lignin (GreenValue SA, Switzerland) were recorded in the mid-infrared region (400–4,000 cm^{-1}) at a resolution of 4 cm^{-1} by using a Bio-Rad FTS 6000 spectrometer (Digilab, Randolph, MA, USA) equipped with a MTEC PAC300 photoacoustic detector.

Transmission electron microscopy (TEM) images were recorded from drop-casted N-lignin on 3 nm carbon coated copper grids. FEI Tecnai 12 microscope was operated at 120 kV to acquire the images under bright field mode.

Water Purification by Dye Adsorption

N-lignin and GreenValue wheat straw soda lignin were tested comparatively as adsorbents for water purification. Aqueous lignin dispersions (5 mL, 0.7 mg/mL) were adjusted to pH 6 and added to aqueous dye solutions of methylene blue, malachite green oxalate, acid red 88 (5 mL, 0.2 mM), or mordant red 11 (5 mL, saturated solution) and magnetically stirred at 22°C during 8 h along with dye solutions at similar initial concentrations as above but without lignin. Absorbance spectra of the filtered (0.45 μm pore size to ensure exclusion of any submicrometer lignin particles that may have affected spectrophotometric measurements) liquid phases were recorded at 200–800 nm. Decolourization was calculated as percentage reduction of absorbance (at λ_{max} in the visible region) compared to the absorbance of the dye solutions without adsorbents. Reported results are mean values of two independent experiments.

RESULTS AND DISCUSSION

The objective of this work was to develop a two-stage hydrothermal-aqueous ammonia pre-treatment of wheat straw with subsequent enzymatic saccharification and valorization of the isolated lignin fraction. The pre-treatment process was scaled up to allow for production of N-lignin for dye adsorption tests. It is well-known that efficient saccharification of the pre-treated biomass requires opening up the recalcitrant lignocellulose structure by the removal or modification of lignin. Our first important task was therefore to investigate the mass balances and compositional changes as a result of the pre-treatment process.

Fractionation of Wheat Straw in the Two-Stage Pre-treatment

The effects of ammonia concentration, treatment time and temperature on ammonolysis of technical lignins have been studied in a series of detailed investigations (Capanema et al., 2001, 2002, 2006). Here, our objective was to use aqueous ammonia to fractionate hydrothermally pre-treated wheat straw (HT-straw) for enzymatic saccharification and isolation of N-lignin for valorization. First, we used response surface modeling to assess how extraction temperature and ammonia concentration influenced dissolution of HT-straw in aqueous ammonia. The yields of soluble lignin and solid fractions are given in **Table 1** along with the carbohydrate and lignin compositions of the solids. In general, dissolution of HT-straw increased as the ammonia concentration and treatment temperature increased. The lowest yield of the solid fraction was 68.6%, while the soluble lignin fraction was obtained at a maximum yield of 15.8% following the treatment at 160°C in 20% aqueous ammonia. The resulting solid straw fraction contained 13.2% of lignin, compared to 23.6% lignin content in HT-straw. It is noteworthy that almost as good yield of soluble lignin (14.2%, entry 10 in **Table 1**) was obtained with 12 wt-% of ammonia at 160°C. This observation suggests that the extent of lignin removal from HT-straw could be increased by increasing the treatment temperature. However, previous results indicate that maintaining hemicellulose and a low content of residual lignin can be beneficial to the enzymatic hydrolysability, presumably by avoiding the collapse of the porous cell wall matrix (Pihlajaniemi et al., 2016; Zhang et al., 2016; An et al., 2019) While the content of pentose sugars decreased slightly, extraction of lignin enriched the solid fractions with cellulose and hemicellulose, reaching 78.1% total carbohydrate content at the highest treatment temperature and ammonia concentration. Calculated from the data in **Table 1**, the mass balance closure decreased only slightly

TABLE 1 | Conditions of aqueous ammonia extraction, mass yield of solids and soluble lignin, and composition of the resulting solid fractions before enzymatic saccharification.

Entry	**Pre-treatment**		**Mass yield**		**Composition of solids, % dry weight basis**			
	NH_3 (wt-%)	**T (°C)**	**Solids (%)**	**Soluble lignin (% of HT-straw)**	**Glc[a]**	**Xyl[a]**	**Ara[a]**	**Lignin[b]**
1	0	0	100.0	0	39.8 ± 0.2	23.5 ± 0.4	2.7 ± 0.0	23.6 ± 0.2
2	0	140	80.2	n.a.	41.5 ± 0.3	21.2 ± 0.3	1.8 ± 0.1	23.9 ± 0.0
3	0	100	92.7	1.3	43.6 ± 0.5	21.1 ± 1.2	0.8 ± 0.1	22.9 ± 0.2
4	4	100	84.9	6.5	47.0 ± 0.6	20.9 ± 1.2	0.8 ± 0.2	22.0 ± 0.0
5	4	130	80.8	9.4	51.1 ± 0.3	20.0 ± 0.5	1.9 ± 1.0	19.7 ± 0.5
6	4	160	77.1	11.6	54.5 ± 0.7	18.3 ± 0.5	0.7 ± 0.2	19.5 ± 0.3
7	12	100	83.8	6.6	48.7 ± 0.5	20.5 ± 0.3	0.5 ± 0.5	20.6 ± 0.5
8	12	130	75.4	12.0	53.5 ± 1.3	18.6 ± 1.2	0.5 ± 0.5	17.3 ± 0.4
9	12	130	76.3	10.7	52.4 ± 0.4	19.2 ± 1.0	0.4 ± 0.4	18.0 ± 0.5
10	12	160	72.7	14.2	54.8 ± 0.8	18.1 ± 1.0	0.5 ± 0.2	16.2 ± 0.8
11	20	100	80.2	8.3	51.7 ± 0.6	20.9 ± 0.1	0.7 ± 0.2	20.1 ± 0.7
12	20	130	73.2	11.5	54.8 ± 0.7	17.5 ± 0.8	0.4 ± 0.4	16.2 ± 0.7
13	20	160	68.6	15.8	59.2 ± 0.5	18.2 ± 0.5	0.7 ± 0.2	13.2 ± 0.2

[a]Calculated as anhydrous sugars; [b]Includes acid-insoluble and acid-soluble lignin. n.a., not analyzed. Entries: 1 = original wheat straw, 2 = wheat straw subjected to 5 h hydrothermal (HT) treatment at 140°C; 3 =100°C water-extracted HT-straw (entry 2), 4–13 = aqueous ammonia pre-treated HT-straw (entry 2).

from 94 to 84% in response to the increasing treatment severity. Two aqueous ammonia pre-treatments that were carried out under identical conditions (130°C, 12 wt% ammonia solution) gave similar results, indicating that the reproducibility of the experiments was sufficient for the modeling of the data.

The response surface shown in **Figure 1A** was obtained when the yield of solid straw fraction from the pre-treatment was fitted to a quadratic model ($R^2 = 0.97$). Though such three-dimensional plots are effective for the visualization of data, combination of the pre-treatment parameters (ammonia concentration, treatment time, and temperature) into a single parameter allows for further analysis of enzymatic hydrolysability of the solid fractions from the pre-treatments at various severities. The best-fit of ammonia concentration and treatment temperature produced a coefficient of determination (R^2) of 0.97 and an exponential factor (n) of 2.23 for the combined severity parameter Log M_0 (**Figure 1B**). A higher n-value of 3.90 has been fitted for lignin removal from cotton stalks by sodium hydroxide treatment (Silverstein et al., 2007), and also used to calculate pre-treatment severity of aqueous ammonia soaking (Huo et al., 2018). However, we reasoned that differences in biomass type (in our case hydrothermally pre-treated straw) and basicity (lower with ammonium hydroxide than sodium hydroxide) rationalize using a different value here. Effectively, the extent of dissolution of lignin increased from 5 to 55% in linear correlation ($R^2 = 0.95$) with the severity parameter, validating its usefulness in comparison of the pre-treatment conditions (**Figure 1C**). Taking into account the yield of the solid fraction, we calculated the loss of individual straw components from the mass balances (**Figure 1D**). There was a negligible loss of glucose (≤4%), but the loss of xylose (maximum 41%) correlated (linear regression, $R^2 = 0.94$) with the loss of lignin (maximum 62%). This simultaneous removal of lignin with xylose suggest that the two components are closely associated with each other. To shed light into the interactions of these polymers, we further analyzed the spent cooking liquor fractions from the ammonia treatments.

Characterization of Aqueous Ammonia-Soluble Lignin

Aqueous size-exclusion chromatography was used to analyze molecular weight distribution of the lignins solubilized during the aqueous ammonia treatment. **Figure 2** shows three chromatograms recorded from lignins obtained at low ($Log\ M_0 = 2.4$), medium ($Log\ M_0 = 5.6$), and high ($Log\ M_0 = 6.1$) severities. The most obvious observation that can be made from the chromatograms is the disappearance of the sharp static light scattering detector signal at 30.8 min as the severity increased. This peak outside of the column calibration range was likely caused by lignin-carbohydrate complexes (LCCs) that contained relatively few lignin fragments, since the associated UV detector signal was very low. Although further analysis of LCCs was out of scope of the present work, it is noted that LCCs from wood and grass biomass have been characterized before (Watanabe et al., 1989; Lawoko et al., 2006; Yuan et al., 2011). The most pre-dominant covalent linkages in LCCs are phenyl glycoside, γ-ester, and benzyl ether (Yuan et al., 2011). We expect that cleavage of these LCCs occurred under the harsh alkaline conditions of the aqueous ammonia pulping enabled retaining a majority of the hemicelluloses in the solid straw fraction. In turn, there was a weak correlation of increasing weight average molecular weight ($\overline{M}_w$) of aqueous ammonia-solubilized lignin fractions with increasing severity ($R^2 = 0.48$) or percentage dissolution of lignin ($R^2 = 0.58$). The $\overline{M}_w$ of the 10 lignin fractions varied from 2,420 g/mol to 3,880 g/mol, which are in the similar range compared to the values of aqueous ammonia lignins isolated from wheat straw (2,200 g/mol) and *Miscanthus*

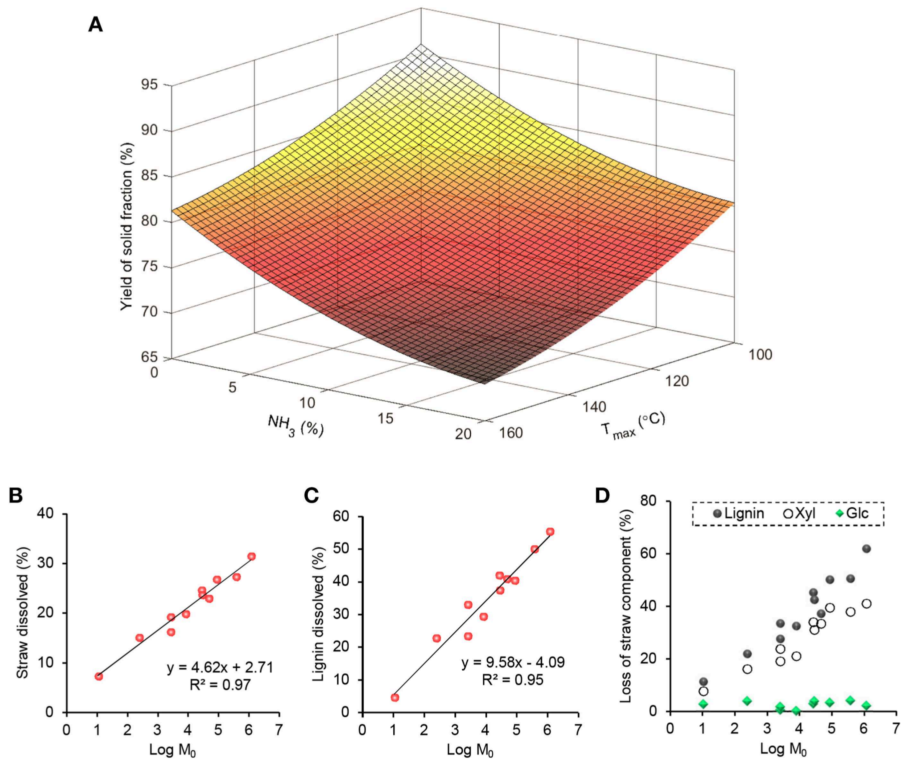

FIGURE 1 | Optimization and modeling of aqueous ammonia extraction of hydrothermally pre-treated wheat straw (HT-straw). **(A)** Response surface showing the effects of aqueous ammonia and maximum treatment temperature on the dry weight yield of solid fractions. Linear fitting of percentage dissolution of **(B)** straw (% of HT-straw dry weight) and **(C)** lignin (% of lignin dry weight of HT-straw) as a function of the combined severity parameter: $Log\ M_0 = Log\ R_0 + Log\ C^{2.23}$. **(D)** Loss of glucose, xylose (both anhydrous basis) and total lignin from straw, based on mass balance calculated from the data in **Table 1**.

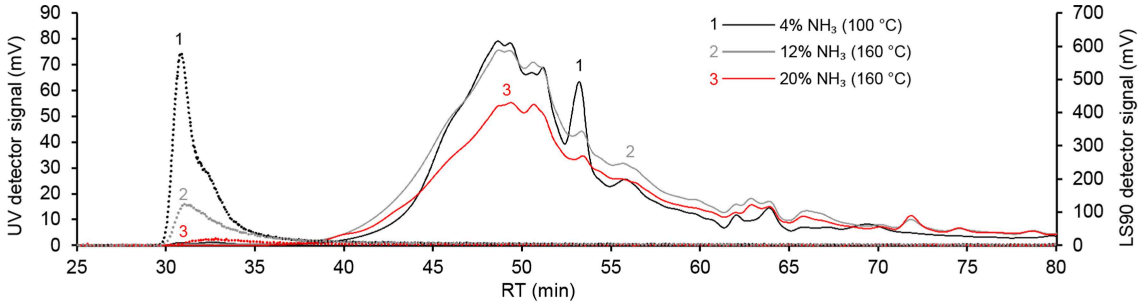

FIGURE 2 | Aqueous SEC traces of lignins extracted from hydrothermally pre-treated wheat straw with aqueous ammonia under varied severity. Dashed lines: light scattering detector (90°) signal.

× *giganteus* (3,140 g/mol) (Kondo et al., 1992; Vanderghem et al., 2011).

Aqueous ammonia was expected to cause incorporation of nitrogen by ammonolysis of lignin in HT-straw. Indeed, elemental analysis revealed that nitrogen content of the partially delignified solid fractions increased as the pre-treatment severity increased (**Figure 3A**). A stronger linear correlation to the severity parameter was observed when the nitrogen content was related to the lignin content of the pre-treated straw fractions (**Figure 3B**). Therefore, nitrogen seemed to bind mainly to lignin as suggested by earlier literature (Lapierre et al., 1994; Potthast et al., 1996).

Adsorption of Cationic Dye on Pre-treated Straw With Different Lignin Content

The compositional and chemical analyses discussed above proved that aqueous ammonia treatment caused severity-dependent lignin removal from HT-straw. Adsorption of the cationic dye Azure B on pre-treated solid fractions was used to assess whether these modifications caused changes in their accessible surface

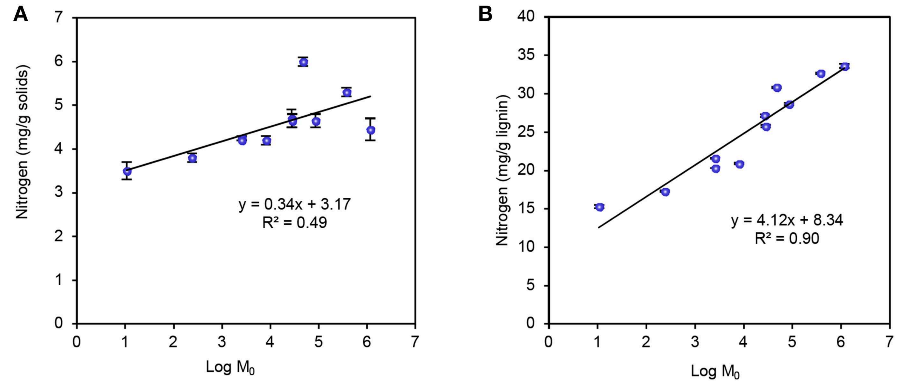

FIGURE 3 | Effect of severity of aqueous ammonia pre-treatment (*Log* M_0) on nitrogen content of recovered solid fractions **(A)** Nitrogen content of the pre-treated solid fractions. **(B)** Nitrogen content calculated relative to the lignin content of the solid fractions.

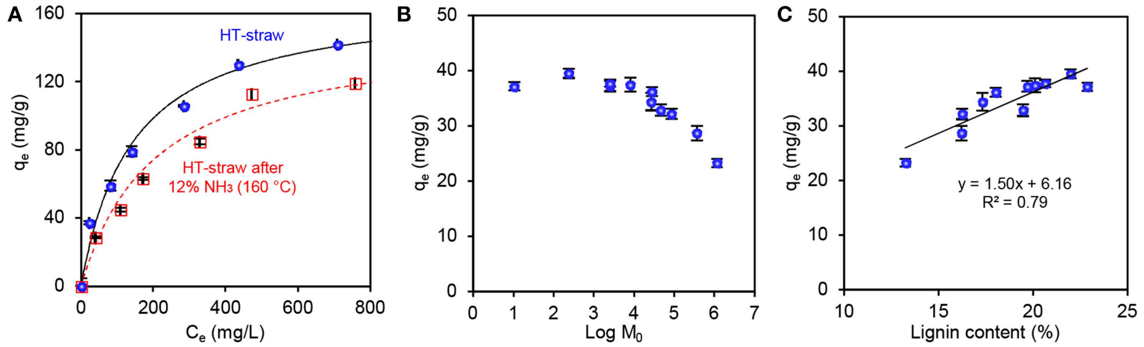

FIGURE 4 | Characterization of aqueous ammonia extracted HT-straw by cationic dye adsorption. **(A)** Langmuir model fitted to adsorption isotherm of Azure B on HT-straw and HT-straw pre-treated with 12% aqueous ammonia at 160°C. Equilibrium adsorption capacities (0.1 g/L initial dye concentration) as a function of **(B)** The severity parameter (Log M_0) of aqueous ammonia extraction. **(C)** Lignin content of pre-treated straw. Data points show mean values ± one standard deviation.

areas. A further aim was to assess how the accessible surface area of the pre-treated straw solids relates to their enzymatic hydrolysability. The adsorption isotherms of Azure B on the HT-straw before and after the aqueous ammonia pre-treatment are shown in **Figure 4A**. The aqueous ammonia pre-treatment caused a clear drop in the adsorption capacity due to the removal of lignin from the solid straw fractions (**Table 1**). This was expected on the basis of prior studies that have shown that lignin has a significantly higher adsorption capacity for Azure B compared to that of cellulose (Sipponen, 2015).

A fixed initial dye concentration (0.1 g/L) was used to compare adsorption capacities and thus evaluate accessible surface area of lignin in relation to the pre-treatment severity. The equilibrium adsorption capacity remained unchanged at low severity levels, but eventually decreased from 188 to 124 mg/g when the severity increased from 2.4 to 6.1 (**Figure 4B**). This decrease in the adsorption capacity correlated ($R^2 = 0.79$, $p < 0.01$, **Figure 4C**) with the decreasing lignin content of the solid fractions, suggesting that aqueous ammonia removed lignin solvolytically in contrast to melting and degradation of lignin under acidic and hydrothermal conditions (Selig et al., 2007).

Enzymatic Hydrolysability of Solids After Aqueous Ammonia Extraction

High yield and volumetric productivity of monomeric sugars from pre-treated biomass is central for the production of bioethanol or other products via microbial conversion routes (Pihlajaniemi et al., 2014). The solid fractions were collected after the various pre-treatments and subjected to enzymatic hydrolysis at low (2 FPU/g) and high (15 FPU/g) cellulase enzyme activity dosages. A response surface plot was created by fitting the enzymatic hydrolysabilities to a quadratic model (**Figure 5A**, $R^2 = 0.95$). The response surface indicates that the enzymatic hydrolysability increased with increasing ammonia concentration and treatment temperature. The shape of the surface suggests that additional increment in hydrolysability could have been reached by further increasing severity of the aqueous ammonia pre-treatment. Similar conclusion can be reached by correlating enzymatic hydrolysability to the combined pre-treatment severity (Log M_0) in **Figure 5B**. There was a clear trend of increasing hydrolysability as the pre-treatment severity increased when using 15 FPU/g enzyme dosage. Enzymatic hydrolysability remained at 41–43% until the pre-treatment

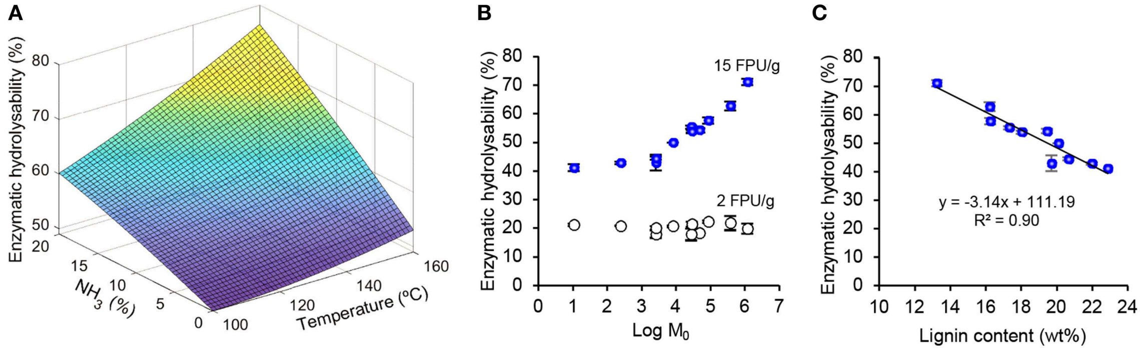

FIGURE 5 | Enzymatic hydrolysability (24 h reaction time) of pre-treated straw solid fractions. **(A)** Response surface plot showing effects of ammonia concentration and treatment temperature on enzymatic hydrolysability (15 FPU/g). **(B)** Hydrolysabilities at 15 FPU/g (filled circles) and 2 FPU/g (open circles) activity dosages as a function of pre-treatment severity *Log* M_0; **(C)** Hydrolysability (15 FPU/g) as a function of lignin content of pre-treated straw prior to enzymatic hydrolysis. Data points show mean values ± one standard deviation.

severity value of 3.4, but increased linearly thereafter to reach a value of 71.1% after the 24 h reaction. Taking into account the mass balances, the most severe pre-treatment conditions (20% NH_3, 160°C, Log $M_0 = 6.1$) led to the highest sugar recovery yield from HT-straw (39.8%), representing a clear augmentation compared to 27.8% obtained from HT-straw without aqueous ammonia treatment.

Inverse linear correlation of enzymatic hydrolysability with the lignin content of the pre-treated solids ($R^2 = 0.90$, **Figure 5C**) also points to the fact that further selective removal of lignin could increase the sugar recovery yield in the overall process. Moreover, the enzymatic hydrolysability (15 FPU/g) showed an inverse correlation with the equilibrium Azure B adsorption capacity (0.1 g/L initial dye concentration, $R^2 = 0.89$). That essentially similar R^2 values were obtained from the two factors is opposite to what has been reported following the autohydrolysis pre-treatment that melts lignin and reduces lignin surface area without major changes in the lignin content (Sipponen et al., 2014). In fact, multiple physical and chemicals changes occur in plant biomass during thermochemical pre-treatment (Pedersen and Meyer, 2010; Pihlajaniemi et al., 2016; Paës et al., 2017). Although the single-parameter correlations do not necessarily indicate causation, the results presented here support the earlier conclusion that cationic dye adsorption can be used as an indirect indicator of the constraint from residual lignin to enzymatic hydrolysis of polysaccharides (Sipponen et al., 2014).

Several wood and grass biomass types have been subjected to aqueous ammonia pre-treatment prior to the enzymatic hydrolysis step for sugar production (Du et al., 2018; Huo et al., 2018; An et al., 2019). The combination of ammonia pulping with ultrasound treatment (Du et al., 2018) and oxidative agents such as hydrogen peroxide (Huo et al., 2018) or oxygen gas (An et al., 2019) has increased subsequent enzymatic hydrolysability at least in a few cases. Sequential pre-treatment with dilute acid and aqueous ammonia has been found beneficial regarding hydrolysability of cellulose (An et al., 2019). Recent studies reported a high sugar recovery yield of 78% (Du et al., 2018) and an enzymatic digestibility of 84%, (Huo et al., 2018) but these were achieved with 30 FPU/g (glucan) cellulase dosage, i.e., much higher dosages than the ones used here. In addition to differences in feedstock types and pre-treatment conditions, it is also important to note that we obtained distinctively different results when a low cellulase activity was used in the saccharification reaction (**Figure 6A**). In contrast to what was observed at 15 FPU/g, the hydrolysability at 2 FPU/g remained low (∼20%) and essentially unchanged regardless of the severity. In contrast to the present work, An et al. (2019) achieved a reasonably high (72%) glucan conversion at 3 FPU/g cellulase dosage, which may be due to the oxygen pressure that enhanced lignin removal in the ammonolysis of dilute acid pre-treated corn stover. Our results suggest that nitrogen incorporation in the residual lignin is an important factor impeding enzymatic hydrolysis at the low cellulase dosage and regardless of the high extent of delignification. One plausible explanation is the competitive adsorption of cellulases on nitrogen-containing residual lignin. This reasoning is in agreement with our results (**Figure 3B**) and recent findings showing a significantly higher affinity and binding strength of cellulase on ammonia lignin residue than on organosolv lignin (Yoo et al., 2017).

Characterization of N-lignin From the Up-Scaled Process

To get a more comprehensive understanding of the nitrogen-containing lignin and to isolate a sufficient amount of material for application tests, a larger batch of hydrothermally pre-treated wheat straw was extracted with aqueous ammonia, and the isolated N-lignin was characterized. The fractionation process involved hydrothermal treatment at 177°C followed by aqueous ammonia extraction (7.5% NH_3, 140°C). These conditions were selected to remove a majority of hemicelluloses before the aqueous ammonia extraction step (20% solubilization of wheat straw, entry 2 in **Table 1**). Compositional analysis showed that N-lignin mainly contained (on dry weight basis) lignin (88.9 ± 0.6%), xylose (2.3 ± 0.3%, anhydrous basis), ash (4.7 ± 0.1%), and trace amounts of other components (**Figure 6A**). The lignin fraction was thus quite pure and had

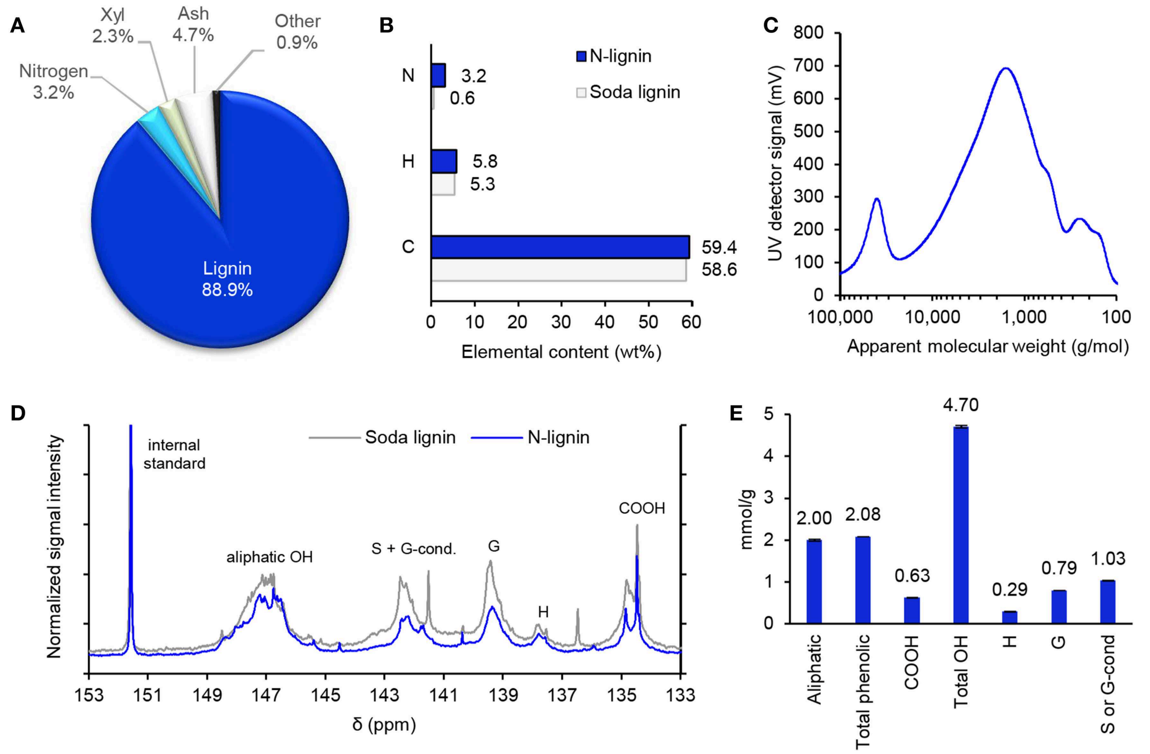

FIGURE 6 | (A) Composition of N-lignin. **(B)** Carbon, hydrogen, and nitrogen contents of N-lignin compared to the published values of wheat straw soda lignin extracted from HT-straw (Sipponen, 2015). **(C)** HPSEC trace of N-lignin. **(D)** ^{31}P NMR spectra of soda lignin (Sipponen, 2015) and N-lignin. **(E)** Quantities of aliphatic and phenolic hydroxyl groups and carboxylic acid groups of N-lignin based on ^{31}P NMR analysis. Error bars indicate ± one standard deviation relative to the mean value.

a low amount of sugar contaminants. Despite their similar carbon and hydrogen contents, the nitrogen content of N-lignin (3.2%) was ~5 times as high as that of soda lignin that was previously isolated from the same batch of HT-straw (**Figure 6B**).

The mass recovery yield of N-lignin (approximately 5% of hydrothermally pre-treated straw dry weight) was lower than expected (12%) based on the severity value ($Log\ M_0 = 4.8$), but its nitrogen content (32 mg/g) was similar as those of the residual lignins in pre-treated straw at comparable severities (**Figure 3B**). The lower extent of lignin dissolution is likely due to the higher temperature (177°C) used in the hydrothermal treatment compared to the milder temperature in the small scale experiments (140°C). In fact, it is well known that acid-catalyzed formation of condensed lignin under high temperatures hampers extraction of lignin from lignocellulose (Lora and Wayman, 1978). Alkaline pulping involves fragmentation of the side chain region of lignin and generation of free phenolic hydroxyl groups (Sipponen et al., 2017a). Molecular weight is one of the key parameters of polymers, and hence we recorded the molecular weight distribution of N-lignin using SEC (**Figure 6C**). Most of the molecules eluted at apparent molecular weights between 400 g/mol and 20,000 g/mol, with $\overline{M}_w$of 3,100 g/mol (PDI = 2.3) that was in the same range as observed above in the small scale experiments.

Quantitative ^{31}P NMR spectra were recorded from N-lignin to get further insight of the chemical changes that may have occurred during the extraction process. The spectrum shown in **Figure 6D** differed slightly from the one recorded earlier from the wheat straw soda lignin (Sipponen, 2015). Quantification of the hydroxyl group moieties (on dry weight basis) revealed that N-lignin contained 4% more aliphatic hydroxyls, while carboxylic acid and free phenolic hydroxyl groups were 24% and 9% lower compared to the values for the soda lignin (**Figure 6E**). These small differences may result from the stronger alkalinity of sodium hydroxide compared to ammonium hydroxide, and effectively a lower extent of oxidation with the latter. Yoo et al. (2017) recently reported that treatment of poplar lignin with 5% aqueous ammonia at 180°C caused a moderate increase in the content of C5-substituted phenolic hydroxyl groups with a concomitant loss of G and H type of phenolic hydroxyl and aliphatic hydroxyl groups.

FTIR spectroscopy was used to analyze the chemical structure of N-lignin in comparison to commercial wheat straw soda lignin. **Figure 7** shows typical lignin signals in both of the lignins that were assigned according to Faix (1992). The signal intensities were calculated relative to the baseline values at 1,900 cm^{-1}. The two lignins showed similar intensities at 1,512 cm^{-1} (aromatic skeletal vibrations) but differences were detected in bands indicating the presence of amides at 3,744 cm^{-1}, 1,653 cm^{-1},

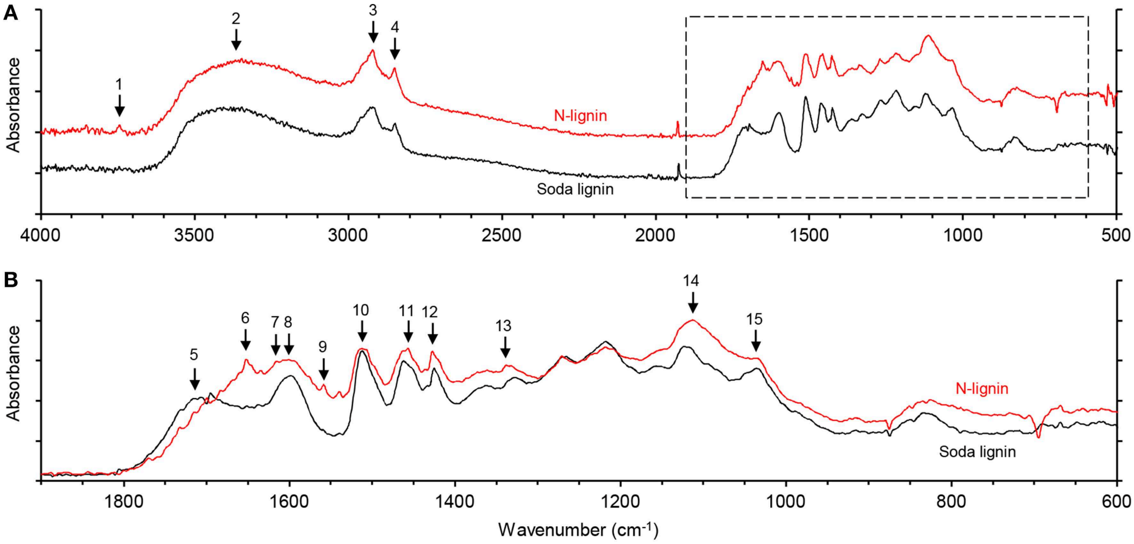

FIGURE 7 | FT-IR spectra of N-lignin and GreenValue wheat straw soda lignin. **(A)** Full spectra. **(B)** Overlaid spectra at 1900–600 cm^{-1}. See text and **Table 2** for signal assignments.

TABLE 2 | Signal intensities relative to the baseline value at 1,900 cm^{-1} of N-lignin and GreenValue wheat straw soda lignin, and differences between the two.

No	cm^{-1}	N-lignin	Soda lignin	Difference	Assignment
1	3744	1.30	1.28	0.02	Amide N-H stretching
2	3388	3.02	2.77	0.13	O–H stretching
3	2920	3.32	2.89	0.43	C–H stretch, methyl, and methylene groups
4	2849	2.84	2.44	0.40	C–H stretching, methyl, and methylene groups
5	1717	2.07	2.33	−0.26	C=O stretching, unconjugated carbonyl
6	1653	3.02	2.19	0.82	Amide I (C=O stretching)
7	1636	2.58	1.78	0.80	Imine (Shiff base) C=N stretching
8	1601	3.01	2.73	0.28	Ar. skeletal vibration; S>G
9	1558	2.58	1.78	0.80	Amide II (C–N stretch coupled with N–H bending)
10	1512	3.21	3.18	0.04	Ar. skeletal vibration; G>S
11	1456	3.21	2.92	0.29	C–H deform. methyl and methylene groups
12	1427	3.16	2.78	0.38	Ar. skeletal vibrations and C–H in-plane deform.
13	1339	2.92	2.60	0.31	Amide III (N–H in-plane bending coupled with C–N stretching plus C–H and N–H deformation); S ring plus G-cond
14	1113	3.71	3.20	0.51	Ar. C–H in-plane deform.; sec. alcohol; C=O stretching
15	1036	3.04	2.87	0.17	Ar. in-plane C-H deform.; C-O deform.; C=O stretching (unconj.)

1,558 cm^{-1}, and 1,427 cm^{-1} (Fu et al., 1994; De Campos Vidal and Mello, 2011; Yoo et al., 2014). Relative signal intensities of these amide bands were stronger in N-lignin than in soda lignin (**Table 2**). These results indicate that the formation of amides occurs under considerably milder ammonolysis conditions than those used in the previous studies (Lapierre et al., 1994; Potthast et al., 1996).

The signal intensity of the unconjugated carbonyl band at 1,717 cm^{-1} was slightly lower in N-lignin compared to soda lignin. In accordance with our results, Yoo et al. (2017) reported that aqueous ammonia treatment of cellulolytic enzyme lignin (CEL) resulted in lower abundance of unconjugated carbonyl moieties. We postulate that the drop in unconjugated carbonyl moieties was due to the Schiff base formation during the aqueous ammonia treatment. This speculation is supported by the appearance in N-lignin of a new band at 1,636 cm^{-1} that was assigned to the C=N stretching in imine (Dos Santos et al., 2005), and though overlapped with other signals in this region, the band was absent in soda lignin.

TEM imaging was lastly employed to get a better understanding of the nanoscaled morphology of the N-lignin. It showed micrometer-sized flakes that contained partially

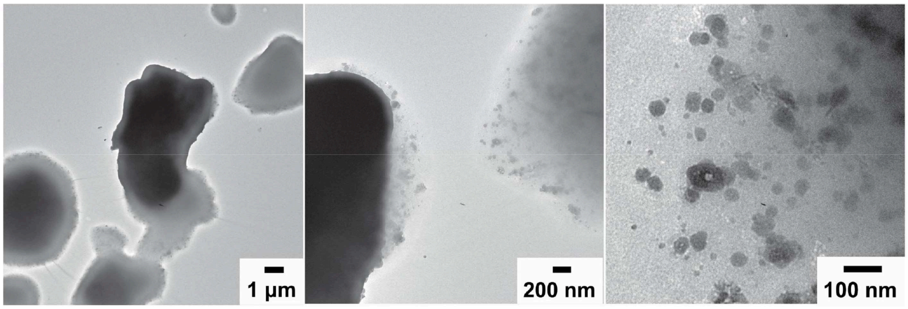

FIGURE 8 | TEM micrographs of N-lignin dried from aqueous suspension.

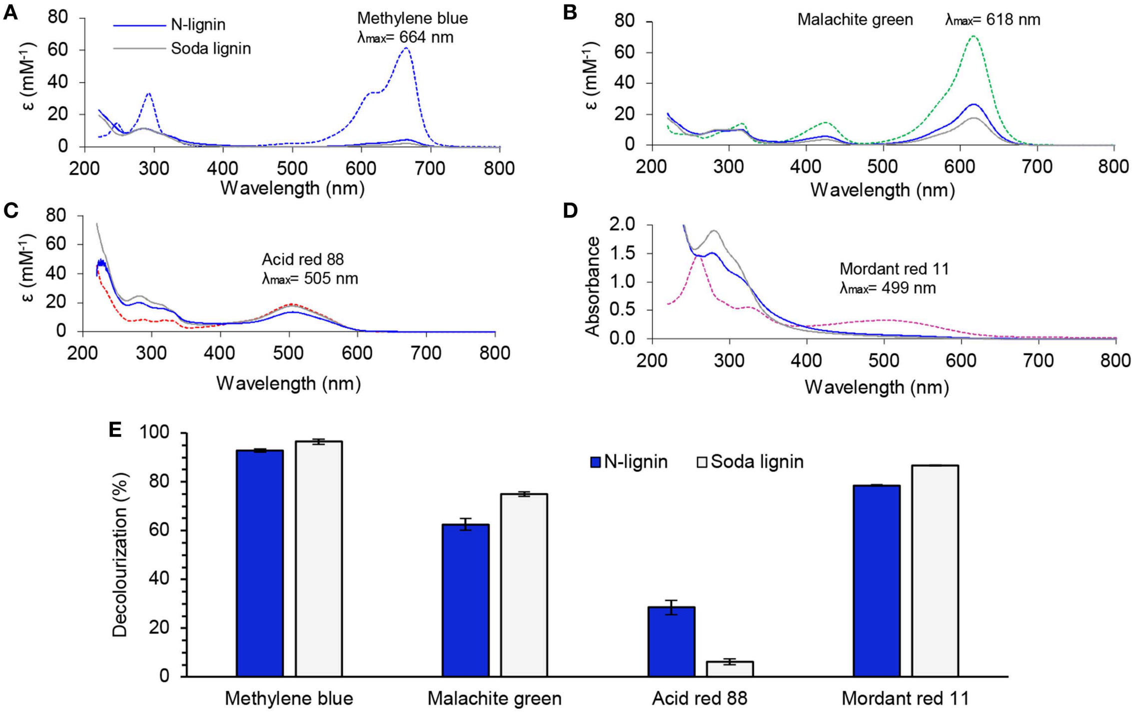

FIGURE 9 | Dye adsorption (8 h, pH 6, 22°C) on lignins. UV-Vis absorbance spectra showing apparent dilution-corrected molar absorptivity of aqueous dye solutions before (dashed spectra) and after adsorption on N-lignin (blue spectra) and GreenValue wheat straw soda lignin (gray spectra): **(A)** Methylene blue; **(B)** Malachite green oxalate; **(C)** Acid red 88; **(D)** Absorbance spectra of Mordant red 11 before and after adsorption. **(E)** Decolourization (absorbance decrement) of the dye solutions by the different lignins. Error bars indicate ± one standard deviation relative to the mean value.

aggregated nanoparticles (**Figure 8**). The smallest particles were ~20 nm and the majority of them were <100 nm in diameter. We anticipated that this fine morphology combined with the incorporated nitrogen could be beneficial for adsorption and flocculation in water remediation applications. Therefore, we carried out proof-of-concept experiments on dye adsorption from aqueous media.

Water Purification Using the N-lignin Particles

Due to their negative charge, many lignins have been shown to adsorb cationic dyes such as methylene blue (Yu et al., 2016; Albadarin et al., 2017) and malachite green (Tang et al., 2016) but this is of limited use in practical applications requiring purification of complex wastewaters. Hence our hypothesis was that the N-lignin could be more universal adsorbent due to its zwitterion character and hence we tested also anionic and neutral dyes. N-lignin and wheat straw soda lignin (GreenValue) were compared as adsorbents for two cationic dyes (methylene blue and malachite green), one anionic dye (acid red 88), and one uncharged dye (mordant red 11). The concentration of cationic and anionic dyes in the adsorption experiments was 0.1 mM. Due to its low water-solubility, a filtered saturated solution of mordant red 11 was used. Absorbance spectra were recorded after

8 h contact time with the adsorbents, and decolourization was calculated from the absorbance maxima in the visible wavelength region (**Figures 9A–D**).

Both of the lignins turned out to be effective adsorbents for methylene blue, with 93–96% decolourization and 84–86 mg/g (non-maximum) equilibrium adsorption capacities, respectively, for N-lignin and soda lignin (**Figure 9E**). In the case of malachite green the highest extent of 75% decolourization was obtained with soda lignin, compared to 63% with N-lignin. As mentioned above, anionic dyes are more demanding pollutants to remove by adsorption due to their electrostatic repulsion with negatively charged lignins. It was thus important to observe that N-lignin was clearly more effective adsorbent for Acid red 88 (29% decolourization) than soda lignin (6% decolourization). In the case of the uncharged dye mordant red 11, 87% decolourization was reached with soda lignin, a slightly higher value compared to 79% with N-lignin. This minor difference could be related to differences in surface area or adsorption sites of the two lignins, but further analysis of this matter was beyond the scope of the present work.

One important feature of any adsorbent is its structural stability in the wastewater. Due to their pH-dependent solubility, leaching of lignin from solid particles is common in aqueous media. Interestingly, due to the electrostatic complex formation absorbance reading at 280 nm did not indicate obvious leaching of lignins in the presence of cationic dyes, unlike in the presence of anionic and non-charged dyes (**Figures 9A–D**). Hydrogels represent another means to stabilize lignin-based adsorbents. Yu et al. (2016) synthesized hydrogels by grafting acrylic acid on the lignosulfonate backbone, and reported that the maximum equilibrium adsorption capacity of methylene blue reached 2,013 mg/g. The hydrogel was quite stable, since the adsorption capacity decreased only to 1,681 mg/g after four desorption/reuse cycles. Combination of lignin with chitin (Duan et al., 2018) and chitosan (Albadarin et al., 2017) has been made to form structurally stabilized composites for water purification. Tang et al. (2016) grafted acrylamide to lignosulfonate, and cross-linked the aromatic rings with formaldehyde under acidic conditions. Others have synthesized cationic lignin for adsorption and flocculation of pollutants (Wahlström et al., 2017). These promising results encourage to continue water remediation research with chemically tailored lignins and colloidal lignin particles (Sipponen et al., 2017b). In retrospect, the sorption of not only cationic but also anionic and uncharged dyes on N-lignin may explain why cellulases tend to adsorb on residual lignin in ammonia pre-treated straw. Cellulases contain charged and uncharged amino acids that may bind non-covalently with amphiphilic N-lignin, which may explain the adsorption affinity of cellulases on ammonia-treated lignin (Yoo et al., 2017).

CONCLUSIONS

This work had two interlinked objectives. The first was to optimize aqueous ammonia extraction of hydrothermally pre-treated wheat straw to isolate lignin and facilitate enzymatic hydrolysis of the cellulosic fraction. The second important goal was to provide improved understanding of the isolated nitrogen-containing lignin, and to assess its valorization as adsorbent in water remediation. Aqueous ammonia extraction improved accessibility to hydrolytic enzymes of the straw polysaccharides mainly by removing lignin without extensive oxidation. However, incorporation of nitrogen in wheat straw lignin reduced hydrolysability at low enzyme activity dosages, presumably by competitive adsorption of cellulases. The nitrogen-containing lignin showed beneficial broad spectrum adsorption of anionic, cationic, and uncharged organic dyes from aqueous solutions. Besides the demonstrated water purification applications, our results suggest that N-lignins could find use as adsorbents in enzyme immobilization.

DATA AVAILABILITY

All datasets generated for this study are included in the manuscript. Raw data is available from the authors upon a reasonable request.

AUTHOR CONTRIBUTIONS

MS carried out the experimental work and analyzed the results with input from MÖ. MS wrote the manuscript with input and critical comments from MÖ.

ACKNOWLEDGMENTS

MS acknowledges funding from Academy of Finland (Grant 296547), the Novo Nordisk Foundation (SUSCELL project, Reference Number: NNF17OC0027658) and Neste Corporation within the Microbial Oil project co-finance by Tekes (nowadays Business Finland). Tiia Juhala is acknowledged for carrying out the CHNS analyses. Dr. Leena Pitkänen (Aalto University) is acknowledged for technical assistance with the SEC analysis of N-lignin.

REFERENCES

Albadarin, A. B., Collins, M. N., Naushad, M., Shirazian, S., Walker, G., and Mangwandi, C. (2017). Activated lignin-chitosan extruded blends for efficient adsorption of methylene blue. *Chem. Eng. J.* 307, 264–272. doi: 10.1016/j.cej.2016.08.089

An, S., Li, W., Liu, Q., Xia, Y., Zhang, T., Huang, F., et al. (2019). Combined dilute hydrochloric acid and alkaline wet oxidation pretreatment to improve sugar recovery of corn stover. *Bioresour. Technol.* 271, 283–288. doi: 10.1016/j.biortech.2018.09.126

Auxenfans, T., Crônier, D., Chabbert, B., and Paës, G. (2017). Understanding the structural and chemical changes of plant biomass following steam explosion pretreatment. *Biotechnol. Biofuels* 10, 1–16. doi: 10.1186/s13068-017-0718-z

Capanema, B. E. A., Chen, C., Gratzl, J. S., Kirkman, A. G., Science, P., Federal, U., et al. (2001). Oxidative ammonolysis of technical lignins part 1. kinetics of the reaction under isothermal condition at 130°C. *Holzforschung* 55, 397–404. doi: 10.1515/HF.2001.066

Capanema, E. A., Balakshin, M. Y., Chen, C., and Gratzl, J. S. (2006). Oxidative ammonolysis of technical lignins. Part 4. Effects of the ammonium hydroxide concentration and pH. *J. Wood Chem. Technol.* 26, 95–109. doi: 10.1080/02773810600582350

Capanema, E. A., Balakshin, M. Y., Chen, C. L., Gratzl, J. S., and Kirkman, A. G. (2002). Oxidative ammonolysis of technical lignins. Part 3. Effect of temperature on the reaction rate. *Holzforschung* 56, 402–415. doi: 10.1515/HF.2002.063

Cayetano, R. D. A., and Kim, T. H. (2017). Effects of Low Moisture Anhydrous Ammonia (LMAA) pretreatment at controlled ammoniation temperatures on enzymatic hydrolysis of corn stover. *Appl. Biochem. Biotechnol.* 181, 1257–1269. doi: 10.1007/s12010-016-2282-6

Cayetano, R. D. A., and Kim, T. H. (2018). Two-stage processing of *Miscanthus giganteus* using anhydrous ammonia and hot water for effective xylan recovery and improved enzymatic saccharification. *Bioresour. Technol.* 255, 163–170. doi: 10.1016/j.biortech.2018.01.135

Chen, F., and Dixon, R. A. (2007). Lignin modification improves fermentable sugar yields for biofuel production. *Nat. Biotechnol.* 25, 759–761. doi: 10.1038/nbt1316

Chong, G. G., He, Y. C., Liu, Q. X., Kou, X. Q., and Qing, Q. (2017). Sequential aqueous ammonia extraction and LiCl/N,N-Dimethyl formamide pretreatment for enhancing enzymatic saccharification of Winter bamboo shoot shell. *Appl. Biochem. Biotechnol.* 182, 1341–1357. doi: 10.1007/s12010-017-2402-y

Chundawat, S. P. S., Beckham, G. T., Himmel, M. E., and Dale, B. E. (2011a). Deconstruction of lignocellulosic biomass to fuels and chemicals. *Annu. Rev. Chem. Biomol. Eng.* 2, 121–145. doi: 10.1146/annurev-chembioeng-061010-114205

Chundawat, S. P. S., Donohoe, B. S., da Costa Sousa, L., Elder, T., Agarwal, U. P., Lu, F., et al. (2011b). Multi-scale visualization and characterization of lignocellulosic plant cell wall deconstruction during thermochemical pretreatment. *Energy Environ. Sci.* 4, 973–984. doi: 10.1039/c0ee00574f

De Campos Vidal, B., and Mello, M. L. S. (2011). Collagen type I amide I band infrared spectroscopy. *Micron* 42, 283–289. doi: 10.1016/j.micron.2010.09.010

Dence, C. W. (1992). "The determination of lignin," in *Methods in Lignin Chemistry*, eds C. W. D. Stephen and Y. Lin (Berlin: Springer), 33–58. doi: 10.1007/978-3-642-74065-7_3

Domanski, J., Borowski, S., Marchut-Mikolajczyk, O., and Kubacki, P. (2016). Pretreatment of rye straw with aqueous ammonia for conversion to fermentable sugars as a potential substrates in biotechnological processes. *Biomass Bioenergy* 91, 91–97. doi: 10.1016/j.biombioe.2016.05.008

Dos Santos, J. E., Dockal, E. R., and Cavalheiro, É. T. G. (2005). Synthesis and characterization of Schiff bases from chitosan and salicylaldehyde derivatives. *Carbohydr. Polym.* 60, 277–282. doi: 10.1016/j.carbpol.2004.12.008

Du, R., Su, R., Qi, W., and He, Z. (2018). Enhanced enzymatic hydrolysis of corncob by ultrasound-assisted soaking in aqueous ammonia pretreatment. *3 Biotech* 8, 1–7. doi: 10.1007/s13205-018-1186-2

Duan, Y., Freyburger, A., Kunz, W., and Zollfrank, C. (2018). Lignin/chitin films and their adsorption characteristics for heavy metal ions. *ACS Sustain. Chem. Eng.* 6, 6965–6973. doi: 10.1021/acssuschemeng.8b00805

Faix, O. (1992). "Fourier transform infrared spectroscopy," in *Methods in Lignin Chemistry*, eds S. Y. Lin and C. W. Dence (Berlin: Springer-Verlag Berlin Heidelberg), 81–109. doi: 10.1007/978-3-642-74065-7_7

Flores-Gómez, C. A., Escamilla Silva, E. M., Zhong, C., Dale, B. E., Da Costa Sousa, L., and Balan, V. (2018). Conversion of lignocellulosic agave residues into liquid biofuels using an AFEX$^{\mathrm{TM}}$-based biorefinery. *Biotechnol. Biofuels* 11, 1–18. doi: 10.1186/s13068-017-0995-6

Fu, F. N., DeOliveira, D. B., Trumble, W. R., Sarkar, H. K., and Singh, B. R. (1994). Secondary structure estimation of proteins using the amide III region of fourier transform infrared spectroscopy: application to analyze calcium-binding-induced structural changes in calsequestrin. *Appl. Spectrosc.* 48, 1432–1441. doi: 10.1366/0003702944028065

Granata, A., and Argyropoulos, D. S. (1995). 2-Chloro-4,4,5,5-tetramethyl-1,3,2-dioxaphospholane, a reagent for the accurate determination of the uncondensed and condensed phenolic moieties in lignins. *J. Agric. Food Chem.* 43, 1538–1544. doi: 10.1021/jf00054a023

Guo, M., Jin, T., Nghiem, N. P., Fan, X., Qi, P. X., Jang, C. H., et al. (2018). Assessment of antioxidant and antimicrobial properties of lignin from corn stover residue pretreated with low-moisture anhydrous ammonia and enzymatic hydrolysis process. *Appl. Biochem. Biotechnol.* 184, 350–365. doi: 10.1007/s12010-017-2550-0

Hage, R., El Brosse, N., Chrusciel, L., Sanchez, C., Sannigrahi, P., and Ragauskas, A. (2009). Characterization of milled wood lignin and ethanol organosolv lignin from miscanthus. *Polym. Degrad. Stab.* 94, 1632–1638. doi: 10.1016/j.polymdegradstab.2009.07.007

Himmel, M. E., Ding, S.-Y., Johnson, D. K., Adney, W. S., Nimlos, M. R., Brady, J. W., et al. (2007). Biomass recalcitrance: engineering plants and enzymes for biofuels production. *Science* 315, 804–807. doi: 10.1126/science.1137016

Huo, D., Yang, Q., Fang, G., Liu, Q., Si, C., Hou, Q., et al. (2018). Improving the efficiency of enzymatic hydrolysis of Eucalyptus residues with a modified aqueous ammonia soaking method. *Nord. Pulp Pap. Res. J.* 33, 165–174. doi: 10.1515/npprj-2018-3025

Kondo, T., Ohshita, T., and Kyuma, T. (1992). Comparison of characteristics of soluble lignins from untreated and ammonia-treated wheat straw. *Anim. Feed Sci. Technol.* 39, 253–263. doi: 10.1016/0377-8401(92)90045-8

Lapierre, C., Monties, B., Meier, D., and Faix, O. (1994). Structural investigation of kraft lignins transformed via oxo-ammoniation to potential nitrogenous fertilizers. *Holzforschung* 48, 63–68. doi: 10.1515/hfsg.1994.48.s1.63

Laurichesse, S., and Avérous, L. (2014). Chemical modification of lignins: towards biobased polymers. *Prog. Polym. Sci.* 39, 1266–1290. doi: 10.1016/j.progpolymsci.2013.11.004

Lawoko, M., Henriksson, G., and Gellerstedt, G. (2006). Characterisation of lignin-carbohydrate complexes (LCCs) of spruce wood (*Picea abies* L.) isolated with two methods. *Holzforschung* 60, 156–161. doi: 10.1515/HF.2006.025

Li, H., Xiong, L., Chen, X., Li, H., Qi, G., Huang, C., et al. (2017). Enhanced enzymatic hydrolysis and acetone-butanol-ethanol fermentation of sugarcane bagasse by combined diluted acid with oxidate ammonolysis pretreatment. *Bioresour. Technol.* 228, 257–263. doi: 10.1016/j.biortech.2016.12.119

Li, M., Pu, Y., and Ragauskas, A. J. (2016). Current understanding of the correlation of lignin structure with biomass recalcitrance. *Front. Chem.* 4:45. doi: 10.3389/fchem.2016.00045

Liu, H., Sun, J., Leu, S.-Y., and Chen, S. (2016). Toward a fundamental understanding of cellulase-lignin interactions in the whole slurry enzymatic saccharification process. *Biofuels Bioprod. Bioref.* 10, 648–663. doi: 10.1002/bbb.1670

Lora, J. H., and Wayman, M. (1978). Delignification of hardwoods by autohydrolysis and extraction. *Tappi J.* 61, 47–50.

Mittal, A., Katahira, R., Donohoe, B. S., Pattathil, S., Kandemkavil, S., Reed, M. L., et al. (2017). Ammonia pretreatment of corn stover enables facile lignin extraction. *ACS Sustain. Chem. Eng.* 5, 2544–2561. doi: 10.1021/acssuschemeng.6b02892

Mousavioun, P., and Doherty, W. O. S. (2010). Chemical and thermal properties of fractionated bagasse soda lignin. *Ind. Crops Prod.* 31, 52–58. doi: 10.1016/j.indcrop.2009.09.001

Nascimento, E. A., Morais, S. A. L., Veloso, D. P., and Menezes, S. M. C. (1994). Oxidative ammonolysis of the *Eucalyptus grandis* Kraft Lignin. *J. Brazilian Chem. Soc.* 5, 5–14. doi: 10.5935/0103-5053.19940002

Niemi, P., Pihlajaniemi, V., Rinne, M., and Siika-aho, M. (2017). Production of sugars from grass silage after steam explosion or soaking in aqueous ammonia. *Ind. Crops Prod.* 98, 93–99. doi: 10.1016/j.indcrop.2017.01.022

Paës, G., Habrant, A., Ossemond, J., and Chabbert, B. (2017). Exploring accessibility of pretreated poplar cell walls by measuring dynamics of fluorescent probes. *Biotechnol. Biofuels* 10, 1–10. doi: 10.1186/s13068-017-0704-5

Pedersen, M., and Meyer, A. S. (2010). Lignocellulose pretreatment severity - relating pH to biomatrix opening. *N. Biotechnol.* 27, 739–750. doi: 10.1016/j.nbt.2010.05.003

Phitsuwan, P., Sakka, K., and Ratanakhanokchai, K. (2016). Structural changes and enzymatic response of Napier grass (*Pennisetum purpureum*) stem induced by alkaline pretreatment. *Bioresour. Technol.* 218, 247–256. doi: 10.1016/j.biortech.2016.06.089

Pihlajaniemi, V., Sipponen, M. H., Liimatainen, H., Sirviö, J. A., Nyyssölä, A., and Laakso, S. (2016). Weighing the factors behind enzymatic hydrolyzability of pretreated lignocellulose. *Green Chem.* 18, 1295–1305. doi: 10.1039/C5GC01861G

Pihlajaniemi, V., Sipponen, S., Sipponen, M. H., Pastinen, O., and Laakso, S. (2014). Enzymatic saccharification of pretreated wheat straw: comparison of solids-recycling, sequential hydrolysis and batch hydrolysis. *Bioresour. Technol.* 153, 15–22. doi: 10.1016/j.biortech.2013.11.060

Potthast, B. A., Schiene, R., Fischer, K., Pflanzenchemie, H.-, and Dresden, T. U. (1996). Structural investigations of N-modified lignins by 15N-NMR spectroscopy and possible pathways for formation of nitrogen containing compounds related to lignin. *Holzforschung* 50, 554–562. doi: 10.1515/hfsg.1996.50.6.554

Ragauskas, A. J., Beckham, G. T., Biddy, M. J., Chandra, R., Chen, F., Davis, M. F., et al. (2014). Lignin valorization: improving lignin processing in the biorefinery. *Science* 344:1246843. doi: 10.1126/science.1246843

Ramírez, F., González, V., Crespo, M., Meier, D., Faix, O., and Zúñiga, V. (1997). Ammoxidized kraft lignin as a slow-release fertilizer tested on *Sorghum vulgare*. *Bioresour. Technol.* 61, 43–46. doi: 10.1016/S0960-8524(97)84697-4

Sakuragi, K., Igarashi, K., and Samejima, M. (2018). Application of ammonia pretreatment to enable enzymatic hydrolysis of hardwood biomass. *Polym. Degrad. Stab.* 148, 19–25. doi: 10.1016/j.polymdegradstab.2017.12.008

Selig, M. J., Viamajala, S., Decker, S. R., Tucker, M. P., Himmel, M. E., and Vinzant, T. B. (2007). Deposition of lignin droplets produced during dilute acid pretreatment of maize stems retards enzymatic hydrolysis of cellulose. *Biotechnol. Prog.* 23, 1333–1339. doi: 10.1021/bp0702018

Silverstein, R. A., Chen, Y., Sharma-Shivappa, R. R., Boyette, M. D., and Osborne, J. (2007). A comparison of chemical pretreatment methods for improving saccharification of cotton stalks. *Bioresour. Technol.* 98, 3000–3011. doi: 10.1016/j.biortech.2006.10.022

Sipponen, M. H. (2015). *Effect of Lignin Structure on Enzymatic Hydrolysis of Plant Residues*, Helsinki: Aalto University Doctoral Dissertations 79/2015.

Sipponen, M. H., Pihlajaniemi, V., Pastinen, O., and Laakso, S. (2014). Reduction of surface area of lignin improves enzymatic hydrolysis of cellulose from hydrothermally pretreated wheat straw. *RSC Adv.* 4, 36591–36596. doi: 10.1039/C4RA06926A

Sipponen, M. H., Rahikainen, J., Leskinen, T., Pihlajaniemi, V., Mattinen, M.-L., Lange, H., et al. (2017a). Structural changes of lignin in biorefinery pretreatments and consequences to enzyme-lignin interactions. *Nord. Pulp Pap. Res. J.* 32, 550–571. doi: 10.3183/NPPRJ-2017-32-04-p550-571

Sipponen, M. H., Smyth, M., Leskinen, T., Johansson, L.-S., and Österberg, M. (2017b). All-lignin approach to prepare cationic colloidal lignin particles: stabilization of durable pickering emulsions. *Green Chem.* 19, 5831–5840. doi: 10.1039/C7GC02900D

Sluiter, J. B., Ruiz, R. O., Scarlata, C. J., Sluiter, A. D., and Templeton, D. W. (2010). Compositional analysis of lignocellulosic feedstocks. 1. Review and description of methods. *J. Agric. Food Chem.* 58, 9043–9053. doi: 10.1021/jf1008023

Tang, Y., Zeng, Y., Hu, T., Zhou, Q., and Peng, Y. (2016). Preparation of lignin sulfonate-based mesoporous materials for adsorbing malachite green from aqueous solution. *J. Environ. Chem. Eng.* 4, 2900–2910. doi: 10.1016/j.jece.2016.05.040

Tolbert, A. K., Yoo, C. G., and Ragauskas, A. J. (2017). Understanding the changes to biomass surface characteristics after ammonia and organosolv pretreatments by using time-of-flight secondary-ion mass spectrometry (TOF-SIMS). *Chempluschem* 82, 686–690. doi: 10.1002/cplu.201700138

Vanderghem, C., Richel, A., Jacquet, N., Blecker, C., and Paquot, M. (2011). Impact of formic/acetic acid and ammonia pre-treatments on chemical structure and physico-chemical properties of *Miscanthus x giganteus* lignins. *Polym. Degrad. Stab.* 96, 1761–1770. doi: 10.1016/j.polymdegradstab.2011.07.022

Wahlström, R., Kalliola, A., Heikkinen, J., Kyllönen, H., and Tamminen, T. (2017). Lignin cationization with glycidyltrimethylammonium chloride aiming at water purification applications. *Ind. Crops Prod.* 104, 188–194. doi: 10.1016/j.indcrop.2017.04.026

Watanabe, T., Ohnishi, L., Yamasaki, Y., Kaizu, S., and Koshijima, T. (1989). Binding-site analysis of the ether linkages between lignin and hemicelluloses in lignin-carbohydrate complexes by ddq-oxidation. *Agric. Biol. Chem.* 53, 2233–2252. doi: 10.1080/00021369.1989.10869603

Xiao, M., Wang, L., Wu, Y., Cheng, C., Chen, L., Chen, H., et al. (2019). Hybrid dilute sulfuric acid and aqueous ammonia pretreatment for improving butanol production from corn stover with reduced wastewater generation. *Bioresour. Technol.* 278, 460–463. doi: 10.1016/j.biortech.2019.01.079

Yoo, C. G., Li, M., Meng, X., Pu, Y., and Ragauskas, A. J. (2017). Effects of organosolv and ammonia pretreatments on lignin properties and its inhibition for enzymatic hydrolysis. *Green Chem.* 19, 2006–2016. doi: 10.1039/C6GC03627A

Yoo, M. J., Kim, H. W., Yoo, B. M., and Park, H. B. (2014). Highly soluble polyetheramine-functionalized graphene oxide and reduced graphene oxide both in aqueous and non-aqueous solvents. *Carbon N. Y.* 75, 149–160. doi: 10.1016/j.carbon.2014.03.048

Yu, C., Wang, F., Zhang, C., Fu, S., and Lucia, L. A. (2016). The synthesis and absorption dynamics of a lignin-based hydrogel for remediation of cationic dye-contaminated effluent. *React. Funct. Polym.* 106, 137–142. doi: 10.1016/j.reactfunctpolym.2016.07.016

Yuan, T. Q., Sun, S. N., Xu, F., and Sun, R. C. (2011). Characterization of lignin structures and lignin-carbohydrate complex (LCC) linkages by quantitative 13C and 2D HSQC NMR spectroscopy. *J. Agric. Food Chem.* 59, 10604–10614. doi: 10.1021/jf2031549

Zakzeski, J., Bruijnincx, P. C. A., Jongerius, A. L., and Weckhuysen, B. M. (2010). The catalytic valorization of lignin for the production of renewable chemicals. *Chem. Rev.* 110, 3552–3599. doi: 10.1021/cr900354u

Zhang, L., Zhang, L., Zhou, T., Wu, Y., and Xu, F. (2016). The dual effects of lignin content on enzymatic hydrolysis using film composed of cellulose and lignin as a structure model. *Bioresour. Technol.* 200, 761–769. doi: 10.1016/j.biortech.2015.10.048

Zhou, L., da Costa Sousa, L., Dale, B. E., Feng, J.-X., and Balan, V. (2018). The effect of alkali-soluble lignin on purified core cellulase and hemicellulase activities during hydrolysis of extracticve ammonia-pretreated lignocellulosic biomass. *R. Soc. Open Sci.* 5, 1–21. doi: 10.1098/rsos.171529

Zhu, J.-Q., Li, W.-C., Qin, L., Zhao, X., Chen, S., Liu, H., et al. (2018). Stepwise pretreatment of aqueous ammonia and ethylenediamine improve enzymatic hydrolysis of corn stover. *Ind. Crops Prod.* 124, 201–208. doi: 10.1016/j.indcrop.2018.07.072

Zhu, X., Tang, M., and Chen, H. (2019). Delignification and hydrolyzation of mycorrhizal black locust biomass pretreated with aqueous ammonia. *BioResources* 14, 965–976. doi: 10.15376/biores.14.1.965-976

Conflict of Interest Statement: The authors declare that the research was conducted in the absence of any commercial or financial relationships that could be construed as a potential conflict of interest.

Copyright © 2019 Sipponen and Österberg. This is an open-access article distributed under the terms of the Creative Commons Attribution License (CC BY). The use, distribution or reproduction in other forums is permitted, provided the original author(s) and the copyright owner(s) are credited and that the original publication in this journal is cited, in accordance with accepted academic practice. No use, distribution or reproduction is permitted which does not comply with these terms.

frontiers in Chemistry

ORIGINAL RESEARCH
published: 14 August 2019
doi: 10.3389/fchem.2019.00578

Acidic Ionic Liquid as Both Solvent and Catalyst for Fast Chemical Esterification of Industrial Lignins: Performances and Regioselectivity

Eric Husson[1]*, *Lise Hulin*[1], *Caroline Hadad*[2], *Chaima Boughanmi*[1], *Tatjana Stevanovic*[3] *and Catherine Sarazin*[1]*

[1] *Unité de Génie Enzymatique et Cellulaire, UMR 7025 CNRS, Université de Picardie Jules Verne, Amiens, France,* [2] *Laboratoire de Glycochimie, des Antimicrobiens et des Agroressources, UMR CNRS 7378, Université de Picardie Jules Verne, Amiens, France,* [3] *Département des Sciences du Bois et de la Forêt, Centre de Recherche sur les Matériaux Renouvelables, Université Laval, Quebec City, QC, Canada*

OPEN ACCESS

Edited by:
Gabriel Paes,
Fractionnation of AgroResources and Environment (INRA), France

Reviewed by:
Paul-Henri Ducrot,
INRA UMR1318 Institut Jean Pierre Bourgin, France
Haaan Sadeghifar,
North Carolina State University, United States

***Correspondence:**
Eric Husson
eric.husson@u-picardie.fr
Catherine Sarazin
catherine.sarazin@u-picardie.fr

Specialty section:
This article was submitted to Green and Sustainable Chemistry, a section of the journal Frontiers in Chemistry

Received: 13 May 2019
Accepted: 30 July 2019
Published: 14 August 2019

Citation:
Husson E, Hulin L, Hadad C, Boughanmi C, Stevanovic T and Sarazin C (2019) Acidic Ionic Liquid as Both Solvent and Catalyst for Fast Chemical Esterification of Industrial Lignins: Performances and Regioselectivity. Front. Chem. 7:578. doi: 10.3389/fchem.2019.00578

Lignin can be considered an essential under-exploited polymer from lignocellulosic biomass representing a key for a profitable biorefinery. One method of lignin valorization could be the improvement of physico-chemical properties by esterification to enhance miscibility in apolar polyolefin matrices, thereby helping the production of bio-based composites. The present work describes for the first time a succeeded chemical esterification of industrial lignins with maleic anhydride in an acidic ionic liquid: 1-butyl-3-methyl imidazolium hydrogen sulfate without additional catalyst. This efficient strategy was applied to four industrial lignins: two softwood Kraft lignins (Indulin AT, Wayagamack), one hardwood Kraft lignin (Windsor), and one softwood organosolv lignin (Lignol), distinct in origin, extraction process and thus chemical structure. The chemical, structural, and thermal properties of modified lignins were characterized by ^{31}P nuclear magnetic resonance, infrared spectroscopy and thermal analyses, then compared to those of unmodified lignins. After 4 h of reaction, between 30 to 52% of the constitutive hydroxyls were esterified depending on the type of lignin sample. The regioselectivity of the reaction was demonstrated to be preferentially orientated toward aliphatic hydroxyls for three out of four lignins (66.6, 65.5, and 83.6% for Indulin AT, Windsor and Lignol, respectively, vs. 51.7% for Wayagamack). The origin and the extraction process of the polymer would thus influence the efficiency and the regioselectivity of this reaction. Finally, we demonstrated that the covalent grafting of maleyl chain on lignins did not significantly affect thermal stability and increased significantly the solubility in polar and protic solvent probably due to additional exposed carboxylic groups resulted from mono-acylation independently of H/G/S ratio. Blending with polyolefins could then be considered in regard of compatibility with the obtained physico-chemical properties.

Keywords: lignin, chemical esterification, acidic ionic liquids, selectivity, thermal properties

INTRODUCTION

The biorefinery concept consists of the development of innovative and sustainable strategies for the valorization of a whole biomass such as a plant in its entirety and in particular the three main constitutive polymers; cellulose, hemicellulose and lignin, respectively (Ferreira, 2017). Lignins are complex highly branched amorphous polymers based on polyphenolic structures constituted of phenylpropane units, e.g., syringylpropane (S), guaiacylpropane (G), and hydroxyphenylpropane (H), providing interesting reactivity for chemical modifications (Erdtman, 1972; Stevanovic and Perrin, 2009; Laurichesse and Avérous, 2014). Lignin is henceforth considered as an essential under-exploited potential offering a key-issue for a profitable biorefinery (Calvo-Flores and Dobado, 2010; Doherty et al., 2011). Indeed, to date, only 2% of industrial lignin is valorized into applications other than energy production: base materials for the production of chemicals, adhesives or fertilizers are some examples (Gandini and Belgacem, 2008; Ion et al., 2018). An emergent way of valorization could be the blending of lignin with apolar matrices of polyolefins to produce partially bio-based composites with improved rheological and thermomechanical properties and better carbon footprint (Thielemans and Wool, 2005; Laurichesse and Avérous, 2014). However, the difference in polarity between lignins and polyolefins such as polyethylene impedes considerably their miscibility. To overcome this constraint, physico-chemical properties of lignin can be modified by chemical esterification with apolar moieties (Nadji et al., 2010; Gordobil et al., 2015). The acyl donors generally used for these modifications are short acyl chains present in acetic, butyric, succinic or maleic anhydrides (Xiao et al., 2001; Thielemans and Wool, 2005; Tamminen et al., 2012) or acyl chlorides (Koivu et al., 2016). Some drawbacks can be the use of tetrahydrofurane, 1,4-dioxane or *N*-methyl pyrrolidone as organic solvents, thionyl chloride as hazardous chemical reagents, and pyridine derivatives or 1-methyl imidazole as catalysts. Besides the use of non-environmentally friendly chemicals, drastic reaction conditions are often applied (high temperature reaction, extreme pH) together with the production of by-products and salts involving purification steps, which are not in agreement with the current environmental requirements and green chemistry framework (Anastas and Eghbali, 2010; Zhao et al., 2017). The development of alternative strategies thus remains a current scientific and technological challenge in the biorefinery concept. In this way, one can take advantage of the use of some ILs able to act both as solvent for lignin and as catalyst for lignin esterification based. For example, a recent study reported the IL to promote lignin acetylation of aliphatic hydroxyl groups while aromatic acetate were deacetylated, in DMSO as solvent (Suzuki et al., 2018). Earlier, based on the acidic properties of 1-butyl-3-methyl imidazolium hydrogen sulfate ([Bmim][HSO_4]), it was evidenced that this IL acts as a catalyst for esterification of linear alcohols (Fraga-Dubreuil et al., 2002).

On the other hand, the access to a lignin fraction with an adequate purity or structural integrity for considering valorization requires an efficient fractioning of lignocellulosic biomass (LCB) upstream. From now on, a very large panel of fractioning, and delignification pretreatments of LCB is described in the literature. These include the use of dilute acid or alkali solutions, liquid hot water, organosolv, steam explosion, liquid hot water, ultrasounds-assisted processes, or high voltage electrical discharges methods (Park and Kim, 2012; Zhu et al., 2012; Putro et al., 2016; Brahim et al., 2017; Gominho et al., 2019). Some imidazolium-based ionic liquids (ILs) are now well-recognized for efficiently fractionate LCB under mild conditions (Brandt et al., 2011; Papa et al., 2012; Auxenfans et al., 2014; Husson et al., 2018; Singh et al., 2018). These ILs constitute promising solvents with unique properties such as low vapor pressure, recyclability, thermostability, and acceptable toxicity for some of them, particularly those with cation alkyl chain length inferior or equal to 4 carbons (García-Lorenzo et al., 2008; Egorova and Ananikov, 2014). In this context, it can be noticed that [Bmim] [HSO_4] would be a suitable candidate to induce lignin removal from LCB as effective as acetate or chloride anion imidazolium-based IL. The acidic properties of this IL coupled with residual water content allow inducing acid-catalyzed hydrolysis of the β-O-4 linkage resulting in its dissociation from the carbohydrate matrix and then its dissolution (Brandt et al., 2011; Carvalho et al., 2015; Bernardo et al., 2019). It can then be imagined that chemical esterification of lignin could be directly implemented in the IL used for pretreatment/fractioning to avoid tremendous procedures of lignin extraction.

Before considering the development of a one-batch process including delignificaton of LCB and subsequent transformation of lignin in the same IL, the study of both the feasibility of chemical esterification of lignin in ([Bmim] [$HSO_4$and the versatility of this strategy is inherent. For this reason, we selected four distinct industrials lignin as representative substrates: two softwood Kraft lignins (Indulin AT, Wayagamack), one hardwood Kraft lignin (Windsor) and one softwood organosolv lignin (Lignol) distinct in origin, extraction process, and thus chemical structure. The raw materials were firstly characterized, especially the hydroxyl groups. Then, the impact of single incubation in [Bmim][HSO_4] on the structural and physicochemical properties was studied. Finally, the feasibility of lignin esterification with maleic anhydride was investigated without additional catalyst. Extracted modified lignins were finely characterized and the performances and selectivity of these non-conventional reaction systems were discussed based on quantitative data.

MATERIALS AND METHODS

Reagent

Maleic anhydride (>99%), 2-chloro-4,4,5,5-tetramethyl-1,3,2-dioxaphospholane (95%), chromium acetylacetonate (>97%), *N*-Hydroxyphtalimide (97%), acetonitrile (HPLC grade), chloroform-d (99.8%), and pyridine (99.8%) were acquired from Sigma-Aldrich (Steinheim, Germany). 1-butyl-3-methylimidazolium hydrogen sulfate [Bmim][HSO_4] (98%) was produced by Solvionic SA (Verniole, France).

Industrial Lignins

Kruger Wayagamack and Domtar Windsor furnished two Kraft black liquors, used to precipitate Kraft lignin. Kruger Wayagamack black liquor was extracted from softwood and exhibited 50.9% of solid content with a pH = 14, and a volumetric mass of 1.27 g.ml^{-1}. Domtar Windsor black liquor was from hardwood and contained 24.0% of solid with a pH = 13 and a volumetric mass of 1.12 g.ml^{-1}. Wayagamack and Windsor lignins were extracted from black liquor followed by a precipitation procedure using carbon dioxyde described in a previous study (Schorr et al., 2014). Indulin AT lignin was extracted from softwood by Kraft process and furnished by the Westvaco Company. Composition in Klason and acid soluble lignins, total sugars and ash contents of these three Kraft lignins were reported by Schorr et al. (2014) and summarized in **Supplementary Table 1** and suggested a satisfactory purity (>95% with around 1% of residual sugars) allowing to consider as significant the result on lignin esterification. Lignol^{TM} lignin was extracted by organosolv process applied on softwood and produced by Lignol Innovation LTD (Berlin et al., 2011).

Esterification of Industrial Lignins

The four industrial lignins were lyophilized and [Bmim][HSO$_4$] was dried at 80°C under vacuum for 4 h (Rotavapor R-200, Büchi, France). Lignins and [Bmim][HSO$_4$] were then stored in desiccator for 48 h before each reaction. The water content and water activity of the industrial lignins and [Bmim][HSO$_4$] were then determined by Karl Fischer coulometry method (831 KF Coulometer, Metrohm, France) and a thermoconstanter (LabTouch Aw, Novasina, Switzerland), respectively. Data were reported in **Table 1** as a mean of two replicates. Reactions were carried out in parallel with a synthesis station (Carousel 12+, Interchim, France) allowing to implement simultaneously 12 identical reactions. In a typical reaction, 300 mg of [Bmim][HSO$_4$] (melting point 28°C) were incubated at 75°C under vigorous stirring until total liquefaction. Reaction was initiated by introducing lignin (10 mg) and maleic anhydride in distinct ratio: 1/1, 1/2, 1/5, 1/7.5, and 1/10 (w/w) and was performed at 75°C for 4 h under vigorous stirring. After this duration, the mixture was cooled down in an ice bath in order to stop the reaction. Acetonitrile was added in the reaction medium to precipitate the modified lignin. The resulted solid residue was collected by vacuum filtration, thoroughly washed with acetonitrile to eliminate unreacted maleic anhydride and [Bmim][HSO$_4$], allowing to check that there is no residual IL, and then dried for 4 h at 100°C. Control experiments without maleic anhydride were also carried out in [Bmim][HSO$_4$] (30/1 IL/lignin ratio, w/w) under the same conditions followed by similar extraction procedure to evaluate the impact of [Bmim][HSO$_4$] on the four industrial lignins. Control, reaction and extraction were replicated three times.

Solubility of Lignins and Their Corresponding Esters

The solubility of Wayagamack and Windsor lignins (distinct by their respective H/G/S ratio) before and after esterification was determined in methanol and chloroform according to experimental procedure reported in previous studies (Cybulska et al., 2012; Sameni et al., 2017). At room temperature, 5 mL of organic solvent were added to 50 mg oven-dried lignin (or maleated lignin). The samples were sonicated for 10 min in a water bath sonicator at 40°C. The resulted suspensions were filtered with paper filter (Whatman no 1). Filters and retentats were air dried and then weighed. The soluble fraction was calculated by subtracting the insoluble fraction from the initial 50 mg lignin weight. Solubility values were expressed as mean values of three replicates with standard deviations (±) in g.L^{-1}.

TABLE 1 | Water content and water activity of lyophilized lignins and dried [Bmim][HSO$_4$].

	Water content (%, w/w)	a_w
Lignins		
Indulin AT	3.24 ± 0.04	0.32
Windsor	3.12 ± 0.88	0.38
Wayagamack	3.23 ± 1.14	0.33
Lignol^{TM}	2.04 ± 0.70	0.34
Ionic Liquid		
[Bmim][HSO$_4$]	0.02 ± 0.01	0.13

Structural and Thermal Analyses

Pyrolysis-GC/MS

Pyrolysis-GC/MS analyses were performed in triplicate according experimental procedure described by Schorr et al. (2014). Each peak of chromatograms was identified according to NIST Mass Spectral Library and literature data (Meier and Faix, 1992). H/G/S ratio was calculated based on relative area (%) of each degradation product. All results were presented in **Supplementary Table 2**.

Infrared Spectroscopy

Raw, control and modified lignins were characterized by infrared spectrometry using a FTIR-8400S (Shimadzu, France) equipped with a universal ATR sampling accessory with diamond crystal. Solid samples, without further preparation, were analyzed between 4,000 and 600 cm^{-1} using 128 scans with a resolution of 4 cm^{-1}. All spectra were normalized at 1,510 cm^{-1}, the band assigned to aromatic rings vibration (Faix, 1991, 1992).

^{31}P NMR Analyses

Based on reference works from Argyropoulos et al., the quantification of lignin hydroxyls groups were performed by ^{31}P NMR analyses (Argyropoulos, 1994, 1995). The sample preparation consisted in the derivatization of lignin hydroxyls with the phosphorylating agent: 2-chloro-tetra-1,3,2-dioxophospholane (TMDP). For this, 15 mg of dried lignin or modified lignin were introduced in a glass vial of 1.5 mL. 350 μL of pyridine/deuterated chloroform mixture (1.6/1 v/v) were then added followed by 100 μL of TMDP and 200 μL of a solution containing 55 mM of *N*-hydryphtalimide (internal standard) and 7.15 mM of chromium acetylacetonate solubilized in pyridine/deuterated chloroform mixture (1.6/1 v/v). Once prepared, the sample was immediately transferred in NMR

TABLE 2 | Assignment of chemical shifts and integration regions in ^{31}P NMR spectra of lignin after derivatization with 2-chloro-tetra-1,3,2-dioxophospholane adapted from literature data (Crestini and Argyropoulos, 1997; Crestini et al., 1998; Pu et al., 2011; Fiţigău et al., 2013).

Structure	Abbreviation	Chemical shift δ (ppm)
Aliphatic-OH	HO_{aliph}	145.4–150.0
Aromatic-OH	HO_{ph}	137.6–144.0
Syringyl-OH		∼142.7
Guaiacyl-OH		139.0–140.2
p-hydroxyphenyl		∼137.8
Carboxylic acid-OH	HO_{COOH}	133.6–136.0

tube. In this way, TMDP reacts with hydroxyl groups of lignin to generate phosphite derivatives, distinguishing aliphatic, phenolic hydroxyls, and carboxylic acids groups by their distinct chemical shift. ^{31}P NMR spectra were acquired on a Bruker Avance III HD 500 MHz spectrometer equipped with BBI 5 mm probe operating at 202,4360 MHz (500,0800 MHz for ^{1}H canal). Spectra acquisition, adapted from literature data (Crestini and Argyropoulos, 1997) was obtained by reverse pulse angle decoupling at 30°. Spectra consisted of 62 scans with spectral width of 81.5 kHz collected with a relaxation delay of 25 s at 298.1 K. Treatments of spectra were performed on Brucker TopSpin 3.2 software. The residual ^{31}P signal of product issued from the reaction of water with the phosphorylating agent at 132.2 ppm was used as reference. Assignment was established according to literature data and gathered in **Table 2** (Crestini and Argyropoulos, 1997; Crestini et al., 1998; Pu et al., 2011; Fiţigău et al., 2013). After integration, esterification yield (Y%) and regioselectivity (R%) were determined according to the equations below:

(1) $Y(HO_{total}) = [(HO_{aliph} + HO_{ph})_{control\ lignin} - (HO_{aliph} + HO_{ph})_{maleated\ lignin}]/(HO_{aliph} + HO_{ph})_{control\ lignin} \times 100$

(2) $R(HO_{aliph}) = [(HO_{aliph})_{control\ lignin} - (HO_{aliph})_{maleated\ lignin}]/[((HO_{aliph})_{control\ lignin} - (HO_{aliph})_{maleated\ lignin}) + ((HO_{ph})_{control\ lignin} - (HO_{ph})_{maleated\ lignin})] \times 100$

(3) $R(HO_{ph}) = [(HO_{ph})_{control\ lignin} - (HO_{ph})_{lignin\ maleated}]/[((HO_{aliph})_{control\ lignin} - (HO_{aliph})_{maleated\ lignin}) + ((HO_{ph})_{control\ lignin} - (HO_{ph})_{maleated\ lignin})] \times 100$

where HO_{aliph}, HO_{ph} and HO_{COOH} correspond, respectively, to hydroxyls groups from aliphatic, phenolic and carboxylic acid moieties.

Thermal Gravimetric Analyses

Thermal Gravimetric Analyses (TGA) were performed on a Simultaneous Thermal Analyzer STA 449 C Jupiter Unit (Netzsch), at a heating rate of 10°C.min^{-1} under a constant argon flow of 50 mL.min^{-1} and from room temperature to 800°C (approximately 20 mg of each compound). Values of isothermal drift and sensitivity are 0.6 μg h^{-1} and 0.1 μg, respectively. The TGA apparatus is coupled with a Quadrupole QMS 403 Aeolos mass spectrometer, MS (Detector SEV/Sekundär Elektronen Vervielfacher (Channeltron), stainless steel capillary, counting time 20 ms per m/z with a resting time of 1 s, scanning width 1/51 amu).

Differential Scanning Calorimetry

Differential scanning calorimetric analyses (DSC) were carried out on a Netzsch DSC 204 F1 heat flux differential calorimeter. A constant heating rate of 10°C.min^{-1} was selected for analyses, from room temperature up to 160°C (1st heating), then cooling down to room temperature and finally heated to 200°C (2nd heating), under a constant argon flow of 200 mL.min^{-1} (approximately 6.0 mg of each compound).

RESULT AND DISCUSSION

Chemical esterification of four industrial lignins were investigated in [Bmim][HSO_4]. The catalytic properties of this IL (Gupta et al., 2007) associated to its β parameter of Kamlett Taft superior to 0.5 (Ventura et al., 2012) suggested that this non-conventional solvent could be a suitable alternative for our strategy in joining both lignin solvation and catalytic activity. However, before considering chemical modification of lignin, the structure of the starting lignins and the impact of incubation in [Bmim][HSO_4] were assessed.

Characterization of the Raw Lignins

As the potential of esterification depends on lignin hydroxyl groups and their accessibility/reactivity, we propose to first quantify each type of hydroxyl for all raw lignins and their respective H/G/S ratio by two methods: pyrolysis-GC/MS (**Supplementary Table 2**) and ^{31}P NMR discussed below. Indulin AT, Lignol, and Wayagamack lignins exhibited similar distribution of the three phenylpropan units: 93–96% of G units, 1–4% of H units, and 2–3% of S units. This similarity can be explained by their softwood origin while the Windsor lignin originated from hardwood exhibits a different H/G/S ratio of 1/32/67. In **Table 3** the hydroxyl quantification from ^{31}P NMR spectra is reported. Indulin AT exhibited a total hydroxyl concentration (5.58 mmol.g^{-1} of lignin) superior to those of all others lignins. Distribution between HO_{Ph} and HO_{aliph} gave a ratio of 0.89 in agreement with previous studies (Fiţigău et al., 2013). Wayagamack lignin exhibited HO_{Ph}/HO_{aliph} ratio of 1.09 (with a total hydroxyl concentration of 2.79 mmol.g^{-1} of lignin). In comparison to Indulin AT, these lower hydroxyls contents determined for Wayagamack lignin could be due to condensation reactions. This could be in agreement with the difference of condensation index between these two lignins (**Supplementary Table 3**). The hydroxyl concentrations can also decrease by oxidation reactions occurring during the precipitation step of the recovery process and leading to the formation of additional carboxylic functions (Gierer, 1985; Asgari and Argyropoulos, 1998; Kouisni, 2011). This could be correlated to the higher concentration of HO_{COOH} groups for Wayagamack in comparison to Indulin AT (0.64 mmol.g^{-1} of lignin for Wayaagmack vs. 0.40-0.48 mmol.g^{-1} of lignin for the three other). The Windsor lignin presented a total hydroxyl concentration of 3.87 mmol.g^{-1} of lignin with a HO_{Ph}/HO_{aliph} ratio of 1.25. 60% of HO_{Ph} provided from S units. HO_{Ph} amount

TABLE 3 | Quantification by ^{31}P NMR of hydroxyl groups (mmol.g^{-1} of lignin) in raw lignins.

Concentration (mmol.g^{-1} of lignin)	Industrial lignins			
	Indulin AT	Wayagamack	Lignol	Windsor
HO_{aliph}	2.19 ± 0.01	1.34 ± 0.07	1.39 ± 0.02	1.56 ± 0.12
HO_{Ph}	1.95 ± 0.06	1.45 ± 0.28	1.37 ± 0.14	1.93 ± 0.01
$HO_{Syringyl}$	nd	nd	nd	1.17 ± 0.06
$HO_{Guaiacyl}$	1.43 ± 0.01	1.17 ± 0.01	1.14 ± 0.11	0.56 ± 0.04
$HO_{Hydroxyphenyl}$	0.08 ± 0.01	0.03 ± 0.01	0.05 ± 0.02	0.04 ± 0.01
Condensed HO_{Ph}	0.44 ± 0.07	0.25 ± 0.04	0.19 ± 0.01	0.17 ± 0.10
HO_{COOH}	0.44 ± 0.03	0.64 ± 0.01	0.48 ± 0.02	0.39 ± 0.02
HO^{a}_{total}	4.58 ± 0.07	3.43 ± 0.05	3.23 ± 0.14	3.87 ± 0.14
$HO^{b}_{esterifiable}$	4.14 ± 0.04	2.79 ± 0.04	2.75 ± 0.12	3.49 ± 0.13
Ratio HO_{Ph}/HO_{aliph}	0.89 ± 0.04	1.09 ± 0.08	0.99 ± 0.11	1.25 ± 0.09
Ratio H/G/S	4/96/0	2/98/0	3/97/0	2/38/60
Ratio H/G/S^{c}	4/94/2	1/96/3	4/93/3	1/32/67

[a] $HO_{total} = HO_{aliph} + HO_{Ph} + HO_{COOH}$.
[b] $HO_{esterifiable} = HO_{aliph} + HO_{Ph}$.
[c] *Calculated using pyrolysis-GC-MS analyses.*
nd, not detected.

of Lignol lignin was similar to those from Indulin AT while the HO_{aliph} was lower. This lignin, issued from hardwood does not seem as sensitive to oxydation reaction as Wayagamack. Finally, Lignol lignin presented a hydroxyl group concentration of 3.23 mmol.g^{-1} of lignin with a HO_{Ph}/HO_{aliph} ratio close to 1.Among the three lignins extracted from softwood, Lignol showed a lower condensed HO_{Ph} content, in agreement with the mild conditions of organosolv process. As the ratios evaluated by both methods are in close agreement, a classification of the four lignins according to their potential of esterification (concentration of hydroxyl groups susceptible to be implied in O-acylation reaction) can be suggested: Indulin AT > Windsor > Wayagamack ≈ Lignol.

Impact of Incubation in [Bmim][HSO_4] on Lignin Properties in View of Further Transformation

Structural Properties

FTIR analyses of the four industrial lignins (Indulin AT, Wayagamack, Lignol, and Windsor) were performed after incubation in [Bmim][HSO4] for 4 h at 75°C, and extraction process. The obtained data were compared to the corresponding raw materials (**Figure 1**). FTIR spectra of Indulin AT (**Figure 1A**) before and after incubation in [Bmim][HSO_4] did not evidence significant differences suggesting the preservation of overall structural integrity of this lignin in these conditions, as already suggested in the literature for other imidazolium-based ILs (Hulin et al., 2015). This observation is in agreement with the similar quantification of hydroxyl group of Indulin AT before (**Table 3**) and after incubation in the IL (**Table 4**). For Wayagamack, Lignol and to a lesser extent Windsor lignins (**Figures 1B–D**), a slight decrease in intensity of the band at 1,707 cm^{-1}, characteristic of carbonyl stretching, was observed. This could be due to reaction implying ketone functions catalyzed by [Bmim][HSO4] (Gupta et al., 2007). It was also noticed that for the Wayagamack and Lignol lignins a slight increase in the band intensity at 1,080 cm^{-1} occurred, assigned to the C-O deformation in aliphatic esters and secondary hydroxyls (Casas et al., 2012). In this way, aldolization and/or ketolization catalyzed by [HSO_4] anion may occur between lignin ketones and electrophile groups, leading to the formation of C-C covalent bonds and secondary alcohols. This aldolization can also be suggested for the Windsor lignin by the diminution of the band intensity at 1,111 cm^{-1}, assigned to C-O of aliphatic ethers. Anyhow, these modifications on FTIR spectra, revealed after incubation in [Bmim][HSO_4] of raw lignins, remained minor. Additional information was provided by ^{31}P NMR spectra on the distinct types of hydroxyl groups than FTIR cannot discriminate (Pu et al., 2011). **Figure 2** shows ^{31}P NMR spectra of the four phosphorylated industrial lignins (Indulin AT, Wayagamack, Windsor and Lignol) before and after incubation in [Bmim][HSO_4]. Decreases of peak intensity of phenolic hydroxyls from G units (HO_{ph}, 139.0–140.2 ppm) and carboxylic acid hydroxyls ($HO_{COOH,}$ 133.6–136.0 ppm) were observed for Wayagamack, Windsor, and Lignol lignins (**Figures 2B–D**). In the case of Indulin AT, the intensity decrease was much less marked (**Figure 2A**). Contrary to other lignins, intensity of HO_{aliph} peak from Lignol decreased significantly (**Figure 2C**). Concerning the Windsor, intensity of peaks assigned to HO_{ph} from the S units was more strongly decreased than those from G units after incubation in [Bmim][HSO_4] (**Figure 2D**). Although the overall structural integrity of lignins would be preserved after incubation in [Bmim][HSO_4], some chemical modifications specifically affecting amount aliphatic, phenolic, and carboxylic acid hydroxyl groups occurred. These observations are reinforced by quantifications reported before incubation in IL of raw lignins (**Table 3**) and after incubation (**Table 4**). This could be due to condensation reactions between β-ketone and hydroxyl or β-carbonyl groups in acidic conditions (Wayman and Lora, 1980; Hussin et al., 2014). In addition, decrease in HO_{ph} may be due to dehydration resulting from acid-catalyzed elimination reactions (El Hage et al., 2009; Hussin et al., 2014).

Thermal Properties

The thermal properties of the four industrial lignins were characterized by thermogravimetric analysis (TGA) before (**Supplementary Figure 1**) and after (**Supplementary Figure 2**) incubation in [Bmim][HSO_4]. TGA curves represent weight loss of lignin relative to temperature of thermal degradation. The first derivative of the corresponding curve (DTG) shows rate of weight loss. The peaks of the DTG curves may be defined as thermal degradation temperatures: T_{onset} as the temperature at which the degradation of the polymer starts, $T_{50\%}$ as the temperature at which lignin sample attained 50% of degradation and DTG as thermal decomposition temperature at which maximal decomposition occurs. **Table 5** summarizes thermal analyses data relative to the four lignins before and after incubation in [Bmim][HSO_4]. TGA thermograms suggested that thermal degradation behavior was different after incubation

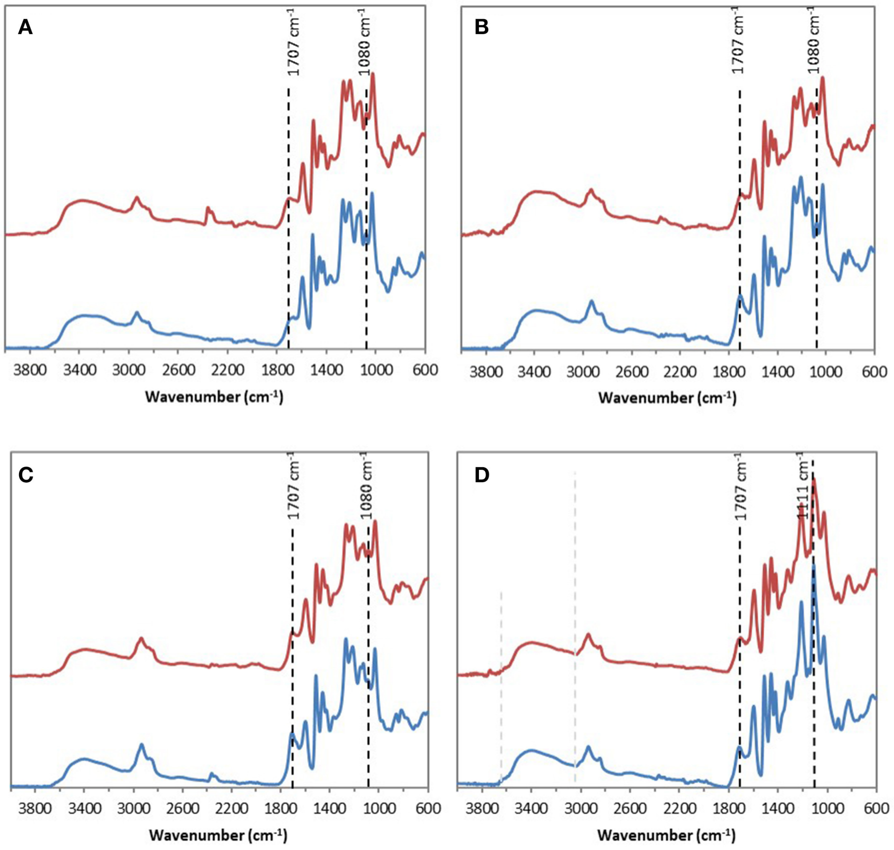

FIGURE 1 | ATR–FTIR spectra of the four industrial lignins: Indulin AT **(A)**, Wayagamack **(B)**, Lignol **(C)**, and Windsor **(D)** before (blue) and after incubation in [Bmim][HSO_4] for 4 h at 75°C (red).

TABLE 4 | Quantification by ^{31}P NMR of hydroxyl groups concentration (mmol.g^{-1} of lignin) in control lignin (incubated in [Bmim][HSO_4] for 4 h at 75°C without maleic anhydride) and in maleated lignins and regioselectivity of the reaction (R%).

	Control lignin (mmol.g^{-1} of lignin)		**Lignin maleate (mmol.g^{-1} of lignin)**		**Regioselectivity (%)**	
	HO_{aliph}	**HO_{ph}**	**HO_{aliph}**	**HO_{ph}**	**HO_{aliph}**	**HO_{ph}**
Indulin AT	2.29 ± 0.17	1.66 ± 0.16	0.88 ± 0.47	1.00 ± 0.36	66.6 ± 3.7	33.4 ± 3.7
Wayagamack	0.79 ± 0.38	1.10 ± 0.07	0.31 ± 0.02	0.77 ± 0.08	51.7 ± 11.7	48.3 ± 11.7
Lignol	1.18 ± 0.29	1.20 ± 0.04	0.50 ± 0.10	1.07 ± 0.01	83.6 ± 0.9	16.4 ± 0.9
Windsor	1.26 ± 0.42	1.43 ± 0.16	0.55 ± 0.01	1.00 ± 0.20	65.5 ± 4.9	34.5 ± 4.9

in IL (**Supplementary Figures 1, 2**). The incubation seemed to minimize the differences between T_{onset} value of each lignin. Indeed, these values ranged between 200.0 and 215.7°C after incubation vs. 145.0 and 183.3°C for raw materials. After incubation in IL, thermal degradation of the four lignins was slower and required higher temperature for starting. However, IndulinAT exhibited a decrease in $T_{50\%}$ and relative mass loss at 798°C after incubation in [Bmim][HSO_4]. The increase of T_{onset} after incubation could be related to the decrease in carboxylic acid hydroxyl groups evidenced by ^{31}P NMR and FTIR spectra. This effect would be particularly marked for Lignol lignin. Previous results obtained by ^{31}P NMR suggested that incubation in [Bmim][HSO_4] decreases the concentration in HO_{ph} of lignins. These HO_{ph} groups allow the prevention of autocondensation of lignin during thermal decomposition (Zhao et al., 2014). We suggested that IL incubation of Wayagamack, Lignol, and Windsor lignins would generate some more condensed aromatic structures leading to higher stability as revealed by increase in T_{onset}. Glass transition temperature (Tg) of the raw lignins were then determined by DSC and ranged between 135.5 and 150.0°C. Although not precisely ascertainable in our experiments, there is an effect of IL incubation that could be due to variation in hydroxyl groups, or maybe the presence of low molecular weight contaminants or residual solvent (Vasile and Zaikov, 2006; Sadeghifar et al., 2012 Cui et al., 2013).

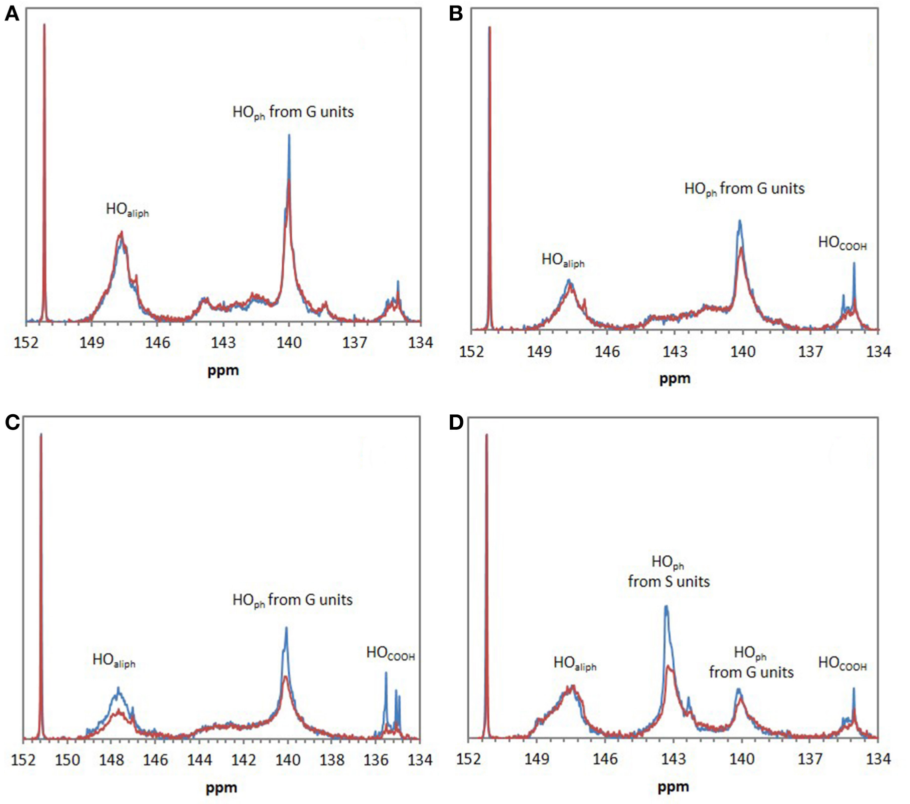

FIGURE 2 | ^{31}P NMR spectra of the four phosphorylated industrial lignins: Indulin AT **(A)**, Wayagamack **(B)**, Lignol **(C)**, and Windsor **(D)** before (blue) and after incubation in [Bmim][HSO$_4$] for 4 h at 75°C (red). *N*-hydroxyphtalimide was used as internal standard with chemical shifts of phosphitylated *N*-hydroxy *N*-hydroxyphtalimide centered on 152.2 ppm.

TABLE 5 | Thermal analyses summary of lignins before and after incubation in [Bmim][HSO$_4$] for 4 h at 75°C.

	Lignins	T_{onset} (°C)	$T_{50\%}$ (°C)	Residual relative mass[a] (%)	DTG max (°C)
Raw	Indulin AT	145.0	645.7	46.6	349.0
	Wayagamack	183.3	516.0	41.3	397.3
	Lignol	162.5	461.2	38.5	390.9
	Windsor	165.0	482.8	39.7	359.9
After incubation in [Bmim][HSO$_4$]	Indulin AT	215.7	572.3	44.0	338.4
	Wayagamack	211.3	552.0	43.6	338.8
	Lignol	200.0	631.6	46.9	335.5
	Windsor	208.8	632.9	46.8	342.4

[a] *Residual relative mass (%) determined at 798°C.*

All together, these characterizations provided evidence that control lignins obtained after IL incubation of raw lignins left a good potential in hydroxyl groups for esterification.

Chemical Esterification of Lignins in [Bmim][HSO$_4$]

Determination of Suitable Lignin/Maleic Anhydride Ratio

Chemical esterifications of Indulin AT and Lignol, two industrial softwood lignins distinct by their respective extraction processes (Kraft vs. organosolv), were firstly performed in [Bmim][HSO$_4$] with various lignin/maleic anhydride ratio (w/w) to target the optimal conditions. For this study, a temperature of 75°C and a duration of 4 h were selected based on a previous work concerning chemical esterification of lignin in dioxane (Schorr et al., 2014). After incubation in [Bmim][HSO$_4$] in presence of various maleic anhydride amount, all FTIR spectra of recovered Indulin AT (**Figure 3**) showed the presence of a characteristic band of ester carbonyl at 1,718 cm^{-1} not observed on the FTIR spectrum of incubated Indulin AT without acyl donor

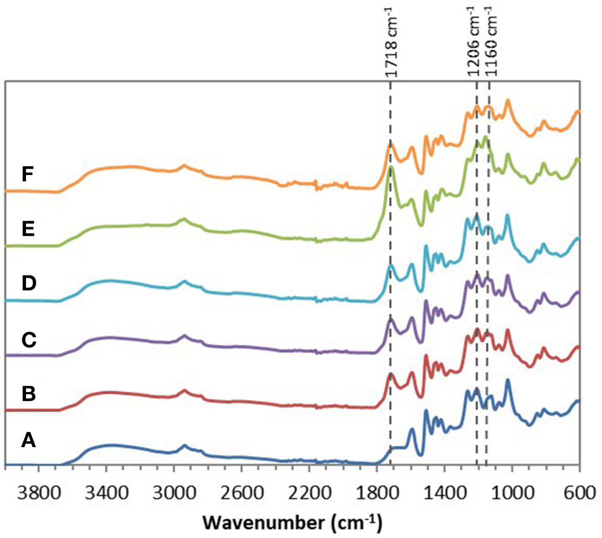

FIGURE 3 | ATR–FTIR spectra of Indulin AT after incubation in [Bmim][HSO_4] for 4 h at 75°C **(A)** and after esterification in similar conditions with the lignin/maleic anhydride ratio of 1/1 w/w **(B)**, 1/2 w/w **(C)**, 1/5 w/w **(D)**, 1/7.5 w/w **(E)**, and 1/10 w/w **(F)**.

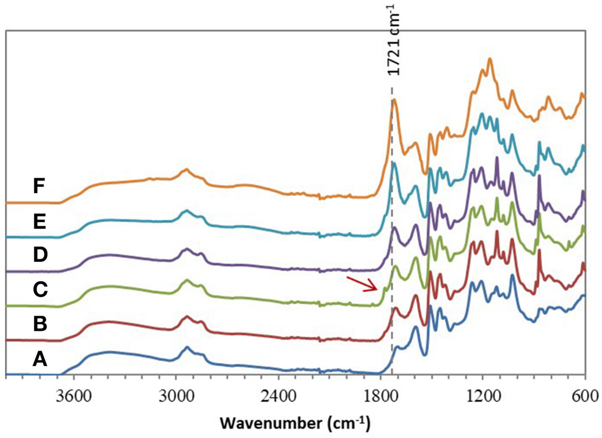

FIGURE 4 | ATR–FTIR spectra of Lignol after incubation in [Bmim][HSO_4] for 4 h at 75°C **(A)** and after esterification in similar conditions with the lignin/maleic anhydride ratio of 1/1 w/w **(B)**, 1/2 w/w **(C)**, 1/5 w/w **(D)**, 1/7.5 w/w **(E)**, and 1/10 w/w **(F)**.

(**Figure 1A**). This carbonyl ester band is distinct from those of maleic anhydride (1,737 cm^{-1}) and those assigned to free carboxylic group (1,707 cm^{-1}). The presence of this band at 1,718 cm^{-1} was supported by significant increase of band intensities at 1,206 cm^{-1} and 1,160 cm^{-1}, corresponding to C-C and C=O stretching and C=O from conjugated ester groups, respectively (Faix, 1992; Boeriu et al., 2004). These characteristic bands suggested the feasibility of the chemical esterification of Indulin AT lignin in [Bmim][HSO_4]. Esterification in this IL would be more efficient with the lignin/maleic anhydride ratio of 1/7.5 w/w (**Figure 3E** and **Figure 5A**) while the best ratio in dioxane was 1/2 w/w (Schorr et al., 2014). To confirm the relevance of this lignin/maleic anhydride ratio, similar reactions were performed with Lignol lignin. The FTIR spectra of recovered Lignol were presented in **Figure 4**. From the ratio of 1/1 w/w, the band at 1,721 cm^{-1}, characteristic of ester carbonyl, appeared. The intensity of this band increased as the higher ratio. A slight band at 1,176 cm^{-1} (see red arrow on **Figure 4C**) can be observed, maybe assigned to carbonyl from aromatic ester (Barra et al., 1999; Maldhure et al., 2012). The increase of band intensity at 1,124 cm^{-1}, assigned to secondary alcohols and ester carbonyl groups, also confirmed the synthesis of lignin maleate (Faix, 1992; Casas et al., 2012). For 1/7.5 and 1/10 w/w ratio, the intensity of the band at 1,161 cm^{-1} increased and constituted thus a supplementary proof of chemical esterification of lignin (see spectra on **Figures 4D–F** and **Figure 5B**). Based on these results, chemical esterifications of the two other industrial lignins (Wayagamack and Windsor) with maleic anhydride were performed with the ratio lignin/maleic anhydride1/7.5 w/w. After extraction from reaction media, FTIR analyses of recovered lignins confirmed the feasibility of chemical esterification of Wayagamack, and Windsor lignins as illustrating by their corresponding infrared footprint (**Figures 5C,D**).

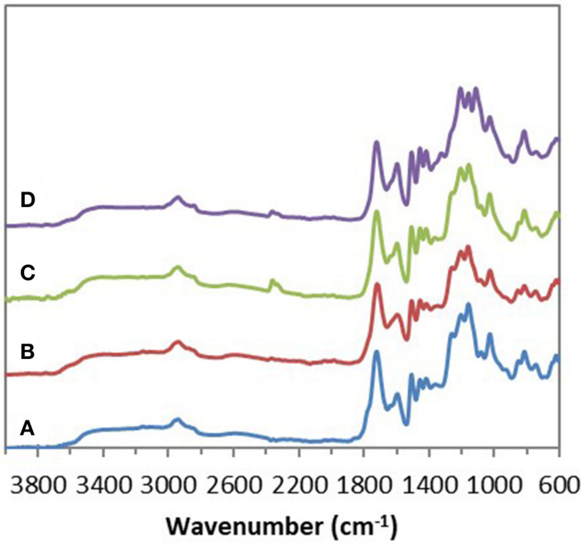

FIGURE 5 | ATR–FTIR spectra of the four maleated lignins: Indulin AT **(A)**, Lignol **(B)**, Wayagamack **(C)**, and Windsor **(D)** after esterification in [Bmim][HSO_4] for 4 h at 75°C with the lignin/maleic anhydride ratio of 1/7.5 w/w.

Reaction Performances and Selectivity

Figure 6 evidences significant differences between ^{31}P NMR spectra of control lignins (incubated in [Bmim][HSO_4] for 4 h at 75°C without maleic anhydride) and esterified lignins. In most of the case, ^{31}P NMR spectra of esterified lignins present a decrease of peak intensity of HO_{aliph} (145.4–150.0 ppm) and HO_{ph} (139.0–140.2 ppm) as compared to control lignins spectra. A sharp increase of peak intensity corresponding to HO_{COOH} (133.6–136.0 ppm) can be noticed. The esterification would thus target both aliphatic and phenolic hydroxyls of lignins

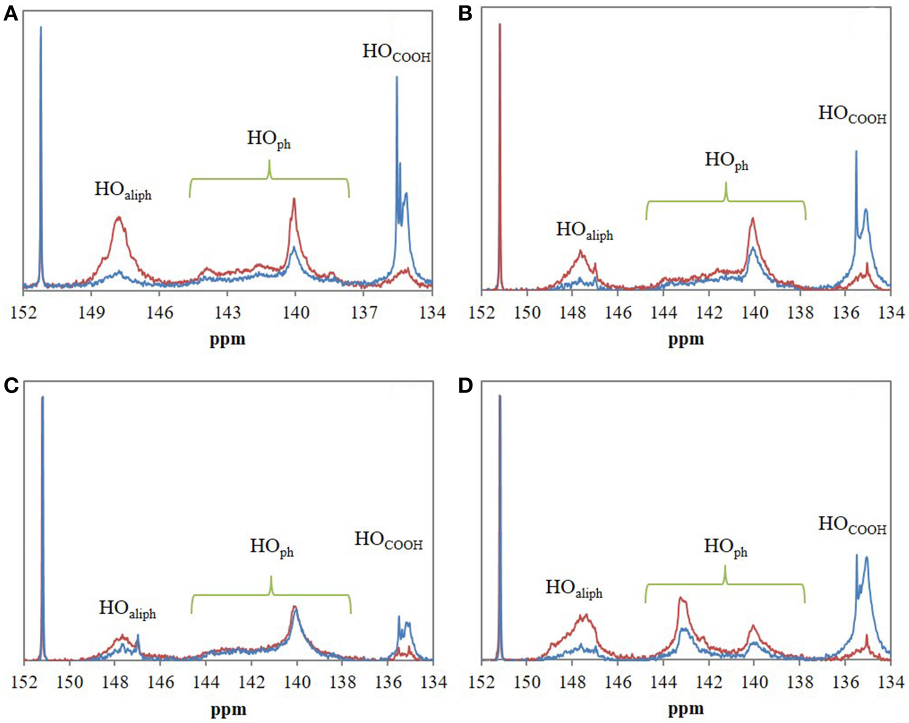

FIGURE 6 | ^{31}P NMR spectra of the four industrial lignins: Indulin AT **(A)**, Wayagamack **(B)**, Lignol **(C)**, and Windsor **(D)** after incubation in [Bmim][HSO_4] for 4 h at 75°C without maleic anhydride (control lignins, red spectra) and with maleic anhydride (maleated lignins, blue spectra). *N*-hydroxyphtalimide was used as internal standard with chemical shifts of phosphitylated *N*-hydroxy *N*-hydroxyphtalimide around 150.7–153.6 ppm. Esterification was performed with the lignin/maleic anhydride ratio of 1/7.5 w/w.

as already observed in FTIR spectra. Moreover, the increase of hydroxyls from carboxylic groups confirmed the presence of grafted maleyl chains on lignin by exposing free one-end carboxylic groups of anhydride. Quantitative analyses of ^{31}P NMR spectra were used to determine esterification yield (Y in%) and then to deduce the regioselectivity of the reaction (**Table 4**). Global esterification yields obtained for Lignol and Wayagamack (30.1 and 38.5%, respectively) were significantly lower than those obtained with Windsor and Indulin AT (47.4 and 52.5%, respectively). The quantitative results thus suggested a difference of esterification performances between these four industrial lignins, maybe influenced either by the origin (softwood or hardwood) or the extraction process (Kraft or organosolv). The comparison of these performances with literature data is not an easy one. Indeed yields were often expressed as the mass increase of recovered lignin after esterification, unfortunately biased by mass loss during extraction from reaction medium and/or residual adsorption of acyl donor (Nadji et al., 2010; Cachet et al., 2014; Chatterjee et al., 2014; Gordobil et al., 2016). However, our obtained yields seemed to be competitive with some of those reported in literature. For instance, a mass increase of 3.3% was determined for esterification of the organosolv lignin with maleic anhydride in tetrahydrofuran. This yield corresponded to 0.5 mmol of esterified hydroxyl groups per gram of lignin (mmol/g_{lignin}) (Chatterjee et al., 2014). This result was significantly lower than those obtained with our greener strategy for the four tested lignins: in average 1.20 mmol/g_{lignin} of esterified hydroxyls achieved in shorter duration.

Literature data usually suggests that esterification would mainly occur directly or indirectly on aliphatic hydroxyls (Thielemans and Wool, 2005; Nadji et al., 2009; Ahvazi et al., 2011; Maldhure et al., 2011, 2012; Chatterjee et al., 2014; Suzuki et al., 2018). In this context, we proposed to finely define the resulted regioselectivity from our reaction system for the four industrial lignins. It can be observed that HO_{aliph} were preferentially esterified for Indulin AT, Lignol, and Windsor lignins (**Table 4**). These results agreed with the low selectivity in favor to HO_{ph} from lignin suggested in a previous study (Ahvazi et al., 2011). Interestingly, similar part of HO_{ph} were esterified (around 33% of total esterified hydroxyl groups) for Indulin AT and Windsor: two lignins extracted from wood by Kraft process. This regioselectivity could be explained by the high amount of syringyl units with two methoxy groups on the aromatic ring inducing probably steric hindrance in the molecular environment of HO_{ph} (Thielemans and Wool, 2005). Concerning the Wayagamack lignin, hydroxyl groups were esterified regardless of their respective nature (51.7% of HO_{aliph} vs. 48.3% of HO_{ph}). This absence of regioselectvity could suggest that chemical modification of lignin occurred during extraction process. About Lignol lignin, HO_{aliph} were preferentially esterified with a regioselectivity of 83.6%. Although organosolv process preserved the native structure of lignin and thus the amount in coniferyl alcohol, we expected a higher availability of HO_{ph} for esterification with maleic anhydride. By this way, we suggested that the solvation in [Bmim][HSO_4] could affected the reactivity of HO_{ph} in agreement with results in dioxane previously reported in the literature (Ahvazi et al., 2011). In solution, maleic anhydride exhibits two carboxylic functions allowing either mono-acylation or di-acylation. The $HO_{COOH}/HO_{esterified}$ ratio can distinguish between these two possible reactions. For Lignol and Wayagamack lignins, the ratio was, respectively, of 0.94 and 0.92 suggesting a mechanism exclusively oriented toward mono-acylation. On the contrary, the ratio of 0.59 determined for Indulin AT, suggested that 1/3 of maleic anhydride induced di-acylation on lignin.

Thermal Properties of Lignin Maleate

Table 6 compares thermal analyses data relative to the four lignins after esterification in [Bmim][HSO_4] with maleic anhydride. TGA and DTG thermograms of the four lignins after esterification exhibited significant differences in comparison with control lignins (**Supplementary Figure 3** vs. **Supplementary Figure 2**). Indeed, thermograms of the four maleated lignins presented henceforth two characteristic temperatures of maximal degradation ($DTG1_{max}$ and $DTG2_{max}$). $DTG1_{max}$ ranged between 192.2 and 196.3°C (**Table 6**). This new $DTG1_{max}$ could be due to the thermal decomposition of the covalently grafted maleyl chains on polymers. Overall, it can be noticed a decrease in thermal stability for the four maleated lignins as illustrated by the lower T_{onset} and $T_{50\%}$ (except for maleated Wayagamack lignin) than those determined for corresponding control (**Table 2**). About maleated Wayagamack, no significative change of $T_{50\%}$ was detected as already reported (Schorr et al., 2014). In addition, TGA-MS coupled analyses of lignin maleates evidenced the generation of degradation fragments with m/z of 26 (C_2H_2) and 44 (CO_2). Example of fragments generated during TGA-MS coupled analysis of maleated Indulin AT lignin was presented in **Supplementary Figure 4**. These fragments would be assigned to thermal decomposition of maleic chains (Cascaval et al., 1996; Chen et al., 2013). Combined with ^{31}P NMR analyses, these thermal degradation fragments strengthen the proof of concept of efficient lignin esterification in [Bmim][HSO_4] with maleic anhydride without additional catalyst. Previous works about esterification of lignins demonstrated that Tg decreased drastically after efficient covalent grafting of alkyl chain on the polymer (Schorr et al., 2014; Hulin et al., 2015). This thermal behavior of modified lignins was thus consistent with a succeeded esterification.

Solubility of Raw Lignins vs. Maleated Lignins

Wayagamack and Windsor lignins were selected for their contrasted H/G/S ratio (1/96/3 vs. 1/32/67, respectively).

TABLE 6 | Thermal analyses summary of lignins after chemical esterification in [Bmim][HSO_4] with maleic anhydride for 4 h at 75°C.

Modified Lignins	T_{onset} (°C)	$T_{50\%}$ (°C)	Residual relative mass[a] (%)	DTG_1 max[b] (°C)	DTG_2 max[c] (°C)
Indulin AT	147.1	478.4	40.0	196.3	324.1
Wayagamack	172.4	557.9	43.8	196.8	318.2
Lignol	155.8	491.5	41.1	192.2	325.0
Windsor	160.0	499.2	40.7	193.5	336.9

[a] *Residual relative mass (%) determined at 798 °C.*
[b] *First maximum degradation temperature.*
[c] *Second maximum degradation temperature.*

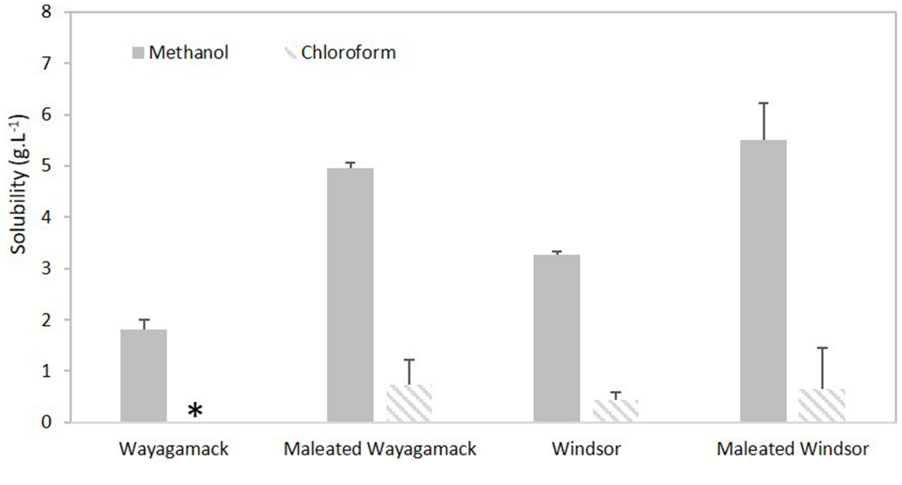

FIGURE 7 | Solubility values of Wayagamack and Windsor lignins in methanol and chloroform before and after esterification. *Insoluble.

Methanol and chloroform, distinct by their solubility parameter δ from Hildebrand theory (14.3 vs. 9.2 (cal/cm^{-3})$^{1/2}$, respectively) and hydrogen bonding parameter δ_H from the Hansen theory (10.9 vs. 2.8 (cal/cm^{-3})$^{1/2}$, respectively), were chosen for this study. The solubility values of Wayagamack and Windsor lignins before and after esterification were presented in the **Figure 7**. Windsor lignin exhibited a higher solubility values than Wayagamack lignin in methanol (3.3 vs. 1.8 g.L^{-1}) and chloroform (0.43 g.L^{-1} vs. insoluble). As expected, methanol was a more suitable solvent than chloroform to solubilize lignins according to their respective δ and δ_H parameters. Based on molecular weight measurements reported in Schorr et al. (2014), we suggested that the higher solubility of Windsor lignin in a given solvent in comparison to Wayagamack lignin could be explained by its lower molecular weight (Mw 3863 vs. 4859, respectively). In addition, this higher solubility could be also related to the higher HO_{total} concentration in Windsor lignin than in Wayagamack lignin (**Table 3**) as already suggested (Sameni et al., 2017). In addition, whatever the lignin, esterification induced an increase in solubility values in methanol (x 2.7 for Wayagamack lignin and x 1.6 for Windsor). This improvement could be related to mono-acylation by maleic anhydride leading to additional exposed carboxylic groups. Indeed, these groups would allow additional hydrogen bonding with solvent and so a better solvation of the polymer. In chloroform, this improvement was less marked with a solubility of maleated lignins inferior to 1 g.L^{-1}. Nevertheless, Wayagamack lignin, initially insoluble in this solvent became slightly more soluble. This weak solubility improvement in aprotic organic solvent as chloroform seemed to be due to a compromise induced by the covalent grafting of maleic anhydride, providing both additional alkyl chains favorable to solvation in this solvent and additional free carboxylic groups which might be unfavorable.

CONCLUSION

Chemical esterifications of four industrial lignins, distinct by their origin, and extraction process, were succeeded for the first time with maleic anhydride in acidic ionic liquid. This route was easy to implement, fast and did not require additional catalyst. An excess of acyl donor favored the efficiency of the reaction whatever the origin and extraction process of lignin. Between 30 to 52% of hydroxyls of lignin were esterified. For three out of four lignins (Indulin AT, Windsor, Lignol), the regioselectivity of the reaction system was mainly orientated toward aliphatic hydroxyls (>60%) reflecting both their accessibility in the molecular environment and their reactivity. For the Wayagamack lignin, esterification yield was the lowest but the absence of selectivity between aliphatic and phenolic hydroxyl suggested an improved reactivity of phenolic hydroxyls in our reaction system. Esterification of lignins with maleic anhydride increased significantly their solubility in polar and protic solvent probably due to additional exposed carboxylic groups resulted from mono-acylation. Although the covalent grafting of maleyl chains on lignin induced a very slight decrease in thermal stability, this remained compatible with temperature conditions of extrusion process for the conception of partially biosourced composites.

DATA AVAILABILITY

All datasets generated for this study are included in the manuscript and the **Supplementary Files**.

AUTHOR CONTRIBUTIONS

EH, CS, TS, and LH conceived and designed the experiments. LH performed and analyzed the experiments with the help of EH, CS for esterification conditions, choices of IL, and analytical methods, and TS for choosing the raw materials and the grafting and the thermal properties analyses. CH helped for physico-chemical interpretations. EH and CS wrote the manuscript on the basis of LH Ph.D. dissertation. CB performed required experiments for the revision. All authors helped with drafting the manuscript and approved the final version.

FUNDING

The authors are grateful for financial support from France Canada Research Fund (FFCR) and the Université de Picardie Jules Verne for its financial support for publication through its S2R action. LH was funded by Ministère Français de l'Enseignement Supérieur et de la Recherche.

ACKNOWLEDGMENTS

We thank Matthieu Courty and Jean-Pierre Bonnet (LRCS UMR 7314 CNRS-UPJV) for DSC and TGA analyses and Dominique Cailleu for his welcoming access to NMR platform.

SUPPLEMENTARY MATERIAL

The Supplementary Material for this article can be found online at: https://www.frontiersin.org/articles/10.3389/fchem.2019.00578/full#supplementary-material

REFERENCES

Ahvazi, B., Wojciechowicz, O., Ton-That, T.-M., and Hawari, J. (2011). Preparation of lignopolyols from wheat straw soda lignin. *J. Agric. Food Chem.* 59, 10505–10516. doi: 10.1021/jf202452m

Anastas, P., and Eghbali, N. (2010). Green chemistry: principles and practice. *Chem. Soc. Rev.* 39, 301–312. doi: 10.1039/B918763B

Argyropoulos, D. S. (1994). Quantitative phosphorus-31 NMR analysis of lignins, a new tool for the lignin chemist. *J. Wood Chem. Technol.* 14, 45–63. doi: 10.1080/02773819408003085

Argyropoulos, D. S. (1995). ^{31}P NMR in wood chemistry: a review of recent progress. *Res. Chem. Intermed.* 21, 373–395. doi: 10.1007/BF03052265

Asgari, F., and Argyropoulos, D. S. (1998). Fundamentals of oxygen delignification. part II, functional group formation/elimination in residual Kraft lignin. *Can. J. Chem.* 76, 1606–1615. doi: 10.1139/cjc-76-11-1606

Auxenfans, T., Buchoux, S., Larcher, D., Husson, G., Husson, E., and Sarazin, C. (2014). Enzymatic saccharification and structural properties of industrial wood sawdust: recycled ionic liquids pretreatments. *Energy Convers. Manage.* 88, 1094–1103. doi: 10.1016/j.enconman.2014.04.027

Barra, G. M. O., Crespo, J. S., Bertolino, J. R., Soldi, V., and Pires, A. T. N. (1999). Maleic anhydride grafting on EPDM: qualitative and quantitative determination. *J. Brazil. Chem. Soc.* 10, 31–34. doi: 10.1590/S0103-50531999000100006

Berlin, A., Balakshin, M. Y., Ma, R., Maximenko Gutman, V., and Ortiz, D. (2011). *Organosolv Process. WO/2011/097720.* Available online at: http://www.freepatentsonline.com/WO2011097720.html

Bernardo, J. R., Gírio, F. M., and Łukasik, R. M. (2019). The effect of the chemical character of ionic liquids on biomass pre-treatment and posterior enzymatic hydrolysis. *Molecules* 24:E808. doi: 10.3390/molecules24040808

Boeriu, C. G., Bravo, D., Grosselink, R. J. A., and van Dam, J. E. G. (2004). Characterization of structure-dependent functional properties of lignin with infrared spectroscopy. *Ind. Crops Prod.* 20, 205–218. doi: 10.1016/j.indcrop.2004.04.022

Brahim, M., Checa Fernandez, B. L., Regnier, O., Boussetta, N., Grimi, N., Sarazin, C., et al. (2017). Impact of ultrasounds and high voltage electrical discharges on physico-chemical properties of rapeseed straw's lignin and pulps. *Bioresour. Technol.* 237, 11–19. doi: 10.1016/j.biortech.2017.04.003

Brandt, A., Ray, M. J., To, T. Q., Leak, D. J., Murphy, R. J., and Welton, T. (2011). Ionic liquid pretreatment of lignocellulosic biomass with ionic liquid-water mixtures. *Green Chem.* 13, 2489–2499. doi: 10.1039/c1gc15374a

Cachet, N., Camy, S., Benjelloun-Mlayah, B., Condoret, J.-S., and Delmas, M. (2014). Esterification of organosolv lignin under supercritical conditions. *Ind. Crops Prod.* 58, 287–297. doi: 10.1016/j.indcrop.2014.03.039

Calvo-Flores, F. G., and Dobado, J. A. (2010). Lignin as renewable raw material. *ChemSusChem* 3, 1227–1235. doi: 10.1002/cssc.201000157

Carvalho, A. V., da Costa Lopes, A. M., and Bogel-Łukasik, R. (2015). Relevance of the acidic 1-butyl-3-methylimidazolium hydrogen sulphate ionic liquid in the selective catalysis of the biomass hemicellulose fraction. *RSC Adv.* 5, 47153–47164. doi: 10.1039/C5RA07159C

Casas, A., Alonso, M. V., Oliet, M., Rojo, E., and Rodriguez, F. (2012). FTIR analysis of lignin regenerated from pinus radiata and eucalyptus globulus woods dissolved in imidazolium-based ionic liquids. *J. Chem. Technol. Biotechnol.* 87, 472–480. doi: 10.1002/jctb.2724

Cascaval, C. N., Chitanu, G., and Carpov, A. (1996). On the thermal decomposition of copolymers of maleic anhydride with styrene. *Thermochim. Acta* 275, 225–233. doi: 10.1016/0040-6031(95)02698-3

Chatterjee, S., Clingenpeel, A., McKenna, A., Rios, O., and Johs, A. (2014). Synthesis and characterization of lignin-based carbon materials with tunable microstructure. *RSC Adv.* 4, 4743–4753. doi: 10.1039/C3RA46928J

Chen, M., Chen, C., Liu, C., and Sun, R. (2013). Homogeneous modification of sugarcane bagasse with maleic anhydride in 1-butyl-3-methylimidazolium chloride without any catalysts. *Ind. Crops Prod.* 46, 380–385. doi: 10.1016/j.indcrop.2013.02.023

Crestini, C., and Argyropoulos, D. S. (1997). Structural analysis of wheat straw lignin by quantitative ^{31}P and 2D NMR spectroscopy. the occurrence of ester bonds and α-O-4 substructures. *J. Agric. Food Chem.* 45, 1212–1219. doi: 10.1021/jf960568k

Crestini, C., Sermanni, G. G., and Argyropoulos, D. S. (1998). Structural modifications induced during biodegradation of wheat lignin by lentinula edodes. *Bioorg. Med. Chem.* 6, 967–973. doi: 10.1016/S0968-0896(98)00047-9

Cui, C., Sadeghifar, H., Sen, S., and Argyropoulos, D. S. (2013). Toward thermoplastic lignin polymers; Part II: thermal and polymer characteristics of Kraft Lignin and derivatives. *BioResources* 8, 864–886.

Cybulska, I., Brudecki, G., Rosentrater, K., Julson, J. L., and Lei, H. (2012). Comparative study of organosolv lignin extracted from prairie cordgrass, switchgrass and corn stover. *Bioresour. Technol.* 118, 30–36. doi: 10.1016/j.biortech.2012.05.073

Doherty, W. O. S., Mousavioun, P., and Fellows, C. M. (2011). Value-adding to cellulosic ethanol: lignin polymers. *Ind. Crops Prod.* 33, 259–276. doi: 10.1016/j.indcrop.2010.10.022

Egorova, K. S., and Ananikov, V. P. (2014). Toxicity of ionic liquids: eco(cyto)activity as complicated, but unavoidable parameter for task-specific optimization. *ChemSusChem* 7, 336–360. doi: 10.1002/cssc.201300459

El Hage, R., Brosse, N., Chrusciel, L., Sanchez, C., Sannigrahi, P., and Ragauskas, A. (2009). Characterization of milled wood lignin and ethanol organosolv lignin from miscanthus. *Polym. Degrad. Stab.* 94, 1632–1638. doi: 10.1016/j.polymdegradstab.2009.07.007

Erdtman, H. (1972). "Lignins: occurrence, formation, structure and reactions,"in *Journal of Polymer Science Part B: Polymer Letters,* eds K. V. Sarkanen and C. H. Ludwig (New York, NY: John Wiley & Sons, Inc.), 228–230. doi: 10.1002/pol.1972.110100315

Faix, O. (1991). Condensation indices of lignins determined by FTIR-spectroscopy. *Holz als Roh- und Werkstoff* 49:356. doi: 10.1007/BF02662706

Faix, O. (1992). "Fourier transform infrared spectroscopy," in *Methods in Lignin Chemistry*, eds S. Y. Lin and C. W. Dence (Berlin, Heidelberg: Springer Berlin Heidelberg), 83–109.

Ferreira, A. F. (2017). "Biorefinery concept," in *Biorefineries: Targeting Energy, High Value Products and Waste Valorisation,* eds M. Rabaçal, A. F. Ferreira, C. A. M. Silva and M. Costa (Cham: Springer International Publishing), 1–20.

Fiţigău, I. F., Peter, F., and Boeriu, C. G. (2013). Structure analysis of lignins from different sources. *World Acad. Sci. Eng. Technol.* 7, 98–103.

Fraga-Dubreuil, J., Bourahla, K., Rahmouni, M., Bazureau, J. P., and Hamelin, J. (2002). Catalysed esterifications in room temperature ionic liquids with acidic counteranion as recyclable reaction media. *Catal. Commu.* 3, 185–190. doi: 10.1016/S1566-7367(02)00087-0

Gandini, A., and Belgacem, M. N. (2008). "Chapter 11 - lignins as components of macromolecular materials," in *Monomers, Polymers and Composites from Renewable Resources*, eds M. N. Belgacem and A. Gandini (Amsterdam: Elsevier), 243–271.

García-Lorenzo, A., Tojo, E., Tojo, J., Teijeira, M., Rodríguez-Berrocal, F. J., González, M. P., et al. (2008). Cytotoxicity of selected imidazolium-derived ionic liquids in the human Caco-2 cell line. sub-structural toxicological interpretation through a QSAR study. *Green Chem.* 10, 508–516. doi: 10.1039/b718860a

Gierer, J. (1985). Chemistry of delignification. *Wood Sci. Technol.* 19, 289–312.

Gominho, J., Costa, R., Lourenço, A., Neiva, D. M., and Pereira, H. (2019). The effect of different pre-treatments to improve delignification of eucalypt stumps in a biorefinery context. *Biores. Technol. Rep.* 6, 89–95. doi: 10.1016/j.biteb.2019.02.004

Gordobil, O., Delucis, R., Egüés, I., and Labidi, J. (2015). Kraft lignin as filler in PLA to improve ductility and thermal properties. *Ind. Crops Prod.* 72, 46–53. doi: 10.1016/j.indcrop.2015.01.055

Gordobil, O., Robles, E., Egüés, I., and Labidi, J. (2016). Lignin-ester derivatives as novel thermoplastic materials. *RSC Adv.* 6, 86909–86917. doi: 10.1039/C6RA20238A

Gupta, N., Sonu, Kad, G. L., and Singh, J. (2007). Acidic ionic liquid [bmim]HSO_4: an efficient catalyst for acetalization and thioacetalization of carbonyl compounds and their subsequent deprotection. *Catal. Commun.* 8, 1323–1328. doi: 10.1016/j.catcom.2006.11.030

Hulin, L., Husson, E., Bonnet, J.-P., Stevanovic, T., and Sarazin, C. (2015). Enzymatic transesterification of kraft lignin with long acyl chains in ionic liquids. *Molecules* 20:16334. doi: 10.3390/molecules200916334

Hussin, M. H., Rahim, A. A., Mohamad Ibrahim, M. N., Yemloul, M., Perrin, D., and Brosse, N. (2014). Investigation on the structure and antioxidant properties of modified lignin obtained by different combinative processes of oil palm fronds (OPF) biomass. *Ind. Crops Prod.* 52, 544–551. doi: 10.1016/j.indcrop.2013.11.026

Husson, E., Auxenfans, T., Herbaut, M., Baralle, M., Lambertyn, V., Rakotoarivonina, H., et al. (2018). Sequential and simultaneous strategies for biorefining of wheat straw using room temperature ionic liquids, xylanases and cellulases. *Bioresour. Technol.* 251, 280–287. doi: 10.1016/j.biortech.2017.12.047

Ion, S., Opris, C., Cojocaru, B., Tudorache, M., Zgura, I., Galca, A. C., et al. (2018). One-pot enzymatic production of lignin-compositesv. *Front. Chem.* 6:124. doi: 10.3389/fchem.2018.00124

Koivu, K. A. Y., Sadeghifar, H., Nousiainen, P. A., Argyropoulos, D. S., and Sipilä, J. (2016). Effect of fatty acid esterification on the thermal properties of softwood kraft lignin. *ACS Sustain. Chem. Eng.* 4, 5238–5247. doi: 10.1021/acssuschemeng.6b01048

Kouisni, L. L. M. (2011). *Method for Separating Lignin From Black Liquor. International US 2011/0297340 A1*.

Laurichesse, S., and Avérous, L. (2014). Chemical modification of lignins: towards biobased polymers. *Prog. Polym. Sci.* 39, 1266–1290. doi: 10.1016/j.progpolymsci.2013.11.004

Maldhure, A. V., Chaudhari, A. R., and Ekhe, J. D. (2011). Thermal and structural studies of polypropylene blended with esterified industrial waste lignin. *J. Thermal Anal. Calorimetry* 103, 625–632. doi: 10.1007/s10973-010-1048-6

Maldhure, A. V., Ekhe, J. D., and Deenadayalan, E. (2012). Mechanical properties of polypropylene blended with esterified and alkylated lignin. *J. Appl. Poly. Sci.* 125, 1701–1712. doi: 10.1002/app.35633

Meier, D., and Faix, O. (1992). "Pyrolysis-gas chromatography-mass spectrometry," in *Methods in Lignin Chemistry*, eds S. Y. Lin, and D. W. Dence (Berlin: Springer Berlin Heidelberg), 177–199.

Nadji, H., Bedard, Y., Benaboura, A., Rodrigue, D., Stevanovic, T., and Riedl, B. (2010). Value-added derivatives of soda lignin from alfa grass (Stipa tenacissima). I. modification and characterization. *J. Appl. Poly. Sci.* 115, 1546–1554. doi: 10.1002/app.31141

Nadji, H., Rodrigue, D., Benaboura, A., Bédard, Y., Stevanovic, T., and Riedl, B. (2009). Value-added derivatives of soda lignin Alfa grass (Stipa tenacissima). II. uses as lubricants in plastic processing. *J. Appl. Poly. Sci.* 114, 3003–3007. doi: 10.1002/app.30925

Papa, G., Varanasi, P., Sun, L., Cheng, G., Stavila, V., Holmes, B., et al. (2012). Exploring the effect of different plant lignin content and composition on ionic liquid pretreatment efficiency and enzymatic saccharification of Eucalyptus globulus L. mutants. *Bioresour. Technol.* 117, 352–359. doi: 10.1016/j.biortech.2012.04.065

Park, Y. C., and Kim, J. S. (2012). Comparison of various alkaline pretreatment methods of lignocellulosic biomass. *Energy* 47, 31–35. doi: 10.1016/j.energy.2012.08.010

Pu, Y., Cao, S., and Ragauskas, A. J. (2011). Application of quantitative ^{31}P NMR in biomass lignin and biofuel precursors characterization. *Energy Environ. Sci.* 4, 3154–3166. doi: 10.1039/c1ee01201k

Putro, J. N., Soetaredjo, F. E., Lin, S.-Y., Ju, Y.-H., and Ismadji, S. (2016). Pretreatment and conversion of lignocellulose biomass into valuable chemicals. *RSC Adv.* 6, 46834–46852. doi: 10.1039/C6RA09851G

Sadeghifar, H., Cui, C., and Argyropoulos, D. S. (2012). Toward thermoplastic lignin polymers. Part 1. Selective masking of phenolic hydroxyl groups in kraft lignins via methylation and oxypropylation chemistries. *Ind. Eng. Chem. Res.* 51, 16713–16720. doi: 10.1021/ie301848j

Sameni, J., Krigstin, S., and Sain, M. (2017). Solubility of lignin and acetylated lignin in organic solvents. *Bioresources* 12, 1548–1565. doi: 10.15376/biores.12.1.1548-1565

Schorr, D., Diouf, P. N., and Stevanovic, T. (2014). Evaluation of industrial lignins for biocomposites production. *Ind. Crops Prod.* 52, 65–73. doi: 10.1016/j.indcrop.2013.10.014

Singh, J. K., Sharma, R. K., Ghosh, P., Kumar, A., and Khan, M. L. (2018). Imidazolium based ionic liquids: a promising green solvent for water hyacinth biomass deconstruction. *Front. Chem.* 6:548. doi: 10.3389/fchem.2018.00548

Stevanovic, T., and Perrin, D. (2009). *Chapitre 5. La Lignine. Chimie du Bois*. Lausanne: Presses Polytechniques et Universitaires Romandes, 145–177.

Suzuki, S., Ishikuro, A., Hirose, D., Ninomiya, K., and Takahashi, K. (2018). Dual catalytic activity of an ionic liquid in lignin acetylation and deacetylation. *Chem. Lett.* 47, 860–863. doi: 10.1246/cl.180350

Tamminen, T., Ropponen, J., Hult, E.-L., and Poppius-Levlin, K. (2012). *Functionalized Lignin and Method of Producing the Same WO*2013050661A1.

Thielemans, W., and Wool, R. P. (2005). Lignin esters for use in unsaturated thermosets: lignin modification and solubility modeling. *Biomacromolecules* 6, 1895–1905. doi: 10.1021/bm0500345

Vasile, C., and Zaikov, G. E. (2006). *New Trends in Natural and Synthetic Polymer Science*. Nova Publishers.

Ventura, S. P. M., de Barros, R. L. F., Sintra, T., Soares, C. M. F., Lima, Á. S., and Coutinho, J. A. P. (2012). Simple screening method to identify toxic/non-toxic ionic liquids: agar diffusion test adaptation. *Ecotoxicol. Environ. Saf.* 83, 55–62. doi: 10.1016/j.ecoenv.2012.06.002

Wayman, M., and Lora, J. H. (1980). Simulated autohydrolysis of aspen milled wood lignin in the presence of aromatic additives: structural modifications. *J. Appl. Polym. Sci.* 25, 2187–2194. doi: 10.1002/app.1980.070251005

Xiao, B., Sun, X. F., and Sun, R. (2001). The chemical modification of lignins with succinic anhydride in aqueous systems. *Polym. Degrad. Stab.* 71, 223–231. doi: 10.1016/S0141-3910(00)00133-6

Zhao, J., Xiuwen, W., Hu, J., Liu, Q., Shen, D., and Xiao, R. (2014). Thermal degradation of softwood lignin and hardwood lignin by TG-FTIR and Py-GC/MS. *Polym. Degrad. Stab.* 108, 133–138. doi: 10.1016/j.polymdegradstab.2014.06.006

Zhao, X., Zhang, Y., Wei, L., Hu, H., Huang, Z., Yang, M., et al. (2017). Esterification mechanism of lignin with different catalysts based on lignin model compounds by mechanical activation-assisted solid-phase synthesis. *RSC Adv.* 7, 52382–52390. doi: 10.1039/C7RA10482K

Zhu, Z., Zhu, M., and Wu, Z. (2012). Pretreatment of sugarcane bagasse with $NH_4OH–H_2O_2$ and ionic liquid for efficient hydrolysis and bioethanol production. *Bioresour. Technol.* 119, 199–207. doi: 10.1016/j.biortech.2012.05.111

Conflict of Interest Statement: The authors declare that the research was conducted in the absence of any commercial or financial relationships that could be construed as a potential conflict of interest.

Copyright © 2019 Husson, Hulin, Hadad, Boughanmi, Stevanovic and Sarazin. This is an open-access article distributed under the terms of the Creative Commons Attribution License (CC BY). The use, distribution or reproduction in other forums is permitted, provided the original author(s) and the copyright owner(s) are credited and that the original publication in this journal is cited, in accordance with accepted academic practice. No use, distribution or reproduction is permitted which does not comply with these terms.

frontiers
in Chemistry

ORIGINAL RESEARCH
published: 23 August 2019
doi: 10.3389/fchem.2019.00585

Wheat Bran Pretreatment by Room Temperature Ionic Liquid-Water Mixture: Optimization of Process Conditions by PLS-Surface Response Design

Monica Araya-Farias [1†], ***Eric Husson*** [1], ***Jorge Saavedra-Torrico*** [2], ***Doriane Gérard*** [3], ***Romain Roulard*** [4], ***Isabelle Gosselin*** [1], ***Harivoni Rakotoarivonina*** [3], ***Virginie Lambertyn*** [1], ***Caroline Rémond*** [3] ***and Catherine Sarazin*** [1*]

[1] Unité de Génie Enzymatique et Cellulaire, UMR 7025 CNRS, Université de Picardie Jules Verne, Amiens, France, [2] Escuela de Ingenieria de Alimentos, Pontificia Universidad Catolica de Valparaíso, Valparaíso, Chile, [3] Chaire AFERE, UMR Fractionnement des AgroRessources et Environnement 614 INRA, Université de Reims Champagne-Ardenne, Reims, France, [4] Plate-forme de Microscopie Electronique, Université de Picardie Jules Verne, Amiens, France

OPEN ACCESS

Edited by:
Pascal Granger,
Lille University of Science and Technology, France

Reviewed by:
Jipeng Yan,
Lawrence Berkeley National Laboratory, United States
Federica Valentini,
University of Rome Tor Vergata, Italy

***Correspondence:**
Catherine Sarazin
catherine.sarazin@u-picardie.fr

†Present address:
Monica Araya-Farias,
Macromolecules and Microsystems in Biology and Medicine, Institut Curie - Centre de Recherche- UMR 168, Institut Pierre Gilles de Gennes pour la Microfluidique, Paris, France

Specialty section:
This article was submitted to Green and Sustainable Chemistry, a section of the journal Frontiers in Chemistry

Received: *14 May 2019*
Accepted: *05 August 2019*
Published: *23 August 2019*

Citation:
Araya-Farias M, Husson E, Saavedra-Torrico J, Gérard D, Roulard R, Gosselin I, Rakotoarivonina H, Lambertyn V, Rémond C and Sarazin C (2019) Wheat Bran Pretreatment by Room Temperature Ionic Liquid-Water Mixture: Optimization of Process Conditions by PLS-Surface Response Design. Front. Chem. 7:585. doi: 10.3389/fchem.2019.00585

Room Temperature Ionic Liquids (RTILs) pretreatment are well-recognized to improve the enzymatic production of platform molecules such as sugar monomers from lignocellulosic biomass (LCB). The conditions for implementing this key step requires henceforth optimization to reach a satisfactory compromise between energy saving, required RTIL amount and hydrolysis yields. Wheat bran (WB) and destarched wheat bran (DWB), which constitute relevant sugar-rich feedstocks were selected for this present study. Pretreatments of these two distinct biomasses with various 1-ethyl-3-methylimidazolium acetate ([C2mim][OAc])-water mixtures prior to hydrolysis catalyzed by hemicellulolytic cocktail (Cellic CTec2) were finely investigated. The main operating conditions such as pretreatment temperature (25–150°C), time (40–180 min), WB and DWB loading (2–5% w/v) and concentration of [C2mim][OAc] in water [10–100% (v/v)] were screened through glucose and xylose yields and then optimized through a Partial Least Square (PLS)—Second Order Design. In an innovative way, the PLS results showed that the four factors and their interactions could be well-fitted by a second-order model ($p < 0.05$). The quadratic PLS models were used to predict optimal pretreatment conditions. Thus, maximum glucose (83%) and xylose (95%) yields were obtained from enzymatic hydrolysis of WB pretreated at 150°C for 40 min with 10% of [C2mim][OAc] in water and 5% of WB loading. For DWB, maximum glucose (100%) and xylose (57%) yields were achieved for pretreatment temperatures of 150°C and 25°C, respectively. The required duration was still 40 min, with 20% of [C2mim][OAc] in water and a 5% DWB loading. Then, Multiple Response Optimization (MRO) performed by Nelder-Mead Simplex Method displayed sugar yields similar to those obtained by individual PLS optimization. This complete statistical study confirmed that the established models were appropriate to predict the sugar yields achieved after different pretreatment conditions from WB and DWB biomasses. Finally, Scanning Electron microscopy (SEM) studies allowed us to establish clearer link between structural changes induced by pretreatment and the best enzymatic performances obtained.

Keywords: wheat bran, room temperature ionic liquid, pretreatment, ionic liquid-water mixture, hemicellulolytic cocktail, enzymatic hydrolysis, partial least square surface response design

INTRODUCTION

Among the sustainable energy resources, lignocellulosic biomass (LCB) constitutes a vast and biorenewable source for producing high value-added molecules and fuels. LCB is composed of two main carbohydrate polymers (cellulose and hemicellulose) and an aromatic polymer (lignin) (Balat, 2011). Cellulose and hemicellulose are starting raw materials for the production of sugar which can be fermented for example into bioethanol while lignin is a potential source for the production of bioplastics, dispersants, and nanocomposites (Norgren and Edlund, 2014). However, as a complex matrix, LCB needs to be pretreated prior to conversion into chemicals and biofuels (Kumar et al., 2009; Alvira et al., 2010; Akhtar et al., 2016). Diluted acid hydrolysis, organosolv pulping, steam explosion have been proposed in the literature as effective pretreatments to improve the biomass digestibility by reducing its recalcitrance (Chandra et al., 2007; Hendriks and Zeeman, 2009; Alvira et al., 2010; Perez-Cantu et al., 2013; Xu et al., 2013; Shi et al., 2014). However, they exhibit some drawbacks such degrading fermentable sugars and producing by-products inhibitory toward biocatalysts (Hendriks and Zeeman, 2009; Ahmed et al., 2016; Akhtar et al., 2016; Elgharbawy et al., 2016). Hot water extraction pretreatment has been proposed as an environmental-friendly as water is the only agent used. For example, from woody biomass, hot water extraction in a pilot-scale allowed to achieve high release of glucose and xylose mainly originated from hemicellulose and also xylose oligomers. Reducing extraction time helped to limit sugars degradation although decreasing sugar yields (Yan and Liu, 2015; Yan et al., 2016).

Alternatively, some Room Temperature Ionic Liquids (RTILs) have achieved success as green solvents for biomass pretreatment due to their double ionic and organic nature that gives them advantageous properties including the ability to dissolve biopolymers, negligible vapor pressure, low flammability, chemical, and thermal stability (Li et al., 2009; Olivier-Bourbigou et al., 2010; Liu et al., 2012; Wang et al., 2012; Elgharbawy et al., 2016; Shi and Wang, 2016; Zhang et al., 2017). It has also been reported that some imidazolium-based RTILs with alkyl chain length of cation inferior to 4 carbons exhibit lower toxicity than those with alkyl chain superior to 4 carbons (Egorova and Ananikov, 2014). Up to date, most reported biomass pretreatment involves 1-ethyl-3-methylimidazolium acetate ([C2mim][OAc]) which have proved to be highly effective to breakdown the lignocellulosic complex and improve enzymatic hydrolysis (Sun et al., 2009; Fu and Mazza, 2011a; Shill et al., 2011; Auxenfans et al., 2012, 2014a, 2017b; Liu et al., 2012, 2016; Yoon et al., 2012; Brandt et al., 2013; da Costa Lopes et al., 2013; Liu and Ng, 2016; Papa et al., 2017; Perez-Pimienta et al., 2017). Moreover, imidazolium-based RTILs can be reused without loss of pretreatment efficiency (Shill et al., 2011; Auxenfans et al., 2012, 2014a,b) present biocompatibility with cellulolytic enzymes (Engel et al., 2012; Auxenfans et al., 2017b) and fermentative microorganisms (Mehmood et al., 2015; Ryu et al., 2015). Moreover, the feasibility of scale-up with this ionic liquid (IL) was demonstrated on switchgrass pointing out as well challenges still existing prior to pilot scale demonstration such as IL recycling and reuse, development of IL-tolerant enzyme cocktails or one-pot process for an economically viable process (Liang et al., in press).

One strategy involves minimizing of the required amount of RTIL in an integrated process. As water is already used in the process (regeneration step, enzymatic hydrolysis, and fermentation), mixing RTIL and water can reduce viscosity of medium facilitating the handling and recycling operations. Indeed, some studies have reported that the addition of water to RTIL can reduce the viscosity of medium and maintain the effectiveness of pretreatment even in the presence of high contents of water (Kamiya et al., 2008; Fu and Mazza, 2011a; Hou et al., 2013; Shi et al., 2013, 2014; Viell et al., 2016; Perez-Pimienta et al., 2017; Hu et al., 2018). On the contrary, several authors have reported that the pretreatment efficiency is drastically reduced when RTIL is mixed with water reinforcing the importance of the use of pure RTIL (Swatloski et al., 2002; Liu et al., 2008; Mazza et al., 2009; Doherty et al., 2010). This raised a dependency on the nature of the IL and the conditions of implementation. It is thus difficult to perform a fair conclusion about the real impact of RTIL-water mixture as biomass pretreatment which raises immediately a question: "Could we minimize the amount of RTIL without incurring a loss of pretreatment efficiency?" Recently, it was highlighted that the success of any pretreatment depends on the physico-chemical properties of the pretreated material as well as the conditions employed which can interact with each other in numerous complex ways (Badgujar and Bhanage, 2015; Papa et al., 2017). Consequently, optimization of pretreatment conditions is highly necessary not only to improve the performance of enzymatic hydrolysis but also to provide additional comprehensive information about the efficiency of the pretreatment. Optimization by the conventional "one-factor-at-one-time" (OFAT) method is time consuming and the interactions between the factors are not estimable from OFAT experiments (Czitrom, 1999). Experimental Design (ED) is an effective statistical approach to investigate and to optimize multivariate processes. To date, many types of LCB have been pretreated by RTILs and optimized by Response Surface Methodology (RSM) (Bajaj and Wani, 2011; Fu and Mazza, 2011b; Tan et al., 2011; Yoon et al., 2012; Lee et al., 2013; Sidik et al., 2013; Qiu et al., 2014; Singh et al., 2015; Wang et al., 2015; Li et al., 2017; Saha et al., 2017; Oliveira Ribeiro et al., 2018; Trinh et al., 2018). Only very few research groups have investigated the optimum conditions for RTIL-based pretreatment using another statistical design (Elgharbawy et al., 2017; Papa et al., 2017; Vergara et al., 2018). The standard Multiple Linear Regression (MLR), which is extensively described in the literature (Myers et al., 2016), requires that each one of variables in the X matrix must be independent (no collinearity and no auto-correlation) and fit to a Normal Statistical Distribution (Gauss). However, these conditions are not always met experimentally. Alternatively, Partial Least Square Regression (PLS) which is supported by the Nonlinear Iterative Partial Least Squares (NIPALS) algorithm (Wold et al., 2001) allows to analysis of a large number of variables, highly correlated and ill-conditioned matrices (Ferrer, 2007) which represents the main advantage of this method compared to MLR.

In the present study, wheat bran (WB) and destarched wheat bran (DWB) were selected as lignocellulosic materials. WB is one of the most important agricultural by-products from wheat milling industry and biorefineries. Annually, over 150 million tons of WB are produced in the world which are basically used for animal feed (Prückler et al., 2014). WB is a complex matrix of cellulose (40–50% of dry matter), hemicellulose (25–35% of dry matter), and lignin (15–20% of dry matter), it constitutes a valuable resource to produce platform molecules and bioethanol (Celiktas et al., 2014; Prückler et al., 2014). Here, we investigated the pretreatments of WB and DWB using RTIL [C2mim][OAc] pure or diluted in aqueous solution. The influence of main operating conditions such as pretreatment temperature, time, RTIL percentage (RTIL to water ratio), and biomass loading (RTIL to WB or DWB ratio) were investigated and optimized through of PLS Methodology never described in the literature for biomass pretreatment. This modeling technique establishes the relationship between a set of predictors (or factors in an Experimental Design) and response variables which can be used to investigate the optimum process conditions (Yañez et al., 2012). The obtained model was experimentally validated and supported by a comprehensive study including chemical composition analysis and structural characterization.

MATERIALS AND METHODS

Wheat Bran, Chemicals, and Enzyme

Wheat Bran (WB) was provided by Chamtor, Bazancourt, France. For the preparation of DWB, WB was washed with water at 40°C during 10 min (solid/liquid ratio: 1/10) and filtrate through a glass filter (40–100 µm pososity). Four successive washings were performed to obtain a total destarching. [C2mim][OAc] were purchased from Solvionic S.A. (Verniole, France). Standards (arabinose, galactose, glucose, xylose, cellobiose, and cellotriose) were purchased from Sigma Aldrich (Steinheim, Germany). All other chemical reagents were purchased from commercial sources in France and used as received. Cellic CTec2 enzymatic cocktail including both cellulolytic and hemicellulolytic activities was supplied by Novozymes (Bagsvaerd, Denmark) and prepared at 15 FPU/g of WB or DWB for the production of hydrolysates rich in glucose and xylose. The value of 2.0 mg of reducing sugar as glucose from 50 mg of filter paper (4% conversion) in 60 min has been designated as the intercept for calculating filter paper cellulase units (FPU) by IUPAC.

TABLE 1 | Experimental range of levels and coding of factors used to evaluate the sugar yields after pretreatment by [C2mim][OAc].

Factors	Coding	Range of levels		
		Low	Middle	High
Temperature (°C)	X_1	25	87.5	150
Time (min)	X_2	40	110	180
RTIL percentage (% v/v)	X_3	10	55	100
Biomass loading (% w/v)	X_4	2.0	3.5	5.0

Pretreatment of WB and DWB Samples With RTIL-Water Mixture

Before the pretreatment, WB and DWB samples were dried at 105°C during 24 h. The dried samples were then weighted in a screw capped Teflon tube and 10 mL of pure RTIL or RTIL-water mixture were added. The pretreatment was performed in a silicone oil bath under vigorous stirring (700 rpm) at various temperature and reaction time ranges as given in **Table 1**. After incubation, the pretreated sample was cooled and mixed with 20 mL of anti-solvent (ultrapure water, 20°C) for 30 min. The resulting suspension was subsequently centrifuged (10.1733 g) (Allegra® 64R Beckman Coulter, Indianapolis, United States) at 20°C for 20 min. This step was repeated 6 times until amber-colored suspension became clear with conductivity lower than 200 µS/cm. This extensive washing step ensured minimization of residual IL to prevent interference with the enzymatic hydrolysis (Liang et al., in press). The resulting insoluble substrate was then freeze-dried at room temperature for 24 h and collected for subsequent enzymatic hydrolysis. Recovered permeate solutions (solvent-RTIL mixture) were stored for a subsequent RTIL-recycling.

Enzymatic Hydrolysis

The enzymatic hydrolysis procedure is adapted from Auxenfans et al. (2014b, 2017a). The Cellic CTec2-catalyzed hydrolysis of the different WB and DWB substrates (untreated or pretreated) was carried out in 1 mL Eppendorf tubes. For hydrolysis reaction, 20 mg of sample was added to 590 µL of citrate-phosphate buffer (50 mM, pH 5.5), 100 µL of fucose preparation (2 mg/mL) which was used as internal standard and 310 µL of Cellic CTec2 preparation (0.974 FPU/mL) with the aim to have an enzyme loading of 15 FPU/g of WB or DWB. The mixture was incubated in a thermomixer (700 rpm) (Eppendorf Thermomixer C, Eppendorf, Hambourg, Germany) at 50°C for 72 h. The reaction was stopped by incubating the mixture at 90°C for 20 min. Then, the sample was dilute (100x) in ultrapure water and filtered (0.22 µm Syringe PTFE filter) prior to quantify the sugar content by High Performance Anion Exchange Chromatography (HPAEC-PAD) (Dionex ICS 5000+ DC, Thermo Fisher Scientific, Massachusetts, United States). The hydrolysis reaction was repeated in duplicate.

Sugar Analysis

To determine the sugar concentrations a method was developed by HPAEC using an analytical CarboPac PA-20 (150 × 3 mm) column equipped with a guard column (30 × 3 mm) (DIONEX, Thermo Fisher Scientific, Massachusetts, United States) and kept at 25°C. Elution was carried out at a flow rate of 0.5 mL/min. A gradient method was used for the separation of monosaccharides and disaccharides using solvent A: 10 mM NaOH, solvent B: 200 mM NaOH, and solvent C: ultra-pure water. The gradient consisted of 25% A and 75% C (0–20 min) followed by a linear increase of A to 100% (20–25 min) then a linear decrease of A to 0% and a linear increase of B to 27.5% and D to 62.5% (25–35 min) after the gradient was maintained to 27.5% B and 62.5% D (35–50 min) followed by a linear increase of B to 100% and a linear decrease of D to 0% (50–60 min). The column was then regenerated with 100% B (60–80 min) and equilibrated with 25% A and 75% C (20 min). The injection volume was 10 μL. Quantification was based on calibration curve using standard sugar solutions (0–0.1 g/L). The retention times of arabinose, galactose, glucose, xylose, mannose, cellobiose, and cellotriose were: 7.90, 9.90, 11.50, 13.6, 14.60, 34.8, and 45.5 min, respectively. The sugar concentrations were expressed in (g/L) from total of each sugar contained in native biomass.

For statistical analysis, the relative glucose and xylose yields for both untreated and pretreated samples were determined after 72 h of enzymatic hydrolysis according to the following equations:

$$Glucose\ yield\ \ (Y_1)\ (\%) = \frac{glucose\ \ released\ after\ enzymatic\ hydrolysis\ \left(g\right)}{glucose\ of\ \ untreated\ \ biomass\ \left(g\right)} \quad (1)$$

$$Xylose\ yield\ \ (Y_2)\ (\%) = \frac{xylose\ \ released\ after\ enzymatic\ hydrolysis\ \left(g\right)}{xylose\ of\ \ untreated\ biomass\ \left(g\right)} \quad (2)$$

Experimental Design and Statistical Analysis

In this research, two kinds of models were performed (a linear and a second order models) to estimate the effect of four factors pertaining ionic liquid pretreatment on the response. Thus, pretreatment temperature (X1), time (X2), RTIL percentage i.e., RTIL to water ratio (X3) and biomass loading (X4) were studied on glucose (Y1) or xylose (Y2) yields, the two major monosaccharides released by enzymatic hydrolysis from WB and DWB. The highest and lowest levels of factors were selected based on the results achieved in preliminary tests. The levels of factors are shown in **Table 1**. The experiments were designed by Statgraphics Centurion XVIII® (FranceSTAT, Neuilly sur Seine, France) and MODDE 12® (Umetrics, Umea, Sweeden) software. The experimental design consists of 2^4 factorial points and 2 central points. A total of 18 experiments were randomly performed in duplicate with 2 repetitions of central point (**Table 2**).

The experimental design was submitted to goodness of fit routine using a first and second order equation by MODDE 12® software as shown in Equations (3) and (4).

$$Y_{1,2} = \beta_0 + \sum_{i=1}^{4} \beta_i X_i + \sum_{i,j=1}^{4} \beta_{ij} X_i X_j + \ \varepsilon \quad (3)$$

$$Y_{1,2} = \beta_0 + \sum_{i=1}^{4} \beta_i X_i + \sum_{i=1}^{4} \beta_{ii} X_i^2 + \sum_{i,j=1}^{4} \beta_{ij} X_i X_j + \ \varepsilon \quad (4)$$

Where Y_1 is the response variable for glucose and Y_2 for xylose, X*i*'s are the independent factor variables. β_0, β_i, β_{ii}, and β_{ij} are the constant, linear, quadratic and two factor interaction coefficients, respectively. Each coefficient in the second-order polynomial model was calculated and the possible interaction effects of pretreatment factors on the glucose and xylose yields were obtained. The experimental error ε is assumed to be randomly drawn from a normal distribution with a mean of 0 and a standard variance equal to σ^2.

The method used to fit the models was PLS supported by NIPALS algorithm (Wold et al., 2001). This method has the properties of support collinearity, no-normality, missing data, and statistical noise (Ferrer, 2007). These conditions allow fitting phenomena with high variability improving the features of the standard method MLR than cannot explain these kinds of situations. We applied a Variable Importance to the Projection (VIP) as part of the PLS computes (Eriksson et al., 2013). This analysis creates a hierarchy of the explanatory capacity of the independent variables on the variable(s). The VIP is based on the weighted sum of squares of the weights of the model factors, allowing a hierarchical ordering of the independent variables (Wold et al., 2001).

The significance of the developed models was checked by Analysis of Variance (ANOVA). The quality of the goodness of fit of second-order model was expressed by the coefficient of determination R^2, R^2_{adj}, and the statistical significance of model was determined by the *F*-test ($p < 0.05$). Optimization (maximum of glucose and xylose yields) was also determined by PLS method and D-Desirability Function. A Multiple Response Optimization (MRO) for Glucose and Xylose yields was also performed using Nelder-Mead Simplex Method (Eriksson et al., 2013). VIP charts and surface response plots were drawn using MODDE 12 software to illustrate the effects of pretreatment factors on sugar yields.

Characterization of WB and DWB Samples

Compositional Analysis

The moisture content of samples (g water/100 g WB or DWB) was determined by drying the samples (1 g) in a hot air oven at 105°C overnight. Protein content was determined using the Kjeldahl method. A factor of 5.7 was used for conversion from nitrogen (N) to protein content (AOAC Official Method, 2001). In order to obtain the destarched WB sample, the soluble starch was removed by washing the WB in hot water (50°C). Starch content in WB and in DWB was quantified with the kit K-TSHK from Megazyme (Megazyme, Pontcharra Sur Turdine, France). Relative contents of cellulose, hemicellulose, lignin and ash were determined according to the Goering and Van Soest method

TABLE 2 | Experimental design matrix of four factors and data for glucose and xylose yields after pretreatment of WB and DWB with [C2mim][OAc].

Pretreatment	Temperature (°C) X_1	Time (min) X_2	RTIL (% v/v) X_3	Biomass loading (% w/v) X_4	WB		DWB	
					Glucose yields[a] Y_1	Xylose yields[b] Y_2	Glucose yields Y_1	Xylose yields Y_2
Untreated	n.a	n.a	n.a	n.a	0.10 ± 0.00[c]	0.28 ± 0.02	0.26 ± 0.01	0.22 ± 0.01
P1	150	40	10	2.0	0.30 ± 0.00	0.45 ± 0.00	1.00 ± 0.09	0.79 ± 0.04
P2	25	180	10	2.0	0.17 ± 0.00	0.25 ± 0.00	0.16 ± 0.03	0.18 ± 0.00
P3	25	40	100	2.0	0.15 ± 0.00	0.36 ± 0.01	0.14 ± 0.02	0.16 ± 0.03
P4	150	180	100	2.0	0.26 ± 0.01	0.07 ± 0.08	0.80 ± 0.01	0.10 ± 0.03
P5	25	40	10	5.0	0.50 ± 0.16	0.74 ± 0.17	0.73 ± 0.03	0.58 ± 0.03
P6	150	180	10	5.0	0.27 ± 0.16	0.39 ± 0.05	0.97 ± 0.04	0.82 ± 0.01
P7	150	40	100	5.0	0.27 ± 0.03	0.54 ± 0.06	0.75 ± 0.01	0.41 ± 0.02
P8	25	180	100	5.0	0.53 ± 0.02	0.69 ± 0.01	0.17 ± 0.01	0.17 ± 0.05
P9	25	40	10	2.0	0.10 ± 0.00	0.63 ± 0.03	0.22 ± 0.01	0.23 ± 0.00
P10	150	180	10	2.0	0.84 ± 0.03	0.54 ± 0.01	1.00 ± 0.08	0.58 ± 0.04
P11	150	40	100	2.0	0.48 ± 0.19	0.22 ± 0.00	0.93 ± 0.00	0.29 ± 0.00
P12	25	180	100	2.0	0.76 ± 0.02	0.76 ± 0.07	0.86 ± 0.07	0.64 ± 0.01
P13	150	40	10	5.0	0.87 ± 0.02	0.91 ± 0.03	1.00 ± 0.11	0.54 ± 0.05
P14	25	180	10	5.0	0.69 ± 0.02	0.84 ± 0.11	0.20 ± 0.06	0.17 ± 0.06
P15	25	40	100	5.0	0.12 ± 0.01	0.26 ± 0.19	0.37 ± 0.02	0.56 ± 0.02
P16	150	180	100	5.0	0.86 ± 0.18	0.51 ± 0.01	0.95 ± 0.02	0.53 ± 0.09
P17	87.5	110	55	3.5	0.26 ± 0.01[d]	0.39 ± 0.03[d]	0.17 ± 0.02[d]	0.40 ± 0.01[d]
P18	87.5	110	55	3.5	0.31 ± 0.01[d]	0.46 ± 0.16[d]	0.22 ± 0.00[d]	0.35 ± 0.00[d]

[a] $Glucose\ yield\ \ (Y_1) = \frac{glucose\ \ released\ after\ enzymatic\ hydrolysis\ (g)}{glucose\ of\ untreated\ biomass\ (g\ )}$.

[b] $Xylose\ yield\ \ (Y_2) = \frac{xylose\ \ released\ after\ enzymatic\ hydrolysis\ (g)}{xylose\ of\ untreated\ biomass(g\ )}$.

[c] *Mean ± SD of duplicate.*

[d] *Central points.*

n.a, not applicable.

(Goering and Van Soest, 1970). Before the experiment, solid samples were dried at 105°C overnight and all the measurements were conducted duplicate. Five hundred milligram of sample (W0) were mixed with 100 mL of neutral detergent at 100°C for 1 h. After filtration and washing with water and acetone, the residue was dried at 105°C for 8 h and then weighed (W1). The residue was then mixed with 100 mL of acid detergent, 0.5 g of sulfite de sodium and 2 mL de decahydronaphtalene at 100°C for 1 h to remove hemicellulose. After this step, the residue was dried at 105°C for 8 h and weighed (W2). Then, the residue was treated with 72% H_2SO_4 at 25°C for 3 h to remove cellulose. After the removal of cellulose, the residue was dried at 105°C for 8 h and weighed (W3). Finally, the residue was incinerated at 550°C for 3 h to remove lignin. After incineration, the residue was dried and weighed (W4). The contents of cellulose, hemicellulose, lignin, and ash were calculated as follows:

$$Hemicellulose\ \ (\%) = \frac{(W_1 - W_2)}{W_0} \times 100 \tag{5}$$

$$Cellulose\ \ (\%) = \frac{(W_2 - W_3)}{W_0} \times 100 \tag{6}$$

$$Lignin\ \ (\%) = \frac{(W_3 - W_4)}{W_0} \times 100 \tag{7}$$

$$Ash\ \ (\%) = \frac{W_4}{W_0} \times 100 \tag{8}$$

Structural and Morphological Characterization of WB and DWB Samples

The morphology of untreated/pretreated WB and DWB samples was investigated by Scanning Electron Microscopy (SEM). In the case of cellulose samples, the gold metallization prior to SEM analysis could induce physical changes and possible artifacts due to the action of the vacuum and/or the gold deposit heating (Husson et al., 2011). Thus, another classical method was preferred for LCB visualization, which consisted of observation in low-vacuum mode (under partial vacuum pressure of water) without any sample preparation step. The microscope was an environmental high-resolution electron scanning microscope QUANTA 200 FEG (FEI Company, USA) with a LF (Large Field) detector. The conditions of observation were the following: acceleration voltage between of 2 kV, work distance between 5 and 9 mm and pressure between 0.5 and 2 m bar. ^{13}C NMR spectra of untreated and pretreated samples were acquired at 25°C by using Cross-Polarization Magic Angle Spinning Nuclear Magnetic Resonance spectroscopy (CP-MAS ^{13}C NMR) on a Bruker DRX-500 spectrometer equipped with a 4 mm probe operating at 125.7452 MHz (^{13}C channel). Samples were spun with a MAS speed of 5 kHz. Calibration of ^{13}C spectra was externally performed using ethylbenzene as a reference. The NMR spectra were processed using Brucker's Topspin 3.1 windows processing software.

RESULTS

The temperature and duration time of IL-pretreatment are important parameters for an efficient LCB deconstruction. Indeed, we have shown, in previous work, a significant effect on improving enzymatic saccharification after IL pretreatment on cellulose or woody residues from 25°C for 20 min or 45°C for 40 min, respectively (Auxenfans et al., 2012, 2014a). However, an increase in the temperature or duration of IL-pretreatment allow to achieve higher sugar yields usually implemented at temperature between 80°C and 160°C from hours to overnight regardless of biomass (Olivier-Bourbigou et al., 2010; Brandt et al., 2013; Badgujar and Bhanage, 2015; Liang et al., in press). Another point that can be connected is the biomass loading, especially with pretreatment with pure IL due to high viscosity (Alayoubi et al., 2019). These studies led us to the choice of experimental range gathered in **Table 1**. The focus of the present work was to optimize pretreatment conditions of IL-water mixture allowing on one hand to reduce viscosity, and thus facilitating the handling in the process, and, on the other hand, to reduce cost due to IL.

Chemical Composition and RTIL-Water Mixture Pretreatment of WB and DWB

As starch can be reserved for other uses and also its content can affect the enzymatic performances on cellulose and hemicellulose, another study was conducted in parallel on DWB. After washing WB in hot water, the starch percentage in the samples was decreased by a factor of 3.7 times (**Table 3**). LCB polysaccharides in raw materials account for 48.4–65.6% of the dry matter where 14.1–21.1% correspond to the cellulose content and 34.2–40.9% to the hemicellulose fraction. Total lignin content of all samples varied between 4.7 and 12.6% and small amounts of various compounds (0.5% ash content) were also found in WB and DWB samples (**Table 4**). The relative composition of remains almost unchanged after the pretreatment.

The influence of pretreatment by [C2mim][OAc]-water mixtures on saccharification performances of WB and DWB samples was then investigated through the sugar yields obtained after 72 h of hydrolysis with the cocktail enzymatic Cellic CTec2. Untreated WB and DWB samples were also hydrolyzed with Cellic CTec2 under the same reaction conditions. Beyond the potential interest in enzymatic hydrolysis, this reaction can be used as test to assess the efficiency of a pretreatment in disrupting the LCB. The pretreatments were performed at different levels of temperature (25–100°C), time (40–180 min), percentage of [C2mim][OAc] (10–100% v/v) and biomass loading (2–5% w/v) following the experimental design shown in **Table 2**. The sugar production obtained after 72 h of enzymatic hydrolysis for untreated and pretreated WB and DWB were plotted as a function of pretreatments (**Figures 1**, **2**). As seen on the figures, the two major monosaccharides released after the enzymatic hydrolysis were glucose and xylose in agreement with the initial composition.

TABLE 3 | Relative chemical composition of raw WB and DWB.

	WB (%)	DWB (%)
Moisture[a]	9.05 ± 0.16[e]	5.41 ± 0.13
Starch[b]	24.50 ± 0.00	6.60 ± 0.00
Protein[c]	16.42 ± 0.48	16.33 ± 0.78
Arabinose[d]	11.43 ± 1.18	12.41 ± 0.36
Galactose[d]	0.83 ± 0.08	0.81 ± 0.09
Glucose[d]	25.69 ± 2.87	13.57 ± 0.07
Xylose[d]	16.61 ± 0.89	19.04 ± 0.47

[a] *Determined at 105°C during 24 h.*

[b] *Determined after washing in hot water.*

[c] *% N × 5.7.*

[d] *Determined by HPAEC-PAD after H_2SO_4 hydrolysis.*

[e] *Mean ± SD of duplicate.*

Model Fitting

Next, the effect of pretreatment factors was further investigate and optimize on the two main sugar released after the enzymatic hydrolysis through a designed experiment using PLS methodology. Thus, **Table 2** shows the design matrix generated by PLS statistical tool according to Equations (1) and (2) as well as the xylose and glucose yields obtained after 72 h of enzymatic hydrolysis of WB and DWB. Pretreatment with [C2mim][OAc]-water mixture increased significantly the glucose and xylose yields of about 3–10 folds as compared to those of untreated samples. A second-order polynomial model was then used to fit the response as shown earlier in Equation (4). Thus, the coefficients β_0, β_i, β_{ii}, and β_{ij} of each model estimated by the MODDE 12® software were obtained which are shown in **Table 5**.

Analysis of variance (ANOVA) was performed to test the significance of the developed model and VIP charts were utilized to evaluate the linear, quadratic and interaction effects on

TABLE 4 | Relative composition of polymers and ash of WB and DWB before and after pretreatment with [C2mim][OAc][a].

Substrate	Cellulose	Hemicellulose	Lignin	Ash
WB-untreated	14.13 ± 6.91[b]	34.24 ± 1.77	4.72 ± 0.47	0.54 ± 0.49
WB-[C2mim][OAc]-water mixture[c]	15.43 ± 3.15	36.28 ± 7.35	6.44 ± 0.49	0.25 ± 0.06
DWB-untreated	21.13 ± 3.25	40.85 ± 4.50	12.64 ± 4.10	0.46 ± 0.13
DWB-[C2mim][OAc]-water mixture[d]	23.35 ± 1.42	42.27 ± 4.01	10.78 ± 1.81	0.15 ± 0.05

[a] *Relative Chemical Composition (g/ 100 g of dry matter) determined by Goering and Van Soest (1970) method.*

[b] *Mean ± SD of duplicate.*

[c] *Pretreatment leading to higher sugar yields [150°C, 40 min, RTIL 10% v/v, biomass loading 5% (w/v)].*

[d] *Pretreatment leading to higher sugar yields [150°C, 40 min, RTIL 10% v/v, biomass loading 5% (w/v)].*

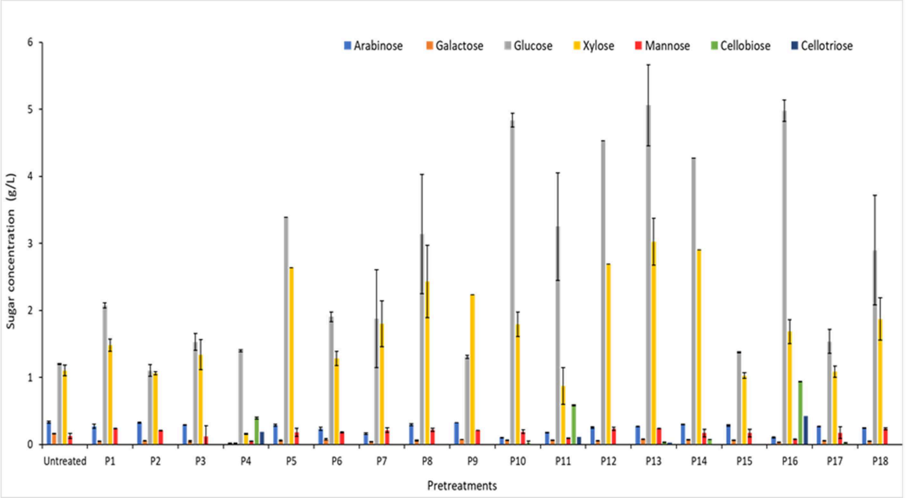

FIGURE 1 | Sugar composition of WB after 72 h of hydrolysis with Cellic CTec2 at 15 FPU/g for different pretreatments. Hydrolysis were performed in duplicate with 2% w/v of WB.

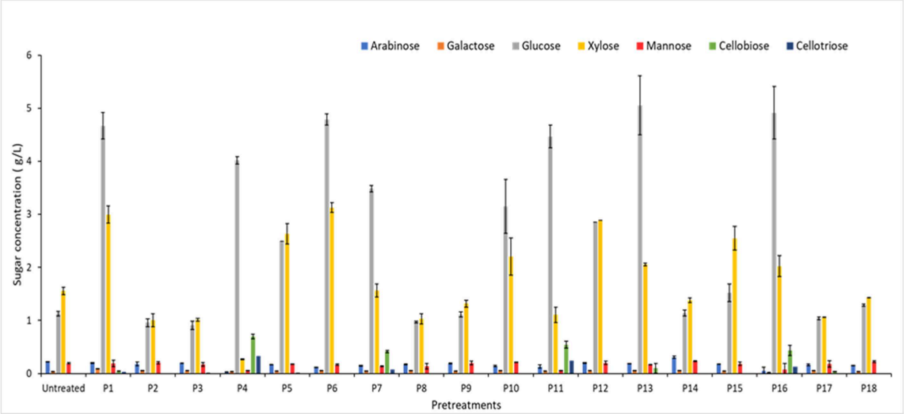

FIGURE 2 | Sugar composition of DWB after 72 h of hydrolysis with Cellic CTec2 at 15 FPU/g for different pretreatments. Hydrolysis were performed in duplicate with 2% w/v of DWB.

the response. ANOVA analysis revealed that model *F*-values ranged from 35.3 to 83.6 and the values of "Prob > F" were <0.001 (**Table 5**). The calculated determination coefficients (R^2) were in agreement with the adjusted determination coefficients (R_2Adj). The Relative Standard Deviation (RSD%) of models were lower than 10% (**Table 5**). As part of PLS analysis, VIP values were graphically represented as a function of the coded factors: temperature (X_1), time (X_2), RTIL percentage (X_3), and biomass loading (X_4) (**Figure 3**). Thus, on the **Figure 3**, any factor (Bar) beyond the specified level of 0.8 (orange horizontal line) was considered as statistically significant ($p < 0.05$). Furthermore, the experimental data and the predicted values were closely grouped close to the line of best fit as shown in **Figure 4**.

Based on the obtained quadratic models, response surface (RS) plots were drawn to evaluate the effect (simple, quadratic, and interaction) of the different factors within the range studied in the present work. The effect on glucose yields are shown in **Figures 5A,C** for WB and DWB, respectively and the effect on xylose yields in **Figures 5B,D** for WB and DWB, respectively. Except for DWB xylose yield, the trend showed a better sugar yield with an increase in the temperature at low pretreatment times.

Morphology and Structure of WB and DWB

Finally, the morphological and structural changes on WB and DWB samples after pretreatment are illustrated in **Figure 6** and **Figure S1**, respectively. The surface morphology of the WB and DWB samples before and after pretreatment was analyzed by SEM. As shown in **Figure 6**, the raw WB and DWB showed a surface compact, irregular and agglomerated as "flakelike" structures (**Figures 6A,D**) where bran starch granules can be randomly observed even after the destarching step (**Figure 6D**). Pretreatment with pure [C2mim][OAc] induced

TABLE 5 | Regression coefficients and ANOVA of quadratic model.

Coefficients	WB		DWB	
	Glucose Yield Y_1	Xylose Yield Y_2	Glucose Yield Y_1	Xylose Yield Y_2
Constant β_0	0.2809	0.4199	0.1952	0.3634
Linear				
β_1	−0.0223	−0.0659	0.2789	0.0678
β_2	−0.0002	−0.0452	−0.0564	−0.0413
β_3	0.0191	−0.0117	−0.0515	0.0056
β_4	0.0901	0.1086	0.0377	0.0636
Quadratic				
β_{11}	0.0129	0.0104	0.1652	0.0475
β_{22}	0.0225	−0.0252	0.0334	−0.0189
β_{33}	0.1499	0.0177	0.0643	−0.0009
β_{44}	−0.0204	0.0105	0.0726	−0.0236
Interaction				
β_{12}	−0.1465	−0.0792	0.0409	0.0565
β_{13}	0.0000	0.0001	0.0007	0.0103
β_{14}	−0.0017	0.0874	−0.0456	−0.0185
β_{23}	0.0908	0.1324	0.0493	0.0089
β_{24}	0.0013	0.0193	−0.0471	−0.0661
β_{34}	−0.1493	−0.0383	−0.0265	0.0025
Model *F*-value	35.28*	62.90*	54.25*	83.57*
p-value Prob > F	<0.0001	<0.0001	<0.0001	<0.0001
R^2	0.96	0.97	0.97	0.98
R^2_{Ajusted}	0.93	0.96	0.95	0.97
RSD (%)	6.10	4.30	7.55	2.69

*$p < 0.001$.

drastic morphological changes (**Figures 6B,E**). As compared to untreated samples, large cavities appeared and the matter seemed completely disorganized. After RTIL-water mixture pretreatment at 150°C for 40 min of WB or DWB (**Figures 6C,F**), a more porous and expanded structure was observed as compared to untreated samples but less impacted than with pure IL pretreatment. In addition, solid state ^{13}C NMR was used to characterize the structure of the WB and DWB samples before and after pretreatment with the aqueous [C2mim][OAc]. The ^{13}C NMR (**Figure S1**) peaks were assigned according to data published in the literature (Ha et al., 1997; Gauthier et al., 2002; Locci et al., 2008). The region at 120–170 ppm and the peak at 56 ppm represent the signals assigned to the aromatic carbons and the aromatic the methyl ester groups of the lignin while the peaks shown at 170–178 ppm and 18–24 ppm represent the signal for the hemicellulose carboxyl and acetyl carbon groups, respectively (Sannigrahi et al., 2011). The intense signal occurring from 60 to 110 ppm represents the C-atoms of the cellulose in the samples. In particular, the signal representing the C4 of cellulose appeared from 83 to 92 ppm as broad signals. In particular, the signal centered at 83 ppm corresponds to the C4 of the amorphous cellulose while the shoulder at 89 ppm represents the C4 of the crystalline cellulose.

DISCUSSION

Impact of RTIL-Water Mixture Pretreatment of WB and DWB on Enzymatic Hydrolysis

Pretreatment with diluted [C2mim][OAc] did not induce a real fractioning of constitutive cellulose/hemicellulose/lignin of WB whatever the presence or absence of starch (DWB) as the relative composition remains almost unchanged after the pretreatment (**Table 4** and **Figure S1**). This behavior was in agreement with the results published in previous works where pure RTIL was used to pretreat the LCB (Auxenfans et al., 2014b; Husson et al., 2018). This suggests that the presence of water in the [C2mim][OAc] medium did not affected the specificitiy of RTIL mild pretreatment. Indeed, fractioning and partial degradation of polysaccharidic and polyphenolic polymers were minimized contrary to the chemical pretreatment such as hydrothermal or diluted-acid pretreatments (Chandra et al., 2007; Hendriks and Zeeman, 2009; Reisinger et al., 2013; Akhtar et al., 2016). The statements based on the comparison of chemical analyses before and after pretreatment with RTIL-water mixture were also supported by NMR spectroscopic measurements as illustrated in **Figure S1**. Indeed, no major modification was evidenced after the pretreatment for each biomass as specific peaks of hemicelluloses and lignins were still observed. It could be due either to the use of IL in water mixture or more specifically to the studied biomass. In effect, it has already been reported that pretreatment with pure [C2mim][OAc] induced partial removal or dissolution of lignin and extractives or induced deacetylation of hemicellulose of wood residues (Çetinkol et al., 2010; Auxenfans et al., 2014b). However, there is a consensus on the effect of IL on the lignin-carbohydrate complex disruption whatever the extent of fractionation and structural changes on cellulose (Singh et al., 2009; Husson et al., 2011). In addition, NMR spectra did not show characteristic peaks of IL in the pretreated WB or DWB, it can be thought that there is no or negligible amount of residual IL that may be entrapped in the pretreated biomass.

Whatever the pretreatment conditions (**Figures 1**, **2**), the enzymatic hydrolysates are mainly composed of glucose and xylose and only small amounts of other sugars (arabinose, galactose and mannose) which were in agreement with the sugar composition (**Table 3**). This is consistent with the high cellulase (97.3 FPU/mL) and xylanase (12082 UI/mL) activities in the Cellic CTec2 cocktail. On the other hand, the low arabinosidase activity in the Cellic CTec2 cocktail (3.4 IU/mL for arabinosidase) did not allow for a significant release of arabinose in any case.

High yields of glucose or xylose can be achieved by enzymatic hydrolysis after RTIL-water pretreatment in mild conditions allowing to consider the reducing use of IL pretreatment to overcome the lignocellulosic recalcitrance prior to enzymatic production of C6 and C5 sugars.

Model Fitting and Statistical Analysis

Utilization of RTIL for WB pretreatment in order to get maximum sugar yields after enzymatic hydrolysis might result in an expensive method to pretreat this biomass. Optimization of pretreatment factors is thus essential to obtain the most suitable levels of the process conditions, especially, the percentage

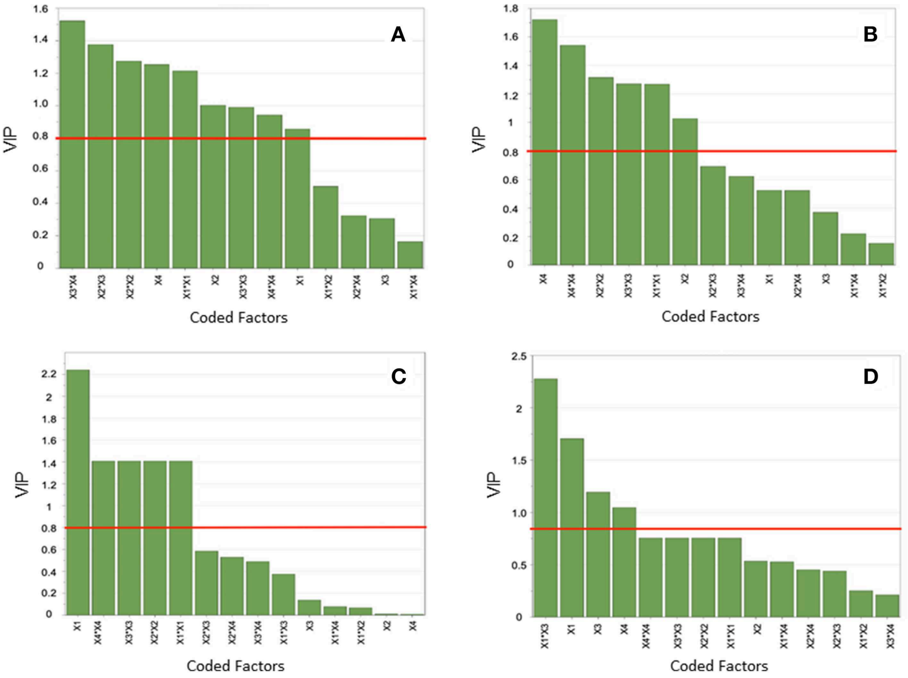

FIGURE 3 | Effect of pretreatment factors by Variable Importance to Projection (VIP) charts on glucose and xylose yields: **(A,B)** for WB and **(C,D)** for DWB. Any factor (green bars) beyond the specified significance level of 0.8 (orange line) is statistically significant ($p < 0.05$).

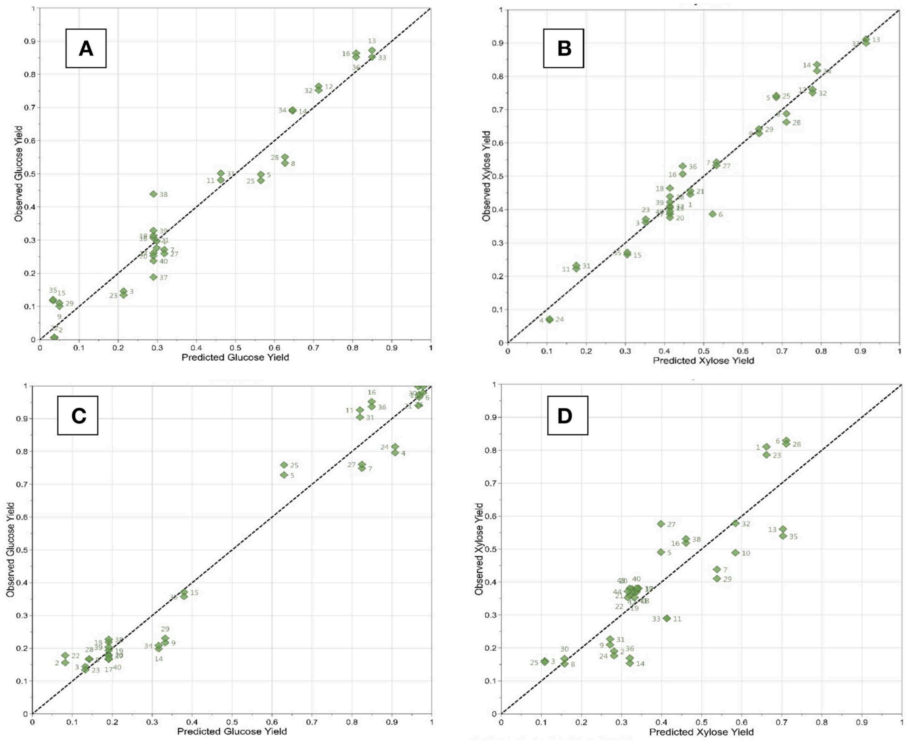

FIGURE 4 | Correlation graphs between the predicted and observed experimental glucose and xylose yields values for WB **(A,B)** and DWB **(C,D)**, respectively.

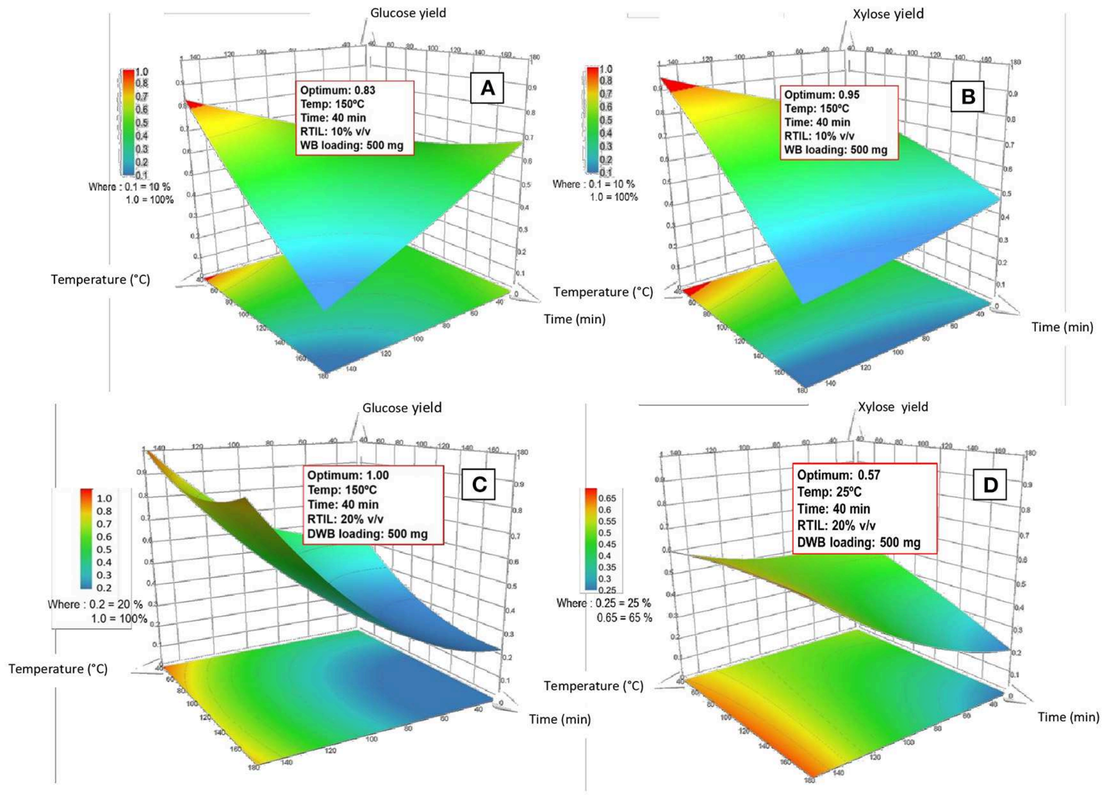

FIGURE 5 | Response surface plots of sugar release after enzymatic hydrolysis for WB **(A,B)** and DWB **(C,D)** as a function of time (40–180 min) and temperature (25–150°C).

of RTIL. The experimental data of glucose and xylose yields presented in **Table 2** were used to fit the model (Equation 4) to predict the responses and identify the regression coefficients of the second order equation (**Table 5**). Based on coefficients presented in **Table 5**, the relation between the investigated factors and the glucose or xylose yields can be obtained.

ANOVA was implemented to test the significance of the established models. A model is considered significant if its "Prob > F" value (*p*-value) is <0.05 and its *F*-value is relatively high ($F > 4$) which implies that there is only a 0.05% chance that a "Model *F*-value" could occur due to noise. In this study, the model *F* values were ≥35.3 indicating that all models were highly significant at the 95% confidence level (**Table 5**). Furthermore, the *p* value was $p < 0.0001$ which indicated that the quadratic model explains adequately the linear, quadratic and interaction effects on the response, in other words, the regression equation (Equation 4) was adequate to explain the glucose and xylose yields. According to the ANOVA results, the lack of fit was not significant for all response variables ($p > 0.05$) which confirm the goodness of the model. The fitness of the quadratic model was checked by means of the coefficients of determination. As can be seen from **Table 5**, the coefficients of determination (R^2) ranged from 0.960 to 0.980 for both glucose and xylose yields implying a 96–98% variability of response explained. That is, only about 2–4% of the total variance could not be explained by the model. In general, quadratic model having R^2 values higher than 0.90 are considered as models with a high degree of correlation (Cadoche and López, 1989; Myers et al., 2016). Moreover, the coefficient of adjusted determination ($R_{2\mathrm{Adj}}$) was calculated as an accurate measure of regression model quality. Thus, the high $R_{2\mathrm{Adj}}$ values (0.93–0.97) implied a high significance of the model. Finally, the precision and model reproducibility were evaluated by the RSD% that is defined as a percentage of error and whose value should not be higher than 10%. Consequently, according to the values of RSD (<10%) shown in **Table 5** we can conclude that the current models for glucose and xylose yields are precise and reproducible.

To complete the PLS analysis, the effect of pretreatment factors on the response (sugar yields) was shown by means of VIP charts (**Figure 3**). It should be noticed that the weight of factors are different since 4 different and independent models (WB and DWB) were fitted for glucose and xylose yields obtained after enzymatic hydrolysis. From those models MRO was developed to obtain the maximum glucose and xylose yields for WB and in the same way another MRO for DWB. In the case of glucose yield for WB, the factors with the largest linear effects were the biomass loading (X_4) followed by the time (X_2) and the temperature (X_1) while the RTIL percentage (X_3) was not a significant factor (**Figure 3A**). For DWB, temperature was the most contributing factor affecting the glucose yield (**Figure 3C**).

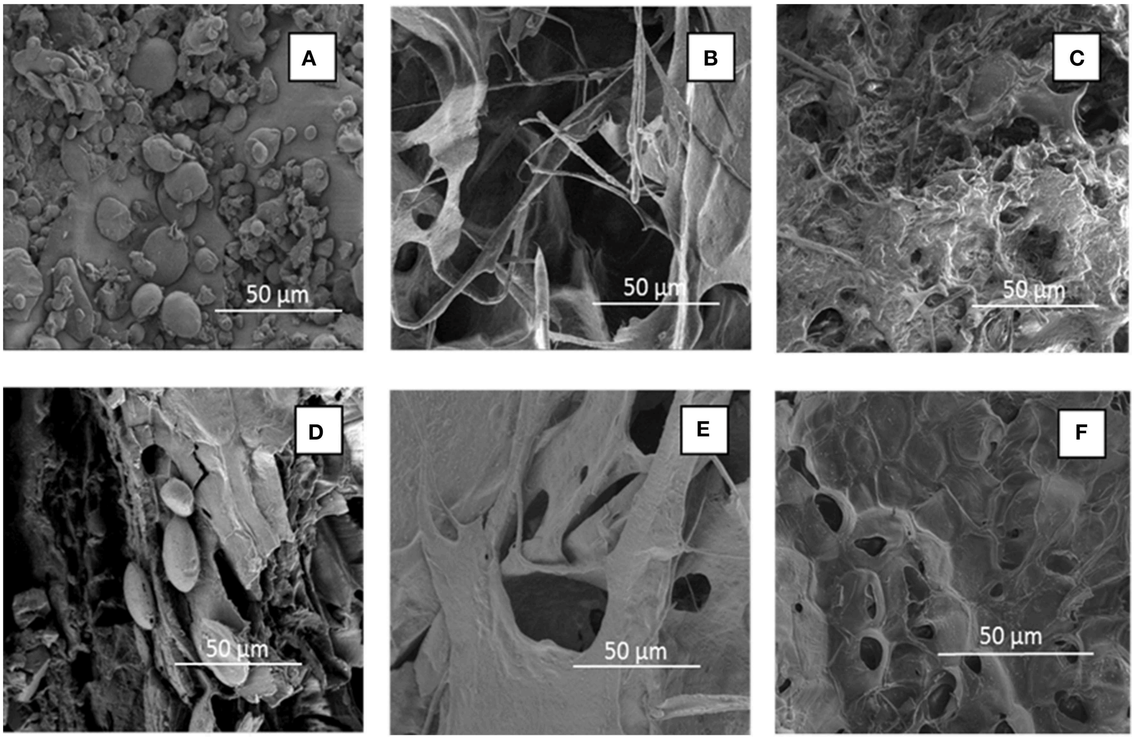

FIGURE 6 | SEM images (x 500) of untreated WB **(A)** and DWB **(D)** and pretreated with pure [C2mim][OAc] WB **(B)** and DWB **(E)** and with [C2mim][OAc]-water mixtures (RTIL content of 10%) [WB **(C)** and DWB **(F)**] at 150°C for 40 min.

For both WB and DWB, the quadratic terms of temperature (X_1X_1), time (X_2X_2), RTIL percentage (X_3X_3), and biomass loading (X_4X_4) exerted a substantial effect on glucose yield at the 95% confidence level (**Figures 3A,C**). In particular, for WB, some interactions such as RTIL percentage and biomass loading (X_3X_4), time and RTIL percentage (X_2X_3) were, according to the model, statistically significant ($p < 0.05$). Otherwise, no interaction effects were observed ($p > 0.005$) in the case of DWB. In addition, for xylose yields, the linear effect of time (X_2) and biomass loading (X_4) and their quadratic terms had the most significant effect during the WB pretreatment (**Figure 3B**). In the case of DWB, it was affected by the single effect of temperature (X_1), RTIL percentage (X_3), biomass loading (X_4) and the interaction of temperature, and RTIL percentage (X_1X_3) (**Figure 3D**).

Finally, the relationship between the observed values of glucose (Y_1) and xylose (Y_2) yields and the predicted values of the response from the models was shown in **Figure 4**. As illustrated in the **Figures 4A–D**, the values were closely grouped along the line of best fit which suggest a high degree of correlation between predicted and observed ones.

The PLS regression method to design of experiment utilize a type of validation named "Full Cross-Validation." This PLS regression variant differs lightly from the routine fit used in other PLS applications, such as the Multivariate Calibration where a "trainee" data and a second "validation" set are normally used (Pontes et al., 2006; Cen et al., 2007). In resume, these statistical results corroborated the efficiency and reliability of the present regression models and demonstrated a good correlation between process factors and their effects on the response.

Effect of Pretreatment Factors on Glucose and Xylose Yields and Optimums

As previously mentioned for WB, the VIP charts revealed that all factors present a clear quadratic tendency indicating that this effect was very critical for the model. Hence, the second order model was the most suitable to adjust the experimental data and to predict the glucose and xylose yields. These findings were supported by the curvatures and twists observed in the RS plots (**Figures 5A,B**). In fact, the RS plot for glucose yield showed a saddle curvature while for xylose yield the RS plot showed a clear convex curvature which is typical of a quadratic–shaped surface (Myers et al., 2016). Moreover, through PLS analysis made, the optimal conditions of WB pretreatment were determined, i.e.,: temperature (X_1) = 150°C, time (X_2) = 40 min, RTIL percentage (X_3) = 10% (v/v) aqueous medium, and biomass loading (X_4) = 5% (w/v) leading to yields predicted values of 83% in glucose and 95% in xylose (**Figures 5A,B**). Under the optimized conditions, slightly lower experimental yields were obtained: 77% for glucose and 90.4% for xylose. The residual values (that is: experimental value—model predicted value, expressed by absolute value) were estimated to be 6 and 4.6% for glucose and xylose yields, respectively.

As for WB, all of quadratic terms had a significant influence on glucose yield for DWB (**Figure 3C**). This phenomenon is reflected in the high yields obtained (100%) and graphically observed in the curvature of RS plot which present a steep slope (**Figure 5C**). In this context, if we compare the glucose yield of WB with that of DWB we can see clearly that in very similar experimental conditions, the performance of pretreatment would be significantly higher for DWB. The difference detected can be attributed to a higher level of RTIL (X_3) (20% for DWB vs. 10% for WB). Maximum glucose yield (100%) was obtained under the following pretreatment conditions: temperature (X_1) = 150°C, time (X_2) = 40 min, RTIL percentage (X_3) = 20% (v/v) in aqueous medium, and biomass loading (X_4) = 5% (w/v) (**Figure 5C**).

On the contrary, in the case of xylose yield for DWB, the linear effects of X_1, X_3, and X_4, the interaction effects of X_1 and X_3 were the ones who had the most significant influence in the fitted second order model (**Figure 3D**). This is agreement with the results obtained. Indeed, the RS plot (**Figure 5D**) presents a slight curvature concave and the optimum performance (57%) was very low when compared to that obtained for WB (95%). This may be partially explained by the effect not significant of interactions in the model (**Figure 3D**), in other words, the interactions have barely contributed to the xylose yield. In this context, a linear model could have been a more adequate solution to adjust the response. However, the slight curvature concave of the plot (**Figure 5D**) shows that the second order model was effectively the most appropriate to fit the xylose yields (lack of fit not significant). The optimal pretreatment conditions were: temperature (X_1) = 25°C, time (X_2) =40 min, RTIL percentage (X_3) = 20% (v/v) in aqueous medium, and biomass loading (X_4) = 5% (w/v) (**Figure 5C**).

Under each optimal condition, yields obtained experimentally with DWB gave 92.1% for glucose and 53% for xylose, again slightly lower than the predicted ones, as for WB. Residual values were thus estimated at 7.9% for glucose and 4%n for xylose.

Finally, a MRO was performed by Nelder-Mead Simplex Method for each biomass (WB and DWB) in order to obtain best pretreatment conditions to maximize both glucose and xylose yields. The MRO for WB displayed optimums of glucose and xylose yields of 83.5 and 95.3%, respectively, which were obtained under the following conditions: temperature (X_1) = 150°C, time (X_2)= 40 min, RTIL percentage (X_3) = 10% (v/v) in aqueous medium, and biomass loading (X_4) = 5% (w/v). Furthermore, MRO for DWB revealed optimum of glucose and xylose yields of 100 and 56.1%, respectively. These optimum yields were obtained with a temperature (X_1) =150°C, time (X_2) = 40 min, RTIL percentage (X_3) = 20% of RTIL (v/v), and a biomass loading (X_4) = 5% w/v. These yields are similar to those obtained by individual optimization with PLS approach, in other words, MRO maintain the yield values for both sugars. Based on the results mentioned above, we can observe that optimal pretreatment conditions for WB further improve the glucose yields while in the opposite case optimal pretreatment conditions for DWB improve the xylose yields. Moreover, pretreatment of WB and DWB with [C2mim][OAc]-water mixtures increased significantly the sugar yields of about 60–100% as compared to those of unpretreated biomass (10–20%). Results from this study were in agreement with others previous reports using [C2mim][OAc] and water as pretreatment media. Fu and Mazza (2011a) reported that a higher sugar yield (81%) was obtained after the [C2mim][OAc]-water pretreatment (50% of water content) of triticale straw at 150°C for 90 min. Perez-Pimienta et al. (2017) reported a glucan conversion efficiency of 98% for Agave bagasse biomass (40% water in [C2mim][OAc] media) and 83% for municipal solid waste biomass (50% water in [C2mim][OAc] media).

To sum up, optimal conditions to pretreat wheat bran by RTIL were determined. Our experimental design demonstrated the possibility to implement efficient pretreatment of wheat bran with diluted [C2mim][OAc] [10–20% (v/v)] in water within the range of study of the present work. Hence, this complete statistical study confirmed that the established models were appropriate to predict the sugar yields under different pretreatment conditions.

Morphological and Textural Properties Associated With WB and DWB Pretreatment

To gain more insight into the effect of [C2mim][OAc]-water mixture, we focused then on the structural characterization of untreated and pretreated WB and DWB samples by performing SEM. For those analyses, we selected two pretreatment conditions leading to highest sugar yields. [C2mim][OAc]-water mixture pretreatments visibly induced a disorganization of WB and DWB leading to the formation of porous and expanded structure (**Figures 6C,F**) while more drastic effect was displayed with pure [C2mim][OAc] pretreatment (**Figures 6B,E**). The aqueous [C2mim][OAc] pretreatment contributed to the formation of a porous material that could account for increasing the enzymatic digestibility as already suggested by other authors (Singh et al., 2009; Hu et al., 2018). However, our optimized pretreatment conditions allowed preserving the structural integrity of cellulose as seen from the NMR signals of C4-carbon of amorphous and crystalline cellulose (**Figure S1**).

CONCLUSION

This is the first work applying PLS methodology to optimize WB and DWB pretreatments with [C2mim][OAc]-water mixtures. Pretreatment conditions were optimized to achieve high glucose and xylose yields from WB biomasses by the proposed quadratic models. Highs glucose (83–100%) and xylose (57–95%) yields were obtained under optimized pretreatment conditions of temperature, time, concentration of [C2mim][OAc] in water and biomass loading. The complete statistical assessment confirmed that our established model is adequate and accurately predicts the glucose and xylose yield within the range of pretreatment conditions employed. Finally, the possibility to minimize the required RTIL amount to implement efficient pretreatment of

WB and DWB was demonstrated which could have a great impact for further implementation at a large scale.

DATA AVAILABILITY

All datasets generated for this study are included in the manuscript/**Supplementary Files**.

AUTHOR CONTRIBUTIONS

EH, CS, and CR conceived the project. EH, CS, MA-F, and JS conceived the experiments and wrote the manuscript. MA-F, DG, VL, IG, and HR achieved chemical composition, RTIL pretreatments, and enzymatic reactions experiments and analysis. MA-F and JS-T realized and interpreted the experimental design and statistical analysis. RR realized the SEM analysis. MA-F, EH, and CS coordinate the study and interpretations. All authors helped with drafting the manuscript.

FUNDING

This research was supported by the Interreg France-Wallonie-Vlaanderen through the ValBran project with the support of the European Regional Development Fund (ERDF) of the regions Grand Est, Walloon and the Province West of Flanders (www.valbran.eu).

ACKNOWLEDGMENTS

The authors thank to Dominique Cailleu, Aurelien Furlan, and Arash Jamali for their technical support with NMR and SEM analyses.

SUPPLEMENTARY MATERIAL

The Supplementary Material for this article can be found online at: https://www.frontiersin.org/articles/10.3389/fchem.2019.00585/full#supplementary-material

REFERENCES

Ahmed, M. A., Seo, Y. H., Terán-Hilares, R., Rehman, M. S. U. R., and Han, J.-I. (2016). Persulfate based pretreatment to enhance the enzymatic digestibility of rice straw. *Bioresour. Technol.* 222, 523–526. doi: 10.1016/j.biortech.2016.09.122

Akhtar, N., Gupta, K., Goyal, D., and Goyal, A. (2016). Recent advances in pretreatment technologies for efficient hydrolysis of lignocellulosic biomass. *Environ. Prog. Sustain. Energy* 35, 489–511. doi: 10.1002/ep.12257

Alayoubi, R., Mehmood, N., Husson, E., Kouzayha, A., Tabcheh, M., Chaveriat, L., et al. (2019). Low temperature ionic liquid pretreatment of lignocellulosic biomass to enhance bioethanol yield. *Renew. Energy* 145, 1808–1816. doi: 10.1016/j.renene.2019.07.091

Alvira, P., Tomás-Pejó, E., Ballesteros, M., and Negro, M. J. (2010). Pretreatment technologies for an efficient bioethanol production process based on enzymatic hydrolysis: a review. *Bioresour. Technol.* 101, 4851–4861. doi: 10.1016/j.biortech.2009.11.093

AOAC Official Method (2001). *AOAC Official Method 2001.11 Protein(Crude)in Animal Feed|Ammonia|Titration Scribd*. Available online at: https://fr.scribd.com/document/230362186/4-2-11-AOAC-Official-Method-2001-11-Protein-Crude-in-Animal-Feed (accessed September 7, 2018).

Auxenfans, T., Buchoux, S., Djellab, K., Avondo, C., Husson, E., and Sarazin, C. (2012). Mild pretreatment and enzymatic saccharification of cellulose with recycled ionic liquids towards one-batch process. *Carbohydr. Polym.* 90, 805–813. doi: 10.1016/j.carbpol.2012.05.101

Auxenfans, T., Buchoux, S., Husson, E., an d Sarazin, C. (2014a). Efficient enzymatic saccharification of Miscanthus: energy-saving by combining dilute acid and ionic liquid pretreatments. *Biomass Bioenergy* 62, 82–92. doi: 10.1016/j.biombioe.2014.01.011

Auxenfans, T., Buchoux, S., Larcher, D., Husson, G., Husson, E., and Sarazin, C. (2014b). Enzymatic saccharification and structural properties of industrial wood sawdust: recycled ionic liquids pretreatments. *Energy Convers. Manag.* 88, 1094–1103. doi: 10.1016/j.enconman.2014.04.027

Auxenfans, T., Crônier, D., Chabbert, B., and Paës, G. (2017a). Understanding the structural and chemical changes of plant biomass following steam explosion pretreatment. *Biotechnol. Biofuels* 10:36. doi: 10.1186/s13068-017-0718-z

Auxenfans, T., Husson, E., and Sarazin, C. (2017b). Simultaneous pretreatment and enzymatic saccharification of (ligno) celluloses in aqueous-ionic liquid media: a compromise. *Biochem. Eng. J.* 117, 77–86. doi: 10.1016/j.bej.2016.10.004

Badgujar, K. C., and Bhanage, B. M. (2015). Factors governing dissolution process of lignocellulosic biomass in ionic liquid: current status, overview and challenges. *Bioresour. Technol.* 178, 2–18. doi: 10.1016/j.biortech.2014.09.138

Bajaj, B. K., and Wani, M. A. (2011). Enhanced phytase production from *Nocardia* sp. MB 36 using agro-residues as substrates: potential application for animal feed production. *Eng. Life Sci.* 11, 620–628. doi: 10.1002/elsc.201100039

Balat, M. (2011). Production of bioethanol from lignocellulosic materials via the biochemical pathway: a review. *Energy Convers. Manag.* 52, 858–875. doi: 10.1016/j.enconman.2010.08.013

Brandt, A., Gräsvik, J., Hallett, J. P., and Welton, T. (2013). Deconstruction of lignocellulosic biomass with ionic liquids. *Green Chem.* 15, 550–583. doi: 10.1039/c2gc36364j

Cadoche, L., and López, G. D. (1989). Assessment of size reduction as a preliminary step in the production of ethanol from lignocellulosic wastes. *Biol. Wastes* 30, 153–157. doi: 10.1016/0269-7483(89)90069-4

Celiktas, M. S., Kirsch, C., and Smirnova, I. (2014). Cascade processing of wheat bran through a biorefinery approach. *Energy Convers. Manage.* 84, 633–639. doi: 10.1016/j.enconman.2014.04.039

Cen, H., He, Y., and Huang, M. (2007). Combination and comparison of multivariate analysis for the identification of oranges varieties using visible and near infrared reflectance spectroscopy. *Eur. Food Res. Technol.* 225, 699–705. doi: 10.1007/s00217-006-0470-2

Çetinkol, Ö. P., Dibble, D. C., Cheng, G., Kent, M. S., Knierim, B., Auer, M., et al. (2010). Understanding the impact of ionic liquid pretreatment on eucalyptus. *Biofuels* 1, 33–46. doi: 10.4155/bfs.09.5

Chandra, R. P., Bura, R., Mabee, W. E., Berlin, A., Pan, X., and Saddler, J. N. (2007). "Substrate pretreatment: the key to effective enzymatic hydrolysis of lignocellulosics?," in *Biofuels Advances in Biochemical Engineering/Biotechnology*, ed L. Olsson (Berlin; Heidelberg: Springer Berlin Heidelberg), 67–93. doi: 10.1007/10_2007_064

Czitrom, V. (1999) One-factor-at-a-time versus designed experiments. *Am. Statist.* 53, 126–131.

da Costa Lopes, A. M., João, K. G., Morais, A. R. C., Bogel-Łukasik, E., and Bogel-Łukasik, R. (2013). Ionic liquids as a tool for lignocellulosic biomass fractionation. *Sustain. Chem. Process.* 1:3. doi: 10.1186/2043-7129-1-3

Doherty, T. V., Mora-Pale, M., Foley, S. E., Linhardt, R. J., and Dordick, J. S. (2010). Ionic liquid solvent properties as predictors of lignocellulose pretreatment efficacy. *Green Chem.* 12, 1967–1975. doi: 10.1039/c0gc00206b

Egorova, K. S., and Ananikov, V. P. (2014). Toxicity of ionic liquids: eco(cyto)activity as complicated, but unavoidable parameter for task-specific optimization. *ChemSusChem* 7, 336–360. doi: 10.1002/cssc.201300459

Elgharbawy, A. A., Alam, M. Z., Kabbashi, N. A., Moniruzzaman, M., and Jamal, P. (2017). Implementation of definite screening design in optimization of *in situ* hydrolysis of EFB in cholinium acetate and locally produced cellulase combined system. *Waste Biomass Valor.* 8, 839–850. doi: 10.1007/s12649-016-9638-6

Elgharbawy, A. A., Alam, M. Z., Moniruzzaman, M., and Goto, M. (2016). Ionic liquid pretreatment as emerging approaches for enhanced enzymatic hydrolysis of lignocellulosic biomass. *Biochem. Eng. J.* 109, 252–267. doi: 10.1016/j.bej.2016.01.021

Engel, P., Krull, S., Seiferheld, B., and Spiess, A. C. (2012). Rational approach to optimize cellulase mixtures for hydrolysis of regenerated cellulose containing residual ionic liquid. *Bioresour. Technol.* 115, 27–34. doi: 10.1016/j.biortech.2011.10.080

Eriksson, L., Byrne, T., Johansson, E., Trygg, J., and Wikstrom, C. (2013). *Multi- and Megavariate Data Analysis Basic Principles and Applications, 3rd Edn*. Umetrics. Available online at: https://webshop.umetrics.com/products/multi-and-megavariate-data-analysis-basic-principles-and-applications-third-revised-edition (*accessed September* 7, 2018).

Ferrer, A. (2007). Multivariate statistical process control based on principal component analysis (MSPC-PCA): some reflections and a case study in an autobody assembly process. *Qual. Eng.* 19, 311–325. doi: 10.1080/08982110701621304

Fu, D., and Mazza, G. (2011a). Aqueous ionic liquid pretreatment of straw. *Bioresour. Technol.* 102, 7008–7011. doi: 10.1016/j.biortech.2011.04.049

Fu, D., and Mazza, G. (2011b). Optimization of processing conditions for the pretreatment of wheat straw using aqueous ionic liquid. *Bioresour. Technol.* 102, 8003–8010. doi: 10.1016/j.biortech.2011.06.023

Gauthier, A., Derenne, S., Dupont, L., Guillon, E., Largeau, C., Dumonceau, J., et al. (2002). Characterization and comparison of two ligno-cellulosic substrates by 13C CP/MAS NMR, XPS, conventional pyrolysis and thermochemolysis. *Anal. Bioanal. Chem.* 373, 830–838. doi: 10.1007/s00216-002-1371-2

Goering, H. K., and Van Soest, P. J. (1970). *Forage Fiber Analyses (Apparatus, Reagents, Procedures, and Some Applications)*. Available online at: https://trove.nla.gov.au/version/46035777 (accessed September 7, 2018).

Ha, M.-A., Jardine, W. G., and Jarvis, M. C. (1997). Solid-state 13 C NMR of cell walls in wheat bran. *J. Agric. Food Chem.* 45, 117–119. doi: 10.1021/jf960311m

Hendriks, A. T. W. M., and Zeeman, G. (2009). Pretreatments to enhance the digestibility of lignocellulosic biomass. *Bioresour. Technol.* 100, 10–18. doi: 10.1016/j.biortech.2008.05.027

Hou, X. D., Li, N., and Zong, M. H. (2013). Significantly enhancing enzymatic hydrolysis of rice straw after pretreatment using renewable ionic-liquid-water mixtures. *Bioresour. Technol.* 136, 469–474. doi: 10.1016/j.biortech.2013.02.118

Hu, X., Cheng, L., Gu, Z., Hong, Y., Li, Z., and Li, C. (2018). Effects of ionic liquid/water mixture pretreatment on the composition, the structure and the enzymatic hydrolysis of corn stalk. *Ind. Crops Prod.* 122, 142–147. doi: 10.1016/j.indcrop.2018.05.056

Husson, E., Auxenfans, T., Herbaut, M., Baralle, M., Lambertyn, V., Rakotoarivonina, H., et al. (2018). Sequential and simultaneous strategies for biorefining of wheat straw using room temperature ionic liquids, xylanases and cellulases. *Bioresour. Technol.* 251, 280–287. doi: 10.1016/j.biortech.2017.12.047

Husson, E., Buchoux, S., Avondo, C., Cailleu, D., Djellab, K., Gosselin, I., et al. (2011). Enzymatic hydrolysis of ionic liquid-pretreated celluloses: contribution of CP-MAS ^{13}C NMR and SEM. *Bioresour. Technol.* 102, 7335–7342. doi: 10.1016/j.biortech.2011.04.097

Kamiya, N., Matsushita, Y., Hanaki, M., Nakashima, K., Narita, M., Goto, M., et al. (2008). Enzymatic *in situ* saccharification of cellulose in aqueous-ionic liquid media. *Biotechnol. Lett.* 30, 1037–1040. doi: 10.1007/s10529-008-9638-0

Kumar, R., Mago, G., Balan, V., and Wyman, C. E. (2009). Physical and chemical characterizations of corn stover and poplar solids resulting from leading pretreatment technologies. *Bioresour. Technol.* 100, 3948–3962. doi: 10.1016/j.biortech.2009.01.075

Lee, K. M., Ngoh, G. C., and Chua, A. S. M. (2013). Process optimization and performance evaluation on sequential ionic liquid dissolution–solid acid saccharification of sago waste. *Bioresour. Technol.* 130, 1–7. doi: 10.1016/j.biortech.2012.11.124

Li, D., Qian, Y., Tian, Y.-J., Yuan, S.-M., Wei, W., and Wang, G. (2017). Optimization of ionic liquid-assisted extraction of biflavonoids from *Selaginella doederleinii* and evaluation of its antioxidant and antitumor activity. *Molecules* 22:586. doi: 10.3390/molecules22040586

Li, Q., He, Y.-C., Xian, M., Jun, G., Xu, X., Yang, J.-M., et al. (2009). Improving enzymatic hydrolysis of wheat straw using ionic liquid 1-ethyl-3-methyl imidazolium diethyl phosphate pretreatment. *Bioresour. Technol.* 100, 3570–3575. doi: 10.1016/j.biortech.2009.02.040

Liang, L., Yan, J., He, Q., Luong, T., Pray, T. R., Simmons, B. A., et al. (in press). Scale-up of biomass conversion using 1-ethyl-3-methylimidazolium acetate as the solvent. *Green Energy Environ*. doi: 10.1016/j.gee.2018.07.002

Liu, Q.-P., Hou, X.-D., Li, N., and Zong, M.-H. (2012). Ionic liquids from renewable biomaterials: synthesis, characterization and application in the pretreatment of biomass. *Green Chem.* 14, 304–307. doi: 10.1039/C2GC16128A

Liu, W., Cheng, L., Zhang, Y., Wang, H., and Yu, M. (2008). The physical properties of aqueous solution of room-temperature ionic liquids based on imidazolium: database and evaluation. *J. Mol. Liq.* 140, 68–72. doi: 10.1016/j.molliq.2008.01.008

Liu, Y., and Ng, P. K. W. (2016). Relationship between bran characteristics and bran starch of selected soft wheats grown in Michigan. *Food Chem.* 197, 427–435. doi: 10.1016/j.foodchem.2015.10.112

Liu, Y.-R., Thomsen, K., Nie, Y., Zhang, S.-J., and Meyer, A. S. (2016). Predictive screening of ionic liquids for dissolving cellulose and experimental verification. *Green Chem.* 18, 6246–6254. doi: 10.1039/C6GC01827K

Locci, E., Laconi, S., Pompei, R., Scano, P., Lai, A., and Marincola, F. C. (2008). Wheat bran biodegradation by Pleurotus ostreatus: a solid-state Carbon-13 NMR study. *Bioresour. Technol.* 99, 4279–4284. doi: 10.1016/j.biortech.2007.08.048

Mazza, M., Catana, D.-A., Vaca-Garcia, C., and Cecutti, C. (2009). Influence of water on the dissolution of cellulose in selected ionic liquids. *Cellulose* 16, 207–215. doi: 10.1007/s10570-008-9257-x

Mehmood, N., Husson, E., Jacquard, C., Wewetzer, S., Büchs, J., Sarazin, C., et al. (2015). Impact of two ionic liquids, 1-ethyl-3-methylimidazolium acetate and 1-ethyl-3-methylimidazolium methylphosphonate, on *Saccharomyces cerevisiae*: metabolic, physiologic, and morphological investigations. *Biotechnol. Biofuels* 8:17. doi: 10.1186/s13068-015-0206-2

Myers, R. H., Montgomery, D. C., and Anderson-Cook, C. M. (2016). *Response Surface Methodology: Process and Product Optimization Using Designed Experiments, 4th Edn*. Hoboken, NJ: John Wiley and Sons.

Norgren, M., and Edlund, H. (2014). Lignin: recent advances and emerging applications. *Curr. Opin. Colloid Interface Sci.* 19, 409–416. doi: 10.1016/j.cocis.2014.08.004

Oliveira Ribeiro, W. C., Silva Lima, A. C., and Araújo Morandim-Giannetti, A. (2018). Optimizing treatment condition of coir fiber with ionic liquid and subsequent enzymatic hydrolysis for future bioethanol production. *Cellulose* 25, 527–536. doi: 10.1007/s10570-017-1554-9

Olivier-Bourbigou, H., Magna, L., and Morvan, D. (2010). Ionic liquids and catalysis: recent progress from knowledge to applications. *Appl. Catal. A Gen.* 373, 1–56. doi: 10.1016/j.apcata.2009.10.008

Papa, G., Feldman, T., Sale, K. L., Adani, F., Singh, S., and Simmons, B. A. (2017). Parametric study for the optimization of ionic liquid pretreatment of corn stover. *Bioresour. Technol.* 241, 627–637. doi: 10.1016/j.biortech.2017.05.167

Perez-Cantu, L., Schreiber, A., Schütt, F., Saake, B., Kirsch, C., and Smirnova, I. (2013). Comparison of pretreatment methods for rye straw in the second generation biorefinery: effect on cellulose, hemicellulose and lignin recovery. *Bioresour. Technol.* 142, 428–435. doi: 10.1016/j.biortech.2013.05.054

Perez-Pimienta, J. A., Sathitsuksanoh, N., Thompson, V. S., Tran, K., Ponce-Noyola, T., Stavila, V., et al. (2017). Ternary ionic liquid–water pretreatment systems of an agave bagasse and municipal solid waste blend. *Biotechnol. Biofuels* 10:72. doi: 10.1186/s13068-017-0758-4

Pontes, M., Santos, S., Araujo, M., Almeida, L., Lima, R., Gaiao, E., et al. (2006). Classification of distilled alcoholic beverages and verification of adulteration by near infrared spectrometry. *Food Res. Intern.* 39, 182–189. doi: 10.1016/j.foodres.2005.07.005

Prückler, M., Siebenhandl-Ehn, S., Apprich, S., Höltinger, S., Haas, C., Schmid, E., et al. (2014). Wheat bran-based biorefinery 1: composition of wheat bran and strategies of functionalization. *LWT Food Sci. Technol.* 56, 211–221. doi: 10.1016/j.lwt.2013.12.004

Qiu, Z., Aita, G. M., and Mahalaxmi, S. (2014). Optimization by response surface methodology of processing conditions for the ionic liquid pretreatment of energy cane bagasse: optimization by RSM of the IL pretreatment of energy cane bagasse. *J. Chem. Technol. Biotechnol.* 89, 682–689. doi: 10.1002/jctb.4167

Reisinger, M., Tirpanalan, Ö., Prückler, M., Huber, F., Kneifel, W., and Novalin, S. (2013). Wheat bran biorefinery—A detailed investigation on hydrothermal and enzymatic treatment. *Bioresour. Technol.* 144, 179–185. doi: 10.1016/j.biortech.2013.06.088

Ryu, S., Labbé, N., and Trinh, C. T. (2015). Simultaneous saccharification and fermentation of cellulose in ionic liquid for efficient production of α-ketoglutaric acid by *Yarrowia lipolytica*. *Appl. Microbiol. Biotechnol.* 99, 4237–4244. doi: 10.1007/s00253-015-6521-5

Saha, K., Dasgupta, J., Chakraborty, S., Antunes, F. A. F., Sikder, J., Curcio, S., et al. (2017). Optimization of lignin recovery from sugarcane bagasse using ionic liquid aided pretreatment. *Cellulose* 24, 3191–3207. doi: 10.1007/s10570-017-1330-x

Sannigrahi, P., Kim, D. H., Jung, S., and Ragauskas, A. (2011). Pseudo-lignin and pretreatment chemistry. *Energy Environ. Sci.* 4, 1306–1310. doi: 10.1039/C0EE00378F

Shi, J., Balamurugan, K., Parthasarathi, R., Sathitsuksanoh, N., Zhang, S., Stavila, V., et al. (2014). Understanding the role of water during ionic liquid pretreatment of lignocellulose: co-solvent or anti-solvent? *Green Chem.* 16, 3830–3840. doi: 10.1039/C4GC00373J

Shi, J., Gladden, J. M., Sathitsuksanoh, N., Kambam, P., Sandoval, L., Mitra, D., et al. (2013). One-pot ionic liquid pretreatment and saccharification of switchgrass. *Green Chem.* 15, 2579–2589. doi: 10.1039/c3gc40545a

Shi, R., and Wang, Y. (2016). Dual ionic and organic nature of ionic liquids. *Sci. Rep.* 6:19644. doi: 10.1038/srep19644

Shill, K., Padmanabhan, S., Xin, Q., Prausnitz, J. M., Clark, D. S., and Blanch, H. W. (2011). Ionic liquid pretreatment of cellulosic biomass: enzymatic hydrolysis and ionic liquid recycle. *Biotechnol. Bioeng.* 108, 511–520. doi: 10.1002/bit.23014

Sidik, D. A. B., Ngadi, N., and Amin, N. A. S. (2013). Optimization of lignin production from empty fruit bunch via liquefaction with ionic liquid. *Bioresour. Technol.* 135, 690–696. doi: 10.1016/j.biortech.2012.09.041

Singh, S., Sambhyal, M., Vaid, S., Singh, P., and Bajaj, B. K. (2015). Two-step sequential optimization for production of ionic liquid stable cellulase from *Bacillus subtilis* I-2. *Biocatal. Biotransform.* 33, 224–233. doi: 10.3109/10242422.2015.1113955

Singh, S., Simmons, B. A., and Vogel, K. P. (2009). Visualization of biomass solubilization and cellulose regeneration during ionic liquid pretreatment of switchgrass. *Biotechnol. Bioeng.* 104, 68–75. doi: 10.1002/bit.22386

Sun, N., Rahman, M., Qin, Y., Maxim, M. L., Rodríguez, H., and Rogers, R. D. (2009). Complete dissolution and partial delignification of wood in the ionic liquid 1-ethyl-3-methylimidazolium acetate. *Green Chem.* 11, 646–655. doi: 10.1039/b822702k

Swatloski, R. P., Spear, S. K., Holbrey, J. D., and Rogers, R. D. (2002). Dissolution of cellose with ionic liquids. *J. Am. Chem. Soc.* 124, 4974–4975. doi: 10.1021/ja025790m

Tan, H. T., Lee, K. T., and Mohamed, A. R. (2011). Pretreatment of lignocellulosic palm biomass using a solvent-ionic liquid [BMIM]Cl for glucose recovery: an optimisation study using response surface methodology. *Carbohydr. Polym.* 83, 1862–1868. doi: 10.1016/j.carbpol.2010.10.052

Trinh, L. T. P., Lee, Y.-J., Lee, J.-W., and Lee, W.-H. (2018). Optimization of ionic liquid pretreatment of mixed softwood by response surface methodology and reutilization of ionic liquid from hydrolysate. *Biotechnol. Bioprocess Eng.* 23, 228–237. doi: 10.1007/s12257-017-0209-x

Vergara, P., Wojtusik, M., Revilla, E., Ladero, M., Garcia-Ochoa, F., and Villar, J. C. (2018). Wheat straw fractionation by ethanol-water mixture: optimization of operating conditions and comparison with diluted sulfuric acid pre-treatment. *Bioresour. Technol.* 256, 178–186. doi: 10.1016/j.biortech.2018.01.137

Viell, J., Inouye, H., Szekely, N. K., Frielinghaus, H., Marks, C., Wang, Y., et al. (2016). Multi-scale processes of beech wood disintegration and pretreatment with 1-ethyl-3-methylimidazolium acetate/water mixtures. *Biotechnol. Biofuels* 9:7. doi: 10.1186/s13068-015-0422-9

Wang, H., Gurau, G., and Rogers, R. D. (2012). Ionic liquid processing of cellulose. *Chem. Soc. Rev.* 41, 1519–1537. doi: 10.1039/c2cs15311d

Wang, S., You, T., Xu, F., Chen, J., and Yang, G. (2015). Optimization of [Amim]Cl pretreatment conditions for maximum glucose recovery from hybrid pennisetum by response surface methodology. *BioResources* 10, 7021–7037. doi: 10.15376/biores.10.4.7021-7037

Wold, S., Sjöström, M., and Eriksson, L. (2001). PLS-regression: a basic tool of chemometrics. *Chemom. Intell. Lab. Syst.* 58, 109–130. doi: 10.1016/S0169-7439(01)00155-1

Xu, C., Liao, B., and Shi, W. (2013). "Organosolv pretreatment of pine sawdust for bio-ethanol production," in *Pretreatment Techniques for Biofuels and Biorefineries Green Energy and Technology*, ed Z. Fang (Berlin; Heidelberg: Springer Berlin Heidelberg), 435–457. doi: 10.1007/978-3-642-32735-3_19

Yan, J., Joshee, N., and Liu, S. (2016). Utilization of hardwood in biorefinery: a kinetic interpretation of pilot-scale hot-water pretreatment of *Paulownia elongata* woodchips. *J. Biobased Mater. Bioenergy* 10, 339–348. doi: 10.1166/jbmb.2016.1609

Yan, J., and Liu, S. (2015). Hot water pretreatment of boreal aspen woodchips in a pilot scale digester. *Energies* 8, 1166–1180. doi: 10.3390/en8021166

Yañez, L., Saavedra, J., Martínez, C., Córdova, A., and Ganga, M. A. (2012). Chemometric analysis for the detection of biogenic amines in Chilean cabernet sauvignon wines: a comparative study between organic and nonorganic production. *J. Food Sci.* 77, T143–T149. doi: 10.1111/j.1750-3841.2012.02796.x

Yoon, L. W., Ang, T. N., Ngoh, G. C., and Chua, A. S. M. (2012). Regression analysis on ionic liquid pretreatment of sugarcane bagasse and assessment of structural changes. *Biomass Bioenergy* 36, 160–169. doi: 10.1016/j.biombioe.2011.10.033

Zhang, Q., Hu, J., and Lee, D.-J. (2017). Pretreatment of biomass using ionic liquids: research updates. *Renew. Energy* 111, 77–84. doi: 10.1016/j.renene.2017.03.093

Conflict of Interest Statement: The authors declare that the research was conducted in the absence of any commercial or financial relationships that could be construed as a potential conflict of interest.

Copyright © 2019 Araya-Farias, Husson, Saavedra-Torrico, Gérard, Roulard, Gosselin, Rakotoarivonina, Lambertyn, Rémond and Sarazin. This is an open-access article distributed under the terms of the Creative Commons Attribution License (CC BY). The use, distribution or reproduction in other forums is permitted, provided the original author(s) and the copyright owner(s) are credited and that the original publication in this journal is cited, in accordance with accepted academic practice. No use, distribution or reproduction is permitted which does not comply with these terms.

frontiers in Chemistry

REVIEW
published: 29 August 2019
doi: 10.3389/fchem.2019.00565

About Making Lignin Great Again—Some Lessons From the Past

*Wolfgang G. Glasser**

Sustainable Biomaterials, Virginia Tech, Blacksburg, VA, United States

Lignin, the second most abundant biopolymer on the planet, serves land-plants as bonding agent in juvenile cell tissues and as stiffening (modulus-building) agent in mature cell walls. The chemical structure analysis of cell wall lignins from two partially delignified wood species representing between 6 and 65% of total wood lignin has revealed that cell wall-bound lignins are virtually invariable in terms of inter-unit linkages, and resemble the native state. Variability is recognized as the result of isolation procedure. In native state, lignin has a low glass-to-rubber transition temperature and is part of a block copolymer with non-crystalline polysaccharides. This molecular architecture determines all of lignin's properties, foremost of all its failure to undergo interfacial failure by separation from (semi-) crystalline cellulose under a wide range of environmental conditions. This seemingly unexpected compatibility (on the nano-level) between a carbohydrate component and the highly aromatic lignin represents a lesson by nature that human technology is only now beginning to mimic. Since the isolation of lignin from lignocellulosic biomass (i.e., by pulping or biorefining) necessitates significant molecular alteration of lignin, isolated lignins are highly variable in structure and reflect the isolation method. While numerous procedures exist for converting isolated (carbon-rich) lignins into well-defined commodity chemicals by various liquefaction techniques (such as pyrolysis, hydrogenolysis, etc.), the use of lignin in man-made thermosetting and thermoplastic structural materials appears to offer greatest value. The well-recognized variabilities of isolated lignins can in large part be remedied by targeted chemical modification, and by adopting nature's principles of functionalization leading to inter-molecular compatibility. Lignins isolated from large-scale industrial delignification processes operating under invariable isolation conditions produce polymers of virtually invariable character. This makes lignin from pulp mills a potentially valuable biopolymeric resource. The restoration of molecular character resembling that in native plants is illustrated in this review via the demonstrated (and in part commercially-implemented) use of pulp lignins in bio-degradable (or compostable) polymeric materials.

Keywords: biobased polymer, compostable plastics, lignin modification, lignin properties, sustainable thermoplastics, natural adhesives, lignin compatibility

OPEN ACCESS

Edited by:
Florent Allais,
AgroParisTech Institut des Sciences et Industries du Vivant et de L'environnement, France

Reviewed by:
Paul-Henri Ducrot,
INRA UMR1318 Institut Jean Pierre Bourgin, France
Gregory Chatel,
Université Savoie Mont Blanc, France
Jean-Michel Lavoie,
Université de Sherbrooke, Canada

***Correspondence:**
Wolfgang G. Glasser
wglasser@vt.edu

Specialty section:
This article was submitted to Green and Sustainable Chemistry, a section of the journal Frontiers in Chemistry

Received: *07 March 2019*
Accepted: *24 July 2019*
Published: *29 August 2019*

Citation:
Glasser WG (2019) About Making Lignin Great Again—Some Lessons From the Past. Front. Chem. 7:565. doi: 10.3389/fchem.2019.00565

INTRODUCTION

Lignin is well-known as the second most abundant biopolymer on Earth (Freudenberg and Neish, 1968; Sarkanen and Ludwig, 1971; Lewis and Sarkanen, 1998). Except for plants grown under water (or in juvenile condition, such as in annual crops), the planet's method of harnessing solar energy and recycling carbon dioxide, water, and oxygen through photosynthesis involves the formation of lignin. Lignin is always the minor component (by mass) of lignocellulosic plant species, and it plays a major and important role in the mechanical (bonding and stiffening), nutritional, and soil preservation role of nature. The process of lignification, and the structural details of lignin, have been the subject of numerous recent articles, and reviews (Forss and Fremer, 2003; The Ljungberg Textbook, 2008). This paper reviews the issue of lignin's variability, and specific aspects of its utilization potential in structural materials. While lignin has captured major markets as water-soluble derivative for many decades, mostly from sulfite pulping (Gargulak and Lebo, 2000), its potential use from other delignification processes has rarely extended beyond that as process-fuel. However, the quest for using renewable resources in place of fossil carbon sources for chemicals and materials has recently led to an accelerated exploration of lignin (and other biomass sources) in structural polymers (Doherty et al., 2011; Thakur et al., 2014; Upton and Kasko, 2016; Graichen et al., 2017). The many options investigated for lignin include chemical products derived from numerous depolymerization techniques (Zakzeski et al., 2010; Xu et al., 2014; Beckham et al., 2016; Kozliak et al., 2016; Cheng et al., 2018; Sun et al., 2018; Van den Bosch et al., 2018); from polymer fractionation using solvents and/or membrane filtration (Huang et al., 2017; Li and Takkellapati, 2018); from thermal conversion (carbon fibers; 3-D products; etc.) (Baker and Rials, 2013; Li et al., 2017); from chemical modification (Wang et al., 2016; Mueller et al., 2019); and many others. Thermosetting and thermoplastic materials have attracted special interest due to their market value and size, but they also present the most formidable obstacles since most natural polymers are neither soluble nor thermally deformable.

This review will attempt to illustrate the fundamental principles of how nature's approach to the assembly of recyclable but interfacial-failure-proof materials can (a) be adopted for the design of structural materials involving lignin; and (b) how these materials can draw specific benefits from lignin's original structural design and properties. Many of these principles have been the result decades ago of studies focused on both biochemical (i.e., wood formation and thus lignification) and papermaking (and thus delignification) techniques, which constitute the basic roots of our understanding of lignin without being readily connected to present-day polymer and materials science literature.

STRUCTURAL ASPECTS

Lignin is formed by the *in-situ* polymerization of a mixture of *para*-hydroxy cinnamyl alcohols with an enzyme-triggered mechanism involving free radicals. In native plants, lignin's aromatic structure is dominated by alky-aryl ether bonds that accommodate a limited variability in relation to precursor supply, which represents a mixture of three *p*-hydroxy cinnamyl alcohols (also called C_9-species), designated as coumaryl (*p*-OH), coniferyl (Gua), and sinapyl (Syr) alcohol (Freudenberg and Neish, 1968). The enzymatic electron-abstracting (oxidation) reaction of the phenolate species generates a series of free phenoxy radical species that exist in a variety of mesomeric forms. The phenoxy radicals react ("couple") with one another either in juvenile plant tissue, which is in need of immobilizing (immature) cells with respect to each other (i.e., bonding), or in mature tissue, which is in need of cell wall stiffening. This process has been studied (experimentally and by computer simulation) and described abundantly (Glasser and Glasser, 1974, 1981; Glasser, 1981; Glasser et al., 1981; Lewis and Sarkanen, 1998). It results in a chemical structure with many different inter-monomer bonds (also called "inter-unit bonds") that are the consequence of the presumed randomness of the bond formation between the different mesomeric forms of the phenoxy radicals. It has recently been established that lignin in different tissue locations (such as stalk vs. endocarp, middle lamella vs. cell wall, etc.) can vary significantly, esp. in relation to Syr:Gua ratio (Rencoret et al., 2018). This creates the possibility of different functionalities in different tissue locations. However, it is well-established that all lignins, regardless of their monomer composition (i.e., "precursor ratio," *p*-OH: Gua: Syr), have a preponderance of alky-aryl ether inter-monomer bonds that amounts to around 50–60% of bond-total in native wood, and it reaches as high as 84% in some other plants (Rencoret et al., 2018). The ether content rises with the methoxy content on the aromatic ring of the monomer species (Glasser et al., 1983b). Because of this linkage distribution, the following corroborating observations can be made:

1. An analytical procedure most qualified to depolymerize lignin by severing exclusively alkyl-aryl ether linkages (i.e., no side-reactions), produces a mixture of building blocks that consists predominantly of monomers (50%), dimers, and some oligomers (Nimz and Das, 1971; Lapierre et al., 1986).
2. Since lignin's average degree of dehydrogenation (i.e., the number of sites per C_9-unit being linked by the coupling of free radicals produced by dehydrogenation) is $<2.00/C_9$ (Freudenberg and Neish, 1968; Glasser and Glasser, 1976), lignin can be considered a predominantly linear chain of monomeric, dimeric, and oligomeric phenylpropane units having molecular sizes of <1,000 g/M that are linked in alkyl-aryl ether fashion (Funaoka, 2013).
3. The concentration of phenolic OH-groups in native lignin is exceedingly low ($<0.25/C_9$).
4. Lignin has a low glass-to-rubber transition point, T_g, making wood thermally-deformable as long as plasticization by water is maintained at temperatures exceeding 100°C as shown in **Figures 1A,B**, i.e., under pressure (Kelley et al., 1987; Ito et al., 1998).
5. There is significant variability in bond types, in addition to different alky-aryl ether types, between monomeric C_9-species that have the potential of influencing thermal, and solubility properties.

This understanding has given rise to the picture of the amorphous component of wood being a block copolymer of modestly sized lignin phases with non-crystalline hetero-polysaccharides (**Figure 1C**) (Košikova et al., 1978;

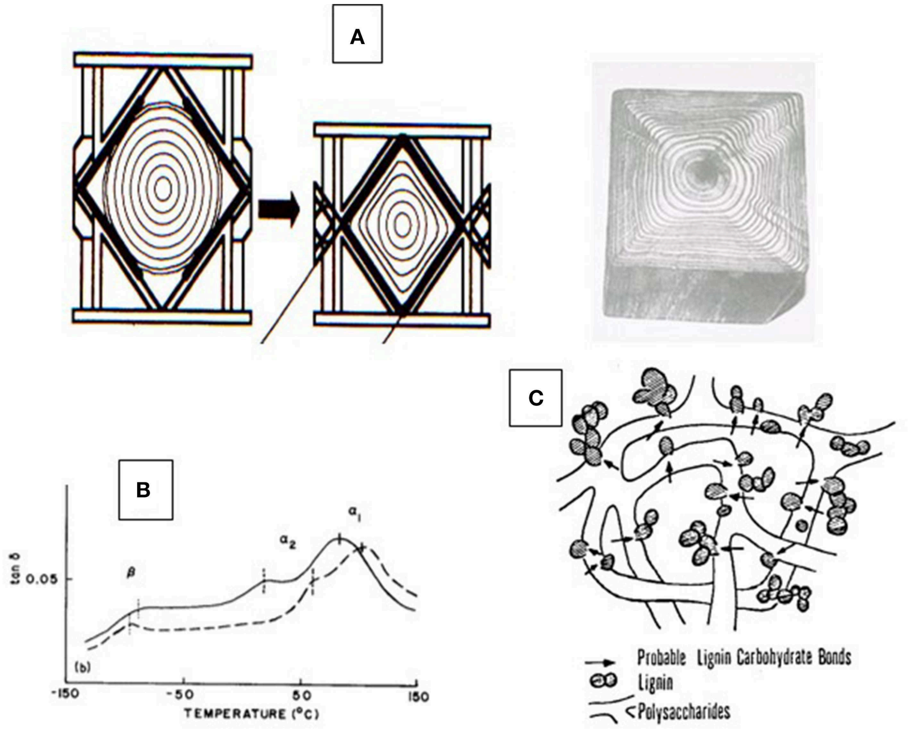

FIGURE 1 | Aspects of thermal properties of wood—**(A)** Illustration of the irreversible thermal deformation of a moisture-plasticized tree trunk under the influence of high-pressure steam and pressure (Ito et al., 1998); **(B)** Glass-to-rubber transitions (T_g) of two moisture-plasticized solid wood slices (spruce and beech) recorded by dynamic mechanical thermal analysis (DMTA) revealing the T_g of native lignin (α_1), native carbohydrates (α_2), and moisture exchange (β) (Kelley et al., 1987); and **(C)** generic proposed model of the lignin-carbohydrate copolymer architecture according to Košikova et al. (1978).

Koshijima and Watanabe, 2003). That the inherently thermoplastic lignin component of the native block copolymer will undergo phase separation and relocation in the cell wall via melt-state after exposure to high temperature (224°C) treatment for short periods of time (180 s) without rapid steam decompression ("explosion") was demonstrated by Debzi et al. (1991) and others. When subjected to delignification treatments during pulp production, wood is exposed to aqueous acid or alkali (Rydholm, 1965; The Ljungberg Textbook, 2008). This fractionation proceeds via two primary reactive lignin intermediates, benzylic cations (in acid), and quinonemethides (in alkali) (**Figure 2**). In acid, fractionation is made possible by the introduction of solubilizing (in water) functional (sulfonate) groups in the lignin polymer without (significant) depolymerization (except for the most labile benzyl-ether bonds) while severing lignin-carbohydrate bonds by hydrolysis; and in alkali, lignin removal requires depolymerization along the alky-aryl ether chain with simultaneous generation of (acidic) phenol groups (Sarkanen and Ludwig, 1971; The Ljungberg Textbook, 2008). This depolymerization is assisted catalytically by the presence of sulfide and hydrosulfide ions in the pulping liquor, which become the preferred reaction partner for the quinonemethide intermediates (**Figure 2**). Both delignification options encounter competitive secondary (condensation) reactions by internal competition for the reactive intermediates, benzylic cations and quinonemethides, thereby generating new carbon-to-carbon bonds. This is particularly significant in acid sulfite pulping where, for example, the indigenous presence of pinosylvin -an aromatic extractive substance with resorcinol structure in the heartwood tissue of pines- out-competes sulfite ions for the reaction with cations, leading to water insolubility of the modified (condensed) lignin (Hillis, 1962). This illustrates the virtual inescapability of lignin structure modification during aqueous pulping resulting in newly created structural variability. That this variability arises *after* lignin removal from cell tissue, in aqueous solution, becomes evident with the analysis of residual lignin isolated from incompletely delignified (also called "high yield") pulp fibers.

In a study examining the structure of residual pulp lignins isolated from NSSC-pulp fibers that had been exposed to neutral sulfite pulping conditions for between 5 min (following a 1.33 h presteaming and impregnation time) and 8½ h, the residual lignin content ranged from 6 to 65% of total lignin (Glasser and Barnett, 1979a). The isolated lignin content was thereby inversely related to delignification time. While there were obvious signs of hydrolytic cleavage of weak (lignin-carbohydrate) ether bonds in the first 5 min of cooking (following pre-steaming) with formation of phenolic OH and sulfonate groups on lignin (**Figure 3A**), the most noticeable change involved the loss of aliphatic OH- groups (**Figure 3B**) and

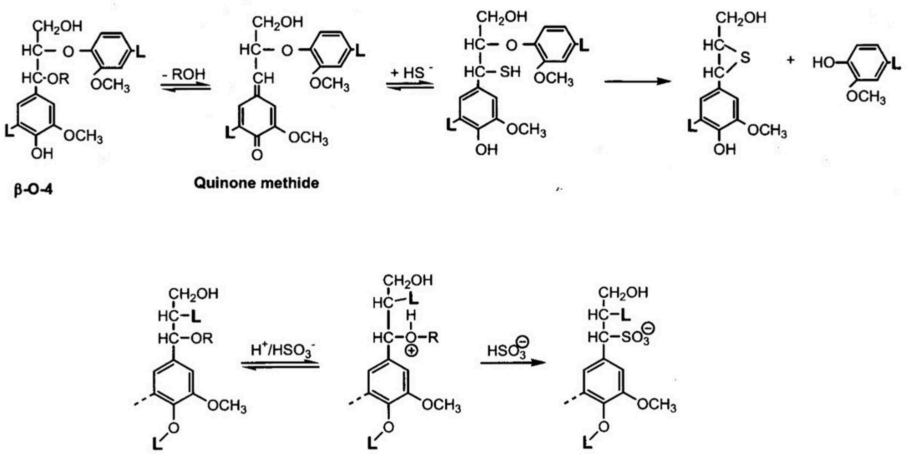

FIGURE 2 | Main reaction mechanisms of lignin during pulping—TOP: Alkyl-aryl ether cleavage and phenolic OH-generation via quinonemethide intermediates in alkali; the involvement of bisulfide ions prevents dissolution-defeating side-reactions from taking place, leading to increased alkali-solubility and effective depolymerization; BOTTOM: Formation of (water-soluble) lignin sulfonates via benzylium ion intermediate aromatic structures in pulping reactions under acidic conditions with bisulfite.

the formation of new lignin-carbohydrate bonds (**Figure 3C**) (Glasser and Barnett, 1979b). The residual lignin isolated from the pulp fibers by the Bjoerkman protocol (milled wood lignin) (Bjoerkman, 1956) revealed progressive attachment to cellulosic, and detachment from non-cellulosic carbohydrates with delignification time (**Figure 3C**). This reversed the initial linking of lignin to, almost exclusively, the non-cellulosic hetero-polysaccharides ("hemicelluloses"). A comparison of the structure of untreated wood lignin with that isolated from the pulp fibers suggested virtually no change in intermonomer bonding (Glasser and Morohoshi, 1979), except for the initial (most likely benzylic) ether hydrolysis with sulfonation (**Figures 3A,B**). Resistance to delignification coincided with significant changes in functionality, especially the loss of aliphatic hydroxyl groups (Glasser et al., 1979), and to the re-established bonding with (progressively cellulosic) carbohydrates (Glasser and Barnett, 1979b). This made delignification appear like a peeling-off phenomenon without obvious lignin degradation in terms of inter-monomer bonds prior to lignin dissolution. The formation of new lignin-carbohydrate bonds has been attributed to quinonemethide structures in lignin (Glasser, 1981), a conclusion consistent with model compound studies by Ohara et al. (1980) (**Figure 3D**) and Leary et al. (1983). The block-copolymer nature of the amorphous component of wood was thereby preserved, but the nature of the association of residual lignins with polysaccharides reflected progressively the more abundant (crystalline) cellulose. This progressive detachment/re-attachment created the misleading impression of lignin structure in fiber solids as being variable, with some fractions of lignin resisting dissolution while others dissolve rapidly.

In separate studies on the behavior of lignin during kraft pulping, similar observations were made (Glasser et al., 1983b). Isolated lignin revealed signs of hydrolytic depolymerization to lower molecular weight structures with lower alkyl-aryl ether and higher phenolic OH-contents, whereas residual lignin continued to resemble the native, untreated form. When (commercial) isolated (pine) kraft lignin was fractionated according to molecular size, it became apparent that degradation strictly followed alkyl-aryl ether cleavage to different extents; high molecular weight lignin fractions were found with partially preserved ether bonding, whereas low molecular weight fractions were enriched in C-C bonding and phenolic OH-content (Glasser et al., 1983b).

The analytical procedure used in these studies, known as permanganate oxidation, follows a protocol adopted from earlier work by Freudenberg (Freudenberg et al., 1936), and later by Larsson and Miksche (1967), and that relies on the treatment of lignin (isolated from, or embedded in pulp fibers) with diethylsulfate, an effective ethylating agent for phenolic hydroxyl groups; subsequent oxidative hydrolysis with alkaline cupric oxide; followed by methylation with dimethylsufate; and oxidation of non-aromatic lignin entities with permanganate and hydrogen peroxide (Morohoshi and Glasser, 1979). The resulting mixture of aromatic carboxylic acids is quantitatively separated by gas and gel chromatography following esterification with diazomethane. The ratio of ethyl- to methyl-ethers among the carboxylic acids produces a "hydrolysis factor" that expresses (quantitatively) the degree of alky-aryl ether bonding of the identified aromatic carboxylic acids. Experimental hydrolysis factors were found to range from 0.1 to 1.0 representing alky-aryl ether contents in the range of 10 to 65 per 100 C_9-units (Glasser et al., 1983a,b).

These results and observations suggest that the variability of native lignin in wood is limited to differences between middle lamella and cell wall lignin; to differences between juvenile and mature plant tissue; and to differences in function (bonding as opposed to stiffening needs) (Monties, 2003). The lack of variability in wood lignin had been a major point of contention in the lignin field in the 1960's and 1970's based on findings by Forss et al. (1966) that seemed to indicate the existence of a

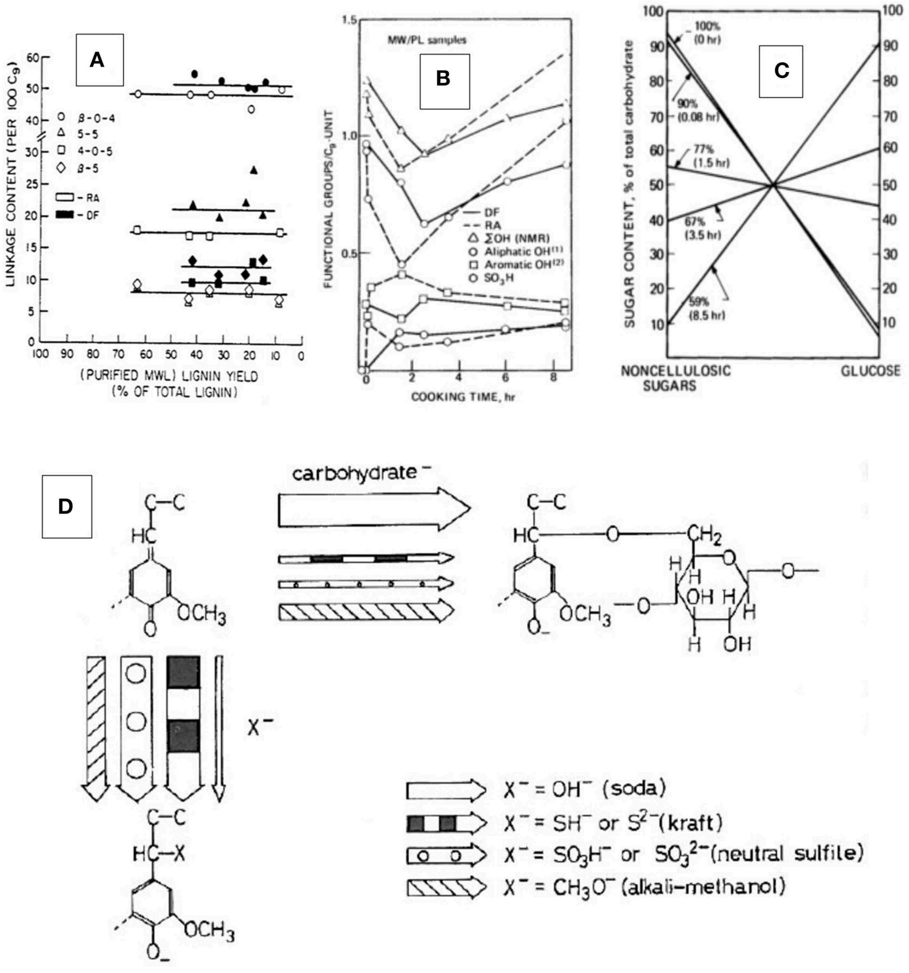

FIGURE 3 | Residual lignin structures in pulp fibers—results of the re-attachment of lignin to carbohydrates in NSSC pulps from Red Alder and Douglas Fir wood (on the basis of ¼ to 8 ½ h of cooking times and representing pulp yields of between 59 and 90%; the recovered, purified and analyzed pulp fiber lignins represented between 6 and 65% of the total lignin content of wood; for more information, see Glasser and Barnett, 1979a): **(A)** Interunit-linkage distribution; **(B)** Functional group distribution (total, aliphatic, phenolic, and sulfonate groups); **(C)** nature of association with carbohydrates (cellulosic vs. non-cellulosic sugar content in % of total carbohydrate content; pulp yield and cooking times indicated on each line; for more information, see Glasser and Barnett, 1979a,b; Glasser and Morohoshi, 1979; Glasser et al., 1979, 1982). **(D)** Proposed mechanism (Glasser, 1981) of the reaction leading to a restored lignin-carbohydrate bond as revealed by Ohara et al. (1980) on the basis of model compound studies.

"repeating unit structure" in lignin. While this hypothesis (Forss, 1968) failed to find general acceptance (Forss and Fremer, 2000) based on advancing analytical techniques, the conclusion that native lignin in wood has limited variability, and that significant variability is created only by the isolation procedure, gained significant evidential support (Forss and Fremer, 2003).

Much of research (and development) with lignin continues to be carried out with non-industrial preparations—such as experimental fractions derived from mild wood treatment (incl. organosolv and all non-chemical isolations, like milled wood lignin, MWL); from selected lignin fractions (i.e., solvent-soluble fractions of isolated kraft lignins); and from experimental laboratory and pilot plant isolations–which focuses on a wide variety of different lignin structures (Glasser et al., 1983b). This variability, however, is misleading, since isolation on industrial scale is likely to be carried out under highly consistent and invariable conditions, which generate isolated lignins that may vary from pulp mill to pulp mill, and from separation protocol to separation protocol, but that remain invariable when isolated using an invariable delignification procedure.

Since the industrial separation of lignins from wood had the generation of pulp fibers as sole objective for many generations, the isolation process was designed to assist to the utmost degree in the preservation of polysaccharide yield, structure, purity, and size (Rydholm, 1965; The Ljungberg Textbook, 2008). This focus helped generate paper fibers in high yield, with high brightness, in high strength, and with high molecular weight. The goal was achieved by the use of acids or bases in aqueous mixtures. An inexpensive and effective acid was based on sulfur dioxide forming bisulfite and/or sulfite ions in combination with inexpensive bases, such as Ca, Mg, NH4, or Na. This mixture converts lignin into a water-soluble derivative, "lignin sulfonate" (also called "lignosulfonate"), in which many of the native structural details of lignin, mostly the alkyl-aryl ether bonds, remain largely intact. This has led to the utilization of sulfonated lignins from sulfite pulping as water-soluble surfactants and dispersants in applications exceeding one million tons per year worldwide (Gargulak and Lebo, 2000). Pulp production using the "sulfite process" has, however, declined globally due mostly to environmental concerns. It has been replaced in most parts of the world with alkaline processes. While delignification with aqueous sodium hydroxide solutions is effective with herbaceous plants, woody plants resist lignin release (into water) in the absence of a suitable catalyst capable of hydrolyzing alky-aryl ether inter-monomer bonds. The almost universally (but not exclusively) used catalyst in alkaline pulping is the sodium salt of hydrogen sulfide, Na_2S, which promotes the cleavage of alkyl-aryl ethers in lignin with the simultaneous generation of new solubilizing acidic (phenolic) functionality (**Figure 2**). Since the alkali-soluble form of lignin can easily be concentrated in water to a level allowing incineration with heat and chemical (ash) recovery, the $NaOH/Na_2S$ based pulping process (called "Kraft" process) has become worldwide norm. Alternatively, alkali-soluble lignin can be recovered in solid form by the adjustment of solution-pH and filtration. In contrast to lignin sulfonates, which become water-soluble as sulfonated lignin derivatives at any pH, alkali (Kraft) lignin becomes soluble in alkali only, and is insoluble under neutral aqueous conditions and in most organic solvents, due to the creation of acidic (phenolic) functionality by alkyl-aryl ether hydrolysis, and depolymerization (**Figure 2**). Reduction of pH thus allows Kraft lignin recovery in powder form. Although this lignin has been known, and has been commercially isolated for decades in at least one commercial installation, it has been attracting attention as an optional sustainable, and biodegradable polymer resource only in the last couple of decades.

As stated above, isolated Kraft lignin is inhomogeneous in terms of molecular size and structural functionality depending on its isolation protocol. While some of its alkyl-aryl ether linkages are preserved; new carbon-to-carbon bonds are created; and thiol (mercaptan) functionality is introduced. With the loss of ether bonds, thermal properties are affected with a significant rise of the glass-to-rubber transition temperature (T_g), and a loss of solubility in all but alkali.

This change, however, is not irreversible. It has been known for several decades that some of the thermal and solution properties of Kraft lignin can be recovered, and lignin can be converted into materials that take advantage of its native design features, bonding and stiffening (modulus-building) (Falkehag, 1975; Glasser and Sarkanen, 1989; Lora and Glasser, 2002). This is the subject of the remaining review.

Lignin in wood is usually a pale-yellow substance. Its isolation under alkaline conditions creates a severe discoloration due to the formation of quinoid structures by phenol oxidation. This discoloration is reversible following modifications that remove phenolic and quinoid functionality (**Figure 4**) (Barnett and Glasser, 1989).

FIGURE 4 | Lignin and lignin derivative color—Typical color of phenolic Kraft lignin (KL) and non-phenolic hydroxypropyl kraft lignin, non-bleached (HPL), and peroxide-bleached (BL. HPL). (According to Barnett and Glasser, 1989).

LIGNIN APPLICATIONS IN MATERIALS

The bonding and stiffening attributes of the different forms of isolated lignins have been harnessed in man-made polymeric materials for many decades with varying success. Owing to lignin's character as small, mostly spherically-shaped, multifunctional molecule, the longest and most intensively investigated application has been the use in thermosetting materials in general, and specifically in phenolic resins for wood bonding (Hemingway and Conner, 1989).

While structurally and performance-wise comparable to phenolic (phenol-formaldehyde, PF) network polymers, as additive to phenolic resins lignin has faced the obstacle of variability, dark color, slow cure rate, and lack of chemical reactivity. Isolated (commercial) lignins often resist thermal deformation attempts unless they involve temperatures close to the onset of lignin's thermal degradation (about 200°C). The resulting resins are frequently limited to low rates of addition and extended cure times (Lewis and Lantzy, 1989). The handicap of the limiting solubility and thermal deformability of isolated commercial (Kraft) lignins has been demonstrated to be reversible to different extents by chemical modification. Lignins from non-commercial, experimental sources, however, such as organosolv or steam explosion lignins, with an abundance of T_g-lowering intermonomer ether bonds, can offer lower T_g's as well as more compatible chemistry (Glasser, 2000).

Other applications in thermosetting polymeric materials have included a range of network-forming polymers crosslinked using isocyanate, polyamine, polyacrylate, epoxy etc. resin chemistry (Glasser, 1989; Wang and Glasser, 1989). Several examples of such applications are illustrated in **Figure 5**. In applications that rely on resin formulations using non-alkaline or non-aqueous conditions, chemical modification or molecular fractionation becomes mandatory since most industrial lignin sources are insoluble in most common solvents. The same is true for applications in thermoplastic materials, where thermal processability requires the restoration of moderate T_g's.

The potential recovery of lignin as a solvent-soluble polymer with improved solubility and reduced T_g by chemical modification must be considered the first challenge to the

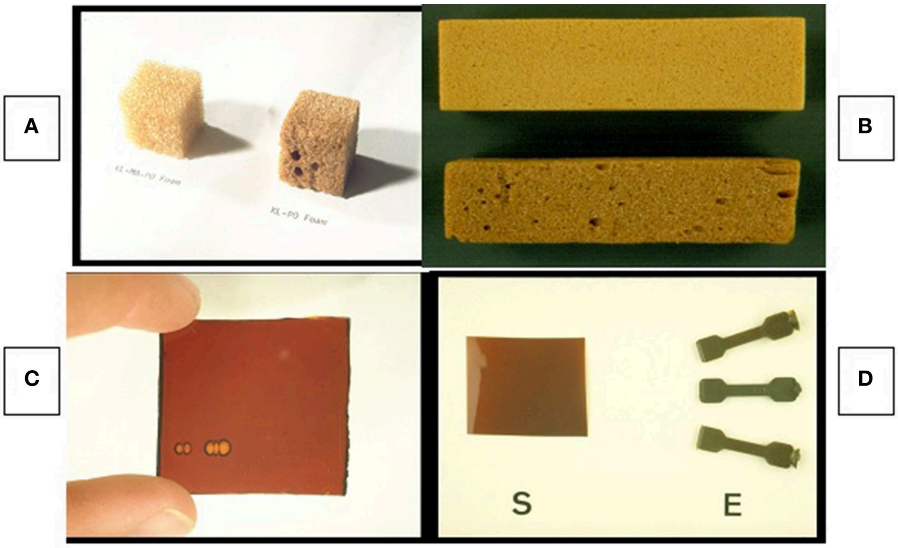

FIGURE 5 | Early lignin-containing structural materials—Polyurethane foams using bleached and unbleached HPL (see **Figure 4**) according to Hsu and Glasser (1975) **(A)**, and foams according to Lora and Glasser (2002) **(B)**; polyacrylate sheet **(C)** according to Wang and Glasser (1989); and solvent-cast polyurethane coating (S) and injection-molded test specimens (E) according to Ciemniecki and Glasser (1989) **(D)**.

reclamation of its performance attributes (Wang et al., 2016; Mueller et al., 2019). It has long been established that the branched nature of lignin combined with its abundance of phenolic OH groups (following isolation involving alkyl-aryl ether cleavage) that give rise to strong internal hydrogen-bonds, is most effectively changed by oxyalkylation as shown in **Figure 6A** (Hsu and Glasser, 1975, 1976; Glasser et al., 1982; Glasser and Leitheiser, 1984). Non-phenolic hydroxyalkyl lignin derivatives are recognized as virtually uniformly functional (with aliphatic OH-groups) branched molecules with good solubility and thermal properties. Their aromatic character offers many opportunities to contribute to the properties of multi-phase materials that resemble those of natural lignocellulosic materials.

Following chemical modification with alkylene oxides (**Figure 6**), lignins become sufficiently soluble to perform well in wood adhesives when crosslinked with isocyanates (Newman and Glasser, 1985) as well as in fire resistant foams (Glasser and Leitheiser, 1984). The former has been accomplished, for example, with rapidly curing wood adhesives using blocked diisocyanates as crosslinking agents (Gillespie, 1985). Blends of hydroxypropyl lignin with soy protein have resulted in materials with significantly increased tensile strength and undiminished elongation at break due the formation of supramolecular domains and strong inter-molecular adhesion (Wei et al., 2006).

Combining (non-phenolic) lignin derivatives with such inherently low-modulus polymer components as polyether glycols mimics the role lignin plays in the amorphous component of wood, where it adds modulus by the formation of copolymer structures with gum-like non-crystalline hetero-polysaccharides (Kelley et al., 1988, 1989). This has been examined repeatedly for the case of both lignin-containing mixtures with, and copolymers of, polyaliphatic glycols (**Figure 6**). Whereas addition of an extended aliphatic polyether glycol chain to lignin (CE-HPL in **Figure 6D**) by chemical modification provides flexibility in terms of thermal and mechanical properties of a polyurethane-based network polymer, simple mixing of Kraft lignin derivatives with aliphatic glycols (HPL/PEG in **Figure 6D**) prior to crosslinking helps introduce a more moderate, but still noticeable, and effective modulus-raising aromaticity to the cured resin structure as well (Moerck et al., 1989). Such mixtures of aromatic and aliphatic polyols have been demonstrated to become the basis of a variety of adhesives, coatings, foams, etc., in which the inherent properties of lignin are adopted for achieving mechanical, thermal, moisture absorbing, sustainability, and other property goals (**Figure 5**).

These examples demonstrate that lignin as isolated by separation from woody biomass performs like a normal polymer in a predictable manner and continues to present the option of re-use in a form it was initially designed for by nature.

In addition to thermosetting materials, lignin can also contribute important properties to thermoplastic mixtures (polyblends) with other polymers as long as it meets thermal and compatibility needs. Lignin in native state, such as in solid wood, will readily undergo thermal deformation if (a) the plasticizing effect of water on amorphous hetero-polysaccharides is assured, and (b) the T_g of (water-plasticized) lignin is exceeded (Ito et al., 1998). This has been demonstrated at temperatures of 135–150°C since lignin's *in-situ* T_g has been reported to be around 60–80°C (**Figure 1**). The Tg of lignin rises with loss of alkyl-aryl ether bonds to >180°C (Falkehag, 1975); it can be restored by suitable chemical modification, most commonly by esterification or etherification (**Figure 6**).

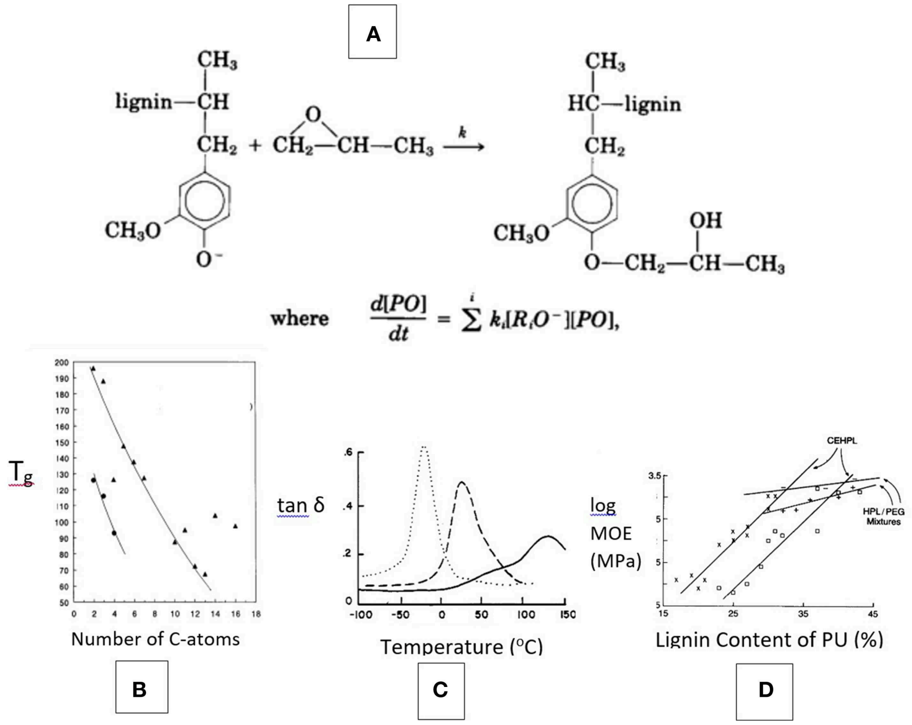

FIGURE 6 | Benefits of lignin modification by propoxylation—**(A)** Derivatization reaction is oxyanion-dependent; **(B)** T_g of lignin esters is related to the size of the acyl substituent (i.e., number of C-atoms), applied to Kraft and organosolv lignin with data from Lewis and Brauns (1947), Glasser and Jain (1993); **(C)** Damping (tan δ) thermograms (by DMTA) of polyurethane films containing lignins with variable degree of propylene oxide-chain extension (Kelley et al., 1988); and **(D)** Modulus of polyurethane films with chain-extended hydroxypropyl lignin (CEHPL) compared with HPL/polyethylene glycol (PEG) mixed solutions in relation to lignin content.

Thermoplastic blend materials with lignin (derivatives) having acceptable T_g's have been widely demonstrated. Ester formation has been studied in terms of the effect on thermal properties as early as 1947 (Lewis and Brauns, 1947; Glasser and Jain, 1993), and etherifications by ring opening reactions with aliphatic oxirans have been pursued by Glasser et al. (Wu and Glasser, 1984; Jain and Glasser, 1993).

For reasons of biodegradability and sustainability, thermally processable natural polymers have attracted attention also in the field of melt-processed materials. Since ester-type lignin derivatives meet those requirements, their feasible incorporation into blend materials has been examined (Ghosh et al., 1999, 2000). Lignin esters were found to be readily miscible with cellulose esters, starch esters and poly(hydroxybutyrate).

Because of its potential contribution to the modulus of rigid multi-phase materials and its resistance to thermal degradation, lignin has also been considered as an attractive source for carbon fibers (Fukuoka, 1969). However, because of its inability to organize in melt-state into liquid crystalline condition, an attribute of benefit for lignin's function in lignocellulosic composite structures, lignin appears to have a limiting effect on building strength in carbon fibers (Davé et al., 1993).

ISOLATED LIGNIN'S LIMITATIONS

Lignin appears to be a relatively small molecule, both *in vivo* and *in vitro,* that serves lignocellulosic multi-phase materials (i.e., cellular tissues of plants) exclusively as a component of a block copolymer with amorphous hetero-polysaccharides (also called "hemicelluloses"). **Figures 1C** and **7** represent widely–used illustrations of the molecular architecture of the amorphous component of wood. Since thermal and solubility characteristics of the two components, hetero-polysaccharides and lignin, are very different, the copolymer behaves like a crosslinked, three-dimensional network structure in native (unplasticized) wood. The polysaccharides provide stability and immobility in dry as well as high-temperature state, and lignin anchors the branched (gum-like) hetero-polysaccharides in place under high-moisture conditions. It can therefore not be expected that lignin by itself will qualify as stand-alone polymeric material. It is most likely performing best as partner with a molecular entity that complements its properties, as it does in wood. This partnership must, by design, experience different levels of stress that results in the separation of molecular components into individual phases. Such molecular stresses are relieved when wood is exposed to high temperature moisture, such as during "steam explosion" treatments involving exposure to high-pressure steam for

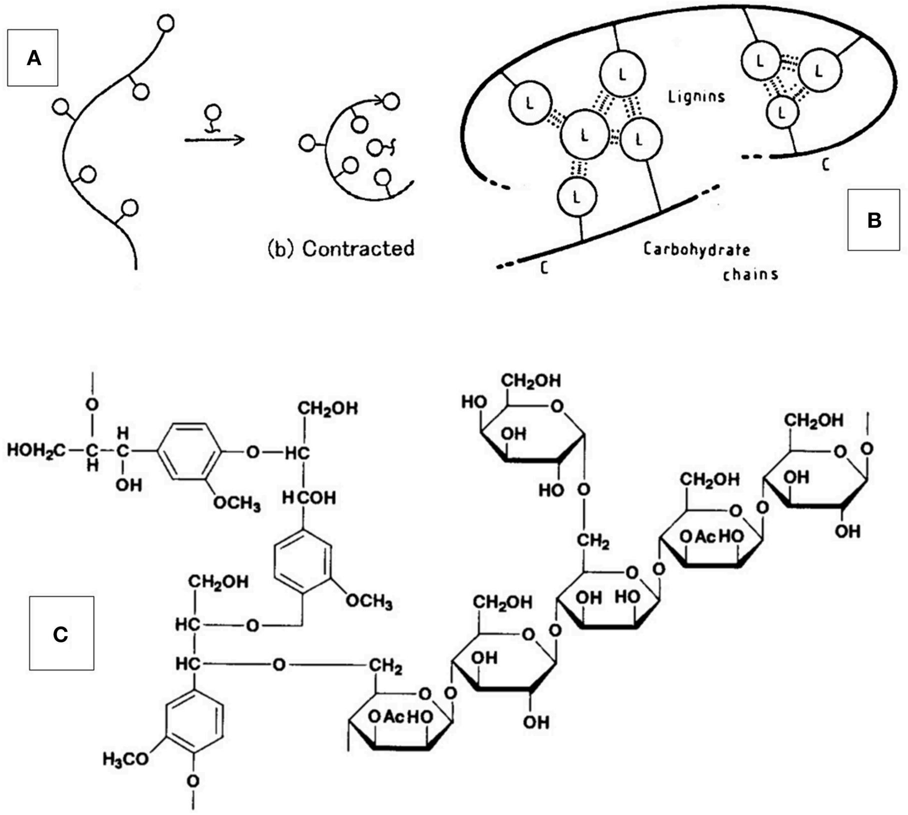

FIGURE 7 | Model of molecular structure and architecture of the amorphous component of wood— **(A,B)** Concept of lignin-carbohydrate copolymer (LCC) self-associating ("contracting") with lignin-rich phases via secondary bonds (on the nano-scale); this effect of copolymer structure on solution behavior has been studied using LCC-model copolymers by Esker et al. (see Gradwell et al., 2004; Westbye et al., 2007; Kaya et al., 2009); **(C)** Schematic lignin-carbohydrate complex with benzyl ether linkage between lignin and branched xylan.

short time periods (Focher et al., 1991). The molecular response involves (a) lignin-carbohydrate separation by hydrolysis, and (b) relocation of the separated lignin within the fibrous tissue (Debzi et al., 1991). Depending on the severity of the steam treatment, other hydrolytic and/or condensation reactions are encountered that change lignin's functionality and molecular character. However, it is obvious that disruption of the block copolymer architecture of the amorphous component of wood results in spontaneous phase-separation of carbohydrates and lignin within the limits of mobility. This results in the opportunity to extract lignin partially with aqueous alkali or organic solvents without further pretreatment (Wright and Glasser, 1998). The re-incorporation of lignin into polymeric materials structures (i.e., the "making lignin great again"-effort), in networks or blends, thermosets or thermoplastics, requires "phase compatibilization." In either case, thermosets or thermoplastics, the molecular mixture proceeds toward solidification via a homogeneous liquid phase at either ambient or elevated temperature. Phases separate on either or both, kinetic and thermodynamic grounds.

Lignin's potential as component in structural materials, both network-forming and thermally processable, is limited by its solution and thermal properties. Restricting the solubility of isolated Kraft lignin to aqueous alkali, and its thermal deformability (i.e., glass transition temperature, T_g) to close to its thermal degradation temperature, leaves little opportunity for incorporation into multi-phase polymeric network materials systems. The degree to which such limitations apply to thermosetting materials has been analyzed by Gillham using a time-temperature-transition (TTT)-diagram (**Figure 8**) (Gillham, 1986); and thermoplastic blend compatibility is often analyzed in terms of thermodynamic solubility characteristics (Rials and Glasser, 1989a,b, 1990). Both approaches have been applied to lignin-containing polymeric materials.

The TTT-diagram records molecular changes of resin mixtures under cure by isothermal heat exposure on a time scale. During isothermal heating of homogeneous thermosetting mixtures at different temperature-levels, three events take place in sequence: (a) separation of molecular phases representing differences in chemical or molecular structures (incl. differences in molecular origin or differences in crosslink density, **Figure 8C**) (i.e., "demixing"); (b) formation of a continuous phase by gelation; and (c) gel densification ("vitrification") with the formation of additional crosslinks resulting in a rise in T_g to

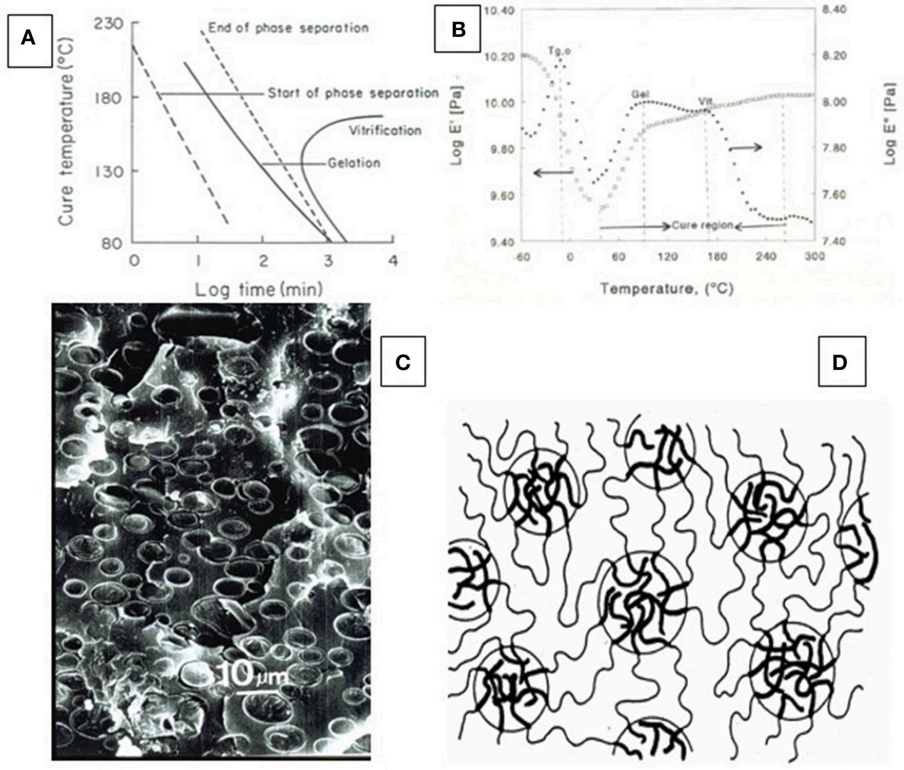

FIGURE 8 | Basis of phase separation in lignin-containing thermosets—**(A)** Schematic time-temperature-transformation (TTT)-diagram identifying phase separation preceding gelation and vitrification on a time scale (after Gillham, 1986); **(B)** Dynamic mechanical thermal analysis (DMTA) diagram of a lignin-containing thermosetting resin mixture undergoing cure with identification of gelation (gel), and vitrification (vit) on the temperature-scale (Toffey and Glasser, 1997); **(C)** SEM picture of cured lignin-containing thermoset with phase separation of (presumably lignin-rich) particulate inclusions (Hsu and Glasser, 1976); **(D)** Schematic phase separation of gel-forming molecules illustrating the clustering that produces regions of greater mass density embedded in a continuous phase of lower-density gel (after Kinloch, 1986).

the point where T_g reaches cure temperature (T_c) (**Figure 8**). This process can, in part, be followed experimentally by thermal analysis (differential scanning calorimetry, DSC, and/or differential mechanical thermal analysis, DMTA) for many network polymers (**Figure 8B**) (Toffey and Glasser, 1997).

Using these analytical principles, it becomes apparent that an excessive separation of phases prior to gelation can produce particulate-filled polymer networks in which the included particles are rubbery or glassy; and the sizes are on the nano-, micron-, or millimeter-scale. In resin mixtures that contain molecules with different character (i.e., functionality, solubility parameter, size, etc.), phase compatibility undergoes a dynamic change as gelation progresses with the consequence of separation. This is illustrated in **Figure 8D** (Kinloch, 1986). In the case of a resin mixture with lignin, phase separation likely results in the formation of glassy (because of high T_g) particles disconnected from the (continuous) network polymer. This formation of a particulate "composite" architecture representing solids dispersed in a continuous polymer matrix must not be detrimental to performance unless the enclosed particles exceed a certain concentration or size. It must be recognized that this formation of an inhomogeneous resin phase depends on both lignin functionality and molecular size, with lower molecular fractions preserving phase compatibility for a greater period during the cure cycle. The employment of low molecular weight lignin fractions is therefore preferable in phenol-formaldehyde (PF) resin products (Gillespie, 1985).

An example of a phase-separated polyurethane network with lignin-rich particulate enclosures is given in **Figure 8C**. Even though the component mixture, polyol and isocyanate, started the curing process as homogeneous mixture, it quickly experienced phase separation as gelation advanced. This phenomenon is observed universally with network forming mixtures, regardless of chemistry. In the case of lignin, it can be retarded by chemical modification aimed at the development of structural compatibility, or by the addition of functionality (chemical modification), that promotes the participation in crosslinking (gelation) reactions before phases separate. Different resins have different tolerances (in terms of molecular size and chemical functionality as well as cure cycle times) to the formation of separate phases during normal gelation.

Similar arguments can be applied to the analysis of phase separation in thermoplastic polymer mixtures (i.e., polyblends),

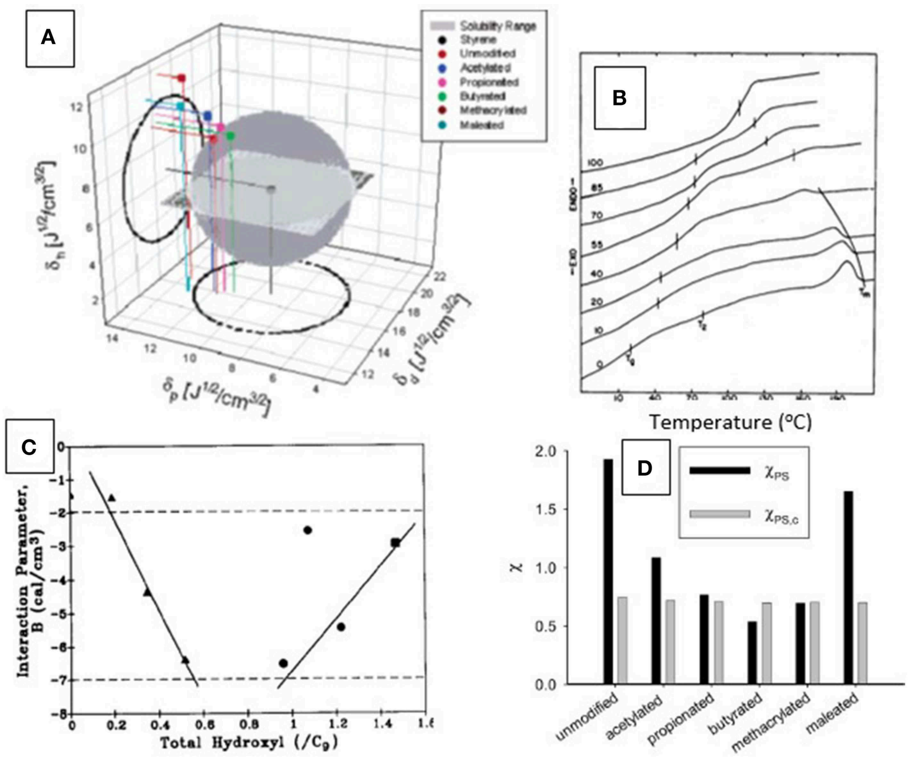

FIGURE 9 | Analysis of phase compatibility—**(A)** Theoretical range of solubility parameters of several (Kraft) lignin esters as predicted by the Hoy model, compared to the solubility range of styrene (from Thielemans and Wool, 2005). Only the points representing the lignin derivatives fitting into the gray sphere can be considered phase compatible with polystyrene. **(B)** Differential scanning thermograms (DSC) of hydroxypropyl cellulose blended with 0 to 100% hydroxypropyl lignin (bottom to top) revealing single T$_g$'s and indicating phase compatibility (adopted from Rials and Glasser, 1990). **(C)** Relationship between experimentally determined Flory-Huggins polymer-polymer interaction parameter, B, of two (organosolv) lignin derivatives [acetate (○), and ethyl ether, (Δ)] and lignin total hydroxyl group content in solvent-cast blends of lignin derivatives and hydroxypropyl cellulose illustrating the importance of optimal lignin functionality on phase compatibility in blends. Phase compatibility rises with the negative magnitude of the B-parameter. Maximum compatibility is reached with lignin derivatives having OH-contents of 0.8 per C$_9$-repeat unit, similar to that of native lignin (from Rials and Glasser, 1990). **(D)** Comparison of the calculated Flory-Huggins interaction parameters χ_{PS} of lignin esters with the critical value, $\chi_{PS,c}$, derived from the ratios of molar volumes of polymer and solvent (polystyrene). Compatibility is reached if $\chi_{PS} < \chi_{PS,c}$. In this graph, only lignin butyrate is predicted to be miscible with polystyrene (from Thielemans and Wool, 2005).

illustrated in **Figure 9**. This has previously been approached experimentally with lignins modified in different ways and to different extents prior to solution-blending with non-crystalline (thermoplastic) cellulose derivatives (**Figures 9B,C**) (Rials and Glasser, 1988, 1990). The results of this study demonstrated that a difference in solubility parameter between lignin and cellulose derivatives was responsible for the formation of regions with greater or lesser molecular compatibility. Calculations based on experimental observations of the shift in T$_g$ with blend composition (**Figure 9C**) resulted in the conclusion that greatest phase compatibility between the derivatives of cellulose and lignin (i.e., most negative polymer-polymer interaction parameter, B) was achieved when the lignin derivative had a free OH-group content comparable to that in wood (i.e., 0.8/C$_9$) (Rials and Glasser, 1989a) (**Figure 9C**).

Phase compatibility of lignin derivatives with polystyrene has also been assessed using a theoretical approach involving solubility parameter calculations (**Figure 9A**). Various chemical modification treatments of lignin were found to allow predicting the compatibilization of lignin derivatives with polystyrene (Thielemans and Wool, 2005). Esters of lignin with selected acids were found to contribute to both compatibility and reduced thermal transitions (**Figure 9D**).

COMPATIBILIZATION BY FUNCTIONALIZATION

Creating single-phase network structures with lignin requires both component miscibility and complementary functionality. This approach is routinely pursued by the attachment of (a) reactive functional groups, such as phenols (by "phenolation"), acrylates, epoxies, amines, vinyl, etc; or (b) by modification with molecular entities that promote the formation of secondary interactions, such as hydrogen bonds, with the surrounding (continuous) polymer phase (Thielemans et al., 2002; Bova et al., 2016; Kun and Pukanszky, 2017).

The desire to use lignin in phenol-formaldehyde (PF) resins has an extremely long history (Lambuth, 1989). It resurfaces any time the price of phenol rises (Lake, 2016). Both, lignin

FIGURE 10 | (Semi-) commercial products with lignin—**(A)** Prototype printed circuit board manufactured with glass fiber-reinforced (organosolv) lignin-containing (50%) epoxy resin (IBM pilot plant) (Kosbar and Gelorme, 1996; Shaw et al., 1996; Kosbar et al., 2001); **(B)** Prototype shell of injection-molded chair made from polypropylene/lignin derivative blend; and **(C,D)** commercial compostable waste bag made with melt-blown films of blends of hydroxypropyl (Kraft) lignin derivative and biodegradable polyester (*Ecoflex* by BASF) (Glasser et al., 2017).

sulfonates and kraft lignins, are amenable to substituting phenol; but this requires either molecular fractionation or chemical modification of the parent lignin if high substitution degrees are to be reached. The most common derivatization involves methylolation by reaction with formaldehyde and/or phenolation (Muller and Glasser, 1984; Hemingway and Conner, 1989).

Another example of phase compatibility gained by functionalization is shown in **Figure 10A**, which represents a prototype printed circuit board based on glass fiber-reinforced epoxy resin containing 50% lignin (Kosbar and Gelorme, 1996; Shaw et al., 1996; Kosbar et al., 2001). Lignin content in epoxy resins can be achieved using several approaches. The functionalization of lignin with oxiran functionality produces resins crosslinkable with amines or phenols (Nieh and Glasser, 1989; Hofmann and Glasser, 1993; Lora and Glasser, 2002), whereas bis-phenol A-based epoxies are capable of serving as crosslinking agents for phenolated or aminated lignin (derivatives).

The introduction of functionality useful for participation in chemical reactions is limited only by sufficient molecular compatibility to prevent premature phase separation, as pointed out above. Like other (natural) polymers, like cellulose and starch for example, the solubilizing and/or plasticizing effect of substituents can be generalized (within limits) based on character and degree of substitution.

In polyblend applications, in which a lignin component is mixed in homogeneous melt-state with a thermoplastic polymer, both thermodynamic and kinetic factors dictate the degree of phase separation. Examples of blends of (lightly modified) lignin with thermoplastic polymers in need of stiffening are shown in **Figures 10B–D**, which represent an injection-molded chair seat with polypropylene (**Figure 10B**), and a melt-blown waste bag

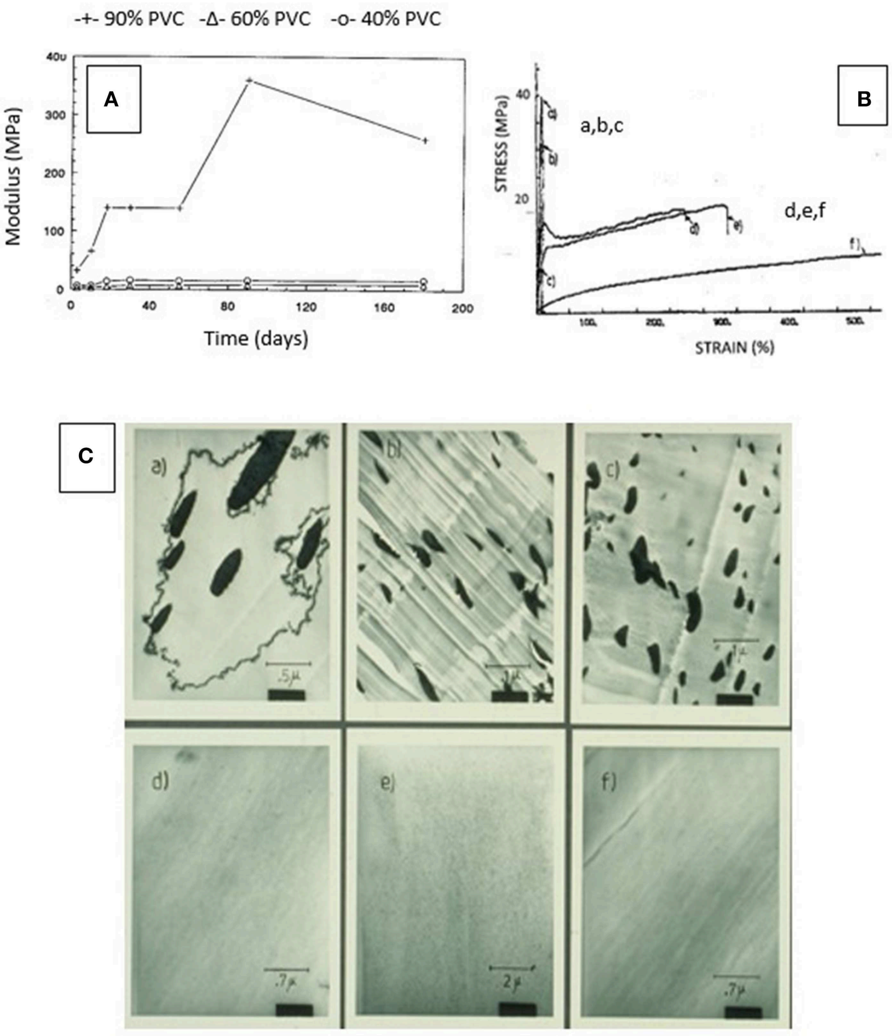

FIGURE 11 | Consequence of phase compatibilization in PVC blends with lignin (derivative)—**(A)** Relationship between modulus and degree of aging (time) for three different lignin derivative/PVC blend formulations (with 10, 40, and 60% lignin content) illustrating the long-lasting plasticizing effect of lignin derivative (de Oliveira and Glasser, 1994b). **(B)** Stress—strain curves of PVC/lignin derivative blends (solvent-cast films) shown in part C: blend formulations a-c reveal brittleness whereas blends d-f display ductile behavior based on phase compatibility (on the nano-level) (de Oliveira and Glasser, 1994b). **(C)** Illustrations by SEM of the degree of compatibility achieved by block copolymer formation of HPL and caprolactone segments (a-c are caprolactone-free, and d-f reveal the impact of the presence of caprolactone as copolymer component). (de Oliveira and Glasser, 1994b).

made with a biodegradable polyester (**Figures 10C,D**) (Glasser et al., 2017). Improving the solubility and thermal properties of isolated (Kraft) lignin thereby helps to compatibilize the two components sufficiently (but incompletely) to assure mutual support. This is a prerequisite for opening important pathways to lignin's use in melt-blended polymeric materials based exclusively on secondary molecular interactions.

Using nature's approach to the design of greater component compatibility required from inherently (thermodynamically) incompatible polymer types employs the creation of co-polymers that help in the dispersion of otherwise incompatible but (structurally) complementary molecular phases. In the case of natural lignocellulosic materials, kinetic phase compatibilization factors are eliminated, and thermodynamic factors become prevalent.

Mimicking the approach of compatibilizing an aromatic polymer (lignin) with a crystalline polysaccharide (i.e., cellulose) on the nano-scale, without ever forming covalent bonds between the blend components, as shown in **Figure 7**, has been adopted for lignins compatibilized with thermoplastic cellulose esters, polystyrene, and poly(vinyl chloride) (PVC) (de Oliveira and Glasser, 1989). In all cases, co-polymer synthesis was achieved by reacting mono-functional (with terminal NCO-groups) synthetic polymer segments (of variable sizes) with lignin derivatives to produce star-like block-copolymer structures resembling native lignin-carbohydrate complexes. These block-copolymer preparations were solution-blended with the linear polymer partner (de Oliveira and Glasser, 1993, 1994a,b).

The response of changes in blend properties to composition was remarkable in terms of mechanical, thermal, crystallinity, and morphological characteristics as is illustrated for PVC blends in **Figure 11** (de Oliveira and Glasser, 1994b). The compatibilizing power of caprolactone attached to lignin resulted in blend compositions that revealed either miscibility or near-miscibility of the aromatic and linear phases. Whereas, blends of (polycaprolactone-free) lignin derivatives with PVC generated structures with macro-phase separation on the scale of 0.1–1.0 µm, the presence of caprolactone revealed copolymer domains sized about 10–30 nm (**Figure 11C**). Similarly astonishing was the consequence on mechanical properties following aging (**Figure 11A**), and on stress- and strain-levels (**Figure 11B**) (de Oliveira and Glasser, 1994b). Blends with copolymer contents above the 30–40%-level were found not to experience the well-known embrittlement with age usually observed with PVC materials and indicated by a time-dependent rise in modulus and tensile strength (**Figure 11A**); and the stress-strain behavior of the blends revealed extreme brittleness for all caprolactone-free compositions (**Figure 11B**).

The compatibilization of lignins for use in thermoplastic polymer systems has found a significant following in recent years. The effect of derivatization with fatty acids of different sizes was found to enhance both phase morphology and melt rheology (Koivu et al., 2016); and the molecular nature of the aliphatic ester substituents of Kraft lignin was found to play a significant role on crystalline and supramolecular complexes of aliphatic polyesters in relation to methylene/carboxylate group ratios (Li and Sarkanen, 2002). Thermoplastic blends of acrylonitrile-butadiene rubber with various lignins in different blend ratios were found to produce tough materials with high failure strains (Bova et al., 2016; Nguyen et al., 2018).

The gradual build-up of lignin-containing phases on cellulose surfaces (mimicking a hydrophobization effect of plant fibers required by native plants) using copolymers of lignin with hetero-polysaccharides has been studied in aqueous environments (Gradwell et al., 2004). "Docking" was registered by surface plasmon resonance spectroscopy, and it was revealed that very low lignin concentrations attached to water-soluble (model) carbohydrates, pullulan and xylan, for example, effectively promote adsorption of these substances on mono-molecular (crystalline) cellulose surfaces (Westbye et al., 2007; Kaya et al., 2009). This suggests that lignin-carbohydrate copolymers serve as phase compatibilizers between cellulose and lignin. It is obvious that this parallels the multi-phase molecular architecture of wood, where a lignin-rich copolymer phase of water-soluble or gum-like non-crystalline polysaccharides becomes attached to cellulose crystals via secondary bonds. The principle of phase compatibilization of lignin and PVC via caprolactone parallels that of lignin-co-hetero-polysaccharides and cellulose. The principle produces non-covalently-linked blends of molecular entities with widely different characteristics on the nano-scale. The principle is adoptable for the development of a virtually unlimited range of sustainable and biodegradable materials.

CONCLUSIONS

(1) The structure of native (especially softwood) lignins is highly invariable in terms of its inter-monomer bonding and functionality. Differences are detectable between middle lamella and secondary cell wall location, among other factors.
(2) The aromatic character of lignin is compatibilized with crystalline cellulose fiber surfaces by the formation of block copolymers with hetero-polysaccharides ("hemicelluloses").
(3) Isolated lignins vary distinctly regarding their alkyl-aryl ether contents, degrees of secondary condensation, molecular weights, solubility, and thermal properties.
(4) Lignins retained by chemical pulps (NSSC and Kraft) exposed to between 5 min (following presteaming and heat-up) and 8½ h to pulping conditions, and representing yields between 6 and 65% of total lignin, are virtually identical to the native wood lignins in structure (esp. inter-unit bonding). Resistance to dissolution is a consequence of re-attachment to polysaccharides (incl. cellulose) via ether bond formation involving quinonemethide intermediates.
(5) Since structural variability of lignins is primarily the result of the isolation protocol, commercial sources of lignin isolated by any procedure under invariable process conditions can be expected to remain invariable.
(6) Isolated lignin represents an important and abundant biopolymer resource the behavior of which is highly predictable and adaptable based on its varied functionality and modifiability.
(7) Structure and properties of isolated lignins are subject to wide-ranging changes via chemical modification. Properties can readily be tailored for uses that require special solubility, thermal and compatibility behaviors.
(8) Modified lignins have the potential of contributing the characteristics of lignin in wood to man-made thermoplastic and thermosetting materials, such as bonding, stiffness (modulus), fire resistance, biodegradability, and sustainability.
(9) Best results are achieved when lignin's structural modification adopts the principles of its nature in wood by partnering with polymers via compatibilization.
(10) A variety of lignin derivatives have been converted into such products as adhesives, coatings, foams, printed circuit boards, melt-blown compostable films and other thermosetting and injection-molded thermoplastic materials.
(11) In many cases, such undesirable properties as malodor associated with the isolation method, esp. Kraft pulping, need to be overcome for lignin to reach its inherent "greatness."

AUTHOR CONTRIBUTIONS

The author confirms being the sole contributor of this work and approved it for publication.

ACKNOWLEDGMENTS

This is to acknowledge the contributions of the many students and research associates that have contributed to the many phases of the research reported here. Many are named in text and references. In addition, numerous private companies have participated in sharing in the risks of implementing the research findings and demonstrating their potential for transitioning into commercial reality. Their contributions are greatly acknowledged as well, and among them were the following (in alphabetical order): ALKO, ARCO Chemicals, BASF, Borregaard, Cyclewood Solutions, Domtar, Eastman Tennessee, Georgia Pacific, IBM, Proctor & Gamble, Quaker Oats Comp., Westvaco, Weyerhaeuser, and un-named others.

REFERENCES

Baker, D. A., and Rials, T. (2013). Recent advances in low-cost carbon fiber manufacture from lignin. *J. Appl. Polym. Sci.* 130, 713–728. doi: 10.1002/app.39273

Barnett, C. A., and Glasser, W. G. (1989). "Bleaching of hydroxypropyl lignin with hydrogen peroxide," in *ACS Symposium Series No. 397* (Washington, DC: American Chemical Society), 436–451.

Beckham, G. T., Johnson, C. W., Karp, E. M., Salvachua, D., and Vardon, D. R. (2016). Opportunities and challenges in biological lignin valorization. *Curr. Opin. Biotechnol.* 42, 40–53. doi: 10.1016/j.copbio.2016.02.030

Bjoerkman, A. (1956). Studies on finely divided wood. I. Extraction of lignin with neutral solvents. *Sv. Papperstidn*. 59, 477–485.

Bova, T., Tran, C. D., Balakshin, M. Y., Chen, J., Capanema, E. A., and Naskar, A. K. (2016). An approach towards tailoring interfacial structures and properties of multiphase renewable thermoplastics from lignin-nitrile rubber. *Green Chem.* 18, 5423–5437. doi: 10.1039/C6GC01067A

Cheng, C., Shen, D., Gu, S., and Luo, K. H. (2018). State-of-the-art catalytic hydrogenolysis of lignin for the production of aromatic chemicals. *Catal. Sci. Technol.* 8, 6275–6296. doi: 10.1039/C8CY00845K

Davé, V., Prasad, A., Marand, H., and Glasser, W. G. (1993). Molecular organization of lignin during carbonization. *Polymer* 34, 3144–3154. doi: 10.1016/0032-3861(93)90382-K

de Oliveira, W., and Glasser, W. G. (1989). Engineering plastics from lignin. XVI. Star-like macromers with propylene oxide. *J. Appl. Polymer Sci*. 37, 3119–3135. doi: 10.1002/app.1989.070371105

de Oliveira, W., and Glasser, W. G. (1993). "Chapter 37. Comparison of some molecular characteristics of star-block copolymers with lignin," in *Cellulosics: Chemical, Biochemical and Materials Aspects*, eds J. F. Kennedy, G. O. Phillips, and P. A. Williams (Hertfordshire: Ellis Horwood Publishers Ltd.), 263–272.

de Oliveira, W., and Glasser, W. G. (1994a). Multiphase materials with lignin. XI. Star-like copolymers with caprolactone. *Macromolecules*. 27, 5–11. doi: 10.1021/ma00079a002

de Oliveira, W., and Glasser, W. G. (1994b). Multiphase materials with lignin. XII. Blends of polyvinyl chloride with lignin-caprolactone copolymers. *J. Appl. Polymer Sci*. 51, 563–571. doi: 10.1002/app.1994.070510320

Debzi, E. M., Excoffier, G., Toussaint, B., and Vignon, M. R. (1991). "Steam explosion treatment of wood: effects of pressure and time on cellulose behavior," in *Steam Explosion Techniques – Fundamentals and Industrial Applications*, eds B. Focher, A. Marzetti, V. Crescenzi (Philadelphia, PA; Reading; Paris; Montreux; Tokyo; Melbourne, VIC: Gordon Breach Science Publishers S. A.), 141–161.

Doherty, W. O. S., Mousavioun, P., and Fellows, C. M. (2011). Value-adding to cellulosic ethanol: lignin polymers. *Indust Crops Prod.* 33, 259–276. doi: 10.1016/j.indcrop.2010.10.022

Falkehag, S. I. (1975). "Lignin in materials," in *Applied Polymer Symposium No. 28* (New York, NY: John Wiley & Sons), 247–257.

Focher, B., Marzetti, A., and Crescenzi, V. (eds.). (1991). *Steam Explosion Techniques – Fundamentals and Industrial Applications*. Philadelphia, PA; Reading; Paris; Montreux; Tokyo; Melbourne, VIC: Gordon Breach Science Publishers S. A., 413.

Forss, K. (1968). Proposal of a formula for spruce lignin. *Comm. Holzforschung* 22, 66–68. doi: 10.1515/hfsg.1968.22.3.66

Forss, K., and Fremer, K.-E. (2000). The nature of lignin: a different view. *ACS Symp Ser.* 742, 100–116. doi: 10.1021/bk-2000-0742.ch002

Forss, K., and Fremer, K.-E. (2003). *The nature and Reactions of Lignin – A New Paradigm*. Helsinki: Oy Nord Print Ab, 555.

Forss, K., Fremer, K.-E., and Stenlund, B. (1966). Spruce lignin and its reactions in sulfite cooking. I. the structure of lignin. *Paperi Ja Puu* 48, 565–574.

Freudenberg, K., Janson, A., Knopf, E., Haag, A., and Meister, M. (1936). Lignin XV. Zur Kenntnis des Lignins (15. Mitteil.). *Chem. Ber*. 69B, 1415–1425. doi: 10.1002/cber.19360690637

Freudenberg, K., and Neish, A. C. (1968). *Constitutionand Biosynthesis of Lignin*. New York, NY: Springer-Verlag Inc., 129.

Fukuoka, Y. (1969). Carbon fiber made from lignin (kayacarbon). *Japan. Chem. Quart*. 5, 63–66.

Funaoka, M. (2013). Sequential transformation and utilization of natural network polymer "Lignin". *React. Funct. Poly*. 73, 396–404. doi: 10.1016/j.reactfunctpolym.2012.05.010

Gargulak, J. D., and Lebo, S. E. (2000). Commercial use of lignin-based materials. *ACS Symp. Ser*. 742, 304–320. doi: 10.1021/bk-2000-0742.ch015

Ghosh, I., Jain, R. K., and Glasser, W. G. (1999). Multiphase materials with lignin. XV. Blends of cellulose acetate butyrate with lignin esters. *J. Applied Polymer Sci*. 74, 448–457. doi: 10.1002/(SICI)1097-4628(19991010)74:2<448::AID-APP28>3.0.CO;2-C

Ghosh, I., Jain, R. K., and Glasser, W. G. (2000). "Chapter 17. Blends of biodegradable thermoplastics with lignin esters," in *Lignin – Historical, Biological, and Materials Perspectives, No. 742. ACS Symposium Series*, eds W. G. Glasser, R. A. Northey, and T. P. Schultz (Washington, DC: American Chemical Society), 331–350. doi: 10.1021/bk-2000-0742.ch017

Gillespie, R. H. (1985). "Chapter 9. Durable wood adhesives from kraft lignin," in *Adhesives From Renewable Resources, No. 385. ACS Symposium Series*, eds R. H. Hemingway and A. H. Conner (Washington, DC: American Chemical Society), 110–125. doi: 10.1021/bk-1989-0385

Gillham, J. K. (1986). "Cure and properties of thermosetting polymers," in *Structural Adhesives: Developments in Resins and Primers*, ed A. J. Kinloch (London; New York, NY: Elsevier Applied Science Publishers Ltd.), 1–28.

Glasser, W. G. (1981). The chemistry of NSSC-pulping from the perspective of the structure of residual pulp lignins. *Svensk Papperstidning* 84, R25–R33.

Glasser, W. G. (1989). "Chapter 4. Cross-linking options for lignins," in *Adhesives From Renewable Resources, No. 385. ACS Symposium Series*, eds R. W. Hemingway and A. H. Conner (Washington, DC: American Chemical Society), 43–54.

Glasser, W. G. (2000). "Chapter 9. Classification of lignin according to chemical and molecular structure," in *Lignin – Historical, Biological, and Materials Perspectives, No. 742. ACS Symposium Series*, eds W. G. Glasser, R. A. Northey, and T. P. Schultz (Washington, DC: American Chemical Society), 216–238.

Glasser, W. G., and Barnett, C. A. (1979a). The structure of lignins in pulps. II. A comparative evaluation of isolation methods. *Holzforschung* 33, 78–86. doi: 10.1515/hfsg.1979.33.3.78

Glasser, W. G., and Barnett, C. A. (1979b). The structure of lignins in pulps. III. The association of isolated lignins with carbohydrates. *Tappi* 62, 101–105.

Glasser, W. G., Barnett, C. A., Muller, P. C., and Sarkanen, K. V. (1983a). The chemistry of several novel bioconversion lignins. *J. Agric. Food Chem*. 31, 921–930. doi: 10.1021/jf00119a001

Glasser, W. G., Barnett, C. A., and Sano, Y. (1983b). Classification of lignins with different genetic and industrial origins. *Appl. Poly. Symp*. 37, 441–460.

Glasser, W. G., and Glasser, H. R. (1974). Simulation of reactions with lignin by computer (Simrel). I. Polymerization of coniferyl alcohol monomers. *Macromolecules* 7, 17–27. doi: 10.1021/ma60037a005

Glasser, W. G., and Glasser, H. R. (1976). Simulation of reactions with lignin by computer (Simrel). III. The distribution of hydrogen bonds in lignin. *Cell. Chem. Techol*. 10, 23–37.

Glasser, W. G., and Glasser, H. R. (1981). The evaluation of lignin's chemical structure by experimental and computer simulation techniques. *Paperi ja Puu* 63, 71–83.

Glasser, W. G., Glasser, H. R., and Morohoshi, N. (1981). Simulation of reactions with lignin by computer (Simrel). VI. Interpretation of primary experimental analysis data ("Analysis Program"). *Macromolecules* 14, 253–262. doi: 10.1021/ma50003a006

Glasser, W. G., Honeycutt, S. S., Barnett, C. A., and Morohoshi, N. (1979). The structure of lignins in pulps. VI. Changes in lignin's functionality. *Tappi* 62, 111–116.

Glasser, W. G., and Jain, R. K. (1993). Lignin derivatives. I. Alkanoates *Holzforschung* 47, 225–233. doi: 10.1515/hfsg.1993.47.3.225

Glasser, W. G., and Leitheiser, R. H. (1984). Engineering plastics from lignin. XI. Hydroxypropyl lignins as componenets of fire resistant foams. *Polymer Bull.* 12, 1–5. doi: 10.1007/BF00258264

Glasser, W. G., Loos, R., Cox, B., and Cao, N. (2017). Melt-blown compostable polyester films with lignin. *TAPPI J.* 16, 111–121. doi: 10.32964/TJ16.3.111

Glasser, W. G., and Morohoshi, N. (1979). The structure of lignins in pulps. VII. The distribution of interunit linkages in lignin. *Tappi* 62, 101–105.

Glasser, W. G., Saraf, V. P., and Newman, W. H. (1982). Hydroxypropylated lignin-isocyanate combinations as bonding agents for wood and cellulosic fibers. *J. Adhesion* 14, 233–255. doi: 10.1080/00218468208073206

Glasser, W. G., and Sarkanen, S. (eds.). (1989). Lignin: properties and materials. *ACS Symp. Ser.* 397:545. doi: 10.1021/bk-1989-0397

Gradwell, S. E., Renneckar, S., Esker, A. R., Heinze, T. H., Gatenholm, P., Vaca-Garcia, C., et al. (2004). Surface modification of cellulose fibers: towards wood composites by biomimetics. *Comptes Rendus Biologies*. 327, 945–953. doi: 10.1016/j.crvi.2004.07.015

Graichen, F. H. M., Grigsby, W. J., Hill, S. J., Raymond, L. G., Sanglard, M., Smith, D. A., et al. (2017). Yes, we can make money out of lignin and other bio-based resources. *Indust. Crops Products* 106, 74–85. doi: 10.1016/j.indcrop.2016.10.036

Hemingway, R. W., and Conner, A. H. (eds.). (1989). Adhesives from renewable resources. *ACS Symp. Ser*. 385:510.

Hillis, W. E. (ed.) (1962). *Wood Extractives and Their Significance to the Pulp and Paper Industries*. New York, NY; London: Academic Press, 513.

Hofmann, K., and Glasser, W. G. (1993). Engineering plastics from lignin. 21. Synthesis and properties of epoxidized lignin-poly(propylene oxide) copolymers. *Wood Chem. J. Technol.* 13, 73–95. doi: 10.1080/02773819308020508

Hsu, O. H.-H., and Glasser, W. G. (1975). Polyurethane foams from carboxylated lignins. *Appl. Poly. Symp.* 28, 297–307.

Hsu, O. H.-H., and Glasser, W. G. (1976). Polyurethane adhesives and coatings from modified lignin. *Wood Sci.* 9, 97–103.

Huang, C., Hu, J., Narron, R., Wang, Y., and Yong, Q. (2017). Characterization of kraft lignin fractions obtained by sequential ultrafiltration and their potential application as a biobased component in blends with polyethylene. *ACS Sustain. Chem. Eng.* 5, 11770–11779. doi: 10.1021/acssuschemeng.7b03415

Ito, Y., Tanahashi, M., Shigematsu, M., Shinoda, Y., and Ohta, C. (1998). Compressive-molding of wood by high-pressure steam-treatment: Pt. 1. Development of compressively molded squares from thinnings. *Holzforschung* 52, 211–216. doi: 10.1515/hfsg.1998.52.2.211

Jain, R. K., and Glasser, W. G. (1993). Lignin derivatives. II. Functional ethers. *Holzforschung*, 47, 325–332. doi: 10.1515/hfsg.1993.47.4.325

Kaya, A., Du, X., Liu, Z., Wu, J. W., Morris, J. R., Glasser, W. G., et al. (2009). Surface plasmon resonance studies of pullulan cinnamate adsorption onto cellulose. *Biomacromolecules* 10, 2451–2459. doi: 10.1021/bm900412g

Kelley, S. S., Glasser, W. G., and Ward, T. C. (1988). Engineering plastics from lignin. XV. Polyurethane films from chain-extended hydroxypropyl lignin. *J. Appl. Poly. Sci.* 36, 759–772. doi: 10.1002/app.1988.070360403

Kelley, S. S., Glasser, W. G., and Ward, T. C. (1989). "Effect of soft-segment content on the properties of lignin-based polyurethanes," in *Lignin – Properties and Materials, ACS Symposium Series No. 397*, eds W. G. Glasser and S. Sarkanen (Washington, DC: American Chemical Society), 402–413.

Kelley, S. S., Rials, T. G., and Glasser, W. G. (1987). Relaxation behavior of the amorphous components of wood. *J. Mater. Sci.* 22, 617–624. doi: 10.1007/BF01160778

Kinloch, A. J. (ed.). (1986). *Structural Adhesives-Developments in Resins and Primers*. London; New York, NY: Elsevier Applied Science Publishers Ltd., 328.

Koivu, K. A. Y., Sadeghifar, H., Nousiainen, P. A., Argyropoulos, D. S., and Sipila, J. (2016). Effect of fatty acid esterification on the thermal properties of softwood kraft lignin. *ACS Sustain. Chem. Eng.* 4, 5238–5247. doi: 10.1021/acssuschemeng.6b01048

Kosbar, L. L., and Gelorme, J. (1996). Bio-based resins for the manufacture of printed wiring boards. *ANTEC* 96, 1378–1381.

Kosbar, L. L., Gelorme, J. D., and Japp, R. M. (2001). Introducing biobased materials into the electronics industry – developing a lignin-based resin for printed wiring boards. *J. Indust. Ecol.* 4, 93–105. doi: 10.1162/108819800300106401

Koshijima, T., and Watanabe, T. (2003). *Association between Lignin and Carbohydrates in Wood and Other Plant Tissues*. Berlin; Heidelberg; New York, NY: Springer-Verlag, 329.

Košikova, B., Zakutna, L., and Joniak, D. (1978). Investigation of the lignin-saccharidic complex by electron microscopy. *Holzforschung* 32, 15–18. doi: 10.1515/hfsg.1978.32.1.15

Kozliak, E. I., A., Kubatova, A., Artemyeva, A. A., Nagel, E., Zhang, C., Rajappagowda, R. B., et al. (2016). Thermal liquefaction of lignin to aromatics: efficiency, selectivity, and product analysis. *ACS Sustain. Chem. Eng.* 4, 5106–5122. doi: 10.1021/acssuschemeng.6b01046

Kun, D., and Pukanszky, B. (2017). Polymer/lignin blends: interactions, properties, applications. *Euro. Poly. J.* 93, 618–641. doi: 10.1016/j.eurpolymj.2017.04.035

Lake, M. (2016, October 3). Has lignin's time finally come? *Michael McCoy, C&E News*. p. 35–37.

Lambuth, A. L. (1989). "Chapter 1. Adhesives from renewable resources," in *Adhesives From Renewable Resources, No. 385. ACS Symposium Series*, eds R. H. Hemingway and A. H. Conner (Washington, DC: American Chemical Society), 1–10.

Lapierre, C., A., Scalbert, B., Monties, R. C. (1986). Thioacidolysis, a new method to characterize lignins: application to wheat straw lignins. *Bull. De Liaison Groupe Polyphenols* 13, 128–135.

Larsson, S., and Miksche, G. E. (1967). Gas chromatographic analysis of lignin oxidation products. Diphenylether linkage in lignin. *Acta Chem. Scand*. 21, 1970–1971. doi: 10.3891/acta.chem.scand.21-1970

Leary, G., Sawtell, D. A., and Wong, H. (1983). The formation of model lignin-carbohydrate compounds in aqueous solution. *Holzforschung* 37, 11–16. doi: 10.1515/hfsg.1983.37.1.11

Lewis, G. N., and Sarkanen, S. (eds.). (1998). Lignin and lignan biosynthesis. *ACS Symp. Ser*. 697:436. doi: 10.1021/bk-1998-0697

Lewis, H. F., and Brauns, F. E. (1947). *Esters of Lignin Material*. US Patent. # 2,429,102. Washington, DC: U.S. Patent Office.

Lewis, N. G., and Lantzy, T. R. (1989). "Chapter 2. Lignin in adhesives, in adhesives - from renewable resources," in *ACS Symposium Ser. No. 385*, eds R. H. Hemingway and A. H. Conner (Washington, DC: American Chemical Society), 13–26.

Li, Q., Ragauskas, A. J., and Yuan, J. S. (2017). Lignin carbon fiber: the path for quality. *Tappi J.* 16, 107–108. doi: 10.32964/TJ16.3.107

Li, T., and Takkellapati, S. (2018). The current and emerging sources of technical lignins and their applications. *Biofuels Bioproducts Biorefining* 12, 756–787. doi: 10.1002/bbb.1913

Li, Y., and Sarkanen, S. (2002). Alkylated kraft lignin-based thermoplastic blends with aliphatic polyesters. *Macromolecules* 35, 9707–9715. doi: 10.1021/ma021124u

Lora, J. H., and Glasser, W. G. (2002). Recent industrial applications of lignin – a sustainable alternative to nonrenewable materials. *J. Polym. Environnt.* 10, 39–48. doi: 10.1023/A:1021070006895

Moerck, R., Reiman, A., and Kringstad, K. P. (1989) "Elastomeric polyurethanes from kraft lignin-polyethylene-TDI system," in *Lignin – Properties and Materials, ACS Symposium Series No. 397*, eds W. G. Glasser and S. Sarkanen (Washington, DC: American Chemical Society), 390–401.

Monties, B. (2003). Botanical variability and mechanical function of lignins: two critical aspects of the plant phenolic secondary metabolism. *Adv. Phytochem.* 1–48.

Morohoshi, N., and Glasser, W. G. (1979). The structure of lignins in pulps. Pt. 5. Gas and gel chromatography of permanganate oxidation products. *Wood Sci. Technol.* 13, 249–264. doi: 10.1007/BF00356968

Mueller, K., Zollfrank, C., and Schmid, M. (2019). Natural polymers from biomass resources as feedstocks for thermoplastic materials. *Macromol. Mater. Eng.* 304:1800760. doi: 10.1002/mame.201800760

Muller, P. C., and Glasser, W. G. (1984). Engineering plastics from lignin. VIII. Phenolic resin prepolymer synthesis and analysis. *Adhesion. J.* 17, 157–173. doi: 10.1080/00218468408079672

Newman, W. H., and Glasser, W. G. (1985). Engineeringplastics from lignin. XI. Synthesis and performance of lignin adhesives with isocyanates and melamine. *Holzforschung* 39, 345–353. doi: 10.1515/hfsg.1985.39.6.345

Nguyen, N. A., Meek, K. M., Bowland, C. C., Barnes, S. H., and Naskar, A. K. (2018). An acrylonitrile-butadiene-lignin renewable skin with programmable and switchable electrical conductivity for stress/strain-sensing applications. *Macromolecules* 51, 115–127. doi: 10.1021/acs.macromol.7b02336

Nieh, L.-S., and Glasser, W. G. (1989). "Lignin epoxide – synthesis and characterization," in *Lignin – Properties and Materials, ACS Symposium Series No. 397*, eds W. G. Glasser and S. Sarkanen (Washington, DC: American Chemical Society), 506–514.

Nimz, H., and Das, K. (1971). Low molecular weight degradation products of lignin. I. Degradation of beech lignin with thioacetic acid. *Chem. Ber.* 104, 1871–1876. doi: 10.1002/cber.19711040626

Ohara, S., Hosoya, S., and Nakano, J. (1980). Study of Lignin. 109. Studies on the formation of lignin-carbohydrate complex during alkaline pulping. *Mokuzai Gakkaishi* 26, 408–413.

Rencoret, J. H., Kim, A. B., Evaristo, A., Gutierrez, J., and Ralph, J. C. delRio (2018). Variability in lignin composition and structure in cell walls of different parts of Macauba palm fruit. *J. Agric. Food Chem.* 66, 138–153. doi: 10.1021/acs.jafc.7b04638

Rials, T. G., and Glasser, W. G. (1988). Thermal and dynamic mechanical properties of hydroxypropyl cellulose films. *J. Appl. Polymer Sci.* 36, 749–758. doi: 10.1002/app.1988.070360402

Rials, T. G., and Glasser, W. G. (1989a). Multiphase materials with lignin. VI. Effect of cellulose derivative structure on blend morphology with lignin. *Wood Fiber Sci.* 21, 80–90.

Rials, T. G., and Glasser, W. G. (1989b). "Phase morphology of blends of lignin with liquid crystalline cellulosics," in *Lignin: Properties and Materials, ACS Symposium Series No. 397*, eds W. G. Glasser and S. Sarkanen (Washington, DC: American Chemical Society), 464–475.

Rials, T. G., and Glasser, W. G. (1990). Multiphase materials with lignin. 5. Effect of lignin structure on hydroxypropyl cellulose blend morphology. *Polymer* 31, 1333–1338. doi: 10.1016/0032-3861(90)90226-O

Rydholm, S. A. (1965). *Pulping Processes*. New York, NY: Wiley-Interscience, 1269.

Sarkanen, K. V., and Ludwig, C. H. (eds.). (1971). *Lignins – Occurrence, Formation, Structure and Reactions*. New York, NY: Wiley-Interscience, 916.

Shaw, J. M., Buchwalter, S. L., Hedrick, J. C., Kang, S. K., Kosbar, L. L., Gelorme, J. D., et al. (1996). BigBlue goes green. *Printed Circuit Fabricat.* 19, 38–44.

Sun, Z., Fridrich, B., de Santi, A., Elangovan, S., and Barta, K. (2018). Bright side of lignin depolymerization: toward new platform chemicals. *Chem. Rev.* 118, 614–678. doi: 10.1021/acs.chemrev.7b00588

Thakur, V. K., Thakur, M. K., Raghavan, P., and Kessler, M. R. (2014). Progress in green polymer composites from lignin for multifunctional applications: a review. *ACS Sustain. Chem. Eng.* 2, 1072–1092. doi: 10.1021/sc500087z

The Ljungberg Textbook (2008). *Wood Chemistry and Wood Biotechnology–KF2010*. Stockholm: Fibre and Polymer Technology, KTH, 384.

Thielemans, W., Can, E., Morye, S. S., and Wool, R. P. (2002). Novel applications of lignin in composite materials. *J. Appl. Polym. Sci.* 83, 323–331. doi: 10.1002/app.2247

Thielemans, W., and Wool, R. P. (2005). Lignin esters for use in unsaturated thermosets: lignin, modification and solubility modeling. *Biomacromolecules*. 6, 1895–1905. doi: 10.1021/bm0500345

Toffey, A., and Glasser, W. G. (1997). Cure characterization of polyurethanes with lignin and cellulose derivatives. *Holzforschung* 51, 71–78. doi: 10.1515/hfsg.1997.51.1.71

Upton, B. M., and Kasko, A. M. (2016). Strategies for the conversion of lignin to high-value polymeric materials: review and perspective. *Chem. Rev.* 116, 2275–2306. doi: 10.1021/acs.chemrev.5b00345

Van den Bosch, S., Koelewijn, S.-F., Renders, T., G., Van den Bossche, Vangeel, T., Schutyser, W., et al. (2018). Catalytic strategies towards lignin-derived chemicals. *Topics Curr. Chem.* 376, 1–40. doi: 10.1007/s41061-018-0214-3

Wang, C., Kelley, S. S., and Venditti, R. A. (2016). Lignin-based thermoplastic materials. *ChemSusChem*. 9, 770–783. doi: 10.1002/cssc.2015 01531

Wang, W.-X., and Glasser, W. G. (1989). "Lignin derivatives with acrylate functionality. (Engineering plastics from lignin. XX.)," in *Lignin: Properties and Materials, ACS Symposium Series No. 397*, eds W. G. Glasser and S. Sarkanen (Washington, DC: American Chemical Society), 515–522.

Wei, M., Fan, L., Huang, J., and Chen, Y. (2006). Role of star-like hydroxypropyl lignin in soy-protein plastics. *Macromol. Mater. Eng.* 291:524. doi: 10.1002/mame.200500372

Westbye, P., Koehnke, T., Glasser, W., and Gatenholm, P. (2007). The influence of lignin on the self-assembly behavior of xylan-rich fractions from birch (*Betula pendula). Cellulose* 14, 603–613. doi: 10.1007/s10570-007-9178-0

Wright, R. S., and Glasser, W. G. (1998). Steam assisted biomass fractionation. II. Fractionation behavior of various biomass resources. *Biomass Bioenergy* 14, 219–235. doi: 10.1016/S0961-9534(97)10037-X

Wu, L. C.-F., and Glasser, W. G. (1984). Engineering plastics from lignin. I. Synthesis of hydroxypropyl lignin. *J. Appl. Polym. Sci.* 29, 1111–1123. doi: 10.1002/app.1984.070290408

Xu, C., Arancon, R. A., Labidi, J., and Luque, R. (2014). Lignin depolymerisation strategies: towards valuable chemicals and fuels. *Chem. Soc. Rev.* 43, 7485–7500. doi: 10.1039/C4CS00235K

Zakzeski, J., Bruijnincx, P. C. A., Jongerius, A. L., and Weckhuysen, B. M. (2010). The catalytic valorization of lignin for the production of renewable chemicals. *Chem. Rev.* 110, 3552–3599. doi: 10.1021/cr90 0354u

Conflict of Interest Statement: The author declares that the research was conducted in the absence of any commercial or financial relationships that could be construed as a potential conflict of interest.

Copyright © 2019 Glasser. This is an open-access article distributed under the terms of the Creative Commons Attribution License (CC BY). The use, distribution or reproduction in other forums is permitted, provided the original author(s) and the copyright owner(s) are credited and that the original publication in this journal is cited, in accordance with accepted academic practice. No use, distribution or reproduction is permitted which does not comply with these terms.

frontiers in Chemistry

ORIGINAL RESEARCH
published: 06 September 2019
doi: 10.3389/fchem.2019.00606

Divanillin-Based Aromatic Amines: Synthesis and Use as Curing Agents for Fully Vanillin-Based Epoxy Thermosets

Etienne Savonnet [1,2], Cedric Le Coz [1], Etienne Grau [1], Stéphane Grelier [1], Brigitte Defoort [2] and Henri Cramail [1]**

[1] Univ. Bordeaux, CNRS, Bordeaux INP, LCPO, UMR 5629, Pessac, France, [2] ArianeGroup, St-Médard-en-Jalles, Bordeaux, France

Bio-based aromatic diamines from vanillin substrate were successfully synthesized and characterized. These amines, i.e., methylated divanillylamine (MDVA) and 3,4-dimethoxydianiline (DMAN), were then tested as curing agents for the design of bio-based epoxy thermosets. The epoxy thermosets obtained from these novel vanillin-based amines exhibited promising thermomechanical properties in terms of glass transition temperature and char residue.

Keywords: di-vanillin, amines, curing agent, thermoset, epoxy

OPEN ACCESS

Edited by:
Florent Allais,
AgroParisTech Institut des Sciences et Industries du Vivant et de L'environnement, France

Reviewed by:
Simonetta Antonaroli,
University of Rome Tor Vergata, Italy
Chengji Zhao,
Jilin University, China

***Correspondence:**
Stéphane Grelier
sgrelier@enscbp.fr
Henri Cramail
cramail@enscbp.fr

Specialty section:
This article was submitted to Green and Sustainable Chemistry, a section of the journal Frontiers in Chemistry

Received: 21 June 2019
Accepted: 19 August 2019
Published: 06 September 2019

Citation:
Savonnet E, Le Coz C, Grau E, Grelier S, Defoort B and Cramail H (2019) Divanillin-Based Aromatic Amines: Synthesis and Use as Curing Agents for Fully Vanillin-Based Epoxy Thermosets. Front. Chem. 7:606. doi: 10.3389/fchem.2019.00606

INTRODUCTION

Epoxy thermosets are the products of the reaction between epoxy-based monomers or prepolymers with curing agents. The cross-linking agents are significant in terms of mass fraction as the latter can represent up to 50% of the formulations. Many efforts are currently undertaken to develop bio-based alternatives to traditional epoxy monomers derived from fossil resources and, in particular, bisphenol-A (Kumar et al., 2018). With similar objectives, some studies already reported the synthesis of bio-based anhydride- or acid-type curing agents from renewable resources, such as vegetable oils (Roudsari et al., 2014), rosin (Wang et al., 2008, 2009; Liu et al., 2009; Qin et al., 2014a), terpens Takahashi et al., 2008, tannins Pizzi, 2008; Shibata and Nakai, 2010, or lignins (Qin et al., 2014b).

Moreover, aliphatic amine curing agents have also been reported from substrates originating from biomasses such as terpenes (Keim and Roeper, 1981; Keim et al., 1983; Garrison and Harvey, 2016), lignin (Fache et al., 2014), cardanol (Thiyagarajan et al., 2011; Shingte et al., 2017) derived from cashew oil or vegetable oils (Stemmelen et al., 2011; Hibert et al., 2016; Samanta et al., 2016). Very recently, amines have been synthesized from vanillin (Mora et al., 2018) by NH_3 addition onto diglycidylated vanillin alcohol. When cured with classical DGEBA, a Tg of 72°C of the so-formed epoxy thermoset was obtained.

Despite all these works, the development of bio-based fully aromatic amine-type curing-agents leading to high Tg epoxy thermosets is still an unmet challenge. In this way, there is a growing interest to find bio-based reactive amines leading to epoxy thermosets with high thermomechanical properties.

Vanillin is a very interesting candidate because it is one of the non-hazardous aromatic compounds industrially available from biomass (Pinto et al., 2012). From vanillin, we developed an efficient C–C coupling reaction through enzymatic catalysis leading to highly pure divanillin substrate (Kobayashi and Makino, 2009; Llevot et al., 2015, 2016). More recently, we have developed a palette of epoxy monomers derived from divanillin, which demonstrated to be valuable, and realistic alternative to DGEBA-based epoxy thermosets (Savonnet et al., 2018). In the following of our previous investigations, this article presents two synthetic pathways to prepare primary aromatic amines from divanillin as starting material. These polyfunctional amines were then used as curing agents for the synthesis of epoxy thermosets.

SYNTHESIS OF BIO-BASED AMINES FROM VANILLIN DERIVATIVES

Herein, two synthetic pathways have been identified for the synthesis of bio-based aromatic amines through the reduction of oxime and the acyl azide rearrangement moieties, leading to bis-benzylamine and bis-aniline moieties, respectively.

The divanillin displays two aldehyde functions which can undergo chemical reaction to get divanillyloxime. A synthetic pathway adapted from literature has been developed and is depicted on **Scheme 1** (Liu et al., 2011; Fache et al., 2015). First, the alkylation of phenol moiety was performed in the presence of iodomethane and a weak base leading to methylated divanillin in a quantitative yield (>95%). Then, the oximation step consisted in the reaction of aldehyde functions with hydroxylamine hydrochloride in the presence of sodium acetate to yield methylated divanillyloxime (MDVO) (>95%). The structure of this intermediate was confirmed by ^{1}H and ^{13}C NMR spectroscopies (**Figure S1**). The appearance of a signal at 3.67 ppm was attributed to the methylated phenols and new signals at 8.10 and 11.13 ppm were attributed to the oxime moieties of methylated divanillyloxime (MDVO). Finally, the so-formed oxime was then reduced into methylated divanillylamine (MDVA) by hydrogenation. The reaction was performed during 16 h at 70°C under 12 bars of H_2 pressure in the presence of Nickel Raney in ethanol. Reduction of the oxime yielded a pale orange solid with a melting temperature of 69°C (DSC). ^{1}H NMR spectrum of this orange solid demonstrated the disappearance of oxime signals at 8.10 and 11.13 ppm and the appearance of a new signal at 3.63 ppm, corresponding to the benzylic-protons of the amine (**Figure 1**). ^{13}C NMR spectrum exhibited also a shift of the alpha-carbon of the oxime from 147.81 to 51.62 ppm, which confirmed the reduction of oxime moieties. The attribution of the signals was also confirmed by HSQC NMR spectroscopy. In addition, the MDVA was also characterized by FTIR. **Figure S2a** shows the infra-red spectra of MDVO and MDVA from which the decrease of O-H stretching signal at 3,227 cm^{-1} and the disappearance of N-O stretching at 945 cm^{-1} were observed and corresponding to the oxime moieties. Besides, ninhydrin test (Friedman, 2004), which reveals amino groups, confirmed the presence of amine moieties on MDVA (**Figure S2b**).

The second pathway is based on the Curtius rearrangement. It involves the synthesis of an acyl azide intermediate. Usually carboxylic acids are precursors of acyl azides. As previously described (Kobayashi and Makino, 2009; Llevot et al., 2015, 2016), methyl vanillate can easily be dimerised into the corresponding dimer and hydrolyzed into the diacid. From divanillic acid, the sequential synthetic pathway is summarized in **Scheme 2**. All the intermediates were obtained without any further purification steps, unless mentioned. ^{1}H and ^{13}C NMR spectroscopies were performed to confirm the structure of the synthesized products. Methyl divanillate was first alkylated using the same procedure described previously and obtained in a high yield (>80%). Thereafter, the hydrolysis of the methylated diester with sodium hydroxide yielded the diacid (>90%). The disappearance of the methyl ester protons at 3.38 ppm and the appearance of acid proton signals of carboxylic acid at 9.20 ppm were attributed to the formation of the methylated divanillic acid. Methylated divanillic acid was then converted into acyl azide in a two-step reaction. Ethyl chloroformate was first reacted with the acid to form *in situ* an acyl chloride and sodium azide was then added to the mixture, yielding the corresponding acyl azide (>60%). Finally, the di-isocyanate was obtained in good yield (>80%) by simply heating the azide compound in dry toluene. The synthesis of these latter compounds was confirmed by ^{1}H NMR spectroscopy (**Figure S3**).

In addition, acyl azide structure was confirmed by the disappearance of carboxylic signal at 9.20 ppm and finally the shift of the aromatic protons from 7.61 and 7.55 to 6.65 and 6.58 ppm was attributed to the so-formed di-isocyanate. These compounds were also characterized by FTIR spectroscopy (**Figure S4**). Infrared spectra exhibited characteristic signal wavelengths of carboxylic acid at 1,720 cm^{-1} (-C=O) and 2,500–3,300 cm^{-1} (O-H), acyl azide at 2,140 cm^{-1} (-N_3), and isocyanate at 2,278 cm^{-1} (-N=C=O).

Finally, 3,4-dimethoxydianiline (DMAN) was recovered by hydrolysis in basic conditions of the corresponding di-isocyanate. After extraction with ethyl acetate and washing with water a mixture of brown and white solids was obtained. However, ^{1}H NMR spectroscopy of the reaction mixture revealed the presence of a by-product (**Figure S5**). These additional signals

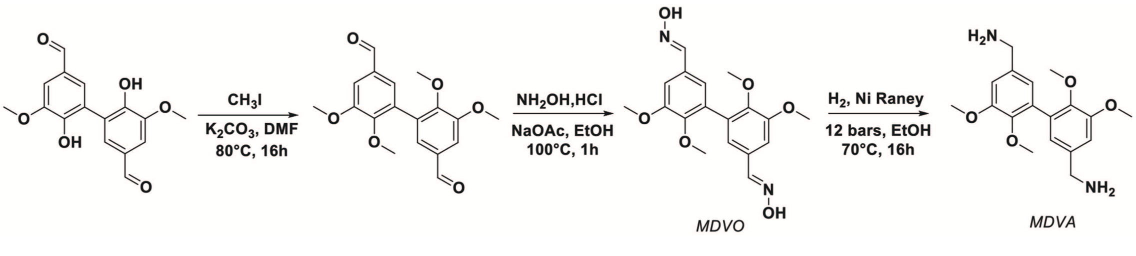

SCHEME 1 | Synthesis of methylated divanillylamine from divanillin.

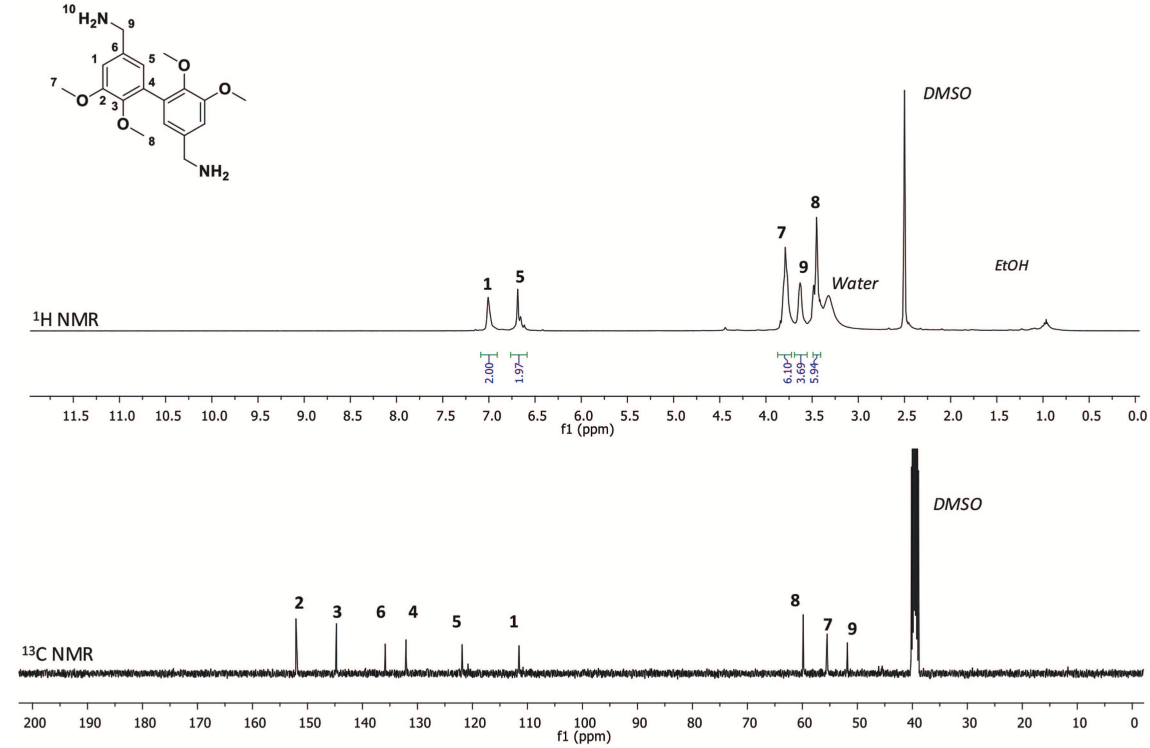

FIGURE 1 | ^1H and ^{13}C NMR spectroscopy of methylated divanillylamine (MDVA) in DMSO-d6.

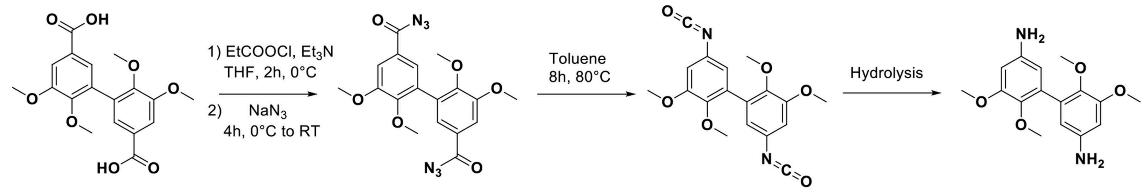

SCHEME 2 | Synthesis of 3,4-dimethoxydianiline (DMAN) from methylated divanillic acid.

could be attributed to the formation of ureas, resulting of the side reaction of amine with the isocyanate or to the oxidation of the amines. Nevertheless, a small fraction was isolated as a white solid corresponding to the DMAN and characterized by ^1H and ^{13}C NMR spectroscopy (**Figure 2**). ^1H NMR spectroscopy displayed proton signals of aromatic rings, amine moieties and alkylated hydroxyl groups at 6.23, 5.90, 4.79, 3.72, and 3.38 ppm, respectively. In addition, the disappearance of the C9 carbon signals of isocyanate at 124.71 ppm, confirmed the obtention of the targeted diamine. DMAN was also characterized by FTIR spectroscopy (**Figure S6**). The following spectrum confirmed the absence of the isocyanate bands (-N=C=O) at 2,278 cm^{-1} and the appearance of amino groups signals at 1,610, 3,240, 3,370, and 3,471 cm^{-1}. In conclusion, the Curtius rearrangement permitted to synthesize the 3,4-dimethoxydianiline from the acyl azide intermediate derived from the methyl divanillate. However, the last step of the synthesis was tedious and only a small amount of the desired product was identified as the diamine. Further investigations and optimizations in the hydrolysis step of the isocyanate substrate are required to recover the bio-based diamine in a better yield.

SYNTHESIS OF FULLY VANILLIN-BASED EPOXY THERMOSETS

The previously synthesized di-amines, i.e., methylated divanillylamine (MDVA) and 3,4-dimethoxydianiline (DMAN) were used as curing agents for the synthesis of epoxy thermosets.

The DGEBA epoxy monomer was stirred vigorously with a stoichiometric amount of MDVA. The thermomechanical properties of the so-formed network were characterized by DSC and TGA. Bio-based thermoset was then compared with DGEBA/IPDA epoxy system. Results are summarized in the **Table S1** and **Figure S7**. Unfortunately, the characterization

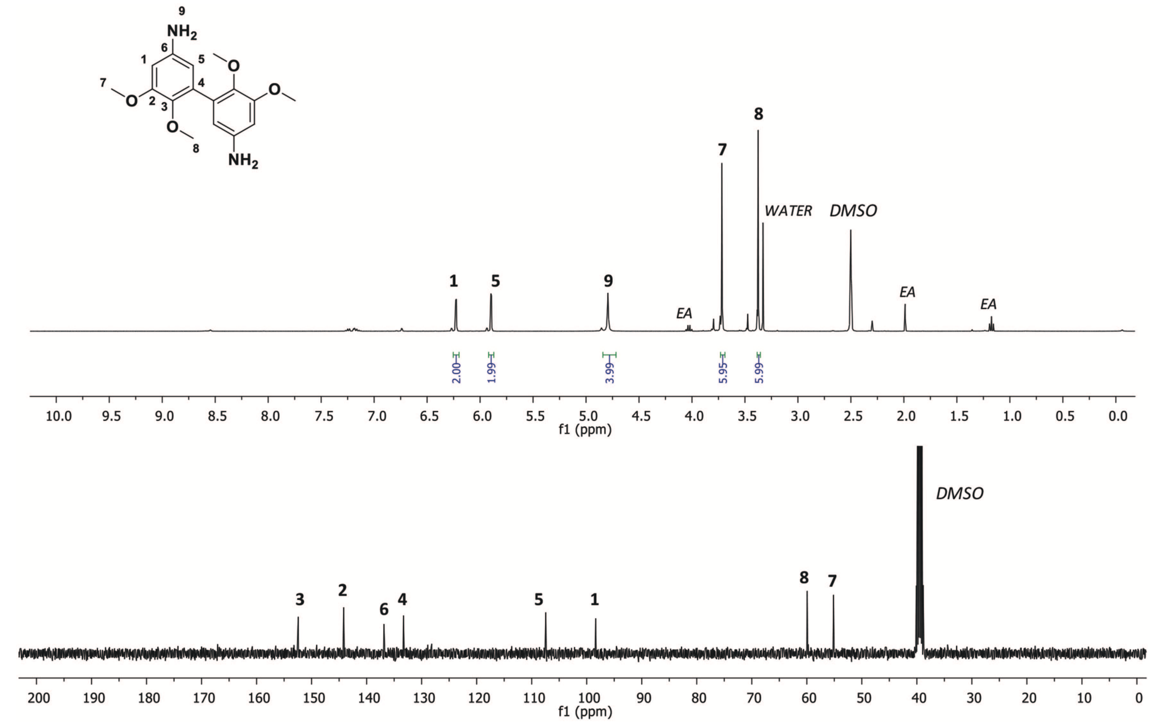

FIGURE 2 | ^{1}H and ^{13}C NMR spectroscopy of 3,4-dimethoxydianiline (DMAN) in DMSO-d6.

of bio-based epoxy networks, using DSC, showed a weak exothermic peak (ΔH=105 J/g for DGEBA/MDVA vs. 430 J/G for DGEBA/IPDA), corresponding to the reaction of amine with epoxy. In addition, no clear glass transition temperature was observed with this network (**Figure S8**). One hypothesis to explain this result could be the poor homogeneity of the mixture between DGEBA and the solid MDVA—MDVA melts at 40°C (DSC)-, which impaired the stoichiometric ratio.

DGEBA epoxy monomer was also cured with bio-based DMAN. However, in view of the small amount recovered, crude DMAN was used for the curing reaction. Thermomechanical properties of the network formed were then determined and compared with DGEBA networks cured with 4,4′-Diaminodiphenyl sulfone (DDS). Results are summarized in **Table 1** and **Figure S8b**. In comparison with conventional amine hardener DDS, epoxy network cured with DMAN exhibited similar properties. Indeed, glass transition temperature of thermoset cured with DMAN displayed a value 30°C below the networks obtained with DDS, i.e., 176°C. This difference can be explained by the presence of by-product compounds, which could impair the stoichiometric ratio. Interestingly, despite the presence of the by-product, the bio-based amine enabled to increase the char yield residue up to 28% (**Figure S8**). This feature could be explained by the C-C bonding between the two aromatic rings of DMAN, which could favor the formation of char and thus increase the residual content. Another important difference between DDS- and DMAN-based epoxy thermosets is the higher reactivity of DDS.

TABLE 1 | Thermomechanical properties of DGEBA and TetraGEDVA cured with DDS and DMAN.

Epoxy/ hardener	**T_{onset} (°C)**	**T_{Exo} (°C)**	**ΔH ($J.g^{-1}$)**	**ΔH ($kJ.mol^{-1}$)**	**Tg (°C)**	**$Char_{900}$ (%)**
DGEBA/DDS	184	226	355	83	204	16
DGEBA/DMAN	99	153	393	95	176	28
TetraGEDVA/DDS	165	208	459	89	-	48
TetraGEDVA/DMAN	110	193	183	39	212	48

At last, a bio-based polyglycidylether, tetraglycidylether of divanillyl alcohol (TetraGEDVA), (Savonnet et al., 2018) was cured with crude DMAN. In this way, a fully bio-based epoxy thermoset was successfully obtained. Such bio-based epoxy network exhibited promising thermomechanical properties as attested by the glass transition temperature of 212°C and the char residue of 48% (**Figure S8**). However, the enthalpy of polymerization is much lower than the enthalpy of the reaction between TetraGEDVA and DDS. Again, the presence of undefined compounds in crude DMAN and the inhomogeneity of the mixture could explain this difference.

CONCLUSION

In summary, the synthesis of bio-based curing agent from divanillin derivatives was investigated. Two routes were chosen to achieve the synthesis of diamines. The first one consisted in the reduction of divanillyloxime obtained from divanillin. The synthesis yielded methylated divanillylamine (MDVA) and the thermomechanical properties of thermosets obtained from epoxy precursors cured with MDVA were investigated. DGEBA epoxy prepolymers were thus cured with MDVA and the networks obtained were compared with the conventional DGEBA/IPDA system. Unfortunately, the characterization by DSC showed a weak exothermic peak, corresponding to the reaction of amine with epoxy, but no clear glass transition temperature could be observed with this system.

Then, the 3,4-dimethoxyaniline (DMAN) was synthesized using the oxidative rearrangement of Curtius. From methyl divanillate and through the synthesis of acyl azide and isocyanate intermediates, the hydrolysis of this latter yielded 3,4-dimethoxyaniline (DMAN). However, the hydrolysis step was tedious and the corresponding amine failed to be isolated efficiently. Nevertheless, crude DMAN was used as curing agent in the polyaddition reaction with DGEBA. Interestingly, the so-formed semi-biobased thermoset exhibited a glass transition temperature of 176°C against 204°C for the conventional DGEBA/DDS system. Moreover, the DMAN permitted to double the char content of the network comparing to DGEBA/DDS network cured in the same conditions. In addition, a fully bio-based epoxy thermoset was obtained by curing tetraglycidylether of divanillyl alcohol (TetraGEDVA) with DMAN. The thermomechanical properties obtained were promising as the epoxy thermoset exhibited a glass transition temperature of 212°C and a char residue of 48%.

Finally, new amine-type curing agents from vanillin-based starting material was successfully attempted and characterized. However, some further optimizations in the synthetic pathways described are still necessary to have a better appreciation of the potential of these new bio-based aromatic diamines in the course of thermoset designs.

DATA AVAILABILITY

All datasets generated for this study are included in the manuscript/**Supplementary Files**.

AUTHOR CONTRIBUTIONS

ES performed the synthesis of the chemicals and performed the polymerization experiments. CL performed the thermo-mechanical analysis. EG, SG, BD, and HC contributed equally to the supervision of the project.

ACKNOWLEDGMENTS

The authors thank Gerard Dimier for the DSC analyses. This study was financially supported by ArianeGroup and ANRT. The authors also thank Equipex Xyloforest ANR-10-EQPX-16 for flash chromatography.

SUPPLEMENTARY MATERIAL

The Supplementary Material for this article can be found online at: https://www.frontiersin.org/articles/10.3389/fchem.2019.00606/full#supplementary-material

REFERENCES

Fache, M., Darroman, E., Besse, V., Auvergne, R., Caillol, S., and Boutevin, B. (2014). Vanillin, a promising biobased building-block for monomer synthesis. *Green Chem*. 16, 1987–1998. doi: 10.1039/C3GC42613K

Fache, M., Montérémal, C., Boutevin, B., and Caillol, S. (2015). Amine hardeners and epoxy cross-linker from aromatic renewable resources. *Eur. Polym. J*. 73, 344–362. doi: 10.1016/j.eurpolymj.2015.10.032

Friedman, M. (2004). Applications of the ninhydrin reaction for analysis of amino acids, peptides, and proteins to agricultural and biomedical sciences. *J. Agric. Food Chem*. 52, 385–406. doi: 10.1021/jf030490p

Garrison, M. D., and Harvey, B. G. (2016). Bio-based hydrophobic epoxy-amine networks derived from renewable terpenoids. *J. Appl. Polym. Sci.* 133:43621. doi: 10.1002/app.43621

Hibert, G., Lamarzelle, O., Maisonneuve, L., Grau, E., and Cramail, H. (2016). Bio-based aliphatic primary amines from alcohols through the 'Nitrile route' towards non-isocyanate polyurethanes. *Eur. Polym. J*. 82, 114–121. doi: 10.1016/j.eurpolymj.2016.07.007

Keim, W., Kurtz, K. R., and Roeper, M. (1983). Palladium catalyzed telomerization of isoprene with secondary amines and conversion of the resulting terpene amines to terpenols. *J. Mol. Catal*. 20, 129–138. doi: 10.1016/0304-5102(83)83002-8

Keim, W., and Roeper, M. (1981). Terpene amine synthesis via palladium-catalyzed isoprene telomerization with ammonia. *J. Org. Chem*. 46, 3702–3707. doi: 10.1021/jo00331a024

Kobayashi, S., and Makino, A. (2009). Enzymatic polymer synthesis: an opportunity for green polymer chemistry. *Chem. Rev*. 109, 5288–5353. doi: 10.1021/cr900165z

Kumar, S., Samal, S. K., Mohanty, S., and Nayak, S. K. (2018). Recent development of biobased epoxy resins: a review. *Polym. Plast. Technol. Eng.* 57, 133–155. doi: 10.1080/03602559.2016.1253742

Liu, H., Lepoittevin, B., Roddier, C., Guerineau, V., Bech, L., Herry, J. M., et al. (2011). Facile synthesis and promising antibacterial properties of a new guaiacol-based polymer. *Polymer* 52, 1908–1916. doi: 10.1016/j.polymer.2011.02.046

Liu, X. W., Xin, W., and Zhang, J. (2009). Rosin-based acid anhydrides as alternatives to petrochemical curing agents. *Green Chem*. 11, 1018–1025. doi: 10.1039/b903955d

Llevot, A., Grau, E., Carlotti, S., Grelier, S., and Cramail, H. (2015). Renewable (semi)aromatic polyesters from symmetrical vanillin-based dimers. *Polym. Chem*. 6, 6058–6066. doi: 10.1039/C5PY00824G

Llevot, A., Grau, E., Carlotti, S., Grelier, S., and Cramail, H. (2016). Selective laccase-catalyzed dimerization of phenolic compounds derived from lignin: towards original symmetrical bio-based (bis). aromatic monomers. *J. Mol. Catal. B Enzym*. 125, 34–41. doi: 10.1016/j.molcatb.2015.12.006

Mora, A. S., Tayouo, R., Boutevin, B., David, G., and Caillol, S. (2018). Vanillin-derived amines for bio-based thermosets. *Green Chem.* 20, 4075–4084. doi: 10.1039/C8GC02006J

Pinto, P. C., Borges da Silva, E. A., and Rodrigues, A. E. (2012). "Lignin as source of fine chemicals: vanillin and syringaldehyde," in *Biomass Conversion*, eds C. Baskar, S. Baskar, and R. S. Dhillon (Berlin, Heidelberg: Springer), 381–420. doi: 10.1007/978-3-642-28418-2_12

Pizzi, A. (2008). "Tannins: major sources, properties and applications," in *Monomers, Polymers and Composites From Renewable Resources*, eds M. N. Belgacem, and A. Gandini (Oxford: Elsevier), 179–199. doi: 10.1016/B978-0-08-045316-3.00008-9

Qin, J., Liu, H., Zhang, P., Wolcott, M., and Zhang, J. (2014a). Use of eugenol and rosin as feedstocks for biobased epoxy resins and study of curing and performance properties. *Polym. Int*. 63, 760–765. doi: 10.1002/pi.4588

Qin, J., Woloctt, M., and Zhang, J. (2014b). Use of polycarboxylic acid derived from partially depolymerized lignin as a curing agent for epoxy application. *ACS Sustain. Chem. Eng*. 2, 188–193. doi: 10.1021/sc400227v

Roudsari, G., Mohanty, A. K., and Misra, M. (2014). Study of the curing kinetics of epoxy resins with biobased hardener and epoxidized soybean oil. *ACS Sustain. Chem. Eng*. 2, 2111–2116. doi: 10.1021/sc500176z

Samanta, S., Selvakumar, S., Bahr, J., Wickramaratne, D. S., Sibi, M., and Chisholm, B. J. (2016). Synthesis and characterization of polyurethane networks derived from soybean-oil-based cyclic carbonates and bioderivable diamines. *ACS Sustain. Chem. Eng*. 4, 6551–6561. doi: 10.1021/acssuschemeng.6b01409

Savonnet, E., Grau, E., Grelier, S., Defoort, B., and Cramail, H. (2018). Divanillin-based epoxy precursors as DGEBA substitutes for biobased epoxy thermosets. *ACS Sustain. Chem. Eng*. 6, 11008–11017. doi: 10.1021/acssuschemeng.8b02419

Shibata, M., and Nakai, K. (2010). Preparation and properties of biocomposites composed of bio-based epoxy resin, tannic acid, and microfibrillated cellulose. *J. Polym. Sci. Part B Polym. Phys*. 48, 425–433. doi: 10.1002/polb.21903

Shingte, R. D., Tawade, B. V., and Wadgaonkar, P. P. (2017). Partially biobased processable polyimides based on aromatic diamine derived from cardanol. *Green Mater*. 5, 74–84. doi: 10.1680/jgrma.17.00010

Stemmelen, M., Pessel, F., Lapinte, V., Caillol, S., Habas, J. P., and Robin, J. J. (2011). A fully biobased epoxy resin from vegetable oils: from the synthesis of the precursors by thiol-ene reaction to the study of the final material. *J. Polym. Sci. Part A Polym. Chem*. 49, 2434–2444. doi: 10.1002/pola.24674

Takahashi, T., Hirayama, K., Teramoto, N., and Shibata, M. (2008). Biocomposites composed of epoxidized soybean oil cured with terpene-based acid anhydride and cellulose fibers. *J. Appl. Polym. Sci.* 108, 1596–1602. doi: 10.1002/app.27866

Thiyagarajan, S., Gootjes, L.,Vogelzang, W.,Wu, J., van Haveren, J., and van Es, D. S. (2011). Chiral building blocks from biomass: 2,5-diamino-2,5-dideoxy-1,4-3,6-dianhydroiditol. *Tetrahedron* 67, 383–389. doi: 10.1016/j.tet.2010.11.031

Wang, H., Liu, B., Liu, X., Zhang, J., and Xian, M. (2008). Synthesis of biobased epoxy and curing agents using rosin and the study of cure reactions. *Green Chem*. 10, 1190–1196. doi: 10.1039/b803295e

Wang, H.,Liu, B., Liu, X., Zhang, J., and Xian, M. (2009). Synthesis synthesis of rosin-based flexible anhydride-type curing agents and properties of the cured epoxy. *Polym. Int*. 58, 1435–1441. doi: 10.1002/pi.2680

Conflict of Interest Statement: BD was employed by ArianeGroup company.

The remaining authors declare that the research was conducted in the absence of any commercial or financial relationships that could be construed as a potential conflict of interest.

Copyright © 2019 Savonnet, Le Coz, Grau, Grelier, Defoort and Cramail. This is an open-access article distributed under the terms of the Creative Commons Attribution License (CC BY). The use, distribution or reproduction in other forums is permitted, provided the original author(s) and the copyright owner(s) are credited and that the original publication in this journal is cited, in accordance with accepted academic practice. No use, distribution or reproduction is permitted which does not comply with these terms.

frontiers in Chemistry

ORIGINAL RESEARCH
published: 18 September 2019
doi: 10.3389/fchem.2019.00633

Chemical Modification of Plasticized Lignins Using Reactive Extrusion

Romain Milotskyi[1,2]*, László Szabó[2], Kenji Takahashi[2] and Christophe Bliard[1]

[1] Institut de Chimie Moléculaire de Reims, ICMR, CNRS UMR 7312, URCA, B18, UFR SEN, Reims, France, [2] Institute of Science and Engineering, Kanazawa University, Kanazawa, Japan

The reaction of esterification of plasticized Kraft lignin (KL) with succinic and maleic anhydrides using reactive extrusion (REX) was studied in detail. DMSO, glycol and glycerol were found to be efficient plasticizers for lignin. The chemical structure of these new lignin esters was determined using Solid-state ^{13}C CP-MAS NMR and FT-IR analysis. ^{31}P NMR analysis of phosphitylated lignins showed that the aliphatic OH groups of lignin had superior reactivity under the reactive extrusion reaction conditions. The formation of monoesters was confirmed by HSQC NMR spectroscopy. Molecular weight changes after extrusion process were studied using GPC/SEC chromatography. Thermal properties of these polymers were assessed by TGA analysis. The results were compared to lignin esters modified in classical batch conditions. These results show that REX can be used as a new fast, solvent free, and continuous process for lignin valorization.

Keywords: plasticizing, kraft lignin, esterification, ^{31}P NMR, DMSO, extrusion

OPEN ACCESS

Edited by:
Florent Allais,
AgroParisTech Institut des Sciences et Industries du Vivant et de L'environnement, France

Reviewed by:
Jean-Marie Raquez,
University of Mons, Belgium
Stephane Grelier,
Université de Bordeaux, France

***Correspondence:**
Romain Milotskyi
romain-mi@se.kanazawa-u.ac.jp

Specialty section:
This article was submitted to Chemical and Process Engineering, a section of the journal Frontiers in Chemistry

Received: 20 June 2019
Accepted: 02 September 2019
Published: 18 September 2019

Citation:
Milotskyi R, Szabó L, Takahashi K and Bliard C (2019) Chemical Modification of Plasticized Lignins Using Reactive Extrusion. Front. Chem. 7:633. doi: 10.3389/fchem.2019.00633

INTRODUCTION

Lignin constitutes one of the main chemical families in plant biomass (Gandini, 2011). Lignins are a polymeric form of variously methoxy-substituted phenylpropane monomeric units. Due to its general abundance (up to 20–30% in hardwood) and its slow biodegradability, lignin is likely to be one of the most abundant biopolymers on earth (Smolarski, 2012). Surprisingly apart from energy production in paper factories lignin finds very few industrial applications (Zakzeski et al., 2010). Production of high value added products such as vanillin has been obtained from lignin (Salvesen et al., 1948; Fache et al., 2016). The aromatic phenylpropane nature of lignin offers some similarity with aromatic polymers. Unfortunately, as its complex mixed structure depends on the extraction process, lignin processing is difficult to carry out and not conducive to chemical process development. Moreover, the difficulty in solubilizing and fractionating renders lignin difficult to process at the industrial level (in non-aqueous media). Various examples of lignin chemical modification have been developed in order to adapt the properties to specific applications (Glasser and Jain, 2009; Laurichesse and Avérous, 2014; Konduri et al., 2015; Kai et al., 2016; Ryohei et al., 2017; Sakai et al., 2018; Szabó et al., 2019). Modification of the aliphatic and aromatic hydroxyl groups of lignin via esterification is a typical approach (Laurichesse and Avérous, 2014). Several esterification agents have been applied to synthesize new lignin derivatives: acetic, propionic and butyric anhydrides (Fox and McDonald, 2010); maleic, succinic and phtalic anhydrides (Chen et al., 2014); palmitic and lauric acid chloride (Hult et al., 2013). Thielemans and Wool (2005) showed that in unsaturated thermosetting composites, incorporated butyrated kraft lignin plays a role in reinforcing, plasticizating, and influencing the cure kinetics of the polymerizing resin. Maleated lignin was successfully mixed with recycled polystyrene showing higher miscibility than native lignin (Schorr et al., 2015) and slightly higher thermal stability compared to native polystyrene (Lisperguer et al., 2013).

Reactive extrusion (REX) is a fast developing technique that shows high potential in producing chemically modified bio-sourced polymeric material from small to large scale (Berzin and Hu, 2004; Formela et al., 2018; Milotskyi et al., 2018). It can be applied to a wide range of highly viscous materials. Reactive extrusion itself can be considered as a green manufacturing process as compared to conventional chemical modification processes: it does not require solvents; it is very energy efficient; it allows clean reaction processes with fast kinetics, even when applied to large scales. Only a few examples of REX modified lignin can be found in the literature (Bridson et al., 2013; Fernandes et al., 2014; Luo et al., 2016). In this paper we describe the chemical modification of lignin with maleic and succinic anhydrides using REX. Both maleic and succinic anhydrides have the potential to be synthesized from biomass-based feedstocks (Bechthold et al., 2008; Li et al., 2018). Moreover, after anhydride opening and reaction with lignin, the free carboxyl group formed can be used for self-polyesterification to form biobased thermosetting polyester coatings (Scarica et al., 2018). More specifically, the main objective of this work was to intensify the process of lignin esterification and investigate the influence of reaction parameters on lignin conversion during REX. New plasticizer systems were developed for lignin processing with relatively low temperature (140°C).

EXPERIMENTAL

Materials

Two Lignins: KL pH6 ("Lignin, alkali" Aldrich 370959, insoluble in water) which will be noted KL in this work and KL pH10.5 ("Lignin, alkali," low sulfonate content, Aldrich 471003, soluble in water) which will be noted KLS were provided by Sigma—Aldrich (St. Louis, USA). Succinic anhydride (SA) and maleic anhydride (MA) were purchased from Alfa Aesar (Karlsruhe, Germany). Glycerol, ethylene glycol and DMSO were purchased from VWR International (Fontenay-sous-Bois, France). The reactor used in this study was the "Minilab Rheomex CTW5" (RHEO S.A., Champlan, France). This apparatus is designed for compounding polymers in a thermostated heat block with a production capacity of 100 g/h. It is also designed for analyzing the rheological behavior of polymer melts on small scale. The system is based on a conical, twin-screw compounder. Two different types of screw geometry (co- and counter- rotating) can be used in order to study the reaction differences according to the mixing mode. Due to a particular design only very small sample amounts (10 g) are needed in its integrated backflow channel. In this study, the conical co-rotating screws mode was chosen over the counter-rotating one because of its superior mixing ability (Milotskyi and Bliard, 2018). The extruder was operated at a screw speed of 60 rpm in the direct and recirculation (loop) modes. The melt-mass flow-rate was determined by weighting extrudates in known time intervals.

Synthetic Procedure

Preparation of Samples for Extrusion

At first, the processability of the two lignins KL and KLS in REX conditions was studied. All attempts to extrude the lignins without any added plasticizer resulted in blocking the extruder due to excessive torque value, exceeding the machine parameters. To address this problem the plasticizing of lignins by using different plasticizers: DMSO, glycerol, ethylene glycol was studied.

Each lignin was milled with a mortar and pestle and then mixed with the corresponding amount of plasticizer at room temperature. The mixture was then introduced into the extruder through the feed hopper and extruded in re-circulation mode to obtain melt viscosity information. The conditions and results of plasticizing are discussed further in this article.

Esterification of Lignins Using REX

To carry out the esterification reaction, 7 g of the plasticized KL was weighed and a corresponding mass of maleic or succinic anhydride calculated with respect to the dry mass of lignin (without plasticizer) was added. The mixture was introduced into the reactor preheated to the selected temperature and was then extruded using the direct mode. In order to evaluate reproducibility, each experiment was repeated at least three times except when noted. The amount of ester reagent (SA or MA) was 0.1, 0.2 and 0.3 equivalents per average phenylpropane unit (Molar mass 178 g/mol, average of the molecular weights of the three monomeric units *p*-coumaryl, coniferyl, and sinapyl alcohol). A reference sample named KL_{ref} was extruded with 25% DMSO without reagents at an extrusion temperature of 140°C and a screw speed of 60 rpm using the direct mode.

Purification of Reacted Extrudates

The KL was purified as follows to remove residues of free maleic or succinic acid or their anhydrides possibly present in the final mixture:

The reaction mixture of KL was crushed in a mortar and the obtained powder was purified with a method adapted from Chen et al. (2014) with some modifications: washing with distilled water and sodium bicarbonate for 24 h with agitation. The resulting powder was then recovered by filtering off the aqueous phase on Whatman filter paper. The modified lignin was dried for 24 h at room temperature in open air, and then overnight in a vacuum oven at 60°C.

Esterification of Lignins in Batch

One gram of kraft lignin (KL) was dissolved in 50 mL pyridine and 0.1/0.2/0.3 equivalent of acylating reagent -succinic anhydride or maleic anhydride- was added to the solution. The reaction was kept for 24 h at room temperature. The obtained product was collected after pouring the solution into 500 mL acetone, and dried in a vacuum drying oven at 70°C for 24 h.

Specific Mechanical Energy (SME)

Specific mechanical energy (SME) is the amount of mechanical energy (work) transferred to the melted mix and dissipated as heat inside the material, expressed per mass unit of the material.

SME is calculated using Equation 1 according to Li et al. (2014) as follows:

$$\text{SME (J/kg)} = (\text{Screw speed (rpm)} \times \text{Torque (N} \times \text{m)} \times 60)/(\text{Feed rate (kg/h)}) \quad (1)$$

Elemental Analysis (C, H, S, N)

A Perkin Elmer 2400 Series II-CHNS/O Elemental Analyzer was used to determine carbon, hydrogen, nitrogen and sulfur contents by catalytic combustion. The oxygen content was estimated on the assumption that the samples contained only C, H, N, S, and O. The samples were dried in vacuum at 80°C prior to the analyses.

Fourier Transform InfraRed Spectroscopy (FTIR)

The FTIR analysis was carried out in absorption mode on KBr pellets mixed with the powdered samples. The spectra were obtained on a Nicolet FT-IR 470 spectrophotometer (Nicolet Instrument Corporation, USA) at 4,000–400 cm^{-1} at a resolution of 4 cm^{-1}. The number of accumulated spectra is 32.

Samples synthesized in batch conditions were analyzed using Thermo Fisher Scientific Nicolet iS10 (Thermo Fisher Scientific, Inc., Tokyo, Japan) spectrophotometer equipped with an attenuated total reflection (ATR) unit. The number of accumulated spectra is 64.

Nuclear Magnetic Resonance Spectroscopy

The HSQC NMR spectra were obtained in DMSO-d_6 as a solvent. The recording was tuned for a one bound coupling of 145 Hz. The number of scans was 48; the acquisition time 0.14 s and the relaxation delay 5 s. The data matrix was 256/2048 (covering 22,640 Hz in F1 and 7,100 Hz in F2).

Phosphorus-31 NMR spectrometry was used in order to quantify aliphatic and aromatic hydroxyl groups as well as carboxylic acid groups in lignins. In order to carry out the analysis it was necessary to phosphitylate the lignins with 2-chloro-4,4,5,5-tetramethyl-dioxaphospholane as the phosphitylating reagent prior to recording. This reagent was synthesized in our laboratory from pinacol and phosphorus trichloride and purified by distillation according to the method described by Zwierzak (1967) as follows. A solution of pinacol (0.2 mole) and distilled triethylamine (0.4 moles) in cyclohexane (150 mL) was added dropwise to a solution of phosphorus trichloride (0.2 mole) in cyclohexane (200 mL) at 5–10°C with efficient stirring and cooling. The mixture was kept for 1 h at room temperature and filtered. The resulting triethylamine hydrochloride crystals were filtered off and washed with cyclohexane (200 mL). Evaporation of the filtrate and careful vacuum distillation of the residue gave pure 2-chloro-4,4,5,5-tetramethyl-dioxaphospholane. The yield after distillation was 36%.

The solvent used for ^{31}P NMR was a mixture of pyridine and deuterated chloroform (1.6:1 v:v) protected from moisture using 4 Å dry molecular sieve. A solution of relaxation agent was prepared by mixing 5 mg of relaxation reagent (chromium III acetylacetonate) in one milliliter of the prepared solvent. The internal standard solution was prepared with 10.85 mg/ml of cyclohexanol in prepared solvent. For this experiment, 30 mg of lignin was accurately weighed into a 1 mL volumetric flask. The sample was then dissolved in 0.5 mL of the above solvent mixture. 2-Chloro-4,4,5,5-tetramethyl-dioxaphospholane (50 μL) was then added, followed by the internal standard and the relaxation agent solution (100 μL each). Finally, the solution was filled to 1 mL with more solvent mixture. The volumetric flask was closed and stirred to ensure complete mixing. The spectra were obtained at 202.45 MHz with inverse-gated decoupling. The pulse lengths corresponded to a 30° pulse. The number of scans was 128, the acquisition time 0.55 s, the relaxation delay 12 s, the spectral widths 294 ppm, the carrier frequency 140 ppm.

Solid-state ^{13}C CP/MAS NMR spectra were obtained at 10 kHz on a ECX-500II spectrometer (JEOL Ltd., Tokyo, Japan). At least 4096 scans were averaged for each spectrum. In the case of sample "Batch KL0.3MA" the number of scans was increased to 10,000 to obtain a spectrum with high resolution. A single contact time of 2 ms, a delay of start of 1.01 s, and proton preparation pulse of 2.71 μs were used. Lignin methoxyl peak (52 ppm) was used as a reference. The DS is calculated using Equation 2 as described by Bridson et al. (2013),

$$DS = I_1/(I_2 * n) \quad (2)$$

where I_1 is the sum of grafted maleic anhydride carbonyl (165 ppm) and CH integrals (126 ppm), I_2 is the methoxyl integral (assuming a stoichiometric number of methoxyl groups), n is the number of maleate carbons (4). The corresponding reaction efficiency (RE) was calculated using Equation 3:

$$RE = DS/(MA/L) * 100\% \quad (3)$$

where DS is the degree of substitution obtained from Equation 2 and MA/L is the mole ratio of maleic anhydride (MA) to lignin C_9 unit.

GPC/SEC Chromatography

The molecular weight of native and modified lignins was determined by size exclusion chromatography (SEC, Prominence UFLC system, Shimadzu Co., Kyoto, Japan) based on polystyrene standards. All GPC/SEC measurements were carried out at 40°C using TSK gel α-M (Tosoh Co., Tokyo, Japan). Samples were dissolved in DMF containing 0.01M of LiBr. The final concentration was 1 mg of polymer in 1 ml of solvent. Before injection, the samples were filtered through a 0.2 μm syringe PTFE filter. The same solvent was used as eluent at the flow rate of 1.0 ml/min. RID-10A Refractive Index Detector (Shimadzu Co., Kyoto, Japan) was used in this study.

Thermogravimetric Analysis

The TA Instruments 2950 Thermogravimetric Analyzer (TGA) 2950 was used to determine the degradation temperature of native and modified lignin samples under nitrogen flow. The samples were analyzed up to a temperature of 650°C at a rate of 10°C/min.

RESULTS AND DISCUSSION

Lignins Processing

At first, the processability of the two native lignins without plasticizer was tested in the extruder within the 140–180°C temperature range. In this case, no melt behavior was observed for both lignins in the chosen range of temperatures. Three plasticizers DMSO, ethylene glycol and glycerol were then studied as potential plasticizers. Results of lignin plasticization using the different plasticizers are given in **Table 1**. The extrusion temperature was fixed at 140°C with a screw speed of 60 rpm during 5 min using recirculation mode.

In the case of the sample where 15% DMSO was used, extrusion is characterized by fairly high SME values; as the maximum torque for the Minilab Rheomex CTW5 is 5.5 N × m, below 15% DMSO the extrusion was not possible on this extruder due to excessive torque values. The addition of supplementary amounts of plasticizer decreased SME and melt viscosity. The melt viscosity values for mixtures prepared with ethylene glycol and glycerol were similar. In conclusion, DMSO gave the best results in providing lignin with a good melting behavior. The two other plasticizers used in this study, polyols -ethylene glycol and glycerol-, were only tested with KLS lignin as they were previously studied for KL lignin (Bouajila et al., 2006). DMSO was then chosen as a main plasticizer as it is compatible with lignin and it has a relatively high boiling point (191°C) compatible with the extrusion conditions and does not interfere with the reagents. In addition, to our knowledge, it had not yet been studied for lignin plasticization applications.

Esterification of Lignins by Reactive Extrusion

At first reactive extrusion of native KL (without plasticizer) with MA and SA was tested at a temperature of 175°C, without plasticizer, as described by Bridson et al. (2013). A molar ratio of 0.2 of MA and SA was used for this test. However, no fusion was observed in our case, indicating that the addition effect of the anhydrides did not improve the melting behavior of KL lignin. REX esterification of lignin was then conducted using previously plasticized KL lignin with 25% of DMSO at 140°C.

TABLE 1 | Results of lignins plasticization with different plasticizers.

Lignin/plasticizer system	Torque (N × m)	SME (kJ/kg)	Melt viscosity (Pa.s)
KL 15% DMSO	3.3	237	4.9×10^3
KL 20% DMSO	2	144	1.2×10^3
KL 25% DMSO	1.8	130	4×10^2
KLS 20% DMSO	1.7	122	8.96×10^3
KLS 20% Et Glycol	1.4	101	2.5×10^3
KLS 20% Glycerol	1,5	108	2.4×10^3

Elemental and FTIR Analysis

In both ester types, elemental analysis showed a decrease in the amount of analyzed carbon in all esterified products, compared to unmodified lignins. For example, the carbon content of native KL before extrusion was 63.42% (±0.11), after extrusion of KL with 0.1 maleic anhydride, it decreased to 62.01% (±0.02) and to 60.02% (±0.13) after extrusion with 0.3 MA. The decrease in carbon content was observed for KL modified with SA, from 61.88% (±0.04) for KL0.1SA to 58.86% (±0.24) for KL0.3SA. This result confirms the addition of succinic and maleic groups to the lignin, which contain a lower proportion of carbon. FTIR results show that in both cases, a band of carbonyl groups is present at 1722 cm^{-1} for 0.1, 0.2, and 0.3 MA and SA, the intensity of this band increases with the quantity of anhydride added (**Figure 1**). All these results confirm the substitution of OH groups in lignins and their transformation into esters. FTIR spectra of samples synthesized in batch are presented in Supporting Information (**Figures S1**, **S2**).

HSQC NMR Analysis

The disperse and complex structure of lignin makes ^1H and ^{13}C NMR analysis very difficult. On the other hand, 2D NMR spectroscopy yields spectra that provide more useful information. HSQC analyses of lignins (in DMSO-d_6) were performed. The signal of DMSO was set at 2.5 ppm for ^1H and 39.5 ppm for ^{13}C. The HSQC spectra of native KL and KL modified with 0.2 MA were compared. As can be seen in the enlargement of this spectrum (**Figure 2**: blue signals for native KL CH or CH_3 and red/pink signals for KL 0.2MA CH or CH_3/CH_2), two new spots appeared at (1) 6.37 ppm (^1H); 128.7 ppm (^{13}C) and (2) 6.39 (^1H); 131.3 (^{13}C). These signals are attributed to the CH groups of the grafted maleic anhydride. These signals are absent for the native KL. In addition, they do not correspond to the signals of MA or maleic acid that could be formed during the washing of samples with water. The appearance of two spots and not only one is due to the different chemical environment of these two CH groups: ester on one side and carboxylic acid on the other. This trend is observed for all samples (0.1; 0.2 and 0.3 MA). This confirms that the esterification reaction has occurred. In this case, the reaction is a mono-esterification. This result is in good agreement with the elemental and FT-IR analysis.

In the same manner, the HSQC spectra of native and succinic anhydride modified lignin 0.2SA KL were superimposed (**Figure 3**) -blue/green signals: CH or CH_3/CH_2 for the native KL; Red/pink signals: CH or CH_3/CH_2 for KL0.2SA-. As in the case of MA, the HSQC enlargement of SA modified KL confirms the appearance of two new signals (pink) corresponding to CH_2 groups with different chemical environment. Full HSQC spectra for KL0.2MA and KL0.2SA are available in Supporting Information (**Figures S3**, **S4**).

Phosphorus NMR Analysis

The obtained proportions of the different hydroxyl and carboxylic acid groups (in mmol/g) for both MA and SA modified KL are summarized in **Table 2**. For both anhydrides, the total amount of hydroxyl decreases during the reaction. After esterification, the hydroxyl content decreased by 34%

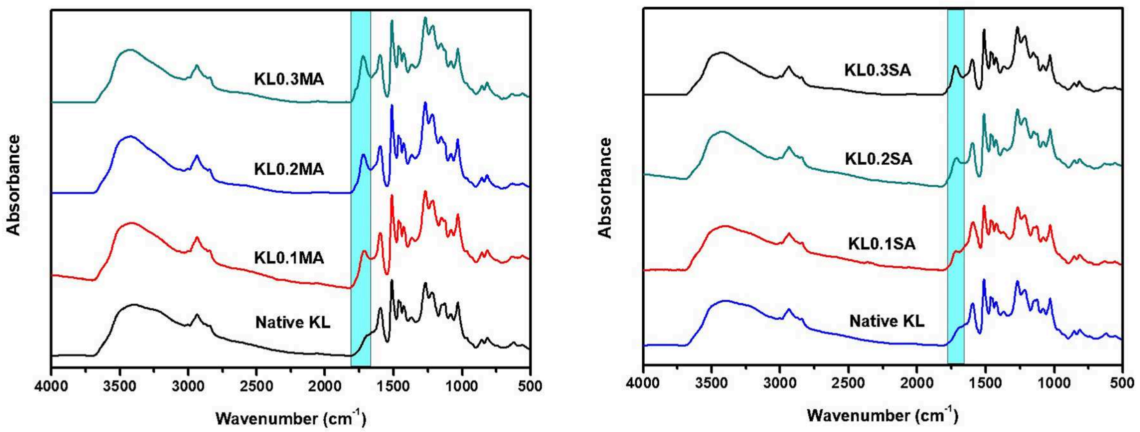

FIGURE 1 | FTIR spectra of KL modified with different ratio of maleic **(Left)** and succinic **(Right)** anhydrides.

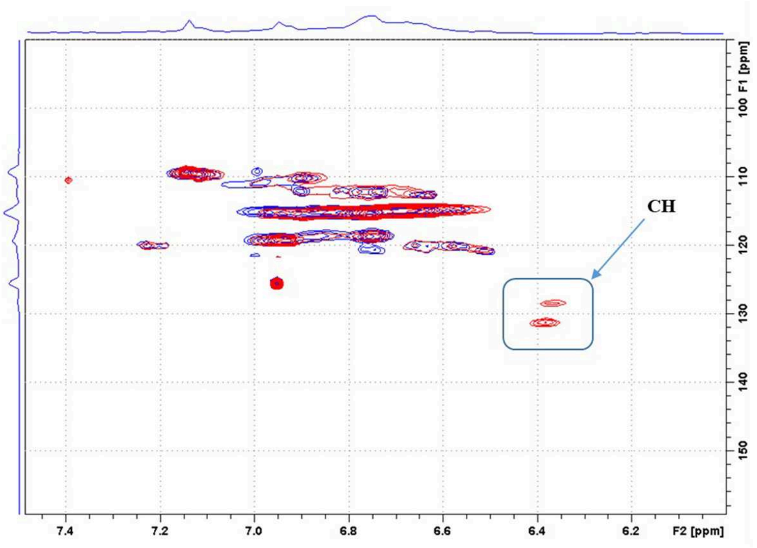

FIGURE 2 | HSQC spectrum of native KL and KL0.2MA in DMSO, aromatic zone.

(KL0.3MA). This also confirms that the esterification has taken place. The carboxylic acid content increased after esterification. Aliphatic and aromatic hydroxyls show a different reactivity. A 48% decrease was observed for the aliphatic hydroxyl content while only 23% of the phenolic hydroxyl reacted. Therefore, esterification was more effective on aliphatic hydroxyl groups than on phenolic hydroxyl groups. This trend was also observed by Ahvazi et al. (2011) during the esterification of kraft lignin with MA in batch. On the other hand, Bridson et al. (2013) described the possible decrease in aliphatic hydroxyl and carboxylic acids after extrusion of kraft lignin without plasticizer. According to them, the decrease in hydroxyl levels is probably due to dehydration reactions leading to condensation. These results highlight condensation reactions when using reactive extrusion for lignin chemical modification. Similar results can be observed for the esterification reaction with succinic anhydride. The percentage of hydroxyl decreases after esterification, with the increase in the amount of carboxylic acid. Aliphatic OHs are also more reactive than aromatic OHs. The sample KL0.3SA was not soluble in the used solvent system. The reference sample (KL_{ref}) showed a decrease in both aromatic and aliphatic OHs as well as carboxyl groups. Phenolic OH groups decreased from 1.81 mmol/g for native KL to 1.42 mmol/g. Aliphatic OHs decreased from 1.54 mmol/g (native KL) to 1.39 mmol/g (KL_{ref}). This result reveals that the structure of lignin changes during the REX process even when no reagent is used. In contrast, the samples of KL modified with MA and SA prepared in batch conditions show very poor solubility in pyridine/deuterated chloroform mixture used for ^{31}P NMR, which might further indicate (along with the increase in molecular weight) a possible crosslinking between free

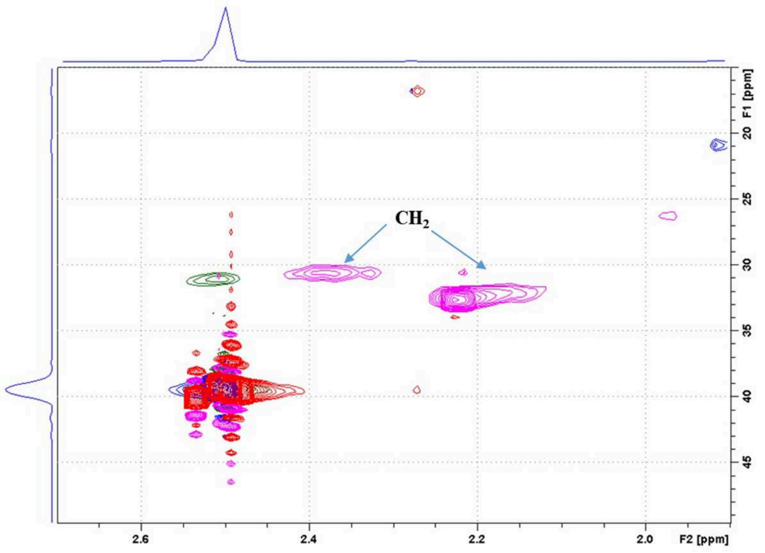

FIGURE 3 | HSQC spectrum of native KL and KL0.2SA in DMSO, aliphatic zone.

TABLE 2 | Proportion in mmol/g of lignin, of the different hydroxyl groups and carboxylic acids of native and esterified KL.

KL	COOH	G-OH	S-OH	H-OH	Total phenolic-OH	Total aliphatic-OH	Total hydroxyl
Native	0.22	1.43	0.23	0.15	1.81	1.54	3.35
0.1 MA	0.28	1.31	0.18	0.12	1.61	1.3	2.91
0.2 MA	0.34	1.25	0.14	0.1	1.49	1.15	2.64
0.3 MA	0.56	1.2	0.12	0.08	1.40	0.8	2.2
0.1 SA	0.27	1.32	0.2	0.1	1.62	1.25	2.87
0.2 SA	0.42	1.29	0.12	0.08	1.49	1.2	2.69

carboxyl groups of grafted anhydride and the residual hydroxyl groups still present in lignin.

Solid-State ^{13}C CP-MAS NMR

It was not possible to calculate the DS of esterified lignin samples using ^{31}P NMR due to possible dehydration involving hydroxyl groups of lignin. On the other hand, Solid-state ^{13}C CP-MAS NMR allows us to calculate the DS using the signals of grafted carbonyl groups after esterification. **Figure 4** shows solid-state ^{13}C CP-MAS NMR spectra of native and modified (KL0.3MA) lignins. It can be seen that after esterification with maleic anhydride the carbonyl group (175 ppm) which is present in native lignin in small quantity increases significantly and shifts to higher field (163 ppm). This shift can be explained by the difference in the chemical environment of carbonyl functions in native and esterified lignins. The DS of modified sample (KL0.3MA) was found to be 0.18 with a corresponding RE of 60%. The Solid-state ^{13}C CP-MAS NMR spectrum of batch modified KL (Batch KL0.3MA) is shown in Supporting Information (**Figure S5**). The DS of this sample is 0.19 with RE of 63%.

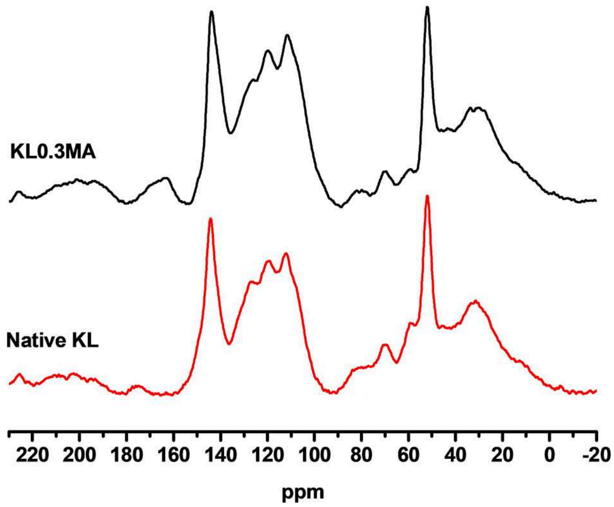

FIGURE 4 | Solid-state ^{13}C CP-MAS NMR spectra of Native KL and KL modified with 0.3 equivalents of MA.

GPC/SEC Chromatography

Chemical modification of lignin in REX conditions, where shear rate and temperature play essential role, can have a direct influence on molecular weight distribution. It was found that for native lignin M_w is 10,800 g/mol with a polydispersity of 8.91. As we can see in **Figure 5**, after extrusion the polydispersity increases significantly for both MA and SA lignin esters. However, the chromatograms are different for two reagents. In the case of KL modified with MA, a new peak with $M_w = 560$ g/mol appeared in the area of low molecular weight fractions, which increases with increasing ratio of the anhydride. This can be explained by possible lignin chain cleavage during REX conditions (Bridson et al., 2013). The original peak of

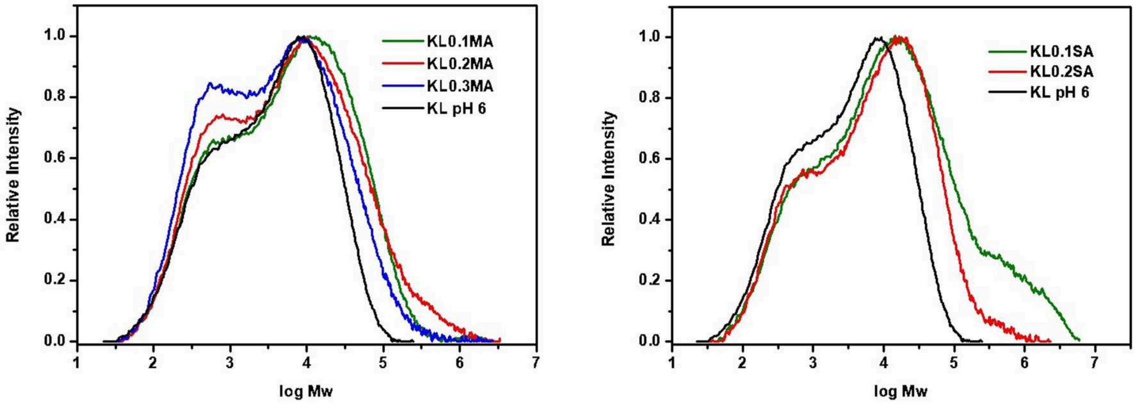

FIGURE 5 | GPC/SEC chromatograms of REX modified KL with maleic **(Left)** and succinic **(Right)** anhydrides.

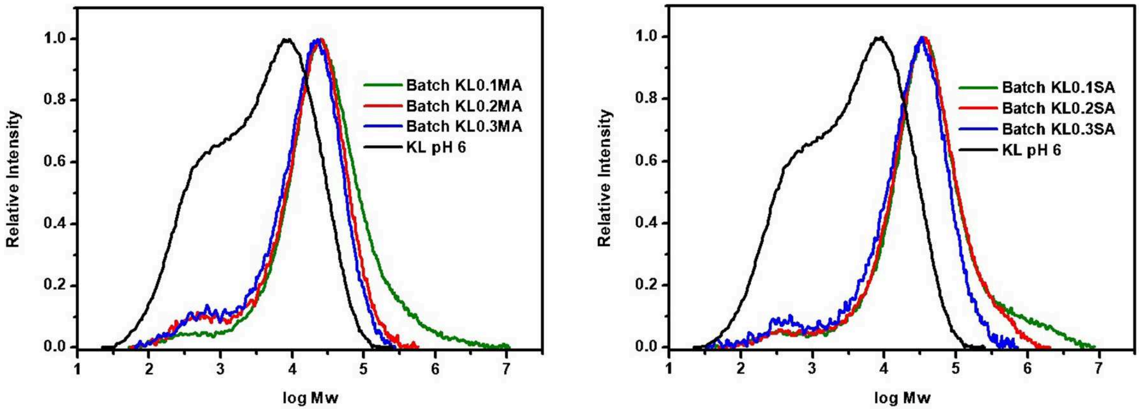

FIGURE 6 | GPC/SEC chromatograms of KL modified in batch with maleic **(Left)** and succinic **(Right)** anhydrides.

lignin becomes broader after the reaction. For KL modified with SA, there are no changes in low molecular weight area. At the same time, the original peak is shifted toward higher molecular weight showing higher polydispersity than native KL. These results show that REX can change the structure and properties of lignin. In contrast, KL esterified in batch conditions (**Figure 6**) shows a shift of molecular weight profiles toward higher molecular weights for both anhydrides. In this case, one possible explanation could be intra- and intermolecular crosslinking between remaining hydroxyls of lignin and free carboxyl groups newly generated after the reaction with the anhydride. As previously mentioned (section Phosphorus NMR analysis), the KL samples esterified in batch show poor solubility in ^{31}P NMR solvent which also indicates the possible crosslinking in the lignin polymer. The crosslinking has an influence not only on lignin molecule but also on the properties of lignin-based materials (Lang et al., 2018). However, the polydispersity decreases in the case of reaction in batch from 8.91 for native KL to 6 for Batch KL0.3MA and 7.82 in case of Batch KL0.3SA. This result could be also due to the purification procedure, with the low molecular weight fractions being more soluble in acetone. To highlight the influence of REX parameters on the lignin transformation, the reference sample KL_{ref} was studied by GPC/SEC. It was found that after extrusion, the molecular weight and polydispersity of lignin increase (M_w = 15900, M_w/M_n = 11). This result confirms that temperature and shear rate have a significant influence on lignin structural changes. The future interest in lignin transformation using REX would be to explore if these changes are directly correlated to SME and if it is possible to control the average molecular weight and polydispersity of the obtained product by the extrusion process parameters.

Thermal Analysis of Native and Modified KL

Native and modified KL were analyzed using TGA (**Figure 7**). For all samples, a weight loss of about 5–8% at temperatures up to 100°C corresponds to water loss. The water loss percentage increases with the increase of succinic anhydride. This result confirms that modified samples become more hydrophilic. During additional heating, the onset of degradation occurred between 135 and 200°C. Typically, the degradation rate reaches a maximum between 300 and 400°C. During this stage (up to 600°C) the pyrolysis of the lignin takes place, resulting

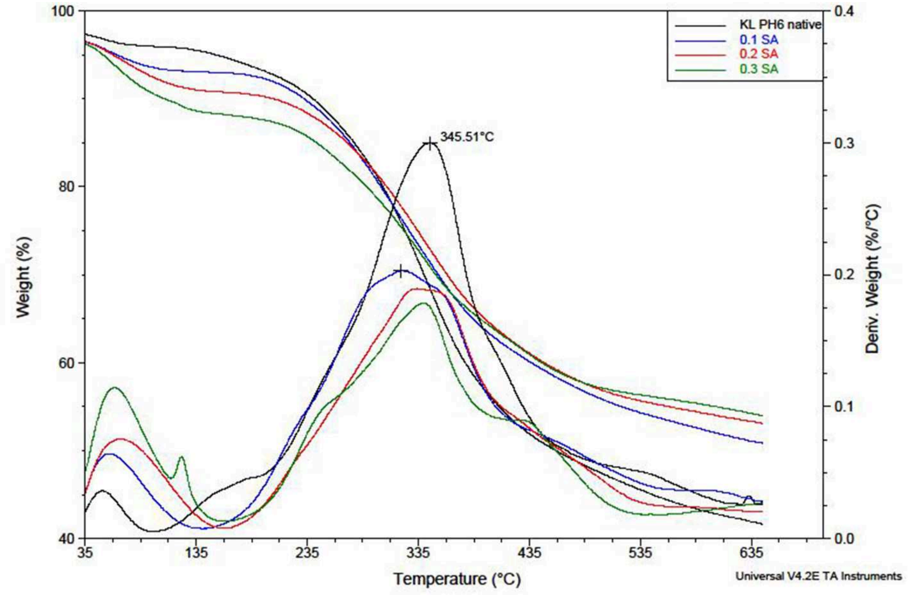

FIGURE 7 | TGA and DTG curves (recorded under nitrogen atmosphere) of native kraft lignin and kraft lignin esterified with SA.

in the breaking of the C-C and C-O bonds of the side chains, the condensed bonds and the breaking of the ether bonds (Cao et al., 2013). From 600°C, the formation of amorphous carbon residue is observed. The samples of KL modified with succinic anhydride all show a slower degradation compared to native lignin. The same behavior is observed in the case of MA. However, no significant changes in thermal behavior between native KL and the reference sample are observed.

CONCLUSION

In summary, we found that kraft lignin maleic and succinic esters can be prepared in very short reaction time (<1 min) in a homogeneous medium and by using low amounts of plasticizer (15–25%) in a reactive extrusion process. Native lignin shows no melting behavior. We showed that small amounts of DMSO renders lignin processable when low extrusion temperature (140°C) is applied. 2D NMR spectroscopy revealed that the reaction of lignin transformation via REX is a monoesterification. At the same time, the molecular weight and polydispersity increase in high shear rate + temperature REX conditions resulting in lignin molecules crosslinking. GPC chromatograms after extrusion showed a shift toward higher molecular weights. A similar shift was also observed for samples prepared in batch conditions. In contrast, the polydispersity decreases for lignin esters synthesized in batch. REX esterified lignin samples show slower degradation compared to native lignins. These new lignin derivatives could be used in combination with other polymers to produce new plastics. Due to the presence of a pendant reactive double bond maleated lignin could be used as a macromonomer for further polymerization or copolymerization synthesis.

DATA AVAILABILITY

All datasets generated for this study are included in the manuscript/**Supplementary Files**.

AUTHOR CONTRIBUTIONS

All the authors have contributed to the work presented in the manuscript to an extent that is consistent with the criteria for authorship. All the authors have agreed with the contents.

ACKNOWLEDGMENTS

The authors would like to thank the Champagne-Ardenne regional council for the financial support of this research through the POLIMER project. A part of this work was supported by the Center of Innovation Science and Technology based Radical Innovation and Entrepreneurship Program [COI stream (JPMJCE1315)] of the Science and Technology Agency of Japan (JST). We would also like to thank Anthony Robert (ICMR, URCA) and Tetsuo Fujie (Institute of Science and Engineering, Kanazawa University) for their help with NMR measurements.

SUPPLEMENTARY MATERIAL

The Supplementary Material for this article can be found online at: https://www.frontiersin.org/articles/10.3389/fchem.2019.00633/full#supplementary-material

REFERENCES

Ahvazi, B., Wojciechowicz, O., and Hawari, J. (2011). Preparation of lignopolyols from wheat straw soda lignin. *J. Agric. Food Chem.* 59, 10505–10516. doi: 10.1021/jf202452m

Bechthold, I., Bretz, K., Kabasci, S., Kopitzky, R., and Springer, A. (2008). Succinic acid: a new platform chemical for biobased polymers from renewable resources. *Chem. Eng. Technol.* 31, 647–654. doi: 10.1002/ceat.200800063

Berzin, F., and Hu, G.-H. (2004). *Procédés d'extrusion réactive*. Techniques de l'ingénieur. AM3654 V1.

Bouajila, J., Dole, P., Joly, C., and Limare, A. (2006). Some laws of a lignin plasticization. *J. Appl. Polym. Sci.* 102, 1445–1451. doi: 10.1002/app.24299

Bridson, J. H., Van De Pas, D. J., and Fernyhough, A. (2013). Succinylation of three different lignins by reactive extrusion. *J. Appl. Polym. Sci.* 128, 4355–4360. doi: 10.1002/app.38664

Cao, J., Xiao, G., Xu, X., Shen, D., and Jin, B. (2013). Study on carbonization of lignin by TG-FTIR and high temperature carbonization reactor. *Fuel Process. Technol.* 106, 41–47. doi: 10.1016/j.fuproc.2012.06.016

Chen, Y., Stark, N. M., Cai, Z., Frihart, C. R., Lorenz, L. F., and Ibach, R. E. (2014). Chemical modification of kraft lignin: effect on chemical and thermal properties. *BioResources* 9, 5488–5500.

Fache, M., Boutevin, B., and Caillol, S. (2016). Vanillin production from lignin and its use as a renewable chemical. *ACS Sust. Chem. Eng.* 4, 35–46. doi: 10.1021/acssuschemeng.5b01344

Fernandes, E. M., Aroso, I. M., Mano, J. F., Covas, J. A., and Reis, R. L. (2014). Functionalized cork-polymer composites (CPC) by reactive extrusion using suberin and lignin from cork as coupling agents. *Compos. Part B Eng.* 67, 371–380. doi: 10.1016/j.compositesb.2014.07.028

Formela, K., Zedler, L., Hejna, A., and Tercjak, A. (2018). Reactive extrusion of bio-based polymer blends and composites – Current trends and future developments. *Express Polym. Lett.* 12, 24–57. doi: 10.3144/expresspolymlett.2018.4

Fox, C. S., and McDonald, A. G. (2010). Chemical and thermal characterization of three industrial lignins and their corresponding lignin esters. *Bioresources* 5, 990–1009.

Gandini, A. (2011). The irruption of polymers from renewable resources on the scene of macromolecular science and technology. *Green Chem.* 13, 1061–1083. doi: 10.1039/c0gc00789g

Glasser, W., and Jain, R. (2009). Lignin Derivatives. I. Alkanoates. *Holzforschung* 47, 225–233. doi: 10.1515/hfsg.1993.47.3.225

Hult, E. L., Koivu, K., Asikkala, J., Ropponen, J., Wrigstedt, P., Sipilä, J., et al. (2013). Esterified lignin coating as water vapor and oxygen barrier for fiber-based packaging. *Holzforschung* 67, 899–905. doi: 10.1515/hf-2012-0214

Kai, D., Tan, M. J., Chee, P. L., Chua, Y. K., Yap, Y. L., and Loh, X. J. (2016). Towards lignin-based functional materials in a sustainable world. *Green Chem.* 18, 1175–2000. doi: 10.1039/C5GC02616D

Konduri, M. K., Kong, F., and Fatehi, P. (2015). Production of carboxymethylated lignin and its application as a dispersant. *Eur. Polym. J.* 70, 371–383. doi: 10.1016/j.eurpolymj.2015.07.028

Lang, J. M., Shrestha, U. M., and Dadmun, M. (2018). The effect of plant source on the properties of lignin-based polyurethanes. *Front. Energy Res.* 6:4. doi: 10.3389/fenrg.2018.00004

Laurichesse, S., and Avérous, L. (2014). Chemical modification of lignins: Towards biobased polymers. *Prog. Polym. Sci.* 39, 1266–1290. doi: 10.1016/j.progpolymsci.2013.11.004

Li, M., Hasjim, J., Xie, F., Halley, P. J., and Gilbert, R. G. (2014). Shear degradation of molecular, crystalline, and granular structures of starch during extrusion. *Starch Stärke* 66, 595–605. doi: 10.1002/star.201300201

Li, X., Ko, J., and Zhang, Y. (2018). Highly efficient gas-phase oxidation of renewable furfural to maleic anhydride over plate vanadium phosphorus oxide catalyst. *ChemSusChem* 11, 612–618. doi: 10.1002/cssc.201701866

Lisperguer, J., Nunez, C., and Perez-Guerrero, P. (2013). Structure and thermal properties of maleated lignin-recycled polystyrene composites. *J. Chil. Chem. Soc.* 58, 1937–1940. doi: 10.4067/S0717-97072013000400005

Luo, S., Cao, J., and McDonald, A. G. (2016). Interfacial improvements in a green biopolymer alloy of poly(3-hydroxybutyrate-co-3-hydroxyvalerate) and lignin via *in situ* reactive extrusion. *ACS Sust. Chem. Eng.* 4, 3465–3476. doi: 10.1021/acssuschemeng.6b00495

Milotskyi, R., and Bliard, C. (2018). Carboxymethylation of plasticized starch by reactive extrusion (REX) with high reaction efficiency. *Starch Stärke* 70:1700275. doi: 10.1002/star.201700275

Milotskyi, R., Bliard, C., Tusseau, D., and Benoit, C. (2018). Starch carboxymethylation by reactive extrusion: Reaction kinetics and structure analysis. *Carbohydr. Polym.* 194, 193–199. doi: 10.1016/j.carbpol.2018.04.040

Ryohei, K., Ninomiya, K., Shibata, Y., Uzawa, K., Ogoshi, T., Maeda, K., et al. (2017). *Method for Producing Polysaccharide Derivative and Lignin Derivative*. EP 3 214 097 A1, European Patent Office, Munich, Germany.

Sakai, H., Kuroda, K., Tsukegi, T., Ogoshi, T., Ninomiya, K., and Takahashi, K. (2018). Butylated lignin as a compatibilizing agent for polypropylene-based carbon fiber-reinforced plastics. *Polym. J.* 50, 997–1002. doi: 10.1038/s41428-018-0088-9

Salvesen, J. R., Brink, D. L., Diddams, D. G., and Owzarski, P. (1948). *Process for Making Vanillin*. U.S. Patent No 2434626A. U.S. Patent Office.

Scarica, C., Suriano, R., Levi, M., Turri, S., and Griffini, G. (2018). Lignin functionalized with succinic anhydride as building block for biobased thermosetting polyester coatings. *ACS Sustain. Chem. Eng.* 6, 3392–3401. doi: 10.1021/acssuschemeng.7b03583

Schorr, D., Rodrigue, D., Diouf, P. N., and Stevanovic, T. (2015). Recycled polystyrene composites reinforced with esterified and non-esterified kraft lignins. *J. Mater. Sci. Res.* 4:63. doi: 10.5539/jmsr.v4n1p63

Smolarski, N. (2012). High-value opportunities for lignin: unlocking its potential. *F&S* 1, 1–15.

Szabó, L., Imanishi, S., Tetsuo, F., Hirose, D., Ueda, H., Tsukegi, T., et al. (2019). Lignin as a functional green coating on carbon fiber surface to improve interfacial adhesion in carbon fiber reinforced composites. *Materials* 12, 1–14. doi: 10.3390/ma12010159

Thielemans, W., and Wool, R. P. (2005). Lignin esters for use in unsaturated thermosets: lignin modification and solubility modeling. *Biomacromolecules* 6, 1895–1905. doi: 10.1021/bm0500345

Zakzeski, J., Bruijnincx, P. C. A., Jongerius, A. L., and Weckhuysen, B. M. (2010). The catalytic valorization of lignin for the production of renewable chemicals. *Chem. Rev.* 110, 3552–3599. doi: 10.1021/cr900354u

Zwierzak, A. (1967). Cyclic organophosphorus compounds I. Synthesis and infrared spectral studies of cyclic hydrogen phosphites and thiophosphites. *Can. J. Chem.* 45:2501. doi: 10.1139/v67-411

Conflict of Interest Statement: The authors declare that the research was conducted in the absence of any commercial or financial relationships that could be construed as a potential conflict of interest.

Copyright © 2019 Milotskyi, Szabó, Takahashi and Bliard. This is an open-access article distributed under the terms of the Creative Commons Attribution License (CC BY). The use, distribution or reproduction in other forums is permitted, provided the original author(s) and the copyright owner(s) are credited and that the original publication in this journal is cited, in accordance with accepted academic practice. No use, distribution or reproduction is permitted which does not comply with these terms.

frontiers in Chemistry

ORIGINAL RESEARCH
published: 30 October 2019
doi: 10.3389/fchem.2019.00730

Hierarchically Structured CeO_2 Catalyst Particles From Nanocellulose/Alginate Templates for Upgrading of Fast Pyrolysis Vapors

Kathleen Moyer[1], Davis R. Conklin[2], Calvin Mukarakate[2], Derek R. Vardon[2], Mark R. Nimlos[2] and Peter N. Ciesielski[3]*

[1] Interdisciplinary Materials Science Program, Vanderbilt University, Nashville, TN, United States, [2] National Renewable Energy Laboratory, National Bioenergy Center, Golden, CO, United States, [3] National Renewable Energy Laboratory, Biosciences Center, Golden, CO, United States

Hierarchically structured porous materials often exhibit advantageous functionality for many applications including catalysts, adsorbents, and filtration systems. In this study, we report a facile approach to achieve hierarchically structured, porous cerium oxide (CeO_2) catalyst particles using a templating method based on nanocellulose, a class of renewable, plant-derived nanomaterials. We demonstrate the catalyst performance benefits provided by this templating method in the context of Catalytic Fast Pyrolysis (CFP) which is a promising conversion technology to produce renewable fuel and chemical products from biomass and other types of organic waste. We show that variations in the porous structures imparted by this templating method may be achieved by modifying the content of cellulose nanofibrils, cellulose nanocrystals, and alginate in the templating suspensions. Nitrogen physisorption reveals that nearly 10-fold increases in surface area can be achieved using this method with respect to commercially available cerium oxide powder. Multiscale electron microscopy further verifies that bio-derived templating can alter the morphology of the catalyst nanostructure and tune the distribution of meso- and macro-porosity within the catalyst particles while maintaining CeO_2 crystal structure. CFP experiments demonstrate that the templated catalysts display substantially higher activity on a gravimetric basis than their non-templated counterpart, and that variations in the catalyst architecture can impact the distribution of upgraded pyrolysis products. Finally, we demonstrate that the templating method described here may be extended to other materials derived from metal chlorides to achieve 3-dimensional networks of hierarchical porosity.

Keywords: nanocellulose (NC), catalysis, fast pyrolysis, hierarchical structure, templated synthesis

OPEN ACCESS

Edited by:
Thomas James Farmer,
University of York, United Kingdom

Reviewed by:
Robin J. White,
Netherlands Organisation for Applied Scientific Research (TNO), Netherlands
Anandarup Goswami,
Vignan's Foundation for Science, Technology and Research, India

****Correspondence:***
Peter N. Ciesielski
peter.ciesielski@nrel.gov

Specialty section:
This article was submitted to Green and Sustainable Chemistry, a section of the journal Frontiers in Chemistry

Received: *15 July 2019*
Accepted: *11 October 2019*
Published: *30 October 2019*

Citation:
Moyer K, Conklin DR, Mukarakate C, Vardon DR, Nimlos MR and Ciesielski PN (2019) Hierarchically Structured CeO_2 Catalyst Particles From Nanocellulose/Alginate Templates for Upgrading of Fast Pyrolysis Vapors. Front. Chem. 7:730. doi: 10.3389/fchem.2019.00730

INTRODUCTION

The development of rapid, scalable, and environmentally sustainable methods to produce hierarchically structured porous materials can provide substantial benefit to many industrial processes due to the importance of these materials in applications such as catalysis, separations, and energy storage (Yang X.-Y. et al., 2017). Recent studies have highlighted the importance of controlling porosity of materials over multiple length scales in order to optimize transport phenomena coupled to adsorption/desorption processes and chemical reactions in filtration (Xu et al., 2014; Wisser et al., 2015; Liu et al., 2019) and catalytic applications (Feliczak-Guzik, 2018; Sierra-Salazar et al., 2018; Bharadwaj et al., 2019). Commonly employed strategies to produce these materials use templating methods that rely upon the self-assembly of surfactants, polymers, and nanomaterials (Yang X.-Y. et al., 2017). Nanocellulose (NC) materials are ideal candidates for such templating purposes for a variety of reasons, including their low cost (Nelson et al., 2016), tunable size and morphology (Brinchi et al., 2013), readily-modified surface chemistry (Habibi, 2014), large production capacity (Shatkin et al., 2014), controllable self-assembly behavior (Habibi et al., 2010), potential to be produced in tandem with renewable biofuels (Yarbrough et al., 2017), and environmental compatibility (Endes et al., 2016). The most common and readily available forms of nanocellulose typically fall into two distinct classes based on the size and shape of the particles: cellulose nanocrystals (CNC) which are typically 50–500 nm long with a diameter of 3–20 nm; and cellulose nanofibrils (CNF) which are classified as having a diameter of ~100 nm or less and length of 500 nm or longer and can form an entangled fibril network (Zhu et al., 2016). **Figure 1** presents images of cellulose nanofibrils (top row) and cellulose nanocrystals (bottom row) obtained by transmission electron microscopy (left column) and atomic force microscopy (right column). Various forms of NC have been investigated previously for catalyst synthesis applications. Many of these applications have used NC directly as a support for metallic nanoparticles as summarized in a recent review by Kaushik and Moores (2016). Alginate, an abundant polysaccharide derived from brown algae, has also been used to prepare high-surface area catalyst supports (Valentin et al., 2005). Additional studies have used NC as a template to achieve mesoporous materials (Shin and Exarhos, 2007; Cai et al., 2015; Kong et al., 2015; Chen et al., 2016; Yang L. et al., 2017; Shen et al., 2018) and hollow tubular structures (Korhonen et al., 2011; Torres-Rendon et al., 2016; Zhu et al., 2017). Several groups have utilized the ordered self-assembly behavior of negatively charged CNCs to achieve chiral mesoporous materials (Dujardin et al., 2003; Shopsowitz et al., 2010, 2011).

Here, we present a facile fabrication method to prepare hierarchically structured mesoporous materials using combinations of NC and alginate We demonstrate the effectiveness of our approach by preparing mesoporous cerium oxide (CeO_2) catalysts used for catalytic fast pyrolysis (CFP) which is promising thermochemical conversion technology for producing renewable fuels and chemicals from biomass (Ciesielski et al., 2018). The chemical composition and structural architecture of catalyst used in the pyrolysis process plays a critical role in determining the product slate that results from upgrading of pyrolysis vapors. Researchers have demonstrated that reducible metal oxides are effective at converting oxygenated pyrolysis products into useful monofunctional molecules (Lu et al., 2010). Based on the choice of catalyst, this process can be tuned to produce functional mono-oxygenated molecules, such as ketones and phenolics. Ketones and alcohols are desired monofunctional intermediates as they can undergo further C-O bond cleavage and C-C bond formation from the initial pyrolytic breakdown to yield various types of chemicals and fuels. A recent study by Mante et al. (2015) revealed that pure CeO_2 exhibits ketonization activity when used to upgrade cellulose pyrolysis vapors. The high catalytic activity of CeO_2 can be ascribed to its active redox properties involving exchange of Ce^{4+} and Ce^{3+} ions, Lewis basicity, and increased oxygen exchange and storage capacity (Mante et al., 2015). These features of CeO_2 imply its utility for the production valuable chemicals alongside biofuels in a CFP format which is a central strategy to improve economic viability (Cai et al., 2018). Native CeO_2 is known to have a high surface area that can effectively transport reactant molecules to active sites (Li et al., 2012); however, the bulk surface area of commercially available CeO_2 powders is low relative to many engineered catalysts used in industrial applications. The development of simple, tunable synthesis methods for high-surface-area CeO_2 catalysts remains a challenge (White et al., 2014).

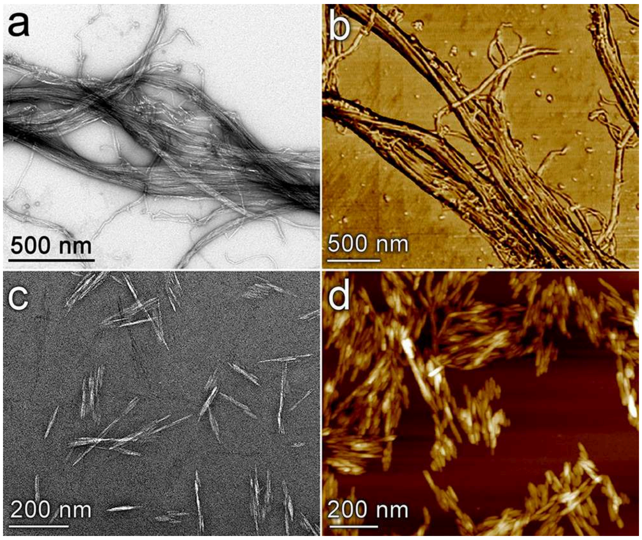

FIGURE 1 | Images of nanocellulose materials used as mesoporous catalyst templates. Cellulose nanofibrils **(a,b)** and cellulose nanocrystals **(c,d)** are visualized by transmission electron microscopy **(a,c)** and atomic force microscopy **(b,d)**. The image in **(b)** is a phase image; **(d)** is a topology image.

A promising approach for increasing the surface area of CeO_2 catalysts was offered by Laha and Ryoo (2003) who synthesized structured CeO_2 nanoparticles using silica templates which resulted in particles with uniform mesoporosity within a nanocrystalline framework. A similar approach was subsequently demonstrated for photocatalytic applications by Ji et al. (2008). While these studies demonstrated that increased surface area could be achieved, the synthesis methods required a premade mesoporous silica template, and the resultant materials lacked higher-order architecture that could serve to further enhance transport of reactants and products within larger catalyst particles. Our objective in the present study is to develop a simple, cost-effective template-assisted synthesis method for hierarchically structured CeO_2 catalyst particles that provide mesoporosity to enhance surface area in tandem with larger pores and channels to improve long-range transport throughout the catalyst.

MATERIALS AND METHODS

Catalyst Synthesis

A schematic illustrating the catalyst the synthesis procedure is presented in **Figure 2**. The first step consists of preparing an aqueous carbohydrate suspension to serve as the templating material. Several mixtures of CNFs, CNCs, and sodium alginate were prepared. Alginate is frequently used for synthesizing biopolymeric materials and is commonly used in the formation of hydrogel micro particles (Paques et al., 2014). This polysaccharide is negatively charged at neutral pH and is easily crosslinked to form a hydrogel in the presence of di- and trivalent cations; thus, dropwise addition of the carbohydrate mixture containing sodium alginate to a saturated $CeCl_3$ solution results in the formation of hydrogel beads crosslinked by Ce^{3+} ions. The bead formation process is similar to that commonly employed to form hydrogels by crosslinking alginate (Valentin et al., 2005), however the trivalent Ce^{3+} used in this study provides the crosslinking function similar to that typically contributed by Ca^{2+} ions. These beads are recovered from the solution and freeze dried to preserve the solution structure of the carbohydrate/Ce^{3+} matrix (De France et al., 2017). The resulting cryogel particles are then placed in a lab oven in air at 773 K for 4 h to burn off the carbohydrate and oxidize the Ce^{3+} to CeO_2.

Four different templating solutions were prepared to investigate the structural features imparted by each component: (a) 1.0 wt.% alginate, (b) 1.0 wt.% CNC 1.0 wt.% alginate, (c) 1.0

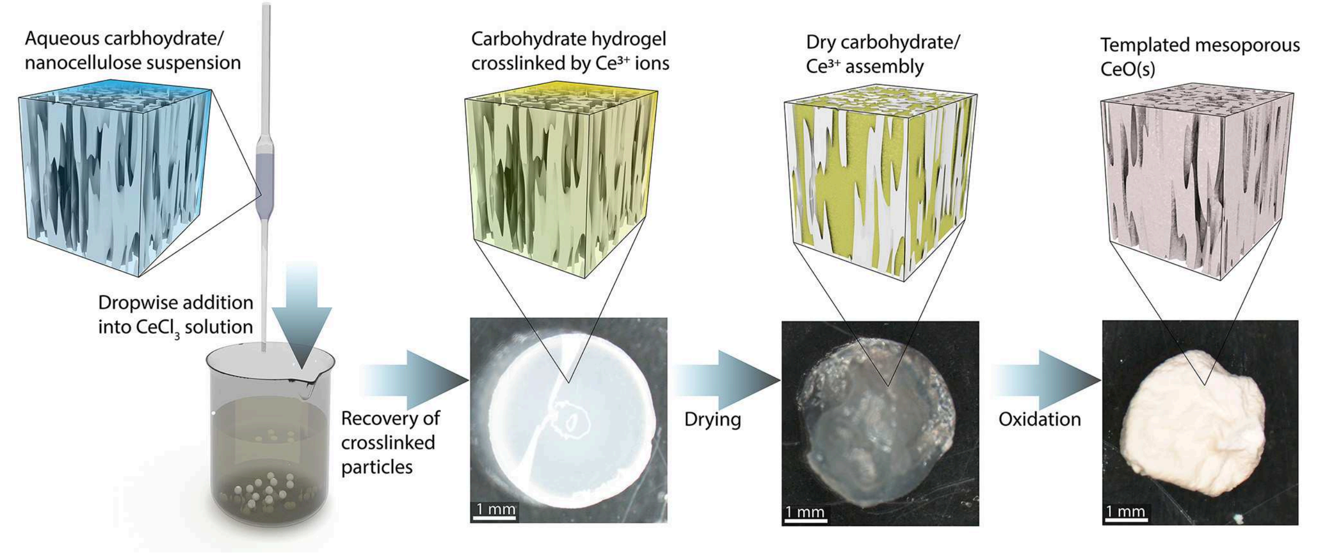

FIGURE 2 | Schematic depiction of the catalyst synthesis process. An aqueous suspension of NC and/or alginate is added dropwise to a solution of $CeCl_3$. The negatively charged carbohydrate components are crosslinked by the Ce^{3+} and form roughly spherical particles. The particles are recovered and freeze-dried. The dried particles are heated to 773 K in air to burn off the carbohydrate scaffold and oxidize the Ce^{3+} to CeO_2 (s).

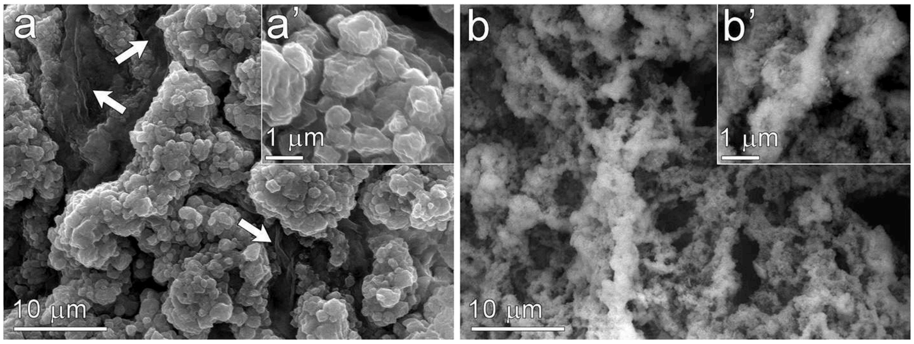

FIGURE 3 | Scanning electron micrographs of the CeO_2 catalyst templated by CNF, CNC, and alginate before **(a,a')** and after **(b,b')** removal of the carbohydrate template by high temperature oxidation. Arrows in **(a)** indicate carbohydrate domains likely contributed by bundles of CNF.

wt.% CNF 1.0 wt.% alginate, (d) 0.5 wt.% CNC 0.5 wt.% CNF 1.0 wt.% alginate. Alginate was included with the NC templating agents to ensure sufficient crosslinking would occur when the carbohydrate suspension was introduced into the $CeCl_3$ solution. A total carbohydrate content of ≤2 wt.% was used in each case in order to achieve a viscosity of the templating solution that facilitated consistent drop formation from the tip of the pipette. Attempts to use carbohydrate contents higher than 2% in the templating solution resulted in inconsistent flow from pipette tip which resulted in catalyst particles of heterogeneous size and shape. Sodium alginate and cerium (III) chloride heptahydrate ($CeCl_3 \cdot 7H_2O$, 99.9%), were purchased from Sigma-Aldrich. CeO_2 powder (Cerium (IV) oxide, powder, 99.995%) for use as a control was also purchased from Sigma-Aldrich. CNF (3 wt.% aqueous suspension, nominal width 50 nm, several 100 microns in length) and CNC produced by sulfuric acid hydrolysis (11.9% aqueous suspension, 5–20 nm width, 150–200 nm length) were purchased from the University of Maine Process Development Center.

Thermal Gravimetric Analysis (TGA)

To verify complete removal of the carbohydrate template during calcination, TGA was performed on cryogel particles templated with both CNC and CNF. Analysis was performed in static air with a ramp rate of 25°C min^{-1} up to 500°C followed by an isothermal hold at 500°C for 1 h.

X-Ray Diffraction (XRD)

The crystal structure of the catalyst materials was analyzed by XRD using a Rigaku Ultima IV X-ray diffractometer. The X-ray voltage was set to 40 kV and 44 mA, with a sampling width of 0.02° and scan speed of 5° min^{-1}. Metal crystallite sizes were estimated using the Williamson-Hall method with PDXL version 1.6.0.1 (Rigaku Corporation). ICDD PDF card number 01-075-9470 was used as a reference pattern for the cubic fluorite crystal structure of cerium (IV) oxide.

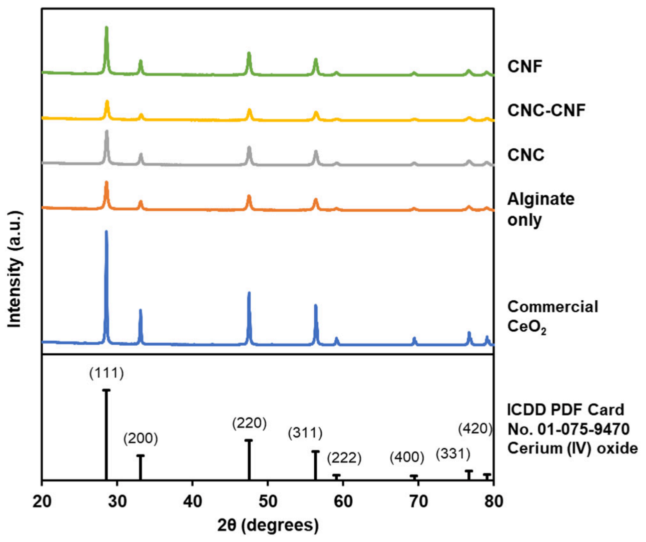

FIGURE 4 | XRD patterns of templated CeO_2 catalyst particles and commercial CeO_2 powder confirm that the templated material consists of polycrystalline CeO_2 in the cubic fluorite crystal structure.

Scanning Electron Microscopy (SEM) and Energy Dispersive X-Ray Spectroscopy (EDS)

SEM was performed using a FEI Quanta 400 FEG instrument. Samples were mounted on aluminum stubs with conductive carbon tape adhesive prior to imaging. The mounted samples were then sputter-coated with 5 nm of Ir. Images were obtained at accelerating voltages of 10 keV for low magnification and 30 keV for high magnification. EDS was performed using EDAX X-ray detector positioned within the same instrument. Elemental composition was obtained from the EDS spectra using the EDAX Genesis software package.

Transmission Electron Microscopy (TEM)

To prepare samples for imaging, catalyst particles were suspended in ethanol and drop-cast onto carbon-coated, 200 mesh copper grids (SPI Supplies, West Chester, PA). Grids were allowed to air dry prior to imaging. Imaging was performed using an accelerating voltage of 200 keV, and images were captured with a four mega-pixel Gatan UltraScan 1000 camera (Gatan, Pleasanton, CA) on a FEI Tecnai G2 20 Twin 200 kV LaB6 TEM (FEI, Hilsboro, OR).

Nitrogen Physisorption

Surface area, pore volume, and average pore diameter were determined by multipoint nitrogen physisorption using a Quantachrome QuadraSorb SI analyzer. Prior to measurement, catalysts were outgassed at 250°C for 18 h. The measurement was performed in liquid nitrogen at −196°C. BET analysis was used to obtain specific surface area, and BJH and t-plot methods were used evaluate pore volume and pore size. Points for BET analysis were selected to include the point of statistical monolayer formation and ensure that the product of the quantity adsorbed with (1–p/p0) was strictly increasing over the range of points included in the calculation (Sing, 2014). All BET fits had $R^2 > 0.998$. BJH analysis was performed on the adsorption branch

TABLE 1 | Material properties of commercial and templated CeO_2.

Templating agent	Surface area ($m^2\ g^{-1}$)	Mesopore volume ($cm^3\ g^{-1}$)	Mean crystallite size (nm)
None-commercial	3	0.0056	48
Alginate	26	0.0677	21
CNC	27	0.0889	24
CNF	23	0.0819	25
CNC-CNF	28	0.0764	21

Surface area and mesopore volume are from BET and BJH analysis of nitrogen physisorption data, respectively. Mean crystallite size is from Williamson-Hall analysis of XRD patterns.

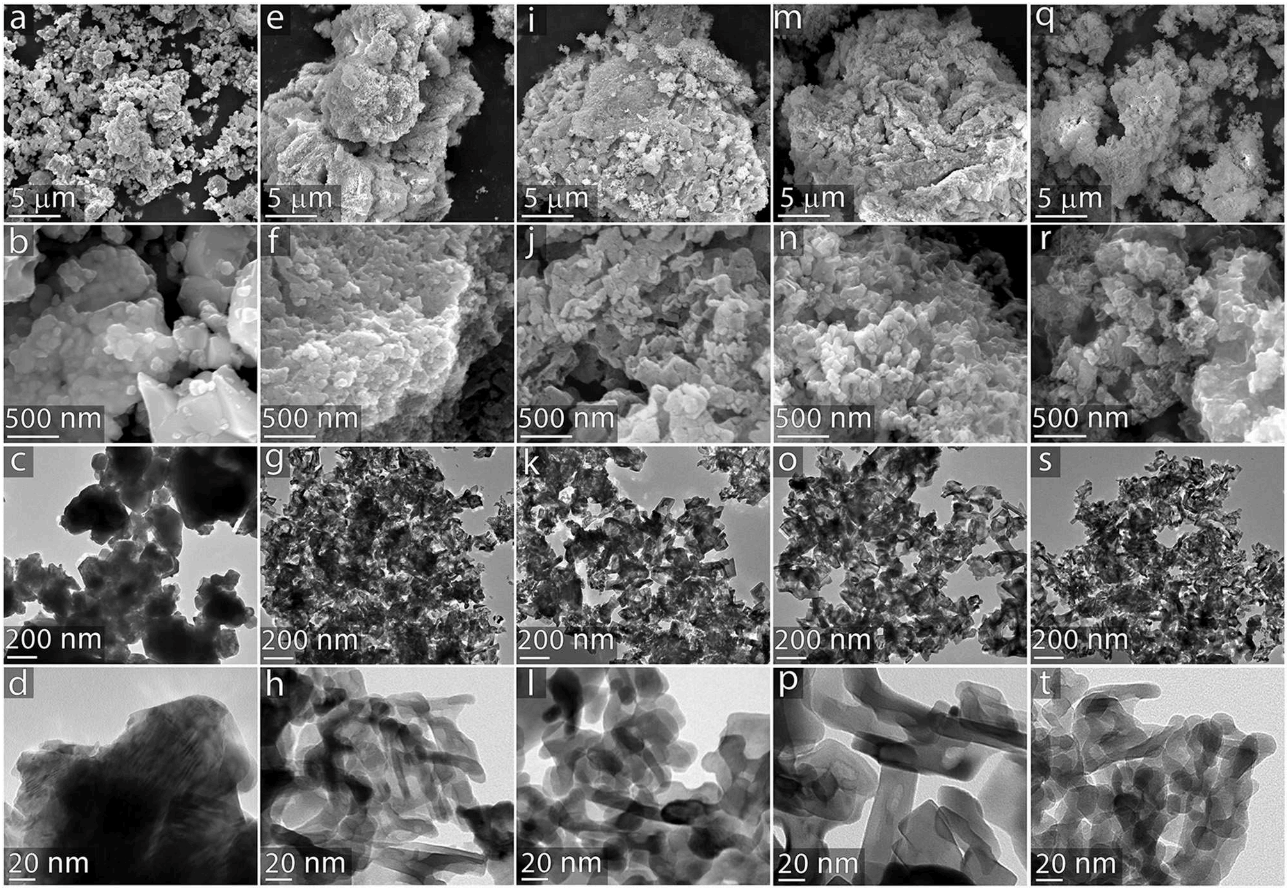

FIGURE 5 | Multiscale electron microscopy of catalyst particles. CeO_2 catalysts from the following templating agents: **(a–d)** commercially available powder control; **(e–h)** 1.0 wt.% alginate; **(i–l)** 1.0 wt.% CNC 1.0 wt.% alginate; **(m–p)** 1.0 wt.% CNF 1.0 wt.% alginate; **(q–t)** 0.5 wt.% CNC 0.5 wt.% CNF 1.0 wt.% alginate. Images on the top two rows were obtained via SEM; images in the bottom two rows were obtained via TEM.

of the isotherm using the Broekhoff-de Boer thickness model and was limited to pore widths >1.7 nm. t-plots were created by using the Harkins-Jura thickness model and fitting points with statistical thickness between 0.3 and 0.5 nm ($R^2 > 0.998$).

Catalytic Fast Pyrolysis and Tandem Micropyrolyzer GC-MS (py-GC-MS/FID)

To evaluate catalyst performance, all synthesized catalysts and CeO_2 powder, which served as a control, were tested in a py-GC-MS micropyrolyzer reactor. Experiments were run in triplicate. The py-GC-MS was coupled to a tandem micropyrolyzer (Rx-3050TR, Frontier Laboratories, Japan) equipped with an auto sampler (AS-1020E) and a microjet cryo-trap (MJT-1030Ex). A detailed description of this system was provided in previous studies (Mukarakate et al., 2014; Xu et al., 2017; Stanton et al., 2018). Briefly, 500 µg of cellulose was loaded in deactivated stainless-steel cups followed by a layer of 10 mg catalysts. The cellulose and catalyst layers were separated by quartz wool. The whole sample cup assembly was loaded into a furnace maintained at 500°C to pyrolyze biomass and pass the generated pyrolysis vapors through the catalyst fixed bed for upgrading. Subsequently, the upgraded vapors were captured using a liquid nitrogen trap (−196°C, housed inside the GC oven) and desorbed into the inlet of the gas chromatograph (7890B, Agilent Technologies, USA) interfaced with the MS (5977A, Agilent Technologies, USA). The GC oven was programmed to hold at 40°C for 3 min followed by a ramp to 240°C at a rate of 6.0°C min^{-1}. The trapped gases were separated by a capillary column (Ultra Alloy-5, Frontier Laboratories, Japan) with a 5% diphenyl and 95% dimethylpolysiloxane stationary phase. Gases (CO and CH_4) not captured by the −196°C liquid N_2 trap were sent to the thermal conductivity detector (TCD) via a separate column (GS-GASPRO) for quantification. The oven was programmed to hold at 40°C for 3 min followed by heating to 300°C. The separated pyrolysis vapors were identified using the NIST GCMS library and quantified using an FID (Budhi et al., 2015; Xu et al., 2017; Stanton et al., 2018). Standard calibrations were checked on a weekly basis by comparing FID areas of at least two compounds. The calibration standards consisted of 30 representative compounds (8 aromatic hydrocarbons, 10 oxygenates, 5 olefins, 5 paraffins, CO, and CO_2). For compounds without standards, the calibration for a compound with similar functional groups of similar molecular weights (C number) was used.

RESULTS

Catalyst Characterization

Scanning electron microscopy (SEM) was used to visualize the structure of the material before and after removal of the carbohydrate template by high temperature oxidation (**Figure 3**). Images of the $CeCl_3$/carbohydrate cryogel following the freeze-drying step but prior to high-temperature oxidation are presented in **Figures 3a,a'**. These images reveal clusters of predominantly inorganic material that are separated by large domains of carbohydrate (indicated by arrows in **Figure 3a**) that likely originated from the bundles of cellulose fibrils present in templating solution. Images of the CeO_2 following removal of the carbohydrate template (**Figures 3b,b'**) reveal a markedly different structure. The large carbohydrate domains observed prior to oxidation are absent, leaving behind channels and void regions within the material. The CeO_2 clusters shown in **Figure 3b'** also exhibit a different nanostructure from the aggregates observed in **Figure 3a'**, and appear lacey and porous. These features likely arise from the removal of the small cellulose nanocrystals and single-chain polysaccharides that were promoting gelation of the templating solution in the presence of Ce^{3+} ions.

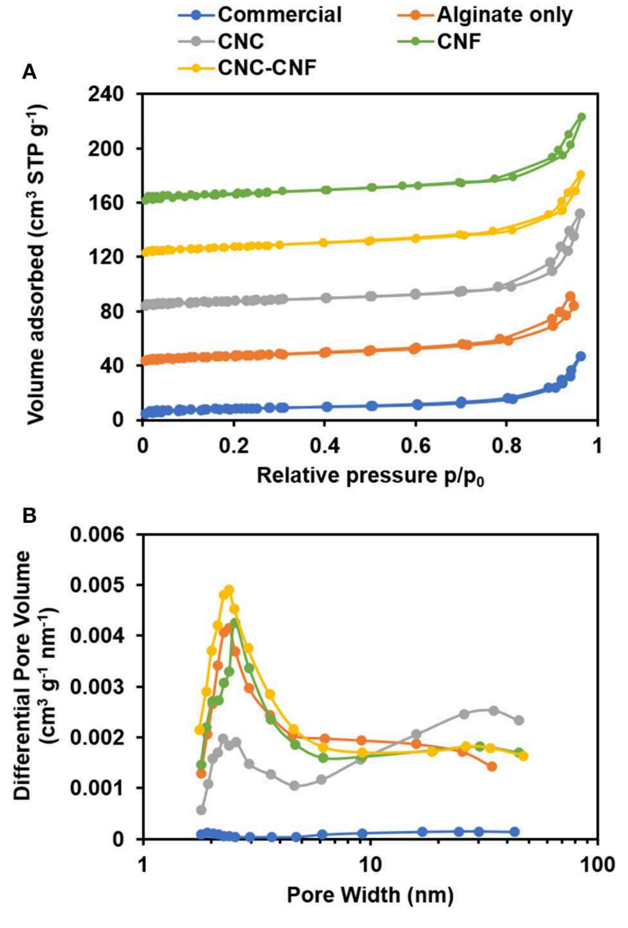

FIGURE 6 | Nitrogen physisorption analysis of CeO_2 catalyst samples. **(A)** Sorption isotherms reveal the introduction of mesopores into the catalyst structure by the carbohydrate templating. Isotherm of the commercial CeO_2 powder is scaled up by a factor of 10 and curves are vertically offset by 40 cm^3 STP g^{-1} to facilitate comparison with other samples. **(B)** The BJH pore volume distribution shows that templates including different carbohydrate components can modify abundance and size of mesopores.

Complete removal of the carbohydrate template from cyrogels during high-temperature oxidation was confirmed by TGA, with a major mass loss around 180°C and insignificant change during a 1 h hold at 500°C. These data are included in the **Figure S1**. The crystal structure of the templated catalysts was investigated by XRD to confirm that the Ce^{3+} within the carbohydrate cryogel was converted to CeO_2 by the oxidation processes. The XRD pattern of each type of templated catalyst, along with that of commercial CeO_2 powder and an ICDD reference pattern, are presented in **Figure 4**. The measured patterns all clearly exhibit diffraction peaks produced by CeO_2 in the cubic fluorite crystal structure, with relative peak intensities all closely matching the ICDD pattern (Chelliah et al., 2012). The peak widths of the templated catalysts are wider than those of the commercial powder which is indicative of increased polycrystallinity (i.e., smaller crystal grain size) in the templated materials relative to the non-templated control. Mean crystallite sizes were determined using the Williamson-Hall method to quantify this observation and are presented in **Table 1**. Templated samples exhibit crystallites roughly 50% smaller than the commercial powder.

The multiscale structural features resulting from the variations in templating agents were examined using SEM and transmission electron microscopy (TEM). These results are summarized in **Figure 5**. SEM images reveal that the commercially available CeO_2 powder (**Figures 5a–d**) is relatively smooth in comparison to the templated samples. Images of the material templated by a 1.0 wt.% alginate solution (**Figures 5e–h**) show that this template introduces mesoporosity into the CeO_2 material; however, the material does not contain a substantial population of larger channels like those displayed by the particles that were templated with NC components. The introduction of nanocellulose to the templating suspension imparts a controlled, well-defined porosity and surface structure to the CeO_2 material. The CNC templating agent (shown in **Figures 5i–l**) introduces fingerlike features to the CeO_2 catalyst that are larger than those imparted by the alginate alone, resulting in a nanostructured network throughout the material. The nanoscale features here are markedly different than the highly ordered mesoporous assemblies formed by pure suspensions of CNC (Dujardin et al., 2003; Shopsowitz et al., 2010, 2011), which is likely due to a disruption of the self-assembly process by interactions between the CNC and the alginage polymers also present in the templating solution. Particles templated by CNFs (shown in **Figures 5m–p**) displayed worm-like channels throughout the material. Particles produced by the templating solution containing both CNCs and CNFs (shown in **Figures 5q–t**) exhibit a combination of features observed in the materials templated by these components individually, consisting of a nanoporous network with larger worm-like channels throughout the structure. These images suggest that the origin of the smaller crystal grain size of the templated catalysts evidenced by the XRD patterns originates from the fingerlike nanostructures observed in **Figures 5h,i,p,t**.

The specific surface area, pore volume, and pore size of the templated materials were characterized by nitrogen physisorption using BET, t-plot, and BJH analysis. Isotherms are presented in **Figure 6A**. The IUPAC Type II sorption isotherm of the commercial CeO$_2$ indicates a lack of mesopores or micropores. In contrast, isotherms of the templated samples exhibit H3-type hysteresis caused by capillary condensation of nitrogen inside mesopores (Sing, 1982). These observations are consistent with SEM and TEM images. All samples show a continuous increase of adsorbed volume as relative pressure approaches one, which is likely caused by macropores and interparticle void spaces observed in SEM images.

BET results revealed that commercial CeO$_2$ powder has a surface area of 3 m^2/g, while the CeO$_2$ materials templated with alginate, CNC, CNF, and CNC/CNF templates exhibited a nearly 10-fold enhancement with surface areas ranging from 27–28 m^2/g. BJH analysis indicates a similar trend in catalyst pore volume, with a greater than 10-fold increase observed for templated samples relative to the commercial sample. The pore volume distribution of each template type is plotted in **Figure 6B**. Though all of the templated catalysts exhibit a much higher mesopore volume than the commercial sample, the choice of templating solution affects the size of pores which are formed during template burn off. Alginate alone produces a significant amount of smaller mesopores around 2–3 nm in width but is less effective at creating larger pores. The addition of CNC significantly increases the population of larger mesopores around 40 nm width, which may arise due to formation of the finger-like structures seen in TEM images. CNF also causes formation of larger mesopores relative to alginate alone, but the difference is less significant because the major impact of this template is the formation of macropore channels which are too large to be directly captured in this measurement. t-plot analysis (included in **Supplemental Material** showed that neither the commercial nor templated materials possess micropores.

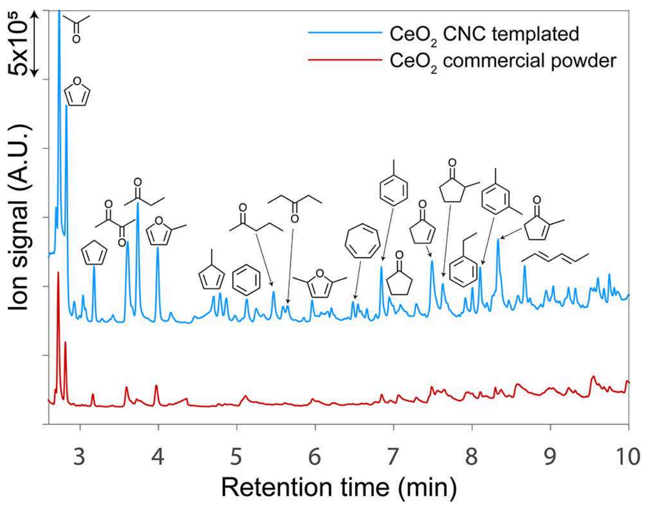

FIGURE 7 | Gas chromatographs from py-GC-MS/FID experiments using a templated CeO$_2$ catalyst (blue) and a non-templated CeO$_2$ powder (red). The templated catalysts consistently produced substantially higher ion signals which is indicative of their enhanced activity on a gravimetric basis relative to the non-templated catalysts.

Catalytic Upgrading of Cellulose Pyrolysis Vapors

The impact of our templating method on catalyst performance was evaluated in the context of upgrading cellulose pyrolysis vapors using CeO$_2$ in a py-GC-MS/FID micropyrolyzer reactor. Representative gas chromatographs from py-GC-MS experiments using commercial CeO$_2$ powder (red trace) and catalyst templated by a CNC/alginate suspension (blue trace) is presented in **Figure 7**. As expected, all of the CeO$_2$ catalysts produced a suite of predominantly monofunctional small oxygenates; however, the templated catalysts consistently produced substantially higher ion counts during the upgrading experiments which is indicative of their higher overall activity than the non-templated catalyst as visualized in **Figure 7**.

Quantification of the py-GC-MS/FID experiments allows for direct comparison of yields of various products from the templated catalyst and non-templated control. These results are presented in **Figure 8** which also includes the yields from cellulose pyrolysis in the absence of a catayst for comparison. In these control experiments the carbon loss to char is ∼40% due to the poor heating rates of the micropyrolyzer which is well documented in previous reports (e.g., Proano-Aviles et al., 2017). The difference between the char carbon yield and measured yield is due to catalyst coking and nonvolatile products which are not measured by GCMS. The total carbon yields of all of the catalytic pyrolysls experiments are lower than that of cellulose pyrolysis performed in the absence of any catalyst, which is expected due to coke formation and condendsation non-volatile products on the catlyst (Mukarakate et al., 2014). Each catalyst variant resulted in nearly complete conversion of the primary cellulose pyrolysis products. None of the of pyrolytic sugars (composed of mostly levoglucosan) present in the primary pyrolysis vapors were detected in the CFP experiments. Molecules classified as primary furans, ketones, and aldehydes were largely different species than those observed in the same classes after catalytic upgrading. Prior to catalytic upgrading the primary furanics observed were furan, 5-hydroxymethylfurfural, furfural, and furfuryl alcohol. After upgrading, partially deoxygenated and alkylated furanics were observed including furan (also observed in the primary pyrolysis vapors), 2-methyl-furan, 2,5-dimethyl-furan, 2-ethyl-furan. Molecules classified as ketones and aldehydes present in the primary pyrolysis vapors consisted mainly of formaldehyde, acetaldehyde, methyl glyoxal, 1-hydroxy-2-propanone, cyclopentanone, and 2-methyl-cyclopentanone. Following catalytic upgrading, the dominant ketone and aldehyde products observed were propenal, butanal, butanone, pentanone, cyclopentanone (which was also observed in the primary pyrolysis products), cyclopentenone, hexanone, cyclohexanone, and methylated variants of these molecules. The templated catalyst variants displayed some differences in yeild ehancments; however, all the templated catalysts produced appreciably higher yeilds then the non-templated control for each class of products. Increases of ∼100% were observed for ketone and aldeyde products for each of the templated catalysts. Yields of furanic compounds from the templated catalyts were similar on average to that of the non-templated control. Slight increases in furans were observed by the materials templated with alinate alone and CNC/CNF, while the other templated materials showed a reduction in furan production. Moderate improvements in aromatic yields were observed for all of the templated catalysts, ranging 10–50%. The increase in olefin production was the highest of any of the product classes analyzed at 100 to nearly 400% with respect to the non-templated control. Production of CO was also higher from all of the templated catalysts. Differences in CO_2 production from the templated catalysts with respect to the control varied substantially, with CNF and CNF/CNC producing more the control, the alginate templated material producing less than the control, and the CNC templated material performing similar to the control.

Extension of the Templating Method to Other Materials

To investigate the generality of the NC-based templating method to other oxide materials, we performed the templating process using a mixture of alginate, CNF, and CNC while substituting several other metal chlorides, consisting of $NiCl_2$, $FeCl_2$, and $MgCl_2$, for $CeCl_3$. SEM micrographs of the resultant materials are presented in **Figure 9**. In each case, hiearhically structured materials were observed. Low magnification images shown in the top row of **Figure 9** reveal high-surface area materials that

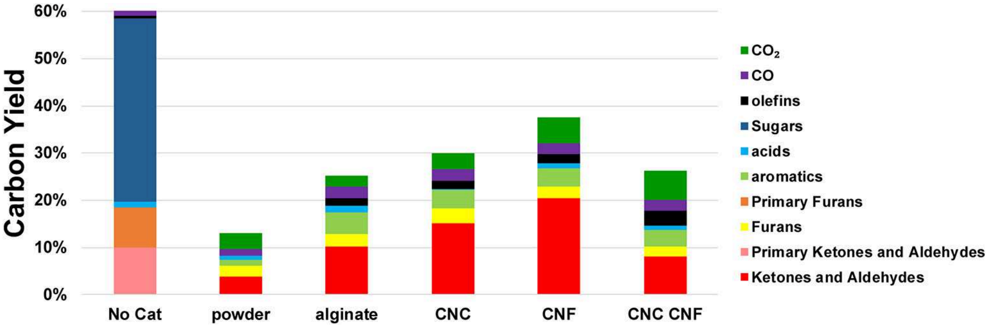

FIGURE 8 | Carbon yields product classes produced by catalytic upgrading of cellulose pyrolysis vapors. Molecules classified as furans, ketones, and aldehydes observed in primary pyrolysis vapors are denoted as Primary Furans and Primary Ketones and Aldehydes and are composed of largely different species than those observed in the same classes after catalytic upgrading.

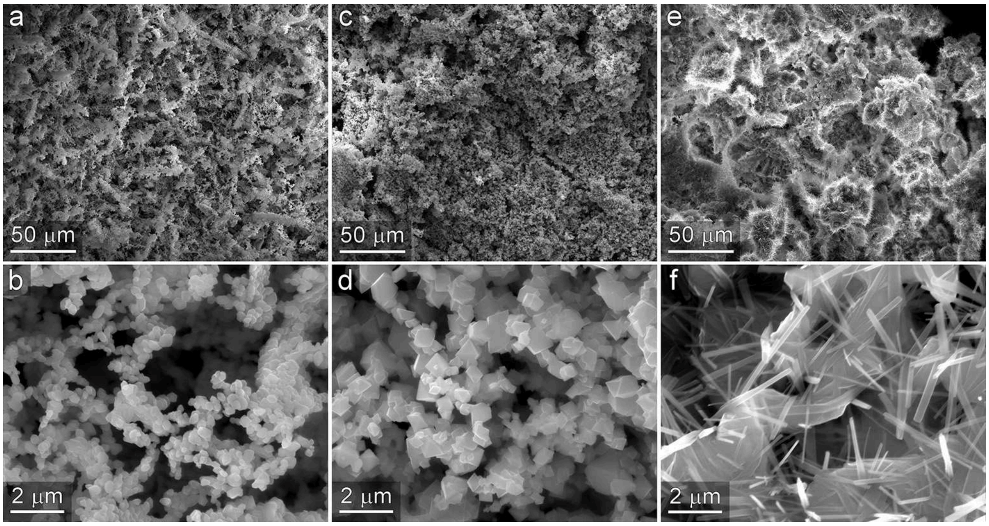

FIGURE 9 | Templated materials prepared from $NiCl_2$ **(a,b)**, $FeCl_2$ **(c,d)**, and $MgCl_2$ **(e,f)**. In each case the resultant material exhibits macroporosity observed in the low magnification images shown in the top row, and a 3-dimensional network of interconnected micro and nanoscale structures shown in the bottom row.

contain macro porosity. Higher magnification images shown in the bottom panel of **Figure 9** reveal that nanostructure of material consists of 3-dimensional interconnected system of micro and nanostructures. The nanoscale characteristics of each material are notably different from each other and reflective of the crystal structure formed by the oxide produced during the high temperature oxidation and template removal step. While comprehensive characterization and evaluation of catalytic activity of these new materials are beyond the scope of the current manuscript, these observations do provide evidence of the extensibility of the templating approach to other materials, and additional support for the assertion that the resultant structures consistently contain 3D interconnected networks of micro- and nanoscale dimensions.

DISCUSSION

Many templating strategies require the use of relatively expensive reagents or nanomaterials that make scaling to industrial demands prohibitive on the basis on cost and/or materials availability. In contrast, the low cost and vast production capacity of NC make it an ideal precursor for many industrial applications. While commercialization of NC is still in its infancy, the development of large volume industrial applications will provide the market pull to incentivize establishment of larger-scale production facilities to meet demands and further reduce the cost of NC.

In the context of CFP, the use of catalysts to increase the yield of desirable products from renewable feedstocks is critical. Some degree of deoxygenation of the primary pyrolysis vapors is necessary to achieve compatibility for blending and co-processing in existing petroleum refineries (Nolte and Shanks, 2017). However, recent studies have suggested that the additional reactivity of oxygenated biofuels may provide performance advantages over conventional hydrocarbon fuels in advanced engine formats, such as homogeneous compression ignition (HCCI) engines (Komninos and Rakopoulos, 2012). Additionally, the oxygenates produced by biomass deconstruction provide rich functionalities that can enable production of commodity chemical co-products. In many cases, biomass-based pathways may be a direct route to produce these oxygenates, while petroleum-based routes often require energy intensive and environmentally damaging oxidation of hydrocarbon precursors (Fitzgerald, 2017). These factors suggest that investigation of reducible metal oxide catalysts that promote formation of useful molecular functionalities from biomass deconstruction products, such as the ketones, aldehydes, and olefins produced by the CeO_2 catalysts produced in the present study. The products obtained from both commercially available and templated CeO_2 material in our experiments are largely expected from amphoteric metal oxides based on previous studies. Ketonization to form linear ketones has previously been reported (Mante et al., 2015) and can result from reactions of acids on the surface (Pham et al., 2013) or aldehydes (Gangadharan et al., 2010) with oxides on the surface to form carboxylate. Aldehydes and acids are commonly found in cellulose pyrolysis vapors and linear ketones, such as 2-butanone, 2-pentanone, and 3-pentanone were observed in the product streams from all of the ceria samples tested. Cyclopentenones are also observed from all of the ceria experiments, and these could result from ketonization reactions of diols or from ring opening of furfural (Omotoso et al., 2019). Extensive alkylation of furans, aromatics and cyclopentenones is also observed and likely results from the acid sites (Vivier and Duprez, 2010) on CeO_2. These bimolecular reactions are strongly dependent on catalyst surface area, which explains the higher yields observed for the hierarchical ceria catalysts.

Among the templated catalysts, the total carbon yield was observed to be highest for the material templated by CNF and CNC, which were the two materials that contained the most mesoporosity. These results suggest that the mesoporosity may faciliate improved access to active sites throughout the catalyst as well as more rapid escape of products from the particle interior thereby reducing coke formation. CNF tend to form relatively large, high aspect ratio bundles in solution. An example of one such bundle observed via TEM is included in **Figure S5**. These structures likely give rise to macroporous channels throughout the material, which enables the higher overall carbon yield from the CNF-templated material by enabling escape of products prior to coke formation. Interestignly, the combination of CNC and CNF in the templating solution did not result in improved carbon yields with respect to the material templated by CNC alone. The origins of this result are not fully understand, however we suspect it may be attributed to the disruption of macro channel formation by CNCs. In addition to the increase in availability of active sites, the smaller average crystallite size present in the templated catalysts likely plays a substantial role in their improved activity. The work of Natile et al. (2005) demonstrated the improved reactivity of nanostructured CeO_2. A recent perspective by Trovarelli and Llorca (2017) highlighted the importance of size, shape, and surface atomic arrangements of nanostructured CeO_2 in determining its catalytic performance. The fingerlike nanoscale features exhibited by the templated catalysts synthesized in this study arise from steric hindrance by the carbohydrate templating materials. These semi-continuous nanostructures will likely result in the exposure of additional high-energy surfaces of CeO_2 which will increase and modify its reactivity with respect to the bulk powder. The overall increase in volatile products from the templated catalyst observed in the py-GCMS experiments could results from the generally more active surface which accelerates reactions of polar pyrolytic sugars (i.e., levoglucosan) and subsequent release of products from the surface. Subtle modifications in the fractions of exposed crystal faces imparted by variations in the templating method may be responsible for the changes in product distribution exhibited by the various catalysts. The changes in total carbon yield and product distribution observed here result from a combination of reaction mechanisms, adsorption/desorption kinetics, and multiscale diffusion and possibly advection through the macropores. The lack of a detailed understanding of these phenomena is a limitation of the present study but should be the topic of future investigations in order to elucidate structure/function relationships and identify optimal synthesis targets for this templating approach.

While successful at introducing meso- and macroporosity to inorganic materials, this templating method does not produce specific surface areas as high as achieved in some previous reports of templating methods that result in mesoporous materials (Laha and Ryoo, 2003; Valentin et al., 2005; Shopsowitz et al., 2010). A potential route to improve the surface-area enhancement of the method described in the present work could be to combine the surfactants used in the aforementioned studies with the nanocellulose components employed here, thereby increasing the surface area by the introduction of more ordered mesoporosity while still maintaining the macroporous channels imparted by the nanocellulose. Another potential means to improve the surface area could be optimization of the drying and template removal process, which has been shown previsouly to have a large impact of the resultant structure of carbhydrate-based structures (Valentin et al., 2005).

CONCLUSIONS

This simple, inexpensive, scalable, synthesis procedure allows for templating metal oxide structures using renewable, bio-derived materials to yield tunable porosity and morphology. In comparison to CeO_2 powder, catalysts synthesized with alginate and nanocellulose templates showed a nearly 10-fold enhancement in surface area and increased meso- and macroporosity. When used for catalytic upgrading of cellulose fast pyrolysis vapors, CeO_2 material produced from carbohydrate templates exhibited substantially higher catalytic activity than an equivalent mass of non-templated CeO_2 powder. Several variations of alginate, CNC, and CNF templates were produced and evaluated. Each templated variant substantially outperformed the non-templated control in CFP experiments, and it was observed that the product distribution was impacted by variations in the catalyst architecture resulting from the different compositions of the carbohydrate templating suspensions. Finally, we demonstrated that this templating methods could be extended materials synthesized from other metal chloride precursors to achieve 3-dimensional networks of hierarchical porosity. Cost-effective routes to increasing the functionality of metal oxide catalysts as demonstrated here can potentially improve the economic feasibility of biomass conversion strategies. Overall, these results demonstrate that nanocellulose can serve as an effective templating agent by introducing controlled porosity and morphology to enhance surface area and introduce higher order architecture within catalyst particles.

AUTHOR CONTRIBUTIONS

Study was conceived by PC, KM, and MN. Catalyst synthesis was performed by KM and PC. Catalyst characterization was performed by KM, DC, DV, and PC. CFP experiments were performed by CM. Manuscript text and figures were prepared by KM and PC with assistance from all authors.

FUNDING

This work was authored by Alliance for Sustainable Energy, LLC, the manager and operator of the National Renewable Energy Laboratory for the U.S. Department of Energy (DOE) under Contract No. DE-AC36-08GO28308. KM was supported in part by the U.S. Department of Energy, Office of Science, Office of Workforce Development for Teachers and Scientists (WDTS) under the Science Undergraduate Laboratory Internships Program (SULI). CM, DV, MN, and PC acknowledge support from the U.S. Department of Energy Office of Energy Efficiency and Renewable Energy Bioenergy Technologies Office.

ACKNOWLEDGMENTS

We greatly appreciate discussions with Dr. Daniel A. Ruddy regarding suggestions to improve the synthesis procedure and interpretation of the characterization results, and assistance from Ms. Kellene McKinney with analyzing the py-GCMS results.

SUPPLEMENTARY MATERIAL

The Supplementary Material for this article can be found online at: https://www.frontiersin.org/articles/10.3389/fchem.2019.00730/full#supplementary-material

REFERENCES

Bharadwaj, V. S., Pecha, M. B., Bu, L., Dagle, V. L., Dagle, R. A., and Ciesielski, P. N. (2019). Multi-scale simulation of reaction, transport and deactivation in a SBA-16 supported catalyst for the conversion of ethanol to butadiene. *Catal. Today* 338, 141–151. doi: 10.1016/j.cattod.2019.05.042

Brinchi, L., Cotana, F., Fortunati, E., and Kenny, J. M. (2013). Production of nanocrystalline cellulose from lignocellulosic biomass: Technology and applications. *Carbohydr. Polym.* 94, 154–169. doi: 10.1016/j.carbpol.2013.01.033

Budhi, S., Mukarakate, C., Iisa, K., Pylypenko, S., Ciesielski, P. N., Yung, M. M., et al. (2015). Molybdenum incorporated mesoporous silica catalyst for production of biofuels and value-added chemicals via catalytic fast pyrolysis. *Green Chem.* 17, 3035–3046. doi: 10.1039/C4GC02477J

Cai, H., Han, J., Wang, M., Davis, R., Biddy, M., and Tan, E. (2018). Life-cycle analysis of integrated biorefineries with co-production of biofuels and bio-based chemicals: co-product handling methods and implications. *Biofuels Bioprod. Bior.* 12, 815–833. doi: 10.1002/bbb.1893

Cai, H., Mu, W., Liu, W., Zhang, X., and Deng, Y. (2015). Sol–gel synthesis highly porous titanium dioxide microspheres with cellulose nanofibrils-based aerogel templates. *Inorg. Chem. Commun.* 51, 71–74. doi: 10.1016/j.inoche.2014.11.013

Chelliah, M., Rayappan, J. B. B., and Krishnan, U. M. (2012). Synthesis and characterization of cerium oxide nanoparticles by hydroxide mediated approach. *J. Appl. Sci.* 12, 1734–1737. doi: 10.3923/jas.2012.1734.1737

Chen, X., Kuo, D.-H., and Lu, D. (2016). N-doped mesoporous TiO_2 nanoparticles synthesized by using biological renewable nanocrystalline cellulose as template for the degradation of pollutants under visible and sun light. *Chemical. Eng. J.* 295, 192–200. doi: 10.1016/j.cej.2016.03.047

Ciesielski, P. N., Pecha, M. B., Bharadwaj, V. S., Mukarakate, C., Leong, G. J., Kappes, B., et al. (2018). Advancing catalytic fast pyrolysis through integrated multiscale modeling and experimentation: challenges, progress, and perspectives. *Wiley Interdisc. Rev.* 7:e297. doi: 10.1002/wene.297

De France, K. J., Hoare, T., and Cranston, E. D. (2017). Review of hydrogels and aerogels containing nanocellulose. *Chem. Mater.* 29, 4609–4631. doi: 10.1021/acs.chemmater.7b00531

Dujardin, E., Blaseby, M., and Mann, S. (2003). Synthesis of mesoporous silica by sol–gel mineralisation of cellulose nanorod nematic suspensions. *J. Mater. Chem.* 13, 696–699. doi: 10.1039/b212689c

Endes, C., Camarero-Espinosa, S., Mueller, S., Foster, E. J., Petri-Fink, A., Rothen-Rutishauser, B., et al. (2016). A critical review of the current knowledge regarding the biological impact of nanocellulose. *J. Nanobiotechnol.* 14:78. doi: 10.1186/s12951-016-0230-9

Feliczak-Guzik, A. (2018). Hierarchical zeolites: Synthesis and catalytic properties. *Micropor. Mesopor. Mater.* 259, 33–45. doi: 10.1016/j.micromeso.2017.09.030

Fitzgerald, N. D. (2017). Chemistry challenges to enable a sustainable bioeconomy. *Nat. Rev. Chem.* 1:0080. doi: 10.1038/s41570-017-0080

Gangadharan, A., Shen, M., Sooknoi, T., Resasco, D. E., and Mallinson, R. G. (2010). Condensation reactions of propanal over CexZr1−xO2 mixed oxide catalysts. *Appl. Catal. A* 385, 80–91. doi: 10.1016/j.apcata.2010.06.048

Habibi, Y. (2014). Key advances in the chemical modification of nanocelluloses. *Chem. Soc. Rev.* 43, 1519–1542. doi: 10.1039/C3CS60204D

Habibi, Y., Lucia, L. A., and Rojas, O. J. (2010). Cellulose nanocrystals: chemistry, self-assembly, and applications. *Chem. Rev.* 110, 3479–3500. doi: 10.1021/cr900339w

Ji, P., Zhang, J., Chen, F., and Anpo, M. (2008). Ordered mesoporous CeO_2 synthesized by nanocasting from cubic Ia3d mesoporous MCM-48 silica: formation, characterization and photocatalytic activity. *J. Phys. Chem. C* 112, 17809–17813. doi: 10.1021/jp8054087

Kaushik, M., and Moores, A. (2016). Review: nanocelluloses as versatile supports for metal nanoparticles and their applications in catalysis. *Green Chem.* 18, 622–637. doi: 10.1039/C5GC02500A

Komninos, N. P., and Rakopoulos, C. D. (2012). Modeling HCCI combustion of biofuels: a review. *Renew. Sustain. Energy Rev.* 16, 1588–1610. doi: 10.1016/j.rser.2011.11.026

Kong, L., Zhang, C., Wang, J., Long, D., Qiao, W., and Ling, L. (2015). Ultrahigh intercalation pseudocapacitance of mesoporous orthorhombic niobium pentoxide from a novel cellulose nanocrystal template. *Mater. Chem. Phys.* 149–150, 495–504. doi: 10.1016/j.matchemphys.2014.10.051

Korhonen, J. T., Hiekkataipale, P., Malm, J., Karppinen, M., Ikkala, O., and Ras, R. H. A. (2011). Inorganic hollow nanotube aerogels by atomic layer deposition onto native nanocellulose templates. *ACS Nano* 5, 1967–1974. doi: 10.1021/nn200108s

Laha, S. C., and Ryoo, R. (2003). Synthesis of thermally stable mesoporous cerium oxide with nanocrystalline frameworks using mesoporous silica templates. *Chem. Commun.* 2138–2139. doi: 10.1039/B305524H

Li, H., Wang, G., Zhang, F., Cai, Y., Wang, Y., and Djerdj, I. (2012). Surfactant-assisted synthesis of CeO2 nanoparticles and their application in wastewater treatment. *RSC Adv.* 2, 12413–12423. doi: 10.1039/c2ra21590j

Liu, J., Ren, B., Wang, Y., Lu, Y., Wang, L., Chen, Y., et al. (2019). Hierarchical porous ceramics with 3D reticular architecture and efficient flow-through filtration towards high-temperature particulate matter capture. *Chem. Eng. J.* 362, 504–512. doi: 10.1016/j.cej.2019.01.065

Lu, Q., Zhang, Z.-F., Dong, C.-Q., and Zhu, X.-F. (2010). Catalytic upgrading of biomass fast pyrolysis vapors with nano metal oxides: an analytical Py-GC/MS STUDY. *Energies* 3, 1805–1820. doi: 10.3390/en3111805

Mante, O. D., Rodriguez, J. A., Senanayake, S. D., and Babu, S. P. (2015). Catalytic conversion of biomass pyrolysis vapors into hydrocarbon fuel precursors. *Green Chem.* 17, 2362–2368. doi: 10.1039/C4GC02238F

Mukarakate, C., Zhang, X., Stanton, A. R., Robichaud, D. J., Ciesielski, P. N., Malhotra, K., et al. (2014). Real-time monitoring of the deactivation of HZSM-5 during upgrading of pine pyrolysis vapors. *Green Chem.* 16, 1444–1461. doi: 10.1039/C3GC42065E

Natile, M. M., Boccaletti, G., and Glisenti, A. (2005). Properties and reactivity of nanostructured CeO_2 powders: comparison among two synthesis procedures. *Chem. Mater.* 17, 6272–6286. doi: 10.1021/cm051352d

Nelson, K., Retsina, T., Iakovlev, M., Van Heiningen, A., Deng, Y., Shatkin, J. A., et al. (2016). "American process: production of low cost nanocellulose for renewable, advanced materials applications," in *Materials Research for Manufacturing: An Industrial Perspective of Turning Materials into New Products,* eds L. D. Madsen and E. B. Svedberg (Cham: Springer International Publishing), 267–302.

Nolte, M. W., and Shanks, B. H. (2017). A perspective on catalytic strategies for deoxygenation in biomass pyrolysis. *Energy Technol.* 5, 7–18. doi: 10.1002/ente.201600096

Omotoso, T., Herrera, L. V., Vann, T., Briggs, N. M., Gomez, L. A., Barrett, L., et al. (2019). Stabilization of furanics to cyclic ketone building blocks in the vapor phase. *Appl. Catal. B* 254, 491–499. doi: 10.1016/j.apcatb.2019.04.079

Paques, J. P., Van Der Linden, E., Van Rijn, C. J. M., and Sagis, L. M. C. (2014). Preparation methods of alginate nanoparticles. *Adv. Colloid Interface Sci.* 209, 163–171. doi: 10.1016/j.cis.2014.03.009

Pham, T. N., Sooknoi, T., Crossley, S. P., and Resasco, D. E. (2013). Ketonization of carboxylic acids: mechanisms, catalysts, and implications for biomass conversion. *ACS Catal.* 3, 2456–2473. doi: 10.1021/cs400501h

Proano-Aviles, J., Lindstrom, J. K., Johnston, P. A., and Brown, R. C. (2017). Heat and mass transfer effects in a furnace-based micropyrolyzer. *Energy Technol.* 5, 189–195. doi: 10.1002/ente.201600279

Shatkin, J. A., Wegner, T. H., Bilek, E. T., and Cowie, J. J. T. J. (2014). Market projections of cellulose nanomaterial-enabled products-part 1: applications. *TAPPI J.* 13, 9–16. Available online at: https://www.fs.usda.gov/treesearch/pubs/46174

Shen, D., Dai, Y., Han, J., Gan, L., Liu, J., and Long, M. (2018). A nanocellulose template strategy for the controllable synthesis of tungsten-containing mesoporous silica for ultra-deep oxidative desulfurization. *Chem. Eng. J.* 332, 563–571. doi: 10.1016/j.cej.2017.09.087

Shin, Y., and Exarhos, G. J. (2007). Template synthesis of porous titania using cellulose nanocrystals. *Mater. Lett.* 61, 2594–2597. doi: 10.1016/j.matlet.2006.10.005

Shopsowitz, K. E., Hamad, W. Y., and Maclachlan, M. J. (2011). Chiral nematic mesoporous carbon derived from nanocrystalline cellulose. *Angew. Chem. Int. Ed.* 50, 10991–10995. doi: 10.1002/anie.201105479

Shopsowitz, K. E., Qi, H., Hamad, W. Y., and Maclachlan, M. J. (2010). Free-standing mesoporous silica films with tunable chiral nematic structures. *Nature* 468:422. doi: 10.1038/nature09540

Sierra-Salazar, A. F., Hulea, V., Ayral, A., Chave, T., Nikitenko, S. I., Kooyman, P. J., et al. (2018). Engineering of silica-supported platinum catalysts with hierarchical porosity combining latex synthesis, sonochemistry and sol-gel process – II. Catalytic performance. *Micropor. Mesopor. Mater.* 256, 227–234. doi: 10.1016/j.micromeso.2017.08.016

Sing, K. S. W. (1982). Reporting physisorption data for gas/solid systems with special reference to the determination of surface area and porosity. *Pure Appl. Chem.* 54, 2201–2218. doi: 10.1351/pac198254112201

Sing, K. S. W. (2014). "Chapter 7–assessment of surface area by gas adsorption," in *Adsorption by Powders and Porous Solids, 2nd Edn*, eds F. Rouquerol, J. Rouquerol, K. S. W. Sing, P. Llewellyn, and G. Maurin (Oxford: Elsevier), 237–268.

Stanton, A. R., Iisa, K., Mukarakate, C., and Nimlos, M. R. (2018). Role of biopolymers in the deactivation of ZSM-5 during catalytic fast pyrolysis of biomass. *ACS Sustain. Chem. Eng.* 6, 10030–10038. doi: 10.1021/acssuschemeng.8b01333

Torres-Rendon, J. G., Köpf, M., Gehlen, D., Blaeser, A., Fischer, H., Laporte, L. D., et al. (2016). Cellulose nanofibril hydrogel tubes as sacrificial templates for freestanding tubular cell constructs. *Biomacromolecules* 17, 905–913. doi: 10.1021/acs.biomac.5b01593

Trovarelli, A., and Llorca, J. (2017). Ceria catalysts at nanoscale: how do crystal shapes shape catalysis? *ACS Catal.* 7, 4716–4735. doi: 10.1021/acscatal.7b01246

Valentin, R., Molvinger, K., Viton, C., Domard, A., and Quignard, F. (2005). From hydrocolloids to high specific surface area porous supports for catalysis. *Biomacromolecules* 6, 2785–2792. doi: 10.1021/bm050264j

Vivier, L., and Duprez, D. (2010). Ceria-based solid catalysts for organic chemistry. *ChemSusChem.* 3, 654–678. doi: 10.1002/cssc.201000054

White, R. J., Fischer, A., Goebel, C., and Thomas, A. (2014). A sustainable template for mesoporous zeolite synthesis. *J. Am. Chem. Soc.* 136, 2715–2718. doi: 10.1021/ja411586h

Wisser, D., Wisser, F. M., Raschke, S., Klein, N., Leistner, M., Grothe, J., et al. (2015). Biological chitin–MOF composites with hierarchical pore systems for air-filtration applications. *Angew. Chem. Int. Ed.* 54, 12588–12591. doi: 10.1002/anie.201504572

Xu, C., Xu, Y., and Zhu, J. (2014). Photocatalytic antifouling graphene oxide-mediated hierarchical filtration membranes with potential applications on water purification. *ACS Appl. Mater. Interfaces* 6, 16117–16123. doi: 10.1021/am5040945

Xu, M., Mukarakate, C., Iisa, K., Budhi, S., Menart, M., Davidson, M., et al. (2017). Deactivation of multilayered MFI nanosheet zeolite during upgrading of biomass pyrolysis vapors. *ACS Sustain. Chem. Eng.* 5, 5477–5484. doi: 10.1021/acssuschemeng.7b00817

Yang, L., Mukhopadhyay, A., Jiao, Y., Yong, Q., Chen, L., Xing, Y., et al. (2017). Ultralight, highly thermally insulating and fire resistant aerogel by encapsulating cellulose nanofibers with two-dimensional MoS2. *Nanoscale* 9, 11452–11462. doi: 10.1039/C7NR02243C

Yang, X.-Y., Chen, L.-H., Li, Y., Rooke, J. C., Sanchez, C., and Su, B.-L. (2017). Hierarchically porous materials: synthesis strategies and structure design. *Chem. Soc. Rev.* 46, 481–558. doi: 10.1039/C6CS00829A

Yarbrough, J. M., Zhang, R., Mittal, A., Vander Wall, T., Bomble, Y. J., Decker, S. R., et al. (2017). Multifunctional cellulolytic enzymes outperform processive fungal cellulases for coproduction of nanocellulose and biofuels. *ACS Nano* 11, 3101–3109. doi: 10.1021/acsnano.7b00086

Zhu, H., Luo, W., Ciesielski, P. N., Fang, Z., Zhu, J., Henriksson, G., et al. (2016). Wood-derived materials for green electronics, biological devices, and energy applications. *Chem. Rev.* 116, 9305–9374. doi: 10.1021/acs.chemrev.6b00576

Zhu, H., Shen, F., Luo, W., Zhu, S., Zhao, M., Natarajan, B., et al. (2017). Low temperature carbonization of cellulose nanocrystals for high performance carbon anode of sodium-ion batteries. *Nano Energy* 33, 37–44. doi: 10.1016/j.nanoen.2017.01.021

Conflict of Interest: The authors declare that the research was conducted in the absence of any commercial or financial relationships that could be construed as a potential conflict of interest.

Copyright © 2019 Moyer, Conklin, Mukarakate, Vardon, Nimlos and Ciesielski. This is an open-access article distributed under the terms of the Creative Commons Attribution License (CC BY). The use, distribution or reproduction in other forums is permitted, provided the original author(s) and the copyright owner(s) are credited and that the original publication in this journal is cited, in accordance with accepted academic practice. No use, distribution or reproduction is permitted which does not comply with these terms.

frontiers in Chemistry

ORIGINAL RESEARCH
published: 31 October 2019
doi: 10.3389/fchem.2019.00735

Influence of Rice Husk and Wood Biomass Properties on the Manufacture of Filaments for Fused Deposition Modeling

Marie-Joo Le Guen[1]*, Stefan Hill[1], Dawn Smith[1], Beatrix Theobald[1], Evamaria Gaugler[1], Abdellatif Barakat[2] and Claire Mayer-Laigle[2]

[1] Scion, Rotorua, New Zealand, [2] IATE, Univ Montpellier, CIRAD, INRA, Montpellier SupAgro, Montpellier, France

Additive manufacturing or 3D printing has the potential to displace some of the current manufacturing techniques and is particularly attractive if local renewable waste resources can be used. In this study, rice husk, and wood powders were compounded in polylactic acid (PLA) by twin screw extrusion to produce filaments for fused-deposition modeling 3D printing. The biomasses were characterized in terms of physical features (e.g., particle size, density) and chemical compositions (e.g., solid state nuclear magnetic resonance, ash content). The two biomasses were found to have a different impact on the rheological behavior of the compounds and the extrusion process overall stability. When comparing the complex viscosity of neat PLA to the biomass/PLA compounds, the integration of wood powder increased the complex viscosity of the compound, whereas the integration of rice husk powder decreased it. This significant difference in rheological behavior was attributed to the higher specific surface area (and chemical reactivity) of the rice husk particles and the presence of silica in rice husks compared to the wood powder. Color variations were also observed. Despite the biomass filler and rheological behavior differences, the mechanical properties of the 3D printed samples were similar and predominantly affected by the printing direction.

Keywords: 3D printing, rice husk, wood, biomass, composites, extrusion

OPEN ACCESS

Edited by:
Caroline Remond,
Université de Reims
Champagne-Ardenne, France

Reviewed by:
Antti Ilmari Koponen,
VTT Technical Research Centre of
Finland Ltd., Finland
Rupinder Singh,
Guru Nanak Dev Engineering
College, India

***Correspondence:**
Marie-Joo Le Guen
mariejoo.leguen@scionresearch.com

Specialty section:
This article was submitted to
Chemical and Process Engineering,
a section of the journal
Frontiers in Chemistry

Received: *15 June 2019*
Accepted: *14 October 2019*
Published: *31 October 2019*

Citation:
Le Guen M-J, Hill S, Smith D,
Theobald B, Gaugler E, Barakat A and
Mayer-Laigle C (2019) Influence of
Rice Husk and Wood Biomass
Properties on the Manufacture of
Filaments for Fused Deposition
Modeling. Front. Chem. 7:735.
doi: 10.3389/fchem.2019.00735

INTRODUCTION

The popularity of incorporating lignocellulosic biomasses in thermoplastic polymers has increased significantly due to their sustainability advantage, low density, thermal, and noise insulation capacity and stiffening performances (Le Guen and Newman, 2007; Müssig, 2010; Gallos et al., 2017; Lammi et al., 2018). The properties of the composites are related to (a) the amount of biomass incorporated and (b) the interactions between the polymeric matrix and the lignocellulosic particles in terms of physical (e.g., surface area, aspect ratio) and chemical interactions (e.g., interface compatibilisation). Amongst the lignocellulosic feedstocks available, rice husk is of particular interest due to its current abundancy (i.e., estimated between 128 and 148 million tons of unutilized waste) (Giddel and Jivan, 2007; Pode, 2016), and chemical make-up. It is composed of around 80–85 wt.% lignocellulosic materials (e.g., cellulose, hemicellulose, lignin), 15–20 wt.% of amorphous silica and 1.1 to 2.5 wt.% of proteins (Juliano et al., 1987; Vadiveloo et al., 2009; Ummah et al., 2015).

Previous research studies have reported its potential applications in composite structures (Kumar et al., 2012), as an energy feedstock (Chungsangunsit, 2009) or amorphous silica feedstock (Yalçin and Sevinç, 2001). In parallel, the incorporation of nanosilica in polylactic acid (PLA) was also reported to improve the thermal stability and mechanical properties of composites (Lv et al., 2016).

3D printing (3DP) or additive manufacturing is an emerging technology that enables the creation of innovative designs and the combination of materials that were previously impossible or impractical to make. The incorporation of fillers in 3DP has demonstrated that the filler's physical features could be transferred to the 3D printed object (Montalvo Navarrete et al., 2018; Zeidler et al., 2018). These attractive traits have been demonstrated with wood (Mirko et al., 2016; Tao et al., 2017), clays (Revelo and Colorado, 2018), metals (Gibson et al., 2018), and seashells (Graichen et al., 2017; Singamneni et al., 2018a; Zeidler et al., 2018).

The combination of (a) the inherent properties of polymer-filled compounds and (b) the control of the 3D printing process directionality, leads to new functionalities to printed objects (Liles et al., 2018; Wang et al., 2018). Examples of such functionalities for lignocellulosic feedstocks include hydromorphic properties (Le Duigou et al., 2016; Sydney Gladman et al., 2016), electrical conductivity (Shao et al., 2018) and vibration damping (Zeidler et al., 2018).

In this present research, the influence of rice husk powder integrated into a PLA matrix is investigated for fused deposition modeling (FDM) 3DP applications, and compared to wood flour PLA 3D prints. The impact of the two biomasses during the extrusion compounding process, and on the mechanical properties of 3D printed rectangular parallelepipeds are observed and quantified.

MATERIALS AND METHODS

Biomasses and Polymer

Carmargue rice (*Oryza*) husks were supplied from Silo des Tourelles- C*omptoir Agricole du Languedoc* (Aigues Mortes, France). The husks were first sieved with a screen of 0.8 mm using a vibratory sieve shaker 400 (Ritec, France) to remove soil dust and stones. The husks were subsequently milled in a vibratory ball mill model DM-1 (Sweco®, USA) consisting of a 36 L abrasion-resistant elastomer grinding chamber filled with 25 kg of ceramics cylinders (diameter and length of 13.5 mm) and 25 kg of ceramics balls (diameter of 13.5 mm). The chamber's motion was controlled by a vibrating mechanism composed of high-tensile steel springs. One kilogram of rice husk was placed in the chamber and milled for 10 h to obtain fine rice husk powder. The ground powder was dried in an oven at 60°C for 12 h and stored in aluminum foil vacuum packaging bags prior to utilization.

Wood flour (*Pinus radiata* D. Don) was supplied by a plywood mill (Carter Holt Harvey, Kinleith Mill, Tokoroa, New Zealand). Only the particles below 125 μm were used after separation using a 43305 F motorized sieve shaker (Humboldt, USA) and 125 μm mesh sieve (Endercotts, UK). The wood flour powder was dried at 100°C for at least 24 h prior to extrusion.

PLA 3001D was obtained from Nature works (USA) and dried overnight prior to extrusion. The PLA and PLA compounds were dried for at least 4 h at 55°C prior to extrusion.

Processing

Compounding

The filaments were made in two sequential steps: (a) compounding the polymer and biomasses at 10 wt.% into pellets and (b) extrusion of the filament for FDM. Both steps were carried out on a 26-mm scientific twin screw, co-rotating extruder LTE26-40 (Labtech Engineering Ltd, Thailand), which had a 40 L/D ratio and was fitted with a vacuum crammer. During Step (a), materials were hand-mixed in plastic bags and fed into the volumetric feeder. The speed of the feeder was set to 20 rpm. The extruder screw speed was set to 200 rpm. The temperature was set to 190°C at the first 5 zones and 200°C at the last 5 zones. Pellets were cut to around 2 mm in length. During Step (b), the settings of the twin-screw extruder were modified (**Table 1**) and the pelletizer replaced by a winding unit set to produce a 1.75 mm diameter filament.

3D Printing

The objects were printed on a M2 fused deposition modeling printer (Makergear, USA) fitted with a 0.75 mm die nozzle. The platform temperature was set at 70°C and the nozzle temperature at 210°C. Rectangular beams (60 × 10 × 2.5 mm) for flexural testing were printed using slicing software (Simplify 3D®, USA) based on 0.2 mm layers thickness and no strand overlap. The 3D printing direction was carried out at either 0° or 90° of the beam length.

Characterization of the Biomasses

Physical Characterization

Particle size distribution

The particle size distribution of the risk husk powder and wood flour powder were measured by a laser diffraction particle size analyzer Hydro 2000S (Malvern Instruments Ltd., UK) with distilled water/ethylic alcohol solution (50:50 in volume) to allow good powder dispersion whilst avoiding swelling. The results are expressed using the Mie method with a refraction index of 1.53 corresponding to those of sawdust particles (Malvern, 2007). The results are generated in volume, based on the assumption that the particles are spherical. Five replicates were carried out for each biomass and the mean average distribution is reported.

TABLE 1 | Extrusion settings for Step (b) to manufacture the FDM filaments.

Temperature (°C)	160, 170, 170, 170, 180, 180, 190, 190, 200, 200
Screw speed (rpm)	200
Feed speed (rpm)	8
Speed of haul-off unit (rpm)	8–13

Scanning electron microscopy (SEM)

Rice husk and wood powders were imaged with a scanning electron microscope Phenom Pro-X (Phenom, France) using a charge reduction sample holder and an acceleration voltage of 5 kV (wood powder) and 10 kV (rice husk powder), respectively.

Tapped density and apparent density

The apparent and tapped density was measured in duplicate using a standard tapped density analyzer (Autotap, Quantachrome instrument®, USA). The experiment consisted of filling a graduated test tube with 200 mL of powder and submitting it to 1,500 taps. The apparent and tapped densities were calculated as the ratio of the mass of the powder to the initial and final volume respectively.

Chemical Characterization

pH measurements

One gram of biomass powder was stirred into 15 mL of distilled water at room temperature. Four pH measurements over 4 h were recorded using a ph meter (Mettler Toledo, USA). The four measurements were then averaged.

Solid-state nuclear magnetic resonance (NMR) spectroscopy

Solid state CP-MAS (Cross Polarization-Magic Angle Spinning) ^{13}C Nuclear Magnetic Resonance spectra were acquired at 50.3 MHz on a Bruker Avance III 200 spectrometer (Bruker BioSpin, Germany) fitted with a 4 mm solid state MAS probe (Bruker BioSpin, Switzerland). The samples were packed into a 4 mm rotor and spun at 5 kHz. Each 3 μs, a 90° proton preparation pulse was followed by a 1 ms contact time and a 30 ms acquisition time, with proton decoupling, and a 1.5 s recycle delay. All spectra were calibrated so that the cellulose Iβ interior C4 peak was assigned a value of 89.3 ppm relative to tetramethylsilane (Newman et al., 1993).

Ash content

Around 2 g of powder was first dried in an oven at 130°C during 90 min and weighed to determine the dry mass (m_s). The sample was subsequently heated at 900°C for 2 h and re-weighted (m_r) after cooling in a desiccator to room temperature. The ash content was calculated according to:

$$Ash = 100 \cdot m_r/m_s \tag{1}$$

Where:

Ash is in percentage,

m_s is the sample dry mass in grams,

m_r is the sample residual mass in grams.

Experiments were carried out in triplicate and averaged.

Chemical composition

Carbohydrates and lignin content of the biomasses were measured after concentrated acid hydrolysis. The lignin content in samples was determined by the Klason method. Briefly, 100 mg of dried samples were treated with 72% v/v H_2SO_4 at ambient temperature for 2 h. The solutions were diluted with water to 12% v/v H_2SO_4 and autoclaved at 100°C for 3 h. The hydrolysates were filtered (10 μm) and the Klason lignin content was determined as the weight of the residue after drying at 105°C for 24 h. The monomeric sugars glucose, xylose, and arabinose were determined using high-pressure liquid chromatography (HPLC). A Waters system, using a BioRad HPX-87H column at 40°C and 0.3 mL/min was used for analysis. All analyses were performed in triplicate.

Characterization of the Biomass Compounds

Rheology

Complex viscosity of the neat PLA and the compounds was measured on a AR 2000 rheometer (TA instruments, USA). The experiments were recorded in triplicate in frequency sweeps from 100 to 1 Hz at 200°C and 1% strain. The linear visco-elastic region was determined at 1 Hz.

Molecular Weight

Gel Permeation Chromatography (GPC) experiments were carried out on a using a styrene divinylbenzene (SDVB) copolymer gel column set consisting of 2 analytical columns (SDV Lux Lin M; 5 μm; 300 × 8 mm; PSS Polymer Standards Service GmbH, Germany) and a precolumn (SDV analytical precolumn, 5 μm; 50 × 8 mm; PSS Polymer Standards Service GmbH, Germany). The flow rate was set to 1 mL/min, the system was conditioned to 30°C and an injection volume of 100 μL was used. Samples were prepared in triplicate by dissolving 6 to 8 mg of sample in chloroform to a concentration of 2.0 mg/mL overnight. The solutions were filtered through a 0.45 μm PTFE filter. The instrument (Knauer, Germany) was calibrated using 12 polystyrene standards (ReadyCal Polystyrene standards; PSS Polymer Standards Service GmbH, Germany) ranging from 370 to 2,520,000 g/mol. A conventional calibration curve was established by measuring the elution volume of the standards and plotting it against the logarithm of the molar mass. The calibration data was fitted with a fourth order polynomial function ($r^2 = 1.00$). Number average molecular weight (Mn), weight average molecular weight (Mw) and polydispersity index (PDI) were calculated from the detector response using the WinGPC UniChrom software (PSS Polymer Standards Service GmbH, Germany).

Dynamic and Quasi-Static Mechanical Test

Specimens for dynamic mechanical thermal analysis (DMTA) and mechanical analysis in flexural mode were tested in 3-point bending mode on a RSA-G2 DMTA (TA instruments, USA) using a 40-mm span. Specimens were conditioned for 48 h at 23°C (±2°C) and 50% (± 5%) relative humidity.

Dynamic testing was carried out from 23 to 80°C at a rate of 5°C/min. Strain oscillations of 0.1% at a frequency of at 1 Hz were applied. The storage modulus (E') and tan δ were recorded throughout the test. Each formulation and printing direction was tested in triplicates.

Flexural testing was carried out on an Instron 5566 universal testing machine (Instron, USA) fitted with a 10 kN load cell at a rate of 2 mm/min. Flexural modulus, strength and strain were recorded throughout the test. At least 5 samples for each formulation were tested.

RESULTS

Characterization of the Biomass Particles

The wood powder particles were larger than those of the rice husks with a median size of 209.9 µm for the wood powder and 28.1 µm for rice husk powder (**Table 2**). Both powders exhibit a widespread distribution with a similar SPAN around 3.3. SPAN expresses the width of the distribution (D90-D10/D50). Rice husk powder contains a considerable proportion of fine particles below 20 µm whereas wood powder has a high content of coarse particle (above 400 µm) as observed in the shape of the particle size distribution graph (**Figure 1**). As a result, the specific surface area calculated from the particle size distribution is approximately 9 times higher for rice husk powder than for wood powder. However, the particle size distributions must be interpreted with caution as laser diffraction model calculations assume spherical homogeneous particles (Bohren and Huffman, 1983).

When looking at the biomass micro-morphology by SEM, large fibrous structures, >125 µm in length, are visible in the wood flour in contrast with low aspect ratio particles of the rice husk particles which supports the laser diffraction measurements (**Figure 2**). The presence of such particle sizes despite the sieving step is explained by their high aspect ratio that allowed them to pass through the mesh. The size and morphological differences contribute to explain the lower apparent density of the wood biomass through a lesser packing efficiency.

TABLE 2 | Physical characterization of the wood and rice husk powders including particle size distribution indicators, specific surface area and densities (D10: 10th percentile, D50: Median Size, D90: 90th percentile).

	Wood powder	Rice husk powder
D10 (µm)	48.4	3.5
D50 (µm)	209.9	28.1
D90 (µm)	748.1	95.2
Specific surface area	0.074	0.65
SPAN ((d90-d10)/d50)	3.26	3.33
Apparent density ($\times 10^{-2}$ kg.L^{-1})	8.2	45.2
Tapped density ($\times 10^{-2}$ kg.L^{-1})	10.0	56.9

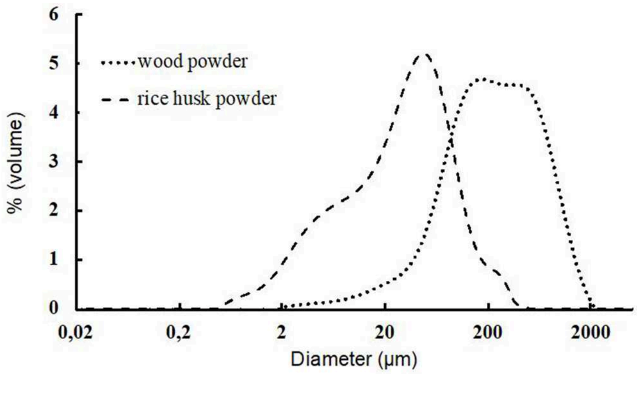

FIGURE 1 | Particle size distribution for the wood powder (dotted line) and rice husk powder (dashed line).

In terms of chemical compositions determined by HPLC, the two biomasses are consistent with literature for lignocellulosic feedstocks (**Table 3**) (Müssig, 2010). The main differences between powders are (a) higher lignin content for the wood powder and (b) higher ash content for the rice husk powder (i.e., 15.7 wt.% compared to 0.16 wt.% for wood). The higher ash content in rice husks is explained by the presence of silica and contributes to the five-fold difference recorded in tapped density (**Table 3**) (Hamdan et al., 1997). The lack of a 100 % mass balance was attributed to the presence of water soluble extractives. Those were found to be present in higher quantities in wood powder than in rice husk powder.

The chemical compositions of the powders as determined by ^{13}C solid-state NMR were consistent with lignocellulosic biomass. The major peaks observed in the wood powder were attributed to cellulose (C1-C6), lignin methoxyl (56 ppm) and aromatic/phenolic groups, with minor contributions from hemicelluloses (**Figure 3A**) (Gil and Neto, 1999). The rice husk powder showed similar signals with the addition of peaks attributed to amide carbonyls (~175 ppm) and signals predominantly from the C_β/C_γ amino acid side chains (C_γ 15-25 ppm and C_β 25-35 ppm) overlapping with signals from acetylated hemicelluloses (**Figure 3B**) (Bruker BioSpin, 2018). The amino acid signals were attributed to the known protein content present in rice husk (Juliano et al., 1987; Vadiveloo et al., 2009).

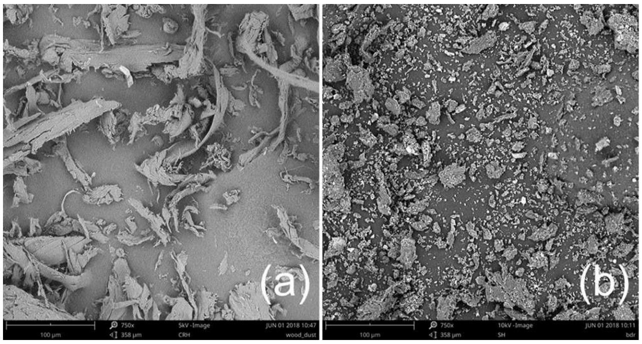

FIGURE 2 | SEM images of wood powder **(a)** and rice husk powder **(b)**.

TABLE 3 | Chemical composition in mass percentage of the biomass.

	Wood powder	Rice husk powder
Hemicellulose	17.1 ± 0.8	21.8 ± 0.7
Cellulose	44.3 ± 1.0	40.6 ± 1.0
Lignin	28.0 ± 0.8	19.4 ± 1.5
Ash (minerals)	0.16 ± 0.1	15.7 ± 0.7
Total	89.6 ± 2.7	97.5 ± 3.9

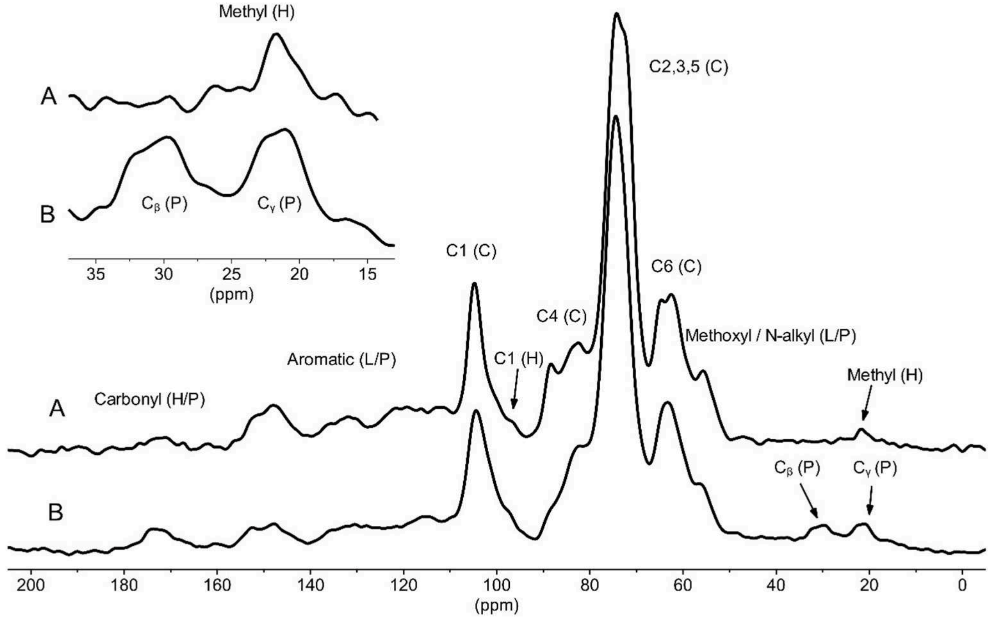

FIGURE 3 | Solid-state NMR of the wood powder **(A)** and rice husk powder **(B)**. P, protein; H, hemicelluloses; L, lignin; C, cellulose. Top left spectrum is a zoom in of the 10–40 ppm range.

Extrusion Process Stability

During the compounding step, the die pressure was significantly different between the wood and the rice husk powders. It ranged from 68 to 73 bars and 22 to 24 bars for the wood and rice husk compounds, respectively. Low die pressure, substantial die surge and color change were observed during rice husk compounding. The processing differences were initially attributed to the particle variation in apparent densities and sizes, however, it did not account for the variation in colors. It is known that compounding lignocellulose biomass in polymer can oxidize the carbohydrates contained in the biomass and lead to a darkening of the compounds depending on the processing conditions (i.e., high shear, high temperature) (Muniyasamy, 2013; Gallos et al., 2017). Yet the variation in color between the raw feedstocks and the compounds was more intense for the PLA rice compound than those of the PLA wood, and accentuated in the FDM filament (**Figure 4**). Ball milling of lignocellulosic biomass during an extended period (i.e., >120 min) is known to increase surface area, decrease cellulose crystallinity and decrease the carbohydrate's degree of polymerization that consequently increases the particle surface reactivity (Vaidya et al., 2016; Gao et al., 2017). This reactivity could explain the difference of coloration caused by chemical reactions triggered by the rice husk compared to the wood powder.

During the FDM filament manufacture, the FDM rice husk filament exhibited a lower melt strength and material surged at the die causing unevenness in the filament shape. These processing effects made the rice husk filament more difficult to manufacture.

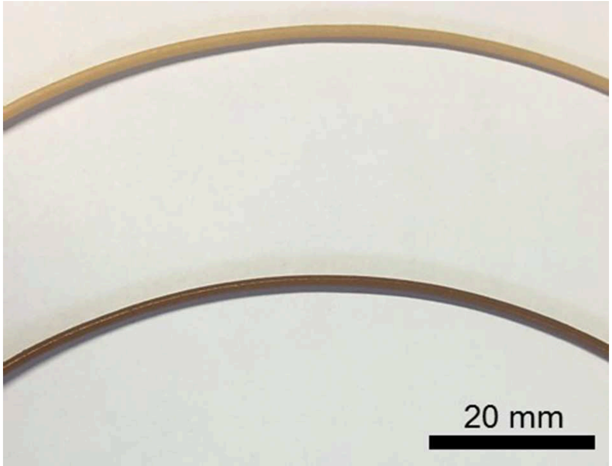

FIGURE 4 | Photographs of the wood flour (top) and rice husk (bottom) FDM filaments.

Influence of the Biomass on the PLA

In terms of rheology, the measurement of the complex viscosities of PLA and the PLA/biomass compounds as a function of frequency indicated that (a) the PLA-wood compound has a higher viscosity than neat PLA and that (b) both are exhibiting shear thinning behaviors (**Figure 5**). The findings are consistent with literature on biomass-filled polymers and the general effect of biomass in polymer melt (Li and Wolcott, 2004; Bettini et al., 2013; Gallos et al., 2017; Chun et al., 2018). Conversely, the rice compound was half the complex viscosity of neat PLA and indicated a poor reproducibility (**Figure 5**). It was hypothesized that the rice husk particles acted as a solid lubricant in the polymer matrix. However, the lack of reproducibility also suggested additional effects such as polymer hydrolysis of the backbone.

When comparing the PLA Mn and Mw of the biomass compounds, the GPC analysis indicated no significant difference between the two fillers (**Table 4**). More specifically, the GPC analysis gave a Mw and Mn of 98,020 g/mol and 52,473 g/mol for the neat PLA. After extrusion with biomass powders, significantly lower average molecular weights were recorded, i.e., Mw = 66,790 g/mol and Mn = 33,780 g/mol for PLA-wood and Mw = 59,853 g/mol and Mn = 31,463 for PLA-rice (**Table 4**, **Figure 6**). This finding is consistent with literature, as PLA is known to hydrolyse in the presence of moisture or acid groups in the biomass during extrusion (Le Guen et al., 2017; Thumm et al., 2018). This translated to an average molecular weight decrease of between 32 and 39% for the PLA compounded with wood and rice husk powders. No significant difference was observed between fillers. The reduction was also observable in the molecular weight distribution (MWD) profiles (**Table 4**). Similarly, no significant changes in the polydispersity indices (PDI) of pure PLA compared to PLA with biomasses were observed (**Table 4**).

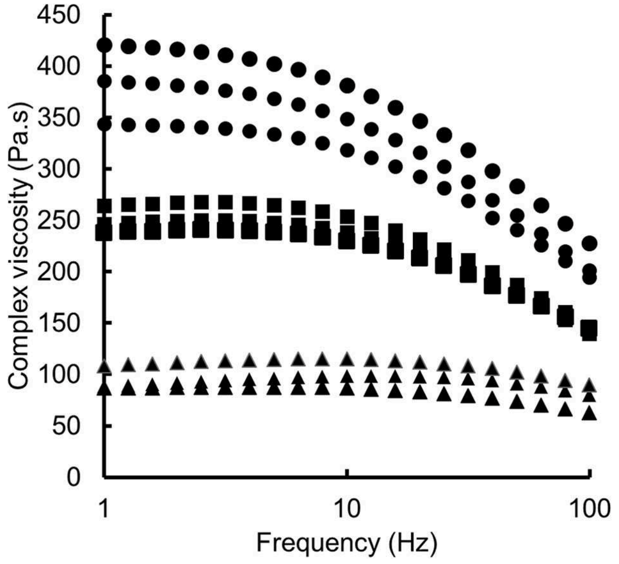

FIGURE 5 | Complex viscosity as a function of frequency for: PLA (Square), PLA-wood (Circle) and PLA-rice (Triangle). Triplicate measurements were carried out and all results are presented on the graph.

TABLE 4 | Molecular weight values and polydispersity indices of the PLA neat and compounded with biomasses.

	Mn (g/mol)	St. Dev. Mn (g/mol)	Mw (g/mol)	St. Dev. Mw (g/mol)	PDI (–)	St. Dev. PDI (–)
PLA	52,473	5,245	98,020	6,294	1.9	0.24
PLA-wood	33,780	2,735	66,790	2,776	2.0	0.08
PLA-rice	31,463	3,526	59,853	5,963	1.9	0.03

n = 3.

When comparing the effect of the fillers onto PLA, the GPC analysis indicated that both resulted in similar level of PLA hydrolysis, hence, the difference rheological behavior could not be attributed to a difference in Mn/Mw.

Mechanical Performances of the 3D Prints at 0° and 90°

The infill of the print direction was carried out at 0° and 90° of the length of the rectangular beam (**Figure 7**). The printing direction influenced the mechanical properties of all formulations, showing a decrease of flexural modulus and strength for the 90° printed beams (**Figure 8**). The anisotropy induced difference in properties between the lengthwise and widthwise printing direction that ranged between 28 and 41% variation in flexural strength, 4 to 15% in strain and 27 to 33% in modulus. Similar mechanical properties results were reported for 3D printed PLA wood rectangular beam where the printing direction (i.e., 0° and 90° of the longitudinal axis of the beam) influenced the tensile stiffness and strength by 20 and 35%, respectively (Le Duigou et al., 2016). They suggested that the mechanical properties differences between the lengthwise and widthwise printing directions were due to the lack of interlayer interactions.

No significant difference was found between the wood and the rice husk fillers in terms of mechanical property except for the flexural stiffness in the lengthwise direction where the PLA-wood sample's modulus is ∼25% higher than the modulus of the PLA-rice samples. The decrease in strength compared to neat PLA and the lack of difference between the PLA-wood and PLA-rice compounds, indicated that the mechanical properties are effectively driven by the PLA inter-strands coalescence as observed by others (Le Duigou et al., 2016). This coalescence

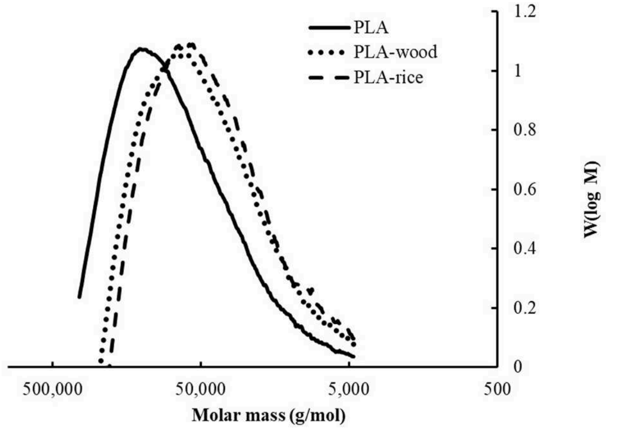

FIGURE 6 | Molecular weight distribution profiles of neat PLA (solid line), PLA-wood (dotted line) and PLA-rice (dashed line) compounds.

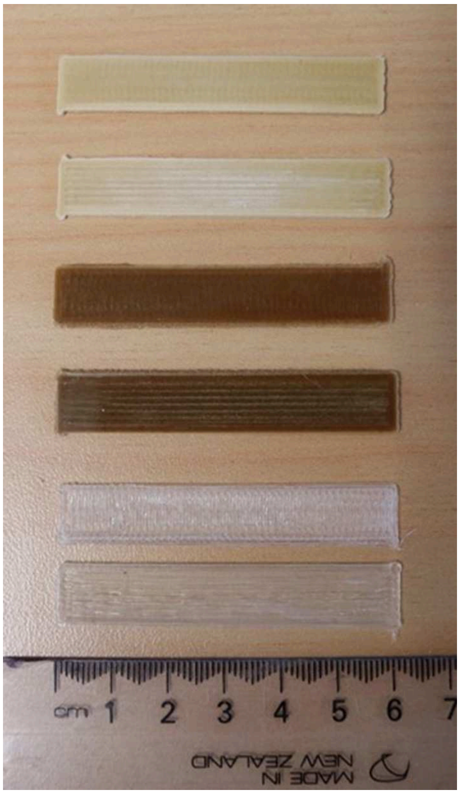

FIGURE 7 | Typical 3D printed rectangular beams for flexural testing. From bottom to top PLA 0°, PLA 90°, PLA-rice 0°, PLA-rice 90°, PLA-wood 0° and PLA-wood 90°.

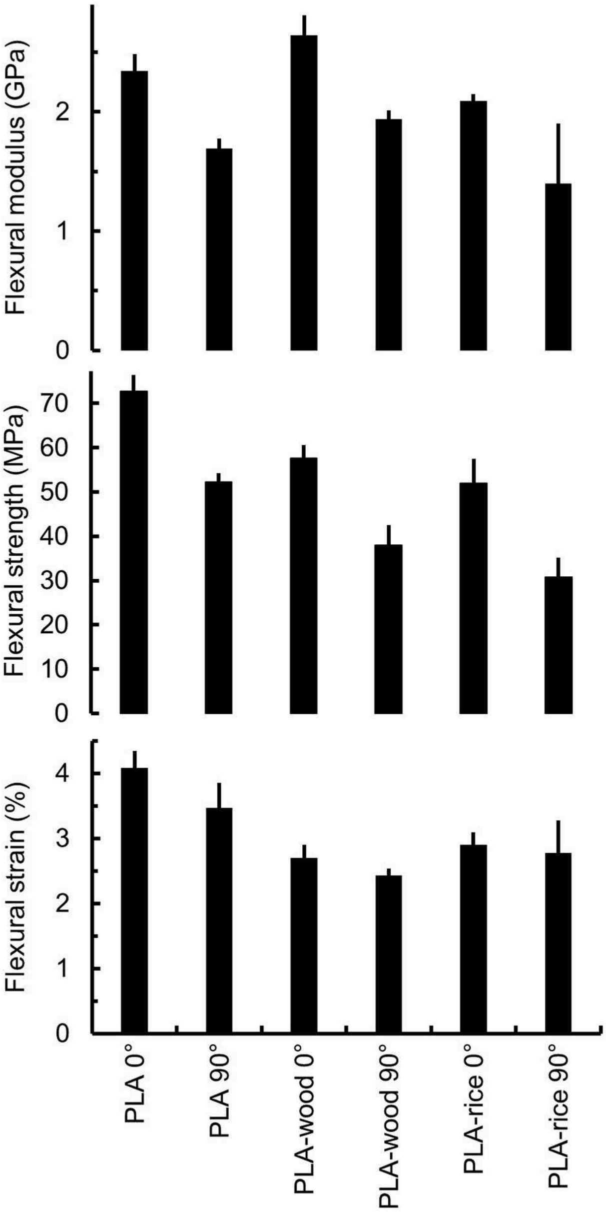

FIGURE 8 | Mechanical properties comparison of the 3D printed beams PLA, (**Top**) Flexural modulus (**Middle**) Flexural strength and (**Bottom**) Flexural strain (Error bars indicate the ± 95 % confidence interval).

is expected to decrease with the introduction of a solid filler that hinders the strand cohesion and creates weak points within the printed object. Singamenni et al., reported a gradual loss of inter-strand and inter-layer coalescence surface, measured by optical microscopy, with increasing amount of wood flour from 5 to 20 wt.% in polybutyrate-adipate-terephthalate–polymer matrix (PBAT) (Singamneni et al., 2018b). They attributed the decrease in flexural properties to the lower strands coalescence (98% coalescence for 5wt.% filler and 64% for 20wt.%). Their findings in terms of flexural strength are consistent with those presented in this study, where the addition of either filler decreases the flexural strength of the printed samples. However, their results relative to the flexural modulus differs. They reported a decrease in flexural modulus at 10 wt.% wood fraction whereas the present results indicate an increase of flexural modulus for the PLA-wood and decrease for the PLA-rice.

The difference was attributed to the polymer matrix as PBAT is more elastomeric than PLA but it raises the possibility of synergetic/competing effects between the type of filler and polymer, leading to different mechanical behavior of the 3D printed object. Similar findings were reported by Badouard et al. who compared the reinforcing ability of flax fibers in different biopolymer matrices (Badouard et al., 2019).

The dynamic thermo-mechanical behavior of the samples tested from 23 to 80°C indicated a single transition, typical of the glass transition temperature of PLA samples (**Table 5**).

The stiffness variation due to the printing direction anisotropy agreed with the quasi-mechanical tests for the neat PLA and filled samples. Storage modulus (E') values indicated a decrease of 28.7, 25.1, and 19.7 % between 0° and 90° printing direction for respectively, the unfilled PLA, PLA-wood and PLA-rice samples, respectively (**Table 5**). The printing direction had no thermo-mechanical effect (e.g., Tg variation, thermal stress relaxation).

TABLE 5 | Storage modulus values at 30 and 75°C, and glass transition temperature (Tg) for PLA, PLA-wood, and PLA-rice samples printed at 0 and 90° of the longitudinal direction.

	PLA 0°	PLA 90°	PLA-wood 0°	PLA-wood 90°	PLA-rice 0°	PLA-rice 90°
E' at 30°C (GPa)	2.66 (0.22)	1.90 (0.15)	2.31 (0.07)	1.73 (0.16)	2.50 (0.15)	2.01 (0.43)
Tg (°C)	65.0 (0.35)	65.5 (0.35)	64.7 (1.7)	65.4 (1.8)	65.3 (0.9)	64.8 (0.4)
E' at 75°C (MPa)	5.6 (0.5)	3.9 (1.6)	12.8 (2.7)	7.8 (1.1)	8.6 (1.7)	13.4 (1.2)

The number in brackets is the standard deviation for n = 3.

However, the filler's contribution to the stiffness could be observed past the glass transition temperature where the storage modulus of the PLA-wood and PLA-rice samples was higher than the unfilled PLA samples. The retention of storage modulus indicated opposite trends between the PLA-wood samples 0° and 90°, and the PLA-rice samples 0° and 90°. Indeed, past the Tg, the wood filled PLA samples displayed a 39% difference in favor of the longitudinal printing direction. Conversely, the rice-husk filled samples displayed an unexpected 56% difference in favor of the transversal printing direction. The former finding is explained by an alignment of wood particles in the printing direction caused by shear forces in the nozzle (Sydney Gladman et al., 2016). The latter finding is more difficult to explain. It was here tentatively attributed to the smaller size of the rice husk particles and their better distribution within the PLA. The rice husk particles are around 10 times smaller than the wood ones (**Figure 2**, **Table 2**). Considering the low aspect ratio of the rice husk particles, it is conceivable that no or little alignment for the rice husk particles occurred. The difference in behavior between the rice husk and the wood was tentatively attributed to the finer particles which created a more uniform and stiffening network. This characteristic was only observed in the widthwise direction as the predominant factor (i.e., the alignment of the polymer chains and fillers) was potentially not present to mask it.

DISCUSSION

Overall, the mechanical behavior of the 3D printed beams at room temperature was governed by the printing direction and the polymer physical properties rather than the type of fillers being used. However, when comparing the wood powder to the rice husk powder as a filler for 3D printing in PLA, particular observations were made on the interaction between the biomasses and PLA.

Process Stability and Thinning Behavior

Whilst both biomass fillers caused a reduction in the PLA molecular chain length, the extrusion process was more unstable during rice husk powder compounding. GPC analysis indicated that the degree of hydrolysis during processing was slightly higher for the rice husk powder than the wood powder, however the difference was not significant and could not alone justify the rheological differences. The complex viscosity analysis indicated a dramatic thinning effect of the rice husk particles on the PLA (∼ 2.5 times lower at 1 Hz). Thinning/plasticization additives is fairly common in polymer processing however, it is much less common in the case of solids in the 10 to 100's micron size range. Coppola et al. found that the addition of 3 and 5 vol.%, powdered hemp shives in PLA reduced the complex viscosity of the compound compared to neat polymer (Coppola et al., 2018). This behavior was attributed to chemical degradation of the pectin contained in hemp shives. Conversely, Cipriano et al. reported the same effect on PLA caused by magnesium silicate particles (Cipriano et al., 2014). They attributed this lubricant effect to a physical interaction between the particles and the polymer chains.

In this study, both chemical and physical phenomena are valid. Rice husk is composed of 15.2 wt.% amorphous silicate which contributes to its higher density compared to wood or other lignocellulosics (e.g., flax) and could contribute to the rheological thinning behavior as reported Cipriano et al. (2014). However, the concurrent presence of organic materials (e.g., carbohydrates) in the particles also points to a chemical triggered mechanism. The difference in chemical reactivity between wood and rice powders was attributed to the particles size and the ball milling. Ball milling of biomass is known to break down the carbohydrates which increases their reactivity (e.g., better enzymatic adsorption) (Vaidya et al., 2016; Gao et al., 2017). The possibility of reacting these carbohydrates at temperatures above 150°C in an extruder is highly probable leading to the faster production of oxidation products such as alcohols, acids or other volatile products (Formela et al., 2018).

Reactive Extrusion of Lignocellulosic Biomass

During compounding of biomass in PLA, hydrolysis of the polymer chains is known to occur (Le Guen et al., 2017; Thumm et al., 2018). A previous study comparing the mechanical behavior of PLA reinforced with protein-based filler and wood flour reported that under accelerated weathering, the protein-based filler hydrolysed the PLA matrix at least twice as fast as a wood flour filler due to the amino-acids produced from protein hydrolysis (Le Guen et al., 2017). Rice husks contain more proteins than wood (Hamdan et al., 1997; Vadiveloo et al., 2009), however, the GPC analysis indicated comparable molecular weights for the PLA compounded with either wood or rice husk powders. This finding ruled out a potential difference solely based on acid hydrolysis of the PLA chains.

In the case of the rice husk compound, the darkening color could be attributed to two chemical reactions:

- Maillard reaction between the amino acids and the carbohydrates (e.g., xylan), that has been previously reported

- to occur during processing of the rice husks at 180°C (Vegas et al., 2008),
- Carbohydrate oxidation (i.e. caramelization) that is known to form volatile organic molecules (Jiang et al., 2008).

In both cases, the reactions release volatile compounds and water that can explain the instability of the rice husk compounding process and the plasticization of the PLA matrix. Whilst the oxidation reactions also occur with wood powder, the higher reactivity of the rice husk powder compared to the wood powder was attributed to the ball-milling pre-treatment.

CONCLUSIONS

Wood and rice husk powders were blended by twin-screw extrusion with PLA to be used for 3D printing applications. It was found that the mechanical properties of the 3D printed samples at room temperature were mainly driven by the properties of PLA and anisotropy was only influenced by the 3D printing directionality. In addition, the mechanical properties were lowered by the integration of either filler which was attributed to a lowering of inter-strand cohesion in the 3D printed samples. Past the glass transition temperature of the PLA, the fillers enabled the retention of stiffness measured by the storage modulus.

In terms of visual assessment and process stability however, differences were observed and attributed to chemical reactions triggered by the (a) silica content of rice husk and/or (b) chemical reactions including Maillard reaction and carbohydrate oxidations. These chemical reactions were potentially enhanced by a particle size difference (i.e., rice husk powder was smaller and denser than the wood powder) and triggered during the temperature and shearing conditions of the extrusion process. Little polymer research has been conducted on the potential of using reactive biomass filler particles based on mechano-chemistry (i.e., ball milling). These unique findings indicate that biomass can trigger chemical reactions that change the polymer rheological behaviors during processing dramatically and reinforces the need for careful attention when matching a biopolymer matrix with a biomass filler.

The ball-milled rice husk powder's effect on thinning PLA, if controlled during the compounding process, is of major interest in the development of reactive sustainable plastic additives.

DATA AVAILABILITY STATEMENT

All datasets generated for this study are included in the manuscript/supplementary files.

AUTHOR CONTRIBUTIONS

M-JL and CM-L contributed to the design of the research. All authors contributed to its implementation and the analysis of the results as per field of expertise and wrote the manuscript.

ACKNOWLEDGMENTS

The authors thank the French GDR Symbiose, and the New Zealand Ministry of Business, Innovation, and Employment funding under High Value Manufacturing and Services (HVMS) Enabling Technologies investment contract C04X1205.

The authors are gratefully acknowledging the contribution of Mr. Ross Anderson and Mr. Bryce McQuillan for supplying and preparing the wood powder. The authors also want to acknowledge the team of the plant-based platform of the JRU IATE, particularly Charlène Fabre for preparing the rice husk powder. In addition, the authors want to express their gratitude to Dr. Mathias Sorieul, Mr. Armin Thumm, and Mr. Elouan Guillou for their helpful advice.

REFERENCES

Badouard, C., Traon, F., Denoual, C., Mayer-Laigle, C., Paës, G., and Bourmaud, A. (2019). Exploring mechanical properties of fully compostable flax reinforced composite filaments for 3D printing applications. *Indus. Crops Products* 135, 246–250. doi: 10.1016/j.indcrop.2019.04.049

Bettini, S. H. P., de Miranda Josefovich, M. P. P., Muñoz, P. A. R., Lotti, C., and Mattoso, L. H. C. (2013). Effect of lubricant on mechanical and rheological properties of compatibilized PP/sawdust composites. *Carbohyd. Polymers* 94, 800–806. doi: 10.1016/j.carbpol.2013.01.080

Bohren, C. F. and Huffman, D. R. (1983). *Absorption and Scattering of Light by Small Particles*. New York, NY: Wiley.

Bruker BioSpin (2018). *TopSpin 4.0.5 NMR Guide [Computer Software]*. Bruker BioSpin.

Chun, K. S., Husseinsyah, S., and Yeng, C. M. (2018). Torque rheological properties of agro-waste-based polypropylene composites: effect of filler content and green coupling agent. *J. Vinyl Addit. Technol.* 24, E30–E35. doi: 10.1002/vnl.21561

Chungsangunsit, T. (2009). Emission assessment of rice husk combustion for power production. *Int. J. Mech. Aerospace, Indus. Mechatr. Manufact. Eng.* 3. Available online at: https://pdfs.semanticscholar.org/7454/b2f04cd9b56de336abe6ac904f100519f123.pdf

Cipriano, T. F. S., da Silva, A. L. N., da Silva, A. H. M., de Sousa, A. M. F., da Silva, G. M., and Rocha, M. G. (2014). Thermal, rheological and morphological properties of poly (Lactic Acid) (PLA) and talc composites. *Polímeros* 24:2. doi: 10.17265/2161-6221/2013.11.002

Coppola, B., Garofalo, E., Maio, L. D., Scarfato, P., and Incarnato, L. (2018). Investigation on the use of PLA/hemp composites for the fused deposition modelling (FDM) 3D printing. *AIP Conference Proc.* 1981:020086. doi: 10.1063/1.5045948

Formela, K., Zedler, Ł., Hejna, A., and Tercjak, A. (2018). Reactive extrusion of bio-based polymer blends and composites – Current trends and future developments. *Exp. Polymer Lett.* 12, 24–57. doi: 10.3144/expresspolymlett.2018.4

Gallos, A., Paës, G., Allais, F., and Beaugrand, J. (2017). Lignocellulosic fibers: a critical review of the extrusion process for enhancement of the properties of natural fiber composites. *RSC Adv.* 7, 34638–34654. doi: 10.1039/C7RA05240E

Gao, C., Xiao, W., Ji, G., Zhang, Y., Cao, Y., and Han, L. (2017). Regularity and mechanism of wheat straw properties change in ball milling process at cellular scale. *Bioresour. Technol.* 241, 214–219. doi: 10.1016/j.biortech.2017.04.115

Gibson, M. A., Mykulowycz, N. M., Shim, J., Fontana, R., Schmitt, P., Roberts, A., et al. (2018). 3D printing metals like thermoplastics: fused filament fabrication of metallic glasses. *Mater. Today* 21, 697–702. doi: 10.1016/j.mattod.2018.07.001

Giddel, M. R., and Jivan, A. P. (2007). "Waste to wealth, potential of rice husk in india a literature review," in *International Conference on Cleaner Technologies and Environmental Management PEC, Pondicherry*, 586–590.

Gil, A. M., and Neto, C. P. (1999). Solid-state NMR studies of wood and other lignocellulosic materials. *Ann. Rep. NMR Spectrosc.* 37, 75–117. doi: 10.1016/S0066-4103(08)60014-9

Graichen, F. H. M., Grigsby, W. J., Hill, S. J., Raymond, L. G., Sanglard, M., Smith, D. A., et al. (2017). Yes, we can make money out of lignin and other bio-based resources. *Indus. Crops Products* 106, 74–85. doi: 10.1016/j.indcrop.2016.10.036

Hamdan, H., Muhid, M. N. M., Endud, S., Listiorini, E., and Ramli, Z. (1997). 29Si MAS NMR, XRD and FESEM studies of rice husk silica for the synthesis of zeolites. *J. Non-Crystalline Solids* 211, 126–131. doi: 10.1016/S0022-3093(96)00611-4

Jiang, B., Liu, Y., Bhandari, B., and Zhou, W. (2008). Impact of caramelization on the glass transition temperature of several caramelized sugars. Part I: chemical analyses. *J. Agric. Food Chem.* 56, 5138–5147. doi: 10.1021/jf703791e

Juliano, B. O., Maniñgat, C. C., Pascual, G. C. (1987). Properties of fraction of rice hull. *Phytochemistry* 26, 3261–3263. doi: 10.1016/S0031-9422(00)82483-8

Kumar, A., Mohanta, K., Kumar, D., and Parkash, O. (2012). Properties and industrial applications of rice husk: a review. *Int. J. Emerg. Technol. Adv. Eng.* 2, 86–90.

Lammi, S., Le Moigne, N., Djenane, D., Gontard, N., and Angellier-Coussy, H. (2018). Dry fractionation of olive pomace for the development of food packaging biocomposites. *Indus. Crops Products* 120, 250–261. doi: 10.1016/j.indcrop.2018.04.052

Le Duigou, A., Castro, M., Bevan, R., and Martin, N. (2016). 3D printing of wood fibre biocomposites: from mechanical to actuation functionality. *Mater. Design* 96, 106–114. doi: 10.1016/j.matdes.2016.02.018

Le Guen, M.-J., Thoury-Monbrun, V., Castellano Roldán, J. M., and Hill, S. J. (2017). Assessing the potential of farm dairy effluent as a filler in novel PLA biocomposites. *J. Polymers Environ.* 25, 419–426. doi: 10.1007/s10924-016-0824-1

Le Guen, M. J., and Newman, R. H. (2007). Pulped Phormium tenax leaf fibres as reinforcement for epoxy composites. Composites Part A. *Appl. Sci. Manufact.* 38, 2109–2115. doi: 10.1016/j.compositesa.2007.07.001

Li, T. Q., and Wolcott, M. P. (2004). Rheology of HDPE–wood composites. I. Steady state shear and extensional flow. Composites Part A. *Appl. Sci. Manufact.* 35, 303–311. doi: 10.1016/j.compositesa.2003.09.009

Liles, K. P., Greene, A. F., Danielson, M. K., Colley, N. D., Wellen, A., Fisher, J. M., Barnes, J. C. Photoredox-Based Actuation of an Artificial Molecular Muscle. *Macromol. Rapid Commun.* (2018) 39:1700781. doi: 10.1002/marc.201700781

Lv, H., Song, S., Sun, S., Ren, L., and Zhang, H. (2016). Enhanced properties of poly(lactic acid) with silica nanoparticles. *Polymers Adv. Technol.* 27, 1156–1163. doi: 10.1002/pat.3777

Malvern (2007). *Sample Dispersion and Refractive Index Guide - Mastersizer* 2000. Malvern.

Mirko, K., Sernek, M., and Kitek Kuzman, M. (2016). Use of wood powder and adhesive as a mixture for 3D printing. *Eur. J. Wood Wood Products* 74:123. doi: 10.1007/s00107-015-0987-9

Montalvo Navarrete, J. I., Hidalgo-Salazar, M. A., Escobar Nunez, E., and Rojas Arciniegas, A. J. (2018). Thermal and mechanical behavior of biocomposites using additive manufacturing. *Int. J. Interact. Design Manufact.* 12, 449–458. doi: 10.1007/s12008-017-0411-2

Muniyasamy, S. (2013). Biodegradability and compostability of lignocellulosic based composite Materials. *J. Renew. Mater.* 1:253.

Müssig, J. (2010). *Industrial Applications of Natural Fibres: Structure, Properties and Technical Applications*. John Wiley & Sons, Ltd. doi: 10.1002/9780470660324

Newman, R. H., Hemmingson, J. A., and Suckling, I. D. (1993). Carbon13 nuclear magnetic resonance studies of kraft pulping. *Holzforschung,* doi: 10.1515/hfsg.1993.47.3.234

Pode, R. (2016). Potential applications of rice husk ash waste from rice husk biomass power plant. *Renew. Sustain. Energy Rev.* 53, 1468–1485. doi: 10.1016/j.rser,.2015.09.051

Revelo, C. F., and Colorado, H. A. (2018). 3D printing of kaolinite clay ceramics using the Direct Ink Writing (DIW) technique. *Ceram. Int.* 44, 5673–5682. doi: 10.1016/j.ceramint.2017.12.219

Shao, Y., Guizani, C., Grosseau, P., Chaussy, D., and Beneventi, D. (2018). Use of lignocellulosic materials and 3D printing for the development of structured monolithic carbon materials. *Compos. Part B Eng.* 149, 206–215. doi: 10.1016/j.compositesb.2018.05.035

Singamneni, S., Behera, M. P., Le Guen, M., and Zeidler, H. (2018a). Mechanism of bonding in seashell powder based ceramic composites used for binder-jet 3D printing. *Bioceram. Dev. Appl.* 108. Available online at: https://www.omicsonline.org/open-access/mechanism-of-bonding-in-seashell-powder-based-ceramic-compositesused-for-binderjet-3d-printing-2090-5025-1000108.pdf

Singamneni, S., Smith, D., LeGuen, M.-J., and Truong, D. (2018b). Extrusion 3D printing of polybutyrate-adipate-terephthalate-polymer composites in the pellet form. *Polymers* 10:922. doi: 10.3390/polym10080922

Sydney Gladman, A., Matsumoto, E. A., Nuzzo, R. G., Mahadevan, L., and Lewis, J. A. (2016). Biomimetic 4D printing. *Nat. Mater.* 15:413. doi: 10.1038/nmat4544

Tao, Y., Wang, H., Li, Z., Li, P., and Shi, S. Q. (2017). Development and application of wood flour-filled polylactic acid composite filament for 3D printing. *Materials* 10:339. doi: 10.3390/ma10040339

Thumm, A., Even, D., Gini, P.-Y., and Sorieul, M. (2018). Processing and properties of MDF fibre-reinforced biopolyesters with chain extender additives. *Int. J. Polymer Sci.* 2018:9. doi: 10.1155/2018/9601753

Ummah, H., Suriamihardja, D., Selintung, M., and Wahab, A. W. (2015). Analysis of chemical composition of rice husk used as absorber plates sea water into clean water. *ARPN J. Eng. Appl. Sci.* 10, 6046–6050.

Vadiveloo, J., Nurfariza, B., and Fadel, J. G. (2009). Nutritional improvement of rice husks. *Anim. Feed Sci. Technol.* 151, 299–305. doi: 10.1016/j.anifeedsci.2009.03.002

Vaidya, A. A., Donaldson, L. A., Newman, R. H., Suckling, I. D., Campion, S. H., Lloyd, J. A., et al. (2016). Micromorphological changes and mechanism associated with wet ball milling of Pinus radiata substrate and consequences for saccharification at low enzyme loading. *Bioresour. Technol.* 214, 132–137. doi: 10.1016/j.biortech.2016.04.084

Vegas, R., Kabel, M., Schols, H. A., Alonso, J. L., and Parajó, J. C. (2008). Hydrothermal processing of rice husks: effects of severity on product distribution. *J. Chem. Technol. Biotechnol.* 83, 965–972. doi: 10.1002/jctb.1896

Wang, Q., Sun, J., Yao, Q., Ji, C., Liu, J., and Zhu, Q. (2018). 3D printing with cellulose materials. *Cellulose* 25, 4275–4301. doi: 10.1007/s10570-018-1888-y

Yalçin, N., and Sevinç, V. (2001). Studies on silica obtained from rice husk. *Ceram. Int.* 27, 219–224. doi: 10.1016/S0272-8842(00)00068-7

Zeidler, H., Klemm, D., Böttger-Hiller, F., Fritsch, S., Le Guen, M. J., and Singamneni, S. (2018). 3D printing of biodegradable parts using renewable biobased materials. *Proc. Manufact.* 21, 117–124. doi: 10.1016/j.promfg.2018.02.101

Conflict of Interest: The authors declare that the research was conducted in the absence of any commercial or financial relationships that could be construed as a potential conflict of interest.

Copyright © 2019 Le Guen, Hill, Smith, Theobald, Gaugler, Barakat and Mayer-Laigle. This is an open-access article distributed under the terms of the Creative Commons Attribution License (CC BY). The use, distribution or reproduction in other forums is permitted, provided the original author(s) and the copyright owner(s) are credited and that the original publication in this journal is cited, in accordance with accepted academic practice. No use, distribution or reproduction is permitted which does not comply with these terms.

frontiers in Chemistry

ORIGINAL RESEARCH
published: 08 November 2019
doi: 10.3389/fchem.2019.00757

Short Carbon Fiber Reinforced Polymers: Utilizing Lignin to Engineer Potentially Sustainable Resource-Based Biocomposites

László Szabó*[1]*, Romain Milotskyi*[1]*, Tetsuo Fujie*[1]*, Takayuki Tsukegi*[2]*, Naoki Wada*[1]*, Kazuaki Ninomiya*[3] *and Kenji Takahashi*[1]*

[1] Institute of Science and Engineering, Kanazawa University, Kanazawa, Japan, [2] Innovative Composite Center, Kanazawa Institute of Technology, Hakusan, Japan, [3] Institute for Frontier Science Initiative, Kanazawa University, Kanazawa, Japan

Carbon fiber reinforced composites have exceptional potential to play a key role in the materials world of our future. However, their success undoubtedly depends on the extent they can contribute to advance a global sustainability objective. Utilizing polymers in these composites that can be potentially derived from biomasses would be certainly vital for next-generation manufacturing practices. Nevertheless, deep understanding and tailoring fiber-matrix interactions are crucial issues in order to design carbon fiber reinforced sustainable resource-based biocomposites. In this study, cellulose derivatives (cellulose propionate and cellulose acetate butyrate) are utilized as model polymer matrices that can be potentially fabricated from biomasses, and the mechanical properties of the prepared short carbon fiber reinforced composites are engineered by means of a functional biobased lignin coating on the fiber surface. Furthermore, polyamide 6 based composites are also prepared, the monomer of this polymer could be obtained using C_6 sugars derived from lignocellulosic biomasses in the future (through 5-hydroxymethylfurfural). Lignin was successfully immobilized on the carbon fiber surface via an industrially scalable benign epoxidation reaction. The surface modification had a beneficial impact on the mechanical properties of cellulose propionate and polyamide 6 composites. Furthermore, our results also revealed that cellulose-based matrices are highly sensitive to the presence of rigid fiber segments that restrict polymer chain movements and facilitate stress development. It follows that the physicochemical properties of the cellulosic matrices (molecular weight, crystallinity), associated with polymer chain mobility, might need to be carefully considered when designing these composites. At the same time, polyamide 6 showed excellent ability to accommodate short carbon fibers without leading to a largely brittle material, in this case, a maximum tensile strength of ∼136 MPa was obtained at 20 wt% fiber loading. These results were further contrasted with that of a petroleum-based polypropylene matrix exhibiting inferior mechanical properties. Our study clearly indicates that carbon fiber reinforced polymers derived and designed using biomass-derived resources can be promising green materials for a sustainable future.

Keywords: lignin, biocomposite, carbon fiber, surface modification, discontinuous reinforcement, cellulose, polyamide 6

OPEN ACCESS

Edited by:
Xavier Coqueret,
Université de Reims Champagne-Ardenne, France

Reviewed by:
Wenbo Wang,
Lanzhou Institute of Chemical Physics (CAS), China
Luke Henderson,
Deakin University, Australia

***Correspondence:**
László Szabó
szabo-laszlo@se.kanazawa-u.ac.jp
Kenji Takahashi
ktkenji@staff.kanazawa-u.ac.jp

Specialty section:
This article was submitted to Green and Sustainable Chemistry, a section of the journal Frontiers in Chemistry

Received: 09 May 2019
Accepted: 22 October 2019
Published: 08 November 2019

Citation:
Szabó L, Milotskyi R, Fujie T, Tsukegi T, Wada N, Ninomiya K and Takahashi K (2019) Short Carbon Fiber Reinforced Polymers: Utilizing Lignin to Engineer Potentially Sustainable Resource-Based Biocomposites. Front. Chem. 7:757. doi: 10.3389/fchem.2019.00757

INTRODUCTION

On account of a seemingly irreversible signature the human activity has already left on Earth, plastics among many manufactured modern materials can be found in geological deposits (Waters et al., 2016; Schneiderman and Hillmyer, 2017). It becomes, therefore, increasingly recognized that a new geological era, "Anthropocene" has certainly arrived due to the anthropogenic activity of the past decades (Waters et al., 2016). In light of the escalated situation, it is time to make right choices and consider the use of biobased biodegradable sources when designing materials (Chen and Patel, 2012; Sheldon, 2014; Graichen et al., 2017; Schneiderman and Hillmyer, 2017). As a result of tremendous research efforts, it appears that most of the important plastics can be derived from renewable sources (Chen and Patel, 2012; Schneiderman and Hillmyer, 2017), and these materials can be further tailored to make sustainable biocomposites for wide range of applications (Mohanty et al., 2018). In order to make the right decisions, deep understanding and tailoring the interactions between matrix segments in these biocomposites are essential, however, pose major scientific challenges in many cases.

Particular sustainability concerns are surrounding advanced structures that are recently gaining interest in several fields, and thereby are predicted to be key components in the materials world of the future. Based on their market growth and exceptional properties (Frank et al., 2014; Witten et al., 2017), carbon fiber reinforced polymers are these types of materials that must be strictly designed from the point of view of sustainability issues. In response to these concerns, pioneering work has started worldwide to prepare carbon fibers from renewable resources (Milbrandt and Booth, 2016). Among the possible candidates, lignin as the most abundant aromatic biopolymer has emerged as a very promising sustainable precursor, opening the gates for the production of low-cost biomass-derived carbon fibers (Fang et al., 2017). In respect to the polymer matrix of carbon fiber reinforced composites, intense research has been focused on changing the most frequently used thermoset epoxy matrix to recyclable thermoplastic resins targeting environmentally more benign compositions (Yao et al., 2018). Short carbon fiber reinforced thermoplastic composites are particularly attractive materials for industrial mass production due to their short production time and recyclability potential (Fu and Lauke, 1996; Fu et al., 2000; Karsli and Aytac, 2011, 2013; Ozkan et al., 2014; Unterweger et al., 2015).

Recent advances achieved in our laboratory hold promise for deriving thermoplastic cellulose derivatives from biomasses (Kakuchi et al., 2017; Suzuki et al., 2018), and utilizing these materials for preparing short carbon fiber reinforced plastics (Szabó et al., 2019a). We have also shown that the adhesion between the cellulosic matrix and carbon fiber can be improved by modifying the carbon fiber surface (Szabó et al., 2018a,b, 2019b). It appeared that immobilizing lignin on carbon fiber surface leads to a great enhancement in interfacial properties due to secondary interactions between lignin and the polymer matrix (Szabó et al., 2019b). It follows that lignin can serve as a functional material to improve the interfacial interactions in green biobased composites. In order to further test these theories, in this study we prepare short carbon fiber reinforced composites utilizing polymers that can be potentially derived from biomasses [cellulose derivatives (Kakuchi et al., 2017; Suzuki et al., 2018) and polyamide 6 (Buntara et al., 2011; Winnacker and Rieger, 2016)] as model materials and tailor the interfacial interactions utilizing lignin as a renewable resource.

While in our previous study we placed interfacial interactions under scrutiny (Szabó et al., 2019b), and therefore, surface modification was achieved via industrially and environmentally less attractive chemistries, here we bind lignin to the carbon fiber surface via a mild, environmentally benign and industrially scalable epoxidation reaction. The surface modified short fibers are embedded in the polymer matrices, and the macroscopic properties of the composites are extensively characterized. Our results are also compared to that obtained with a purely petroleum-derived polypropylene matrix.

EXPERIMENTAL

Materials

The short carbon fiber used in this study was a 3 mm long PX35 type fiber obtained from Zoltek (Toray Group, St. Charles, MO, USA). These chopped fibers have no sizing agent on the surface and are characterized by a nominal diameter of 7.2 μm. Prior to the experiments, the fibers were dried in a vacuum oven at 130°C for 72 h. In the cyclic voltammetry experiments due to the experimental setup, long fibers were used (T700SC-12000-50C, Toray Industries, Tokyo, Japan), in this case, the sizing agent was removed according to our previously elaborated procedure (Szabó et al., 2018a,b, 2019b).

As cellulose-based matrices, two commercially available thermoplastic esters (cellulose propionate and cellulose acetate butyrate) were used, these polymers showed excellent processability in preliminary experiments. Cellulose propionate ($M_\mathrm{n} \approx 79\ 000$ g mol^{-1}) was purchased from Scientific Polymer Products, Inc. (Ontario, NY, USA; Catalog number 321), the degree of substitution (DS) value has been determined previously as DS = 2.76 (92% of the hydroxyl groups are functionalized) (Szabó et al., 2018a). Cellulose acetate butyrate ($M_\mathrm{n} \approx 70\ 000$ g mol^{-1}) was provided by Eastman Chemical Company (Kingsport, TN, USA; Catalog number 381-20), the degree of substitution value is as follows: $\mathrm{DS}_\mathrm{acetyl} = 1.00$ (33.3% of the originally available hydroxyl groups), $\mathrm{DS}_\mathrm{butyryl} = 1.66$ (55.3% of the originally available hydroxyl groups). Furthermore, polyamide 6 resin (melt flow rate of 15 g per 10 min at 230°C) was obtained from Toray Industries (Tokyo, Japan; Catalog number CM1006). Polypropylene (melt flow rate of 25 g per 10 min at 230°C) was from Japan Polypropylene Corporation (Yokkaichi, Japan; Catalog number WINTEC™ WSX03). The cellulosic resins and polyamide 6 were dried in a vacuum oven at 120°C for 1 day before the experiments, and all the resins were kept in a dry box (containing silica gel) prior to use.

Kraft lignin ($M_\mathrm{w} \approx 10000$ g mol^{-1}; low sulfonate content) was purchased from Sigma Aldrich (St. Louis, MO, USA; Lot # 04414PEV), distribution of the hydroxyl groups has been determined in our previous study as follows (Szabó et al., 2019b): $OH_{phenolic} = 2.12$ mmol g^{-1}, $OH_{aliphatic} = 1.65$ mmol g^{-1}, $OH_{carboxylic} = 0.59$ mmol g^{-1}, $OH_{total} = 4.36$ mmol g^{-1}.

Anhydrous pyridine, *N*,*N*-dimethylformamide (DMF) and ferrocenemethanol were provided by Sigma Aldrich (St. Louis, MO, USA). The solvents acetonitrile (ACN) and dichloromethane (DCM) were obtained from Naclai Tesque, Inc. (Kyoto, Japan) and Kanto Chemical (Tokyo, Japan), respectively. All the other chemicals were from Tokyo Chemical Industry Co., Ltd. (Tokyo, Japan).

Synthetic Procedures

Lignin Modification

Kraft lignin was tosylated according to our previously reported procedure using tosyl chloride (and pyridine as solvent), a detailed description can be found elsewhere (Szabó et al., 2019b). The synthetic procedure affords tosylated lignin derivative with a tosyl group content of 0.26 mmol g^{-1} (calculated from elemental analysis). The tosylation procedure is necessary to render the original lignin soluble in the conventional solvent used for the grafting procedure (*N*,*N*-dimethylformamide, see **Figure 1**).

Carbon Fiber Surface Modification

The surface of carbon fibers was epoxidized according to a recently reported procedure applying mild conditions (Koutroumanis et al., 2018), the synthetic method was previously elaborated for carbon nanotubes (Ogrin et al., 2006). The grafting procedure is outlined in **Figure 1**.

Briefly, 6 g chopped carbon fibers are immersed in a solution containing 30 g 3-chloroperoxybenzoic acid [by dry weight, note that due to instability issues the reagent has around 30% water content; equals 29.2 mmol g^{-1} fibers, following the stoichiometries elaborated in our previous works (Szabó et al., 2018a,b, 2019b)] in 500 mL dichloromethane. The reaction is conducted for 5 min, and the fibers are immediately washed using around 1 L dichloromethane to remove the unreacted reagents, and then they are placed in a solution containing 10 g tosylated lignin in 300 mL DMF. The reaction is conducted at room temperature overnight in a double shaker operating at 80 min^{-1} speed (Double Shaker NR-30, Taitec Corporation, Koshigaya, Japan). The functionalized fibers are washed with water, dichloromethane and acetone. The fibers are then dried in a vacuum drying oven at 50°C for 24 h.

It should be noted that 5 min reaction time was reported to be sufficient to reach the maximum amount of epoxide functions on the surface (Koutroumanis et al., 2018). In line with these findings, we could not observe improvement in the amount of epoxide functions when we applied 10 min reaction time (electrochemical analysis after Reaction 3, see in **Figure 2**, note that data for 10 min are not shown).

Cyclic Voltammetry Experiments

Cyclic voltammetry experiments were conducted to confirm the epoxidation reaction and prove the reactivity of the newly generated oxygen functions toward an aliphatic hydroxyl group. For this purpose, after the epoxidation reaction (Reaction 1 in **Figure 1**), 25 mg carbon fibers were placed in a solution containing 0.158 g ferrocenemethanol (0.73 mmol) in DMF, for 24 h at room temperature. After the reaction, the fibers were exhaustively washed according to the previously mentioned cleaning procedure, and then applied as working electrodes in the following cyclic voltammetry setup. The reaction is depicted in **Figure 2**.

The three-electrode cyclic voltammetry cell included a Pt auxiliary electrode, an Ag/Ag^+ reference electrode (0.01 M $AgNO_3$ and 0.1 M tetrabutylammonium perchlorate in acetonitrile; ALS Co., Ltd, Tokyo, Japan) and carbon fiber was applied as working electrode. The SVC3 type voltammetry cell was connected to an ALS/CH Instruments Electrochemical Analyzer Model 1200A potentiostat (ALS Co., Ltd, Tokyo, Japan). Further experimental details can be found in our previous work (Szabó et al., 2019b).

Composite Preparation

Carbon fibers and the resin were compounded in an Xplore MC5 microcompounder equipped with short co-rotating twin-screw (Xplore Instruments BV, Sittard, The Netherlands). The composites were subjected to an injection molding step using an Imoto IMC-5705 injection molding machine to prepare standard dumbbell-shaped specimens (JIS K 7161-2:2014 1BA) for the mechanical tests. The experimental details for each type of resins are given in **Table 1**.

The flow characteristics of the resins were analyzed using a Shimadzu CFT-500EX Constant Test Force Extrusion Type Capillary Rheometer (Kyoto, Japan) following our previously reported procedures (Szabó et al., 2019a). The flow characteristics of the neat polymers can be found in the Supplementary Material (**Figure S1**).

Mechanical Test

Tensile test was performed according to JIS K7161 standard (in line with ISO 527) using a Shimadzu Autograph AG-X Plus 5 kN tensile tester (Kyoto, Japan) equipped with a non-contact video type extensometer (TRViewX, Shimadzu; Kyoto, Japan). The crosshead-speed was 5 mm min^{-1} and a clamping pressure of 0.5 MPa was applied. Ten specimens were prepared for each composition.

Multiple *t*-test was performed to identify statistically significant differences (with a P-value <0.05) in the results of the tensile test, assuming that the data represent a population with equal variance.

Surface Analysis

X-ray photoelectron spectra were recorded on a Thermo Scientific K-Alpha X-ray Photoelectron Spectrometer System using Al K_α monochromated X-ray radiation (1486.6 eV, 36 W; Waltham, MA, USA). Data were collected from a spot size of 400 μm and the binding energy scale was calibrated to the hydrocarbon C1s peak at 285.0 eV. Survey spectra were obtained with a resolution of 1 eV and high-resolution C1s, N1s, O1s, and S2p spectra were recorded using a pass energy of 20 eV and a spectral resolution of 0.1 eV. Data were processed with a Thermo Scientific Avantage Software version 5.89 (Waltham, MA, USA). Overlapping peaks were resolved using the Powel method with

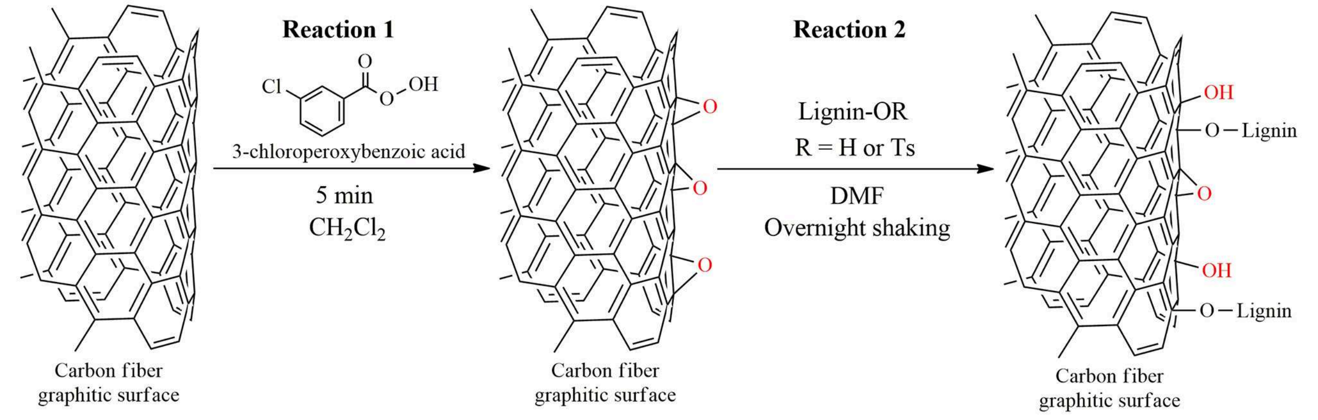

FIGURE 1 | Representative reaction scheme depicting the functionalization procedure (illustrative example).

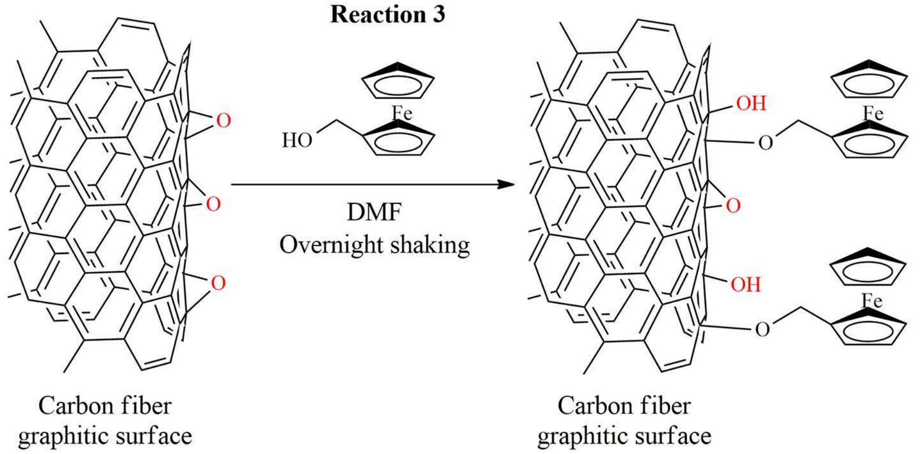

FIGURE 2 | Representative reaction scheme for binding an electrochemical probe to the carbon fiber surface after the epoxidation step (illustrative example).

Gauss-Lorentz Mix algorithm and a built-in Smart algorithm for background correction.

Morphological analysis was performed with a JSM-7610F field emission scanning electron microscope (FE-SEM) applying 8 mm working distance and 15 kV accelerating voltage (JEOL, Tokyo, Japan). Prior to the analysis, Au/Pd layer was sputtered on the sample surface using a Hitachi E1030 type equipment and a deposition time of 40 s (Hitachi, Ltd., Tokyo, Japan).

Thermal Analysis

Thermogravimetric analysis was performed using a Shimadzu DTG-60AH thermal analyzer (Shimadzu Corporation, Kyoto, Japan) with a heating rate of 20°C $\min^{-1}$ under nitrogen atmosphere. Differential Scanning Calorimetry (DSC) experiments were conducted on a Shimadzu DSC-60A Plus equipment (Shimadzu Corporation, Kyoto, Japan) to determine the glass transition temperature of the polymers and their composites. DSC thermographs were recorded between −50 and 250°C using a heating rate of 10°C $\min^{-1}$ and a cooling rate of 50°C $\min^{-1}$. The second heating cycle was analyzed to determine the glass transition temperature.

Fiber Length Analysis

Carbon fibers were extracted from the prepared composites using DMF as a solvent in case of the cellulosic matrices. Furthermore, for polyamide 6 and polypropylene based composites the matrix was separated from the fibers via a burning process performed at 550°C for 10 min in an electric furnace (ROP-001 type, ASONE Corporation, Osaka, Japan), and the obtained fibers were dispersed in water (Fu et al., 2000; Karsli and Aytac, 2013). Optical images of the fibers were recorded on an Olympus BX50 microscope (Tokyo, Japan). The images were analyzed with ImageJ program extended with the ridge/line detection algorithm (Steger, 1998).

RESULTS AND DISCUSSION

It has been revealed in our previous work that lignin can improve the shear tolerance at the carbon fiber-matrix interface in green

TABLE 1 | Processing conditions for the extrusion and injection molding steps.

Polymer resin	Extrusion process			Injection molding		
	Rotation speed	**Retention time**	**Processing temperature**	**Barrel temperature**	**Mold temperature**	**Injection pressure**
Cellulose propionate	60 rpm	5 min	203°C	210°C	140°C	0.6 MPa
Cellulose acetate butyrate						
Polyamide 6			238°C	233°C	80°C	
Polypropylene			180°C	180°C	60°C	0.2 MPa

cellulose-based (cellulose propionate) and commercially available epoxy-based composites (Szabó et al., 2019b). An exceptionally high interfacial shear strength was experienced as matrix failure took place before interfacial failure. Stimulated by the functional and green nature of lignin, we decided to take a step forward and scale-up the process using industrially attractive benign chemistries. Furthermore, we were not only interested in the macroscopic/mechanical outcome of the surface modification but also had a curiosity of how the interfacial effects are expressed for different type of matrices with sustainability potentials. Therefore, in addition to two cellulosic matrices (cellulose propionate and cellulose acetate butyrate), we extended our work to polyamide 6, which could be prepared using C_6 sugars derived from lignocellulosic biomasses in the future (Buntara et al., 2011). Furthermore, we also compare these results with a potentially non-sustainable fully petroleum-based polypropylene matrix.

Carbon Fiber Surface Modification

Our surface modification procedure was inspired by the convenient and efficient way of nanotube sidewall functionalization exploiting the ring-opening reactions between newly generated epoxide functions and nucleophilic agents (Markiewicz et al., 2014). Furthermore, the epoxidation process was recently applied for carbon fibers revealing the non-destructive, short, and benign nature of the functionalization procedure (Koutroumanis et al., 2018). Our surface treatment starts with a conventional epoxidation reaction carried out with short carbon fibers, which are placed in contact immediately with the tosylated lignin derivative (**Figure 1**). The main purpose of the tosylation reaction is to render the lignin derivative soluble in DMF. The tosylation procedure adopted from our previous study (Szabó et al., 2019b) affords a lignin derivative with a tosyl group content of 0.26 mmol g^{-1} (involving a range of aliphatic and aromatic hydroxyl groups, due to solubility issues ^{31}P-NMR experiments could not be performed to investigate the hydroxyl group distribution profile), and leaves 4.1 mmol g^{-1} free hydroxyl groups behind. These free hydroxyl groups are expected to react with the epoxide groups present on carbon fiber surface. The nucleophilic attack on an epoxide typically follows S_N2 mechanism, however, due to steric reasons (the reaction would require 180° attack on the epoxide carbon) this cannot be the case on the surface of carbon fibers. Nevertheless, it might be possible that the reaction eventually proceeds via a carbocation intermediate as it was shown before on arene oxides (Loew et al., 1980). Reactions on surfaces often follow atypical pathways owing to steric effects, the nucleophilic attack on the epoxidized carbon fiber surface might represent an interesting example, which would merit further attention.

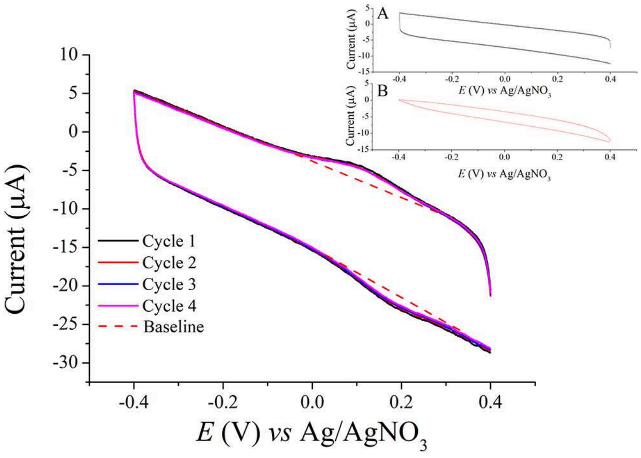

FIGURE 3 | Cyclic voltammogram recorded with carbon fibers as working electrodes functionalized via Reaction 3 (**Figure 2**). Inset A shows the cyclic voltammetry response of a control sample; in this case Reaction 3 was performed with ferrocene instead of ferrocenemethanol to observe any interferences arising from π-π stacking interactions. Inset B shows another control sample, in this case unmodified carbon fibers (before epoxidation) were incubated with ferrocenemethanol under the conditions outlined in Reaction 3 to investigate the possibility of H-bonding interactions with surficial functional groups (-OH, -COOH, and -NH_2 moieties).

The formation of epoxide groups, their reactivity as well as their quantity were investigated through cyclic voltammetry experiments. In these experiments, the epoxidized carbon fibers were reacted with ferrocenemethanol to immobilize the redox probe on the surface (**Figure 2**). Thereafter, the fibers were applied as working electrodes in a three-electrode cyclic voltammetry setup. The recorded voltammograms are shown in **Figure 3**. From the anodic and cathodic peaks, a standard electrode potential of $E^0 = 0.15\,V$ vs. Ag/$AgNO_3$ can be calculated, which is typical for ferrocene structures covalently bound to electrode surfaces (Umaña et al., 1980; Goff et al., 2010). The electrochemical response does not change over several cycles suggesting that stable structures have been immobilized on the substrates. Furthermore, in parallel experiments the possibility of π-π stacking interactions was firmly excluded since when ferrocene was applied in Reaction 3 (**Figure 2**) instead of ferrocenemethanol, no electrochemical response was obtained (**Figure 3** Inset A). The possibility of H-bonding

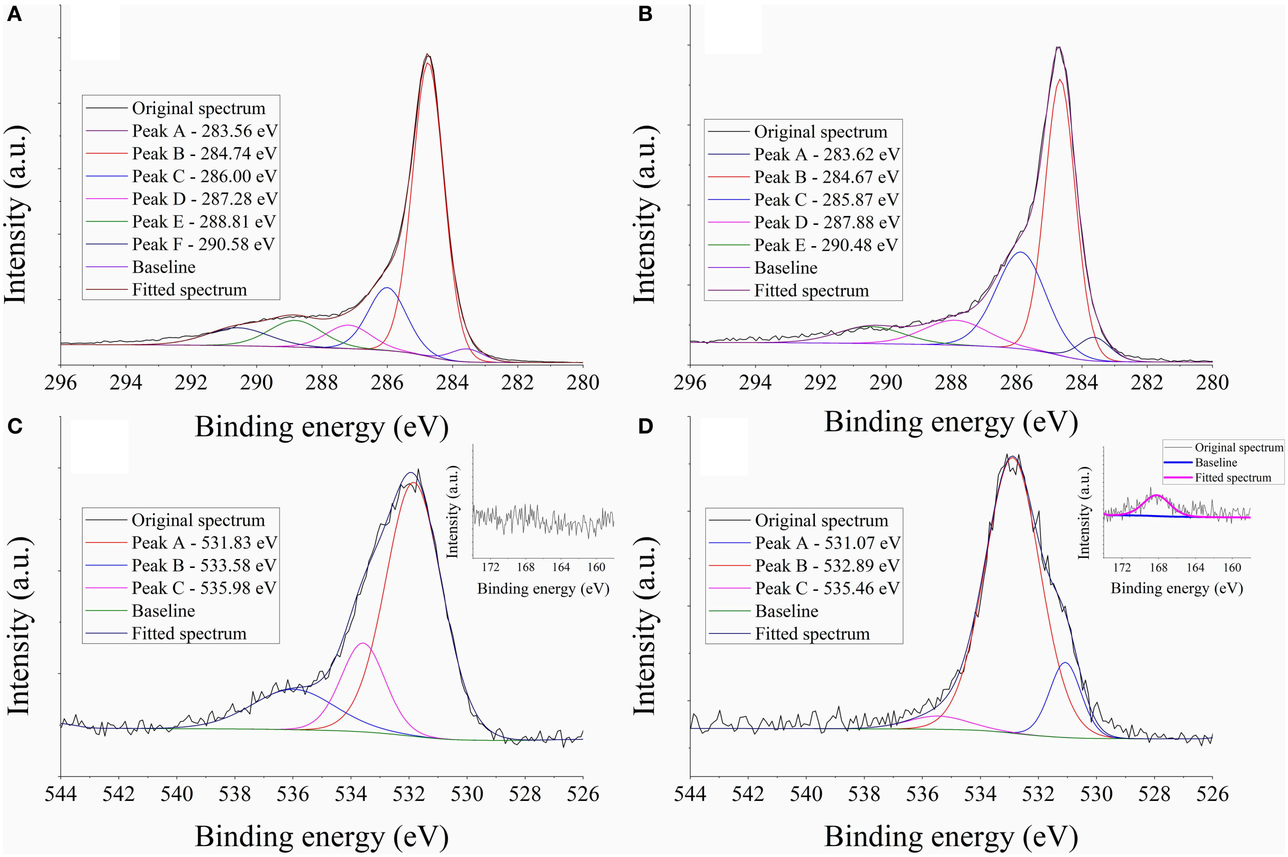

FIGURE 4 | High-resolution C1s **(A,B)**, O1s **(C,D)** and S2p (Insets) X-ray photoelectron spectra of carbon fiber samples before modification **(A,C)** and after immobilizing lignin on the surface **(B,D)**.

interactions between ferrocenemethanol and surficial functional groups [-OH, -COOH and -NH_2 moieties that are known to be present on carbon fiber surface (Xie and Sherwood, 1989)] was also excluded as no electrochemical response can be seen for the corresponding control sample in **Figure 3** (Inset B). By integrating the anodic/cathodic current (in **Figure 3**), the amount of transferred electrons can be calculated and thereby, the number of molecules determined. The surface coverage amounts to a value of 6.5×10^{11} molecules mg^{-1} according to these calculations. This value is much lower than that reported in our previous study (Szabó et al., 2019b), where we used much more aggressive chemistries (free radical-mediated reaction). However, it is considered that a high surface coverage might not be necessary for polymeric substrates having large amount of reactive functions in their structure. Therefore, the results of the cyclic voltammetry experiments indicate that the epoxidation reaction might be an appropriate measure to covalently bind lignin to the carbon fiber surface.

In order to confirm the immobilization of lignin on the surface, the high-resolution C1s, O1s, and S2p X-ray photoelectron spectra of the unmodified and functionalized carbon fiber samples were recorded, the results are shown in **Figure 4**. The high-resolution C1s spectra of the unmodified/modified samples (**Figures 4A,B**) can be resolved into a main peak centered at ∼285 eV, typical for the graphitic carbon present in the structure of carbon fibers (Xie and Sherwood, 1989; Zhang et al., 2008). The C1s spectrum of the unmodified sample (**Figure 4A**) consists of peaks typically assigned to C-OH/C-O-C (286.00 eV; note that C=N moieties also give signal around this region), C=O (287.28 eV) and –COOH (288.81 eV) groups (Xie and Sherwood, 1989). Furthermore, the peak located at higher energies (290.58 eV) is attributed to π-π^* shake up satellites (Xie and Sherwood, 1989; Zhang et al., 2008). In addition, the O1s spectrum (**Figure 4C**) is dominated by a peak centered at 531.83 eV, assigned to C=O or C-O-C moieties (Xie and Sherwood, 1989), while the peaks located at 533.58 and 535.98 eV are usually assigned to C=O groups and probably to some chemisorbed oxygen, respectively (Xie and Sherwood, 1989). After the functionalization process, an increase in the intensity of the peak located at ∼286 eV is observable in the C1s spectrum (**Figure 4B**), this peak was assigned to –C-OH/C-O-C functions. Furthermore, the peak intensity at higher energies decreases, C=O and –COOH functions give signals around this region. The O1s spectrum also changes appreciably after the functionalization process (**Figure 4D**). It is dominated by a peak assigned to C-OH groups

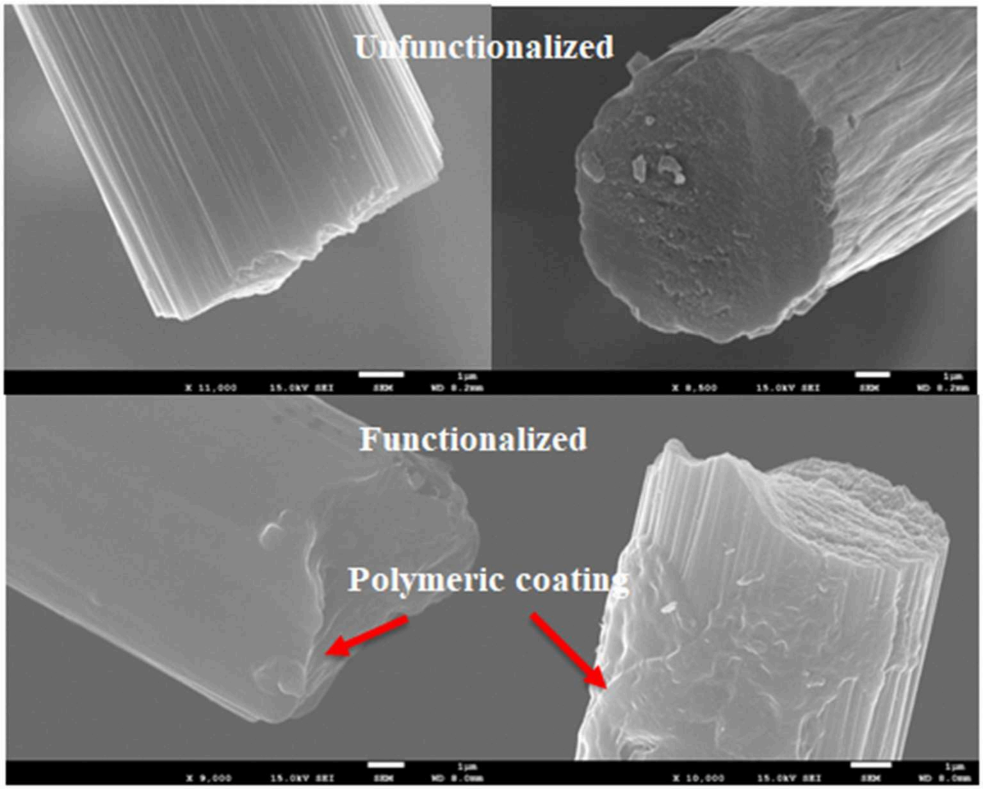

FIGURE 5 | FE-SEM micrographs of carbon fiber samples before **(upper part)** and after **(lower part)** the functionalization process performed with the lignin derivative.

and the previously dominating peak arising from C=O signals is considerably suppressed. Therefore, the C1s and O1s spectra in line with each other indicate that the structure deposited onto the surface has large amount of –OH groups, typical for lignin. Furthermore, while the unmodified carbon fiber has no sulfur on its surface, after the functionalization process, sulfur can be clearly detected (**Figures 4C,D**, Insets). The broad feature of the peak that is observable in the S2p spectrum of the functionalized sample indicates that several types of sulfur-containing functions are present, which is reasonable since kraft lignin has sulfur in its structure originally, and sulfur is also incorporated in tosyl groups after the tosylation process. It should be pointed out that based on the XPS analysis, the lignin coated surface has free hydroxyl groups as well as tosyl functions. This is reasonable since the hydroxyl groups of lignin were only partially substituted as it was mentioned before. As a result of the XPS analysis, the chemical composition of the functionalized carbon fiber sample is in line with the structural features of a lignin derivative.

The FE-SEM micrograph of the unmodified sample shows the striations typical for unsized carbon fiber samples (**Figure 5**), while it is clear that a polymeric coating is present on the surface after the functionalization process. The deposited lignin coating composes a submicron layer on the surface.

We also performed thermogravimetric analysis (TGA) to provide more information about the amount of coating on the fibers, the results of the TGA analysis are shown in the Supplementary Material (**Figure S2**). Given that at 800°C around 44% weight loss takes place for the tosylated lignin sample, and assuming that the same process occurs at the carbon fiber surface, we can predict that around 3% lignin is present as coating on the surface by weight. The amount of lignin coating on the carbon fiber could be controlled by decreasing the amount of epoxide functions on the surface (e.g., by changing the reaction time, note that the amount of epoxide functions on the surface reaches a plateau in our study), this issue will be the matter of future optimization experiments.

In the following sections, short carbon fiber reinforced composites will be prepared using the surface modified carbon fibers (along with unmodified control samples), and their mechanical properties will be evaluated in light of their morphological features, fiber-length distribution and fiber orientation in the composite.

Effect of Surface Modification on the Mechanical and Morphological Properties of Short Carbon Fiber Reinforced Composites

The mechanical properties of a short fiber reinforced composite can be discussed in light of a range of interconnected phenomena involving interfacial interactions, fiber length, and orientation distribution factors, the latter two being extremely sensitive to processing conditions (Fu and Lauke, 1996; Molnár et al., 1999; Fu et al., 2000; Karsli and Aytac, 2011, 2013; Ozkan et al., 2014; Li et al., 2015; Unterweger et al., 2015). The mechanical properties (σ_{cu}–the strength of the composite) can be predicted using the frequently referred modified rule of mixtures theory as it is outlined in Equation 1 (Fu and Lauke, 1996; Fu et al., 2000; Ozkan et al., 2014; Li et al., 2015):

$$\sigma_{\mathrm{cu}} = \chi_1 \chi_2 V_f \sigma l + V_m \sigma m \tag{1}$$

where σ_{l} and σ_{m} are the strength, V_{f} and V_{m} are the volume fraction of the fiber and matrix, respectively. χ_1 and χ_2 are the fiber orientation and fiber length factors, respectively. In this expression (Equation 1), the interfacial interactions are included in χ_2 as it involves the critical fiber length (l_{c}) given by Equation 2 according to the Kelly-Tyson model (Kelly and Tyson, 1965):

$$l_c = \frac{\sigma_{fu} r}{\tau} \tag{2}$$

where σ_{fu} is fiber tensile strength at the critical length [determined via single fiber tensile strength experiments (Kettle et al., 1997)], r is the fiber radius and τ is the interfacial shear strength characterizing fiber-matrix interactions.

According to these theories, the results of the mechanical tests will be discussed in terms of interfacial interactions [morphology of fracture surfaces (see **Figures S3–10**)], fiber orientation, and fiber length distribution aspects (see **Figures S11–14**). It has been shown in our previous work that lignin can improve interfacial adhesion due to secondary interactions and probably also due to plasticizing effects, and thereby it can serve as a functional material at the interface (Szabó et al., 2019b). Interfacial mechanical properties will not be further determined for the different matrices herein (it will be followed by examining morphological changes on the fracture surfaces). Whether the beneficial interfacial effects previously discovered can be transferred to the macroscopical properties of different composites will be the focus of the following sections.

Composites Based on Cellulosic Matrices

The tensile test results of the composite samples prepared using cellulose propionate (CP) and cellulose acetate butyrate (CAB) matrices are shown in **Figures 6A,B**, respectively (strain at break values are shown in **Figures 7A,B**). The tensile strength of the neat polymers lies very close to each other (~80 MPa, see **Figures 6A,B**). Nevertheless, CP and CAB show quite different response for the presence of fibers. The tensile strength decreases initially when 5 wt% short carbon fiber is present in the CP matrix (**Figure 6A**), however, an increase in tensile strength can be observed for the CAB matrix. It has been observed in previous studies that the presence of fibers in a composite can bring about an increase but also a decrease in composite strength (Fu et al., 2000). Due to the shear that develops during the extrusion and injection molding steps when preparing the composites, the initial fiber length (3 mm) decreases appreciably (in our study the mean fiber length is 50–100 µm (**Figure 8**), similar results can be found in other studies (Molnár et al., 1999; Karsli and Aytac, 2013; Ozkan et al., 2014; Li et al., 2015). When the fiber length drops below the critical fiber length determined by interfacial interactions, the fibers do not exhibit considerable reinforcing effects, however, their mere presence can diminish mechanical properties since they can serve as cores for crack formation and propagation leading to material failure (Fu and Lauke, 1996; Molnár et al., 1999). The fiber length observed in our study is much lower than the critical fiber length determined in our previous work for the cellulose propionate matrix (~840 µm) (Szabó et al., 2018a,b), which makes it possible that no reinforcement occurs at low fiber content in the CP matrix. At the same time, it is not expected that the critical fiber length differs considerably for the CAB matrix. Therefore, it is surprising that in this case an increase can be observed in tensile strength as 5 wt% fiber is included in the composite (**Figure 6B**). The difference between the CP and CAB matrices can possibly be connected to the variations in the freedom of polymer chain movements in the prepared composites. The addition of rigid fiber segments to the composite restricts the movement of molecular chains and increases the possibility of microcrack formation (Karsli and Aytac, 2011). Since the molecular weight of CAB ($M_{\mathrm{n}} \approx 70\,000$ g mol^{-1}) is smaller compared to CP ($M_{\mathrm{n}} \approx 79\,000$ g mol^{-1}), the mobility of polymer chains might be higher for CAB. This might be associated with a smaller extent of stress development and accumulation when rigid segments are present in the CAB matrix, giving an explanation for our findings. It should be noted, however, that increase in crystalline regions can also be connected to more restricted polymer chain mobility (this is not further evaluated herein).

At the same time, a monotonous increase in elastic modulus is observed for both the CP and CAB matrices with increasing fiber content, as a stiffer material is formed. It is known that the elastic modulus is mostly dependent on the fiber volume fraction and therefore, no strict correlation can be found with fiber length or surface modification in our study either (**Figures 6A,B**) (Molnár et al., 1999; Fu et al., 2000).

The initial decrease in tensile strength is followed by a monotonous increase as the fiber content increases in the cellulose propionate matrix (**Figure 6A**). The tensile strength further increases when lignin is immobilized on the surface (at 20 wt% carbon fiber loading ~8% improvement in tensile strength could be obtained compared to the neat polymer matrix). Since the presence of lignin increases fiber-matrix adhesion for the cellulose propionate matrix (Szabó et al., 2019b), the load that is applied during tensile test is more efficiently transferred to the inherently stronger fiber, eventually leading to a higher tensile strength. This improved fiber-matrix adhesion can clearly be noticed on the fracture surfaces (**Figure 9**, Cellulose propionate composite) since after the functionalization process, polymer is attached to the fiber surface and also tight connection is observable between the matrix and fibers compared to the composite containing unfunctionalized fibers. Furthermore, as fibers are included in the matrix the strain at break value decreases to its half, exhibiting no significant dependence on fiber volume fraction or surface modification (**Figure 7A**). The decrease in strain at break is explained by the presence of the rigid filler that restricts polymer chain mobility and thus facilitates microcrack formation (Karsli and Aytac, 2011). Furthermore, it

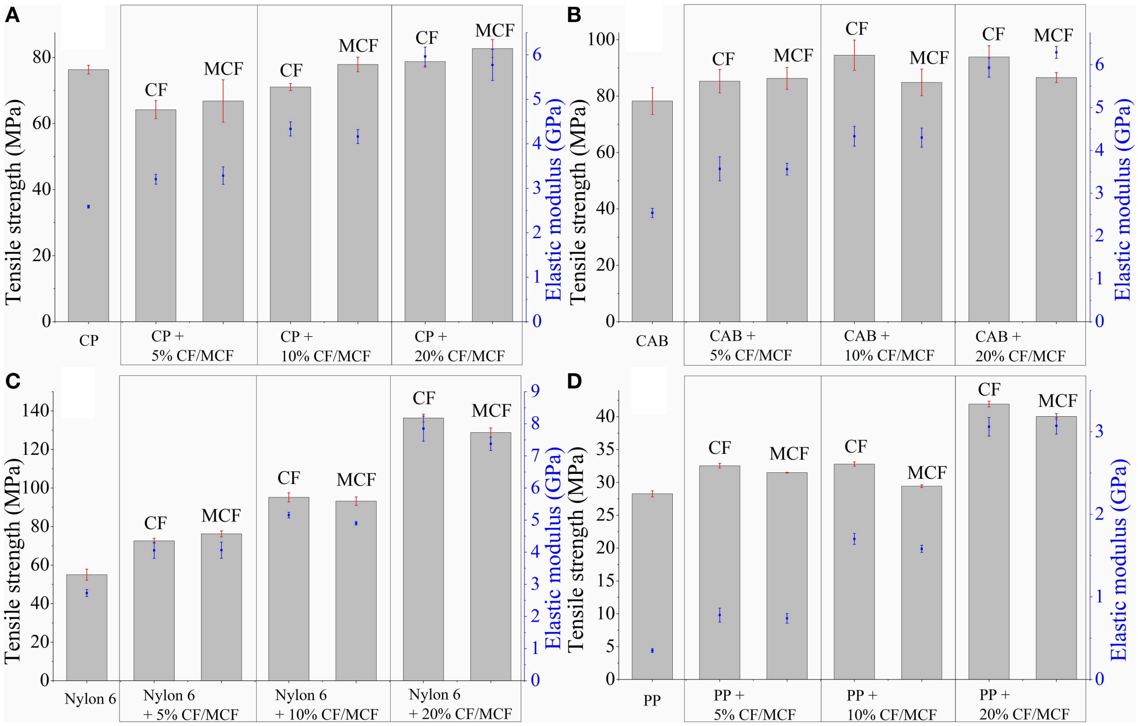

FIGURE 6 | Tensile strength and elastic modulus values for **(A)** cellulose propionate (CP), **(B)** cellulose acetate butyrate (CAB), **(C)** polyamide 6 (Nylon 6), and **(D)** polypropylene (PP) based composites. CF, carbon fiber; MCF, modified carbon fiber (lignin coated).

is also known that on account of the stress accumulation at the fiber ends, strain at break value decreases with increasing number of fiber ends (Fu et al., 2000; Karsli and Aytac, 2011, 2013). In our case, it appears that the brittleness of the material already reaches its limit after adding 5 wt% carbon fiber in the composite (i.e., no further decrease in strain at break can be observed). The mean fiber length does not show appreciable variation with increasing fiber content for the CP matrix (**Figure 8**; fiber length distributions can be found in **Figure S11**). Interestingly, when lignin is present on the surface, the fiber length appreciably decreases. This phenomenon can be explained in terms of the enhanced fiber-matrix interaction that results in the development of increased shear stress during the composite preparation.

An increase in tensile strength can be noticed for the CAB matrix with increasing unmodified fiber content (**Figure 6B**). The tensile strength, however, decreases when surface modified fibers are added to the matrix, indicating that lignin coating results in disadvantageous fiber-matrix interactions. In line with this phenomenon, the fracture surfaces do not indicate improved matrix adhesion to the fibers (**Figure 9**), and also the mean fiber length remains relatively constant with increasing fiber content (**Figure 8**; fiber length distributions can be found in **Figure S12**) anticipating poor fiber-matrix interactions. This poor interaction might be attributed to the presence of longer butyryl chains compared to the propionyl groups in CP (note that the degree of substitution value is $DS_{butyryl} = 1.66$ and $DS_{acetyl} = 1.00$ for CAB and $DS_{propionyl} = 2.76$ for CP), which might restrict secondary interactions (steric reasons or due to enhanced hydrophobicity of CAB) between lignin and the –OH and C=O groups of the cellulose derivative. Furthermore, the strain at break value does not change appreciably with increasing fiber content until 10 wt% fiber loading, and it drops to its half when 20 wt% fibers are present in the composite. This drop can be associated with a thicker skin layer in this type of composite containing fibers perpendicularly aligned to the flow direction (see **Figure S6**), this alignment can also be attributed to weak polymer-fiber interactions. At 10 wt% carbon fiber content (unmodified fiber surface) a maximum tensile strength of ∼94 MPa is obtained (∼20% improvement compared to the neat polymer matrix, **Figure 7B**), while the brittleness of the material does not change considerably if compared with the neat polymer (see the strain at break values in **Figure 7B**). This type of composite has therefore, superior properties over any other cellulose-based short carbon fiber reinforced polymers prepared in this study.

Composites Based on Polyamide 6

The tensile test results for the composites prepared using polyamide 6 as matrix are shown in **Figures 6C**, **7C**. The tensile strength and modulus significantly increase as fibers are added to this polymer, and it appears that surface modification has no impact on these properties. A large increase in tensile strength is obtained at 20 wt% fiber loading, with exceptional ∼250% improvement (∼136 MPa; **Figure 6C**, unmodified fibers) compared to the neat polymer. This large enhancement can be attributed to very good fiber-matrix adhesion, as it can be seen on the fracture surfaces in **Figure 9**. Both the functionalized

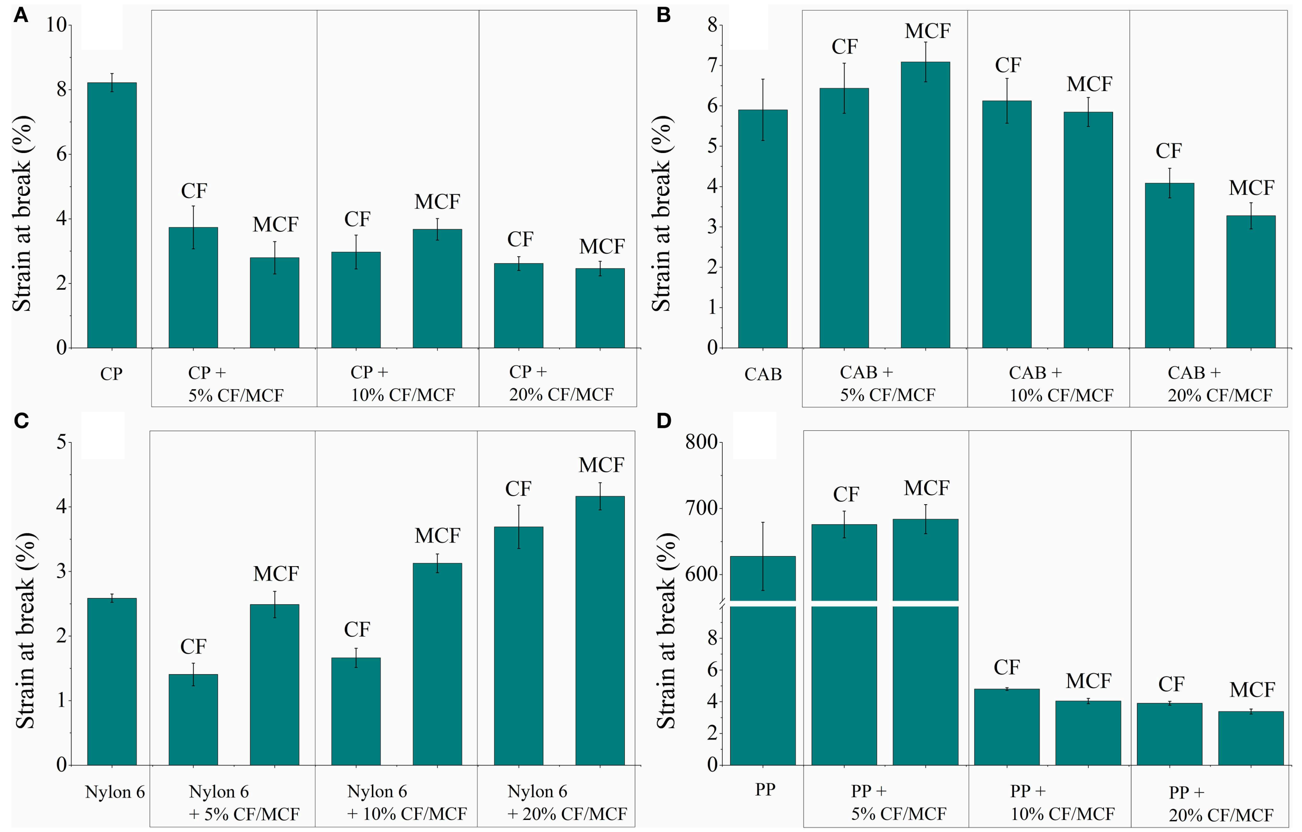

FIGURE 7 | Strain at break values for **(A)** cellulose propionate (CP), **(B)** cellulose acetate butyrate (CAB), **(C)** polyamide 6 (Nylon 6), and **(D)** polypropylene (PP) based composites. CF, carbon fiber; MCF, modified carbon fiber (lignin coated).

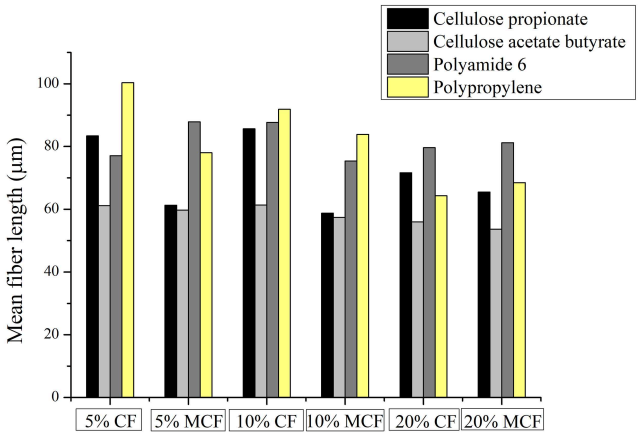

FIGURE 8 | Mean fiber length in the composite samples. CF, carbon fiber; MCF, modified carbon fiber (lignin coated).

and unfunctionalized fibers are well-covered by the polymer, the interfacial layer resists the applied load during the tensile test, and it appears that matrix failure occurs first. The fiber orientation at the skin and at the core of the specimen is parallel to the flow direction (see **Figures S7, S8**), which is also advantageous with respect to the mechanical properties. In this work, the unmodified short fibers have no sizing agent on the surface, and it appears that this results in beneficial fiber-polymer interactions. In a previous study, short fibers with sizing agent have been applied, in that case, on the fracture surfaces the fibers are well-separated from the matrix and also less improvement could be obtained in the tensile strength results compared to our findings (at 20 wt% carbon fiber loading a tensile strength of ∼90 MPa has been reported) (Karsli and Aytac, 2013).

The fiber length mostly remains longer in polyamide 6 based composites compared to the cellulosic matrices (**Figure 8**). Furthermore, an interesting phenomenon can be noticed on the strain at break values, as the carbon fiber surface is functionalized with lignin the fracture strain increases (**Figure 7C**). Such an increase might be connected to plasticizing effects acting at the interface, which can help in dissipating the stress along the fiber axis, eventually rendering the material less prone to stress accumulation. When 20 wt% carbon fiber is embedded in the matrix, the strain at break value is appreciably improved regardless of the surface modification. This might be attributed to fiber-fiber interactions [“bridge effect” (Fu et al., 2000)] due to the high fiber loading, helping to dissipate the stress.

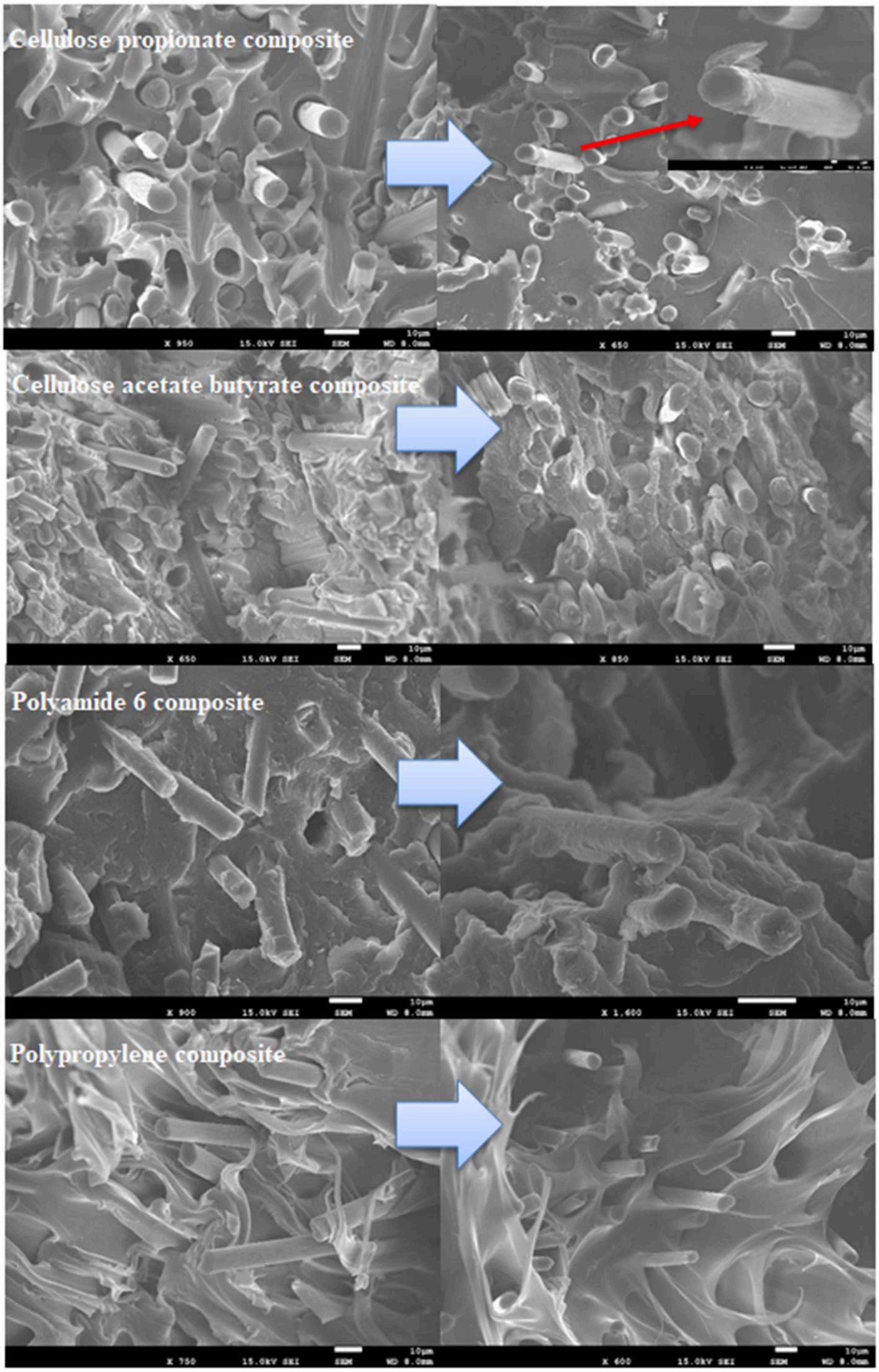

FIGURE 9 | Fracture surfaces of composite samples containing 20 wt% carbon fiber. Pictures on the left and right site depict composite samples prepared with unmodified and modified carbon fibers, respectively.

It is noteworthy to mention that the polyamide based composite containing 20 wt% carbon fiber has superior characteristics in terms of tensile strength and fracture strain.

Composites Based on Polypropylene

It is obvious on the tensile test results that short carbon fiber reinforced polypropylene composites have inferior mechanical properties compared to other composites prepared in this study (**Figure 6D**). The tensile strength is slightly increased at 5 and 10 wt% fiber loadings (∼14% increase compared to the neat polymer), and it reaches ∼40 MPa at 20 wt% fiber content (∼50% increase compared to the neat polymer). The large increase at relatively high fiber loading is attributed to fiber-fiber interactions resulting in "bridge effects" (Fu et al., 2000). It appears that surface modification detrimentally affects the mechanical properties as slight decrease in tensile strength can be noticed. It is reasonable to think that the originally hydrophilic lignin with -OH and -COOH groups in its structure will not establish beneficial secondary interactions with the polypropylene matrix that has a hydrophobic character. On the fracture surfaces, fiber-matrix separation can be observed, which becomes more significant after surface modification (**Figure 9**). The compatibility between polypropylene and lignin can, however, be improved if lignin is functionalized with aliphatic groups, as it has been shown in other studies from our laboratory (Sakai et al., 2018a,b). The elastic modulus monotonously increases (**Figure 6D**) with fiber loading, this is in line with previous reports pointing out that this mechanical property is mainly dependent on the fiber volume fraction and less dependent on other factors (Molnár et al., 1999; Fu et al., 2000). The mean fiber length remains relatively longer in these composites compared to other cases due to poor fiber-matrix interactions (**Figure 8**). Furthermore, while the material retains its ductile nature at 5 wt% fiber loading, the fracture strain falls to a low value after 10 wt% fiber is included in the polymer matrix (**Figure 7D**).

Thermal Analysis

It has been shown before that the presence of fibers has an effect on the glass transition temperature (T_g) of a polymer (Rezaei et al., 2009; Karsli and Aytac, 2013). At low carbon fiber loading, it was reported that fibers can increase the degree of crystallinity of the polymer matrix via increasing crystal growth rate and the number of nucleation sites, however, they can exert opposite effects as the amount of fiber increases in the matrix (Karsli and Aytac, 2013). Furthermore, it has also been shown that glass transition temperature increases with increasing fiber length (Rezaei et al., 2009). It is clear from these studies that glass transition temperature of short carbon fiber reinforced composites stems from the complex interplay of many factors.

The glass transition temperature values were determined for the cellulosic matrices and for polyamide 6 (the polypropylene used in this study is a metallocene catalyzed random copolymer, which made it difficult to analyze the wide range of glass transitions appearing during the thermal analysis), including the composites with 20 wt% fiber loading (the highest fiber loading was chosen since the amount of sizing on the surface is only ∼3 wt%). As it can be seen in **Table 2**, the T_g value is not affected by the presence of fibers appreciably in case of the cellulosic matrices, however, a slight decrease occurs when lignin is present on the surface. The T_g value decreases more significantly for polyamide 6 after adding fibers, and an even sharper drop is observable when lignin-coated fibers are applied. The similar tendency that can be seen for these polymer matrices indicates that similar phenomenon might take place that eventually determines the glass transition in these materials when lignin is present at the interface. The mobility of polymer chains might increase close to the interface where lignin is present compared to the case when polymer chains face a rigid graphitic carbon layer at the interphase. When we compare the results of the mechanical tests and the thermomechanical analysis, it becomes clear that we cannot draw conclusion connecting the glass transition temperature and the mechanical properties of the materials. This might be due to the fact that these mechanical properties are determined mostly by the bulk matrix properties for short fiber reinforced composites and interfacial interactions (the interphase represents only a small fraction of the matrix) might be of lesser importance.

TABLE 2 | Glass transition temperature values.

	Glass transition temperature (°C)
CP	129.8
CP + 20% CF	129.5
CP + 20% MCF	128.9
CAB	132.3
CAB + 20% CF	132.2
CAB + 20% MCF	131.6
Nylon	54.8
Nylon + 20% CF	53.5
Nylon + 20% MCF	51.4

CP, cellulose propionate; CAB, cellulose acetate butyrate; CF, carbon fiber; MCF, modified (lignin coated) carbon fiber.

CONCLUSIONS

Our study aimed at preparing short carbon fiber reinforced composites using polymers that can be potentially derived from biomasses (cellulose derivatives, and polyamide 6) and thereby, have promising sustainability potential. Furthermore, interfacial interactions were engineered by immobilizing lignin, a renewable resource, on carbon fiber surface applying industrially scalable benign chemistries.

It appears that cellulosic matrices are relatively sensitive to the presence of rigid fiber segments that restrict polymer chain movement and facilitate microcrack formation. Increasing fiber-matrix interactions appears to bring about only slight improvement in the mechanical properties. Therefore, in these cases, further advancement might be achieved considering the physicochemical properties of the polymers (molecular weight, crystallinity).

At the same time, polyamide 6 has exceptional potential to accommodate fibers. A large improvement in tensile strength was obtained (reaching a maximum value of ∼136 MPa at 20 wt% fiber loading) without leading to a largely brittle material.

Our study makes it clear that biomass-based short carbon fiber reinforced polymers can be promising green materials for a sustainable resource based society.

DATA AVAILABILITY STATEMENT

All datasets generated for this study are included in the article/**Supplementary Material**.

AUTHOR CONTRIBUTIONS

All the authors have contributed to the work presented in the manuscript to an extent that is consistent with the criteria for authorship. All the authors have agreed with the contents.

ACKNOWLEDGMENTS

The authors gratefully acknowledge the financial support received from the COI program Construction of next-generation infrastructure using innovative materials—Realization of a safe and secure society that can coexist with the Earth for centuries supported by the Ministry of Education, Culture, Sports, Science and Technology (MEXT) and the Japan Science and Technology Agency (JST).

SUPPLEMENTARY MATERIAL

The Supplementary Material for this article can be found online at: https://www.frontiersin.org/articles/10.3389/fchem.2019.00757/full#supplementary-material

REFERENCES

Buntara, T., Noel, S., Phua, P. H., Melián-Cabrera, I., de Vries, J. G., and Heeres, H. J. (2011). Caprolactam from renewable resources: catalytic conversion of 5-hydroxymethylfurfural into caprolactone. *Angew. Chem. Int. Ed.* 50, 7083–7087. doi: 10.1002/anie.201102156

Chen, G.-Q., and Patel, M. K. (2012). Plastics derived from biological sources: present and future: a technical and environmental review. *Chem. Rev.* 112, 2082–2099. doi: 10.1021/cr200162d

Fang, W., Yang, S., Wang, X.-L., Yuan, T.-Q., and Sun, R.-C. (2017). Manufacture and application of lignin-based carbon fibers (LCFs) and lignin-based carbon nanofibers (LCNFs). *Green Chem.* 19, 1794–1827. doi: 10.1039/C6GC03206K

Frank, E., Steudle, L. M., Ingildeev, D., Spörl, J. M., and Buchmeiser, M. R. (2014). Carbon fibers: precursor systems, processing, structure, and properties. *Angew. Chem. Int. Ed.* 53, 5262–5298. doi: 10.1002/anie.201306129

Fu, S.-Y., and Lauke, B. (1996). Effects of fiber length and fiber orientation distributions on the tensile strength of short-fiber-reinforced polymers. *Compos. Sci. Technol.* 56, 1179–1190. doi: 10.1016/S0266-3538(96)00072-3

Fu, S.-Y., Lauke, B., Mäder, E., Yue, C.-Y., and Hu, X. (2000). Tensile properties of short-glass-fiber- and short-carbon-fiber-reinforced polypropylene composites. *Comp. Part A* 31, 1117–1125. doi: 10.1016/S1359-835X(00)00068-3

Goff, A. L., Moggia, F., Debou, N., Jegou, P., Artero, V., Fontecave, M., et al. (2010). Facile and tunable functionalization of carbon nanotube electrodes with ferrocene by covalent coupling and π-stacking interactions and their relevance to glucose bio-sensing. *J. Electroanal. Chem.* 641, 57–63. doi: 10.1016/j.jelechem.2010.01.014

Graichen, F. H. M., Grigsby, W. J., Hill, S. J., Raymond, L. G., Sanglard, M., Smith, D. A., et al. (2017). Yes, we can make money out of lignin and other bio-based resources. *Ind. Crop. Prod.* 106, 74–85. doi: 10.1016/j.indcrop.2016.10.036

Kakuchi, R., Ninomiya, K., Shibata, Y., Uzawa, K., Ogoshi, T., Maeda, K., et al. (2017). *Method for Producing Polysaccharide Derivative and Lignin Derivative*. EP 3 214 097 A1. Munich: European Patent Office.

Karsli, N. G., and Aytac, A. (2011). Effects of maleated polypropylene on the morphology, thermal and mechanical properties of short carbon fiber reinforced polypropylene composites. *Mater. Design* 32, 4069–4073. doi: 10.1016/j.matdes.2011.03.021

Karsli, N. G., and Aytac, A. (2013). Tensile and thermomechanical properties of short carbon fiber reinforced polyamide 6 composites. *Compos. Part B* 51, 270–275. doi: 10.1016/j.compositesb.2013.03.023

Kelly, A., and Tyson, W. R. (1965). Tensile properties of fibre-reinforced metals: copper/tungsten and copper/molybdenum. *J. Mech. Phys. Solids* 13, 329–338. doi: 10.1016/0022-5096(65)90035-9

Kettle, A. P., Beck, A. J., O'Toole, L., Jones, F. R., and Short, R. D. (1997). Plasma polymerisation for molecular engineering of carbon-fibre surfaces for optimised composites. *Comp. Sci. Technol.* 57, 1023–1032. doi: 10.1016/S0266-3538(96)00162-5

Koutroumanis, N., Manikas, A. C., Pappas, P. N., Petropoulos, F., Sygellou, L., Tasis, D., et al. (2018). A novel mild method for surface treatment of carbon fibers in epoxy-matrix composites. *Comp. Sci. Technol.* 157, 178–184. doi: 10.1016/j.compscitech.2018.01.048

Li, F., Liu, Y., Qu, C.-B., Xiao, H.-M., Hua, Y., Sui, G. X., et al. (2015). Enhanced mechanical properties of short carbon fiber reinforced polyethersulfone composites by graphene oxide coating. *Polymer* 59, 155–165. doi: 10.1016/j.polymer.2014.12.067

Loew, G. H., Pudzianowski, A. T., Czerwinski, A., and Ferrell, J. E. (1980). Mechanistic studies of addition of nucleophiles to arene oxides and diol epoxides: candidate ultimate carcinogens. *Int. J. Quantum Chem.* 7, 223–244. doi: 10.1002/qua.560180723

Markiewicz, K. H., Wilczewska, A. Z., Chernyaeva, O., and Winkler, K. (2014). Ring-opening reactions of epoxidized SWCNT with nucleophilic agents: a convenient way for sidewall functionalization. *New J. Chem.* 38, 2670–2678. doi: 10.1039/C4NJ00148F

Milbrandt, A., and Booth, S. (2016). *Carbon Fiber from Biomass.* Technical Report NREL/TP-6A50-66386, Clean Energy Manufacturing and Analysis Center. Available online at: www.nrel.gov/docs/fy16osti/66386.pdf (accessed May 8, 2019).

Mohanty, A. K., Vivekanandhan, S., Pin, J.-M., and Misra, M. (2018). Composites from renewable and sustainable resources: challenges and innovations. *Science* 362, 536–542. doi: 10.1126/science.aat9072

Molnár, S. Z., Rosenberger, S., Gulyás, J., and Pukánszky, B. (1999). Structure and impact resistance of short carbon fiber reinforced polyamide 6 composites. *J. Macromol. Sci. B* 38, 721–735. doi: 10.1080/00222349908248134

Ogrin, D., Chattopadhyay, J., Sadana, A. K., Billups, W. E., and Barron, A. R. (2006). Epoxidation and deoxygenation of single-walled carbon nanotubes: quantification of epoxide defects. *J. Am. Chem. Soc.* 128, 11322–11323. doi: 10.1021/ja061680u

Ozkan, C., Karsli, N. G., Aytac, A., and Deniz, V. (2014). Short carbon fiber reinforced polycarbonate composites: effects of different sizing materials. *Compos. Part B* 62, 230–235. doi: 10.1016/j.compositesb.2014.03.002

Rezaei, F., Yunus, R., and Ibrahim, N. A. (2009). Effect of fiber length on the thermomechanical properties of short carbon fiber reinforced polypropylene composites. *Mater. Design* 30, 260–263. doi: 10.1016/j.matdes.2008.05.005

Sakai, H., Kuroda, K., Muroyama, S., Tsukegi, T., Kakuchi, R., Takada, K., et al. (2018b). Alkylated alkali lignin for compatibilizing agents of carbon fiber-reinforced plastics with polypropylene. *Polym. J.* 50, 281–284. doi: 10.1038/s41428-017-0009-3

Sakai, H., Kuroda, K., Tsukegi, T., Ogoshi, T., Ninomiya, K., and Takahashi, K. (2018a). Butylated lignin as a compatibilizing agent for polypropylene-based carbon fiber-reinforced plastics. *Polym. J.* 50, 997–1002. doi: 10.1038/s41428-018-0088-9

Schneiderman, D. K., and Hillmyer, M. A. (2017). 50th anniversary perspective: there is a great future in sustainable polymers. *Macromolecules* 50, 3733–3749. doi: 10.1021/acs.macromol.7b00293

Sheldon, R. A. (2014). Green and sustainable manufacture of chemicals from biomass: state of the art. *Green Chem.* 16, 950–963. doi: 10.1039/C3GC41935E

Steger, C. (1998). An unbiased detector of curvilinear structures. *IEEE T. Pattern Anal.* 20, 113–125. doi: 10.1109/34.659930

Suzuki, S., Shibata, Y., Hirose, D., Endo, T., Ninomiya, K., Kakuchi, R., et al. (2018). Cellulose triacetate synthesis via one-pot organocatalytic transesterification and delignification of pretreated bagasse. *RSC Adv.* 8, 21768–21776. doi: 10.1039/C8RA03859G

Szabó, L., Imanishi, S., Kawashima, N., Hoshino, R., Hirose, D., Tsukegi, T., et al. (2018b). Interphase engineering of a cellulose-based carbon fiber reinforced composite by applying click chemistry. *Chem. Open* 7, 720–729. doi: 10.1002/open.201800180

Szabó, L., Imanishi, S., Kawashima, N., Hoshino, R., Takada, K., Hirose, D., et al. (2018a). Carbon fiber reinforced cellulose-based polymers: intensifying interfacial adhesion between the fibre and the matrix. *RSC Adv.* 8, 22729–22736. doi: 10.1039/C8RA04299C

Szabó, L., Imanishi, S., Tetsuo, F., Hirose, D., Ueda, H., Tsukegi, T., et al. (2019b). Lignin as a functional green coating on carbon fiber surface to improve interfacial adhesion in carbon fiber reinforced composites. *Materials* 12, 1–14. doi: 10.3390/ma12010159

Szabó, L., Imanishi, S., Tetsuo, F., Nishio, M., Hirose, D., Tsukegi, T., et al. (2019a). Electron beam induced strengthening of a short carbon fiber reinforced green thermoplastic composite: key factors determining materials performance. *Compos. Part A* 121, 386–396. doi: 10.1016/j.compositesa.2019.03.046

Umaña, M., Rolinson, D. R., Nowak, R., Daum, P., and Murray, R. W. (1980). X-ray photoelectron spectroscopy of metal, metal oxide, and carbon electrode surfaces chemically modified with ferrocene and ferricenium. *Surf. Sci.* 101, 295–309. doi: 10.1016/0039-6028(80)90623-8

Unterweger, C., Duchoslav, J., Stifter, D., and Fürst, C. (2015). Characterisation of carbon fiber surfaces and their impact on the mechanical properties of short carbon fiber reinforced polypropylene composites. *Comp. Sci. Technol.* 108, 41–47. doi: 10.1016/j.compscitech.2015.01.004

Waters, C. N., Zalasiewicz, J., Summerhayes, C., Barnosky, A. D., Poirier, C., Galuszka, A., et al. (2016). The Anthropocene is functionally and stratigraphically distinct from the Holocene. *Science* 351:aad226. doi: 10.1126/science.aad2622

Winnacker, M., and Rieger, B. (2016). Biobased polyamides: recent advances in basic and applied research. *Macromol. Rapid Commun.* 37, 1391–1413. doi: 10.1002/marc.201600181

Witten, E., Sauer, M., and Kühnel, M. (2017). *Composites Market Report 2017. Market Developments, Trends, Outlook and Challenges*. Industrievereinigung Verstärkte Kunststoffe e.V. Federation of Reinforced Plastics, Frankfurt.

Xie, Y., and Sherwood, P. M. A. (1989). X-ray photoelectron spectroscopic studies of carbon fiber surfaces. 10. Valence-band studies interpreted by X-α calculations and the differences between poly(acrylonitrile)- and pitch-based carbon fibers. *Chem. Mater.* 1, 427–432. doi: 10.1021/cm00004a009

Yao, S.-S., Jin, F.-L., Rhee, K. Y., Hui, D., and Park, S.-J. (2018). Recent advances in carbon-fiber-reinforced thermoplastic composites: a review. *Compos. Part B* 142, 241–250. doi: 10.1016/j.compositesb.2017.12.007

Zhang, G., Sun, S., Yang, D., Dodelet, J.-P., and Sacher, E. (2008). The surface analytical characterization of carbon fibers functionalized by H_2SO_4/HNO_3 treatment. *Carbon* 46, 196–205. doi: 10.1016/j.carbon.2007.11.002

Conflict of Interest: The authors declare that the research was conducted in the absence of any commercial or financial relationships that could be construed as a potential conflict of interest.

Copyright © 2019 Szabó, Milotskyi, Fujie, Tsukegi, Wada, Ninomiya and Takahashi. This is an open-access article distributed under the terms of the Creative Commons Attribution License (CC BY). The use, distribution or reproduction in other forums is permitted, provided the original author(s) and the copyright owner(s) are credited and that the original publication in this journal is cited, in accordance with accepted academic practice. No use, distribution or reproduction is permitted which does not comply with these terms.

frontiers in Chemistry

ORIGINAL RESEARCH
published: 09 December 2019
doi: 10.3389/fchem.2019.00842

First Total Synthesis of (β-5)-(β-*O*-4) Dihydroxytrimer and Dihydrotrimer of Coniferyl Alcohol (G): Advanced Lignin Model Compounds

Amandine L. Flourat [1,2]*, ***Aurélien A. M. Peru*** [1], ***Arnaud Haudrechy*** [2], ***Jean-Hugues Renault*** [2] ***and Florent Allais*** [1]*

[1] URD Agro-Biotechnologies Industrielles (ABI), CEBB, AgroParisTech, Pomacle, France, [2] Université de Reims Champagne Ardenne, CNRS, Institut de Chimie Moléculaire de Reims, UMR 7312, SFR Condorcet FR CNRS 3417, Reims, France

To investigate lignin degradation, scientists commonly use model compounds. Unfortunately, these models are most of the time simple β-*O*-4 dimers and do not sufficiently mimic the wide complexity of lignin structure (i.e., aliphatic side chains and robust C-C bonds). Herein, we present a methodology to access advanced lignin models through the first synthesis of two trimers of monolignol **G**—possessing side-chains and both robust β-5 bond and labile β-*O*-4 bond—via a chemo-enzymatic pathway. Key steps were (1) the C-C coupling via laccase-mediated oxidation, (2) the C-O coupling via a simple S_{N2} between a phenolate and a bromoketoester, and (3) a modified Upjohn dihydroxylation or a palladium-catalyzed hydrogenation. (β-5)-(β-*O*-4) dihydroxytrimer and dihydrotrimer of coniferyl alcohol (**G**) were obtained in good global yield, 9 and 20%, respectively, over nine steps starting from ferulic acid.

Keywords: lignin models, coniferyl alcohol, monolignol, trimers, total synthesis, C-C coupling, biocatalysis, laccase

OPEN ACCESS

Edited by:
Marc Pera-Titus,
UMI3464 Eco-Efficient Products and Processes Laboratory (E2P2L), Fudan University, China

Reviewed by:
Simonetta Antonaroli,
University of Rome Tor Vergata, Italy
Hoon Kim,
Great Lakes Bioenergy Research Center (DOE), United States

****Correspondence:***
Amandine L. Flourat
amandine.flourat@agroparistech.fr
Florent Allais
florent.allais@agroparistech.fr

Specialty section:
This article was submitted to Green and Sustainable Chemistry, a section of the journal Frontiers in Chemistry

Received: *16 August 2019*
Accepted: *19 November 2019*
Published: *09 December 2019*

Citation:
Flourat AL, Peru AAM, Haudrechy A, Renault J-H and Allais F (2019) First Total Synthesis of (β-5)-(β-O-4) Dihydroxytrimer and Dihydrotrimer of Coniferyl Alcohol (G): Advanced Lignin Model Compounds. Front. Chem. 7:842. doi: 10.3389/fchem.2019.00842

INTRODUCTION

Lignins are the second most abundant biopolymer on Earth and the first potential source of aromatic compounds. However, due to their tridimensional architecture and the large diversity of linkages between their three principal constitutive units, they are under exploited. In order to provide a better understanding of this extremely complex biopolymer and design efficient degradation processes, models of lignin have been used for a long time. To the best of our knowledge, the first reported synthesis of lignin model compounds emerged in 1952 (Sen, 1952). Recent studies still involved lignin model compounds (Gao et al., 2018; Lee and Yang, 2018; Rinesch and Bolm, 2018; Shimizu et al., 2018). They mainly used (β-*O*-4) dimers without side chains as models to study oxidative cleavage of the ether bond, known as the non-condensed linkage in lignin. Not only such approach does not address the steric effect and electronical interaction due to the side chains, but it also bypasses the robust C-C bond in the lignins, the ones that are responsible for lignin recalcitrance to degradation. Even if (β-*O*-4) linkage is abundant, it seems to us important also to look at the impact of oxidative treatments on condensed bond, such as (β-5) C-C bond, in order to efficiently depolymerize lignins. Recently, Forsythe et al. have described an interesting route to obtain controlled oligomers containing (5-5), (β-5), and (β-*O*-4) linkages but always without functionalization of the side chain (Forsythe et al., 2013). In previous works, we have synthesized model compounds with elaborated side chains to (1) conduct electrochemical study (Cottyn et al., 2015), (2) develop analytical method and immunohistochemistry approaches (Mouterde et al., 2013), or (3) unveil the chemical reactivity of lignosulfonates (Broussard et al., 2016). Such models can be used for numerous applications such as determining energetic level for electronic excitation (e.g., photochemistry), determining preferential pathways of (de)lignification, or estimating the required energy to break specific C-C bonding and release monomers from lignin. Herein, we describe the first total chemo-enzymatic synthesis of both the (β-5)-(β-*O*-4) dihydroxytrimer of monolignol **G** and the naturally occurring dihydrotrimer (Ono et al., 1998; Ye et al., 2016; Jiang et al., 2017). Monolignol **G** is the most widespread in nature, as it is the main constituent of softwoods lignin (>90%) and is present in large amount in hardwood (30–40%) and grasses (35–50%). (Bouxin, 2011) These two trimers will allow comparison of reactivity with (β-5) and (β-*O*-4) dimers and determining the impact of side chain complexity in depolymerization for instance. The chosen synthetic methodology is a convergent pathway starting from ferulic acid and acetovanillone, involving (1) the enzymatic dimerization of coniferyl alcohol (**G**) to obtain the (β-5) C-C bond, (2) the formation of the (β-*O*-4) C-O linkage using nucleophilic substitution (S_{N2}) between a phenolate and a bromoketoester, and (3) the dihydroxylation of the double bond to finalize the formation of (β-5)/(β-*O*-4) dihydroxytrimer of monolignol **G**, or the hydrogenation of this double bond to achieve the (β-5)/(β-*O*-4) dihydrotrimer of monolignol **G** (**Scheme 1**).

RESULTS AND DISCUSSION

The synthesis of the two targets started with the preparation of di-acetylated (β-5)-dimer **1** from ferulic acid (**2**), in five steps. Using the strategy previously reported for sinapyl alcohol (Jaufurally et al., 2016), **2** was transformed into ethyl ferulate (**3**) through a Fischer esterification. Subsequent DibalH-mediated reduction of **3** provided coniferyl alcohol (aka monolignol **G**) in 77% overall yield from **2**. Enzymatic dimerization of **G** in the presence of laccase isolated from *Trametes versicolor* (EC.420-150-4) was performed in an emulsion of ethyl acetate and aqueous acetate buffer pH = 5 at room temperature. It is noteworthy to mention that a slow addition of laccase solution via a syringe pump allowed controlling the ratio between **G** and radical species in

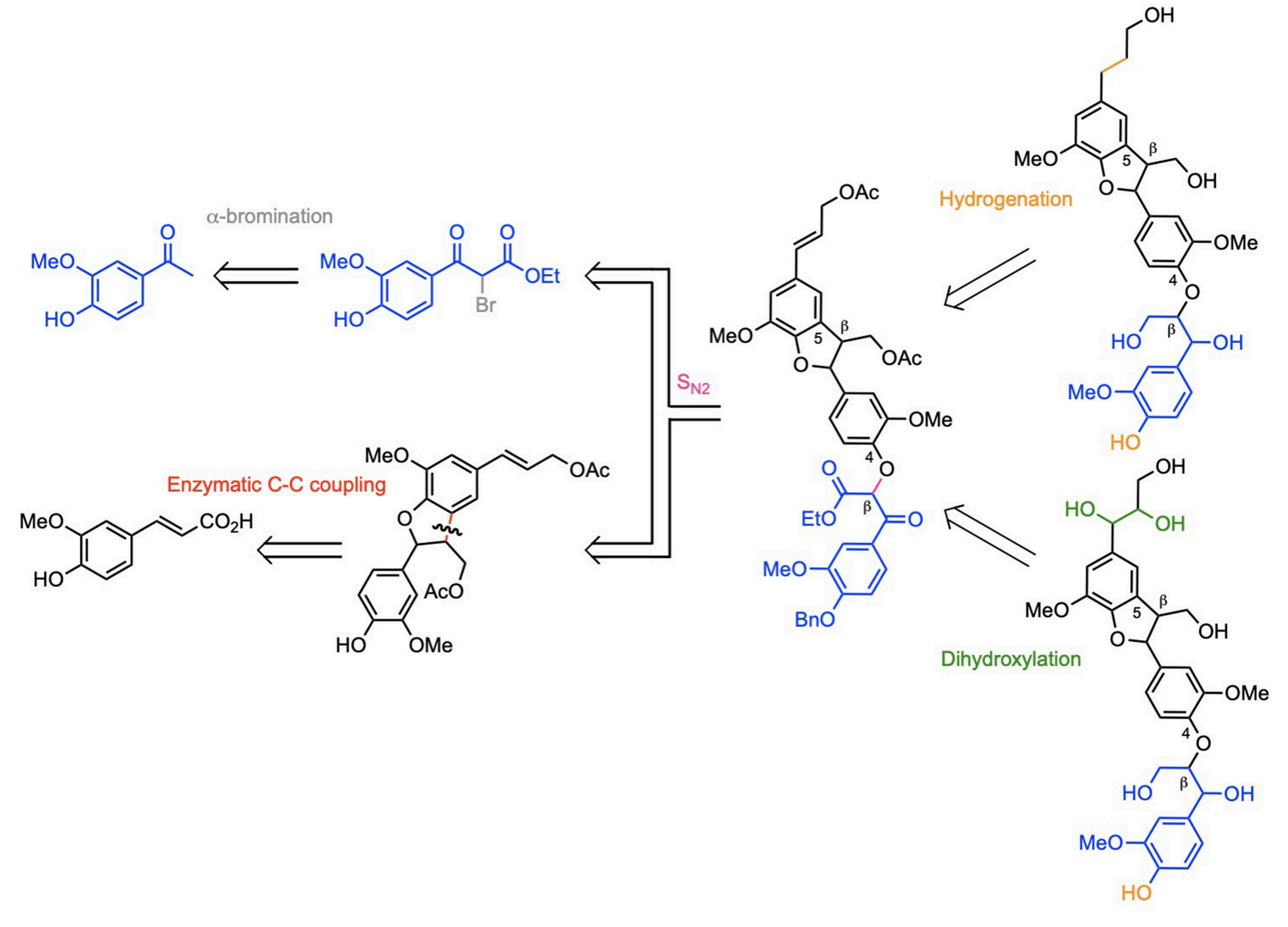

SCHEME 1 | Retrosynthetic routes towards dihydroxy-(β-5)-(β-O-4) trimer and naturally occurring dihydro-(β-5)-(β-O-4) trimer of coniferyl alcohol G.

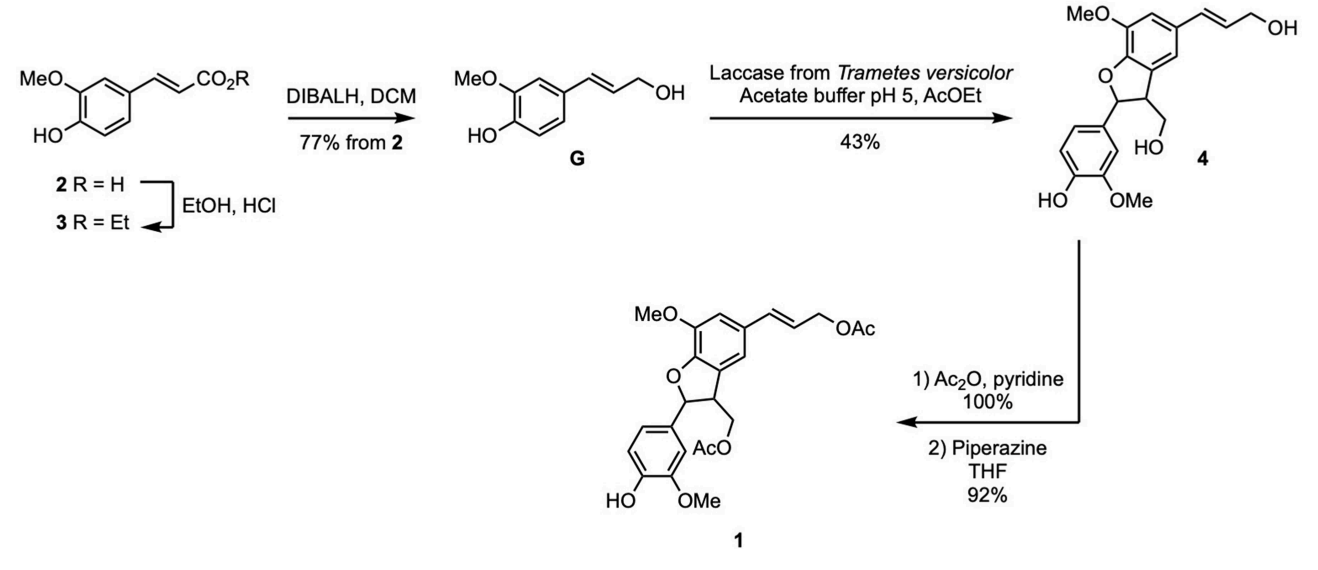

SCHEME 2 | Synthesis of **1** from ferulic acid **(2)**.

the reaction medium, thus limiting the formation of oligomers. Only *trans* diastereoisomer of β-5 dimer of **G** (**4**) was obtained as determined by NMR and according to Lou et al. (2018) (43% yield) (data shown in **Supplementary Material**). The two aliphatic alcohols and the phenol moiety were subsequently acetylated (Ac_2O, pyridine), prior to specific deacetylation of the latter in the presence of piperazine in THF to provide compound **1** (92% yield, 30% overall yield in five steps starting from ferulic acid) (**Scheme 2**).

In another hand, the synthesis of bromoketoester of guaiacol (**6**) was performed from acetovanillone (**7**) in three steps (**Scheme 3**). Benzylation of **7** (BnBr, KI, K_2CO_3, DMF, quant.) gave *O*-benzylacetovanillone that was then reacted with diethylcarbonate and sodium hydride to provide the corresponding β-ketoester (**8**) in 78% yield. The latter then underwent bromination (NBS, Amberlyst A15) giving **6** (79% yield, 62% overall yield from **7**).

Formation of the β-*O*-4 bond was achieved through the coupling between **6** and **1** via a S_{N2} process as previously reported by Forsythe et al. (2013) and Kishimoto et al. (2006). It is worth mentioning that, to achieve (β-*O*-4) bond, such S_{N2} was preferred to the aldolization strategy we previously applied for the preparation of (5-5′)-(8′-*O*-4′′) dihydrotrimer of ferulic acid (Mouterde et al., 2013), due to easier operation conditions and higher reported yields [49% in acetone (Lancefield and Westwood, 2015) and 97% in DMF (Kishimoto et al., 2006)]. Performing this reaction with potassium carbonate in DMF provided the per-protected (β-5)-(β-*O*-4) trimer of **G** (**9**) in 83% yield (**Scheme 3**). To access the desired targets, it was necessary to reduce the ketone and ester moieties. To do so, the procedure reported by Patil and Yan (2016) was applied ($NaBH_4$, THF/H_2O) and provided the intermediate **10** in 82% yield. Even if the molecular ion of these adducts cannot be identified in HRMS, probably because of a high reactivity leading to decomposition of the molecule, the disappearance of all peaks between 2.5 and 1.5 ppm and those at 4.24 and 1.21 ppm in the ^1H NMR spectrum proved the cleavage of the acetates and esters, respectively (data shown in **Supplementary Material**). Moreover, ^{13}C NMR spectrum further confirmed this result and proved also the reduction of the ketone as the peak at 190.0 ppm disappeared.

To access the dihydrotrimer **11**, intermediate **10** was submitted to a palladium-catalyzed hydrogenation step in order to simultaneously cleave the benzyl protecting group and reduce the double bond. It was observed that performing the reaction in ethanol, resulted only in the reduction of the double bond, leaving the benzyl protective group untouched. The cleavage of recalcitrant benzyl moieties being facilitated in highly polar solvent and in the presence of an acid, the successful concomitant debenzylation and reduction of **10** was achieved by using a 95/5 mixture of methanol and acetic acid, providing dihydrotrimer (β-5)-(β-*O*-4) (**11**) in 98% yield (**Scheme 3**, 67% overall yield from **1**, and 20% from ferulic acid in nine steps). It is worth mentioning that despite many attempt, no HRMS data could be obtained for **11**. Nevertheless, ^1H & ^{13}C NMR analyses proved the reduction of the double bond and the cleavage of the benzyl protecting group.

Another pathway to intermediate **10** was designed to reduce the number of steps. Ethyl ferulate (**3**) was enzymatically dimerized using the same procedure applied for **4** leading to a phenolic diester (**12**) in similar yield. This procedure circumvented the reduction of **3** into **G,** the acetylation and the specific deacetylation. As the phenol moiety was free, the phenolate was directly generated by action of potassium carbonate and reacted with bromoketoester **6** to provide the desired ketotriester (**13**) in excellent yield (84%). The aluminum-mediated reduction (Dibal-H) of **13** proved troublesome due to extreme difficulty to recover the desired

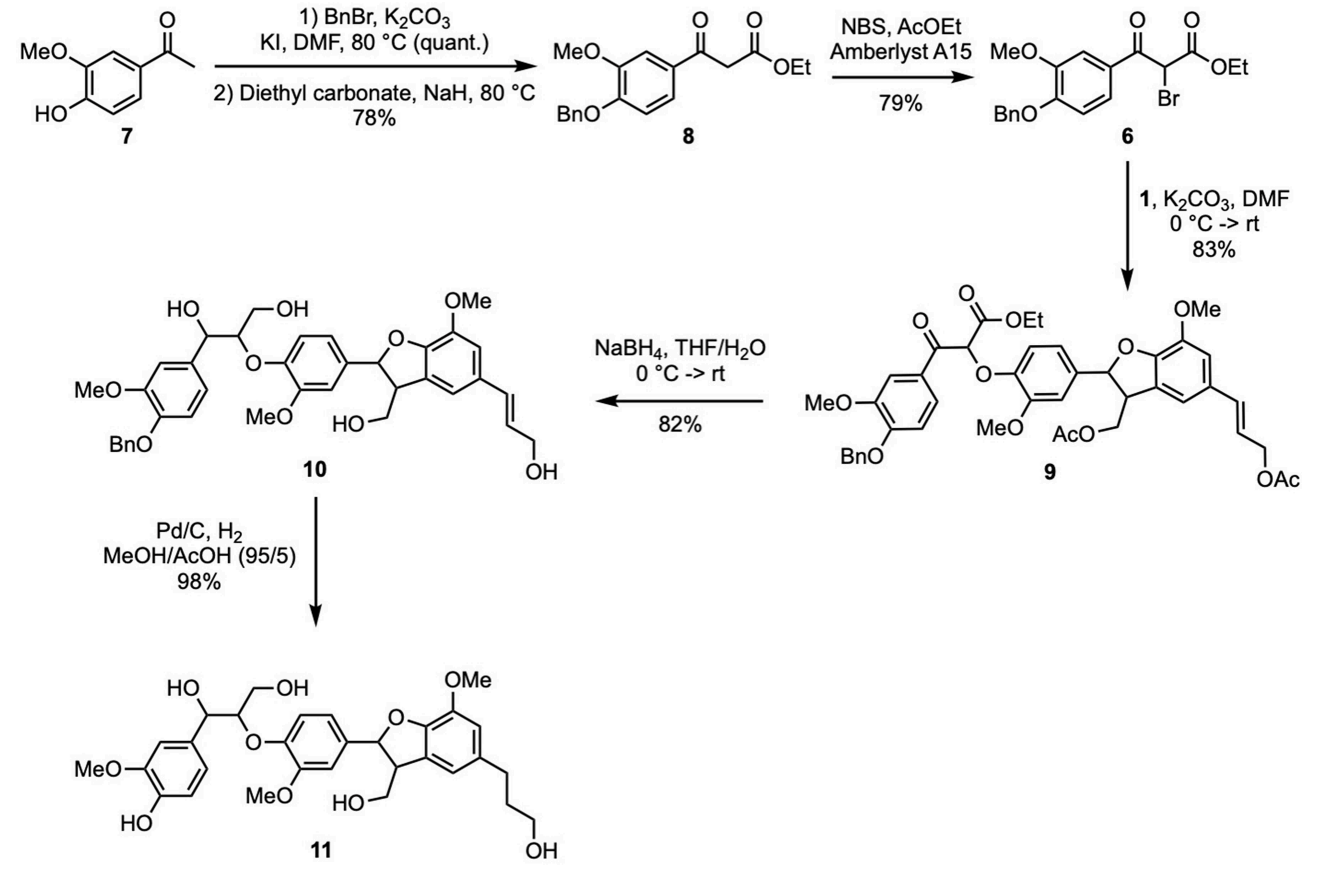

SCHEME 3 | Synthesis of naturally occurring dihydrotrimer (β-5)-(β-O-4) **(11)**.

product from the quenched reaction mixture. Unfortunately, although there have been reports on the successful $NaBH_4$-mediated reduction of aromatic/conjugated esters (Bianco et al., 1988; Boechat et al., 2004; da Costa et al., 2006) the $NaBH_4$-mediated reduction of **13** proved unsuccessful even with longer reaction time (4 days) or addition of more $NaBH_4$ (up to 20 equivalents) (**Scheme 4**).

Finally, in order to access naturally occurring (β-5)-(β-*O*-4) dihydroxytrimer **14**, the double bond in **9** had to be converted into the corresponding 1,2-diol through a dihydroxylation step (**Scheme 5**). The use of a modified osmium tetroxide-based Upjohn approach (K_2OsO_4, NMO, $EtOH/H_2O$, citric acid) (Moreaux et al., 2019) allowed the formation of compound **15** (58% yield). The latter was then deprotected in the presence of sodium borohydride to provide **16** in 65% yield. Compound **16** exhibiting a high polarity, its purification through flash chromatography had to be performed in reverse phase. Finally, dihydroxytrimer (β-5)-(β-*O*-4) **14** was obtained after the removal of the benzyl group using the same hydrogenation procedure as previously described. Efficient removal of acetic acid and ethanol was achieved through azeotropic distillation, providing pure **14** in excellent yield (99% overall yield starting from ferulic acid in nine steps).

MATERIALS AND METHODS

Material

Ferulic acid, 1 M diisobutyl aluminum hydride in dichloromethane, benzyl bromide, laccase from *Trametes versicolor* (776 U/g), piperazine, and sodium hydride were purchased from Sigma-Aldrich and used as received. Acetovanillone, sodium borohydride, pyridine, and diethylcarbonate were purchased from TCI and used as received. Palladium on carbon and anhydrous magnesium sulfate were purchased from Acros Organics and used as received. Deuterated solvents were purchased from Euriso-top. Other reagents, salts, and solvents were purchased from VWR.

DMF was dried using mBraun SPS 800. Evaporations were conducted under reduced pressure (Vario Vacuubrand pump) on Buchi R300. Flash chromatographies were performed on a Puriflash 4100 (Interchim) equipped with and pre-packed INTERCHIM PF-30SI-HP (30 μm silica gel) columns. IR analyses were performed on Cary 630 FTIR (Agilent). NMR analyses were recorded on a Bruker Fourier 300. ^1H NMR spectra of samples were measured on a 300 MHz apparatus, chemicals shifts were reported in parts per million relative to solvent residual peak ($CDCl_3$ $\delta = 7.26$ ppm; DMSO-d_6 $\delta = 2.50$ ppm).

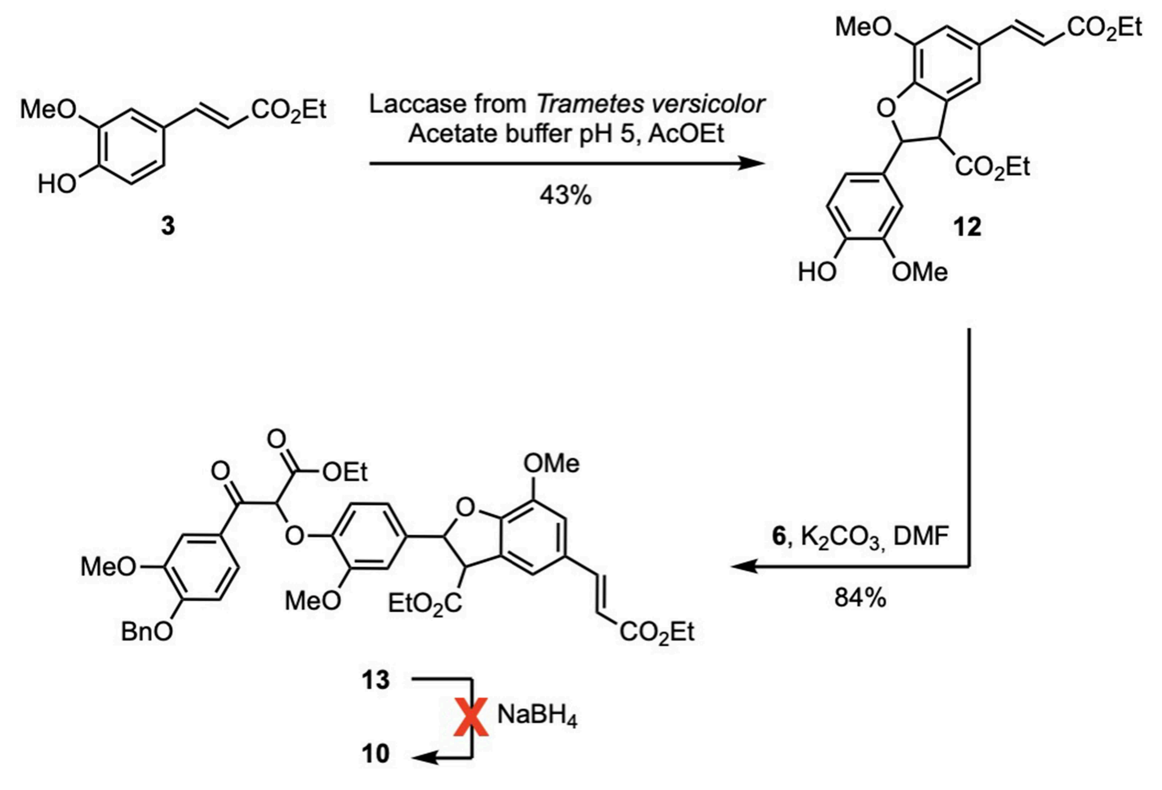

SCHEME 4 | Unsuccessful alternative pathway to **10**.

^{13}C NMR spectra of samples were recorded at 75 MHz and calibrated on solvent peak ($CDCl_3$ $\delta = 77.16$ ppm; DMSO-d$_6$ $\delta = 39.52$ ppm).

Methods

Synthesis of Dimer (β-5) (4)

Coniferyl alcohol **G** (3.0 g, 16.6 mmol) was dissolved in ethyl acetate (170 mL) at room temperature, then citrate/phosphate buffer 4.5 (170 mL) was added and the mixture was vigorously stirred (1,000 rpm). Laccase from *Trametes versicolor* (21 mg, 16.3 U/mmol) was dissolved in pH 4.5 buffer (50 mL) and added at 10 mL.h^{-1} to the mixture. At the end of the addition, layers were separated and aqueous layer was extracted twice with AcOEt (75 mL). Organic layers were then combined, washed with brine, dried over anhydrous $MgSO_4$, filtered and concentrated to dryness. Product was purified by flash chromatography over silica gel in 10/90 cyclohexane/AcOEt, providing **4** as an orange foam (1.28 g, 43%).

IR (neat): ν = 3,332 (O-H), 2,926 + 2,869 (C=C), 1,610 + 1,516 + 1,496 + 1,461 (C=C arom) cm^{-1}.

^{1}H NMR (DMSO-d$_6$, 300 MHz) δ = 9.02 (s, 1H, H_{23}), 6.93 (m, 3H, $H_{10} + H_{20} + H_{21}$), 6.75 (s, 2H, $H_6 + H_{17}$), 6.46 (d, 1H, J =15.9 Hz, H_4), 6.21 (dt, 1H, J = 15.9 Hz, J = 5.4 Hz, H_3), 5.45 (d, 1H, J = 6.9 Hz, H_{15}), 5.02 (t, 1H, J = 5.4 Hz, H_{14}), 4.78, (t, 1H, J = 5.7 Hz, H_1), 4.08 (td, 2H, J =5.4 Hz, J = 1.2 Hz, H_2), 3.79 (s, 3H, H_{22}), 3.74 (s, 3H, H_{11}), 3.58–3.74 (m, 2H, H_{13}), 3.43 (m, 1H, H_{12}) ppm.

^{13}C NMR (DMSO-d$_6$, 75 MHz) δ = 147.6 + 147.1 (Cq, $C_8 + C_{19}$), 146.4 + 143.7 (Cq, $C_7 + C_{18}$), 132.3 (Cq, C_{16}), 130.5 (Cq, C_5), 129.5 (Cq, C_9), 129.0 (Cs, C_4), 128.0 (Cs, C_3), 118.5 + 115.3 (Cs, $C_6 + C_{17}$), 114.9 (Cs, C_{20}), 110.3 (Cs, $C_{10} + C_{21}$), 87.2 (Cs, C_{15}), 62.9 (Cd, C_{13}), 61.7 (Cd, C_2), 55.6 (Ct, $C_{11} + C_{22}$), 53.0 (Cs, C_{12}) ppm.

HRMS (EI): Calcd for $C_{20}H_{22}O_6$ [M]: 358.1416 and for $C_{20}H_{23}O_6^+$ [M+H]$^+$: 359.1489, found 359.1566.

Synthesis of Tri-O-Acetylated Dimer (β-5) (5)

4 (2.6 g, 7.25 mmol) was dissolved in pyridine (18 mL) and acetic anhydride (11 mL, 109 mmol, 5 equiv/function) was added. The reaction was stirred at room temperature overnight. Reaction medium was poured into acidified iced water. The precipitate was filtered off and rinsed with water until neutral pH. After drying, **5** was recovered in quantitative yield and used in the next step without further purification.

IR (neat): ν = 2,940 (C-C), 1,733 (C=O), 1,603 + 1,506 + 1,462 + 1,421 + 1,366 + 1,332 (C=C arom), 1,214 + 1,187 + 1,146 + 1,127 (C-O) cm^{-1}.

^{1}H NMR ($CDCl_3$, 300 MHz) δ = 6.98 (m, 3H, $H_{10} + H_{20} + H_{21}$) 6.88 (m, 2H, $H_6 + H_{17}$), 6.59 (m, 1H, H_4), 6.15 (dt, 1H, J = 15.6 Hz, J = 6.6 Hz, H_3), 6.54 (d, 1H, J = 6.6 Hz, H_{15}), 4.70 (dd, 2H, J = 6.6 Hz, 1.2 Hz, H_2), 4.26–4.47 (m, 2H, H_{13}), 3.91 (s, 3H, H_{22}), 3.78 (m, 4H, $H_{15} + H_{11}$), 2.30 (s, 3H, H_{26}), 2.09 (s, 3H, H_{24}), 2.05 (s, 3H, H_{25}) ppm.

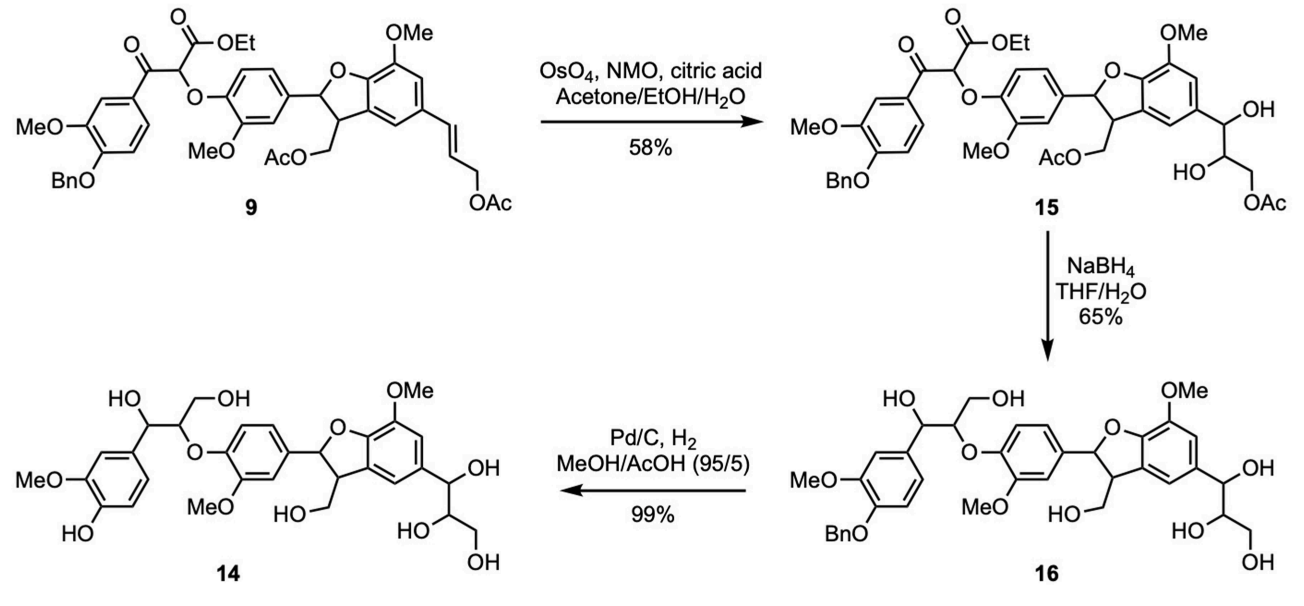

SCHEME 5 | Synthesis of naturally occurring (β-5)-(β-*O*-4) dihydroxytrimer (**14**).

^{13}C NMR ($CDCl_3$-d_6) δ = 171.0 + 170.8 (Cq, C_{14} + C_1), 169.0 (Cq, C_{23}), 151.3 (Cq, C_{18}), 148.2 (Cq, C_8), 144.4 (Cq, C_7), 139.7 + 139.4 (Cq, C_{16} + C_{19}), 134.3 (Cs, C_4), 130.7 (Cq, C_5), 127.3 (Cq, C_9), 122.9 (Cs, C_{20}), 121.3 (Cs, C_3), 118.2 (Cs, C_{21}), 115.4 (Cs, C_{10}), 110.6 (Cs, C_{17}), 109.9 (Cs, C_6), 88.1 (Cs, C_{15}), 65.4 (Cd, C_{13}), 65.2 (Cd, C_2), 56.0 + 55.9 (Ct, C_{11} + C_{22}), 50.5 (Cs, C_{12}), 20.6–21.1 (Ct, C_{24} + C_{25} + C_{26}) ppm.

HRMS (EI): Calcd for $C_{26}H_{28}O_9$ [M]: 484.1733 and for $C_{26}H_{28}O_9Na^+$ $[M+Na]^+$: 507.1631 found 507.1637.

Synthesis of diO-Acetylated Dimer (β-5) (1)

5 (7.25 mmol) was dissolved in THF (70 mL) and piperazine (1.87 g, 21.75 mmol, 3 equiv) was added. Reaction mixture was stirred 4 h at room temperature. After completion, THF was removed under reduced pressure. The crude mixture was dissolved in AcOEt (50 mL), washed with HCl 1 M (3*15 mL) and brine (20 mL), dried over anhydrous $MgSO_4$, filtered and concentrated. After purification by flash chromatography in 40/60 cyclohexane/AcOEt, **1** was recovered as colorless oil (2.95 g, 92%).

IR (neat): ν = 3,443 (OH), 2,939 (C-C), 1,732 (C=O), 1,601 + 1,515 + 1,493 + 1,460 + 1,423 + 1,364 + 1,331 (C=C arom), 1,216 + 1,144 (C-O) cm^{-1}.

^{1}H NMR ($CDCl_3$, 300 MHz) δ = 6.88 (m, 5H, H_6 + H_{10} + H_{17} + H_{20} + H_{21}), 6.60 (d, 1H, *J* =15.9 Hz, H_4), 6.16 (dt, 1H, *J* = 15.9 Hz, *J* = 6.6 Hz, H_3), 5.65 (s, 1H, H_{23}), 5.47 (d, 1H, *J* = 7.5 Hz, H_{15}), 4.71 (dd, *J* = 1.2 Hz, *J* = 6.6 Hz, 2H, H_2) 4.37 (m, 2H, H_{13}), 3.91 (s, 3H, H_{22}), 3.86 (s, 3H, H_{11}), 3.77 (m, 1H, H_{12}), 2.10 (s, 3H, H_{24}), 2.03 (s, 3H, H_{25}) ppm.

^{13}C NMR ($CDCl_3$-d_6, 75 MHz) δ = 171.1 (Cq, C_{14}), 171.0 (Cq, C_1), 148.4 (Cq, C_8), 146.8 (Cq, C_{18}), 146.0 (Cq, C_{19}), 144.5 (Cq, C_7), 134.5 (Cq, C_{16}), 132.3 (Cs, C_4), 130.6 (Cq, C_5), 127.8 (Cq, C_9), 121.2 (Cs, C_3), 119.7 (Cs, C_{21}), 115.4 (Cs, C_{20}), 114.4 (Cs, C_{10}), 110.6 (Cs, C_{17}), 108.7 (Cs, C_6), 89.0 (Cs, C_{15}), 65.4 (Cd, C_2 + C_{13}), 56.1 (Ct, C_{11} + C_{22}), 50.4 (Cs, C_{12}), 21.2 (Ct, C_{24}), 21.0 (Ct, C_{25}) ppm.

HRMS (EI): Calcd for $C_{24}H_{26}O_8$ [M]: 442.1628 and for $C_{24}H_{27}O_8^+$ $[M+H]^+$: 443.1700 found 443.1867.

Synthesis of 9

Under N_2, **1** (1.4 g, 3.16 mmol) was dissolved in dry DMF (10 mL) and K_2CO_3 (0.66 g, 4.75 mmol, 1.5 equiv) was added (reaction turned yellow). After cooling to 0°C, a solution of **6** (1.9 g, 4.75 mmol, 1.5 equiv) in DMF (9 mL) was added dropwise. Reaction mixture was stirred at room temperature for 3 h, then quenched with water (50 mL) and extracted with AcOEt (3*50 mL). Organic layers were combined, washed with brine, dried over anhydrous $MgSO_4$, filtered and concentrated. After purification by flash chromatography in 5/5 cyclohexane/AcOEt, **9** was recovered as an oil (2.04 g, 83%).

IR (neat): ν = 2,953 (C-C), 1,734 (C=Oester), 1,676 (C=Oketone), 1,593 + 1,508 + 1,459 + 1,420 + 1,379 + 1,332 (C=Carom), 1,209 + 1,143 (C-O) cm^{-1}.

^{1}H NMR ($CDCl_3$, 300 MHz) δ = 7.77 (dd, *J* = 8.4 Hz, *J* = 2.1 Hz, 1H, H_{31}), 7.68 (d, *J* = 2.1 Hz, 1H, H_{27}), 7.27–7.45 (m, 5H, H_{35} + H_{36} + H_{37}), 6.74–6.94 (m, 6H, H_6 + H_{10} + H_{17} + H_{20} + H_{21} + H_{30}), 6.59 (d, *J* =15.6 Hz, 1H, H_4), 6.15 (dt, *J* = 15.6 Hz, *J* = 6.6 Hz, 1H, H_3), 5.73 (s, 1H, H_{23}), 5.47 (d, *J* = 6.9 Hz, 1H, H_{15}), 5.23 (s, 2H, H_{33}), 4.71 (d, *J* = 6.6 Hz, 2H, H_2), 4.43 (m, 1H, H_{13a}), 4.24 (m, 3H, H_{13b} + H_{38}), 3.92 (s, 3H, H_{32}), 3.90 (s, 3H, H_{11}), 3.75 (m, 4H, H_{22} + H_{12}), 2.09 (s, 3H, H_{41}), 2.01 (s, 3H, H_{40}), 1.21 (t, *J* = 7.2 Hz, 3H, H_{39}) ppm.

^{13}C NMR ($CDCl_3$, 75 MHz) δ =190.0 (Cq, C_{25}), 170.9–171.3 (Cq, C_1 + C_{14}), 167.0 (Cq, C_{24}), 153.3 (Cs, C_{29}), 150.7 (Cs, C_{18}), 150.6 (Cs, C_8), 149.5 (Cs, C_{28}), 148.2 (Cs, C_{34}), 146.3 (Cs, C_{19}), 144.5 (Cs, C_7), 136.2 (Cs, C_5 + C_{16}), 134.4 (Cs, C_4), 130.7 (Cs,

C_9), 128.8 (Cs, C_{36}), 128.3 (Cs, C_{26}), 127.5 (Cs, C_{37}), 127.3 (Cs, C_{35}), 124.8 (Cs, C_{31}), 121.3 (Cs, C_3), 118.7 (Cs, C_{20}), 118.3 (Cs, C_{21}), 115.4 (Cs, C_{10}), 112.1 (Cs, C_{30}), 112.0 (Cs, C_{27}), 110.5 (Cs, C_{17}) 110.4 (Cs, C_6), 88.4 (Cs, C_{15}), 82.7 (Cs, C_{23}), 70.9 (Cd, C_{33}), 65.3 (Cd, $C_2 + C_{13}$), 62.3 (Cd, C_{38}), 56.0–56.1 (Ct, $C_{11} + C_{22} + C_{32}$), 50.4 (Cs, C_{12}), 21.2 (Ct, C_{41}), 20.9 (Ct, C_{40}), 14.3 (Ct, C_{39}) ppm.

HRMS (EI): Calcd for $C_{43}H_{44}O_{13}$ [M]: 768.2782 and for $C_{43}H_{44}O_{13}Na^+$ $[M+Na]^+$: 791.2680 found 791.2668.

Synthesis of 10

9 (700 mg, 0.91 mmol) was dissolved in THF (7.6 mL) and water was added (2.4 mL). At 0°C, $NaBH_4$ (344 mg, 9.1 mmol, 10 equiv) was added by portions. At the end of the addition, reaction mixture was stirred for two more hours at room temperature, then quenched by a saturated aqueous solution of NH_4Cl (10 mL) and extracted with AcOEt (2*30 mL). Organic layers were combined, washed with brine, dried over anhydrous $MgSO_4$, filtered and concentrated. After purification by flash chromatography in 100% AcOEt, **10** was recovered as an oil (432 mg, 82%).

IR (neat): ν = 3,346 (O-H), 2,934 (C-C), 1,595 + 1,508 + 1,459 + 1,420 + 1,379 + 1,326 (C=Carom), 1,257 + 1,217 + 1,137 (C-O) cm^{-1}.

^1H NMR (DMSO-d$_6$, 300 MHz) δ = 7.30–7.44 (m, 5H, $H_{35} + H_{36} + H_{37}$), 6.75–7.15 (m, 8H, $H_6 + H_{10} + H_{17} + H_{20} + H_{21} + H_{27} + H_{30} + H_{31}$), 6.60 (d, *J* =15.6 Hz, 1H, H_4), 6.21 (dt, *J* = 15.6 Hz, *J* = 6.6 Hz, 1H, H_3), 5.49 (m, 1H, H_{15}), 5.45 (m, 1H, H_{25}), 5.05 (m, 3H, $H_{33} + H_{39}$), 4.74 (m, 1H, H_{23}), 4.64 (m, 2H, H_2), 4.33 (m, 1H, H_{24a}), 3.80 (s, 3H, H_{11}), 3.73 (m, 4H, $H_{32} + H_1$), 3.67 (s, 3H, H_{22}), 3.60 (m, 3H, $H_{13} + H_{24b}$), 3.42 (m, 1H, H_{12}) ppm.

^{13}C NMR (DMSO, 75 MHz) δ =150.0 (Cq, C_8), 148.9 (Cq, C_{19}), 148.3 (Cq, C_{28}), 148.1 (Cq, C_{18}), 147.2 (Cq, C_{29}), 144.2 (Cq, C_7), 137.8 (Cq, C_{34}), 135.7 (Cq, C_{16}), 134.4 (Cq, C_5), 134.3 (Cs, C_4), 130.1 (Cq, C_9), 129.9 (Cq, C_{26}), 128.8 (Cs, $C_{36} + C_{37}$), 128.2 (Cs, C_{35}), 121.4 (Cs, C_3), 119.6 (Cs, C_{31}), 118.5 (Cs, C_{21}), 116.0 (Cs, C_{10}), 115.7 (Cs, C_{20}), 113.2 (Cs, C_{30}), 111.8 (Cs, C_{27}), 111.0 (Cs, C_{17}) 110.8 (Cs, C_6), 87.5 (Cs, C_{15}), 84.0 (Cs, C_{25}), 71.9 (Cs, C_{23}), 70.3 (Cd, C_{33}), 65.1 (Cd, C_2), 60.4 (Ct, C_{24}), 60.2 (Ct, C_{13}), 56.1 (Ct, $C_{11} + C_{22}$), 55.8 (Ct, C_{32}), 53.5 (Cs, C_{12}) ppm.

Synthesis of 11

10 (250 mg, 0.38 mmol) was dissolved in methanol/acetic acid (95/5) mixture (5 mL). Reaction medium was purged with nitrogen during 15 min, then palladium on charcoal (25 mg, 10% w/w) was added. The reaction was put under dihydrogen flux overnight at room temperature. Upon completion, reaction medium was purged with nitrogen during 20 min, filtered through PTFE syringe filter, rinsed twice with 5 mL of ethanol and concentrated. **11** was recovered as a foam (217 mg, 98%) without the need of further purification.

IR (neat): ν = 3,388 (O-H), 2,934 (C-C), 1,602 + 1,509 + 1,460 + 1,421 + 1,366 (C=Carom), 1,258 + 1,210 + 1,138 (C-O) cm^{-1}.

^1H NMR (DMSO-d$_6$, 300 MHz) δ = 8.75 (s, 1H, H_{33}), 7.02–6.64 (m, 8H, $H_6 + H_{10} + H_{17} + H_{20} + H_{21} + H_{27} + H_{30} + H_{31}$), 5.43 (m, 1H, H_{15}), 5.28 (m, 1H, H_{25}), 5.00 (s, 1H, H_{35}), 4.70 (m, 1H, H_{23}), 4.59 (s, 1H, H_{14}), 4.44 (s, 1H, H_1), 4.29 (m, 1H, H), 3.77–3.69 (m, 12H, $H_{11} + H_{22} + H_{32} + H$), 3.59 (m, 4H, H), 3.40 (m, 8H, $H_2 + H_4$), 1.69 (m, 2H, H_3) ppm.

^{13}C NMR (DMSO, 75 MHz) δ = 150.4, (Cq, C_8), 148.2 (Cq, C_{19}), 147.4 (Cq, C_{28}), 146.1 (Cq, C_{18}), 145.9 (Cq, C_{29}), 143.9 (Cq, C_7), 140.0 (Cq, C_{16}), 134.6 (Cq, C_5) 133.7 (Cq, C_9), 128.2 (Cq, C_{26}), 119.9 (Cs $C_{21} + C_{31}$), 116.9 (Cs, $C_{10} + C_{20}$), 112.9 (Cs, $C_{30} + C_{27}$), 111.0 (Cs, $C_{17} + C_6$), 95.5 (Cs, C_{15}), 84.0 (Cs, C_{25}), 72.0 (Cs, C_{23}), 63.8 (Cd, C_2), 63.5 (Ct, C_{24}), 60.4 (Ct, C_{13}), 56.1 (Cs, $C_{11} + C_{22} + C_{32}$), 55.9 (Cs, C_{12}) 31.8 (Cd, C_3), 30.6 (Cd, C_4) ppm.

Synthesis of 15

9 (840 mg, 1.1 mmol) and citric acid (275 mg, 1.3 mmol) were dissolved in a mixture of acetone (3 mL), ethanol (2 mL) and water (1.5 mL). Osmium tetroxide solution 4% in water (170 μL, 27 μmol) was added and then N-methyl morpholine solution 0.5 M in water (270 μL, 1.3 mmol) was added too. The reaction media was stirred overnight, quenched with $Na_2S_2O_3$ (10 mL) and extracted thrice with ethyl acetate (10 mL). Organic layers were combined washed with water and brine, dried over anhydrous $MgSO_4$, filtered and concentrated. Flash purification was conducted on silica gel with cyclohexane/AcOEt (1/1) and then AcOEt (100%) to afford 512 mg of pure **15** as an oil (58%).

IR (neat): ν = 3,456 (O-H), 2,937 (C-C), 1,734 (C=O ester), 1,675 (C=O ketone), 1,592 + 1,508 + 1,454 + 1,419 + 1,368 (C=C arom), 1,209 + 1,135 (C-O) cm^{-1}.

^1H NMR ($CDCl_3$, 300 MHz) δ = 7.77 (dd, *J* = 8.4 Hz, *J* = 2.1 Hz, 1H, H_{31}), 7.68 (d, *J* = 2.1 Hz, 1H, H_{27}), 7.31–7.44 (m, 5H, $H_{35} + H_{36} + H_{37}$), 6.82–6.93 (m, 6H, $H_6 + H_{10} + H_{17} + H_{20} + H_{21} + H_{30}$), 5.73 (s, 1H, H_{23}), 5.47 (d, *J* = 6.9 Hz, 1H, H_{15}), 5.23 (s, 2H, H_{33}), 4.57 (m, 1H, H), 4.39 (m, 1H, H), 4.21–4.35 (m, 3H, $H_{13b} + H_{38}$), 4.12 (m, 1H, H), 3.87–4.01 (m, 9H, H), 3.78 (m, 4H, $H_{22} + H_{12}$), 2.10 (s, 3H, H_{41}), 2.00 (s, 3H, H_{40}), 1.21 (t, *J* = 7.2 Hz, 3H, H_{39}) ppm.

^{13}C NMR ($CDCl_3$, 75 MHz) δ =190.0 (Cq, C_{25}), 170.9 and 171.4 (Cq, $C_1 + C_{14}$), 167.0 (Cq, C_{24}), 153.3 (Cs, C_{29}), 150.6 (Cs, C_{18}), 149.5 (Cs, C_8), 149.5 (Cs, C_{28}), 148.2 (Cs, C), 146.3 (Cs, C_{19}), 144.5 (Cs, C_7), 136.2 (Cs, $C_{34} + C_5 + C_{16}$), 134.4 (Cs, C_4), 130.7 (Cs, C_9), 128.8 (Cs, C_{36}), 128.3 (Cs, C_{26}), 127.5 (Cs, C_{37}), 127.4 (Cs, C_{35}), 124.8 (Cs, C_{31}), 118.8 (Cs, C_{20}), 118.3 (Cs, C_{21}), 115.0 (Cs, C_{10}), 112.1 (Cs, C_{30}), 112.0 (Cs, C_{27}), 110.9 (Cs, C_{17}) 110.4 (Cs, C_6), 88.4 (Cs, C_{15}), 82.7 (Cs, C_{23}), 77.4, 74.6, 74.3 (Cd, C_4), 70.9 (Cd, C_{33}), 65.5+ 65.3 (Cd, $C_2 + C_{13}$), 62.3 (Cd, C_{38}), 56.0–56.2 (Ct, $C_{11} + C_{22} + C_{32}$), 50.6 (Cs, C_{12}), 21.0 (Ct, C_{41}), 20.9 (Ct, C_{40}), 14.2 (Ct, C_{39}) ppm.

HRMS (EI): Calcd for $C_{43}H_{46}O_{15}$ [M]: 802.2837 and for $C_{43}H_{46}O_{15}Na^+$ $[M+Na]^+$: 825.2726 found 825.2734.

Synthesis of 16

15 (794 mg, 0.99 mmol) was dissolved in a THF/water mixture (8.2 mL/2.6 mL). At 0°C, sodium borohydride (375 mg, 9.9 mmol, 10 equiv) was added by portion. The reaction medium was stirred at room temperature during 18 h. THF was removed by distillation under reduce pressure and 2.5 mL of methanol was added. The crude mixture was purified by flash chromatography over C18-grafted silica gel with water/MeOH (1/1) and then water/ MeOH (1/4). **16** was recovered as a white foam (448 mg, 65%).

IR (neat): ν = 3,344 (O-H), 2,932 + 2,873 (C-C), 1,602 + 1,507 + 1,451 + 1,419 + 1,321 (C=C arom), 1,258 + 1,213 + 1,135 (C-O) cm^{-1}.

^{1}H NMR (DMSO, 300 MHz) δ = 7.31–7.41 (m, 5H, $H_{35} + H_{36} + H_{37}$), 6.81–7.06 (m, 8H, $H_6 + H_{10} + H_{17} + H_{20} + H_{21} + H_{27} + H_{30} + H_{31}$), 5.38–5.47 (m, 2H, $H_{23} + H_{41}$), 5.04 (s, 3H, $H_{33} + H_1$), 4.99 (t, *J* = 4.5 Hz, 1H, H_{39}), 4.76 (m, 1H, H_3), 4.66 (m, 1H, H_{14}), 4.53 (m, 1H, H_{38}), 4.45 (m, 2H, $H_{25} + H_{40}$), 4.33 (m, 1H, H_1), 3.68–3.77 (m, 10H, $H_{11} + H_{22} + H_{32} + H_{13a}$), 3.60 (m, 3H, $H_2 + H_{13b}$), 3.43–3.48 (m, 2H, $H_{12} + H_{24a}$), 3.31 (m, 1H, H_4), 3.19 (m, 1H, H_{24b}) ppm.

^{13}C NMR (DMSO, 75 MHz) δ =149.6 (Cq, C_7), 148.5 (Cq, C_{18}), 147.8 (Cq, C_8), 146.8 (Cq, C_{28}), 146.3 (Cq, C_{29}), 143.0–143.1 (Cq, C_{19}), 137.4 (Cq, C_{34}), 136.8 (Cq, C_{16}), 135.3 (Cq, C_{26}), 134.4 (Cs, C_5), 128.4 (Cs, C_{36} +Cq, C_9), 127.8 (Cs, $C_{37} + C_{35}$), 119.2 (Cs, C_{31}), 118.0 (Cs, C_{21}), 115.1–115.4 (Cs, C_{10}), 112.9 (Cs, C_{30}), 11.4 (Cs, C_{17}), 111.0–111.4 (C_{20}), 110.4 (C_6), 86.8 (Cs, C_{23}), 83.5 (Cs, C_{15}), 75.9 (Cs, C_4), 72.8–73.0 (Cs, C_{25}), 71.5 (Cs, C_3), 69.9 (Cd, C_{33}), 63.2 (Cd, C_{13}), 62.7 (cd, C_{24}), 60.0 (Cd, C_2), 55.7 and 55.4 (Ct, $C_{22} + C_{32} + C_{11}$), 53.5 (Cs, C_{12}) ppm.

HRMS (EI): Calcd for $C_{37}H_{42}O_{12}$ [M]: 678.7310 and for $C_{37}H_{42}O_{12}Na^{+}$ $[M+Na]^{+}$: 701.2574 found 701.2565.

Synthesis of 14

16 (325 mg, 0.48 mmol) was dissolved in a MeOH/AcOH (95/5) mixture (4.8 mL). The reaction medium was purged for 15 min under nitrogen flow before palladium on charcoal (32 mg, 10% w/w) was added. The mixture was then stirred under hydrogen flow overnight. Upon completion, reaction medium was purged with nitrogen during 20 min, filtered through PTFE syringe filter, rinsed twice with 5 mL of ethanol and concentrated. Crude product was submitted to azeotropic evaporation with toluene thrice, then thrice with water to eliminate acetic acid residues. Light yellow oil was recovered (99%).

IR (neat): ν = 3,324 (O-H), 2,933 (C-C), 1,601 + 1,507 + 1,451 + 1,420 (C=C), 1,261 + 1,214 + 1,134 (C-O) cm^{-1}.

^{1}H NMR (DMSO-d_6, 300 MHz) δ = 6.52–7.01 (m, 13H, $H_6 + H_{10} + H_{17} + H_{20} + H_{21} + H_{27} + H_{30} + H_{31}$), 5.45 (m, 1H, H_{23}), 4.70 (m, 3H, $H_3 + H_{37} + H_{36}$), 4.39 (m, 3H, H_{25}), 4.24 (m, 2H, H_{15}), 3.63–3.77 (m, 14H, $H_{11} + H_{22} + H_{32} + H_{13a}$), 3.08–3.55 (m, 14H, $H_2 + H_3 + H_4 + H_{12} + H_{13b} + H_{23} + H_{24}$) ppm.

^{13}C NMR (DMSO, 75 MHz) δ = 149.6–145.5 (Cq, $C_7 + C_{18} + C_8 + C_{28} + C_{29}$), 142.9–143.1 (Cq, C_{19}), 136.8–136.9 (Cq, C_{16}), 132.9–134.4 (Cq, $C_5 + C_{26}$), 128.2–128.4 (Cq, C_9), 118.0–120.7 (Cs, $C_{21} + C_{31}$), 114.6–115.5 (Cs, $C_{10} + C_{30}$), 113.2–113.3 (Cs, C_{27}), 110.4–111.4 (Cs, $C_{17} + C_{20}$), 107.8–108.0 (Cs, C_6), 86.8 (Cs, C_{23}), 83.7 (Cs, C_{15}), 75.9–76.1 (Cd, C_4), 72.8–73.1 (Cs, C_{25}), 71.5 (Cs, C_3), 63.2–64.3 (Cd, C_{13}), 62.6 (Cd, C_{24}), 59.9–60.0 (Cd, C_2) 55.4–55.7 (Ct, $C_{11} + C_{22} + C_{32}$), 53.5 (Cs, C_{12}) ppm.

HRMS (EI): Calcd for $C_{30}H_{36}O_{12}$ [M]: 588.2207 and for $C_{30}H_{36}O_{12}Na^{+}$ $[M+Na]^{+}$: 611.2104 found 611.2110.

CONCLUSION

The total convergent synthesis of the β-5/β-*O*-4 dihydroxytrimer of monolignol **G** (**11**) and that of the naturally occurring dihydrotrimer (**10**) have been successfully achieved in nine steps and in 9 and 20% yield, respectively, starting from ferulic acid using laccase-mediated dimerization, nucleophilic substitution (S_{N2}), and dihydroxylation as key steps.

DATA AVAILABILITY STATEMENT

All datasets generated for this study are included in the article/**Supplementary Material**.

AUTHOR CONTRIBUTIONS

AF and FA wrote the publication. AP performed main bibliographical research. AF and AP designed and performed experimental work. AH, J-HR, and FA supervised this work and corrected the proof of article.

FUNDING

This work was fund through the financial support brought to URD ABI by the Grand Reims, the Conseil Général de la Marne and the Région Grand Est.

ACKNOWLEDGMENTS

The authors are grateful to Grand Reims, Département de la Marne, and Grand Est for financial support. Authors also want to acknowledge analytical platform PLANET (Reims) for performing HRMS analysis.

SUPPLEMENTARY MATERIAL

The Supplementary Material for this article can be found online at: https://www.frontiersin.org/articles/10.3389/fchem.2019.00842/full#supplementary-material

REFERENCES

Bianco, A., Passacantilli, P., and Righi, G. (1988). Synthetic communications: an international journal for rapid communication of synthetic organic chemistry. *Synth. Commun.* 15, 1765–1771. doi: 10.1080/00397918808060931

Boechat, N., Santos Da Costa, J. C., De Souza Mendonça, J., De Oliveira, P. S. M., and De Souza, M. V. N. (2004). A simple reduction of methyl aromatic esters to alcohols using sodium borohydride-methanol system. *Tetrahedron Lett.* 45, 6021–6022. doi: 10.1016/j.tetlet.2004.06.034

Bouxin, F. (2011). *Solvolyse Des Lignines: Production de Synthons Aromatiques de Faibles Masses*. Available online at: https://www.theses.fr/2011REIMS004

Broussard, O., Petit, M., Elie, N., Baumberger, S., Arnaud, A., Ducrot, P.-H., et al. (2016). Monitoring of free phenol content in lignosulfonates by ClO_2 titration and UV difference spectroscopy. *Holzforschung* 70, 719–724. doi: 10.1515/hf-2015-0111

Cottyn, B., Rivard, M., Majira, A., Beauhaire, J., Allais, F., Martens, T., et al. (2015). Comparative electrochemical study on monolignols and dimers relevant for the comprehension of the lignification process. *Phytochem. Lett.* 13, 280–285. doi: 10.1016/j.phytol.2015.07.002

da Costa, J. C. S., Pais, K. C., Fernandes, E. L., De Oliveira, P. S. M., Mendonça, J. S., De Souza, M. V. N., et al. (2006). Simple reduction of ethyl, isopropyl and benzyl aromatic esters to alcohols using sodium borohydride-methanol system. *Arkivoc* 1, 128–133. doi: 10.3998/ark.5550190.0007.115

Forsythe, W. G., Garrett, M. D., Hardacre, C., Nieuwenhuyzen, M., and Sheldrake, G. N. (2013). An efficient and flexible synthesis of model lignin oligomers. *Green Chem.* 15, 3031–3038. doi: 10.1039/c3gc41110a

Gao, R., Li, Y., Kim, H., Mobley, J. K., and Ralph, J. (2018). Selective oxidation of lignin model compounds. *ChemSusChem* 11, 2045–2050. doi: 10.1002/cssc.201800598

Jaufurally, A. S., Teixeira, A. R. S., Hollande, L., Allais, F., and Ducrot, P. H. (2016). Optimization of the laccase-catalyzed synthesis of (±)-syringaresinol and study of its thermal and antiradical activities. *ChemistrySelect* 1, 5165–5171. doi: 10.1002/slct.201600543

Jiang, H., Yang, L., Ma, G. X., Xing, X. D., Yan, M. L., Zhang, Y. Y., et al. (2017). New phenylpropanoid derivatives from the fruits of xanthium sibiricum and their anti-inflammatory activity. *Fitoterapia* 117, 11–15. doi: 10.1016/j.fitote.2016.12.007

Kishimoto, T., Uraki, Y., and Ubukata, M. (2006). Chemical synthesis of B-O-4 type artificial lignin. *Org. Biomol. Chem.* 4, 1343–1347. doi: 10.1039/b518005h

Lancefield, C. S., and Westwood, N. J. (2015). The synthesis and analysis of advanced lignin model polymers. *Green Chem.* 17, 4980–4990. doi: 10.1039/C5GC01334H

Lee, T. W., and Yang, J. W. (2018). Transition-metal-free, conversion of lignin model compounds to high-value aromatics: scope and chemoselectivity. *Green Chem.* 20, 3761–3771. doi: 10.1039/C8GC01886C

Lou, L. L., Yao, G. D., Wang, J., Zhao, W. Y., Wang, X. B., Huang, X. X., et al. (2018). Enantiomeric neolignans from picrasma quassioides exhibit distinctive cytotoxicity on hepatic carcinoma cells through ros generation and apoptosis induction. *Bioorgan. Med. Chem. Lett.* 28, 1263–1268. doi: 10.1016/j.bmcl.2018.03.043

Moreaux, M., Bonneau, G., Peru, A. A. M., Brunissen, F., Janvier, M., Haudrechy, A., et al. (2019). High-yielding diastereoselective *syn*-dihydroxylation of protected HBO: an access to D-(+)-Ribono-1,4-Lactone and 5-O-protected analogues. *Eur. J. Organ. Chem*. 7, 1600–1604. doi: 10.1002/ejoc.201801780

Mouterde, L. M. M., Flourat,A. L., Cannet, M. M. M., Ducrot, P.-H., and Allais, F. (2013). Chemoenzymatic total synthesis of a naturally occurring (5-5′)/(8′-O-4″) dehydrotrimer of ferulic acid. *Eur. J. Organ. Chem.* 1, 173–79. doi: 10.1002/ejoc.201201290

Ono, M., Masuoka, C., Ito,Y., and Nohara, T. (1998). Antioxidative constituents from viticis trifoliae fructus (fruit of vitex *Rotundifolia* L.). *Food Sci. Technol. Int. Tokyo* 4, 9–13. doi: 10.3136/fsti9596t9798.4.9

Patil, N. D., and Yan, N. (2016). Study of the nitroxyl radical catalyst in aerobic oxidative cleavage and functionalization of lignin model compounds. *Catal. Commun.* 84, 155–158. doi: 10.1016/j.catcom.2016.06.015

Rinesch, T., and Bolm, C. (2018). Cobalt-catalyzed oxidation of the β-O-4 bond in lignin and lignin model compounds. research-article. *ACS Omega* 3, 8386–8392. doi: 10.1021/acsomega.8b00994

Sen, B. (1952). Synthesis of lignin model compounds. *J. Am. Chem. Soc.* 74, 3445–3447. doi: 10.1021/ja01133a531

Shimizu, S., Posoknistakul, P., Akiyama, T., Yokoyama, T., and Matsumoto, Y. (2018). Effects of aromatic ring type on reactions subsequent to the β-O-4 bond cleavage of non-phenolic lignin model compounds under alkaline pulping conditions. *J. Wood Sci.* 64, 664–674. doi: 10.1007/s10086-018-1739-3

Ye, F., Xie, Y., Ren, J., Ye, J., Guo, Y., Kai Yan, S., et al. (2016). Six new dihydrobenzofuran lignans from the branches and leaves of illicium wardii and their cytotoxic activities. *Phytochem. Lett.* 17, 263–269. doi: 10.1016/j.phytol.2016.07.010

Conflict of Interest: The authors declare that the research was conducted in the absence of any commercial or financial relationships that could be construed as a potential conflict of interest.

Copyright © 2019 Flourat, Peru, Haudrechy, Renault and Allais. This is an open-access article distributed under the terms of the Creative Commons Attribution License (CC BY). The use, distribution or reproduction in other forums is permitted, provided the original author(s) and the copyright owner(s) are credited and that the original publication in this journal is cited, in accordance with accepted academic practice. No use, distribution or reproduction is permitted which does not comply with these terms.

frontiers in Chemistry

ORIGINAL RESEARCH
published: 17 December 2019
doi: 10.3389/fchem.2019.00871

Lignin-Rich PHWE Hemicellulose Extracts Responsible for Extended Emulsion Stabilization

Maarit H. Lahtinen[1]*, Fabio Valoppi[1,2], Venla Juntti[1], Sami Heikkinen[3], Petri O. Kilpeläinen[4], Ndegwa H. Maina[1] and Kirsi S. Mikkonen[1,2]

[1] Department of Food and Nutrition, University of Helsinki, Helsinki, Finland, [2] Faculty of Agriculture and Forestry, Helsinki Institute of Sustainability Science, University of Helsinki, Helsinki, Finland, [3] Department of Chemistry, University of Helsinki, Helsinki, Finland, [4] Natural Resources Institute Finland (Luke), Helsinki, Finland

Wood hemicelluloses have an excellent capacity to form and stabilize oil-in-water emulsions. Galactoglucomannans (GGM) from spruce and glucuronoxylans (GX) from birch provide multifunctional protection against physical breakdown and lipid oxidation in emulsions. Phenolic residues, coextracted with hemicelluloses using the pressurized hot water (PHWE) process, seem to further enhance emulsion stability. According to hypothesis, phenolic residues associated with hemicelluloses deliver and anchor hemicelluloses at the emulsion interface. This study is the first to characterize the structure of the phenolic residues in both GGM- and GX-rich wood extracts and their role in the stabilization of emulsions. PHWE GGM and GX were fractionated by centrifugation to obtain concentrated phenolic residues as one fraction (GGM-phe and GX-phe) and partially purified hemicelluloses as the other fraction (GGM-pur and GX-pur). To evaluate the role of each fraction in terms of physical and oxidative stabilization, rapeseed oil-in-water emulsions were prepared using GGM, GX, GGM-pur, and GX-pur as stabilizers. Changes in droplet-size distribution and peroxide values were measured during a 3-month accelerated storage test. The results for fresh emulsions indicated that the phenolic-rich fractions in hemicelluloses take part in the formation of emulsions. Furthermore, results from the accelerated storage test indicated that phenolic structures improve the long-term physical stability of emulsions. According to measured peroxide values, all hemicelluloses examined inhibited lipid oxidation in emulsions, GX being the most effective. This indicates that phenolic residues associated with hemicelluloses act as antioxidants in emulsions. According to chemical characterization using complementary methods, the phenolic fractions, GGM-phe and GX-phe, were composed mainly of lignin. Furthermore, the total carbohydrate content of the phenolic fractions was clearly lower compared to the starting hemicelluloses GGM and GX, and the purified fractions GGM-pur and GX-pur. Apparently, the phenolic structures were enriched in the GGM-phe and GX-phe fractions, which was confirmed by NMR spectroscopy as well as by other characterization methods. The frequency of the main bonding pattern in lignins, the β-O-4 structure, was clearly very high, suggesting that extracted lignin remains in native form. Furthermore, the lignin carbohydrate complex of γ-ester type was found, which could explain the excellent stabilizing properties of PHWE hemicelluloses in emulsions.

Keywords: hemicellulose, lignin, lignin carbohydrate complex, emulsion, lipid oxidation

OPEN ACCESS

Edited by:
Gabriel Paes,
Fractionnation of AgroResources and Environment (INRA), France

Reviewed by:
Federica Valentini,
Department of Chemical Sciences and Technologies, University of Rome Tor Vergata, Italy
Patrik Eklund,
Åbo Akademi University, Finland

***Correspondence:**
Maarit H. Lahtinen
maarit.lahtinen@helsinki.fi

Specialty section:
This article was submitted to Green and Sustainable Chemistry, a section of the journal Frontiers in Chemistry

Received: *06 August 2019*
Accepted: *03 December 2019*
Published: *17 December 2019*

Citation:
Lahtinen MH, Valoppi F, Juntti V, Heikkinen S, Kilpeläinen PO, Maina NH and Mikkonen KS (2019) Lignin-Rich PHWE Hemicellulose Extracts Responsible for Extended Emulsion Stabilization. Front. Chem. 7:871. doi: 10.3389/fchem.2019.00871

INTRODUCTION

The sustainable use of natural resources requires the development of new functional materials from side streams of industrial processes. Woody material is renewable biomass, which contains unexploited components that can be used for valorized products. The main components of wood are cellulose (33–51%), lignin (21–32%), and hemicelluloses (23–31%), and it contains minor amounts of other compounds, such as extractives and minerals (Fengel and Wegener, 1983; Sjöström, 1993). The processes of pulp mills are optimized and efficient for the production of cellulosic fibers from wood, which are still needed for many traditional products, such as paper and board materials (van Heiningen, 2006). New technologies are also under development for cellulosic fibers, for example as textile fibers, as reinforcing structures in composite materials, and in the form of nanocellulose (Faruk et al., 2012; Kim et al., 2015; Sixta et al., 2015). However, there is also a general need and will to produce valorized products and processes for the currently underutilized parts of wood as well as other sources of biomass, namely, hemicelluloses and lignin (Faruk et al., 2012; Sainio et al., 2013).

Hemicelluloses can be extracted from biomass prior to other processing steps by using pressurized hot water (Kilpeläinen et al., 2014). During pressurized hot water extraction (PHWE), hemicelluloses and sulfur-free lignin are released from woody material at temperatures of 160–170°C. Hemicelluloses and lignin are partially separated, and extracts enriched with hemicelluloses can be further purified from lignin using other methods, such as ultrafiltration or precipitation with ethanol, if necessary (Bhattarai et al., 2019). We have recently developed a method of using differing centrifugal forces to separate hemicellulose- and lignin-rich fractions of PHWE extracts (Valoppi et al., 2019a).

The chemical structure of wood components reflects their material properties. The role of hemicelluloses is to provide flexibility to the cell wall. In contrast to cellulose, hemicelluloses and lignin are heterogeneous materials with a complex chemical structure, which is further dependent on the type of wood (Sjöström, 1993). Thus, the main hemicelluloses in softwoods and hardwoods are glucomannans and glucuronoxylans, respectively, although softwoods also contain minor amounts of glucuronoxylans and hardwoods have some glucomannans (Sjöström, 1993).

In spruce, the main hemicelluloses are galactoglucomannans (GGM) (Lundqvist et al., 2002; Hannuksela and Hervé du Penhoat, 2004; Xu et al., 2007). The backbone of GGM consists of (1 → 4)-linked β-D-mannopyranosyl (Man*p*) units and (1 → 4)-linked β-D-glucopyranosyl (Glc*p*), and some α-galactopyranosyl (Gal*p*) units are (1 → 6)-linked to the backbone as single-unit side groups. The proportions of the carbohydrates in GGM are 4:1:0.5 for Man*p*:Glc*p*:Gal*p* (Willför et al., 2003). In birch, the main hemicelluloses are 4-O-methylglucuronoxylans (GX) (Teleman et al., 2002). The backbone of GX consists of (1 → 4)-linked β-D-xylopyranosyl (Xyl*p*) units, to which α-4-O-methylglucuronic (MeGlcA) substituents are (1 → 2)-linked. The proportions are 0.5–1:10 for MeGlcA:Xyl*p* (Teleman et al., 2002). Both GGM and GX contain O-acetyl (OAc) groups at C-2 and/or C-3 positions of Man*p* and Xyl*p* units. The reported degrees of acetylation are about 15–20% for spruce GGM and 25% for birch GX (Lundqvist et al., 2002; Xu et al., 2007; Du et al., 2013).

Lignin is an aromatic polyphenol composed of phenylpropane units (Sjöström, 1993; Boerjan et al., 2003; Vanholme et al., 2010). The role of lignin in plants is to provide mechanical strength, enable efficient liquid transportation, and provide protection against microbial attack (Fengel and Wegener, 1983; Boudet, 2000). The building blocks of lignin are the monolignols *p*-coumaryl alcohol (minor component of wood plants), coniferyl alcohol (major component of softwoods), and sinapyl alcohol (major component of hardwoods). During lignin biosynthesis, the monolignols are oxidized to form phenoxy radicals, which leads to radical polymerization and the formation of different types of bonding patterns. The most frequent structure in lignin is the β-aryl ether type (β-O-4), which is prone to react with different chemicals, leading to degradation of lignin, for example in kraft pulping process (Sjöström, 1993). The other frequent linkage types include phenyl coumaran type (β-5) and resinol type (β-β).

Hemicelluloses and lignin are closely associated in the wood cell wall. In addition to non-covalent interactions, the presence of covalently bound lignin-carbohydrate complexes (LCCs) was suggested decades ago (Fengel and Wegener, 1983). However, even today, unequivocal proof of different types of LCCs is lacking, because these structures have low frequencies and because structural modifications may occur during their isolation for characterization (Giummarella et al., 2019). Recently, isolation and characterization of the α-ether type LCC was successfully performed (Nishimura et al., 2018) and was made possible by the development of a methodology for enriching LCCs and characterizing by nuclear magnetic resonance (NMR) spectroscopy. To date, the structure of phenolic residues and their associations with hemicelluloses in PHWE extracts are largely unknown.

Hemicellulose- and phenolic-rich PHWE extracts exhibit excellent emulsifying ability and physical emulsion stabilization capacity, which gives them great potential in both bulky and specialized industrial applications, such as food, paints, cosmetics, and pharmaceuticals (Mikkonen et al., 2016, 2019; Valoppi et al., 2019b). Furthermore, PHWE hemicelluloses containing phenolic co-components offer excellent oxidative stability in rapeseed oil-in-water emulsions (Lehtonen et al., 2016, 2018). For comparison, emulsions prepared from rapeseed oil, which has been purified from natural antioxidants of the oil, tocopherols, and stabilized with Tween 20 or gum Arabic, are oxidized in a few days (Heinonen et al., 1997; Lehtonen et al., 2016). The presence of tocopherols retards the oxidation, which is, however, modest compared to PHWE GGM, which improves the oxidative stability for several weeks in an accelerated storage test (Lehtonen et al., 2018). The strong, previously developed hypothesis was that phenolic residues associated with hemicelluloses would be responsible for improved physical and oxidative stability, but their exact chemical structure was still unclear (Lehtonen et al., 2018).

The aim of this study was to reveal the structure of phenolic residues responsible for the efficient emulsion stabilization capacity of PHWE spruce GGM and birch GX. In this study, aqueous GGM and GX were centrifuged in a parallel manner to separate hemicellulose-rich supernatants and lignin-rich pellets. For the first time, the fractions were characterized in detail using complementary chemical analyses to investigate the role of the lignin-rich fraction in the physical and oxidative stability of emulsions. Furthermore, characterization of both GGM and GX using various methods enabled a comparison of softwood and hardwood hemicelluloses and different analytical methods. The results explain the structural elements in hemicellulose-rich wood extracts that are responsible for their excellent performance in emulsions.

MATERIALS AND METHODS

Hemicelluloses

A pressurized hot water flow-through extraction (PHWE) system was used to obtain GGM-rich extract from spruce and GX-rich extract from birch (Kilpeläinen et al., 2014). Spruce sawdust (from Herralan Saha, Finland, 96.9 kg, 43.5 kg on dry basis) was extracted at 170°C for 60 min at a rate of 20 l min^{-1}, and 1,000 l of the extract was collected. Birch sawdust (from Haka-Wood, Finland, 103.7 kg, 54.2 kg on dry basis) was extracted at 170°C for 60 min at a rate of 20 l min^{-1}, and 700 l of the extract was collected. Both the spruce and birch extracts were ultrafiltrated to obtain concentrated extracts, as described previously (Bhattarai et al., 2019). The concentrated extracts were finally spray dried to powdered form using a Buchi Mini Spray Dryer B-290 (Buchi, Switzerland), which has the evaporation capacity of 1 l h^{-1} for water. The conditions for the spray drying used were as follows: inlet temperature 170°C, outlet temperature 65°C, and drying air flow rate 667 l h^{-1}. The moisture contents of the materials were 6.0% for GGM and 3.9% for GX after storage in the dark at room temperature.

Reagents

Rapeseed oil (Keiju, Bunge Finland Ltd, Raisio, Finland) was purchased in a local supermarket. Monosaccharides used for the analysis of carbohydrate content were L(+)-arabinose (Ara), D(+)-xylose (Xyl), D(+)-galactose (Gal), D(+)-glucose (Glc), D(+)-mannose (Man) from Merck (Darmstadt, Germany), L(+)rhamnose monohydrate (Rha) from Sigma (St. Louis, MO, USA), D(+)-sorbitol, D(+)-galacturonic acid monohydrate (GalA) from Fluka (St. Louis, MO, USA), and D(+)-glucuronic acid sodium salt monohydrate (GlcA) from Aldrich. The reagents used for silylation were bis(trimethylsilyl)trifluoroacetamide (BSTFA) from Merck (Darmstadt, Germany) and trimethylsilyl chloride (TMSCl) from Fluka (St. Louis, USA). Pullulan kit standards (Z-POS-pulkith) were used for size-exclusion chromatography (SEC; Postnova Analytics, Landsberg am Lech, Germany). Vanillin (Sigma-Aldrich) and syringaldehyde (Aldrich) were used for the quantification of phenols.

The solvents used for NMR analysis were D_2O and d_6-DMSO, which were purchased from Eurisotop (Saint-Aubin, France). All other solvents used were HPLC or LC-MS grade. Milli-RO water was used in centrifugal separation, and Milli-Q was used as a solvent in chemical analysis.

Centrifugation of Hemicelluloses

The 10% solutions of GGM and GX were dissolved in Milli-RO water and stirred for 2 h at room temperature (total amount 150 ml). The solutions were then centrifuged at 18,677 g at room temperature for 20 min. The supernatants (GGM-pur and GX-pur) and pellets (GGM-phe and GX-phe) were collected and freeze-dried separately. The recovered yields were 91.0% for GGM-pur, 4.6% for GGM-phe, 86.6% for GX-pur, and 5.8% for GX-phe (based on dry material).

Purification of Rapeseed Oil

Rapeseed oil (Keiju, Bunge Finland Ltd, Raisio, Finland) was purchased from a supermarket and stripped of tocopherols using a previously described method (Lampi et al., 1999). The composition has been determined in earlier publications (for example Lehtonen et al., 2016, 2018).

Preparation of Emulsions

The amount of oil and emulsifier, and the applied buffer and pH used, were based on optimizations performed in previous studies (Mikkonen et al., 2016). Emulsions containing hemicelluloses (1 w-%), GGM or GX, or their supernatants, GGM-pur and GX-pur, in 25 mM Na-citrate buffer, pH 4.5, and stripped rapeseed oil (5 w–%) were prepared by high-pressure homogenization using a previously described method with some modifications (Lehtonen et al., 2016). The total weight of each emulsion was 80 g. First, carbohydrate was dissolved in buffer by stirring overnight at room temperature. After the addition of oil, the coarse emulsion was prepared by stirring the resulting mixture with Ultra-Turrax (T25 basic, IKA, Staufen, Germany) at 22,000 rpm for 2 min. The mixture was further homogenized by passing it continuously through a high-pressure homogenizer for 32 s at a pressure of 800 bar (Microfluidizer 110Y, Microfluidics, Westwood, MA, USA). The homogenizer was configured with 75 µm Y-type F20Y and 200 µm Z-type H30Z chambers in series.

Accelerated Storage Test

For the accelerated storage test, emulsions were stored in glass bottles (100 ml) at 40°C in the dark for 3 months. For all the determinations, emulsions were gently mixed by turning their containers upside down 10 times before sampling. The properties of emulsions were monitored on the day of preparation, after 1 and 2 weeks of preparation, and after that approximately every 2 weeks. The properties, which were monitored during the storage test, were droplet-size distribution and peroxide value. At the end of the storage period, optical microscopy was used to visualize the morphology of emulsions (AxioScope A1, Carl Zeiss Inc., 203 Oberkochen, Germany). For microscopic imaging, the 100x objective was used, with a Zeiss Phase Contrast condenser with a Ph3 port.

Droplet-Size Distribution

The droplet-size distribution was determined by static light scattering technique using a Mastersizer Hydro 3000 (Malvern Instruments Ltd, Worcestershire, UK). The refractive indexes used were 1.33 for water and 1.47 for rapeseed oil (Rumble, 2018–2019). The emulsions were added directly into the dispersion accessory, which allowed dilution to avoid multiple scattering effects. The rotor speed during measurement was 2,400 rpm. Each sample was measured three times.

Determination of Peroxide Value

Peroxide values (PVs), as an indicator of primary oxidation of emulsions, were determined by a previously reported method, in which lipids are first released and extracted and then analyzed using the ferric thiocyanate method (Lehtonen et al., 2011, 2016). Analytical samples of extracted lipids were prepared in duplicate, and from both samples of extracted lipids, two samples were withdrawn for the determination of PVs. Thus, the results were calculated as averages and standard deviations of four measured values.

Quantitative Analysis of Carbohydrates

The carbohydrate content of GGM and GX and of their centrifuged fractions, GGM-pur, GGM-phe, GX-pur, and GX-phe, were analyzed by GC using the acid methanolysis and silylation method described previously (Sundberg et al., 1996). The instrumental details of the analysis were described previously as well (Chong et al., 2013). External calibration of five levels of concentration was used to calculate the amount of each monosaccharide in the samples. Methyl glucuronic acid (MeGlcA) was quantified based on the two major signals and the D-glucuronic acid standard (Chong et al., 2013). All samples were analyzed in triplicate ($n = 3$).

Structural Characterization of Starting Materials GGM and GX (Non-acetylated) and Phenolic Samples GGM-Phe and GX-Phe (Acetylated) by 2D HSQC and HSQC-TOCSY NMR, and Evaluation of Diffusion Constants by 2D DOSY NMR (Acetylated or Partially Acetylated Samples)

For structural characterization of the starting hemicelluloses, GGM and GX, and the fractions enriched with phenolic compounds, GGM-phe and GX-phe, 2D Heteronuclear Single Quantum Coherence (HSQC) spectra, 2D Heteronuclear Single Quantum Coherence—Total Correlation SpectroscopY (HSQC-TOCSY) spectra and 2D Diffusion Ordered SpectroscopY (DOSY) data were acquired using a Varian Unity Inova 500-MHz spectrometer equipped with a 5-mm pulsed-field-gradient triple resonance probehead (^{1}H, ^{13}C, ^{15}N) capable of delivering z-gradient amplitudes up to 20 G/cm. The pulse sequences used in this study were readily available in Varian VNMR 6.1C spectrometer operating software.

All samples were analyzed in DMSO-d$_6$ at 27°C. Of the starting hemicelluloses, GGM and GX, 30 mg was first dispersed in D_2O (0.7 ml), freeze-dried, and finally dissolved in DMSO-d$_6$ (0.7 ml). Of the phenolic fractions, GGM-phe and GX-phe, 40 mg was acetylated in pyridine/acetic anhydride (1:1), and the remaining reagents/solvents were removed by evaporating the mixture with ethanol twice, with toluene four times, and finally with chloroform under reduced pressure twice. The acetylated sample was then dissolved in DMSO-d$_6$ (0.7 ml) and analyzed.

All HSQC spectra were recorded with a standard, phase-sensitive, gradient-selected HSQC sequence using echo-antiecho acquisition mode in the indirectly detected dimension. The hard, rectangular 90° pulse widths were 6.7 and 11.5 μs for ^{1}H and ^{13}C, respectively. The spectral width was 5,573 Hz for ^{1}H (carrier at 5.47 ppm) and 25,133 Hz for ^{13}C (carrier at 90.01 ppm). The relaxation delay was 1 s, and the acquisition time was 0.128 s. Experiments were acquired using 64 steady-state scans, 64 transients, and a data matrix size of 713 (^{1}H, complex points) $\times$ 200 (^{13}C, complex points). The data matrices were apodized by a Gaussian function (gf = 0.032) in ^{1}H-dimension and a Gaussian function (gf = 0.004) in ^{13}C-dimension and zero-filled up to 1,024 (^{1}H, complex points) x 1,024 (^{13}C, complex points) prior to Fourier transformation.

For HSQC-TOCSY, a standard phase-sensitive, gradient-selected (echo-antiecho) pulse sequence was applied. The hard, rectangular 90° pulse widths were 6.7 and 11.5 μs for ^{1}H and ^{13}C, respectively. The spectral width was 5,573 Hz for ^{1}H (carrier at 5.47 ppm) and 25,133 Hz for ^{13}C (carrier at 90.01 ppm). Relaxation delay was 1 s and acquisition time was 0.184 s. The TOCSY mixing was performed using the windowed MLEV-17 spin-lock scheme (Griesinger et al., 1988) to suppress possible ROESY correlations. TOCSY mixing was applied for 100 ms at an RF power of 7.9 kHz. Experiments were acquired using 64 steady-state scans, 64 transients, and a data matrix size of 1,024 (^{1}H, complex points) $\times$ 200 (^{13}C, complex points). The data matrices were apodized by a Gaussian function (gf = 0.037) in ^{1}H-dimension and a Gaussian function (gf = 0.003) in ^{13}C-dimension and zero-filled up to 1,024 (^{1}H, complex points) $\times$ 1024 (^{13}C, complex points) prior to Fourier transformation.

2D DOSY spectra were measured using Bipolar Pulse Pair Stimulated Echo sequence with convection compensation (BPPSTE-cc) (Wu et al., 1995; Jerschow and Müller, 1997). The spectral width of 8,000 Hz in ^{1}H-dimension was covered by the acquired 8,002 complex points, resulting in 1-s acquisition time. The relaxation delay was 1 s. In order to map diffusion coefficients (D_c), 20 spectra were acquired with increasing amplitudes of rectangular diffusion gradient pulses (from 0.5 to 20 G/cm). The diffusion gradient pulse duration was 2 ms, and the diffusion delay was 600 ms. The eddy-current recovery delay was 150 μs. A total of four steady-state scans and 32 transients were used to collect all 20 of these spectra. The free induction decays (FIDs) were apodized using an exponential weighting function (10-Hz line broadening) and zero-filled up to 8,192 complex points before the Fourier transform. The 2D DOSY plots were calculated using the dosy macro (a monoexponential fit on the peak tops) incorporated into VNMR 6.1C software. The final size of the diffusion dimension in 2D DOSY was 256 data points. The diffusion coefficients of the macromolecule and the residual DMSO signal were estimated from each DOSY spectrum (see **Figures S2A–D**); the horizontal line shows the estimated values for D_c(GGM), D_c(GGM-phe), D_c(GX), and D_c(GX-phe). Moreover, the D_c(DMSO) value for each sample is shown. In order to compensate the effects of possible sample viscosity differences in the diffusion coefficient results, the estimated diffusion coefficients of the macromolecules were corrected using the measured diffusion coefficient values for residual DMSO signal of the solvent (Kavakka et al., 2009). In the correction procedure, the D_c(DMSO) value in the GGM sample was selected as the reference [D_c(DMSO$_{ref}$)], and the DOSY results for each sample were multiplied by D_c(DMSO$_{ref}$)/D_c(DMSO); that is, after the correction, D_c(DMSO) was the same for all four 2D DOSY spectra.

Analysis of Molar Masses

Molar masses of GGM, GX, and their centrifuged fractions were analyzed by SEC (GPCmax, Viscotek Corp., Houston, TX, USA). The instrumental details were described in a previous study (Pitkänen et al., 2011). The samples were dissolved in 0.01 M LiBr in DMSO overnight to a concentration of 10 mg ml^{-1} and filtered through a 0.45 µm syringe filter (GHP Acrodisc 13 mm, Pall Corp., Ann Arbor, MI, USA). The volume of the sample injected was 100 µl. DMSO, containing 0.01 M LiBr, was used as the eluent, with a flow rate of 0.8 ml min^{-1}. The molar mass of samples was estimated using pullulan standards for calibration (342, 1,320, 5,900, 11,800, and 22,800 Da). The elution data were processed using the OmniSEC 4.5 software (Viscotek Corp.).

Determination of Phenolic Content by Pyrolysis GC-MS

Pyrolysis of the starting hemicellulose samples GGM and GX and the centrifuged pellets GGM-phe and GX-phe was performed using a foil pulse-type Pyrola 2000 MultiMatic pyrolyzer (Pyrol AB, Lund, Sweden). The pyrolysis unit was connected to an Agilent GC model 7890B equipped with an HP5-MS column (25 m x 0.20 mm, film thickness 0.33 µm), coupled with an Agilent 5977B quadrupole-MSD with EI ionization (Agilent Technologies, Santa Clara, CA, USA). Approximately 100 µg of dry sample and a drop of acetone was applied to the Pt filament and pyrolyzed at 600°C for 2 s. Conditions for the GC analysis were as follows: gas flow (helium) 0.8 ml min^{-1}, injector temperature 300°C, split 1:20; the column oven temperature was 50°C for 1 min, then heated with a rate of 8°C min^{-1} to 320°C, which was maintained for 5 min; the transfer line temperature was 250°C.

Compounds were identified by comparing acquired spectra with spectra in the Laboratory of Wood and Paper Chemistry, Åbo Akademi, Finland (own database) and with Wiley 10th/NIST2012. The results were calculated as the relative abundance of each pyrolysis product (peak area-% of total peak area).

Quantitative Determination of Extractable Phenolic Residues by UHPLC-DAD-FLD and Identification by LC-MS

Phenolic residues of the pellets were extracted and quantified based on a previously described method, which was slightly modified (Lehtonen et al., 2016). For extraction, 10 mg of GGM-phe or GX-phe was dissolved in 80% ethanol (1 ml) and centrifuged three times. The supernatants were combined and evaporated under reduced pressure. The ethanol-soluble phenolic residues were then extracted with ethyl acetate (3 × 500 µl), after adjusting the pH by adding 400 µl of 6 M HCl, and finally the ethyl acetate was evaporated under nitrogen stream. The ethanol-soluble phenolics were analyzed after extraction (neutral) or after acid or base hydrolysis. The pellets containing remaining carbohydrates from GGM-phe were also hydrolyzed after extraction with acid or base, as described previously (Lehtonen et al., 2016). No pellet remained from GX-phe after extraction of phenol. All treatments were performed in triplicate ($n = 3$).

For the analysis, all samples were redissolved in 10% MeOH (1 ml), filtered through a 0.2-µm PTFE syringe filter (VWR International, Radnor, PA, USA), and separated with an ACQUITY UPLC system (Waters, Milford, MA, USA), as described previously (Kylli et al., 2011; Lehtonen et al., 2016). The injection volume for all samples was 10 µl. In addition, the sample containing the ethanol-soluble phenols hydrolyzed with base was diluted to 1/10 for quantification at the concentration levels explained below.

For the identification of the main phenolic compounds extracted, the same UPLC system equipped with a Waters Synapt G2-S*i* high definition mass spectrometer with a LockSpray Exact Mass Ionization Source was used. The LC-MS spectra were processed with MassLynx 4.1 software, which uses an *m/z* lockmass value of 556.2771 for leucine eukephalin (equal to *m/z* of $[M+H]^+ + e^-$). Based on identification with MS, the main phenolic compounds extracted were quantified using vanillin and syringaldehyde as the reference compounds, with three levels of concentration in the range of 10–45 ng/injection. LC-MS spectra are presented in the **Supplementary Material**. ESI-MS vanillin: *m/z* 153.0552 $[M + H]^+$ ($C_8H_9O_3 + e^-$ requires 153.0552), syringaldehyde *m/z* 183.0657 $[M + H]^+$ ($C_9H_{11}O_4 + e^-$ requires 183.0657).

RESULTS AND DISCUSSION

Fractionation of Hemicelluloses and Preparation of Emulsions

The starting hemicelluloses, spray-dried hot-water-extracted GGM and GX, were fractioned by centrifugation. As will be explained in the characterization of materials, supernatants consisted of hemicelluloses partially purified from phenolic compounds (GGM-pur and GX-pur fractions), and pellets contained mainly lignin and other phenolic residues (GGM-phe and GX-phe). This solvent-free fractionation method takes advantage on the low solubility of lignin in water, which enables partial separation of precipitated lignin and water-soluble hemicelluloses (Valoppi et al., 2019a). In a recently published study (Valoppi et al., 2019a), the effect of using different centrifugal treatments on the degree of purification and properties of GGM-rich PHWE extracts was evaluated in detail. In the present study, we used high centrifugal forces, optimized in the previous study (Valoppi et al., 2019a), on both GGM and GX to compare softwood and hardwood hemicelluloses for the first time by this fractionation method and to reveal the structure of phenolic residues coextracted with hemicelluloses.

Oil-in-water emulsions were then prepared from rapeseed oil stripped from tocopherols, using the starting hemicelluloses (GGM and GX) and the purified fractions (GGM-pur and GX-pur) as emulsifiers. The resulting emulsions were characterized to investigate the effect of removed phenolic residues on the physical and oxidative stability of emulsions. During the accelerated storage test of emulsions, the droplet-size distribution was measured periodically to monitor the physical stability, and the morphology was further confirmed by microscopy.

Physical Properties and Stability of Emulsions

The droplet-size-distribution curves of all emulsions are presented in **Figure 1**, and values from selected time points of measurements are presented in **Table 1** (All other values for droplet-size measurements are found in **Table S1**). Only the fresh emulsion stabilized with GGM-pur had unimodal droplet-size distribution, and the more bimodal distribution observed previously for GX emulsions (Mikkonen et al., 2016) was most evident for fresh emulsion stabilized with GX-pur. The surface average droplet size D[3,2] for all fresh emulsions was in the range of 120–150 nm, which is similar to the previous result for PHWE GGM (Lehtonen et al., 2018). However, the D[3,2] value of GGM-pur and GX-pur (120 nm) emulsions was smaller than that of emulsions with the starting GGM and GX (140–150 nm). The more pronounced bimodal droplet-size distribution of GX-pur compared to GX emulsion also increased the volume average droplet size D[4,3], which is affected more by the larger droplets compared to D[3,2]. During the storage test, the droplet size increased for all samples, and the change was more apparent for the emulsions stabilized with the purified hemicelluloses GGM-pur and GX-pur. This was most clearly observed in the D90 values, which take into account 90% of the oil droplets, which are equal or smaller than D90. In conclusion, it seems that the fraction that was removed from both of the purified hemicelluloses GGM-pur and GX-pur by centrifugation was responsible for a slightly larger droplet size of fresh emulsions, but on the other hand, it enhanced the long-term physical stability of emulsions, in agreement with previously published results for GGM (Valoppi et al., 2019a).

The microscopic images obtained at the end of the 3-month storage period (**Figure 2**) confirm the results from the droplet-size-distribution measurements. The average droplet size D[3,2] for GGM and GGM-pur was still fairly low, 210–220 nm, at the

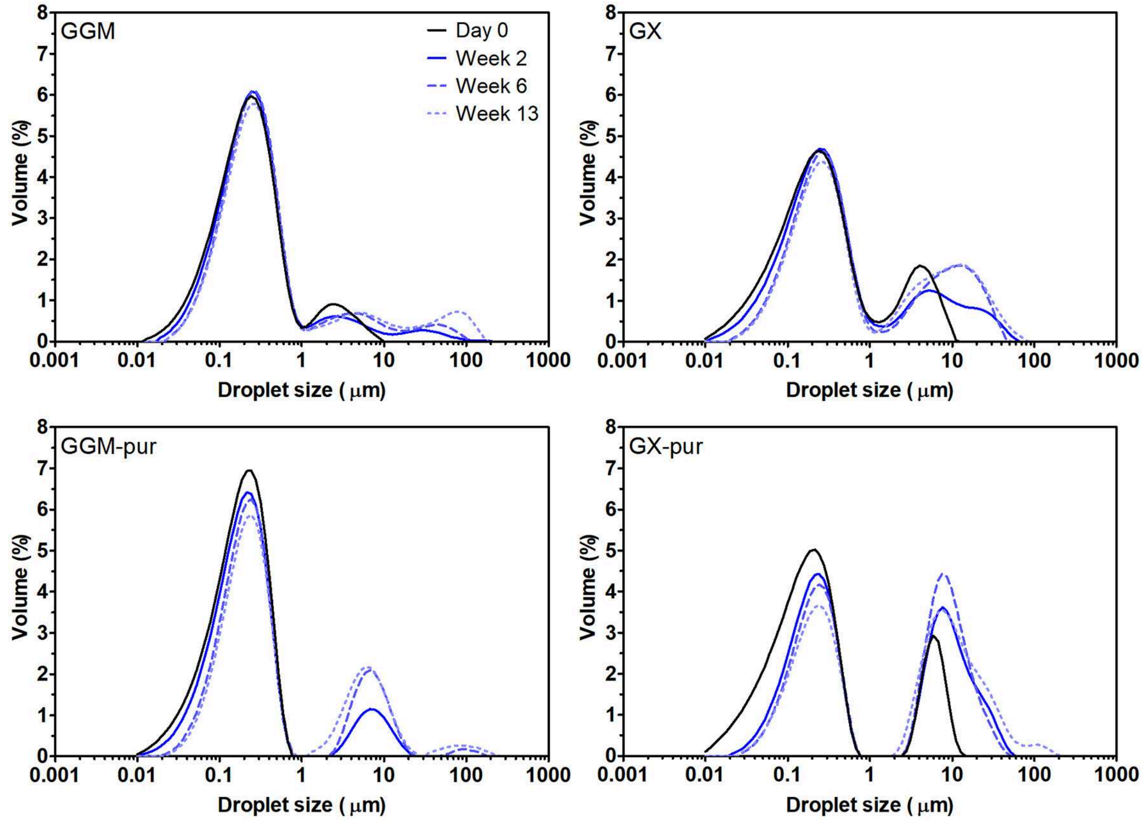

FIGURE 1 | Droplet-size distribution of emulsions using the starting hemicelluloses, GGM and GX, and purified fractions, GGM-pur and GX-pur, as the emulsifiers. The physical stability of emulsions was observed during the storage test at 40°C by measuring droplet-size distribution periodically. The values for selected measurements are presented in **Table 1**.

TABLE 1 | Average droplet-size values for fresh o/w emulsions.

Emulsifier	Storage time	D[3,2] (μm)	D[4,3] (μm)	D10 (μm)	D50 (μm)	D90 (μm)
GGM	Fresh	0.152	0.552	0.070	0.237	1.050
	2 weeks	0.176	1.970	0.081	0.255	1.820
	3 months	0.212	6.950	0.095	0.294	11.50
GGM-pur	Fresh	0.117	0.215	0.056	0.187	0.415
	2 weeks	0.144	1.130	0.068	0.214	4.180
	3 months	0.226	4.870	0.100	0.295	8.850
GX	Fresh	0.137	1.070	0.057	0.259	4.020
	2 weeks	0.171	3.100	0.073	0.301	9.440
	3 months	0.260	5.350	0.104	0.413	17.90
GX-pur	Fresh	0.116	1.400	0.048	0.205	6.160
	2 weeks	0.263	5.670	0.103	0.402	16.80
	3 months	0.343	9.580	0.122	3.940	24.60

The D[3,2] and D[4,3] are the surface and volume weighted mean diameters. The D10, D50, and D90 values mean, respectively, that 10, 50, and 90% of droplets are smaller compared to that value.

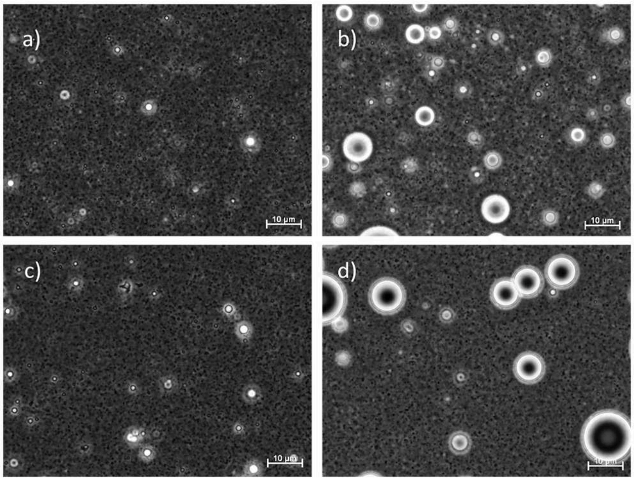

FIGURE 2 | Light microscope images of emulsions at the end of the 3-month storage period. The emulsifiers are in **(a)** starting GGM, **(b)** starting GX, **(c)** GGM-pur, and **(d)** GX-pur. The length of the scale bar is 10 μm in all images.

end of the storage period, and these droplets were hardly visible by optical microscopy with the magnification used. In the image of GGM-pur in **Figure 2c**, there are possibly a couple of larger droplets compared to the image of GGM in **Figure 2a**. In the case of GX and GX-pur (**Figures 2b,d**), the difference in the number and size of larger droplets was more evident and clearly reflects the droplet-size-distribution data.

Oxidative Stability of Emulsions

In order to observe the oxidative stability of emulsions, their peroxide values were measured periodically during the accelerated storage test. The oxidative stability of emulsions stabilized with GX was then investigated for the first time.

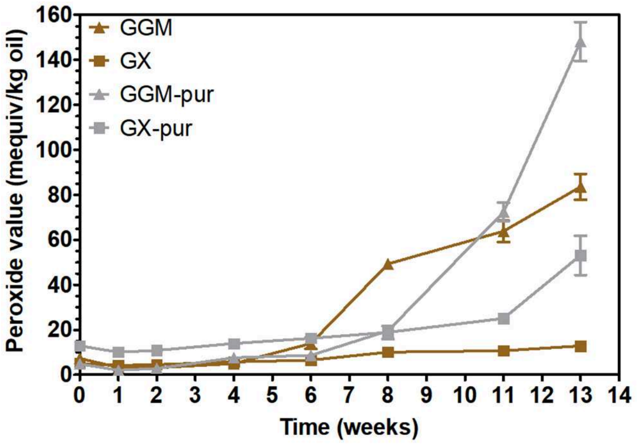

FIGURE 3 | Peroxide values for rapeseed oil in emulsions using starting GGM and GX and using purified GGM-pur and GX-pur as the emulsifiers.

Peroxide values indicate the formation of hydroperoxides, the initial oxidation products of rapeseed oil (Lehtonen et al., 2011, 2016). The results clearly show (**Figure 3**) that the phenolic fraction removed from the starting hemicelluloses GGM and GX was responsible for inhibiting lipid oxidation in emulsions.

The peroxide values for all emulsions were practically unchanged during the first 6 weeks of storage, which is compatible with the previously published results for concentrated PHWE GGM (Lehtonen et al., 2018). The peroxide values of all emulsions started to increase after 6 weeks, but the extent of oxidation was different at the end of the storage period. The starting hemicellulose GX was the most stabilizing of all the emulsifiers tested, because the increase of peroxide values during the 3-month storage period was fairly modest compared to other emulsifiers, although the stabilization of 6 weeks for GGM is also a notable result.

Carbohydrate Composition of Starting Hemicelluloses and Fractionated Materials From Centrifugation

The carbohydrate composition of the starting hemicelluloses, GGM and GX, and their purified (pur) and phenolic (phe) fractions (**Table 2**) was analyzed in order to evaluate both the total amount of carbohydrates in each fraction and possible differences in carbohydrate composition. The total amount of carbohydrates was around 735 mg g^{-1} for GGM and 615 mg g^{-1} for GX, which is in agreement with results previously obtained for spray-dried PHWE GGM and GX (Mikkonen et al., 2019). The total carbohydrate contents for the purified fractions were 845 and 621 mg g^{-1}, implying that the fractionation method increased the ratio of carbohydrates for GGM-pur but was very similar when starting GX and GX-pur were compared. For the fractions GGM-phe and GX-phe, the amount of carbohydrates was clearly lower: 251 and 181 mg g^{-1}. This result indicates that 75–82% of these fractions are of an origin other than

TABLE 2 | Carbohydrate composition of starting GGM and GX, and the centrifugated fractions GGM-phe and GX-phe obtained from quantitative GC analysis of acid methanolyzed and silylated samples.

Sample	Ara	Xyl	Rha	Gal	Glc	Man	GalA	MGA	Total
GGM	9.4 ± 0.2	74.5 ± 2.2	7.1 ± 0.1	54.0 ± 1.2	102.9 ± 2.4	441.2 ± 10.3	20.4 ± 0.8	25.2 ± 2.1	734.7 ± 17.7
	2.1	***16.9***	***1.6***	***12.2***	***23.3***	***100.0***	***4.6***	***5.7***	***166.5***
GGM-pur	9.9 ± 0.1	84.7 ± 1.5	7.3 ± 0.1	64.2 ± 2.9	117.7 ± 3.9	509.6 ± 4.3	23.6 ± 0.5	27.5 ± 1.3	844.6 ± 21.27
	1.9	***16.6***	***1.4***	***12.6***	***23.1***	***100.0***	***4.6***	***5.4***	***165.7***
GGM-phe	6.1 ± 0.4	22.1 ± 7.8	5.2 ± 0.4	17.8 ± 6.3	46.1 ± 9.2	137.6 ± 45.0	5.7 ± 3.7	10.7 ± 4.3	251.3 ± 75.8
	4.4	***16.1***	***3.8***	***13.0***	***33.5***	***100.0***	***4.1***	***7.8***	***182.7***
GX	2.2 ± 0.1	495.9 ± 3.2	7.7 ± 0.1	13.5 ± 0.3	13.3 ± 0.2	18.1 ± 0.1	11.2 ± 0.1	52.8 ± 0.4	614.8 ± 3.5
	0.5	***100.0***	***1.6***	***2.7***	***2.7***	***3.7***	***2.3***	***10.7***	***124.0***
GX-pur	2.4 ± 0.1	499.7 ± 14.4	7.7 ± 0.2	13.7 ± 0.6	13.0 ± 0.6	18.5 ± 0.4	11.8 ± 0.2	54.5 ± 1.2	621.4 ± 15.4
	0.5	***100.0***	***1.6***	***2.8***	***2.6***	***3.7***	***2.4***	***10.9***	***124.4***
GX-phe	1.6 ± 0.4	132.3 ± 11	5.0 ± 0.1	5.1 ± 0.0	6.0 ± 0.3	6.4 ± 0.3	4.5 ± 0.5	20.5 ± 2.4	181.3 ± 13.7
	1.2	***100.0***	***3.8***	***3.9***	***4.5***	***4.9***	***3.4***	***15.5***	***137.1***

The results presented in normal font are expressed as mg/g of dry sample. For results presented in bold and italic font, the results have been normalized by setting a value of 100 for the main carbohydrate in the sample (i.e., for GGM, Man = 100, and for GX, Xyl = 100). Glucuronic acid (GlcA) was not detected.

carbohydrates, which in the case of wood-based hot-water-extracted material is most likely composed of lignin or other phenolic residues.

The carbohydrate composition of the starting materials and purified fractions was more similar to that of the phenolic-rich fractions. Furthermore, certain carbohydrates seemed to be associated more closely with the phenolic fractions. In both GGM-phe and GX-phe, the presence of Ara*f*, Rha*p*, Glc*p*, and MeGlcA was pronounced, even taking into account the high standard errors in the results. Different types of lignins are known to be associated with certain carbohydrates: glucomannan-lignin complexes have been isolated mainly from softwoods, whereas glucan-lignins have been found in hardwoods and xylan-lignins in both softwoods and hardwoods (Lawoko et al., 2005; Li et al., 2011; Du et al., 2013; del Río et al., 2016). Further separation and characterization of the different types of carbohydrate-lignins were beyond the scope of this work, and thus any clear conclusions about the identity of potentially different polysaccharides associated with lignin cannot be made at this point.

Structural Characterization of Starting Hemicelluloses GGM and GX and Precipitated Fractions GGM-Phe and GX-Phe by 2D HSQC NMR Spectroscopy

For more detailed chemical characterization, the non-acetylated starting hemicelluloses were analyzed by 2D HSQC NMR spectroscopy. The HSQC spectra for GGM and GX are presented in **Figures 4**, **5**, respectively. The spectra of samples dissolved in d_6-DMSO were tentatively identified based on existing data for GGM (Hannuksela and Hervé du Penhoat, 2004; Kim and Ralph, 2014; Berglund et al., 2019), for GX (Teleman et al., 2000, 2002; Rencoret et al., 2012; Kim and Ralph, 2014), for lignin (Liitiä et al., 2003), and for LCC γ-ester (Giummarella et al., 2019), combined with the HSQC-TOCSY NMR spectra (presented in **Figures S1A,B**). Furthermore, the centrifuged fractions GGM-phe and GX-phe were acetylated prior to analysis to improve solubility in d_6-DMSO. The HSQC spectra of acetylated GGM-phe and GX-phe side-chain area are presented in **Figure 6**, for which the signals were identified according to previously published data (Ämmälahti et al., 1998; Qu et al., 2011; Wen et al., 2012; Du et al., 2013). The color codes and symbols used for the chemical structures identified are presented in **Figure 7**, and the list of peaks is presented in **Table S2**.

The NMR results support the analysis of carbohydrate composition, and the main carbohydrates shown in **Table 2** were also present in the NMR spectra of the starting materials GGM and GX (**Figures 4**, **5**). Thus, the most intensive signals in the spectra of GGM and GX were assigned to Man*p* and Xyl*p*, respectively. Glc*p* could be assigned for both samples, whereas MeGlcA was found only in the spectrum of GX and Gal*p* only in the spectrum of GGM. Interestingly, considering the signal of MeGlcA, for which the MGA4 (see the **Figure 7** text for abbreviations used in NMR spectra) does not overlap with other signals, it seems that the threshold limit of this 2D NMR technique prevents the observation of MeGlcA in GGM, in which the relative amount of MeGlcA was lower compared to GX. Both starting hemicelluloses also contained acetates, which are naturally present in wood hemicelluloses, GGM and GX (Sjöström, 1993). The $XG1_{3OAc}$ was identified based on a previous structural characterization of GX of birch, beech, and aspen, because the position of the cross-signal between $X1_{2,3OAc}$ and $X1_{2OAc}$ fits very well with the published data (Teleman et al., 2000, 2002). The abbreviation $XG1_{3OAc}$ refers to the structural element (→ 4)[4O-Me-α-D-Glc*p*A-(1 → 2)][O-Ac-(1 → 3)]-β-D-Xyl*p*-(1 →). Because the previously published NMR data were obtained in a different solvent (D_2O), and because there were now more overlapping signals, assignment of the other signals belonging to this xylopyranosyl ring was not possible.

The NMR spectra show also that both starting hemicelluloses contained lignin, for which the signals of β-aryl ether type

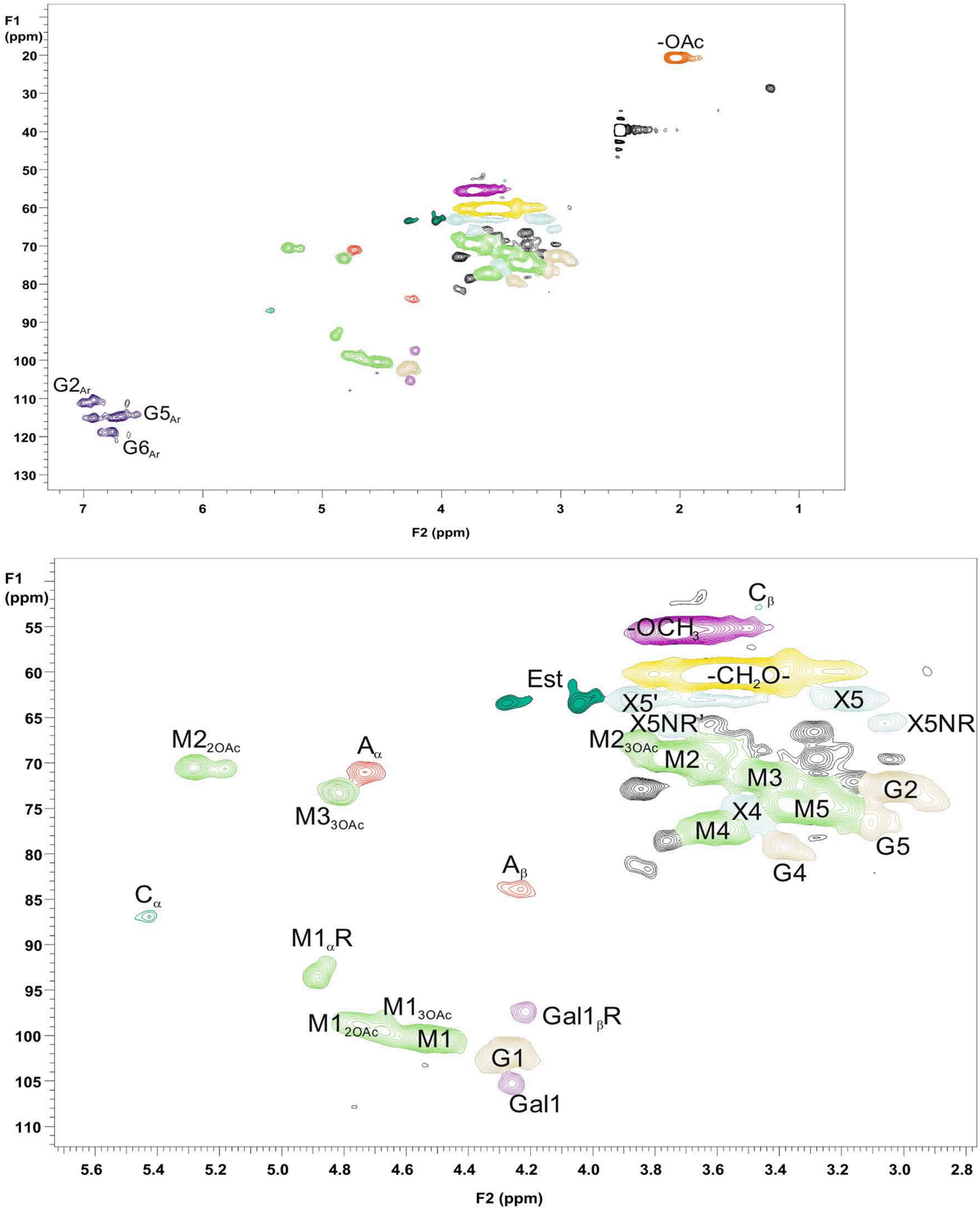

FIGURE 4 | 2D HSQC NMR spectrum of PHWE GGM starting material. Upper figure is the entire NMR spectrum, and lower figure is a magnification of the side-chain area. The nonacetylated sample was characterized dissolved in d_6-DMSO. The symbols and chemical structures are presented and explained in **Figure 7**.

were the most intensive (**Figures 4**, **5**). Further, the results provide further evidence of the fact that lignin is the phenolic material improving emulsifying/functional properties of PHWE extracts. Because β-O-4 linkage is the most abundant type in native lignin (Sjöström, 1993), the intensity of the signals indicated that the structure of lignin was not extensively degraded but instead preserved during the PHWE process. The other lignin bonding types found in the spectra of the starting hemicelluloses were phenyl coumaran type (β-5), found for both hemicelluloses, and resinol type (β-β), found only

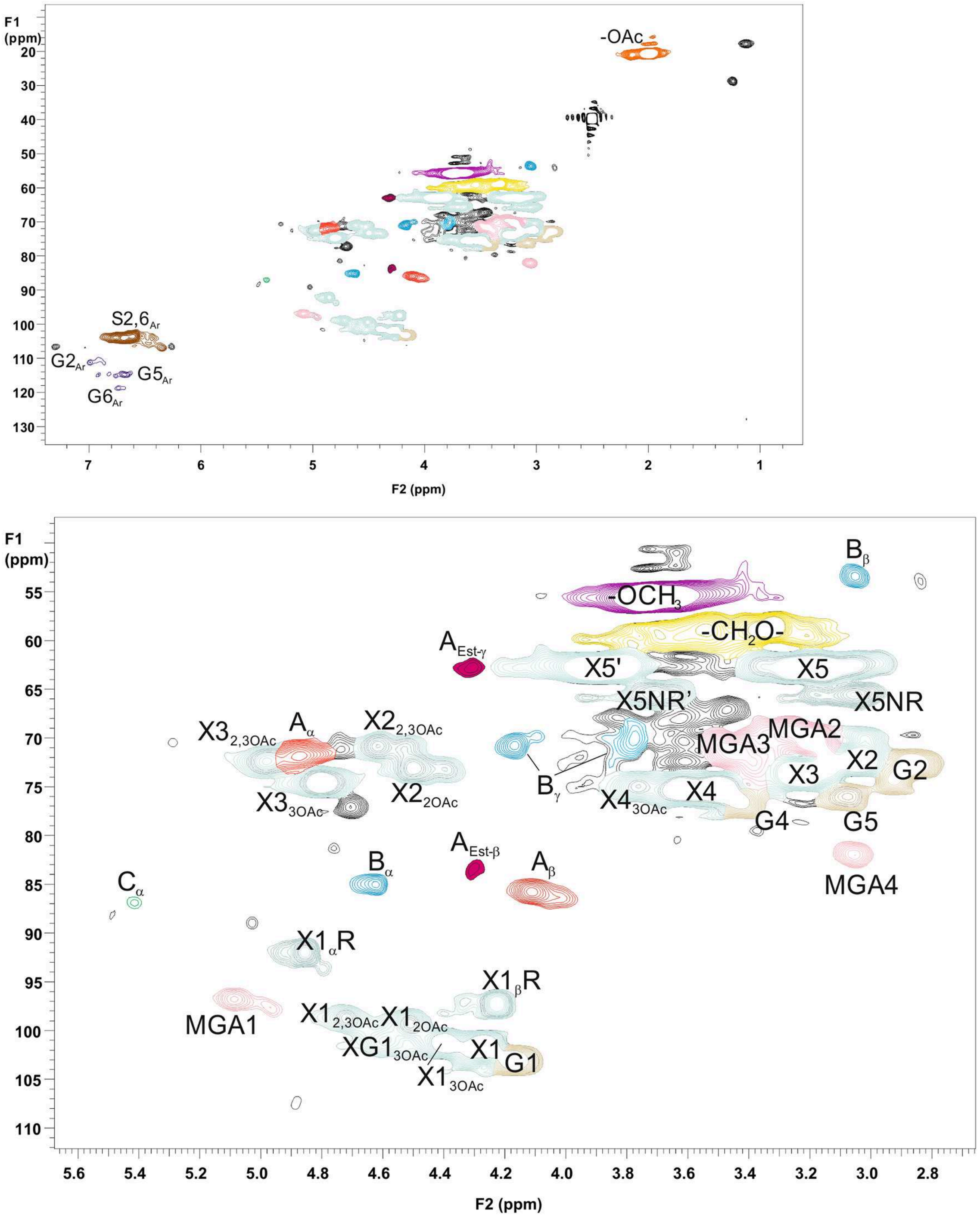

FIGURE 5 | 2D HSQC NMR spectrum of PHWE GX starting material. Upper figure is the entire NMR spectrum, and lower figure is a magnification of the side-chain area. The nonacetylated sample was dissolved in d_6-DMSO for analysis. The symbols and chemical structures are presented and explained in **Figure 7**.

for GX. According to the signals in the aromatic region at around 7 ppm, GGM contained only aromatic protons of the guaiacyl type, and GX contained mainly aromatic protons of the syringyl type and a small amount of guaiacyl type protons.

The starting hemicelluloses also contained -CH_2- protons connected to ester functionality. For GX (**Figure 5**), the signal at 4.30/62.92 ppm was assigned to the γ-proton of the β-O-4-structure linked to MeGlcA through an ester bond, which is also known as the γ-ester type LCC bond (Li and Helm,

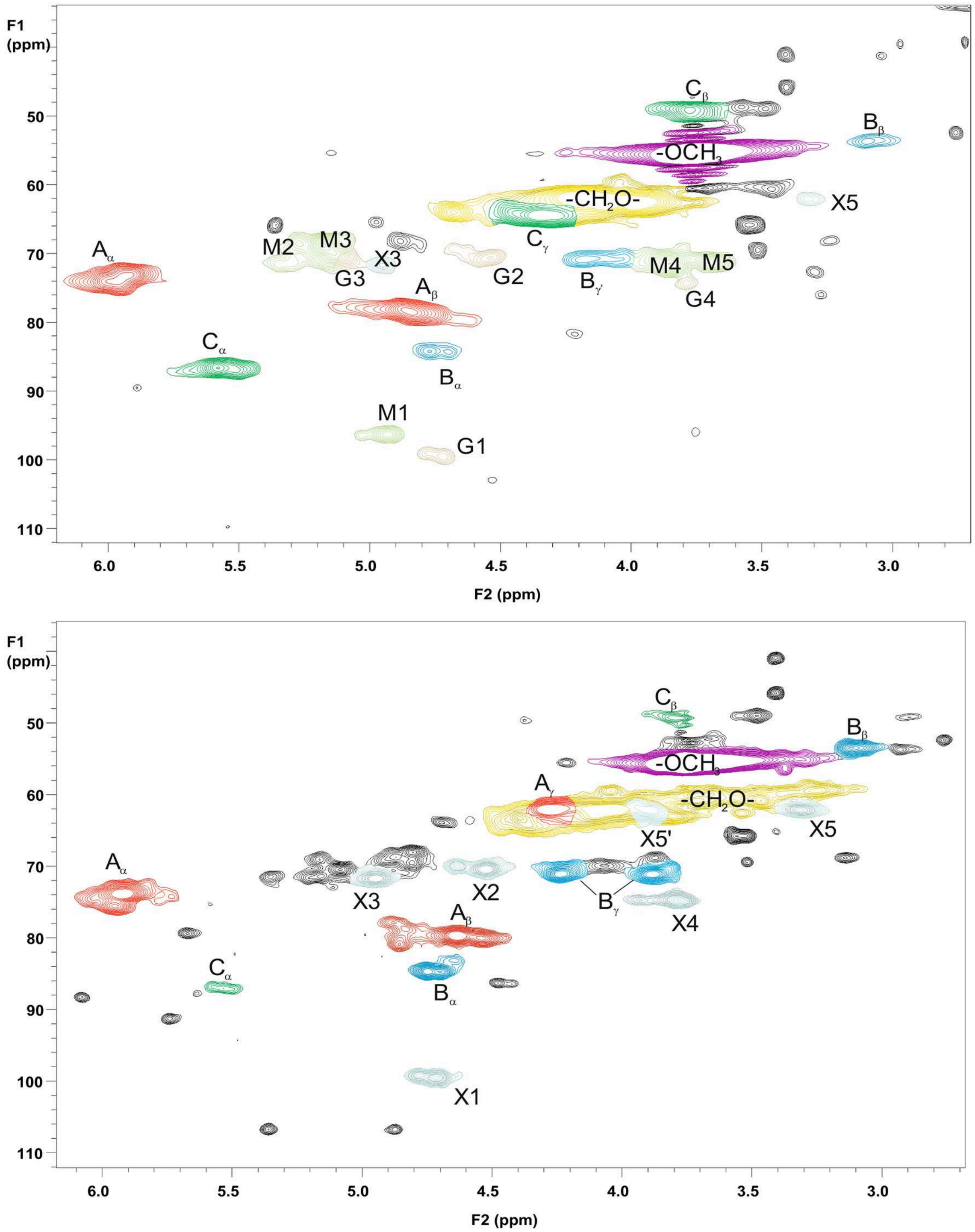

FIGURE 6 | 2D HSQC NMR spectrum of the fractions GGM-phe (upper figure) and GX-phe (lower figure). Only magnification of the side-chain areas is shown. The acetylated samples were dissolved in d_6-DMSO for analysis. The symbols and chemical structures are presented and explained in **Figure 7**.

1995; Giummarella et al., 2019). In addition, the signal at 4.30/83.46 ppm was assigned to the β-proton belonging to the same LCC-bonding pattern type, confirming that γ-ester LCC bonds must be rather frequent in GX hemicelluloses produced by the PHWE process. According to model compound studies using smaller synthesized molecules, as well as to those using lignin dehydropolymer (DHP), urunosyl units can migrate to the γ-position (Li and Helm, 1995; Giummarella et al., 2019),

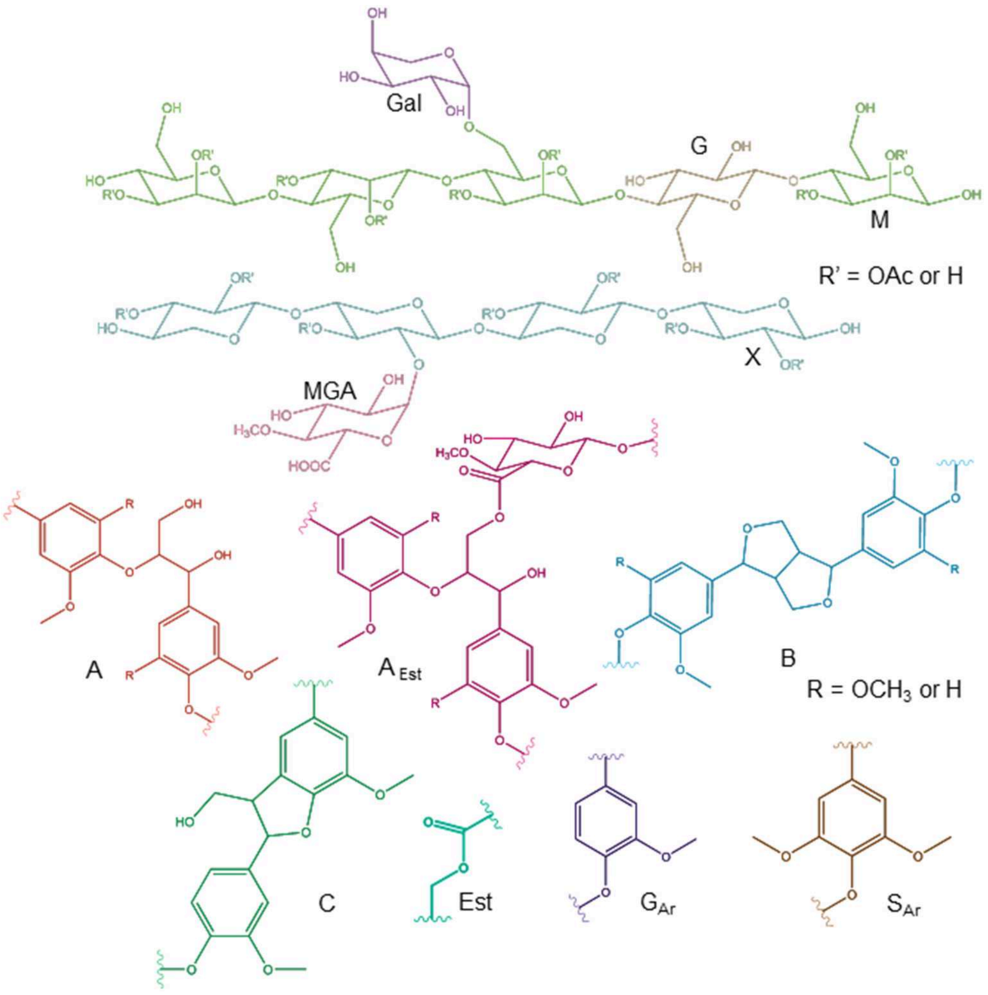

FIGURE 7 | Chemical structures identified by NMR. The symbols and abbreviations used in NMR spectra are G (Glc), M (Man), MGA (MeGlcA), X (Xyl), A (β-O-4/β-aryl ether), B (β-β/resinol), C (β-5/phenyl coumaran), A_{Est} (β-O-4 connected with MeGlcA by γ-ester bond), Est (acyl ester), G_{Ar} (guaiacyl), and S_{Ar} (syringyl). For acetylated carbohydrates, for example, the abbreviation $X1_{2OAc}$ refers to xylose C-1 containing acetyl group in the C-2 position.

and thus it is also possible that LCCs are formed during the PHWE process. Similarly for GGM (**Figure 4**), the signals at 4.04 and 4.27/63.25–63.4 ppm could be assigned to $-CH_2-$ protons connected to ester, but because no more of the signals present belonged to the β-O-4-type LCC-bonding pattern, these signals could not be unequivocally identified as originating from lignin. For example, the GGM of *Aloe barbadensis* contains acetyl groups at the C-6 position of Man*p*, which give signals at the same positions in the HSQC spectrum (Campestrini et al., 2013).

As already suggested by the small amount of carbohydrates, the centrifuged fractions GGM-phe and GX-phe (**Figure 6**) were composed mainly of lignin. The samples were also acetylated prior to analysis in order to improve their solubility in d_6-DMSO. The typical bonding patterns for lignin were found, and the signals for the β-O-4 bond type were clearly the most intense, similarly to the starting hemicelluloses. For both GGM-phe and GX-phe, the other lignin bonding patterns, the β-5 and β-β structures, were also more clearly identified compared to the NMR spectra of the starting hemicelluloses. The LCC structures could not be clearly identified from these acetylated phenolic fractions, because the signals of γ-esters would in this case overlap with all the acetylated γ-signals in lignin.

Molar Mass Analysis of Starting Hemicelluloses GGM and GX, Purified Fractions GGM-Pur and GX-Pur, and Precipitated Fractions GGM-Phe and GX-Phe

The results from molar mass analysis by SEC for the starting hemicelluloses GGM and GX and for the purified and phenolic fractions are presented in **Table 3**. The molar masses of starting GGM, M_w of around 7,300 Da, and starting GX, M_w of around 3,100 Da, were in a similar range, but slightly lower compared to the previously reported values (Mikkonen et al., 2019). However, the previously obtained results, 8,200 Da for GGM and 4,000 Da

TABLE 3 | Molar masses for starting hemicelluloses, GGM and GX, and the purified and phenolic fractions analyzed by size-exclusion chromatography (SEC) in DMSO.

	GGM	GGM-pur	GGM-phe	GX	GX-pur	GX-phe
M_n (Da)	917	949	363	632	710	326
M_w (Da)	7,312	7,155	2,769	3,064	3,355	2,472
M_z (Da)	20,371	18,276	25,362	6,571	8,243	8,041
M_w/M_n	7.97	7.53	7.63	4.85	4.73	7.58

TABLE 4 | Diffusion coefficients (D_c) obtained from DOSY NMR of acetylated (or partially acetylated) starting GGM and GX and phenolic fractions GGM-phe and GX-phe.

	D_c ($\times 10^{-10}$ m^2s^{-1})			
Sample	**D_c(MM)**	**D_c(DMSO)**	**Correction factor**	**D_c(MM_{Corr})**
GGM	0.17	1.30	1.00	0.17
GGM-phe	0.21	1.29	1.01	0.21
GX	0.21	1.39	0.94	0.22
GX-phe	0.22	1.35	0.96	0.21

D_c(MM) is the diffusion constant of macromolecule.

for GX, were analyzed in water solutions compared to the DMSO used in this study, which could have affected the results slightly. The molar masses of both purified fractions were similar to those of the starting materials, 7,200 Da for pur-GGM and 3,400 Da for pur-GX.

For phenolic fractions containing mainly lignin, the estimated molar masses were lower than those of the starting materials, for GGM-phe significantly lower 2,800 Da and for GX-phe 2,500 Da. Although present knowledge indicates that analysis by SEC gives underestimated molar masses for lignins (Zinovyev et al., 2018), the results show that GGM-phe and GX-phe have similar molar masses but that their molar masses are different from those of the starting hemicelluloses and fractions of purified hemicelluloses. Furthermore, the polydispersity, M_w/M_n, for all GGM samples was in the range of 7.5–8.0, although for GX samples the value was higher for GX-phe (7.6) and lower for starting GX (4.9) and GX-pur (4.7). In this respect, the variation of molar masses was similar within the phenolic fractions (GGM-phe and GX-phe) as well as for the GGM starting material and purified fraction GGM-pur, whereas dispersity was slightly lower for starting GX and GX-pur.

Evaluation of Diffusion Constants by DOSY NMR (Acetylated or Partially Acetylated Samples)

The 2D DOSY results are shown in **Table 4**. The viscosity corrected value D_c(GGM) (0.17×10^{-10} m^2s^{-1}) is clearly lower than D_c(GGM-phe) (0.21×10^{-10} m^2s^{-1}), D_c(GX) (0.22×10^{-10} m^2s^{-1}), and D_c(GX-phe) (0.21×10^{-10} m^2s^{-1}), the latter three being practically identical. This is in line with the SEC results (**Table 3**), indicating approximately 7 kDa for GGM-pur and 3 kDa for the others. However, it must be pointed out that the absolute differences in these diffusion coefficients are not large. Because there is a spread in the DOSY-correlations (i.e., all the peaks of the molecule do not appear with the same D_c value), it is difficult to pick a representative average value. There are various reasons for the spread, such as possible overlap with other residual entities, success of DOSY fitting, non-optimized diffusion time/diffusion gradient area (in order to achieve sufficient decay), noise, etc. This, combined with the aforementioned small absolute differences, makes these DOSY results indicative at best, but still usable for qualitative purposes. Improvement could be achieved by optimizing the diffusion delays and/or diffusion gradient areas, increasing the number of diffusion steps in DOSY measurement, and increasing number of transients.

Furthermore, the lignin signals, which do not overlap with other residues, the β-O-4 (1H 5.95 ppm) and ArH (1H 6.65 ppm for GX and 6.97 ppm for GGM), have similar diffusion coefficients compared to carbohydrate signals. This means that lignin has a very similar diffusion coefficient compared to hemicelluloses, which provides further support for covalent association of carbohydrates and lignin.

Analysis of Phenolic Contents of Starting Hemicelluloses and Phenolic Fractions GGM-Phe and GX-Phe Using Pyrolysis GC/MS

The pyrolysis GC/MS technique (py-GC/MS) was used to evaluate the usefulness of this method for fast characterization of the phenolic content of the starting hemicelluloses and phenolic fractions. Py-GC/MS correlates with the lignin and carbohydrate composition, especially for pulp samples, and can be used fairly reliably for the determination of the S/G ratio, which is the ratio of syringyl and guaiacyl types of units in lignin (del Rio et al., 2002; Ohra-aho et al., 2013, 2018). Thus, a rough estimation of the lignin and carbohydrate content of the starting hemicelluloses GGM and GX and for the lignin-rich residues GGM-phe and GX-phe was made by grouping all the peaks from py-GC/MS and calculating areas of all groups, as presented in **Table 5**.

The results were then compared to the acid methanolysis followed by GC analysis of total carbohydrates (in **Table 2**). Assuming that the starting hemicelluloses and phenolic fractions contained only hemicelluloses and lignin, the results of the methods should be compatible. However, the carbohydrate contents from determined py-GC/MS were much lower compared to the results obtained from acid methanolysis-GC method. On the other hand, the lignin content from py-GC/MS seemed fairly reasonable when compared to total carbohydrate content from acid methanolysis. When the total carbohydrate content from acid methanolysis and lignin content from py-GC/MS were summed, the total content (lignin + carbohydrates) was 94.34% for starting GGM, 100.01% for GGM-phe, 86.54% for starting GX, and 91.73% for GX-phe. According to previous results, the py-GC/MS-analysis of carbohydrate content is not necessarily reliable for comparing samples containing different carbohydrates (Ohra-aho et al., 2018), which probably affected

TABLE 5 | The products found in py-GC/MS of starting hemicelluloses GGM and GX and phenolic fractions GGM-phe and GX-phe.

Compound	**GGM**	**GGM-phe**	**GX**	**GX-phe**	**Origin**
Acetic acid			12.34	4.47	Carb
Methyl acetate	11.25				Carb
1-Hydroxypropan-2 one		0.58			Carb
2,3-Pentanedione			0.71		Carb
3-Hydroxypropanal	12.21	1.55	9.76	1.92	Carb
1,4-Butanedial	2.61				Carb
Methyl-2-oxopropanoate	4.79				Carb
3-Furfural			0.50		Carb
Furfural	3.12		6.68	0.43	Carb
2-Furanmethanol	2.73				Carb
2-Butanone			1.42		Carb
Cyclopent-2-ene-1,4-dione	0.44				Carb
2-Methyl-1-cyclopent-2-enone			0.72		Carb
2-(5H)-Furanone	1.60				Carb
2,5-Dihydropyran-6-one	0.82				Carb
2-Hydroxy-2-cyclopenten-1-one	0.88		0.71		Carb
3-Methyl-2-cyclopentenone			0.80		Carb
Phenol	0.83	0.34	0.67		Ar
4-Hydroxy-5,6-dihydro-(2H)-pyran-2-one	1.05		0.59	0.43	Carb
2-Hydroxy-3-methyl-2-cyclopenten-1-one	1.83		1.85		Carb
D-arabinal				0.09	Carb
2,3-Dimethyl-2-cyclopenten-1-one			0.34		Carb
o-Cresol	0.49	0.22	0.29	0.13	Ar
3,4-Dimethyl-2-hydroxy-2-cyclopentanone			0.34		Carb
p-Cresol	0.35	0.47	0.40	0.15	H
Guaiacol	3.32	6.98	1.28	1.50	G
2-Methylpyran-3,4-dione	0.36				Carb
3-Methylguaiacol		0.20	0.14	0.15	G
4-Methylguaiacol	1.34	5.50	0.51	0.69	G
Catechol	1.30				G
5-Hydroxymethylfurfural	0.88				Carb
Methylveratrol	0.14				Ar
3-Methylcatechol	0.57	0.14			Ar
Guaiacyl acetate			0.20		G
3-Methoxycatechol				0.80	Ar
4-Ethylguaiacol	0.79	1.09	0.22	0.24	G
4-Methylcatechol	0.57				Ar
5-Acetoxymethyl-2-furaldehyde	0.39				Carb
4-Vinylguaiacol	3.16	8.34	1.04	1.24	G
Syringol		0.24	6.64	7.37	S
Eugenol	0.67	2.27	0.37	0.41	G
4-Propylguaiacol	0.26	0.33			G
Vanillin	0.64	5.25		1.66	G
cis-Isoeugenol	0.32	1.57		0.25	G
4-Methylsyringol			1.23	2.09	S
trans-Isoeugenol	1.69	6.54	0.57	0.99	G
Homovanillin	0.52	4.25		0.68	G
Acetovanillone	0.59	3.26		0.90	G
4-Ethylsyringol			0.69	0.66	S
Guaiacylacetone	0.37	1.26		0.20	G
4-Vinylsyringol			4.07	5.31	S
Guaiacylvinylketone				0.53	G
Guaiacylpropenol	0.51	0.88			G
4-Prop-2-enyl syringol*			1.55	1.62	S
Dihydroconiferyl alcohol	0.97	3.67			G
Syringaldehyde			0.15	7.56	S
cis-Coniferyl alcohol		2.16		0.41	G
4-Propynesyringol			0.31	1.52	S
cis-4-Prop-1-enyl syringol*			3.80	4.97	S
Homosyringaldehyde				4.38	S
Acetosyringone			0.20	3.59	S
trans-Coniferyl alcohol	4.07	20.62		2.63	G
Syringylacetone			0.79	1.10	S
2,6-Dimethoxy-4-[(1e)-1-propenyl]phenyl acetate			0.43		S
Propiosyringone				0.44	S
Syringyl vinyl ketone				1.41	S
Dihydrosinapyl alcohol				0.40	S
cis-Sinapyl alcohol			0.47	2.34	S
trans-Sinapaldehyde				2.32	S
trans-Sinapyl alcohol				13.89	S
Methyldehydroabietate		0.19			RA
9-Oxodehydroabietic acid methyl ester		0.19			RA
Total Carb	**44.96**	**2.13**	**36.76**	**7.34**	
Total H	0.35	0.47	0.40	0.15	
Total G	20.52	74.17	4.33	12.48	
Total S	0.00	0.24	20.33	60.97	
Total Lig (H + G + S)	**20.87**	**74.88**	**25.06**	**73.60**	
Other units	2.60	1.08			
S/G ratio			**4.70**	**4.89**	

The compounds originated from carbohydrates (Carb), p-hydroxyphenyl (H), guaiacyl (G), or syringyl-type (S) lignin units, other aromatic units (Ar), or rosin acids (RA).

**May contain areas of two signals identified to the same compound by GC-MS. The significance to the total value is 1% or less.*

The values are presented as percentages of the peak area compared to the total peak area.

the results presented here as well. However, for the rough evaluation of lignin content in samples of hemicelluloses, the method could be suitable, and it could provide estimations of the carbohydrate content in an indirect way.

The S/G ratio of the starting GX and GX-phe samples was very similar (4.70 and 4.89, respectively; **Table 5**). The reliability of analyzing the S/G ratio by py-GC/MS has been shown for eucalyptus samples (Ohra-aho et al., 2013), and the method is most likely valid for GX hemicelluloses. A recently published S/G ratio for birch wood from Sweden was 3.25 (Wang et al., 2018). Although the results are not necessarily comparable for samples from different wood materials, the S/G ratio obtained for lignin associated with GX seems fairly high, also taking into consideration the results obtained for other hardwood species. For example, in another study of eucalyptus samples, the S/G ratio was 1.9–3.1 (Ohra-aho et al., 2013).

Analysis and Quantitation of Small Extractable Phenolic Compounds From Phenolic Fractions GGM-Phe and GX-Phe—Vanillin and Syringaldehyde as Indicators in Lignin Participating in Formation of Emulsions

A previous study showed that certain types of extractable small phenolic compounds of PHWE GGM concentrate were adsorbed on the oil droplets of rapeseed oil emulsions (Lehtonen et al., 2018). It was then assumed that LCC structures composed of phenolic and carbohydrate residues would improve the emulsification and stabilization ability of PHWE hemicelluloses. We now assume also that the extractable phenolic compounds would be associated with lignin present in the samples. The phenolic fractions GGM-phe and GX-phe were extracted and analyzed with UPLC, and the main peaks were identified with LC-MS and then quantified using corresponding standards.

The main small phenolic compounds identified according to LC-MS were vanillin (in both GGM and GX) and syringaldehyde (only in GX). The amounts found in GGM-phe and GX-phe are shown in **Table 6**. Both compounds were found mainly in the ethanol soluble fractions; GX was not even precipitated during extractions. The amounts of compounds dissolved in neutral solvent and additionally acid hydrolyzed were very similar. Clearly, the highest amount of these compounds was released by base hydrolysis.

The total amount of vanillin and syringaldehyde extracted was <0.1 m-%, meaning that the amount was still much lower considering the starting hemicelluloses. However, the classification of vanillin and syringaldehyde would fit that of hydroxycinnamic acids (OHCs) in terms of the previously used classification (Lehtonen et al., 2018). On the other hand, ethanol soluble phenols belonging to OHCs were found solely adsorbed in the oil of the emulsion, which means that vanillin bound to GGM-phe and syringaldehyde bound to GX-phe also participate in the formation of emulsions. Furthermore, because these compounds are clearly mainly covalently bound to the phenolic fractions containing lignin, it is also likely that lignin is involved in the formation and stabilization of emulsions.

The S/G ratio of syringaldehyde and vanillin extracted and base-hydrolyzed from GX-phe was 4.79, which is very close to the value obtained from py-GC/MS for the whole lignin. Although the values could be similar by coincidence, it is more likely that the similar S/G ratio obtained reflects the presence of lignin adsorbed with hemicelluloses to the surface of emulsion droplets. Because we have not thus far been able to completely release hemicelluloses adsorbed on rapeseed oil droplets, this quantitation by UPLC is by far the best method for identifying the presence of lignin in emulsions stabilized with PHWE hemicelluloses, and it can be used to tag on lignin associated with hemicelluloses.

TABLE 6 | The amounts obtained from UPLC analysis of main small extractable phenolic compounds, vanillin and syringaldehyde, which were identified as the main products extracted from the phenolic residues GGM-phe and GX-phe.

Sample	Extraction method	Vanillin (μg/g)	Syringaldehyde (μg/g)	S/G ratio
GGM-phe	Ethanol soluble	818 ± 109	ND	
	Ethanol soluble + acid hydrolysis	995 ± 156	ND	
	Ethanol soluble + base hydrolysis	6,148 ± 635	ND	
	Ethanol precipitated + acid hydrolysis	28 ± 5	ND	
	Ethanol precipitated + base hydrolysis	101 ± 26	ND	
GX-phe	Ethanol soluble	255 ± 21	760 ± 55	2.98
	Ethanol soluble + acid hydrolysis	313 ± 40	948 ± 122	3.02
	Ethanol soluble + base hydrolysis	1,603 ± 23	7,677 ± 170	4.79

ND, not detected.

Properties of Hemicelluloses Affecting the Physical Properties and Stability of Emulsions

The results regarding the droplet-size distribution of emulsions (**Figure 1**, **Table 1**) can be explained by the presence of lignin. For fresh emulsions prepared using purified GGM-pur and GX-pur fractions, the D[3,2] values were smaller compared to starting GGM and GX. It is reasonable to assume that lignin's participation in the formation of oil droplets would increase their size.

Regarding the physical stability of emulsions, the droplet size increased faster during the storage of emulsions stabilized with GGM-pur and GX-pur compared to emulsions stabilized with the starting hemicelluloses. This indicates that the presence of lignin stabilizes the physical structure of emulsions. For PHWE GGM, it was recently demonstrated that the mixed mechanism involves Pickering stabilization with interfacial adsorption of GGM, which are probably associated with lignin (Valoppi et al., 2019a). In addition, the bimodal distribution of GX into smaller and larger droplets was less enhanced in the presence of lignin.

It is evident that lignin, as a natural antioxidant, is also responsible for the improved oxidative stability of emulsions. However, oxidation of phenolic compounds may also change their chemical structure, which could further induce structural changes and affect the physical stability of emulsions. The presence of LCC bonds was evident from the NMR spectrum of starting GX, and the γ-ester structures found could be at least partially responsible for the functional properties of PHWE hemicelluloses, allowing the lignin part anchor to the oil droplet surface, as hypothesized previously (Lehtonen et al., 2018). In this case, it is not necessary to debate whether the LCCs are derived from the starting wood material or produced during the PHWE process; the essential point is the excellent functional properties of hemicelluloses produced by the PHWE process.

CONCLUSIONS

We showed that phenolic structures, which were partially removed from both GGM- and GX-rich wood extracts by using centrifugal forces, played a key role in emulsion stability. The proportions, chemical compositions, and molar masses of the phenolic-rich fraction varied between GGM and GX hemicelluloses. Complementary chemical characterization of centrifuged materials showed that the phenolic-rich fraction contained mainly native lignin and a small amount of carbohydrates.

Using various approaches, the results confirmed that this phenolic-rich fraction improved both the physical and the oxidative stability of emulsions stabilized with PHWE extracts. The antioxidative properties of phenolic compounds coextracted with hemicelluloses may also be interlinked with the physical stability of emulsions. Furthermore, NMR analysis confirmed the presence of a high concentration of γ-ester type LCCs, which could explain the excellent emulsifying capacity of PHWE hemicelluloses. Both GGM and GX produced emulsions with high physical and oxidative stability, although the emulsions had slightly different types of characteristics depending on the source of hemicellulose. The results also showed that in order to achieve desired emulsifying properties, the total removal of lignin is not advisable; in fact, it introduces unnecessary complexities into the PHWE biorefining process.

DATA AVAILABILITY STATEMENT

All datasets generated for this study are included in the article/**Supplementary Material**.

AUTHOR CONTRIBUTIONS

KM planned and received funding for the project. ML mainly designed the experimental plan, with expertise in wood chemistry, with the help of KM (emulsions and hemicelluloses) and FV (emulsions, fractionation of hemicelluloses by centrifugal forces). ML performed and analyzed the 2D HSQC NMR of hemicelluloses, did part of the practical work during the preparation and characterization of emulsions, performed and analyzed the phenolic extraction procedures by UPLC and LC-MS, and assumed the main responsibility for writing the manuscript and interpreting the data. PK provided the materials for the study as well as knowledge about PHWE hemicelluloses and the process. VJ analyzed the carbohydrate content under the guidance of ML. VJ also contributed to the preparation and characterization of emulsions. SH designed and performed the DOSY NMR analysis, provided technical support during NMR analysis, and contributed to the writing of the experimental details of NMR for the manuscript. NM contributed to the calibration of SEC data and determination of molar masses. All authors read and commented on the manuscript.

FUNDING

This research and project Novel wood-derived emulsifiers for superior lipid stabilization (WOODLIPS) was funded by Jane and Aatos Erkko Foundation.

ACKNOWLEDGMENTS

From the Department of Food and Nutrition, University of Helsinki, Dr. Sun-Li Chong is thanked for helping with carbohydrate analysis, Satu Kirjoranta for helping with the procedures regarding preparation and characterization of emulsions, Mamata Bhattarai for discussions about the results obtained from size exclusion chromatography, and Miikka Olin is thanked for the technical assistance with chromatographic analyzers. Prof. Martin Lawoko from KTH, Stockholm is acknowledged for discussions about assigning LCC-structures in NMR-spectra. Annika Smeds from Åbo Akademi is thanked for performing the py-GC/MS. Jane and Aatos Erkko Foundation is acknowledged for the funding.

SUPPLEMENTARY MATERIAL

The Supplementary Material for this article can be found online at: https://www.frontiersin.org/articles/10.3389/fchem.2019.00871/full#supplementary-material

REFERENCES

Ämmälahti, E., Brunow, G., Bardet, M., Robert, D., and Kilpeläinen, I. (1998). Identification of side-chain structures in a poplar lignin using three-dimensional HMQC–HOHAHA NMR spectroscopy. *J. Agric. Food Chem.* 46, 5113–5117. doi: 10.1021/jf980249o

Berglund, J., Azhar, S., Lawoko, M., Lindström, M., Vilaplana, F., Wohlert, J., et al. (2019). The structure of galactoglucomannan impacts the degradation under alkaline conditions. *Cellulose* 26, 2155–2175. doi: 10.1007/s10570-018-1737-z

Bhattarai, M., Pitkänen, L., Kitunen, V., Korpinen, R., Ilvesniemi, H., Kilpeläinen, P. O., et al. (2019). Functionality of spruce galactoglucomannans in oil-in-water emulsions. *Food Hydrocolloids* 86, 154–161. doi: 10.1016/j.foodhyd.2018.03.020

Boerjan, W., Ralph, J., and Baucher, M. (2003). Lignin biosynthesis. *Annu. Rev. Plant Biol.* 54, 519–546. doi: 10.1146/annurev.arplant.54.031902.134938

Boudet, A.-M. (2000). Lignins and lignification: selected issues. *Plant Physiol. Biochem.* 38, 81–96. doi: 10.1016/S0981-9428(00)00166-2

Campestrini, L. H., Silveira, J. L. M., Duarte, M. E. R., Koop, H. S., and Noseda, M. D. (2013). NMR and rheological study of Aloe barbadensis partially acetylated glucomannan. *Carbohydr. Polym.* 94, 511–519. doi: 10.1016/j.carbpol.2013.01.020

Chong, S.-L., Koutaniemi, S., Virkki, L., Pynnönen, H., Tuomainen, P., and Tenkanen, M. (2013). Quantitation of 4-O-methylglucuronic acid from plant cell walls. *Carbohydr. Polym.* 91, 626–630. doi: 10.1016/j.carbpol.2012.08.078

del Río, J. C., Prinsen, P., Cadena, E. M., Martínez, Á. T., Gutiérrez, A., and Rencoret, J. (2016). Lignin–carbohydrate complexes from sisal (Agave sisalana) and abaca (Musa textilis): chemical composition and structural modifications during the isolation process. *Planta* 243, 1143–1158. doi: 10.1007/s00425-016-2470-1

del Rio, J. C., Speranza, M., Gutiérrez, A., Martinez, M. J., and Martinez, A. T. (2002). Lignin attack during eucalypt wood decay by selected basidiomycetes: a Py-GC/MS study. *J. Anal. Appl. Pyrolysis* 64, 421–431. doi: 10.1016/S0165-2370(02)00043-8

Du, X., Gellerstedt, G., and Li, J. (2013). Universal fractionation of lignin-carbohydrate complexes (LCCs) from lignocellulosic biomass: an example using spruce wood. *Plant J.* 74, 328–338. doi: 10.1111/tpj.12124

Faruk, O., Bledzki, A. K., Fink, H.-P., and Sain, M. (2012). Biocomposites reinforced with natural fibers: 2000–2010. *Prog. Polym. Sci.* 37, 1552–1596. doi: 10.1016/j.progpolymsci.2012.04.003

Fengel, D., and Wegener, G. (1983). *Wood: Chemistry, Ultrastructure, Reactions. Berlin/Boston,* Germany: De Gruyter, Inc.

Giummarella, N., Pu, Y., Ragauskas, A. J., and Lawoko, M. (2019). A critical review on the analysis of lignin carbohydrate bonds. *Green Chem.* 21, 1573–1595. doi: 10.1039/C8GC03606C

Griesinger, C., Otting, G., Wuethrich, K., and Ernst, R. R. (1988). Clean TOCSY for proton spin system identification in macromolecules. *J. Am. Chem. Soc.* 110, 7870–7872. doi: 10.1021/ja00231a044

Hannuksela, T., and Hervé du Penhoat, C. (2004). NMR structural determination of dissolved O-acetylated galactoglucomannan isolated from spruce thermomechanical pulp. *Carbohydr. Res.* 339, 301–312. doi: 10.1016/j.carres.2003.10.025

Heinonen, M., Haila, K., Lampi, A.-M., and Piironen, V. (1997). Inhibition of oxidation in 10% oil-in-water emulsions by β-carotene with α- and γ-tocopherols. *J. Am. Oil. Chem. Soc.* 74, 1047–1052. doi: 10.1007/s11746-997-0023-2

Jerschow, A., and Müller, N. (1997). Suppression of convection artifacts in stimulated-echo diffusion experiments. double-stimulated-echo experiments. *J. Magn. Reson.* 125, 372–375. doi: 10.1006/jmre.1997.1123

Kavakka, J. S., Kilpeläinen, I., and Heikkinen, S. (2009). General chromatographic NMR method in liquid state for synthetic chemistry: polyvinylpyrrolidone assisted DOSY experiments. *Org. Lett.* 11, 1349–1352. doi: 10.1021/ol9001398

Kilpeläinen, P. O., Hautala, S. S., Byman, O. O., Tanner, L. J., Korpinen, R. I., Lillandt, M. K.-J., et al. (2014). Pressurized hot water flow-through extraction system scale up from the laboratory to the pilot scale. *Green Chem.* 16, 3186–3194. doi: 10.1039/C4GC00274A

Kim, H., and Ralph, J. (2014). A gel-state 2D-NMR method for plant cell wall profiling and analysis: a model study with the amorphous cellulose and xylan from ball-milled cotton linters. *RSC Adv.* 4, 7549–7560. doi: 10.1039/C3RA46338A

Kim, J.-H., Shim, B. S., Kim, H. S., Lee, Y.-J., Min, S.-K., Jang, D., et al. (2015). Review of nanocellulose for sustainable future materials. *Int. J. Precis. Eng. Manuf.* 2, 197–213. doi: 10.1007/s40684-015-0024-9

Kylli, P., Nohynek, L., Puupponen-Pimiä, R., Westerlund-Wikström, B., Leppänen, T., Welling, J., et al. (2011). Lingonberry (Vaccinium vitis-idaea) and European Cranberry (Vaccinium microcarpon) proanthocyanidins: isolation, identification, and bioactivities. *J. Agric. Food Chem.* 59, 3373–3384. doi: 10.1021/jf104621e

Lampi, A.-M., Dimberg, L. H., and Kamal-Eldin, A. (1999). A study on the influence of fucosterol on thermal polymerisation of purified high oleic sunflower triacylglycerols. *J. Sci. Food Agric.* 79, 573–579.

Lawoko, M., Henriksson, G., and Gellerstedt, G. (2005). Structural differences between the lignin–carbohydrate complexes present in wood and in chemical pulps. *Biomacromolecules* 6, 3467–3473. doi: 10.1021/bm0 58014q

Lehtonen, M., Kemmo, S., Lampi, A.-M., and Piironen, V. (2011). Effects of esterification on the formation and decomposition of steryl hydroperoxides. *Eur. Food Res. Technol.* 232, 255–264. doi: 10.1007/s00217-010-1384-6

Lehtonen, M., Merinen, M., Kilpeläinen, P. O., Xu, C., Willför, S. M., and Mikkonen, K. S. (2018). Phenolic residues in spruce galactoglucomannans improve stabilization of oil-in-water emulsions. *J. Colloid Interface Sci.* 512, 536–547. doi: 10.1016/j.jcis.2017.10.097

Lehtonen, M., Teräslahti, S., Xu, C., Yadav, M. P., Lampi, A.-M., and Mikkonen, K. S. (2016). Spruce galactoglucomannans inhibit lipid oxidation in rapeseed oil-in-water emulsions. *Food Hydrocolloids* 58, 255–266. doi: 10.1016/j.foodhyd.2016.03.006

Li, J., Martin-Sampedro, R., Pedrazzi, C., and Gellerstedt, G. (2011). Fractionation and characterization of lignin-carbohydrate complexes (LCCs) from eucalyptus fibers. *Holzforschung* 65, 43–50 doi: 10.1515/hf.2011.013

Li, K., and Helm, R. F. (1995). Synthesis and rearrangement reactions of ester-linked lignin-carbohydrate model compounds. *J. Agric. Food Chem.* 43, 2098–2103. doi: 10.1021/jf00056a026

Liitiä, T. M., Maunu, S. L., Hortling, B., Toikka, M., and Kilpeläinen, I. (2003). Analysis of technical lignins by two- and three-dimensional NMR spectroscopy. *J. Agric. Food Chem.* 51, 2136–2143. doi: 10.1021/jf0204349

Lundqvist, J., Teleman, A., Junel, L., Zacchi, G., Dahlman, O., Tjerneld, F., et al. (2002). Isolation and characterization of galactoglucomannan from spruce (Picea abies). *Carbohydr. Polym.* 48, 29–39. doi: 10.1016/S0144-8617(01)00210-7

Mikkonen, K. S., Kirjoranta, S., Xu, C., Hemming, J., Pranovich, A., Bhattarai, M., et al. (2019). Environmentally-compatible alkyd paints stabilized by wood hemicelluloses. *Ind. Crops Prod.* 133, 212–220. doi: 10.1016/j.indcrop.2019.03.017

Mikkonen, K. S., Merger, D., Kilpeläinen, P., Murtomäki, L., Schmidt, U. S., and Wilhelm, M. (2016). Determination of physical emulsion stabilization mechanisms of wood hemicelluloses via rheological and interfacial characterization. *Soft Matter* 12, 8690–8700. doi: 10.1039/C6SM01557C

Nishimura, H., Kamiya, A., Nagata, T., Katahira, M., and Watanabe, T. J. S. (2018). Direct evidence for α ether linkage between lignin and carbohydrates in wood cell walls. *Sci. Rep.* 8:6538. doi: 10.1038/s41598-018-24328-9

Ohra-aho, T., Gomes, F. J. B., Colodette, J. L., and Tamminen, T. (2013). S/G ratio and lignin structure among Eucalyptus hybrids determined by Py-GC/MS and nitrobenzene oxidation. *J. Anal. Appl. Pyrol.* 101, 166–171. doi: 10.1016/j.jaap.2013.01.015

Ohra-aho, T., Gomes, F. J. B., Colodette, J. L., and Tamminen, T. (2018). Carbohydrate composition in Eucalyptus wood and pulps – Comparison between Py-GC/MS and acid hydrolysis. *J. Anal. Appl. Pyrol.* 129, 215–220. doi: 10.1016/j.jaap.2017.11.010

Pitkänen, L., Tuomainen, P., Mikkonen, K. S., and Tenkanen, M. (2011). The effect of galactose side units and mannan chain length on the macromolecular characteristics of galactomannans. *Carbohydr. Polym.* 86, 1230–1235. doi: 10.1016/j.carbpol.2011.06.018

Qu, C., Kishimoto, T., Kishino, M., Hamada, M., and Nakajima, N. (2011). Heteronuclear single-quantum coherence nuclear magnetic resonance (HSQC NMR) characterization of acetylated fir (Abies sachallnensis MAST) wood regenerated from ionic liquid. *J. Agric. Food Chem.* 59, 5382–5389. doi: 10.1021/jf200498n

Rencoret, J., del Río, J. C., Gutiérrez, A., Martínez, Á. T., Li, S., Parkås, J., et al. (2012). Origin of the acetylated structures present in white birch (Betula pendula Roth) milled wood lignin. *Wood Sci. Technol.* 46, 459–471. doi: 10.1007/s00226-011-0417-z

Rumble, J. R. (Ed.). (2018–2019). *CRC Handbook of Chemistry and Physics*. Boca Raton, FL: CRC Press/Taylor and Francis.

Sainio, T., Kallioinen, M., Nakari, O., and Mänttäri, M. (2013). Production and recovery of monosaccharides from lignocellulose hot water extracts in a pulp mill biorefinery. *Bioresour. Technol.* 135, 730–737. doi: 10.1016/j.biortech.2012.08.126

Sixta, H., Michud, A., Hauru, L., Asaadi, S., Ma, Y., King, A. W. T., et al. (2015). Ioncell-F: a high-strength regenerated cellulose fibre. *Nord. Pulp Pap. Res. J.* 30, 43–57. doi: 10.3183/npprj-2015-30-01-p043-057

Sjöström, E. (1993). *Wood Chemistry: Fundamentals and Applications*. San Diego, CA: Academic Press, Inc.

Sundberg, A., Sundberg, K., Lillandt, C., and Holmbom, B. (1996). Determination of hemicelluloses and pectins in wood and pulp fibres by acid methanolysis and gas chromatography. *Nord. Pulp Pap. Res. J.* 11, 216–219, 226. doi: 10.3183/npprj-1996-11-04-p216-219

Teleman, A., Lundqvist, J., Tjerneld, F., Stålbrand, H., and Dahlman, O. (2000). Characterization of acetylated 4-O-methylglucuronoxylan isolated from aspen employing 1H and 13C NMR spectroscopy. *Carbohydr. Res.* 329, 807–815. doi: 10.1016/S0008-6215(00)00249-4

Teleman, A., Tenkanen, M., Jacobs, A., and Dahlman, O. (2002). Characterization of O-acetyl-(4-O-methylglucurono)xylan isolated from birch and beech. *Carbohydr. Res.* 337, 373–377. doi: 10.1016/S0008-6215(01)00327-5

Valoppi, F., Lahtinen, M. H., Bhattarai, M., Kirjoranta, S. J., Juntti, V. K., Peltonen, L. J., et al. (2019a). Centrifugal fractionation of softwood extracts improves the biorefinery workflow and yields functional emulsifiers. *Green Chem.* 21, 4691–4705. doi: 10.1039/C9GC02007A

Valoppi, F., Maina, N., Allén, M., Miglioli, R., Kilpeläinen, P. O., and Mikkonen, K. S. (2019b). Spruce galactoglucomannan-stabilized emulsions as essential fatty acid delivery systems for functionalized drinkable yogurt and oat-based beverage. *Eur. Food Res. Technol.* 245, 1387–1398. doi: 10.1007/s00217-019-03273-5

van Heiningen, A. (2006). Converting a kraft pulp mill into an integrated forest biorefinery. *Pulp Pap. Can.* 107, T141–T146.

Vanholme, R., Demedts, B., Morreel, K., Ralph, J., and Boerjan, W. (2010). Lignin biosynthesis and structure. *Plant Physiol.* 153:895. doi: 10.1104/pp.110.155119

Wang, Z., Winestrand, S., Gillgren, T., and Jönsson, L. J. (2018). Chemical and structural factors influencing enzymatic saccharification of wood from aspen, birch and spruce. *Biomass Bioenergy* 109, 125–134. doi: 10.1016/j.biombioe.2017.12.020

Wen, J.-L., Xue, B.-L., Xu, F., and Sun, R.-C. (2012). Unveiling the structural heterogeneity of Bamboo Lignin by *in situ* HSQC NMR technique. *Bioenergy Res.* 5, 886–903. doi: 10.1007/s12155-012-9203-5

Willför, S., Rehn, P., Sundberg, A., Sundberg, K., and Holmbom, B. (2003). Recovery of water-soluble acetylgalactoglucomannans from mechanical pulp of spruce. *Tappi J.* 2, 27–32.

Wu, D. H., Chen, A. D., and Johnson, C. S. (1995). An improved diffusion-ordered spectroscopy experiment incorporating bipolar-gradient pulses. *J. Magn. Reson. Ser. A* 115, 260–264. doi: 10.1006/jmra.1995.1176

Xu, C., Willfor, S., Sundberg, K., Pettersson, C., and Holmbom, B. (2007). Physico-chemical characterization of spruce galactoglucomannan solutions: stability, surface activity and rheology. *Cell. Chem. Technol.* 41:51.

Zinovyev, G., Sulaeva, I., Podzimek, S., Rössner, D., Kilpeläinen, I., Sumerskii, I., et al. (2018). Getting closer to absolute molar masses of technical lignins. *ChemSusChem* 11, 3259–3268. doi: 10.1002/cssc.201801177

Conflict of Interest: The authors declare that the research was conducted in the absence of any commercial or financial relationships that could be construed as a potential conflict of interest.

Copyright © 2019 Lahtinen, Valoppi, Juntti, Heikkinen, Kilpeläinen, Maina and Mikkonen. This is an open-access article distributed under the terms of the Creative Commons Attribution License (CC BY). The use, distribution or reproduction in other forums is permitted, provided the original author(s) and the copyright owner(s) are credited and that the original publication in this journal is cited, in accordance with accepted academic practice. No use, distribution or reproduction is permitted which does not comply with these terms.

frontiers in Chemistry

MINI REVIEW
published: 18 December 2019
doi: 10.3389/fchem.2019.00874

Lignocellulosic Biomass: Understanding Recalcitrance and Predicting Hydrolysis

*Aya Zoghlami and Gabriel Paës**

FARE Laboratory, INRAE, University of Reims Champagne-Ardenne, Reims, France

Lignocellulosic biomass (LB) is an abundant and renewable resource from plants mainly composed of polysaccharides (cellulose and hemicelluloses) and an aromatic polymer (lignin). LB has a high potential as an alternative to fossil resources to produce second-generation biofuels and biosourced chemicals and materials without compromising global food security. One of the major limitations to LB valorisation is its recalcitrance to enzymatic hydrolysis caused by the heterogeneous multi-scale structure of plant cell walls. Factors affecting LB recalcitrance are strongly interconnected and difficult to dissociate. They can be divided into structural factors (cellulose specific surface area, cellulose crystallinity, degree of polymerization, pore size and volume) and chemical factors (composition and content in lignin, hemicelluloses, acetyl groups). Goal of this review is to propose an up-to-date survey of the relative impact of chemical and structural factors on biomass recalcitrance and of the most advanced techniques to evaluate these factors. Also, recent spectral and water-related measurements accurately predicting hydrolysis are presented. Overall, combination of relevant factors and specific measurements gathering simultaneously structural and chemical information should help to develop robust and efficient LB conversion processes into bioproducts.

Keywords: lignocellulose, recalcitrance, chemical composition, structure, enzymatic hydrolysis

OPEN ACCESS

Edited by:
Jose Luis Sanchez,
University of Zaragoza, Spain

Reviewed by:
David B. Hodge,
Montana State University,
United States
Mark F. Davis,
National Renewable Energy
Laboratory (DOE), United States

****Correspondence:***
Gabriel Paës
gabriel.paes@inra.fr

Specialty section:
This article was submitted to
Chemical and Process Engineering,
a section of the journal
Frontiers in Chemistry

Received: *14 June 2019*
Accepted: *04 December 2019*
Published: *18 December 2019*

Citation:
Zoghlami A and Paës G (2019)
Lignocellulosic Biomass:
Understanding Recalcitrance and
Predicting Hydrolysis.
Front. Chem. 7:874.
doi: 10.3389/fchem.2019.00874

INTRODUCTION

The environment is suffering from climate change, worsened by over-exploitation of resources thus increasing global greenhouse gas emission (Anderson et al., 2019; Hassan et al., 2019). Sustainable and environmentally friendly energy based on renewable resources are required in order to meet the world's future energy needs. Lignocellulosic biomass (LB) continues to attract global interest as a sustainable alternative to fossil carbon resources to produce second-generation biofuels and other biobased chemicals without compromising global food security (Menon and Rao, 2012; Chandel et al., 2018). These include agricultural wastes such as cereal straw (Yuan et al., 2018) and bagasse (Dias et al., 2009), forest residues such as pine (Cotana et al., 2014) and dedicated crops and short rotation coppices such as miscanthus (Lewandowski et al., 2000), switchgrass (Schmer et al., 2008), and poplar (Sannigrahi et al., 2010). LB is mainly composed of cellulose, hemicelluloses and lignin, making a complex assembly of polymers naturally recalcitrant to enzymatic conversion. That is why some pre-treatment steps are mandatory to make cellulose more accessible by changing the physical and/or the chemical structure of LB and facilitating the conversion of polysaccharides into fermentable sugars (Zhao et al., 2012a; Kumar and Sharma, 2017). Factors affecting LB recalcitrance are strongly interconnected and difficult to dissociate (Zhao et al., 2012b; Bichot et al., 2018). They can be divided into structural factors, which mainly refer to cellulose specific surface area, cellulose crystallinity, degree of polymerization, pore size and volume; chemical factors, related to composition and content in lignin, hemicelluloses and acetyl groups. Although many studies have investigated the impact of these factors on recalcitrance by examining different LB feedstocks and operating process conditions, conclusions obtained are not always obvious and even sometimes contradictory.

This review aims to propose an up-to-date survey of the role of chemical and structural factors on biomass recalcitrance and of the most advanced techniques to evaluate these factors. Resulting from the assessment of these factors, some promising methods aimed at predicting hydrolysis are presented and discussed, so that they should help to develop robust LB conversion processes into biofuels and biobased chemicals.

FACTORS CONTRIBUTING TO THE RECALCITRANCE OF LIGNOCELLULOSIC BIOMASS

LB is naturally recalcitrant to microbial and enzymatic degradation, which constitutes a real obstacle to its industrial valorisation into bioenergy and biomaterials. To optimize deconstruction, it is necessary to understand and overcome the chemical and the structural factors conferring the recalcitrance property to lignocellulose in plant cell walls.

Chemical Factors Impacting Enzymatic Hydrolysis

Cellulose

Cellulose, the most abundant LB polymer, representing 40–60% in weight (Sharma et al., 2019), consists of ß-D-glucopyranose units linked via ß-(1,4) glycosidic bonds, with cellobiose as the fundamental repeating unit. The cellulose chains made up of 500–1400 D-glucose units are arranged together to form microfibrils, which are packed together to form cellulose fibrils (McKendry, 2002; Robak and Balcerek, 2018). Cellulose fibrils are embedded in a lignocellulosic matrix that makes it very resistant to enzymatic hydrolysis. Yoo et al. reported that the cellulose content was positively correlated with the glucose release (Yoo et al., 2017a). The degree of polymerization (DP) of cellulose which is the number of glucose units in the polymer playing a crucial role on LB recalcitrance. But its exact role is still not quite clear and difficult to investigate individually with the current knowledge. Indeed, altering DP is always accompanied by changes in structural parameters such as crystallinity and porosity. For example, Sinitsyn et al. (1991) found that reduction in DP of cotton linters by γ-irradiation had a minor effect on the saccharification rate. Ioelovich et al. got similar conclusion (Ioelovich and Morag, 2011). However, Lu et al. (2019) reported that the cellulose DP was negatively correlated to the cellulose hydrolysis. It is assumed that long cellulose chains contain more hydrogen bonds and are difficult to hydrolyze, whereas shorter cellulose chains contain a weaker hydrogen-bonding system and therefore are believed to facilitate enzyme accessibility (Hallac and Ragauskas, 2011; Meng et al., 2017).

Hemicelluloses and Acetyl Groups

Hemicelluloses are heterogeneous groups of biopolymers, representing 20–35% of the biomass weight (Chandel et al., 2018). It contains various monosaccharide subunits to form xylans, xyloglucan, mannans and glucomannans, and others (McKendry, 2002). The DP of hemicelluloses is in the range of 100–200 units (Mota et al., 2018), which is much lower than that of cellulose, but it can present a high degree of more or less complex substitutions. Hemicellulose is amorphous, with little physical strength. It is readily hydrolysed by dilute acids or bases, as well as hemicellulase enzymes (Isikgor and Becer, 2015). Hemicelluloses act as a physical barrier limiting the accessibility of enzymes. It has been reported that removal of hemicelluloses by dilute acid or steam explosion pre-treatment could increase cellulose conversion by improving the accessibility of enzymes to cellulose (Auxenfans et al., 2017a; Herbaut et al., 2018; Santos et al., 2018). Kruyeniski et al. (2019) reported that the removal of hemicelluloses on pre-treated pine improved the fibers porosity and the area available for enzymes. The impact of hemicelluloses on LB recalcitrance still not quite clear as some lignin is often removed with hemicelluloses. Some studies have reported that hemicelluloses removal was more efficient than lignin removal for improving enzymatic hydrolysis rate (Yoshida et al., 2008; Leu and Zhu, 2013; Lv et al., 2013), whereas others indicated that lignin removal was much more important (Gao et al., 2013; Kruyeniski et al., 2019).

LB hemicelluloses can be extensively acetylated with acetyl groups (OAc). OAc may restrict cellulose accessibility by interfering with enzyme recognition (Pan et al., 2006). It also might hinder the formation of productive binding between cellulose and the catalytic domain of cellulases through increasing the diameter of cellulose chain or changing its hydrophobicity (Zhao et al., 2012a). Previous studies on corn stover reported that reducing the acetyl content improved enzyme effectiveness (Kumar and Wyman, 2009a,b). Whereas, other studies on poplar wood, wheat straw, switchgrass and bagasse pointed out that the effect of deacetylation was more significant on hemicellulose digestibility than on cellulose digestibility (Grohmann et al., 1989; Chang and Holtzapple, 2000; Liu et al., 2014). Chang and Holtzapple (2000) and Zhu et al. (2008) showed that the impact of OAc depends on the lignin and cellulose content and biomass crystallinity.

Lignin

Lignin is the second most abundant polymer in LB after cellulose, corresponding to 15–40% of dry weight (Ragauskas et al., 2014). It is a very complex amorphous heteropolymer of phenylpropanoid building units (*p*-coumaryl, coniferyl, and sinapyl alcohol) (Agbor et al., 2011). Lignin is responsible for hydrophobicity and structural rigidity. It binds hemicelluloses to cellulose in the cell wall. It is well-known that lignin plays a negative role in the conversion of cellulose influenced by several factors such as total lignin content, lignin composition/structure (in particular hydroxyl groups content and S and G units content) (Santos et al., 2012). First of all, lignin can physically limit polysaccharide accessibility: it plays a role as physical barrier that blocks the access of enzymes to cellulose. Also, it can irreversibly adsorb cellulases and other enzymes during enzymatic hydrolysis due to its hydrophobic structural features including hydrogen bonding, methoxy groups, and polyaromatic structures (Kumar and Wyman, 2009b; Zeng et al., 2014). Previous studies showed that the lignin content was negatively correlated with enzymatic digestibility in poplar (Meng et al., 2017; Yoo et al., 2017a), also in miscanthus, in wheat straw (Herbaut et al., 2018) and in transgenic rice (Huang et al., 2017). The removal of lignin generally disrupts the lignin-carbohydrates matrix, increases the porosity and reduces non-productive adsorption sites for enzymes (Pihlajaniemi et al., 2016; Kruyeniski et al., 2019). It has been reported that phenolic hydroxyl groups (lignin-derived compounds) cause reversible inhibition of cellulases (Yu et al., 2014; Yang and Pan, 2016; Yao et al., 2018). Blocking free phenolic hydroxyl groups by chemical reaction such as hydroxypropylation significantly reduced (by 65–91%) the inhibitory effect of lignin (Yang and Pan, 2016). Yoo et al. showed that lignin S/G ratio is important as an independent recalcitrance factor (Yoo et al., 2017a). However, the correlation between lignin S/G ratio and recalcitrance is still not obvious. For example, Herbaut et al. and Yu et al. showed a positive correlation between the S/G ratio and the hydrolysis yields for miscanthus and woody chips (Yu et al., 2014; Herbaut et al., 2018) because of the higher binding capacity of G (with branched structure) over S (with linear structure and low degree of polymerisation) to cellulase (Guo et al., 2014; Yoo et al., 2017b). By contrast, others found a negative correlation between S/G ratio and the enzymatic hydrolysis in woody chips (Papa et al., 2012), in pre-treated miscanthus (Xu et al., 2012; Li et al., 2014), in pre-treated wheat straw (Jiang et al., 2016) and in genetically engineering poplar (Escamez et al., 2017). On the other hand, previous studies showed that changes in S/G ratio of untreated LB did not influence the enzymatic hydrolysis: for untreated poplar with S/G ratio between 1.0 and 3.0 (Studer et al., 2011), for Arabidopsis stems containing G- and S-rich lignin (Li et al., 2010) and for transgenic alfalfa (Chen and Dixon, 2007). Overall, lignin contributes strongly to LB recalcitrance influenced by its chemical composition and its structure, limiting the accessibility of enzymes to cellulose.

Interactions Between Polymers

We detailed the impact of each polymer on LB recalcitrance above. There is a need to find out how interactions between them increase the recalcitrance of the cell walls to the enzymatic hydrolysis. Cellulose and hemicelluloses are intimately associated together through hydrogen bonds (Lee et al., 2014), meanwhile lignin are covalently linked to hemicelluloses to form lignin-carbohydrate complex (LCC) (Tarasov et al., 2018; Giummarella and Lawoko, 2019). There are five different types of lignin-carbohydrate bonds, phenyl glycosides (PG), benzyl ethers (BE), γ-esters esters (GE), ferulate/coumarate esters (FE/CE) and hemiacetal/acetal linkages that are linked to lignin at 4-OH and 4-O positions (Giummarella and Lawoko, 2019). It has been suggested that the interactions between the microfibers from cellulose and hemicelluloses, as well as the LCC linkage plays a significant role in wood structure and affects significantly its enzymatic hydrolysis by reducing the area of cellulose accessible for enzymes (Balan et al., 2009; Du et al., 2014). Until now, the study of LCC is still a controversial topic in lignocellulosic chemistry, due to difficulties in the characterization of heterogeneous biomass substrate in addition to the low concentration of LCC (Obst, 1982). That is why there is a need to develop efficient methods to enrich the LCC such as mild chemical methods or the use of pure enzymes in order to achieve a quantitative analysis of LCC using NMR (Giummarella and Lawoko, 2019).

Physical Factors Impacting Enzymatic Hydrolysis

Crystallinity

Crystallinity has been identified as one of the most extensively studied supramolecular properties of cellulose. It represents the proportion of crystalline regions to amorphous regions. Crystalline cellulose fibers are closely related to each other by non-covalent hydrogen bonds that make their enzymatic hydrolysis 3–30 times lower than in amorphous zones (Zhao et al., 2012b). But the impact of crystallinity on hydrolysis differs. Some studies reported that crystallinity correlated negatively with enzymatic hydrolysis especially at the initial hydrolysis rate on pre-treated wheat straw (Pihlajaniemi et al., 2016), on pre-treated corn stover (Liu et al., 2014; Xu et al., 2019) and on hybrid polar, switchgrass, and bagasse (Chang and Holtzapple, 2000). Others showed that crystallinity was less critical in limiting hydrolysis than other physical features such as DP, pore volume, accessible surface area, and particle size (Mansfield et al., 1999; Ioelovich and Morag, 2011; Aldaeus et al., 2015; Auxenfans et al., 2017a; Meng et al., 2017; Zhang et al., 2018). Another piece of evidence is that in the majority of cases, pure cellulose is used as a substrate to correlate the crystallinity to the saccharification yield, which is not representative of the heterogeneous of LB substrate.

Particle Size

Particle size was identified as a key parameter affecting cellulose hydrolysis potential (Barakat et al., 2014; Vaidya et al., 2016). The reduction of particle size through milling, grinding, and extrusion could enhance the affinity between cellulose and enzymes, deconstruct lignocellulose compact structure and thus increase the rate of hydrolysis (Silva et al., 2012; Pang et al., 2018; Yu et al., 2019). Studies have demonstrated that mechanical deconstruction facilitates enzymatic hydrolysis of various feedstocks such as wood chips (Jiang et al., 2017), miscanthus and wheat straw (Kim et al., 2018) and corn stover (Yu et al., 2019). However, some researchers pointed out that there is a size threshold depending on the lignocellulosic feedstocks. Chang and Holtzapple (2000), observed that a particle size reduction below 400 μm has a negligible effect on the hydrolysis yield of poplar. Whereas, Silva et al. (2012) reported that the size threshold was 270 μm for wheat straw.

Accessible Surface Area (ASA)

Accessible surface area (ASA) of LB is a critical factor for enzymatic hydrolysis, highly related to porosity structure properties, such as specific surface area (SSA) and pore volume

(Liu et al., 2014). Reduction in the particle size or increase in pore volume causes an increase of ASA. It has been shown that theenzymatic conversion of pre-treated pine wood is increased with ASA (Torr et al., 2016). Also Goshadrou et al. (2013) reported that ASA could enhance the fiber accessibility of aspen wood to the hydrolytic enzymes. However, ASA is difficult to estimate, SSA is often used to measure the real surface that is available to enzymes (Silvi Octavia et al., 2017). Moreover, just like crystallinity, it is impossible to consider only SSA (Karimi and Taherzadeh, 2016a). The smaller the particle is, the higher the SSA is (Silvi Octavia et al., 2017). Zhang et al. (2018) reported that the hydrothermal pre-treated corn stover increased the SSA by 2-fold, resulting in 138% enhancement of enzymatic digestibility. Lu et al. (2019) also found that ball milling increased the SAA of cellulose by a factor of two due to the reduction in particle size; these changes made cellulose more accessible and more reactive and resulted in higher glucose yield. However, Peciulyte et al. (2015) pointed out the absence of significant correlation between the yield of cellulose conversion of cellulosic substrates and the SSA.

Accessible Volume (Pore Size: Internal Surface Area)

Accessible volume of cellulose in LB is considered as an important factor influencing enzymatic deconstruction (Jeoh et al., 2007). According to their sizes or their shapes, pore volumes are more or less accessible to enzymes. The size of a cellulase is typically around 5.1 nm, and so, only the pores larger than 5.1 nm are supposed to be accessible to enzyme (Grethlein, 1985). Some authors found that there is a strong correlation between pore size of the biomass and the enzymatic conversion yield for dilute acid pre-treated poplar (Meng et al., 2013) and cellulosic substrates (Peciulyte et al., 2015). Herbaut et al. demonstrated that correlations with specific porosity ranges are biomass specific and pre-treatment dependent. For example, hydrolysis yield correlated strongly to pore size range 15–30 nm for wheat straw, whereas it correlated to pore size range 10–15 nm for poplar. For miscanthus, only pores below 10 nm correlated strongly with hydrolysis, which proved that there is no generic pore size allowing an enhancement of hydrolysis yield and that diffusion of enzymes within the plant cell wall is specific to each biomass species (Herbaut et al., 2018). Other reports found that there is no correlation between pore size and hydrolysis yield, for dilute acid pre-treated corn stover (Ishizawa et al., 2007), pre-treated pine (Kruyeniski et al., 2019), and dilute acid pre-treated and delignified sugarcane (Santos et al., 2018). Moreover, Stoffel et al. (2014) and Vaidya et al. (2016) also showed that the increase of pore volume when lignin contents does not exceed 15% has a negligible effect on enzymatic digestibility of pre-treated pine.

PREDICTING ENZYMATIC HYDROLYSIS

LB recalcitrance to enzymatic degradation was found to be a multi-variant and multi-scale phenomenon, affected by several physical and chemical factors such as hemicelluloses and lignin content, DP of cellulose and accessible surface area and volume (**Figure 1**). However, various studies have demonstrated opposing trends in the effects of these factors due to the complexity of LB and the unknown interactions between these factors.

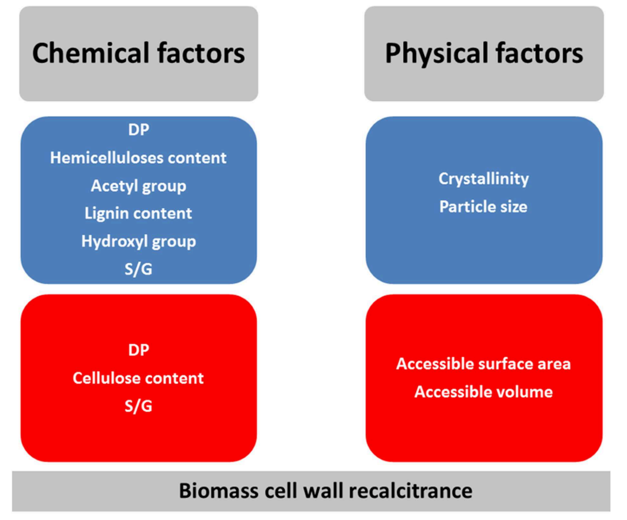

FIGURE 1 | Factors influencing LB recalcitrance. In blue box: the increase in value of the factor increases LB recalcitrance; in red box: the increase in value of the factor decreases LB recalcitrance. When factors are in two boxes, their effect is variable.

Several studies have developed high throughput methodologies to characterize the composition and the structure of large sets of LB samples using wet chemistry and spectroscopy (Studer et al., 2010; Krasznai et al., 2018). These methods have the advantages of being fast and automatic with a very low sample mass and minimal sample preparation (Decker et al., 2018). For instance, Selig et al. developed a high throughput method to determine glucan and xylan content in poplar, pine, wheat stover and pine using a glucose oxidase and a xylose dehydrogenase-based assays instead of HPLC analysis which reduced remarkably the duration of the analysis from 48 to 5-6 h (Selig et al., 2011). Pyrolysis-molecular beam mass spectrometry was used as a high throughput technique to analyse lignin content and structure and polysaccharides content in LB feedstocks (Penning et al., 2014; Decker et al., 2015; Sykes et al., 2015; Harman-Ware et al., 2017). Decker et al. (2012) developed a high throughput method to investigate the effect of the starch content in a set of 250 switchgrass variants on the recalcitrance after hydrothermal pre-treatment and enzymatic hydrolysis (5 days).

High throughput techniques provide useful information to characterize LB while saving time and effort. However, those techniques are not fully automatic (some manual transfers between operations is often necessary), also specialized costly robots, reactors, and sophisticated computational tools are required. More importantly, conducting enzymatic hydrolysis takes several days, whereas there is a need to predict from initial properties of biomass how it will behave during biotechnological transformation in order to adapt the process conditions.

As detailed in the previous section, measuring conventional factors such as lignin content (for example using standard wet-chemistry analysis), cellulose crystallinity or porosity (for example using Simons's staining or thermoporosimetry) provide reliable information about composition, accessibility and structure and can be carried out by several techniques with their advantages and drawbacks (**Table 1**).

In many cases, they are very useful to understand the relationship between assayed factors and hydrolysis. But these parameters are far from being universal to predict hydrolysis, for several reasons:

- Hydrolysis conditions depend on biomass species, pre-treatments, and enzymatic cocktails, which are not standard from one research report to another;
- Measurements of the chemical and structural parameters depend on the instrument, methods and conditions of analysis which are difficult to compare (for example, there are at least 6 different techniques to evaluate porosity, **Table 1**);
- Most importantly, due to the multi-scale architecture of LB, not a single chemical or structural parameter can so far explain hydrolysis.

Therefore, some other methods are required to evaluate, as a single measurement, the interactions existing between several parameters which are responsible for recalcitrance, in order to predict enzymatic hydrolysis. Among them, spectral and water-related properties of LB appear as relevant measurements to be correlated to hydrolysis.

Infra-Red Spectroscopy

Quantitative spectroscopy is a fast, relatively low-cost, non-destructive alternative to classic analytical methods for the chemical analysis of biomass. Several spectroscopic techniques have been applied to analyse biomass properties, including fast-Fourier Transform InfraRed (FT-IR) spectroscopy, near-infrared (NIR) spectroscopy, and Raman scattering spectroscopy.

NIR is a good method for qualitative and quantitative screening of large population of samples. It has also been used to predict LB composition and enzymatic digestibility (Hou and Li, 2011; Huang et al., 2012, 2017).

FTIR spectroscopy is a reliable technique used to determine the effect of pre-treatment (monitor the crystallinity changes), and the degradation of cellulose during the enzymatic saccharification. However, it provides especially qualitative structural information rather than quantitative information. Bekiaris et al. (2015) demonstrated that FTIR spectroscopy combined with chemometric techniques can be used to predict sugar conversions and yields from enzymatic saccharification of pre-treated wheat straw. Earlier study on untreated and pre-treated switchgrass and corn stover got similar conclusion (Sills and Gossett, 2012). Raman spectroscopy is also a robust analytical technique coupled to FTIR spectroscopy allowed the prediction of lignin syringyl/guaiacyl content in diverse lignocellulosic feedstocks (Lupoi et al., 2014).

Overall, even if infrared spectroscopy is very powerful to predict the composition and the saccharification of LB, it requires the creation of mathematical models which needs hundreds of samples, which represents an intensive work. Also, models are specific to biomass species and hydrolysis conditions, which can limit their use.

Fluorescence Spectroscopy

Plant cell walls are autofluorescent materials, containing some endogenous fluorophores, especially aromatic molecules: monolignols in lignin, ferulic, acid and cinnamic acids in hemicellulose (Auxenfans et al., 2017b). Fluorescence can be easily and fastly measured on lignocellulosic samples through spectrofluorimetry. Auxenfans et al. reported that fluorescence intensity correlated strongly with the glucose released from untreated and steam exploded lignocellulosic feedstocks (miscanthus, poplar, and wheat straw) and concluded that fluorescence can predict the LB saccharification.

Fluorescence lifetime as a rapid method can also be used to explain and even predict saccharification with efficiency: Chabbert et al. (2018) reported a strong positive correlation between lifetime fluorescence and saccharification yields. Fluorescence Recovery After Photobleaching (FRAP) technique allowed to explore LB accessibility. Herbaut et al., studied the mobility of PEG-rhodamine probes in cell walls of poplar samples and demonstrated a strong correlation between the accessibility of probes and the saccharification yields (Herbaut et al., 2018). Overall, even if fluorescence by itself cannot be related to a single parameter (lignin content, polymer interactions,…), this can be turned into an advantage since it provides a fingerprint of lignin organization and architecture in LB, which is likely directly related to cellulose accessibility and thus to hydrolysis potential.

Water-Related Properties

Water acts as a swelling agent allowing enzymes diffusion toward plant cell wall. It has been reported that water retention value (WRV) can serve as predictor of hydrolysis rate (Noori and Karimi, 2016; Crowe et al., 2017; Williams et al., 2017; Paës et al., 2019). WRV is a complex function related to chemical and structural properties of the cell wall, such as accessible surface area and particle size. Several works reported a positive correlation between WRV and cellulose conversion rate for various lignocellulosic feedstocks: untreated maize (Li et al., 2015), pre-treated poplar, pine and miscanthus with dilute sulfuric acid (Weiss et al., 2018) and pre-treated corn stover and switchgrass with liquid hot water (Williams and Hodge, 2014). This method is rapid, simple, inexpensive, and provides results comparable to the results of more advanced methods, e.g., NMR and Simons' staining (Karimi and Taherzadeh, 2016a).

Another experimental parameter related to water that can be easily and fastly measured is the contact angle value that indirectly quantifies the hydrophobicity of lignin. This parameter could predict the inhibitory effect of lignin. Yang et al. reported that softwood lignin more hydrophobic than the hardwood lignin, was more able to absorb cellulase and inhibit enzymatic cellulose hydrolysis than the hardwood lignin (Yang and Pan, 2016).

TABLE 1 | Approaches to study the chemical and physical factors influencing LB recalcitrance.

Factors influencing LB recalcitrance			Techniques	Advantages	Disadvantages	References
Chemical factors	Cellulose	Content	Acid-detergent methods Acid-hydrolysis followed by HPLC analysis	Quantitative analysis	Under estimation of cellulose content	Herbaut et al., 2018; Krasznai et al., 2018
		Degree of polymerization (DP)	Gel Permeation Chromatography (GPC)	Dedicated method	Dissolution of cellulose can be uncomplete	Engel et al., 2012; Meng et al., 2017
			Viscometry	No calibration	Instability of cellulose in the alkaline solvent	Karimi and Taherzadeh, 2016a; Neto et al., 2016
	Hemicelluloses	Content	Acid hydrolysis followed by HPLC analysis	Robust	Methyl esterified samples non detected	Herbaut et al., 2018
		Acetyl groups	Nuclear Magnetic Resonance (NMR)	Sensitive	Sample preparation	Arai et al., 2019
			Gas Chromatography-Mass Spectrometry (GC-MS)	Robust	Sample derivative preparation	Benouadah et al., 2019
			Acid-hydrolysis followed by HPLC analysis	Rapid	Global analysis	Li et al., 2015
	Lignin	Content	Acid hydrolysis followed by Klason lignin (insoluble) and UV absorbance (acid-soluble lignin).	Simple and relatively fast	Over estimation of the soluble lignin content	Auxenfans et al., 2017a
			Acetyl bromide soluble	Rapid, simple, precise, appropriate for small sample size	Lignin standard needed Sample solubilisation	Hatfield and Fukushima, 2005
		Molecular weight	GPC	Dedicated method	Formation of aggregates	Yoo et al., 2017a
		Phenolic hydroxyl group	NMR	Fast and sensitive	Sample solubilisation	Yao et al., 2018
			Infrared spectroscopy (IR) and Raman spectroscopy	Fast and sensitive	Only chemical functions analysis	
		Structural information	NMR	In-depth information, fast and sensitive	Complex sample preparation	Yao et al., 2018
			IR	Non-invasive, easy and fast	Only chemical functions analysis	Over et al., 2017
Physical factors	Crystallinity (CrI)		NMR	In-depth information and sensitive to the crystalline phase and amorphous phase	Results highly dependent on the instrument and the method used to analyse data	Yoo et al., 2017a
			X-Ray Diffraction (XRD)	High sensitivity to the crystalline phase	Qualitative estimation and lack of precision Depending on the method used to analyse data, the CrI value can vary drastically XRD is less sensitive to the amorphous phase	Lee et al., 2015; Chen et al., 2018

(Continued)

TABLE 1 | Continued

Factors influencing LB recalcitrance	Techniques	Advantages	Disadvantages	References
	IR and Raman spectroscopy	Semi-quantitative and sensitive Minimal sample preparation	Chemometric techniques required Only relative values	Monrroy et al., 2015; Agarwal et al., 2016
	Sum-Frequency-Generation (SFG) vibration spectroscopy	Selective detection of crystalline cellulose		Barnette et al., 2011; Lee et al., 2015
Particle size	Laser granulometry	Fast and simple	Method based on the assumption that the particles are spherical, which is not always the case	Pang et al., 2018
	Scanning Electron Microscopy (SEM)	The morphology and microstructure of the particles can be observed and their sizes can be quantified	Image processing is needed	Vaidya et al., 2016; Pang et al., 2018
Accessible surface area (ASA)	Simons' staining (SS)	Can be done in wet samples, measures both internal and external surface	Semi-quantitative Measurement depends on the shape and tortuosity of the pores	Meng et al., 2017; Santos et al., 2018
	Water Retention Value (WRV)	Reflects correctly the swelling of the lignocellulosic matrix	WRV depends on the chemical composition and the structure of biomass Overestimation of ASA	Weiss et al., 2017, 2018
Pore volume	Mercury porosimetry	Provides a wide range of information: pore size distribution, total area and pore volume, average pore diameter	Suitable for macro-pores (14–200 μm) Over estimation of the pore volume (the smallest one)	Grigsby et al., 2013; Brewer et al., 2014; Meng et al., 2015
	Brunauer-Emmett-Teller (BET)	Sensitive	Over estimation of pore volume	Liu et al., 2019
	Solute exclusion	Quantitative	Does not determine accessibility of external surfaces	Ishizawa et al., 2007
	NMR cryoporometry and relaxometry NMR	Non-destructive	Requires complex setup	Meng and Ragauskas, 2014
	Thermoporometry (TP-DSC)	Simple	Over estimation of pore volume	Gustafsson et al., 2019; Kruyeniski et al., 2019
	Soft X-ray Tomography (SXT)	High resolution and quantitative information	SXT data collection is challenging	An et al., 2019
Surface morphology	SEM and Transmission electron microscopy (TEM)	High resolution 2D images. Provide qualitative and quantitative informations.	Sample preparation may damage the samples	Karimi and Taherzadeh, 2016b; Li et al., 2018
	Atomic Force Microscopy (AFM)	No sample preparation	Low scanning speed	Isaac et al., 2018

SUMMARY AND PERSPECTIVES

Biomass recalcitrance is a multi-variant and multi-scale phenomenon, and thus cannot simply be assayed by one single chemical or structural factor due to the complex and still unknown interactions between these parameters (**Figure 1**). Nonetheless, spectral analysis based on infrared and fluorescence properties of LB together with water-related characteristics seem to be able to represent chemical and structural properties of LB, thus relating nano- and macro-scale properties. Regarding future developments, the integration of large amount of data (chemical properties, images, spectra) by the means of machine learning approaches should help devising more complex models predicting not only composition but also dynamical behavior of LB over transformation such as hydrolysis. In this context, imaging and quantification of structural features at the cellular/tissular scale (by fluorescence confocal microscopy based on previous reports studying for example plant morphogenesis) or at nano-scale (by atomic force microscopy) might be relevant paths to follow.

AUTHOR CONTRIBUTIONS

AZ and GP discussed the outline, content of the article, and approved the content of the manuscript. AZ drafted the manuscript. GP finalized the manuscript.

ACKNOWLEDGMENTS

Ph.D. studentship of AZ was granted by Grand Est Region and FEDER (TECMI-4D project).

REFERENCES

Agarwal, U. P., Ralph, S. A., Reiner, R. S., and Baez, C. (2016). Probing crystallinity of never-dried wood cellulose with Raman spectroscopy. *Cellulose* 23, 125–144. doi: 10.1007/s10570-015-0788-7

Agbor, V. B., Cicek, N., Sparling, R., Berlin, A., and Levin, D. B. (2011). Biomass pretreatment: fundamentals toward application. *Biotechnol. Adv.* 29, 675–685. doi: 10.1016/j.biotechadv.2011.05.005

Aldaeus, F., Larsson, K., Srndovic, J. S., Kubat, M., Karlström, K., Peciulyte, A., et al. (2015). The supramolecular structure of cellulose-rich wood pulps can be a determinative factor for enzymatic hydrolysability. *Cellulose* 22, 3991–4002. doi: 10.1007/s10570-015-0766-0

An, S., Li, W., Liu, Q., Xia, Y., Zhang, T., Huang, F., et al. (2019). Combined dilute hydrochloric acid and alkaline wet oxidation pretreatment to improve sugar recovery of corn stover. *Bioresour. Technol.* 271, 283–288. doi: 10.1016/j.biortech.2018.09.126

Anderson, E. M., Stone, M. L., Katahira, R., Reed, M., Muchero, W., Ramirez, K. J., et al. (2019). Differences in S/G ratio in natural poplar variants do not predict catalytic depolymerization monomer yields. *Nat. Commun.* 10, 2033–2043. doi: 10.1038/s41467-019-09986-1

Arai, T., Biely, P., Uhliariková, I., Sato, N., Makishima, S., Mizuno, M., et al. (2019). Structural characterization of hemicellulose released from corn cob in continuous flow type hydrothermal reactor. *J. Biosci. Bioeng.* 127, 222–230. doi: 10.1016/j.jbiosc.2018.07.016

Auxenfans, T., Crônier, D., Chabbert, B., and Paës, G. (2017a). Understanding the structural and chemical changes of plant biomass following steam explosion pretreatment. *Biotechnol. Biofuels* 10, 36–52. doi: 10.1186/s13068-017-0718-z

Auxenfans, T., Terryn, C., and Paës, G. (2017b). Seeing biomass recalcitrance through fluorescence. *Sci. Rep.* 7, 8838–8846. doi: 10.1038/s41598-017-08740-1

Balan, V., Sousa, L. C., Chundawat, S. P., Marshall, D., Sharma, L. N., Chambliss, C. K., et al. (2009). Enzymatic digestibility and pretreatment degradation products of AFEX-treated hardwoods (*Populus nigra*). *Biotechnol. Progr.* 25, 365–375. doi: 10.1002/btpr.160

Barakat, A., Mayer-Laigle, C., Solhy, A., Arancon, R. A., De Vries, H., Luque., et al. (2014). Mechanical pretreatments of lignocellulosic biomass: towards facile and environmentally sound technologies for biofuels production. *RSC Adv.* 4, 48109–48127. doi: 10.1039/C4RA07568D

Barnette, A. L., Bradley, L. C., Veres, B. D., Schreiner, E. P., Park, Y. B., Park, J., et al. (2011). Selective detection of crystalline cellulose in plant cell walls with sum-frequency-generation (SFG) vibration spectroscopy. *Biomacromolecules* 12, 2434–2439. doi: 10.1021/bm200518n

Bekiaris, G., Lindedam, J., Peltre, C., Decker, S. R., Turner, G. B., Magid, J., et al. (2015). Rapid estimation of sugar release from winter wheat straw during bioethanol production using FTIR-photoacoustic spectroscopy. *Biotechnol. Biofuels* 8, 85–97. doi: 10.1186/s13068-015-0267-2

Benouadah, N., Aliouche, D., Pranovich, A., and Willför, S. (2019). Chemical characterization of *Pinus halepensis* sapwood and heartwood. *Wood Mater. Sci. Eng.* 14, 157–164. doi: 10.1080/17480272.2018.1448436

Bichot, A., Delgenès, J.-P., Méchin, V. H. C., Bernet, N., and Garcia-Bernet, D. (2018). Understanding biomass recalcitrance in grasses for their efficient utilization as biorefinery feedstock. *Rev. Environ. Sci. Biotechnol.* 17, 707–748. doi: 10.1007/s11157-018-9485-y

Brewer, C. E., Chuang, V. J., Masiello, C. A., Gonnermann, H., Gao, X., Dugan, B., et al. (2014). New approaches to measuring biochar density and porosity. *Biomass Bioenergy* 66, 176–185. doi: 10.1016/j.biombioe.2014.03.059

Chabbert, B., Terryn, C., Herbaut, M., Vaidya, A., Habrant, A., Paës, G., et al. (2018). Fluorescence techniques can reveal cell wall organization and predict saccharification in pretreated wood biomass. *Ind. Crops Prod.* 123, 84–92. doi: 10.1016/j.indcrop.2018.06.058

Chandel, A. K., Garlapati, V. K., Singh, A. K., Antunes, F. A. F., and da Silva, S. S. (2018). The path forward for lignocellulose biorefineries: bottlenecks, solutions, and perspective on commercialization. *Bioresour. Technol.* 264, 370–381 doi: 10.1016/j.biortech.2018.06.004

Chang, V. S., and Holtzapple, M. T. (2000). Fundamental factors affecting biomass enzymatic reactivity. *Appl. Biochem. Biotechnol.* 84, 5–37. doi: 10.1007/978-1-4612-1392-5_1

Chen, F., and Dixon, R. A. (2007). Lignin modification improves fermentable sugar yields for biofuel production. *Nat. Biotechnol.* 25, 759. doi: 10.1038/nbt1316

Chen, S., Ling, Z., Zhang, X., Kim, Y. S., and Xu, F. (2018). Towards a multi-scale understanding of dilute hydrochloric acid and mild 1-ethyl-3-methylimidazolium acetate pretreatment for improving enzymatic hydrolysis of poplar wood. *Ind. Crops Prod.* 114, 123–131. doi: 10.1016/j.indcrop.2018.02.007

Cotana, F., Cavalaglio, G., Gelosia, M., Nicolini, A., Coccia, V., Petrozzi., et al. (2014). Production of bioethanol in a second generation prototype from pine wood chips. *Energy Proc.* 45, 42–51. doi: 10.1016/j.egypro.2014.01.006

Crowe, J. D., Zarger, R. A., and Hodge, D. B. (2017). Relating nanoscale accessibility within plant cell walls to improved enzyme hydrolysis yields in corn stover subjected to diverse pretreatments. *J. Agric. Food Chem.* 65, 8652–8662. doi: 10.1021/acs.jafc.7b03240

Decker, S. R., Carlile, M., Selig, M. J., Doeppke, C., Davis, M., Sykes, R., et al. (2012). Reducing the effect of variable starch levels in biomass recalcitrance screening. *Methods Mol. Biol.* 908, 181–95, doi: 10.1007/978-1-61779-956-3_17

Decker, S. R., Harman-Ware, A. E., Happs, R. M., Wolfrum, E. J., Tuskan, G. A., Kainer, D., et al. (2018). High throughput screening technologies in biomass characterization. *Front. Energy Res.* 6:120. doi: 10.3389/fenrg.2018.00120

Decker, S. R., Sykes, R. W., Turner, G. B., Lupoi, J. S., Doepkke, C., Tucker, M. P., et al. (2015). High-throughput screening of recalcitrance variations in lignocellulosic biomass: total lignin, lignin monomers, and enzymatic sugar release. *JoVE* 103:e53163. doi: 10.3791/53163

Dias, M. O., Ensinas, A. V., Nebra, S. A., Maciel Filho, R., Rossell, C. E., and Maciel, M. R. W. (2009). Production of bioethanol and other bio-based materials from sugarcane bagasse: integration to conventional bioethanol production process. *Chem. Eng. Res Des.* 87, 1206–1216. doi: 10.1016/j.cherd.2009.06.020

Du, X., Pérez-Boada, M., Fernández, C., Rencoret, J., del Río, J. C., Jiménez-Barbero, J., et al. (2014). Analysis of lignin–carbohydrate and lignin–lignin linkages after hydrolase treatment of xylan–lignin, glucomannan–lignin and glucan–lignin complexes from spruce wood. *Planta* 239, 1079–1090. doi: 10.1007/s00425-014-2037-y

Engel, P., Hein, L., and Spiess, A. C. (2012). Derivatization-free gel permeation chromatography elucidates enzymatic cellulose hydrolysis. *Biotechnol. Biofuels* 5:77. doi: 10.1186/1754-6834-5-77

Escamez, S., Latha Gandla, M., Derba-Maceluch, M., Lundqvist, S. -O., Mellerowicz, E. J., Jönsson, L. J., et al. (2017). A collection of genetically engineered Populus trees reveals wood biomass traits that predict glucose yield from enzymatic hydrolysis. *Sci. Rep.* 7:15798. doi: 10.1038/s41598-017-16013-0

Gao, Y., Xu, J., Zhang, Y., Yu, Q., Yuan, Z., Liu., et al. (2013). Effects of different pretreatment methods on chemical composition of sugarcane bagasse and enzymatic hydrolysis. *Bioresour. Technol.* 144, 396–400. doi: 10.1016/j.biortech.2013.06.036

Giummarella, N., and Lawoko, Y. P. A. J. R. a. M. (2019). A critical review on the analysis of lignin carbohydrate bonds in plants. *Green Chem.* 21, 1573–1595. doi: 10.1039/C8GC03606C

Goshadrou, A., Karimi, K., and Lefsrud, M. (2013). Characterization of ionic liquid pretreated aspen wood using semi-quantitative methods for ethanol production. *Carbohydr. Polym.* 96, 440–449. doi: 10.1016/j.carbpol.2013.04.017

Grethlein, H. E. (1985). The effect of pore size distribution on the rate of enzymatic hydrolysis of cellulosic substrates. *Biotechnology* 3:155. doi: 10.1038/nbt0285-155

Grigsby, W. J., Kroese, H., and Dunningham, E. A. (2013). Characterisation of pore size distributions in variously dried *Pinus radiata*: analysis by thermoporosimetry. *Wood Sci. Technol.* 47, 737–747. doi: 10.1007/s00226-013-0537-8

Grohmann, K., Mitchell, D., Himmel, M., Dale, B., and Schroeder, H. (1989). The role of ester groups in resistance of plant cell wall polysaccharides to enzymatic hydrolysis. *Appl. Biochem. Biotech.* 20:45. doi: 10.1007/BF02936472

Guo, F., Shi, W., Sun, W., Li, X., Wang, F., Zhao, J., et al. (2014). Differences in the adsorption of enzymes onto lignins from diverse types of lignocellulosic biomass and the underlying mechanism. *Biotechnol. Biofuels* 7:38. doi: 10.1186/1754-6834-7-38

Gustafsson, S., Westermann, F., Hanrieder, T., Jung, L., Ruppach, H., Mihranyan., et al. (2019). Comparative analysis of dry and wet porometry methods for characterization of regular and cross-linked virus removal filter papers. *Membranes* 9:1. doi: 10.3390/membranes9010001

Hallac, B. B., and Ragauskas, A. J. (2011). Analyzing cellulose degree of polymerization and its relevancy to cellulosic ethanol. *Biofuels, Bioprod. Bioref.* 5, 215–225. doi: 10.1002/bbb.269

Harman-Ware, A. E., Davis, M. F., Peter, G. F., Wang, Y., and Sykes, R. W. (2017). Estimation of terpene content in loblolly pine biomass using a hybrid fast-GC and pyrolysis-molecular beam mass spectrometry method. *J. Anal. Appl. Pyrolysis.* 124, 343–348. doi: 10.1016/j.jaap.2017.01.011

Hassan, S. S., Williams, G. A., and Jaiswal, A. K. (2019). Moving towards the second generation of lignocellulosic biorefineries in the EU: drivers, challenges, and opportunities. *Renew. Sust. Energ. Rev*. 101, 590–599. doi: 10.1016/j.rser.2018.11.041

Hatfield, R., and Fukushima, R. S. (2005). Can lignin be accurately measured? *Crop Sci.* 45, 832–839. doi: 10.2135/cropsci2004.0238

Herbaut, M., Zoghlami, A., Habrant, A., Falourd, X., Foucat, L., Chabbert, B., et al. (2018). Multimodal analysis of pretreated biomass species highlights generic markers of lignocellulose recalcitrance. *Biotechnol. Biofuels* 11:52. doi: 10.1186/s13068-018-1053-8

Hou, S., and Li, L. (2011). Rapid characterization of woody biomass digestibility and chemical composition using near-infrared spectroscopy free access. *J. Integr. Plant Biol.* 53, 166–175. doi: 10.1111/j.1744-7909.2010.01003.x

Huang, J., Li, Y., Wang, Y., Chen, Y., Liu, M., Wang, Y., et al. (2017). A precise and consistent assay for major wall polymer features that distinctively determine biomass saccharification in transgenic rice by near-infrared spectroscopy. *Biotechnol. Biofuels* 10:294. doi: 10.1186/s13068-017-0983-x

Huang, J., Xia, T., Li, A., Yu, B., Li, Q., Tu, Y., et al. (2012). A rapid and consistent near infrared spectroscopic assay for biomass enzymatic digestibility upon various physical and chemical pretreatments in Miscanthus. *Bioresour. Technol.* 121, 274–281. doi: 10.1016/j.biortech.2012.06.015

Ioelovich, M., and Morag, E. (2011). Effect of cellulose structure on enzymatic hydrolysis. *BioResources* 6, 2818–2835. doi: 10.15376/biores.6.3.2818_2835

Isaac, A., Antunes, F. A., Conti, R., Montoro, L. A., Malachias, A., Massara, P., et al. (2018). Unveiling 3D physicochemical changes of sugarcane bagasse during sequential acid/alkali pretreatments by synchrotron phase-contrast imaging. *Ind. Crops Prod.* 114, 19–27. doi: 10.1016/j.indcrop.2018.01.028

Ishizawa, C. I., Davis, M. F., Schell, D. F., and Johnson, D. K. (2007). Porosity and its effect on the digestibility of dilute sulfuric acid pretreated corn stover. *J. Agric. Food Chem.* 55, 2575–2581. doi: 10.1021/jf062131a

Isikgor, F. H., and Becer, C. R. (2015). Lignocellulosic biomass: a sustainable platform for the production of bio-based chemicals and polymers. *Polym. Chem.* 6, 4497–4559. doi: 10.1039/C5PY00263J

Jeoh, T., Ishizawa, C. I., Davis, M. F., Himmel, M. E., Adney, W. S., and Johnson, D. K. (2007). Cellulase digestibility of pretreated biomass is limited by cellulose accessibility. *Biotechnol. Bioeng.* 98, 112–122. doi: 10.1002/bit.21408

Jiang, B., Wang, W., Gu, F., Cao, T., and Jin, Y. (2016). Comparison of the substrate enzymatic digestibility and lignin structure of wheat straw stems and leaves pretreated by green liquor. *Bioresour. Technol.* 199, 181–187. doi: 10.1016/j.biortech.2015.08.104

Jiang, J., Wang, J., Zhang, X., and Wolcott, M. (2017). Assessing multi-scale deconstruction of wood cell wall subjected to mechanical milling for enhancing enzymatic hydrolysis. *Ind. Crops Prod.* 109, 498–508. doi: 10.1016/j.indcrop.2017.09.009

Karimi, K., and Taherzadeh, M. J. (2016a). A critical review on analysis in pretreatment of lignocelluloses: degree of polymerization, adsorption/desorption, and accessibility. *Bioresour. Technol.* 203, 348–356. doi: 10.1016/j.biortech.2015.12.035

Karimi, K., and Taherzadeh, M. J. (2016b). A critical review of analytical methods in pretreatment of lignocelluloses: composition, imaging, and crystallinity. *Bioresour. Technol.* 200, 1008–18. doi: 10.1016/j.biortech.2015.11.022

Kim, S., Um, B., Im, D., Lee, J., and Oh, K. (2018). Combined ball milling and ethanol organosolv pretreatment to improve the enzymatic digestibility of three types of herbaceous biomass. *Energies* 11:2457. doi: 10.3390/en11092457

Krasznai, D. J., Champagne Hartley, R., Roy, H. M., Champagne, P., and Cunningham, M. F. (2018). Compositional analysis of lignocellulosic biomass: conventional methodologies and future outlook. *Crit. Rev. Biotechnol.* 38, 199–217. doi: 10.1080/07388551.2017.1331336

Kruyeniski, J., Ferreira, P. J., Carvalho, M. G. V. S., Vallejos, M. E., Felissia, F. E., Area, M. C., et al. (2019). Physical and chemical characteristics of pretreated slash pine sawdust influence its enzymatic hydrolysis. *Ind. Crops Prod.* 130, 528–536. doi: 10.1016/j.indcrop.2018.12.075

Kumar, A. K., and Sharma, S. (2017). Recent updates on different methods of pretreatment of lignocellulosic feedstocks: a review. *Bioresour. Bioprocess* 4:7. doi: 10.1186/s40643-017-0137-9

Kumar, R., and Wyman, C. (2009a). Effect of enzyme supplementation at moderate cellulase loadings on initial glucose and xylose release from corn stover solids pretreated by leading technologies. *Biotechnol. Bioeng.* 102, 457–467. doi: 10.1002/bit.22068

Kumar, R., and Wyman, C. E. (2009b). Cellulase adsorption and relationship to features of corn stover solids produced by leading pretreatments. *Biotechnol. Bioeng.* 103, 252–267. doi: 10.1002/bit.22258

Lee, C., Dazen, K., Kafle, K., Moore, A., Johnson, D. K., Park, S., et al. (2015). Correlations of apparent cellulose crystallinity determined by XRD, NMR, IR, Raman, and SFG methods. *Cell. Chem. Prop.* 115–131. doi: 10.1007/12_2015_320

Lee, H. V., Hamid, S. B., and Zain, S. K. (2014). Conversion of lignocellulosic biomass to nanocellulose: structure and chemical process. *ScientificWorldJournal.* 2014:631013. doi: 10.1155/2014/631013

Leu, S.-Y., and Zhu, J. (2013). Substrate-related factors affecting enzymatic saccharification of lignocelluloses: our recent understanding. *Bioenerg. Res.* 6, 405–415. doi: 10.1007/s12155-012-9276-1

Lewandowski, I., Clifton-Brown, J., Scurlock, J., and Huisman, W. (2000). Miscanthus: European experience with a novel energy crop. *Biomass Bioenergy* 19, 209–227. doi: 10.1016/S0961-9534(00)00032-5

Li, J., Lu, M., Guo, X., Zhang, H., Li, Y., Han., et al. (2018). Insights into the improvement of alkaline hydrogen peroxide (AHP) pretreatment on the enzymatic hydrolysis of corn stover: chemical and microstructural analyses. *Bioresour. Technol.* 265, 1–7. doi: 10.1016/j.biortech.2018.05.082

Li, M., Heckwolf, M., Crowe, J. D., Williams, D. L., Magee, T. D., Kaeppler, S. M., et al. (2015). Cell-wall properties contributing to improved deconstruction by alkaline pre-treatment and enzymatic hydrolysis in diverse maize (Zea mays L.) lines. *J. Exp. Bot.* 66, 4305–4315. doi: 10.1093/jxb/erv016

Li, M., Si, S., Hao, B., Zha, Y., Wan, C., Hong, S., et al. (2014). Mild alkali-pretreatment effectively extracts guaiacyl-rich lignin for high lignocellulose digestibility coupled with largely diminishing yeast fermentation inhibitors in Miscanthus. *Bioresour. Technol.* 169, 447–454. doi: 10.1016/j.biortech.2014.07.017

Li, X., Ximenes, E., Kim, Y., Slininger, M., Meilan, R., Ladisch, M., et al. (2010). Lignin monomer composition affects Arabidopsis cell-wall degradability after liquid hot water pretreatment. *Biotechnol. Biofuels* 3:27. doi: 10.1186/1754-6834-3-27

Liu, M., Wang, L., Si, M., Wang, Z., Zhang, T., Cheng, X., et al. (2019). New insight into enzymatic hydrolysis of the rice straw and poplar: an in-depth statistical analysis on the multiscale recalcitrance. *Bioenerg. Res.* 12, 1–13. doi: 10.1007/s12155-019-9959-y

Liu, Z.-H., Qin, L., Li, B.-Z., and Yuan, Y.-J. (2014). Physical and chemical characterizations of corn stover from leading pretreatment methods and effects on enzymatic hydrolysis. *ACS Sustain. Chem. Eng.* 3, 140–146. doi: 10.1021/sc500637c

Lu, M., Li, J., Han, L., and Xiao, W. (2019). An aggregated understanding of cellulase adsorption and hydrolysis for ball-milled cellulose. *Bioresour. Technol.* 273, 1–7. doi: 10.1016/j.biortech.2018.10.037

Lupoi, J. S., Singh, S., Davis, M., Lee, D. J., Shepherd, M., Simmons, B. A., et al. (2014). High-throughput prediction of eucalypt lignin syringyl/guaiacyl content using multivariate analysis: a comparison between mid-infrared, near-infrared, and Raman spectroscopies for model development. *Biotechnol. Biofuels* 7:93. doi: 10.1186/1754-6834-7-93

Lv, S., Yu, Q., Zhuang, X., Yuan, Z., Wang, W., Wang, Q., et al. (2013). The influence of hemicellulose and lignin removal on the enzymatic digestibility from sugarcane bagasse. *Bioenerg. Res.* 6, 1128–1134. doi: 10.1007/s12155-013-9297-4

Mansfield, S. D., Mooney, C., and Saddler, J. N. (1999). Substrate and enzyme characteristics that limit cellulose hydrolysis. *Biotechnol. Progr.* 15, 804–816. doi: 10.1021/bp9900864

McKendry, P. (2002). Energy production from biomass (part 1): overview of biomass. *Bioresour. Technol.* 83, 37–46. doi: 10.1016/S0960-8524(01)00118-3

Meng, X., Foston, M., Leisen, J., DeMartini, J., Wyman, C. E., and Ragauskas, A. J. (2013). Determination of porosity of lignocellulosic biomass before and after pretreatment by using Simons' stain and NMR techniques. *Bioresour. Technol.* 144, 467–476. doi: 10.1016/j.biortech.2013.06.091

Meng, X., Pu, Y., Yoo, C. G., Li, M., Bali, G., Park, D. Y., et al. (2017). An in-depth understanding of biomass recalcitrance using natural poplar variants as the feedstock. *ChemSusChem* 10, 139–150. doi: 10.1002/cssc.201601303

Meng, X., and Ragauskas, A. J. (2014). Recent advances in understanding the role of cellulose accessibility in enzymatic hydrolysis of lignocellulosic substrates. *Curr. Opin. Biotechnol.* 27, 150–158. doi: 10.1016/j.copbio.2014.01.014

Meng, X., Wells, T., Sun, Q., Huang, F., and Ragauskas, A. (2015). Insights into the effect of dilute acid, hot water or alkaline pretreatment on the cellulose accessible surface area and the overall porosity of Populus. *Green Chem.* 17, 4239–4246. doi: 10.1039/C5GC00689A

Menon, V., and Rao, M. (2012). Trends in bioconversion of lignocellulose: biofuels, platform chemicals and biorefinery concept. *Prog. Energy Combust. Sci.* 38, 522–550. doi: 10.1016/j.pecs.2012.02.002

Monrroy, M., Garcia, J. R., Troncoso, E., and Freer, J. (2015). Fourier transformed near infrared (FT-NIR) spectroscopy for the estimation of parameters in pretreated lignocellulosic materials for bioethanol production. *J. Chem. Technol. Biot.* 90, 1281–1289. doi: 10.1002/jctb.4427

Mota, T. R., Oliveira, D. M., Rogério Marchiosi, O., Ferrarese-Filho and Santos, W. D. (2018). Plant cell wall composition and enzymatic deconstruction. *Bioengineering.* 5, 63–77. doi: 10.3934/bioeng.2018.1.63

Neto, W. P. F., Putaux, J.-L., Mariano, M., Ogawa, Y., Otaguro, H., Pasquini, D., et al. (2016). Comprehensive morphological and structural investigation of cellulose I and II nanocrystals prepared by sulphuric acid hydrolysis. *RSC Adv.* 6, 76017–76027. doi: 10.1039/C6RA16295A

Noori, M. S., and Karimi, K. (2016). Detailed study of efficient ethanol production from elmwood by alkali pretreatment. *Biochem. Eng. J.* 105, 197–204. doi: 10.1016/j.bej.2015.09.019

Obst, J. R. (1982). Frequency and alkali resistance of wood lignin-carbohydrate bonds in wood. *Tappi* 65, 109–112. Available online at: https://www.fpl.fs.fed.us/products/publications/specific_pub.php?posting_id=17447

Over, L. C., Grau, E., Grelier, S., Meier, M. A., and Cramail, H. (2017). Synthesis and characterization of epoxy thermosetting polymers from glycidylated organosolv lignin and Bisphenol a. *Macromol. Chem. Phys.* 218:1600411. doi: 10.1002/macp.201600411

Paës, G., Navarro, D., Benoit, Y., Blanquet, S., Chabbert, B., Chaussepied, B., et al. (2019). Tracking of enzymatic biomass deconstruction by fungal secretomes highlights markers of lignocellulose recalcitrance. *Biotechnol. Biofuels* 12:76. doi: 10.1186/s13068-019-1417-8

Pan, X., Gilkes, N., and Saddler, J. N. (2006). Effect of acetyl groups on enzymatic hydrolysis of cellulosic substrates. *Holzforschung* 60, 398–401. doi: 10.1515/HF.2006.062

Pang, J., Zheng, M., Li, X., Sebastian, J., Jiang, Y., Zhao, Y., et al. (2018). Unlock the compact structure of lignocellulosic biomass by mild ball milling for ethylene glycol production. *ACS Sustain. Chem. Eng.* 7, 679–687. doi: 10.1021/acssuschemeng.8b04262

Papa, G., Varanasi, P., Sun, L., Cheng, G., Stavila, V., Holmes, B., et al. (2012). Exploring the effect of different plant lignin content and composition on ionic liquid pretreatment efficiency and enzymatic saccharification of *Eucalyptus globulus* L. mutants. *Bioresour. Technol.* 117, 352–359. doi: 10.1016/j.biortech.2012.04.065

Peciulyte, A., Karlström, K., Larsson, P. T., and Olsson, L. (2015). Impact of the supramolecular structure of cellulose on the efficiency of enzymatic hydrolysis. *Biotechnol. Biofuels* 8:56. doi: 10.1186/s13068-015-0236-9

Penning, B. W., Sykes, R. W., Babcock, N. C., Dugard, C. K., Held, M. A., Klimek, J. F., et al. (2014). Genetic determinants for enzymatic digestion of lignocellulosic biomass are independent of those for lignin abundance in a maize recombinant inbred population. *Plant Physiol.* 165, 1475–1487. doi: 10.1104/pp.114.242446

Pihlajaniemi, V., Sipponen, M. H., Liimatainen, H., Sirviö, J. A., Nyyssölä, A., Laakso., et al. (2016). Weighing the factors behind enzymatic hydrolyzability of pretreated lignocellulose. *Green Chem.* 18, 1295–1305. doi: 10.1039/C5GC01861G

Ragauskas, A. J., Beckham, G. T., Biddy, M. J., Chandra, R., Chen, F., Davis, M. F., et al. (2014). Lignin valorization: improving lignin processing in the biorefinery. *Science* 344:1246843. doi: 10.1126/science.1246843

Robak, K., and Balcerek, M. (2018). Review of second generation bioethanol production from residual biomass. *Food Technol. Biotech.* 56, 174–187. doi: 10.17113/ftb.56.02.18.5428

Sannigrahi, P., Ragauskas, A. J., and Tuskan, G. A. (2010). Poplar as a feedstock for biofuels: a review of compositional characteristics. *Biofuels Bioprod. Bioref.* 4, 209–226. doi: 10.1002/bbb.206

Santos, R. B., Lee, J. M., Jameel, H., Chang, H. -M., and Lucia, L. A. (2012). Effects of hardwood structural and chemical characteristics on enzymatic hydrolysis for biofuel production. *Bioresour. Technol.* 110, 232–238. doi: 10.1016/j.biortech.2012.01.085

Santos, V. T. O., Siqueira, G., Milagres, A. M. F., and Ferraz, A. (2018). Role of hemicellulose removal during dilute acid pretreatment on the cellulose accessibility and enzymatic hydrolysis of compositionally diverse sugarcane hybrids. *Ind. Crops Prod.* 111, 722–730. doi: 10.1016/j.indcrop.2017.11.053

Schmer, M. R., Vogel, K. P., Mitchell, R. B., and Perrin, R. K. (2008). Net energy of cellulosic ethanol from switchgrass. *Proc. Natl. Acad. Sci. U.S.A.* 105, 464–469. doi: 10.1073/pnas.0704767105

Selig, M. J., Tucker, M. P., Law, C., Doeppke, C., Himmel, M. E., and Decker, S. R. (2011). High throughput determination of glucan and xylan fractions in lignocelluloses. *Biotechnol. Lett.* 33, 961–967. doi: 10.1007/s10529-011-0526-7

Sharma, H. K., Xu, C., and Qin, W. (2019). Biological pretreatment of lignocellulosic biomass for biofuels and bioproducts: an overview. *Waste Biomass Valori.* 10, 235–251. doi: 10.1007/s12649-017-0059-y

Sills, D. L., and Gossett, J. M. (2012). Using FTIR to predict saccharification from enzymatic hydrolysis of alkali-pretreated biomasses. *Biotechnol. Bioeng.* 109, 353–62. doi: 10.1002/bit.23314

Silva, G. G., Couturier, M., Berrin, J. -G., Buléon, A., and Rouau, X. (2012). Effects of grinding processes on enzymatic degradation of wheat straw. *Bioresour. Technol.* 103, 192–200. doi: 10.1016/j.biortech.2011.09.073

Silvi Octavia, R. P., Arsa, P. I. D. G., and Tatang, H. (2017). Soerawidjaja: determining the enzyme accessibility of ammonia pretreated lignocellulosic substrates by Simon's Stain method. *J. Eng. Appl. Sci.* 12.

Sinitsyn, A., Gusakov, A., and Vlasenko, E. Y. (1991). Effect of structural and physico-chemical features of cellulosic substrates on the efficiency of enzymatic hydrolysis. *Appl. Biochem. Biotech.* 30, 43–59. doi: 10.1007/BF02922023

Stoffel, R. B., Felissia, F. E., Curvelo, A. A. S., Gassa, L. M., and Area, M. C. (2014). Optimization of sequential alkaline–acid fractionation of pine sawdust for a biorefinery. *Ind. Crops Prod.* 61, 160–168. doi: 10.1016/j.indcrop.2014.06.047

Studer, M. H., DeMartini, J. D., Brethauer, S., McKenzie, H. L., and Wyman, C. E. (2010). Engineering of a high-throughput screening system to identify cellulosic biomass, pretreatments, and enzyme formulations that enhance sugar release. *Biotechnol. Bioeng.* 105, 231–238. doi: 10.1002/bit.22527

Studer, M. H., DeMartini, J. D., Davis, M. F., Sykes, R. W., Davison, B., Keller, M., et al. (2011). Lignin content in natural Populus variants affects sugar release. *Proc. Natl. Acad. Sci. U.S.A.* 108, 6300–6305. doi: 10.1073/pnas.1009252108

Sykes, R. W., Gjersing, E. L., Doeppke, C. L., and Davis, M. F. (2015). High-throughput method for determining the sugar content in biomass with pyrolysis molecular beam mass spectrometry. *Bioenerg. Res.* 8, 964–972. doi: 10.1007/s12155-015-9610-5

Tarasov, D., Leitch, M., and Fatehi, P. (2018). Lignin-carbohydrate complexes: properties, applications, analyses, and methods of extraction: a review. *Biotechnol. Biofuels* 11:269. doi: 10.1186/s13068-018-1262-1

Torr, K. M., Love, K. T., Simmons, B. A., and Hill, S. J. (2016). Structural features affecting the enzymatic digestibility of pine wood pretreated with ionic liquids. *Biotechnol. Bioeng.* 113, 540–549. doi: 10.1002/bit.25831

Vaidya, A. A., Donaldson, L. A., Newman, R. H., Suckling, I. D., Campion, S. H., Lloyd, J. A., et al. (2016). Micromorphological changes and mechanism associated with wet ball milling of *Pinus radiata* substrate and consequences for saccharification at low enzyme loading. *Bioresour. Technol.* 214, 132–137. doi: 10.1016/j.biortech.2016.04.084

Weiss, N. D., Felby, C., and Thygesen, L. G. (2018). Water retention value predicts biomass recalcitrance for pretreated lignocellulosic materials across feedstocks and pretreatment methods. *Cellulose* 25, 3423–3434. doi: 10.1007/s10570-018-1798-z

Weiss, N. D., Thygesen, L. G., Felby, C., Roslander, C., and Gourlay, K. (2017). Biomass-water interactions correlate to recalcitrance and are intensified by pretreatment: an investigation of water constraint and retention in pretreated spruce using low field NMR and water retention value techniques. *Biotechnol. Progr.* 33, 146–153. doi: 10.1002/btpr.2398

Williams, D. L., Crowe, J. D., Ong, R. G., and Hodge, D. B. (2017). Water sorption in pretreated grasses as a predictor of enzymatic hydrolysis yields. *Bioresour. Technol.* 245, 242–249. doi: 10.1016/j.biortech.2017.08.200

Williams, D. L., and Hodge, D. B. (2014). Impacts of delignification and hot water pretreatment on the water induced cell wall swelling behavior of grasses and its relation to cellulolytic enzyme hydrolysis and binding. *Cellulose* 21, 221–235. doi: 10.1007/s10570-013-0149-3

Xu, H., Che, X., Ding, Y., Kong, Y., Li, B., Tian., et al. (2019). Effect of crystallinity on pretreatment and enzymatic hydrolysis of lignocellulosic biomass based on multivariate analysis. *Bioresour. Technol.* 279, 271–280. doi: 10.1016/j.biortech.2018.12.096

Xu, N., Zhang, W., Ren, S., Liu, F., Zhao, C., Liao, H., et al. (2012). Hemicelluloses negatively affect lignocellulose crystallinity for high biomass digestibility under NaOH and H 2 SO 4 pretreatments in Miscanthus. *Biotechnol. Biofuels* 5:58. doi: 10.1186/1754-6834-5-58

Yang, Q., and Pan, X. (2016). Correlation between lignin physicochemical properties and inhibition to enzymatic hydrolysis of cellulose. *Biotechnol. Bioeng.* 113, 1213–1224. doi: 10.1002/bit.25903

Yao, L., Yoo, C. G., Meng, X., Li, M., Pu, Y., Ragauskas, A. J., et al. (2018). A structured understanding of cellobiohydrolase I binding to poplar lignin fractions after dilute acid pretreatment. *Biotechnol. Biofuels* 11:96. doi: 10.1186/s13068-018-1087-y

Yoo, C. G., Dumitrache, A., Muchero, W., Natzke, J., Akinosho, H., Li, M., et al. (2017b). Significance of lignin S/G ratio in biomass recalcitrance of populus trichocarpa variants for bioethanol production. *ACS Sustain. Chem. Eng.* 6, 2162–2168. doi: 10.1021/acssuschemeng.7b03586

Yoo, C. G., Yang, Y., Pu, Y., Meng, X., Muchero, W., Yee, K. L., et al. (2017a). Insights of biomass recalcitrance in natural *Populus trichocarpa* variants for biomass conversion. *Green Chem.* 19, 5467–5478. doi: 10.1039/C7GC02219K

Yoshida, M., Liu, Y., Uchida, S., Kawarada, K., Ukagami, Y., Ichinose, H., et al. (2008). Effects of cellulose crystallinity, hemicellulose, and lignin on the enzymatic hydrolysis of Miscanthus sinensis to monosaccharides. *Biosci. Biotechnol. Biochem.* 72, 805–810. doi: 10.1271/bbb.70689

Yu, H., Xiao, W., Han, L., and Huang, G. (2019). Characterization of mechanical pulverization/phosphoric acid pretreatment of corn stover for enzymatic hydrolysis. *Bioresour. Technol.* 282, 69–74. doi: 10.1016/j.biortech.2019.02.104

Yu, Z., Gwak, K. S., Treasure, T., Jameel, H., Chang, H., M., and Park, S. (2014). Effect of lignin chemistry on the enzymatic hydrolysis of woody biomass. *ChemSusChem* 7, 1942–1950. doi: 10.1002/cssc.201400042

Yuan, Z., Wen, Y., and Li, G. (2018). Production of bioethanol and value added compounds from wheat straw through combined alkaline/alkaline-peroxide pretreatment. *Bioresour. Technol.* 259, 228–236 doi: 10.1016/j.biortech.2018.03.044

Zeng, Y., Zhao, S., Yang, S., and Ding, S.-Y. (2014). Lignin plays a negative role in the biochemical process for producing lignocellulosic biofuels. *Curr. Opin. Biotechnol.* 27, 38–45. doi: 10.1016/j.copbio.2013.09.008

Zhang, H., Li, J., Huang, G., Yang, Z., and Han, L. (2018). Understanding the synergistic effect and the main factors influencing the enzymatic hydrolyzability of corn stover at low enzyme loading by hydrothermal and/or ultrafine grinding pretreatment. *Bioresour. Technol.* 264, 327–334. doi: 10.1016/j.biortech.2018.05.090

Zhao, X., Zhang, L., and Liu, D. (2012a). Biomass recalcitrance. Part II: fundamentals of different pre-treatments to increase the enzymatic digestibility of lignocellulose. *Biofuels Bioprod. Bioref.* 6, 561–579. doi: 10.1002/bbb.1350

Zhao, X., Zhang, L., and Liu, D. (2012b). Biomass recalcitrance. Part I: the chemical compositions and physical structures affecting the enzymatic hydrolysis of lignocellulose. *Biofuels, Bioprod. Bioref.* 6, 465–482. doi: 10.1002/bbb.1331

Zhu, L., O'Dwyer, J. P., Chang, V. S., Granda, C. B., and Holtzapple, M. T. (2008). Structural features affecting biomass enzymatic digestibility. *Bioresour. Technol.* 99, 3817–3828. doi: 10.1016/j.biortech.2007.07.033

Conflict of Interest: The authors declare that the research was conducted in the absence of any commercial or financial relationships that could be construed as a potential conflict of interest.

Copyright © 2019 Zoghlami and Paës. This is an open-access article distributed under the terms of the Creative Commons Attribution License (CC BY). The use, distribution or reproduction in other forums is permitted, provided the original author(s) and the copyright owner(s) are credited and that the original publication in this journal is cited, in accordance with accepted academic practice. No use, distribution or reproduction is permitted which does not comply with these terms.

ORIGINAL RESEARCH
published: 28 January 2020
doi: 10.3389/fchem.2020.00011

Quantitative Comparison of Pyranose Dehydrogenase Action on Diverse Xylooligosaccharides

Johanna Karppi[1], Hongbo Zhao[2], Sun-Li Chong[2,3], Antti E. Koistinen[1], Maija Tenkanen[2] and Emma Master[1,4]*

[1] Department of Bioproducts and Biosystems, Aalto University, Espoo, Finland, [2] Department of Food and Nutrition, University of Helsinki, Helsinki, Finland, [3] State Key Laboratory of Subtropical Silviculture, Zhejiang A&F University, Hangzhou, China, [4] Department of Chemical Engineering and Applied Chemistry, University of Toronto, Toronto, ON, Canada

OPEN ACCESS

Edited by:
Caroline Remond,
Université de Reims
Champagne-Ardenne, France

Reviewed by:
Dietmar Haltrich,
University of Natural Resources and
Life Sciences Vienna, Austria
Paul-Henri Ducrot,
INRA UMR1318 Institut Jean Pierre
Bourgin, France

***Correspondence:**
Emma Master
emma.master@utoronto.ca

Specialty section:
This article was submitted to
Chemical and Process Engineering,
a section of the journal
Frontiers in Chemistry

Received: *07 October 2019*
Accepted: *07 January 2020*
Published: *28 January 2020*

Citation:
Karppi J, Zhao H, Chong S-L,
Koistinen AE, Tenkanen M and
Master E (2020) Quantitative
Comparison of Pyranose
Dehydrogenase Action on Diverse
Xylooligosaccharides.
Front. Chem. 8:11.
doi: 10.3389/fchem.2020.00011

Pyranose dehydrogenases (PDHs; EC 1.1.99.29; AA3_2) demonstrate ability to oxidize diverse carbohydrates. Previous studies of these enzymes have also uncovered substrate-dependent regioselectivity, along with potential to introduce more than one carbonyl into carbohydrate substrates. Enzymatic oxidation of carbohydrates facilitates their further derivatization or polymerization into bio-based chemicals and materials with higher value; accordingly, PDHs that show activity on xylooligosaccharides could offer a viable approach to extract higher value from hemicelluloses that are typically fragmented during biomass processing. In this study, AbPDH1 from *Agaricus bisporus* and AmPDH1 from *Leucoagaricus meleagris* were tested using linear xylooligosaccharides, along with xylooligosaccharides substituted with either arabinofuranosyl or 4-*O*-(methyl)glucopyranosyluronic acid residues with degree of polymerization of two to five. Reaction products were characterized by HPAEC-PAD to follow substrate depletion, UPLC-MS-ELSD to quantify the multiple oxidation products, and ESI-MS^n to reveal oxidized positions. A versatile method based on product reduction using sodium borodeuteride, and applicable to carbohydrate oxidoreductases in general, was established to facilitate the identification and quantification of oxidized products. AbPDH1 activity toward the tested xylooligosaccharides was generally higher than that measured for AmPDH1. In both cases, activity values decreased with increasing length of the xylooligosaccharide and when using acidic rather than neutral substrates; however, AbPDH1 fully oxidized all linear xylooligosaccharides, and 60–100% of all substituted xylooligosaccharides, after 24 h under the tested reaction conditions. Oxidation of linear xylooligosaccharides mostly led to double oxidized products, whereas single oxidized products dominated in reactions containing substituted xylooligosaccharides. Notably, oxidation of specific secondary hydroxyls vs. the reducing end C-1 depended on both the enzyme and the substrate. For all substrates, however, oxidation by both AbPDH1 and AmPDH1 was clearly restricted to the reducing and non-reducing xylopyranosyl residues, where increasing the length of the xylooligosaccharide did not lead to detectable oxidation of internal xylopyranosyl substituents. This detailed analysis of AbPDH1 and AmPDH1 action on diverse xylooligosaccharides reveals an opportunity to synthesize bifunctional molecules directly from hemicellulose fragments, and to enrich for specific products through appropriate PDH selection.

Keywords: carbohydrate oxidoreductases, pyranose dehydrogenase, xylooligosaccharide, degree of oxidation, telechelic molecules

INTRODUCTION

Hemicelluloses comprise a diverse group of polysaccharides present in plant cell walls, and are thought to strengthen cell wall structures through interactions with both cellulose and lignin (Ebringerová, 2006; Scheller and Ulvskov, 2010). Xylans are the dominant hemicellulose in cell walls of both grasses and deciduous trees. In deciduous trees, the main xylan is glucuronoxylan, where the β-(1→ 4)-linked D-xylopyranose (Xyl*p*) backbone can be substituted with 4-*O*-methylated glucopyranosyluronic acid (MeGlc*p*A); the Xyl*p* backbone can also be acetylated (Ebringerová, 2006; Scheller and Ulvskov, 2010). Arabinoxylans (AXs) are the main xylans in grasses, where the Xyl*p* backbone can be substituted with L-arabinofuranose (Ara*f*). In addition to Ara*f*, arabinoglucuronoxylans found in cell walls of both grasses and coniferous trees, contain glucuronic acid and MeGlc*p*A substitutions (Scheller and Ulvskov, 2010).

So far, biocatalysts that transform hemicelluloses have mainly been studied and developed to deconstruct corresponding polysaccharides to sugars that can be fermented to fuels and chemicals (Chundawat et al., 2011). These enzymes include glycoside hydrolases (GHs), carbohydrate esterases (CEs), and auxiliary activities (AAs) that are classified by the Carbohydrate-active enzyme (CAZy) database (www.cazy.org) into multiple GH, CE, and AA families (Lombard et al., 2014). Alternatively, enzymatic functionalization of hemicelluloses, including oligosaccharides liberated during lignocellulose processing, opens new possibilities to make high value bioproducts that retain the carbon and energy stored in starting carbohydrate structures.

Carbohydrate oxidoreductases that act on hemicelluloses without cleaving them are attractive targets for further functionalization (Parikka et al., 2012). Among these are AA3 and AA7 FAD-containing oxidoreductases. Briefly, AA7 activity is restricted to the anomeric carbon of carbohydrate substrates (Huang et al., 2005; Vuong et al., 2013); the resulting lactone undergoes spontaneous ring-opening to the carboxylic acid that can be used in polymerization reactions (MacCormick et al., 2018). On the other hand, AA3 oxidoreductases are reported to oxidize the anomeric carbon and secondary hydroxyls to carboxylic acid or ketone functional groups, respectively (Giffhorn et al., 2000; Levasseur et al., 2013; Sützl et al., 2018). Based on phylogenetic analyses, AA3 sequences have been divided into four subfamilies, including activities such as cellobiose dehydrogenase, alcohol oxidase and pyranose oxidase in subfamilies 1, 3, and 4, respectively. Subfamily 2 is the most complex one of these, comprising enzymes with aryl-alcohol oxidase, aryl-alcohol dehydrogenase, glucose oxidase, glucose dehydrogenases, or pyranose dehydrogenase (PDH) activities (Levasseur et al., 2013; Sützl et al., 2018). From these, AA3_2 PDHs have been shown to oxidize several monosaccharides and some oligosaccharides through single or double oxidation and substrate dependent regioselectivity (Peterbauer and Volc, 2010; Rafighi et al., 2018), which increases their attractiveness on oligosaccharide modification.

PDHs have been found in a narrow group of litter-decomposing fungi within the fungal division Basidiomycota (Peterbauer and Volc, 2010). These extracellular enzymes contain two domains, an FAD-binding and substrate-binding domain (Tan et al., 2013). The active site contains two conserved histidines. His512 of AmPDH1 from *Leucoagaricus meleagris* acts as the main base in the first reductive half-reaction and His556 together with Gln392 and Tyr510 take part in substrate interactions that likely influence the observed substrate specific regioselectivity (Graf et al., 2013, 2015; Tan et al., 2013). After the first half-reaction, the reduced flavin is oxidized by an electron acceptor which acts as the second substrate in the reaction. Along with AmPDH1, AbPDH1 from *Agaricus bisporus* are the two most studied PDHs. AbPDH1 and AmPDH1 oxidize D-xylose to 2,3-diketo-D-xylose (Volc et al., 2000; Sedmera et al., 2006) and display slightly higher relative activity toward D-xylose compared to D-glucose (Volc et al., 2000; Sedmera et al., 2006). In addition to D-xylose, AmPDH1 was shown to oxidize xylobiose (X_2) (Sygmund et al., 2008). PDH activity on oligosaccharides with degree of polymerization (DP) greater than two has been tested using cello- and maltooligosaccharides. Those studies confirm that AbPDH1 and AmPDH1 are both active toward cellotetraose and maltotriose (Volc et al., 1997; Peterbauer and Volc, 2010), and that AmPDH1 is also active toward maltooligosaccharides up to maltoheptaose (Tasca et al., 2007; Peterbauer and Volc, 2010; Rafighi et al., 2018). Among the characterized PDHs, AmPDH1 showed highest catalytic efficiency (k_{cat}/K_m) toward D-xylose (Sygmund et al., 2012), whereas AbPDH1 showed highest catalytic efficiency toward cellobiose, maltose and lactose (Gonaus et al., 2016).

PDH action toward xylooligosaccharides common to hardwood and agricultural resources has not been investigated. Herein, AbPDH1 and AmPDH1 were directly compared in terms of activity toward linear and substituted xylooligosaccharides, and ability to oxidize corresponding substrates at more than one position to create a new class of telechelic building blocks. The analysis of corresponding oligosaccharide products is complicated by the multiple hydroxyl groups that could potentially be oxidized. Moreover, the oxidized products are inherently unstable in water because they can further transform into various end products. For example, oxidation of the anomeric carbon leads to a lactone which spontaneously hydrolyzes to the carboxylic acid in water (Vuong et al., 2013). Furthermore, secondary hydroxyls that are oxidized to ketones and primary hydroxyls that are oxidized to aldehydes, exist primarily as hydrates (geminal diols) in water (Volc et al., 2002; Andberg et al., 2017). In this study, a new analytical method was developed to simplify and clarify the analysis of oxidized xylooligosaccharides utilizing deuterium to label the oxidized position. By following the deuterated residues by HILIC-MS-ELSD and ESI-MS^n, the oxidation positions were identified and the proportion of each reaction product was quantified. Both AbPDH1 and AmPDH1 were shown to oxidize X_2, xylotriose (X_3) and xylotetraose (X_4) with and without Ara*f* substitution; however, activity toward acidic glucuronoxylooligosaccharides was 10-times lower than with neutral substrates.

MATERIALS AND METHODS

Materials

Below mentioned growth medium chemicals, yeast extract, yeast nitrogen base, and peptone were purchased from Lab M Ltd. (UK). Salts and vitamins were obtained from Sigma-Aldrich or Merck (Germany). Neutral substrates X_2, X_3, X_4, 3^2-α-L-arabinofuranosyl-xylobiose (A^3X), 2^3-α-L-arabinofuranosyl-xylotriose (A^2XX), 3^3-α-L-arabinofuranosyl-xylotetraose (XA^3XX) were purchased from Megazyme (UK). 2^3-(4-*O*-methyl-α-D-glucuronyl)-xylotriose ($U^{4m2}XX$) and 2^3-(4-*O*-methyl-α-D-glucuronyl)-xylotetraose ($XU^{4m2}XX$) substrates were prepared as in Koutaniemi et al. (2012) by Dr. T. Vuong, University of Toronto and Dr. S. Koutaniemi, University of Helsinki and kindly provided to the study. The commercial laccase from *Trametes versicolor* (Sigma-Aldrich, Germany) was used in oxidation reactions (described below) to recycle 1,4-benzoquinone (BQ; Sigma-Aldrich, Germany) electron acceptor.

PDH Production and Purification

Agaricus bisporus and *Agaricus meleagris* pyranose dehydrogenases (AbPDH1 and AmPDH1; pyranose:acceptor oxidoreductase, EC 1.1.99.29, CAZy family AA3_2) were expressed in *Pichia pastoris* strain KM71H. Codon optimized genes encoding AbPDH1 and AmPDH1 amino acid sequences (AAW92124 and AAW82997, respectively) were obtained as subcloned in pPICZB plasmids with C-terminal 6 x His tag (GenScript, New Jersey, USA). PDHs were produced in eight 2 l shake-flasks each containing 250 ml of medium. Precultures were grown over night in buffered glycerol-complex medium [BMGY; 100 mM potassium phosphate buffer, pH 6.0, 2% (w/v) peptone, 1% (w/v) yeast extract, 1.34% (w/v) yeast nitrogen base, 4×10^{-5}% (w/v) biotin, 1% (v/v) glycerol] at 30°C and 220 rpm. Cells were then transferred to methanol-complex medium (BMMY) containing 0.5% (v/v) methanol instead of glycerol. Methanol was added to 0.5% (v/v) every 24 h and induction was continued 4 d at 25°C and 220 rpm. After the induction, culture supernatants were recovered and filtered, and the secreted recombinant proteins were purified by affinity chromatography; AbPDH1 was further purified by anion exchange and size exclusion (**Figure S2**). Final protein concentrations were measured using the Bradford method (Bio-Rad Laboratories, US); purified proteins were then aliquoted and stored in −80°C.

Initial Activity Measurements

To select the optimal conditions for the xylooligosaccharide oxidation, the activity of AbPDH1 and AmPDH1 was screened at 30°C with 25 mM substrate (D-xylose or D-glucose) and 5 mM BQ in 50 mM sodium acetate, 50 mM ammonium acetate (at pH values 3.0–5.5), and in 50 mM sodium phosphate (at pH values 6.0–7.0) buffers. Reduction of BQ ($\varepsilon_{abs290nm} = 2.24\ mM^{-1}\ cm^{-1}$) in 250 μl reaction was followed at 290 nm; all reactions were performed in triplicate.

Enzyme loading for PDH conversion of xylooligosaccharides was based on activity units determined in 50 mM ammonium acetate buffer (pH 5.5). PDH activity was measured using 25 mM D-xylose and 5 mM BQ similarly as mentioned above. Laccase activity was measured using 5 mM hydroquinone (HQ, Sigma Aldrich, Germany), and oxidation of HQ ($\varepsilon_{abs249} = 17.25\ mM^{-1}\ cm^{-1}$) in 250 μl reaction was followed at 249 nm.

Initial AbPDH1 and AmPDH1 activity toward xylooligosaccharides was measured using 10 mM neutral or 2 mM of acidic substrates, and 0.2 mM ferrocenium hexafluorophosphate (Fc+, Sigma Aldrich, Germany) as the electron acceptor. Reactions (100 μl) were performed at 30°C in 50 mM sodium phosphate buffer (pH 7.5), and the reduction of the Fc+ ion ($\varepsilon_{abs250nm} = 10.6\ mM^{-1}\ cm^{-1}$) was measured for up to 1 h at 250 nm. All the activity measurements were followed using an Eon plate reader (BioTek, USA).

Enzymatic Conversion of Xylooligosaccharides

Reactions (30–400 μl reaction volume in 1.5 ml Eppendorf tubes) were performed at 30°C for up to 48 h with shaking (500 rpm) in 10 mM ammonium-acetate buffer (pH 5.5) containing 1 mM BQ as the electron acceptor, and 5 mM of neutral xylooligosaccharides or 4 mM of acidic xylooligosaccharides (**Table 1**). Enzyme loadings for reactions containing neutral xylooligosaccharides were 50 mU of AbPDH or AmPDH, and 50 mU of *T. versicolor* laccase. Enzyme loadings for reactions containing acidic xylooligosaccharides were 800 mU of AbPDH1 or AmPDH1, and 800 mU of *T. versicolor* laccase. Time course sampling (25 or 10 μl) for the HPAEC-PAD analyses was done at 1, 4, and 8 h for the neutral substrates and 24 h for acidic substrates. Total reaction time was 24 or 48 h. Oxygen availability was not controlled during the reactions. Reactions were stopped by filtrating the samples through 10 kDa cut off Vivaspin 500 spin columns (Sartorius, Germany) and then kept frozen at −80°C before analysis by High-Performance Anion-Exchange Chromatography Coupled

TABLE 1 | Structures of xylooligosaccharides and oxidation reaction details.

Substrate	Substrate (mM)	PDH (U/ml)	Reaction[a] time (h)
Xylobiose (X_2) 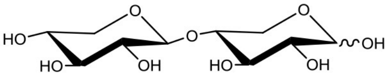	5	0.2	Up to 24
Xylotriose (X_3) 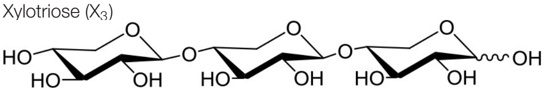	5	0.2	Up to 24
Xylotetraose (X_4) 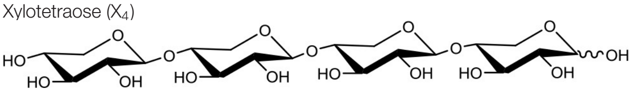	5	0.2	Up to 24
3^2-α-L-arabinofuranosyl-xylobiose (A^3X) 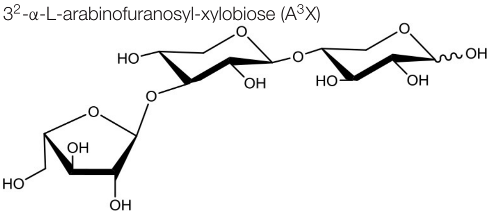	5	0.2	Up to 24
2^3-α-L-arabinofuranosyl-xylotriose (A^2XX) 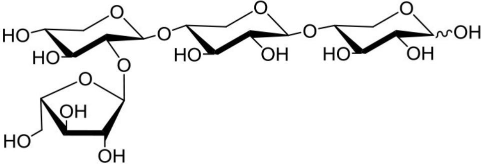	5	0.2	Up to 24
3^3-α-L-arabinofuranosyl-xylotetraose (XA^3XX) 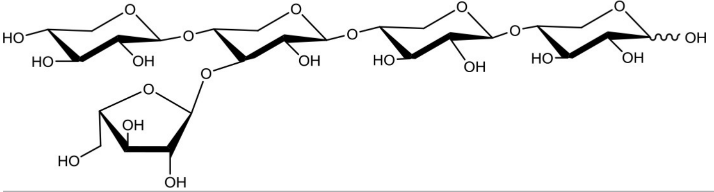	5	0.2	Up to 24
2^3-(4-*O*-methyl-α-D-glucuronyl)-xylotriose ($U^{4m2}XX$) 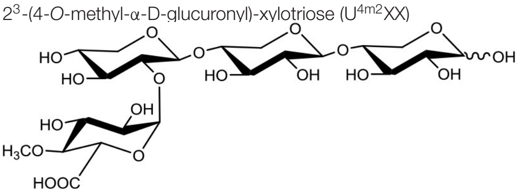	4 4	0.2 2	Up to 48 Up to 24
2^3-(4-*O*-methyl-α-D-glucuronyl)-xylotetraose ($XU^{4m2}XX$) 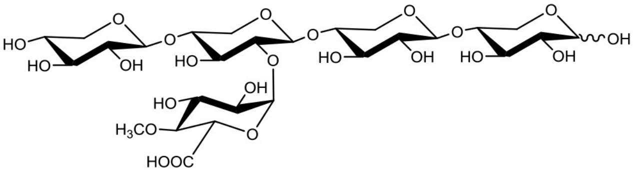	4 4	0.2 2	Up to 48 Up to 24

[a] *All the reactions contained 0.2 U/ml of laccase and 1 mM BQ as electron acceptor.*

with Pulsed Electrochemical Detection (HPAEC-PAD) and mass spectrometry as described below.

Quantification of Substrate Depletion by HPAEC-PAD

Products of reactions described above (section *Enzymatic Conversion of Xylooligosaccharides*) were diluted in ultrapure water to 50–100 ppm concentrations depending on the sensitivity of substrate detection by HPAEC-PAD. Substrate depletion over the course of the reaction was followed using a DionexTM-5000^{+} system equipped with a Dionex^{TM} CarboPac^{TM} PA1 IC column and corresponding precolumn (Thermo Scientific, USA). The samples were eluted at 1 ml/min with eluent A (0.1 M NaOH) in a linear gradient toward an increasing proportion of eluent B (1 M NaOAc in 0.1 M NaOH). The gradient reached 21.7% B at 20 min after injection, 38% B at 25 min and 100% B at 27 min after which it was kept at 100% for 7 min. Data were analyzed using the Thermo Scientific Dionex Chromeleon 7 Chromatography Data System (version 7.2 SR4, Thermo Fisher Scientific). Corresponding xylooligosaccharides with three known concentrations were used to create a standard curve for each run. Integrated peak areas of the enzyme treated xylooligosaccharides were compared against the corresponding control reactions without the PDH enzyme.

Mass Spectrometric Analysis of Oxidized Products by Direct Infusion

A 5 µl sample from 24 h reactions described above (section *Enzymatic Conversion of Xylooligosaccharides*) was mixed with 5 µl of 10 mg/ml NH_4Cl and 500 µl 50% acetonitrile (ACN) in water. Each sample solution was then introduced into Quadruple Time-of-flight (Q-Tof) mass spectrometry with an ESI source (SYNAPT G2-Si, Waters, MA, USA) at a flow rate of 5 µl/min. The capillary was set to 3 kV; source temperature to 80°C and desolvation temperature to 150°C. The cone gas was 100 l/h and desolvation gas was 600 l/h with nebulizer set at 6.5 bar. The analysis was done in negative mode and the ions were collected in *m/z* range of 50–800. The products of acidic xylooligosaccharides oxidized by 2 U/ml PDH for 24 h were analyzed directly by ESI-Q-Tof-MS without the addition of NH_4Cl.

Identification of Oxidized Positions Through Fragmentation Analysis of Products After $NaBD_4$ Reduction

The multiple potential oxidations and reactivity of oxidized products in water complicate the interpretation of MS spectra. Therefore, after confirming the production of oxidized xylooligosaccharides by direct infusion mass spectrometry, reaction products were reduced using $NaBD_4$ to facilitate their identification. Specifically, $NaBD_4$ was added to the 24 h reactions described above (section *Enzymatic Conversion of Xylooligosaccharides*) at 3 mol equivalent $NaBD_4$ per mole of substrate in the initial reaction; the resulting solution was then stirred overnight to reduce the carbonyls back to hydroxyls.

After reduction, samples were desalted using Porous Graphitic Carbon (PGC) columns (Hyper carb PGC 50 mg, Thermo Fisher, MA, USA). Briefly, a column was pre-washed with 0.1% trifluoroacetic acid (TFA) 80% ACN and water before loading a sample. The impurities were washed away with Milli Q water and the reaction products were eluted with 50% ACN. The purified samples were then lyophilized, dissolved in 200 µl MilliQ-water, and diluted to 10 µg/ml using 50% ACN, after which ammonium chloride (10 mg/ml) was added to a final concentration of 40 µg /ml. The negative ion MS and MS^n spectra were obtained by direction infusion of the solutions to the Finnigan LXQ Ion Trap (IT) mass spectrometer equipped with ESI source (Thermo Fisher, MA, USA) at a flow rate of 5 µl/min. The parameters were automatically tuned by the instrument based on X_3. The collision energy for fragmentation was optimized based on each substrate.

X_2 and its oxidized products after reduction were not successfully purified by the PGC column. Instead, they were analyzed by Acquity Ultra High Performance Liquid Chromatography (UPLC) coupled to an ESI-Q-Tof mass spectrometer (Waters, MA. USA) as described in **Figure S12**.

Quantification of Oxidized Products by UPLC-ESI-Q-Tof-MS and UPLC Evaporative Light Scattering Detection (ELSD)

The reaction products after $NaBD_4$ reduction and PGC purification were quantified using an Acquity UPLC coupled with ELSD (Waters, MA, USA). A 1.7 µm, 2.1*150 mm Acquity UPLC BEH Amide column (Waters, MA, USA) was used to separate the reaction products. The mobile phases were (A) ACN with 0.1% ammonium hydroxide and (B) 20% ACN with 0.1% ammonium hydroxide. The elution gradient was as follows: from 96% ACN to 50% ACN in 10 min, isocratic (50% ACN) for 2 min, back to 96% ACN in 0.01 min, and 18 min re-equilibrium in initial conditions. The flow was at 250 µl/min with column temperature at 35°C. The ELSD drift tube temperature was set to 40°C and the gain to 200. The nebulizer was set to cooling and pressure to 40 psi. Reaction products were diluted with pure ACN to ∼3,000 ng of reaction products per 7 µl of injected sample. External standards were made by reducing and purifying the pure substrates using the PGC column as described in section *Identification of Oxidized Positions Through Fragmentation Analysis of Products After $NaBD_4$ Reduction*. Standard curves were made by injecting 200–3,750 ng of each reduced substrate for each injection. The Acquity UPLC coupled with ESI-Q-Tof-MS was used to identify the peaks in ELSD chromatogram. The parameters for ESI-Q-Tof were set to the same as mentioned in section *Mass Spectrometric Analysis of Oxidized Products by Direct Infusion*, except that the desolvation temperature was set to 400°C. Quantitative analysis of the reaction products using the UPLC-ELSD and mass spectra collected in section *Identification of Oxidized Positions Through Fragmentation Analysis of Products After $NaBD_4$ Reduction* was then achieved as described below (section *Quantitative Interpretation of Mass Spectra*).

Quantitative Interpretation of Mass Spectra

Following $NaBD_4$ reduction of oxidized xylooligosaccharides, the same *m/z* value can be obtained for isotopic non-oxidized xylooligosaccharides and specific oxidized products. For example, the monoisotopic mass of X_3 has an *m/z* of 452, and the naturally present isotopic chloride, carbon, hydrogen and oxygen generate *m/z* values of 453 and 454. At the same time, single oxidation of a secondary hydroxyl in X_3 followed by $NaBD_4$ reduction will also generate a peak at *m/z* 453, and double oxidation of secondary hydroxyls in X_3 followed by $NaBD_4$ reduction will generate a peak at *m/z* 454 (**Figure S1**). Therefore, the following system of equations (Equations 1–4) was established to calculate the percent of single oxidized and double oxidized products, taking into account the abundance of naturally present isotopic substrate:

$$\begin{aligned}&\text{Abundance of isotopic } m/z \text{ for a given reduced oligosaccharide}\\&= \text{abundance of non-oxidized oligosaccharide}\\&+ \text{abundance of single oxidized oligosaccharide}\\&+ \text{abundance of double oxidized oligosaccharide}\\&= a + \left(b - a \times r1 \div 100\right)\\&+ \left\{c - a \times r2 \div 100 - \left(b - a \times r1 \div 100\right) \times r1 \div 100\right\} \qquad (1)\end{aligned}$$

where a, b, and c are the abundance of *m/z* values corresponding to non-oxidized, single oxidized, and double oxidized oligosaccharides in reactions following enzymatic oxidation (e.g., *m/z* 452, 453, and 454, respectively, for X_3); and r1 and r2 are the abundances of corresponding *m/z* values naturally present the isotopic substrate.

Therefore:

$$\begin{aligned}\text{Non-oxidation\%} = {}& 100\% - \text{single oxidation\%}\\&- \text{double oxidation\%} \qquad (2)\end{aligned}$$

where:

$$\begin{aligned}&\text{Single oxidation\%}\\&= \frac{\text{Abundance of single oxidized oligosaccharide}}{\text{Abundance of isotopic } m/z \text{ for a given reduced oligosaccharide}}\\&\times 100\% \qquad (3)\end{aligned}$$

$$\begin{aligned}&\text{Double oxidation\%}\\&= \frac{\text{Abundance of double oxidized oligosaccharide}}{\text{Abundance of isotopic } m/z \text{ for a given reduced oligosaccharide}}\\&\times 100\% \qquad (4)\end{aligned}$$

When an oligosaccharide is oxidized at the reducing end C-1, the reaction product containing the carboxyl acid forms an anionic, deprotonated species. For example, X_3 oxidized at the C-1 position will have an *m/z* of 429. Herein, the theoretical isotopic distribution of C-1 oxidized oligosaccharides was generated by Masslynx V4.1. When additional oxidations take place at the secondary hydroxyls, the deuterium label would increase the corresponding *m/z* value by a corresponding number of Daltons.

Therefore, Equations (1)–(4) can be extended by Equations (5)–(8), to calculate the extent of oxidized products with at least one oxidation at the reducing end C-1:

$$\begin{aligned}&\text{Abundance of isotopic m/z for a given oligosaccharide}\\&\text{oxidized at the reducing end C-1}\\&= \text{abundance of C-1 oxidized oligosaccharide}\\&+ \text{abundance of double oxidized oligosaccharide}\\&+ \text{abundance of triple oxidized oligosaccharide}\\&= a' + \left(b' - a' \times r1' \div 100\right)\\&+ \left\{c' - a' \times r2' \div 100 - \left(b' - a' \times r1' \div 100\right) \times r1' \div 100\right\} \qquad (5)\end{aligned}$$

where a′, b′, and c′ are the abundance of *m/z* values corresponding to C-1 oxidized, C-1 oxidized + single oxidation at a secondary hydroxyl, and C-1 oxidized + double oxidation at secondary hydroxyls (e.g., *m/z* 429, 430, and 431, respectively, for X_3); and r1′ and r2′ are the relative abundance of theoretically generated isotopic oligosaccharide with one oxidation at reducing end C-1.

In this case, the double oxidation consists of one reducing end C-1 oxidation and one secondary hydroxyl oxidation, and a the triple oxidation consists of one reducing end C-1 oxidation and two secondary hydroxyl oxidation.

Therefore:

$$\begin{aligned}\text{Reducing end C-1 oxidation\%} = {}& 100\% - \text{double oxidation\%}\\&- \text{triple oxidation\%} \qquad (6)\end{aligned}$$

where:

$$\begin{aligned}&\text{Double oxidation\%}\\&= \frac{\text{Abundance of double oxidized } X_3}{\begin{array}{l}\text{Abundance of isotopic m/z for a given}\\\text{oligosaccharideoxidized at the reducing end C-1}\end{array}} \times 100\% \qquad (7)\end{aligned}$$

$$\begin{aligned}&\text{Triple oxidation\%}\\&= \frac{\text{Abundance of triple oxidized } X_3}{\begin{array}{l}\text{Abundance of isotopic m/z for a given oligosaccharide}\\\text{oxidized at the reducing end C-1}\end{array}} \times 100\% \qquad (8)\end{aligned}$$

See **Figure S1** for example calculations.

RESULTS

Initial Rates of PDH Action on Xylooligosaccharides

The yield of recombinantly produced and purified AbPDH1 and AmPDH1 was 1.65 and 11.5 mg/l, respectively, where over 90% purity was reached for both enzymes (**Figure S2**). The activity and pH optima of each PDH was comparable to previous studies when using glucose as the substrate (**Table S1**). Activity on xylose and xylooligosaccharides was then measured using Fc+ ion as the electron acceptor, given the particular sensitivity of the corresponding assay (Sygmund et al., 2008). Both AbPDH1 and AmPDH1 were active on 10 mM X-X_4 and A^3X; furthermore, AbPDH1 was distinguished by its additional activity on A^2XX and XA^3XX under the conditions used (**Figure 1**).

Activity of both enzymes on xylose (43–45 U/mg; **Figure 1**) were similar to those previously reported for the native AmPDH1 (39 U/mg; Sygmund et al., 2008). Overall, AbPDH1 had higher activities toward X_3, X_4, and A^3X compared to corresponding activity of AmPDH1. Notably, the activity of AbPDH1 toward A^3X was comparable to unsubstituted X_2, and AbPDH1 activity toward A^2XX and XA^3XX was ∼40 and 55% of the corresponding unsubstituted X_3 and X_4 substrates. By contrast, the activity of AmPDH1 on A^3X was only 38% of its activity on X_2 and initial activity values could not be obtained for AmPDH1 oxidation of A^2XX or XA^3XX under these conditions. Similarly, initial activities were not obtained for AbPDH1 and AmPDH1 toward $U^{4m2}XX$ or $XU^{4m2}XX$; however, oxidation of all tested xylooligosaccharides by AbPDH1 and AmPDH1 was observed after reaction optimization and prolonged incubation time, as described below.

Measuring Xylooligosaccharide Conversion by AbPDH1 and AmPDH1

To maximize xylooligosaccharide oxidation by AmPDH1 and AbPDH1, the Fc+ electron acceptor used to measure initial rates was replaced with BQ that can be regenerated using laccase (Baminger et al., 2001). In an effort to optimize PDH and laccase activities, glucose and xylose oxidation by AmPDH1 and AbPDH1 was tested at pH values ranging from pH 3.0 to 7.0 (**Figure S3**). Based on these analyses, subsequent reactions were performed at pH 5.5. Notably, the addition of laccase clearly increased substrate conversions by both enzymes (**Figure S4**), where up to 85% depletion of xylose (50 mM starting concentration) was reached in 24 h using 5 mM BQ.

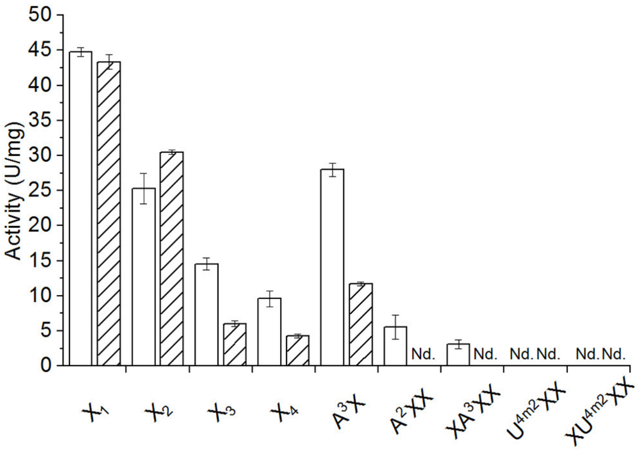

FIGURE 1 | Activity of AbPDH1 (white) and AmPDH1 (with diagonal stripes) on 10 mM of neutral or 2 mM of acidic xylooligosaccharides at pH 7.5 using Fc+ ion as electron acceptor. X_1, xylose; X_2, xylobiose; X_3, xylotriose; X_4, xylotetraose; A^3X, 3^2-α-L-arabinofuranosyl-xylobiose; A^2XX, 2^3-α-L-arabinofuranosyl-xylotriose; XA^2XX, 3^3-α-L-arabinofuranosyl-xylotetraose; $U^{4m2}XX$, 2^3-(4-*O*-methyl-α-D-glucuronyl)-xylotriose; $XU^{4m2}XX$, 2^3-(4-*O*-methyl-α-D-glucuronyl)-xylotetraose. Error bars represent standard deviation of three replicate reactions. Reactions with $U^{4m2}XX$ and $XU^{4m2}XX$ were done in duplicates. Nd., no activity detected under these conditions after 24 h.

Both AbPDH1 and AmPDH1 fully depleted X_2, X_3, and A^3X after 24 h; AbPDH1 also fully depleted X_4 after 24 h (**Figure 2**). With the exception of X_2, substrate depletion was more rapid in reactions containing AbPDH1 than AmPDH1 (**Figure 2**). Differences in substrate conversion were most apparent after 8 h, where X_3 and X_4 conversion by AbPDH1 was 1.2 and 3.9 times higher than by AmPDH1, respectively (**Figures 2B,C**).

When testing AbPDH1 and AmPDH1 activity over 24 h on A^3X, A^2XX, and XA^3XX, minor α-arabinofuranosidase activity was detected in the commercial laccase. Specifically, after 24 h in reactions containing laccase alone, 7.5, 11.5, and 20% of Ara*f* was hydrolyzed from A^3X, A^2XX, and XA^3XX, respectively (**Figures S5–S7**). This reduction of substrate by hydrolysis was taken into account by comparing the substrate depletion in PDH reactions to corresponding control reactions containing laccase alone. Whereas, both AbPDH1 and AmPDH1 were able to fully deplete A^3X by 8 h (**Figure 2D**), A^2XX conversion by AbPDH1 was 1.6 times higher than AmPDH1 after 24 h (**Figure 2E**), and both AbPDH1 and AmPDH1 transformed ∼60% of XA^3XX after 24 h (**Figure 2F**).

When using the same enzyme loading (0.2 U/ml) as for neutral xylooligosaccharides, only AbPDH1 showed clear conversion of both $U^{4m2}XX$ and $XU^{4m2}XX$ (**Figure S8**). Detectable conversion of $U^{4m2}XX$ and $XU^{4m2}XX$ by AmPDH1 was only observed after increasing the enzyme loading 10 times (to 2 U/ml). When comparing AbPDH1 and AmPDH1 after 24 h at the higher enzyme loading, AbPDH1 depleted nearly 100% of both $U^{4m2}XX$ and $XU^{4m2}XX$ whereas substrate depletion by AmPDH1 was ∼30 and 20% for $U^{4m2}XX$ and $XU^{4m2}XX$, respectively (**Figure S8**).

Direct Infusion ESI-Q-Tof Mass Spectrometry Confirms the Formation of Oxidized Xylooligosaccharides

Direct infusion ESI-Q-Tof analyses confirmed that all the tested substrates were oxidized by both AbPDH1 and AmPDH1. The C-1 oxidation products were negatively charged and detected in their anionic form, while neutral oligosaccharides were detected as chlorine adducts. X_2, X_3, X_4, A^3X, A^2XX, XA^3XX gave peaks at mass-to-charge ratios (*m/z*) 317, 449, 581, 449, 581, and 713, respectively (**Figures S9, S10**). Consistent with the HPAEC-PAD analyses summarized above, low levels of products with a loss of pentose (132 Da) were detected in reactions containing Ara*f* substituted xylooligosaccharides, resulting from α-arabinofuranosidase side activity in the commercial laccase preparation. $U^{4m2}XX$ and $XU^{4m2}XX$ were detected deprotonated $[M\text{-}H]^-$ with peaks at *m/z* 603 and 735, respectively (**Figure S11**).

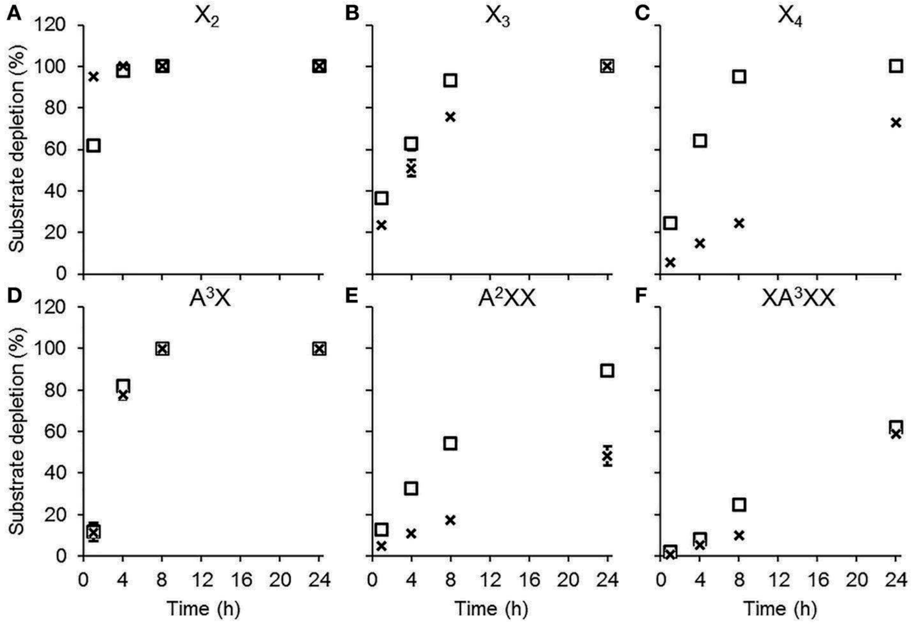

FIGURE 2 | Substrate depletion by AbPDH1 (square) and AmPDH1 (cross) followed by HPAEC-PAD. Substrates: **(A)** xylobiose, X_2, **(B)** xylotriose, X_3, **(C)** xylotetraose, X_4, **(D)** 3^2-α-L-arabinofuranosyl-xylobiose A^3X, **(E)** 2^3-α-L-arabinofuranosyl-xylotriose, A^2XX, and **(F)** 3^3-α-L-arabinofuranosyl-xylotetraose XA^3XX. Depletion of 5 mM substrate using 0.2 U/ml PDHs, 1 mM BQ and 0.2 U/ml laccase was compared to the control reaction containing all reaction components except PDH. Error bars show the data range of duplicate reactions. Error bars are not visible when the data range fits inside the drawn data point.

Both AbPDH1 and AmPDH1 completely consumed X_2 and X_3 after 24 h treatment. By contrast, varying amounts of residual substrate could be detected for X_4 and all substituted xylooligosaccharides. AbPDH1 and AmPDH1 treatment of X_2, A^3X, and XA^3XX resulted in similar MS spectra and thus end products; however, clear differences in product profiles were seen for the other tested substrates. For example, highest peaks following X_3 oxidation by AbPDH1 and AmPDH1 were at *m/z* 463 and 427, respectively; and highest peaks following X_4 oxidation were at *m/z* 595/597 and 561, respectively (**Figure S9**). Considering substituted xylooligosaccharides, a peak at *m/z* 597 represented the highest product peak from A^2XX following 24 h treatment with AbPDH1, whereas the most abundant peak after 24 h AmPDH1 treatment was the non-oxidized A^2XX (*m/z* 581; **Figure S10**). Consistent with the greater oxidation of neutral xylooligosaccharides by AbPDH1 compared to AmPDH1, the ESI-Q-Tof analyses confirmed significant oxidation of $U^{4m2}XX$ and $XU^{4m2}XX$ by the higher dose of AbPDH1, resulting in peaks at *m/z* 619 and 751, respectively. By contrast, AmPDH1 oxidized $U^{4m2}XX$ and $XU^{4m2}XX$ to a small percentage (**Figure S11**). Given the higher oxidation of neutral substrates by both enzymes, the corresponding products were analyzed in greater detail.

Qualitative Comparison of Oxidized Xylooligosaccharides Generated by AbPDH1 and AmPDH1

Due to the multiple potential oxidations and reactivity of the oxidized products in water, MS spectra interpretation is challenging. Taking the AbPDH1 oxidized X_3 as an example (**Figure S1C**), the main peak *m/z* 463 is expectedly representing a chlorine adduct of a double oxidized product with two carbonyl groups of which the other one has reacted with water to a hydrate (compound A in **Table S2**). Peak *m/z* 481 is presumably the chorine adduct of the same double oxidized product in which both carbonyls are in the hydrate form. The second most abundant peak *m/z* 427 is most probably the double oxidized product carrying carboxylic acid group at the reducing end C-1 and one carbonyl group (compound B in **Table S2**) whereas peak *m/z* 445 can represent the same product in a hydrate form. Mass to charge ratio of 445 can also represent a chlorine adduct of the original double oxidized product with two carbonyl groups. Thus, one compound that is oxidized at two secondary hydroxyls is shown as three peaks in the mass spectrum (compound A in **Table S2**).

To facilitate the interpretation of MS spectra, the oxidized products were treated with $NaBD_4$, and analyzed by ESI-MS after purification. Thus, a PDH oxidation at secondary hydroxyl resulting in a ketone is equivalent to one Dalton difference in mass after $NaBD_4$ reduction compared to substrate (**Figure 3A**). Instead, the oxidation at the reducing end C-1 forms a carboxyl group, which is resistant to $NaBD_4$ reduction (**Figure 3B**). Compared to the chloride adduct of $NaBD_4$ reduced substrate, the oxidation at reducing end C-1 will result in a deprotonated *m/z* peak that is 23 Da less. Therefore, by counting the Dalton difference between the reduced oxidation products and the reduced original substrates, the number of oxidations occurring in one molecule can be determined.

After $NaBD_4$ reduction, the predominant peak in mass spectra of oxidized X_2 by both PDHs was *m/z* 322, which is

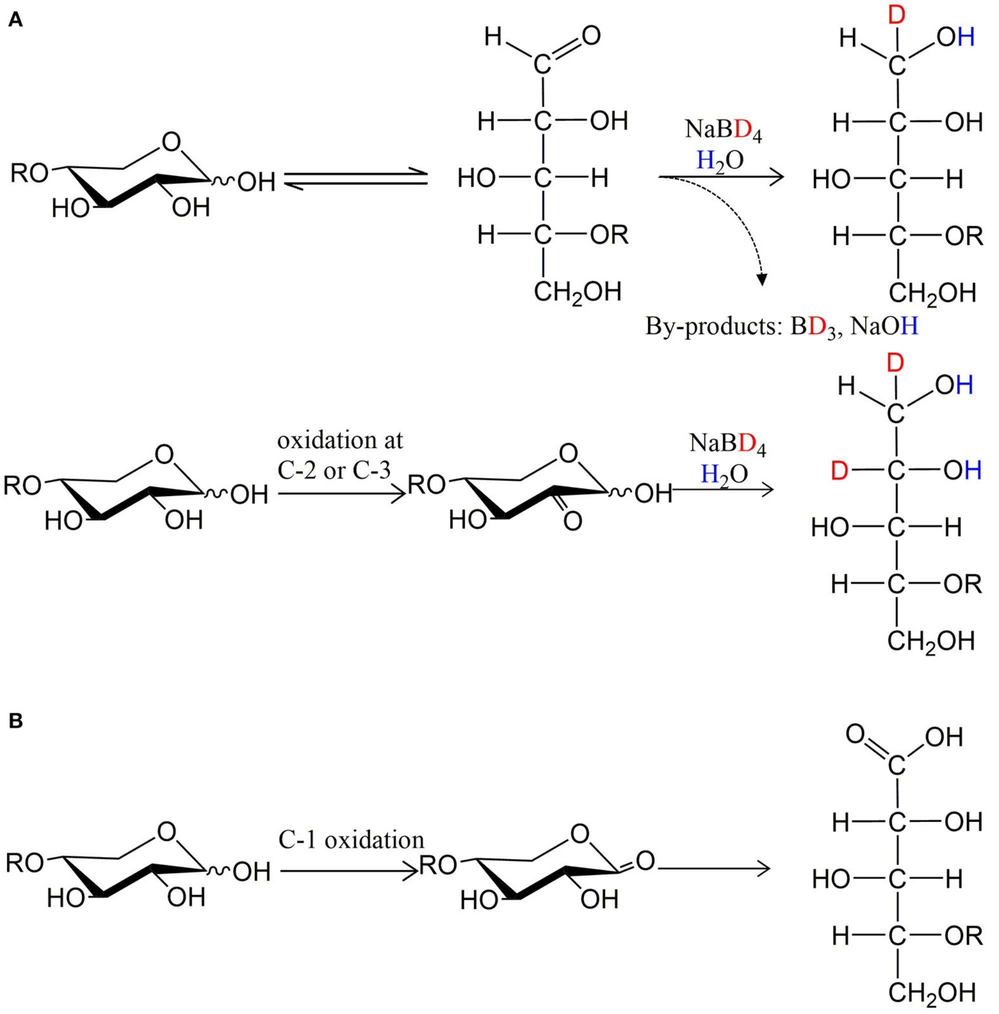

FIGURE 3 | The principle of isotopic labeling with $NaBD_4$ reduction. **(A)** One oxidation at secondary hydroxyls is equivalent to one Dalton difference in mass and **(B)** oxidation at C-1 hydroxyl is resistant to $NaBD_4$ reduction.

2 Da more than the control X_2 indicating double oxidation at two secondary hydroxyls (**Figure S12**). The 2 Da increase in mass was also seen for oxidized X_3. Oxidation of X_4 by both PDHs resulted in single and double oxidized products after 24 h reaction. Notably, Ara*f* substitution inhibited multiple oxidation of corresponding substrates; A^3X and A^2XX were mostly single oxidized at a secondary hydroxyl while the XA^3XX was still largely non-oxidized by both PDHs after 24 h reaction (**Figure S13**).

In addition to oxidizing secondary hydroxyls, both AbPDH1 and AmPDH1 oxidized the reducing end C-1 of all substrates. Moreover, mass spectra of X_2, $X_{3,}$ and X_4 products revealed that reducing end C-1 oxidation and secondary hydroxyl oxidations could co-exist in one molecule, resulting in final products with a mass that is 22 Da (reducing end C-1 oxidation + one secondary hydroxyl oxidation) or 21 Da (reducing end C-1 oxidation + two secondary hydroxyls oxidation) less than the control substrate (**Figure S12**).

Direct infusion mass spectrometry after $NaBD_4$ reduction thus confirmed the ability of both AbPDH1 and AmPDH1 to oxidize xylooligosaccharides at multiple positions. Quantification of the reaction products was subsequently important to uncover the specificity of each PDH.

Separate Quantification of Xylooligosaccharides Oxidized at Secondary Hydroxyl Positions and the Reducing End C-1

A two-stage MS-based approach was developed in this study to quantify single and multiply oxidized oligosaccharides, and as well as oxidations at secondary hydroxyls vs. the reducing end C-1 (section *Quantitative Interpretation of Mass Spectra*; see **Figure S1** for example calculation).

Product profiles were first calculated based on mass spectra, where different ionization intensities are obtained for neutral and acidic products, preventing the direct quantitative comparison of residual substrate products with ketone groups, and acidic products with reducing end C-1 oxidation. As a result, the extent of oxidized secondary hydroxyls and the reducing end C-1 were calculated separately (**Figure 4**). Overall, products with two ketones (i.e., oxidation of two secondary hydroxyls) were dominant for linear xylooligosaccharides. The only exception was AmPDH1 oxidation of X_4, which was only partially oxidized and mainly to a single oxidized product (**Figure 4A**). For all linear xylooligosaccharides treated for 24 h with AbPDH1, products oxidized at the reducing end C-1 were mostly also oxidized at a secondary hydroxyl group (i.e., were double oxidized products, **Figure 4B**). This same pattern was observed for AmPDH1 oxidation of X_3; however, a triple oxidized product (C-1 oxidation + two ketones) represented more than 50% of acidic products generated through AmPDH1 oxidization of X_2. Whereas, oxidation of linear xylooligosaccharides mostly led to double oxidized products, single oxidized products dominated in reactions containing Ara*f* substituted xylooligosaccharides (**Figures 4A,B**).

Total Comparative Quantification of Oxidized Xylooligosaccharides Generated by AbPDH1 and AmPDH1

Using hydrophilic interaction chromatography (HILIC), acidic and neutral reaction products were successfully separated and identified by MS (**Figures S14, S15**). The acidic products (C-1 oxidation) eluted earlier than the neutral ones and these two classes of products could be quantified after HILIC separation with on-line ELSD using external standards. The ELSD quantification was successfully done for X_3, X_4, A^3X, A^2XX, and XA^3XX products. Due to co-elution with salts, X_2 products could not be quantified. Six reaction species could be quantified: non-oxidized substrate, one oxidation at a secondary hydroxyl, two oxidations at secondary hydroxyls, one oxidation at the reducing end C-1, one oxidation at reducing end C-1 with one oxidation at secondary hydroxyl, and one oxidation at reducing end C-1 with two oxidations at secondary hydroxyls (**Figure 5**).

AbPDH1 and AmPDH1 primarily oxidized secondary hydroxyls, and to a lesser extent the anomeric C-1. The main, double oxidized derivative with two ketone groups represented 81 and 56% of X_3 products after 24 h treatment by AbPDH1 and AmPDH1, respectively (**Figure 5**). AbPDH1 also mainly oxidized X_4 at secondary hydroxyls with 38% being single ketone and 48% being double ketone products, whereas the most abundant reaction product after AmPDH1 treatment was C-1 oxidized X_4 (34%). Dominating A^3X products (73–78%) carried single ketone group whereas A^2XX was primary oxidized by AbPDH1 to one (50%) and two (21%) ketone derivatives. After AmPDH1 treatment, 48% of A^2XX remained non-oxidized and 39% of products carried single ketone group. The composition of reaction products from XA^3XX treatments by both PDHs was rather similar, with ~50% of substrates being non-oxidized after 24 h reaction; ~25% converted to products with one ketone group, and 22% were oxidized only at the reducing end C-1 (**Figure 5**).

MS Fragmentation to Determine the Oxidized Residues

The oxidized products after reduction were analyzed using Q-Tof or ion trap by following the deuterium label in the fragment ions. For example, the MS/MS spectrum of reduced X_2 shows the glycosidic linkage cleavage generating Y_1 ion containing the reduced Xyl*p* residues at *m/z* 152 (**Figure 6A**). The molecular masses of Y_1 ions carrying 1 Da more than the control sample (**Figures 6B,C**), indicate that one oxidation had taken place at the reducing Xyl*p* residue by both AbPDH1 and AmPDH1. The mass of precursor ions increased by 2 Da for oxidized samples, thus the other oxidation was at the non-reducing end Xyl*p* residue. The C-1 oxidized X_2 would have *m/z* 297 and generate the Y_1 ion at *m/z* 165 (data not shown). The *m/z* 298 ion produced the Y_1 ion also at *m/z* 165 (**Figure 6D**), suggesting one secondary hydroxyl oxidation took place at the non-reducing Xyl*p* moiety together with the oxidation at reducing end C-1. The Y_1 ion shown in **Figure 6E** increased by 1 Da compared to the compound shown in **Figure 6D**, indicating that AmPDH1 can even generate triple oxidized X_2 with a ketone group at the non-reducing Xyl*p* residue, a ketone at the reducing Xyl*p* residue, and a reducing end carboxylic acid.

Following the same procedure as described above for X_2, the oxidized positions for other linear xylooligosaccharides were determined (**Figure 5**; see example MS^n spectra in **Figures S16, S17**). Oxidation by both AbPDH1 and AmPDH1 was clearly restricted to the reducing and non-reducing Xyl*p* residues. Consistent with quantification using ELSD (section *Separate Quantification of Xylooligosaccharides Oxidized at Secondary Hydroxyl Positions and the Reducing End C-1*), the MS fragmentation confirmed that linear xylooligosaccharides were mostly multi-oxidized by both PDHs, with the exception of X_4 oxidation by AmPDH1 which was dominated by single oxidation. The MS fragmentation further revealed that the oxidation of X_4 by AmPDH1 was localized to the reducing end secondary hydroxyls or reducing end C-1. Surprising, whereas single oxidation of X_4 by both AbPDH1 and AmPDH1 was restricted to the reducing Xyl*p*, single oxidation of X_3 by both PDHs was mainly at the non-reducing end Xyl*p* secondary hydroxyls (**Figure 5**). Double oxidation by PDHs included products oxidized at (1) secondary hydroxyls of both the reducing and non-reducing Xyl*p,* or (2) the reducing C-1 position and a secondary hydroxyl at the non-reducing end. Increasing the length of the xylooligosaccharide to X_3 and X_4 did not lead to detectable oxidation of internal Xyl*p* substituents. Interestingly, in addition to the regioselectivity of single and double oxidations, a product of *m/z* 299 was detected in the AmPDH1 oxidized X_2 after reduction, representing products that were triple oxidized. In this case, it is conceivable that the reducing Xyl*p* is oxidized at both the reducing end C-1, and a secondary hydroxyl. This was the only detected triple oxidized product.

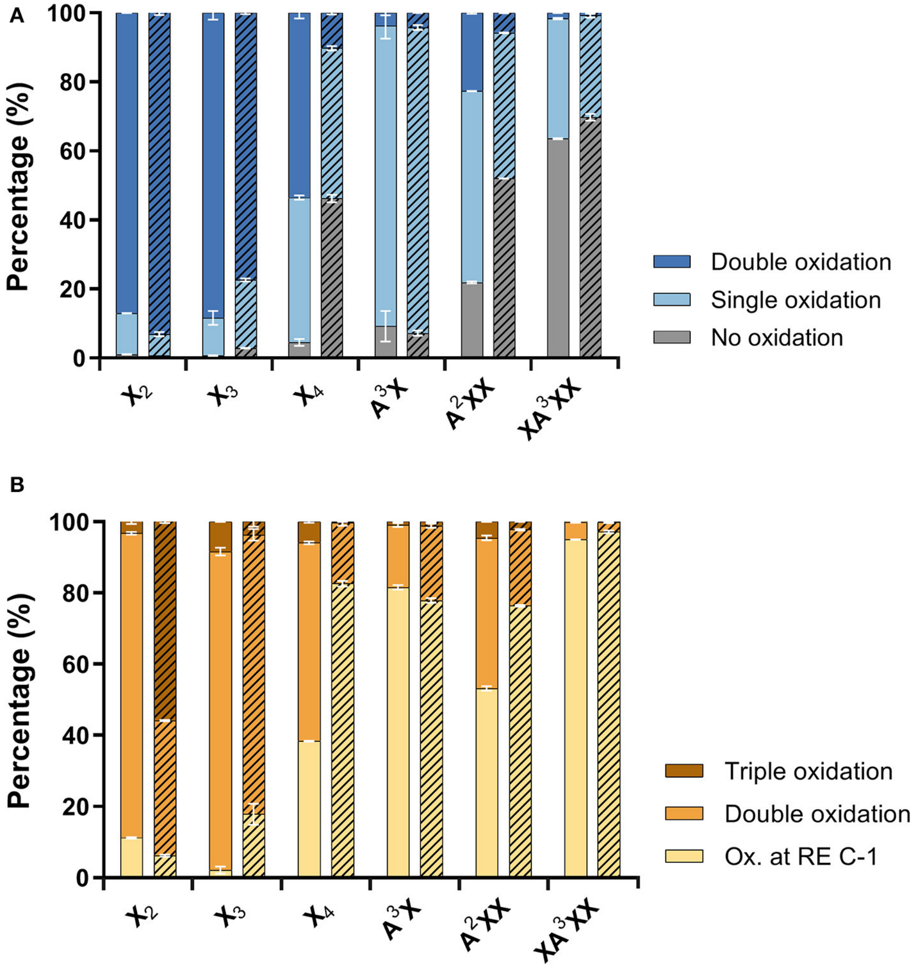

FIGURE 4 | Distribution of **(A)** neutral products (unreacted substrate and oxidations at secondary hydroxyls) and **(B)** acidic products (reducing end C-1 oxidation with zero, one or two secondary hydroxyls oxidations). Reactions with AbPDH1 are indicated by solid color and reactions with AmPDH1 are indicated by diagonal stripes.

The Ara*f* substituted substrates were mainly single oxidized or non-oxidized after 24 h treatment. A^3X containing α-(1→ 3)-linked Ara*f* substitution at the non-reducing end Xyl*p* residue, was single oxidized by both PDHs at the reducing end Xyl*p* resulting in a ketone group or C-1 oxidized carboxylic acid. A^2XX with α-(1→ 2)-linked Ara*f* substitution was similarly oxidized at the secondary hydroxyl or C-1 of the reducing end Xyl*p* by both PDHs. Interestingly, in some A^2XX products, a second ketone group was detected at the non-reducing end Xyl*p*, which carries the Ara*f* substituent. Moreover, AmPDH1 showed unique ability to form products with a single ketone group at the non-reducing end Xyl*p* of A^2XX. No clear oxidation of Ara*f* was detected in any of the samples.

DISCUSSION

AbPDH1 was first isolated over 20 years ago (Volc et al., 1997), and was followed nearly 10 years later by the isolation of AmPDH1 (Sedmera et al., 2006). Since then, AbPDH1 and AmPDH1 have been biochemically characterized using a broad collection of monosaccharides, heteroglycosides, and selected oligosaccharides, revealing their potential for single and double oxidation of many plant-derived carbohydrates, and motivating their application in biofuel cells and organic syntheses (Giffhorn et al., 2000; Peterbauer and Volc, 2010). Herein, AbPDH1 and AmPDH1 were directly compared in terms of potential to oxidize diverse xylooligosaccharides, both linear and branched, acid and neutral. In particular, we investigated the impact of xylooligosaccharide length and substitution on the extent and position of oxidation by each enzyme. In this way, we evaluated the potential of AbPDH1 and AmPDH1 to serve as catalysts in the synthesis of telechelic building blocks from xylan fragments common to wood and agricultural residues.

Consistent with reported AmPDH1 activity toward X_2 (Sygmund et al., 2008) and glucose-containing oligosaccharides (Volc et al., 1997; Tasca et al., 2007; Peterbauer and Volc, 2010; Rafighi et al., 2018) both AbPDH1 and AmPDH1 produced herein oxidized X_2 as well as X_3 and X_4. As observed for PDH activity toward cellooligosaccharides and maltooligosaccharides

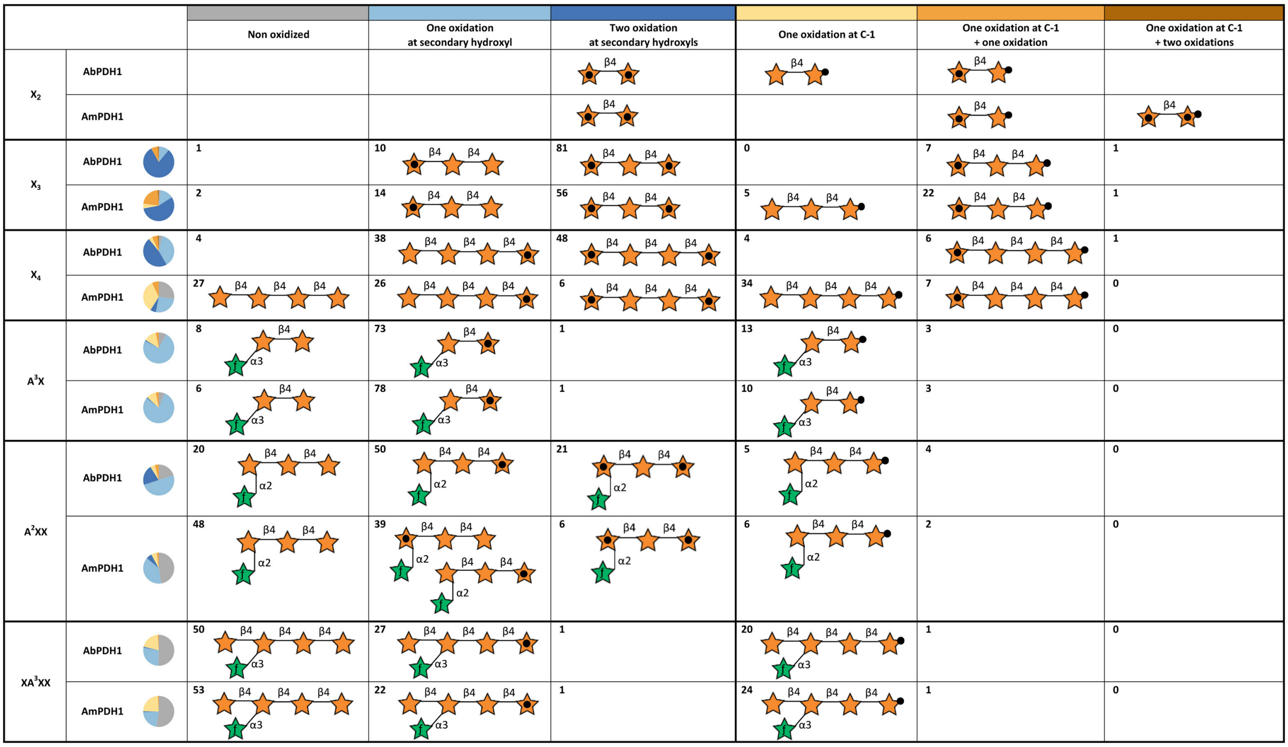

		Non oxidized	One oxidation at secondary hydroxyl	Two oxidation at secondary hydroxyls	One oxidation at C-1	One oxidation at C-1 + one oxidation	One oxidation at C-1 + two oxidations
X_2	AbPDH1						
	AmPDH1						
X_3	AbPDH1	1	10	81	0	7	1
	AmPDH1	2	14	56	5	22	1
X_4	AbPDH1	4	38	48	4	6	1
	AmPDH1	27	26	6	34	7	0
A^3X	AbPDH1	8	73	1	13	3	0
	AmPDH1	6	78	1	10	3	0
A^2XX	AbPDH1	20	50	21	5	4	0
	AmPDH1	48	39	6	6	2	0
XA^3XX	AbPDH1	50	27	1	20	1	0
	AmPDH1	53	22	1	24	1	0

FIGURE 5 | Summary of main oxidation products and oxidized positions following xylooligosaccharide treatment by AbPDH1 and AmPDH1. Representative product structures are drawn for those representings > 5% of the reaction mixture; the symbol nomenclature for glycans was adopted from Varki et al. (2015). A black dot in the center of a star represents a secondary hydroxyl oxidation, and a black dot at the tip of a star represents oxidation at the reducing end C-1. The proportion of each reaction product is shown by the number in each cell and summarized by the pie chart shown in each row.

(Kujawa et al., 2007; Sygmund et al., 2008; Peterbauer and Volc, 2010; Graf et al., 2017), the specific activity (U/mg) of both AbPDH1 and AmPDH1, as well as the rate of the substrate depletion detected with HPAEC-PAD, decreased with increasing degree of polymerization, where the impact of substrate length on activity was greater for AmPDH1 than for AbPDH1. Notably, AmPDH1 depleted X_2 faster than AbPDH1, which is in line with the previous studies, where AmPDH1 shows higher catalytic turnover toward disaccharides, cellobiose, maltose and lactose than AmPDH1 (Sygmund et al., 2008; Gonaus et al., 2016). However, the reverse pattern was observed for longer linear oligosaccharides; AbPDH1 activity toward substituted xylooligosaccharides was also substantially higher than that measured for AmPDH1. In both cases, however, activities toward A^3X were higher than X_3, and activities toward neutral substrates were higher than for the acidic xylooligosaccharides $U^{4m2}XX$ and $XU^{4m2}XX$. The structural basis for these differences in AbPDH1 and AmPDH1 activity toward oligosaccharides awaits a solved structure for AbPDH1 and of enzyme-substrate complexes for this enzyme family. Still, as found in Gonaus et al. (2016), a homology model of AbPDH1 based on the solved structure of AmPDH1 revealed two amino acid deletions in the loop 1 region, differences in the loop 3 region, and substitution of Phe508 in AmPDH1 to the smaller Val505 in AbPDH1. These differences vary the amino acid content in loop regions at the entrance of the substrate binding pocket, and could impact accessibility of the active site (Gonaus et al., 2016).

When considering the synthesis of telechelic molecules from xylooligosaccharides, it is especially important to evaluate the extent and positions of oxidation in each reaction product. To facilitate this analysis, we established an alternative method for the identification and quantification of oxidized carbohydrates, which utilizes $NaBD_4$ reduction and is solely based on MS and UPLC systems. This method enables fast quantification of formed carbonyl groups as the results are readily interpreted by counting the Dalton difference. In addition, the analysis can be accomplished with reaction products in microgram levels, allowing it to be an attractive technique for characterizing carbohydrate oxidoreductases where enzyme or substrate quantities are limiting. For example, even though specific activity values could not be obtained using the acidic xylooligosaccharides $U^{4m2}XX$ and $XU^{4m2}XX$, the near-complete oxidation of both substrates by AbPDH1 after 24 h was confirmed using this method. Given the higher activity of both AbPDH1 and AmPDH1 on neutral xylooligosaccharides, corresponding product profiles were quantified in more detail. Consistent with activity values, AbPDH1 reached a higher level of double oxidized end products from X_4 and A^2XX compared to AmPDH1. An exception was for X_2, where treatment with AmPDH1 led even to a triple-oxidized product. The ESI-MS^n analyses confirmed

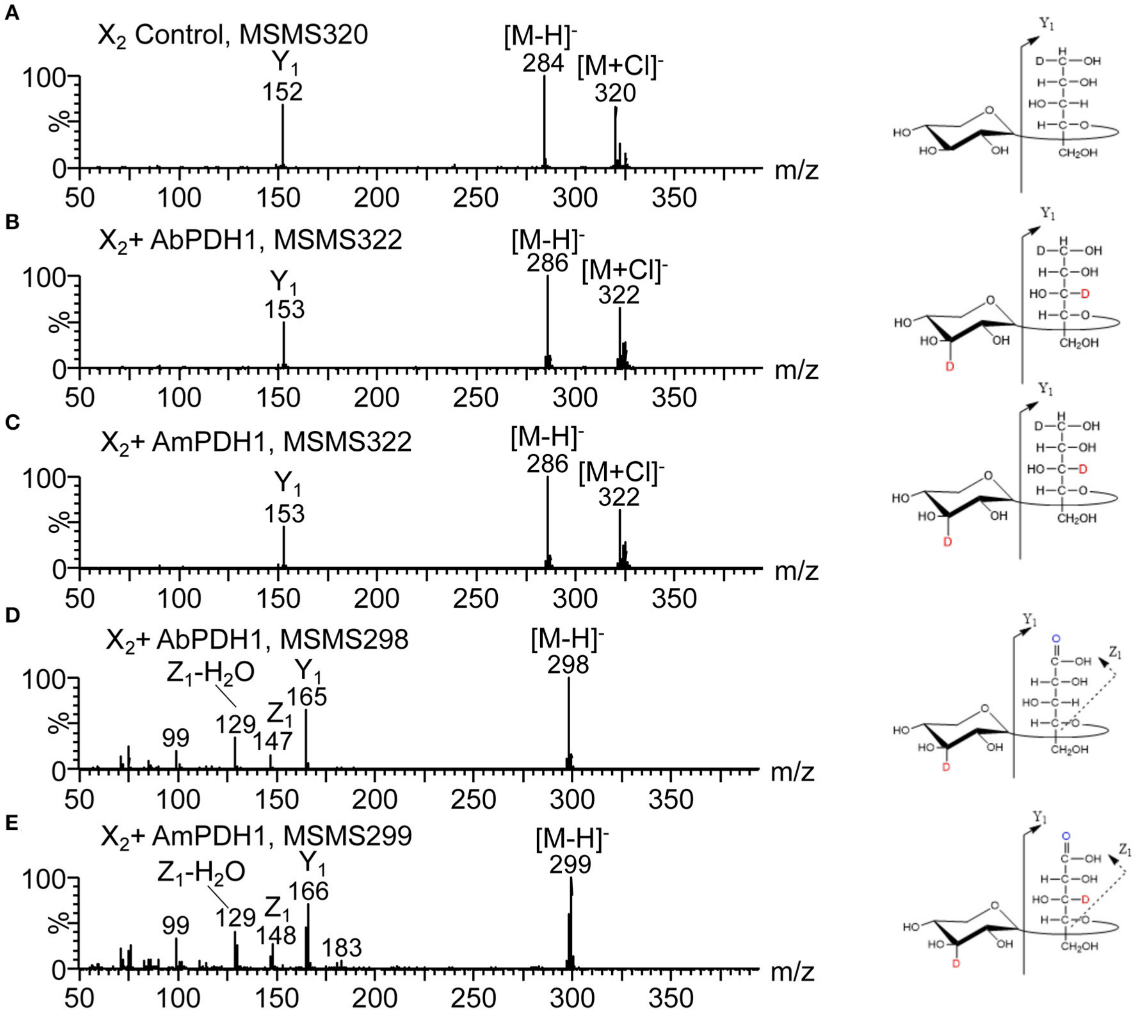

FIGURE 6 | HILIC-MS/MS spectra collected in negative ion mode showing fragmentation of X_2 after enzymatic oxidation by PDHs followed by $NaBD_4$ reduction. **(A)** Negative MS/MS 320 of the X_2 control, **(B)** negative MS/MS 322 of the X_2 oxidized by AbPDH1, **(C)** negative MS/MS 322 of the X_2 oxidized by AmPDH1, **(D)** negative MS/MS 298 of the X_2 oxidized by AbPDH1, **(E)** negative MS/MS 299 of the X_2 oxidized by AmPDH1. Product ions named according to Domon and Costello (1988). Oxidations at C-2, C-3, and C-4 are not distinguishable.

that oxidations were targeted to the reducing and non-reducing ends of all tested xylooligosaccharide substrates. Interestingly, yet unexplained, selectivity was noticed by both enzymes. For example, a single keto group was formed at the non-reducing Xyl*p* residue of X_3, whereas in X_4 a single keto group was found solely at the reducing end Xyl*p*. Also, AmPDH1 produced more C-1 oxidized acidic products from X_3 and X_4 than AbPDH1. As previously reported for activity toward cellobiose, maltose and lactose (Volc et al., 2004; Sygmund et al., 2012; Gonaus et al., 2016), AbPDH1 and AmPDH1 oxidized the anomeric carbon together with secondary hydroxyls of xylooligosaccharides.

Although cross-ring fragmentation was observed in some oxidation products (e.g., with C-1 oxidation), we were not able to identify which secondary hydroxyl was targeted by each enzyme due to proton transfer during the fragmentation (Domon and Costello, 1988). Nevertheless, as reported for glucose-containing oligosaccharides (Sedmera et al., 2006; Peterbauer and Volc, 2010; Rafighi et al., 2018), the context of the secondary hydroxyls at C-2 and C-3 positions clearly impacted AbPDH1 and AmPDH1 activity toward xylooligosaccharides. Most notably, the alpha-(1→ 3)-linked Ara*f* in A^3X and XA^3XX shifted AbPDH1 and AmPDH1 activity toward the reducing end of both substrates. By contrast, both the reducing and non-reducing ends of A^2XX were oxidized.

In summary, with the newly developed method to identify and quantify oxidized carbohydrates, we successfully determined the degree of oxidation and analyzed the regioselectivity of AbPDH1 and AmPDH1 toward xylooligosaccharides present in wood and agricultural fiber. The widened carbohydrate profile of AbPDH1 and AmPDH1 provides further support for their proposed biological function in evading plant defense mechanisms through reducing plant-derived quinones, or promoting lignin depolymerization through reducing lignin-derived radicals generated by lignin-active peroxidases and laccases (Peterbauer and Volc, 2010; Sützl et al., 2018; Herzog et al., 2019). Confirming herein that oxidative activity is restricted to the ends of xylooligosaccharides, and that both linear and substituted xylooligosaccharides are accepted, also opens new applications of PDHs that transform underused xylan streams into telechelic molecules primed for polymerization.

DATA AVAILABILITY STATEMENT

The datasets generated for this study are available on request to the corresponding author.

AUTHOR CONTRIBUTIONS

JK, HZ, AK, MT, and EM contributed conception and design of the study. JK, HZ, and AK performed the experiments. JK, HZ, S-LC, and AK analyzed the data. MT and EM contributed reagents, materials, and analysis tools. JK, HZ, MT, and EM wrote the paper. All authors read and approved the submitted version.

FUNDING

This work was conducted with the funding from Academy of Finland for COCOA (project codes 308996 and 308997).

ACKNOWLEDGMENTS

Dr. Thu Vuong and Dr. Sanna Koutaniemi are acknowledged for kindly providing acidic substrates for this study. Dr. Anne Usvalampi was acknowledged for the eminent technical support and expertise in HPAEC-PAD analyses.

SUPPLEMENTARY MATERIAL

The Supplementary Material for this article can be found online at: https://www.frontiersin.org/articles/10.3389/fchem.2020.00011/full#supplementary-material

REFERENCES

Andberg, M., Mollerup, F., Parikka, K., Koutaniemi, S., Boer, H., Juvonen, M., et al. (2017). A novel *Colletotrichum graminicola* raffinose oxidase in the AA5 family. *Appl. Environ. Microbiol.* 83, 1–17. doi: 10.1128/AEM.01383-17

Baminger, U., Ludwig, R., Galhaup, C., Leitner, C., Kulbe, K. D., and Haltrich, D. (2001). Continuous enzymatic regeneration of redox mediators used in biotransformation reactions employing flavoproteins. *J. Mol. Catal.* 11, 541–550. doi: 10.1016/S1381-1177(00)00034-5

Chundawat, S., Beckham, G. T., Himmel, M. E., and Dale, B. E. (2011). Deconstruction of lignocellulosic biomass to fuels and chemicals. *Annu. Rev. Chem. Biomol.* 2, 121–145. doi: 10.1146/annurev-chembioeng-061010-114205

Domon, B., and Costello, C. E. (1988). A systematic nomenclature for carbohydrate fragmentations in FAB-MS/MS spectra of glycoconjugates. *Glycoconj. J.* 5, 397–409. doi: 10.1007/BF01049915

Ebringerová, A. (2006). Structural diversity and application potential of hemicelluloses. *Macromol. Symp.* 232, 1–12. doi: 10.1002/masy.200551401

Giffhorn, F., Köpper, S., Huwig, A., and Freimund, S. (2000). Rare sugars and sugar-based synthons by chemo-enzymatic synthesis. *Enzyme Microb. Technol.* 27, 734–742. doi: 10.1016/S0141-0229(00)00293-3

Gonaus, C., Kittl, R., Sygmund, C., Haltrich, D., and Peterbauer, C. (2016). Transcription analysis of pyranose dehydrogenase from the basidiomycete *Agaricus bisporus* and characterization of the recombinantly expressed enzyme. *Protein Expr. Purif.* 119, 36–44. doi: 10.1016/j.pep.2015.11.003

Graf, M. M., Bren, U., Haltrich, D., and Oostenbrink, C. (2013). Molecular dynamics simulations give insight into d-glucose dioxidation at C2 and C3 by *Agaricus meleagris* pyranose dehydrogenase. *J. Comput. Aided Mol. Des.* 27, 295–304. doi: 10.1007/s10822-013-9645-7

Graf, M. M., Weber, S., Kracher, D., Kittl, R., Sygmund, C., Ludwig, R., et al. (2017). Characterization of three pyranose dehydrogenase isoforms from the litter-decomposing basidiomycete *Leucoagaricus meleagris* (syn. *Agaricus meleagris*). *Appl. Microbiol. Biotechnol.* 101, 2879–2891. doi: 10.1007/s00253-016-8051-1

Graf, M. M. H., Sucharitakul, J., Bren, U., Chu, D. B., Koellensperger, G., Hann, S., et al. (2015). Reaction of pyranose dehydrogenase from *Agaricus meleagris* with its carbohydrate substrates. *FEBS J.* 282, 4218–4241. doi: 10.1111/febs.13417

Herzog, P. L., Sützl, L., Eisenhut, B., Maresch, D., Haltrich, D., Obinger, C., et al. (2019). Versatile oxidase and dehydrogenase activities of bacterial pyranose 2-oxidase facilitate redox cycling with manganese peroxidase *in vitro*. *Appl. Environ. Microbiol.* 85, 1–15. doi: 10.1128/AEM.00390-19

Huang, C. H., Lai, W. L., Lee, M. H., Chen, C. J., Vasella, A., Tsai, Y. C., et al. (2005). Crystal structure of glucooligosaccharide oxidase from *Acremonium strictum*: a novel flavinylation of 6-S-cysteinyl, 8α-N1-histidyl FAD. *J. Biol. Chem.* 280, 38831–38838. doi: 10.1074/jbc.M506078200

Koutaniemi, S., Guillon, F., Tranquet, O., Bouchet, B., Tuomainen, P., Virkki, L., et al. (2012). Substituent-specific antibody against glucuronoxylan reveals close association of glucuronic acid and acetyl substituents and distinct labeling patterns in tree species. *Planta* 236, 739–751. doi: 10.1007/s00425-012-1653-7

Kujawa, M., Volc, J., Halada, P., Sedmera, P., Divne, C., Sygmund, C., et al. (2007). Properties of pyranose dehydrogenase purified from the litter-degrading fungus *Agaricus xanthoderma*. *FEBS J.* 274, 879–894. doi: 10.1111/j.1742-4658.2007.05634.x

Levasseur, A., Drula, E., Lombard, V., Coutinho, P. M., and Henrissat, B. (2013). Expansion of the enzymatic repertoire of the CAZy database to integrate auxiliary redox enzymes. *Biotechnol. Biofuels* 6:41. doi: 10.1186/1754-6834-6-41

Lombard, V., Golaconda Ramulu, H., Drula, E., Coutinho, P. M., and Henrissat, B. (2014). The carbohydrate-active enzymes database (CAZy) in 2013. *Nucleic Acids Res.* 42, D490–D495. doi: 10.1093/nar/gkt1178

MacCormick, B., Vuong, T. V., and Master, E. R. (2018). Chemo-enzymatic Synthesis of Clickable Xylo-oligosaccharide Monomers from Hardwood 4-O-Methylglucuronoxylan. *Biomacromolecules* 19, 521–530. doi: 10.1021/acs.biomac.7b01642

Parikka, K., Leppänen, A. S., Xu, C., Pitkänen, L., and Eronen, P., Österberg, M., et al. (2012). Functional and anionic cellulose-interacting polymers by selective chemo-enzymatic carboxylation of galactose-containing polysaccharides. *Biomacromolecules* 13, 2418–2428. doi: 10.1021/bm300679a

Peterbauer, C. K., and Volc, J. (2010). Pyranose dehydrogenases: biochemical features and perspectives of technological applications. *Appl. Microbiol. Biotechnol.* 85, 837–848. doi: 10.1007/s00253-009-2226-y

Rafighi, P., Bollella, P., Pankratova, G., Peterbauer, C. K., Conghaile, P. Ó., Leech, D., et al. (2018). Substrate preference pattern of *Agaricus meleagris* pyranose dehydrogenase evaluated through bioelectrochemical flow injection amperometry. *ChemElectroChem* 6, 801–809. doi: 10.1002/celc.201801194

Scheller, H. V., and Ulvskov, P. (2010). Hemicelluloses. *Annu. Rev. Plant Biol.* 61, 263–289. doi: 10.1146/annurev-arplant-042809-112315

Sedmera, P., Halada, P., Kubátová, E., Haltrich, D., Prikrylová, V., and Volc, J. (2006). New biotransformations of some reducing sugars to the corresponding (di)dehydro(glycosyl) aldoses or aldonic acids using fungal pyranose dehydrogenase. *J. Mol. Catal.* 41, 32–42. doi: 10.1016/j.molcatb.2006.04.004

Sützl, L., Laurent, C. V. F. P., Abrera, A. T., Schütz, G., Ludwig, R., and Haltrich, D. (2018). Multiplicity of enzymatic functions in the CAZy AA3 family. *Appl. Microbiol. Biotechnol.* 102, 2477–2492. doi: 10.1007/s00253-018-8784-0

Sygmund, C., Gutmann, A., Krondorfer, I., Kujawa, M., Glieder, A., Pscheidt, B., et al. (2012). Simple and efficient expression of *Agaricus meleagris* pyranose dehydrogenase in *Pichia pastoris*. *Appl. Microbiol. Biotechnol.* 94, 695–704. doi: 10.1007/s00253-011-3667-7

Sygmund, C., Kittl, R., Volc, J., Halada, P., Kubátová, E., Haltrich, D., et al. (2008). Characterization of pyranose dehydrogenase from *Agaricus meleagris* and its application in the C-2 specific conversion of D-galactose. *J. Biotechnol.* 133, 334–342. doi: 10.1016/j.jbiotec.2007.10.013

Tan, T. C., Spadiut, O., Wongnate, T., Sucharitakul, J., Krondorfer, I., Sygmund, C., et al. (2013). The 1.6 Å crystal structure of pyranose dehydrogenase from *Agaricus meleagris* rationalizes substrate specificity and reveals a flavin intermediate. *PLoS ONE* 8: e53567. doi: 10.1371/journal.pone.0053567

Tasca, F., Timur, S., Ludwig, R., Haltrich, D., Volc, J., Antiochia, R., et al. (2007). Amperometric biosensors for detection of sugars based on the electrical wiring of different pyranose oxidases and pyranose dehydrogenases with osmium redox polymer on graphite electrodes. *Electroanalysis* 19, 294–302. doi: 10.1002/elan.200603740

Varki, A., Cummings, R. D., Aebi, M., Packer, N. H., Seeberger, P. H., Esko, J. D., et al. (2015). Symbol nomenclature for graphical representations of glycans. *Glycobiology* 25, 1323–1324. doi: 10.1093/glycob/cwv091

Volc, J., Kubátová, E., Wood, D. A., and Daniel, G. (1997). Pyranose 2-dehydrogenase, a novel sugar oxidoreductase from the basidiomycete fungus *Agaricus bisporus*. *Arch. Microbiol.* 167, 119–125. doi: 10.1007/s002030050424

Volc, J., Sedmera, P., Halada, P., Daniel, G., Prikrylová, V., and Haltrich, D. (2002). C-3 oxidation of non-reducing sugars by a fungal pyranose dehydrogenase: spectral characterization. *J. Mol. Catal.* 17, 91–100. doi: 10.1016/S1381-1177(02)00014-0

Volc, J., Sedmera, P., Halada, P., Prikrylová, V., and Haltrich, D. (2000). Double oxidation of D-xylose to D-glycero-pentos-2,3-diulose (2,3-diketo-D-xylose) by pyranose dehydrogenase from the mushroom *Agaricus bisporus*. *Carbohydr. Res.* 329, 219–225. doi: 10.1016/S0008-6215(00)00167-1

Volc, J., Sedmera, P., Kujawa, M., Halada, P., Kubátová, E., and Haltrich, D. (2004). Conversion of lactose to β-D-galactopyranosyl-(1 → 4)-D-arabino-hexos-2-ulose-(2-dehydrolactose) and lactobiono-1,5-lactone by fungal pyranose dehydrogenase. *J. Mol. Catal.* 30, 177–184. doi: 10.1016/j.molcatb.2004.05.006

Vuong, T. V., Vesterinen, A. H., Foumani, M., Juvonen, M., Seppälä, J., Tenkanen, M., et al. (2013). Xylo- and cello-oligosaccharide oxidation by gluco-oligosaccharide oxidase from *Sarocladium strictum* and variants with reduced substrate inhibition. *Biotechnol. Biofuels* 6:148. doi: 10.1186/1754-6834-6-148

Conflict of Interest: The authors declare that the research was conducted in the absence of any commercial or financial relationships that could be construed as a potential conflict of interest.

Copyright © 2020 Karppi, Zhao, Chong, Koistinen, Tenkanen and Master. This is an open-access article distributed under the terms of the Creative Commons Attribution License (CC BY). The use, distribution or reproduction in other forums is permitted, provided the original author(s) and the copyright owner(s) are credited and that the original publication in this journal is cited, in accordance with accepted academic practice. No use, distribution or reproduction is permitted which does not comply with these terms.

Advantages of publishing in Frontiers

OPEN ACCESS
Articles are free to read
for greatest visibility
and readership

FAST PUBLICATION
Around 90 days
from submission
to decision

HIGH QUALITY PEER-REVIEW
Rigorous, collaborative,
and constructive
peer-review

TRANSPARENT PEER-REVIEW
Editors and reviewers
acknowledged by name
on published articles

Frontiers
Avenue du Tribunal-Fédéral 34
1005 Lausanne | Switzerland

Visit us: www.frontiersin.org
Contact us: info@frontiersin.org | +41 21 510 17 00

REPRODUCIBILITY OF RESEARCH
Support open data
and methods to enhance
research reproducibility

DIGITAL PUBLISHING
Articles designed
for optimal readership
across devices

FOLLOW US
@frontiersin

IMPACT METRICS
Advanced article metrics
track visibility across
digital media

EXTENSIVE PROMOTION
Marketing
and promotion
of impactful research

LOOP RESEARCH NETWORK
Our network
increases your
article's readership